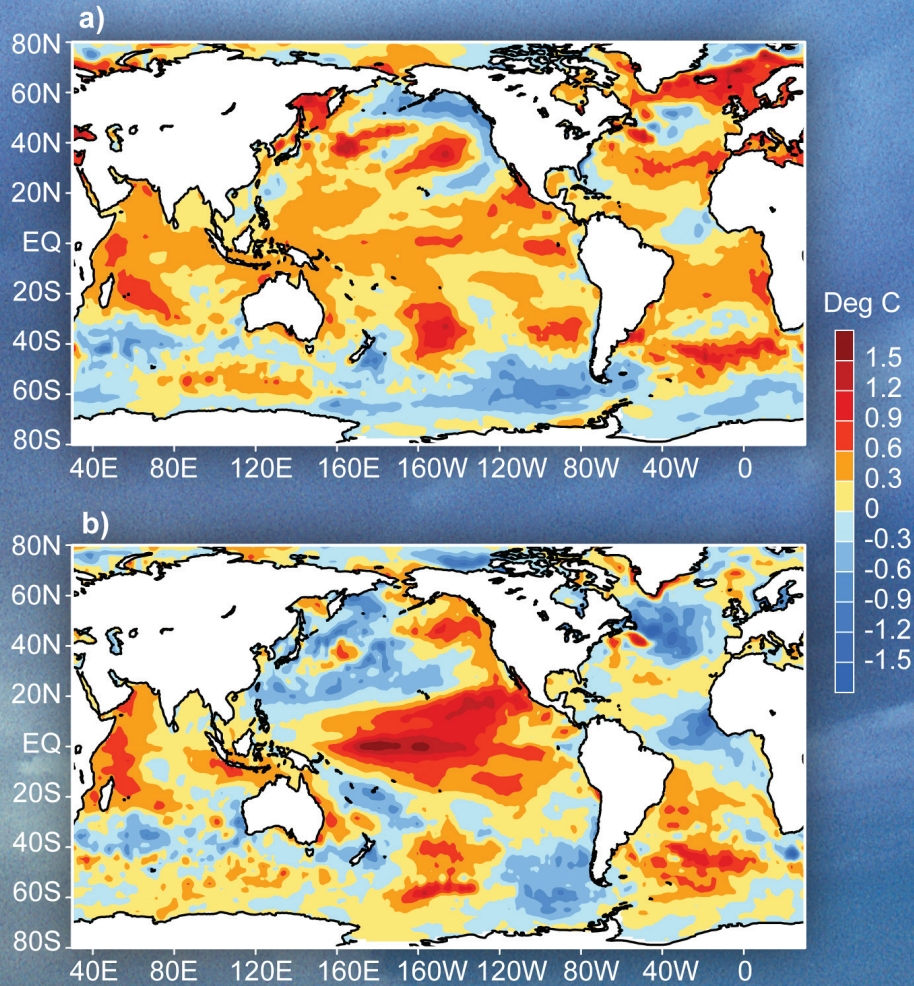# STATE OF THE CLIMATE IN 2009

D.S. Arndt, M.O. Baringer and M.R. Johnson, Eds.

Associate Eds. L.V. Alexander, H.J. Diamond, R.L. Fogt, J.M. Levy,
J. Richter-Menge, P.W. Thorne, L.A. Vincent, A.B. Watkins and K.M. Willett

(a) Yearly mean sea surface temperature anomalies (SSTA) in 2009 and (b) SSTA differences between 2009 and 2008. Anomalies are defined as departures from the 1971-2000 climatology. Refer to Chapter 3, Figure 3.1 for a more detailed description.

STATE of THE CLIMATE in 2009

HOW TO CITE THIS DOCUMENT

Citing the complete report:

Arndt, D. S., M. O. Baringer, and M. R. Johnson, Eds., 2010: State of the Climate in 2009. *Bull. Amer. Meteor. Soc.*, **91** (6), S1–S224.

Citing a chapter (example):

Diamond, H. J., Ed., 2010: The tropics [in "State of the Climate in 2009"]. *Bull. Amer. Meteor. Soc.*, **91** (6), S79–S106.

Citing a section (example):

Halpert, M., G. D. Bell, and M. L'Heureux, 2010: ENSO and the Tropical Pacific [in "State of the Climate in 2009"]. *Bull. Amer. Meteor. Soc.*, **91** (6), S79–S82.

EDITOR & AUTHOR AFFILIATIONS (ALPHABETICAL BY NAME)

EDITORS

Alexander, Lisa V., Climate Change Research Centre, University of New South Wales, Sydney, New South Wales, Australia

Arndt, Derek S., NOAA/NESDIS National Climatic Data Center, Asheville, North Carolina

Baringer, Molly O., NOAA/OAR Atlantic Oceanographic and Meteorological Laboratory, Physical Oceanography Division, Miami, Florida

Diamond, Howard J., NOAA/NESDIS National Climatic Data Center, Silver Spring, Maryland

Fogt, Ryan L., Department of Geography, Ohio University, Athens, Ohio

Johnson, Michael R., NOAA National Marine Fisheries Service, Gloucester, Massachusetts

Levy, Joel M., NOAA/OAR Climate Program Office, Silver Spring, Maryland

Richter-Menge, Jacqueline, US Army Corps of Engineers, ERDC-Cold Regions Research and Engineering Laboratory, Hanover, New Hampshire

Thorne, Peter W., Met Office Hadley Centre, Exeter, Devon, United Kingdom

Vincent, Lucie A., Environment Canada, Toronto, Canada

Watkins, Andrew B., National Climate Centre, Australian Bureau of Meteorology, Melbourne, Australia

Willett, Katharine M., Met Office Hadley Centre, Exeter, Devon, United Kingdom

AUTHORS

Aceituno, Patricio, Universidad de Chile, Santiago, Chile

Achberger, Christine, Earth Sciences Centre, University of Gothenburg, Gothernburg, Sweden

Ackerman, Steven A., CIMSS University of Wisconsin - Madison, Madison, Wisconsin

Aguilar, Enrique, University Rovira I Virgili de Tarragona, Tarragona, Spain

Ahmed, Farid H., Météo Nationale Comorienne, Comores

Alexander, Lisa V., Climate Change Research Centre, University of New South Wales, Sydney, New South Wales, Australia

Alfaro, Eric J., Center for Geophysical Research and School of Physics, University of Costa Rica, San Jose, Costa Rica

Allan, Robert J., Met Office Hadley Centre, Exeter, Devon, United Kingdom

Alves, Lincoln, Centro de Ciências do Sistema Terrestre (CCST), Instituto Nacional de Pesquisas Espaciais (INPE), São Paulo, Brazil

Amador, Jorge A., Center for Geophysical Research and School of Physics, University of Costa Rica, San Jose, Costa Rica

Ambenje, Peter, Kenya Meteorological Department, Nairobi, Kenya

Amelie,Vincent, Seychelles Meteorological Services, Seychelles

Antonov, John I., NOAA/NESDIS National Ocean Data Center, Silver Spring, Maryland

Ashik, Igor, Arctic and Antarctic Research Institute, St. Petersburg, Russia

Atheru, Zachary, IGAD Climate Prediction and Applications Centre, Nairobi, Kenya

Attaher, Samar M., Agricultural Research Center, MALR, Cairo, Egypt

Baez, Julian, DMH-DINAC / CTA-UCA, Asunción, Paraguay

Banda, Joyce, Zimbabwe Meteorological Service, Zimbabwe

Banzon, Viva, NOAA/NESDIS National Climatic Data Center, Asheville, North Carolina

Baringer, Molly O., NOAA/OAR Atlantic Oceanographic and Meteorological Laboratory, Physical Oceanography Division, Miami, Florida

Barreira, Sandra, Argentine Naval Hydrographic Service, Buenos Aires, Argentina

Barriopedro, David, Centro de Geofísica da Universidade de Lisboa, Lisbon, Portugal

Beal, Lisa M., Rosenstiel School of Marine and Atmospheric Science, Division of Meteorology and Physical Oceanography, Miami, Florida

Behrenfeld, Michael J., Oregon State University, Corvallis, Oregon

Bell, Gerald D., NOAA/NWS/NCEP Climate Prediction Center, Camp Springs, Maryland

Belward, Alan S., Global Environment Monitoring Unit, IES, EC Joint Research Centre, Ispra, Italy

Benedetti, Angela, European Centre for Medium-Range Weather Forecasts (ECMWF), Reading, United Kingdom

Beszczynska-Moeller, Agnieszka, Alfred Wegener Institute, Germany

Bhatt, Uma S., Geophysical Institute, University of Alaska Fairbanks, Fairbanks, Alaska

Bhattacharya, Indrajit, Byrd Polar Research Center and Department of Geography, The Ohio State University, Columbus, Ohio

Bidegain, Mario, Universidad de la República, Uruguay

Birkett, Charon, ESSIC, University of Maryland, College Park, Maryland

Bissolli, Peter, Deutscher Wetterdienst (German Meteorological Service, DWD), WMO RA VI Regional Climate Centre on Climate Monitoring, Offenbach, Germany

Blake, Eric S., NOAA/NWS/NCEP National Hurricane Center, Miami, Florida

Blunden, Jessica, STG, Inc., Asheville, North Carolina

Booneeady, Prithiviraj, Mauritius Meteorological Services, Vacoas, Mauritius

Bowling, Laura C., Department of Agronomy, Purdue University, West Lafayette, Indiana

Box, Jason E., Byrd Polar Research Center and Department of Geography, The Ohio State University, Columbus, Ohio

Boyer, Timothy P., NOAA/NESDIS National Ocean Data Center, Silver Spring, Maryland

Bromwich, David H., Byrd Polar Research Center, The Ohio State University, Columbus, Ohio

Brown, Ross, Climate Research Division, Environment Canada, Montréal, Quebec, Canada

Bryden, Harry L., Ocean Observing and Climate Research Group, National Oceanography Centre, Southampton, United Kingdom

Bulygina, Olga N., All-Russian Research Institute of Hydro-meteorological Information – World Data Center, Obninsk, Russia

Calderon, Blanca, Center for Geophysical Research, University of Costa Rica, San Jose, Costa Rica

Camargo, Suzana J., Lamont-Doherty Earth Observatory, The Earth Institute at Columbia University, Palisades, New York

Cappelen, John, Danish Meteorological Institute, Copenhagen, Denmark

Carmack, Eddy, Institute of Ocean Sciences, Sidney, Canada

Carrasco, Gualberto, Servicio Nacional de Meteorología e Hidrología de Bolivia (SENAMHI), La Paz, Bolivia

Carrión Romero, Ana M., Institute of Meteorology of Cuba, La Habana, Cuba

Christy, John R., Earth System Science Center, University of Alabama in Huntsville, Huntsville, Alabama

Coelho, Caio A. S., CPTEC/INPE, Center for Weather Forecasts and Climate Studies, Cachoeira Paulista, Brazil

Colwell, Steve, British Antarctic Survey, Cambridge, United Kingdom

Comiso, Josefino C., NASA Goddard Space Flight Center, Greenbelt, Maryland

Crouch, Jake, NOAA/NESDIS National Climatic Data Center, Asheville, North Carolina

Cunningham, Stuart A., Ocean Observing and Climate Research Group, National Oceanography Centre, Southampton, United Kingdom

Cutié Cancino, Virgen, Institute of Meteorology of Cuba, La Habana, Cuba

Davydova-Belitskaya, Valentina, National Meteorological Service of Mexico

Decker, David, Byrd Polar Research Center and Department of Geography, The Ohio State University, Columbus, Ohio

Derksen, Chris, Climate Research Division, Environment Canada, Downsview, Ontario, Canada

Diamond, Howard J., NOAA/NESDIS National Climatic Data Center, Silver Spring, Maryland

Dlugokencky, Ed J., NOAA Global Monitoring Division, Earth System Research Laboratory, Boulder, Colorado

Doelling, David R., NASA Langley Research Center, Hampton, Virginia

Dohan, Kathleen, Earth and Space Research, Seattle, Washington

Drozdov, Dmitry S., Earth Cryosphere Institute, Tumen, Russia

Dutton, Geoffrey S., NOAA Earth Science Research Laboratory/Cooperative Institute for Research in Environmental Sciences (CIRES), Boulder, Colorado

Elkins, James W., NOAA Earth Science Research Laboratory, Boulder, Colorado

Epstein, Howard E., Department of Environmental Sciences, University of Virginia, Charlottesville, Virginia

Feely, Richard A., NOAA/OAR Pacific Marine Environmental Laboratory, Seattle, Washington

Fekete, Balázs M., NOAA CREST Center, The City College of New York, New York, New York

Fenimore, Chris, NOAA/NESDIS National Climatic Data Center, Asheville, North Carolina

Fettweis, Xavier, Department of Geography, University of Liège, Belgium

Fogt, Ryan L., Department of Geography, Ohio University, Athens, Ohio

Fonseca-Rivera, Cecilia, Institute of Meteorology of Cuba, La Habana, Cuba

Foster, Michael J., AOS/CIMSS University of Wisconsin - Madison, Madison, Wisconsin

Free, Melissa, NOAA Air Resources Laboratory, Silver Spring, Maryland

Frolov, Ivan, Arctic and Antarctic Research Institute, St. Petersburg, Russia

Gibney, Ethan J., IMSG Inc., Asheville, North Carolina

Gill, Stephen, NOAA/NOS Center for Operational Oceanographic Products and Services, Silver Spring, Maryland

Gitau, Wilson, Department of Meteorology, University of Nairobi, Kenya

Gleason, Karin L., NOAA/NESDIS National Climatic Data Center, Asheville, North Carolina

Gobron, Nadine, Global Environment Monitoring Unit, IES, EC Joint Research Centre, Ispra, Italy

Goldammer, Johann G., Global Fire Monitoring Centre, Max Planck Institute for Chemistry, Freiburg University / United Nations University (UNU), Germany and European Centre for Medium-Range Weather Forecasts (ECMWF), Reading, United Kingdom

Goldenberg, Stanley B., NOAA/OAR Atlantic Oceanographic and Meteorological Laboratory, Miami, Florida

Goni, Gustavo, NOAA/OAR Atlantic Oceanographic and Meteorological Laboratory, Physical Oceanography Division, Miami, Florida

González García, Idelmis, Institute of Meteorology of Cuba, La Habana, Cuba

Good, Simon A., Met Office Hadley Centre, Exeter, Devon, United Kingdom

Gottschalck, Jonathan, NOAA/NWS/NCEP Climate Prediction Center, Camp Springs, Maryland

Gould, William A., USDA Forest Service, International Institute of Tropical Forestry, San Juan, Puerto Rico

Gouveia, Celia M., Centro de Geofísica da Universidade de Lisboa, Lisbon, Portugal

Griffiths, Georgina, National Institute of Water & Atmospheric Research Ltd., Auckland, New Zealand

Guard, Charles P., NOAA National Weather Service Forecast Office, Barrigada, Guam

Haimberger, Leopold, University of Vienna, Vienna, Austria

Haines, Keith, Reading University, Reading, United Kingdom

Halpert, Michael S., NOAA/NWS/NCEP Climate Prediction Center, Camp Springs, Maryland

Hassane, Ahmed Farid, Météo Nationale Comorienne, Comores

Heidinger, Andrew K., NOAA/NESDIS University of Wisconsin – Madison, Madison, Wisconsin

Heim, Richard R., Jr., NOAA/NESDIS National Climatic Data Center, Asheville, North Carolina

Henry, Greg H.R., Geography Department, University of British Columbia, Vancouver, British Columbia, Canada

Hidalgo, Hugo G., Center for Geophysical Research and School of Physics, University of Costa Rica, San Jose, Costa Rica

Hilburn, Kyle A., Remote Sensing Systems, Santa Rosa, California

Hirschi, Joël J.M., Ocean Observing and Climate Research Group, National Oceanography Centre, Southampton, United Kingdom

Ho, Shu-peng B., NCAR COSMIC, Boulder, Colorado

Hoerling, Martin P., NOAA/NESDIS Earth System Research Laboratory, Boulder, Colorado

Jaimes, Ena, Servicio Nacional de Meteorología e Hidrología de Perú, Lima, Perú

Jezek, Kenneth C., Byrd Polar Research Center, The Ohio State University, Columbus, Ohio

Jia, Gensu J., RCE-TEA, CAS, Chinese Academy of Sciences, Institute for Atmospheric Physics, Beijing, China

Johns, William E., Rosenstiel School of Marine and Atmospheric Science, Division of Meteorology and Physical Oceanography, Miami, Florida

Johnson, Bryan, NOAA Earth System Research Laboratory, Global Monitoring Division, and University of Colorado, Boulder, Colorado

Johnson, Gregory C., NOAA/OAR Pacific Marine Environmental Laboratory, Seattle, Washington

Jumaux, Guillaume, Météo-France, Réunion

Kabidi, Khadija, Direction de la Météorologie Nationale, Rabat, Morocco

Kaiser, Johannes W., European Centre for Medium-Range Weather Forecasts (ECMWF), Reading, United Kingdom

Kanzow, Torsten O., Ocean Observing and Climate Research Group, National Oceanography Centre, Southampton, United Kingdom

Keller, Linda M., Department of Atmospheric and Oceanic Sciences, University of Wisconsin-Madison, Madison, Wisconsin

Kennedy, John J., Met Office Hadley Centre, Exeter, Devon, United Kingdom

Khatiwala, Samar, Lamont-Doherty Earth Observatory, Columbia University, Palisades, New York

Kholodov, Alexander L., Geophysical Institute, University of Alaska – Fairbanks, Fairbanks, Alaska

Khoshkam, Mahbobeh, Islamic Republic of Iran Meteorological Organization, Tehran, Iran

Kimberlain, Todd B., NOAA/NWS/NCEP National Hurricane Center, Miami, Florida

Knaff, John A., NOAA/NESDIS Center for Satellite Applications and Research, Fort Collins, Colorado

Knorr, Wolfgang, Department of Earth Science, University of Bristol, Bristol, United Kingdom

Kokelj, Steve V., Water Resources Division, Indian and Northern Affairs Canada, Yellowknife, Northwest Territories, Canada

Korshunova, Natalia N., All-Russian Research Institute of Hydrometeorological Information – World Data Center, Obninsk, Russia

Kratz, David P., NASA Langley Research Center, Hampton, Virginia

Krishfield, Richard, Woods Hole Oceanographic Institution, Woods Hole, Massachusetts

Kruger, Andries, South African Weather Service, South Africa

Kruk, Michael C., STG Inc., Asheville, North Carolina

Kuo, Ying-Hwa, NCAR COSMIC, Boulder, Colorado

Kwok, Ron, Jet Propulsion Laboratory, Pasadena, California

L'Heureux, Michelle, NOAA/NWS/NCEP Climate Prediction Center, Camp Springs, Maryland

Lammers, Richard B., WSAG/CSRC Institute for the Study of Earth, Oceans, and Space, University of New Hampshire, Durham, New Hampshire

Lander, Mark A., Water and Environmental Research Institute, University of Guam, Mangilao, Guam

Landsea, Chris W., NOAA/NWS/NCEP National Hurricane Center, Miami, Florida

Lantz, Trevor C., School of Environmental Studies, University of Victoria, Victoria, British Columbia, Canada

Lapinel Pedroso, Braulio, Institute of Meteorology of Cuba, La Habana, Cuba

Lawford, Richard, Hydrological and Biospheric Sciences, NASA GSFC, Greenbelt, Maryland

Lawrimore, Jay H., NOAA/NESDIS National Climatic Data Center, Asheville, North Carolina

Lazzara, Matthew A., Space Science and Engineering Center, University of Wisconsin-Madison, Madison, Wisconsin

León, Gloria, Instituto de Hidrología de Meteorología y Estudios Ambientales de Colombia (IDEAM), Bogotá, Colombia

León Lee, Antonia, Institute of Meteorology of Cuba, La Habana, Cuba

Leuliette, Eric, NOAA/NESDIS Laboratory for Satellite Altimetry, Silver Spring, Maryland

Levinson, David H., NOAA/NESDIS National Climatic Data Center, Asheville, North Carolina

Levitus, Sydney, NOAA/NESDIS National Ocean Data Center, Silver Spring, Maryland

Levy, Joel M., NOAA/OAR Climate Program Office, Silver Spring, Maryland

Lin, I.-I., Department of Atmospheric Sciences, National Taiwan University, Taipei, Taiwan

Liu, Hongxing, Department of Geography, University of Cincinnati, Cincinnati, Ohio

Loeb, Norman G., NASA Langley Research Center, Hampton, Virginia

Long, Craig S., NOAA National Center for Environmental Prediction, Camp Springs, Maryland

Lorrey, Andrew M., National Institute of Water and Atmospheric Research, Ltd., Auckland, New Zealand

Lumpkin, Rick, NOAA/OAR Atlantic Oceanographic and Meteorological Laboratory, Physical Oceanography Division, Miami, Florida

Luo, Jing-Jia, Research Institute for Global Change, JAMSTEC, Yokohama, Japan

Lyman, John M., NOAA/OAR Pacific Marine Environmental Laboratory, Seattle, Washington and Joint Institute for Marine and Atmospheric Research, University of Hawaii, Honolulu, Hawaii

Macdonald, Alison M., Woods Hole Oceanographic Institution, Woods Hole, Massachussets

Maddux, Brent C., AOS/CIMSS University of Wisconsin - Madison, Madison, Wisconsin

Malkova, Galina, Earth Cryosphere Institute, Tumen, Russia

Marchenko, Sergey S., Geophysical Institute, University of Alaska – Fairbanks, Fairbanks, Alaska

Marengo, Jose A., Centro de Ciências do Sistema Terrestre (CCST), Instituto Nacional de Pesquisas Espaciais (INPE), São Paulo, Brazil

Maritorena, Stephane, University of California at Santa Barbara, Santa Barbara, California

Marotzke, Jochem, Max-Planck-Institut für Meteorologie, Hamburg, Germany

Martínez, Rodney, Centro Internacional para la Investigación del Fenómeno El Niño (CIIFEN), Guayaquil, Ecuador

Mascarenhas, Affonso, Centro Internacional para la Investigación del Fenómeno El Niño (CIIFEN), Guayaquil, Ecuador

Massom, Robert A., Australian Antarctic Division and Antarctic Climate and Ecosystems Cooperative Research Center (ACE CRC), University of Tasmania, Sandy Bay, Tasmania, Australia

McBride, Charlotte, South African Weather Service, Pretoria, South Africa

McGree, Simon, National Climate Centre, Australian Bureau of Meteorology, Melbourne, Victoria, Australia

McLaughlin, Fiona, Institute of Ocean Sciences, Sidney, Canada

Mears, Carl A., Remote Sensing Systems, Santa Rosa, California

Medany, Mahmoud A., Agricultural Research Center, MALR, Cairo, Egypt

Meier, Walt, CIRES/NSIDC, University of Colorado, Boulder, Colorado

Meinen, Christopher S., NOAA/OAR Atlantic Oceanographic and Meteorological Laboratory, Physical Oceanography Division, Miami, Florida

Menne, Matthew J., NOAA/NESDIS National Climatic Data Center, Asheville, North Carolina

Mercado-Díaz, Joel A., USDA Forest Service, International Institute of Tropical Forestry, San Juan, Puerto Rico

Merrifield, Mark A., University of Hawaii at Manoa, Honolulu, Hawaii

Mhanda, Albert S., Climate Change Office, Harare, Zimbabwe

Miller, Laury, NOAA/NESDIS Laboratory for Satellite Altimetry, Silver Spring, Maryland

Mitchum, Gary T., College of Marine Science, University of South Florida, St. Petersburg, Florida

Montfraix, Brice, Commission de l'Océan Indien (Projet AC-CLIMATE), Quatre-Bornes, Maurice

Montzka, Steve A., NOAA Global Monitoring Division, Earth System Research Laboratory, Boulder, Colorado

Morcrette, Jean-Jacques, European Centre for Medium-Range Weather Forecasts (ECMWF), Reading, United Kingdom

Morison, James, Polar Science Center, University of Washington, Seattle, Washington

Mote, Thomas, Department of Geography, University of Georgia, Athens, Georgia

Mullan, A. Brett, National Institute of Water and Atmospheric Research, Ltd., Wellington, New Zealand

Na, Hyun-Jong, Climate Prediction Division, Korea Meteorological Administration, Soel, Korea

Nash, Eric R., Science Systems and Applications, Inc., NASA Goddard Space Flight Center, Greenbelt, Maryland

Nerem, Steven R., University of Colorado, Boulder, Colorado

Newman, Paul A., Laboratory for Atmospheres, NASA Goddard Space Flight Center, Greenbelt, Maryland

Nghiem, Son, Jet Propulsion Laboratory, Pasadena, California

Nguyen, Louis C., NASA Langley Research Center, Hampton, Virginia

Njau, Leonard, African Centre of Meteorological Applications for Development (ACMAD), Niamey, Niger

O'Malley, Robert T., Oregon State University, Corvallis, Oregon

Oberman, Naum G., MIREKO, Syktivkar, Russia

Obregón, Andre, Laboratory for Climatology and Remote Sensing (LCRS), Department of Geography, University of Marburg, Germany

Ogallo, Laban, IGAD Climate Prediction and Applications Centre, Nairobi, Kenya

Oludhe, Christopher, Department of Meteorology, University of Nairobi, Kenya

Osawa, Kazuhiro, Climate Prediction Division, Japan Meteorological Agency, Tokyo, Japan

Overland, James, NOAA Pacific Marine Environmental Laboratory, Seattle, Washington

Palmer, Matthew D., Met Office Hadley Centre, Exeter, Devon, United Kingdom

Park, Geun-Ha, NOAA/OAR Atlantic Oceanographic and Meteorological Laboratory, Ocean Chemistry Division, Miami, Florida

Parker, David E., Met Office, FitzRoy Road, Exeter, Devon, United Kingdom

Pasch, Richard J., NOAA/NWS/NCEP National Hurricane Center, Miami, Florida

Peltier, Alexandre, Meteo-France, New Caledonia, Wallis and Futuna Service, Climatology Division, Noumea

Pelto, Mauri S., Nichols College, Dudley, Massachusetts

Penalba, Olga, Departamento de Ciencias de la Atmósfera y los Océanos, Universidad de Buenos Aires, Argentina

Pérez-Suarez, Ramón, Institute of Meteorology of Cuba, La Habana, Cuba

Perovich, Donald, ERDC-Cold Regions Research and Engineering Laboratory, Hanover, New Hampshire

Peterson, Thomas C., NOAA/NESDIS National Climatic Data Center, Asheville, North Carolina

Pezza, Alexandre B., The University of Melbourne, Melbourne, Victoria, Australia

Phillips, David, Environment Canada, Toronto, Canada

Pinty, Bernard, Monitoring Unit, IES, EC Joint Research Centre, Ispra, Italy (Seconded to the Earth Observation Directorate, ESA-ESRIN, Frascati, Italy)

Pinzon, Jorge E., NASA Goddard Space Flight Center, Greenbelt, Maryland

Pitts, Michael C., NASA Langley Research Center, Hampton, Virginia

Polyakov, Igor, International Arctic Research Center, Fairbanks, Alaska

Proshutinsky, Andrey, Woods Hole Oceanographic Institution, Woods Hole, Massachusetts

Quintana, Juan, Dirección Meteorológica de Chile, Santiago, Chile

Quintero, Alexander, Servicio de Meteorología de l'Aviación (SEMETAVIA), Venezuela

Rachid, Sebbari, Direction de la Météorologie Nationale, Rabat, Morocco

Rahimzadeh, Fatemeh, Atmospheric Science and Meteorological Research Center, Tehran, Iran

Rajeevan, Madhavan, National Atmospheric Research Laboratory, Tirupati, India

Randel, William, Atmospheric Chemistry Division, NCAR, Boulder, Colorado

Randriamarolaza, Luc Y.A., Service Météorologique de Madagascar, Madagascar

Rayner, Darren, Ocean Observing and Climate Research Group, National Oceanography Centre, Southampton, United Kingdom

Raynolds, Martha K., Institute of Arctic Biology, University of Alaska Fairbanks, Fairbanks, Alaska

Razuvaev, Vyacheslav N., All-Russian Research Institute of Hydrological Information, Obninsk, Russia

Reid, Phillip, Australian Bureau of Meteorology and ACE CRC, University of Tasmania, Sandy Bay, Tasmania, Australia

Renwick, James, National Institute of Water and Atmospheric Research, Ltd., Wellington, New Zealand

Revadekar, Jayashree, Indian Institute of Tropical Meteorology, Pune, India

Reynolds, Richard W., NOAA Cooperative Institute for Climate and Satellites, Asheville, North Carolina

Richter-Menge, Jacqueline, US Army Corps of Engineers, ERDC-Cold Regions Research and Engineering Laboratory, Hanover, New Hampshire

Rivera, Erick R., Center for Geophysical Research, University of Costa Rica, San Jose, Costa Rica

Robinson, David A., Rutgers University, Piscataway, New Jersey

Rogers, Mark, Joint Operational Meteorology and Oceanography Centre, Met Office, Exeter, United Kingdom

Romanovsky, Vladimir, Geophysical Institute, University of Alaska – Fairbanks, Fairbanks, Alaska

Romero-Cruz, Fernando, National Meteorological Service of Mexico, Mexico City, Mexico

Ronchail, Josyane, Université of Paris, France

Rossi, Shawn, National Weather Service, San Juan, Puerto Rico

Ruedy, Reto A., Sigma Space Partners LLC, NASA Goddard Institute for Space Studies, New York, New York

Sabine, Christopher L., NOAA/OAR Pacific Marine Environmental Laboratory, Seattle, Washington

Saindou, Madjidi, Météo National Comorienne, Comores

Santee, Michelle L., NASA Jet Propulsion Laboratory, Pasadena, California

Sayouri, Amal, Direction de la Météorologie Nationale, Rabat, Morocco

Schemm, Jae, NOAA/NWS/NCEP Climate Prediction Center, Camp Springs, Maryland

Schnell, Russ C., NOAA Global Monitoring Division, Earth System Research Laboratory, Boulder, Colorado

Schreiner, William, NCAR COSMIC, Boulder, Colorado

Schueller, Dominique, Météo-France, Réunion

Sensoy, Serhat, Turkish State Meteorological Service, Kalaba, Ankara, Turkey

Sharp, Martin, University of Alberta, Department of Earth and Atmospheric Sciences

Shaver, Gus R., Ecosystem Center, Marine Biological Laboratory, Woods Hole, Massachusetts

Shiklomanov, Alexander, University of New Hampshire, Durham, New Hampshire

Shimada, Koji, Institute of Observational Research for Global Change, Japan Agency for Marine-Earth Science and Technology, Yokosuka, Japan

Siegel, David A., University of California at Santa Barbara, Santa Barbara, California

Skansi, Maria, Servicio Meteorológico Nacional, Argentina

Sokolov, Vladimir, Arctic and Antarctic Research Institute, St. Petersburg, Russia

Solonomenjanahary, Andrianjafinirina, Service Météorologique de Madagascar, Madagascar

Spence, Jacqueline M., Meteorological Service of Jamaica, Kingston, Jamaica

Srivastava, Arvind Kumar, National Climate Centre, India Meteorological Department, Pune, India

Stackhouse, Paul W., Jr., NASA Langley Research Center, Hampton, Virginia

Stammerjohn, Sharon, University of California Santa Cruz, Santa Cruz, California

Steele, Mike, Polar Science Center, University of Washington, Seattle, Washington

Steinbrecht, Wolfgang, Met. Obs. Hohenpeissenberg, German Weather Service (DWD), Germany

Stephenson, Tannecia S., University of the West Indies, Mona, Jamaica

Stott, Peter A., Met Office Hadley Centre, Exeter, Devon, United Kingdom

Tahani, Lloyd, Solomon Islands Meteorological Service, Honiara, Solomon Islands

Takahashi, Taro, Lamont-Doherty Earth Observatory, Columbia University, Palisades, New York

Taylor, Michael A., University of the West Indies, Mona, Jamaica

Tedesco, Marco, Department Earth and Atmospheric Sciences, City College of New York, New York

Thiaw, Wassila M., NOAA/NWS/NCEP Climate Prediction Center, Camp Springs, Maryland

Thorne, Peter W., Met Office Hadley Centre, Exeter, Devon, United Kingdom

Timmermans, Mary-Louise, Yale University, New Haven, Connecticut

Titchner, Holly A., Met Office Hadley Centre, Exeter, Devon, United Kingdom

Toole, John, Woods Hole Oceanographic Institution, Woods Hole, Massachusetts

Trewin, Blair C., National Climate Centre, Australian Bureau of Meteorology, Melbourne, Victoria, Australia

Trigo, Ricardo M., Centro de Geofísica da Universidade de Lisboa, Lisbon, Portugal

Tucker, Compton J., NASA Goddard Space Flight Center, Greenbelt, Maryland

Tweedie, Craig E., Department of Biology, The University of Texas at El Paso, El Paso, Texas

Vincent, Lucie A., Environment Canada, Toronto, Canada

Virasami, Renganaden, Mauritius Meteorological Services, Vacoas, Mauritius

Walker, David A., Institute of Arctic Biology, University of Alaska Fairbanks, Fairbanks, Alaska

Walsh, John, International Arctic Research Center, Fairbanks, Alaska

Wang, Junhong, Earth Observation Laboratory, NCAR, Boulder, Colorado

Wang, Lei, Department of Geography and Anthropology, Louisiana State University, Baton Rouge, Louisiana

Wang, Libo, Climate Research Division, Environment Canada, Downsview, Ontario, Canada

Wang, Muyin, Joint Institute for the Study of the Atmosphere and Ocean, University of Washington, Seattle, Washington

Wang, Sheng-Hung, Byrd Polar Research Center, The Ohio State University, Columbus, Ohio

Wanninkhof, Rik, NOAA/OAR Atlantic Oceanographic and Meteorological Laboratory, Ocean Chemistry Division, Miami, Florida

Watkins, Andrew B., National Climate Centre, Australian Bureau of Meteorology, Melbourne, Australia

Webber, Patrick J., Department of Plant Biology, Michigan State University, East Lansing, Michigan

Weber, Mark, Institute of Environmental Physics, University of Bremen, Bremen, Germany

Weller, Robert A., Woods Hole Oceanographic Institution, Woods Hole, Massachusetts

Weyman, James, NOAA/NWS Central Pacific Hurricane Center, Honolulu, Hawaii

Whitewood, Robert, Environment Canada, Toronto, Canada

Wilber, Anne C., Science Systems Applications, Inc., Hampton, Virginia

Willett, Katharine M., Met Office Hadley Centre, Exeter, Devon, United Kingdom

Willis, Joshua K., NASA Jet Propulsion Laboratory, California Institute of Technology, Pasadena, California

Wolken, Gabriel, Alaska Division of Geological & Geophysical Surveys, Fairbanks, Alaska

Wong, Takmeng, NASA Langley Research Center, Hampton, Virginia

Woodgate, Rebecca, Polar Science Center, University of Washington, Seattle, Washington

Woodworth, Philip L., Proudman Oceanographic Laboratory, Liverpool, United Kingdom

Xue, Yan, NOAA/NWS Climate Prediction Center, National Centers for Environmental Prediction, Camp Springs, Maryland

Yu, Lisan, Woods Hole Oceanographic Institution, Woods Hole, Massachusetts

Zhang, Liangying, Earth Observation Laboratory, National Center for Atmospheric Research, Boulder, Colorado

Zhang, Peiqun, National Climate Centre, China Meteorological Administration, Beijing, China

Zhou, Xinjia, NCAR COSMIC, Boulder, Colorado

Zhu, YanFeng, National Climate Centre, China Meteorological Administration, Beijing, China

TABLE OF CONTENTS

ABSTRACT—M. O. BARINGER, D. S. ARNDT, AND M. R. JOHNSON

The year was characterized by a transition from a waning La Niña to a strengthening El Niño, which first developed in June. By December, SSTs were more than 2.0°C above average over large parts of the central and eastern equatorial Pacific. Eastward surface current anomalies, associated with the El Niño, were strong across the equatorial Pacific, reaching values similar to the 2002 El Niño during November and December 2009. The transition from La Niña to El Niño strongly influenced anomalies in many climate conditions, ranging from reduced Atlantic basin hurricane activity to large scale surface and tropospheric warmth.

Global average surface and lower-troposphere temperatures during the last three decades have been progressively warmer than all earlier decades, and the 2000s (2000–09) was the warmest decade in the instrumental record. This warming has been particularly apparent in the mid- and high-latitude regions of the Northern Hemisphere and includes decadal records in New Zealand, Australia, Canada, Europe, and the Arctic. The stratosphere continued a long cooling trend, except in the Arctic.

Atmospheric greenhouse gas concentrations continued to rise, with CO_2 increasing at a rate above the 1978 to 2008 average. The global ocean CO_2 uptake flux for 2008, the most recent year for which analyzed data are available, is estimated to have been 1.23 Pg C yr^{-1}, which is 0.25 Pg C yr^{-1} smaller than the long-term average and the lowest estimated ocean uptake in the last 27 years. At the same time, the total global ocean inventory of anthropogenic carbon stored in the ocean interior as of 2008 suggests an uptake and storage of anthropogenic CO_2 at rates of 2.0 and 2.3 ±0.6 Pg C yr^{-1} for the decades of the 1990s and 2000s, respectively. Total-column ozone concentrations are still well below pre-1980 levels but have seen a recent reduction in the rate of decline while upper-stratospheric ozone showed continued signs of ongoing slow recovery in 2009. Ozone-depleting gas concentrations continued to decline although some halogens such as hydrochlorofluorocarbons are increasing globally. The 2009 Antarctic ozone hole was comparable in size to recent previous ozone holes, while still much larger than those observed before 1990. Due to large interannual variability, it is unclear yet whether the ozone hole has begun a slow recovery process.

Global integrals of upper-ocean heat content for the last several years have reached values consistently higher than for all prior times in the record, demonstrating the dominant role of the oceans in the planet's energy budget.

Aside from the El Niño development in the tropical Pacific and warming in the tropical Indian Ocean, the Pacific Decadal Oscillation (PDO) transitioned to a positive phase during the fall/winter 2009. Ocean heat fluxes contributed to SST anomalies in some regions (e.g., in the North Atlantic and tropical Indian Oceans) while dampening existing SST anomalies in other regions (e.g., the tropical and extratropical Pacific). The downward trend in global chlorophyll observed since 1999 continued through 2009, with current chlorophyll stocks in the central stratified oceans now approaching record lows since 1997.

Extreme warmth was experienced across large areas of South America, southern Asia, Australia, and New Zealand. Australia had its second warmest year on record. India experienced its warmest year on record; Alaska had its second warmest July on record, behind 2004; and New Zealand had its warmest August since records began 155 years ago. Severe cold snaps were reported in the UK, China, and the Russian Federation. Drought affected large parts of southern North America, the Caribbean, South America, and Asia. China suffered its worst drought in five decades. India had a record dry June associated with the reduced monsoon. Heavy rainfall and floods impacted Canada, the United States, the Amazonia and southern South America, many countries along the east and west coasts of Africa, and the UK. The U.S. experienced its wettest October in 115 years and Turkey received its heaviest rainfall over a 48-hr period in 80 years.

Sea level variations during 2009 were strongly affected by the transition from La Niña to El Niño conditions, especially in the tropical Indo-Pacific. Globally, variations about the long-term trend also appear to have been influenced by ENSO, with a slight reduction in global mean sea level during the 2007/08 La Niña event and a return to the long-term trend, and perhaps slightly higher values, during the latter part of 2009 and the current El Niño event. Unusually low Florida Current transports were observed in May and June and were linked to high sea level and coastal flooding along the east coast of the United States in the summer. Sea level significantly decreased along the Siberian coast through a combination of wind, ocean circulation, and steric effects. Cloud and moisture increased in the tropical Pacific. The surface of the western equatorial Pacific freshened considerably from 2008 to 2009, at least partially owing to anomalous eastward advection of fresh surface water along the equator during this latest El Niño. Outside the more variable tropics, the surface salinity anomalies associated with evaporation and

precipitation areas persisted, consistent with an enhanced hydrological cycle.

Global tropical cyclone (TC) activity was the lowest since 2005, with six of the seven main hurricane basins (the exception is the Eastern North Pacific) experiencing near-normal or somewhat below-normal TC activity. Despite the relatively mild year for overall hurricane activity, several storms were particularly noteworthy: Typhoon Morakot was the deadliest typhoon on record to hit Taiwan; Cyclone Hamish was the most intense cyclone off Queensland since 1918; and the state of Hawaii experienced its first TC since 1992.

The summer minimum ice extent in the Arctic was the third-lowest recorded since 1979. The 2008/09 boreal snow cover season marked a continuation of relatively shorter snow seasons, due primarily to an early disappearance of snow cover in spring. Preliminary data indicate a high probability that 2009 will be the 19th consecutive year that glaciers have lost mass. Below normal precipitation led the 34 widest marine terminating glaciers in Greenland to lose 101 km^2 ice area in 2009, within an annual loss rate of 106 km^2 over the past decade. Observations show a general increase in permafrost temperatures during the last several decades in Alaska, northwest Canada, Siberia, and Northern Europe. Changes in the timing of tundra green-up and senescence are also occurring, with earlier green-up in the High Arctic and a shift to a longer green season in fall in the Low Arctic.

The Antarctic Peninsula continues to warm at a rate five times larger than the global mean warming. Associated with the regional warming, there was significant ice loss along the Antarctic Peninsula in the last decade. Antarctic sea ice extent was near normal to modestly above normal for the majority of 2009, with marked regional contrasts within the record. The 2008/09 Antarctic-wide austral summer snowmelt was the lowest in the 30-year history.

This 20th annual *State of the Climate* report highlights the climate conditions that characterized 2009, including notable extreme events. In total, 37 Essential Climate Variables are reported to more completely characterize the *State of the Climate* in 2009.

I. INTRODUCTION—M. O. Baringer and D. S. Arndt

The primary goal of the annual *State of the Climate* collection of articles is to document the weather and climate events in 2009 from around the world and put them into accurate historical perspective, with a particular focus on unusual or anomalous events. The year also marks the end of the first decade of the 21st century, so whenever possible the climate anomalies over this decade are highlighted.

This year the *State of the Climate* report brings together more than 300 authors from every continent and from over 160 different research groups to collaborate, share data and insights, and describe the observed changes in climate from different perspectives. The 2009 El Niño and the global consequences described herein highlight the global scope of connections between weather, climate, and, one could argue, climate scientists. In keeping with the increasingly global perspective of this report, the authors and editors seek to provide an inclusive synthesis of diverse weather and climate data to describe what took place across our planet last year. For example, recognizing the importance of providing error statistics, differing analysis products and datasets are included where possible (e.g., see sidebar on ocean heat content analyses in Chapter 3). We expect this trend to continue in future reports. Notably, the document's editors represented three disciplinary backgrounds (meteorology, oceanography, and biology). This composition reflects the increasing recognition that the natural world is embedded within, impacted by, and exerts influence on the physical climate system. We expect these connections to be explored in future issues of *State of the Climate*.

As a guiding principle behind the inclusion of certain climatic events into this report, the Global Climate Observing System has identified Essential Climate Variables (ECVs, see GCOS 2003) (see appendix for a full list of abbreviations) necessary to support the United Nations Framework Convention on Climate Change and the Intergovernmental Panel on Climate Change. These variables are defined as those required for international exchange and should be economically and technically feasible to acquire (Table 1.1). The *State of the Climate* report has evolved to include an increasing number of these climatically important variables as data availability increases and the analysis techniques and attributions improve. The degree to which each of these ECVs can be assessed and reported depends largely on the level of data availability both currently and as a homogeneous historical record and, hence, can be divided into cat-

egories: (1) being monitored, (2) partially monitored, and (3) not yet monitored. To be listed as monitored, the ECV not only must be observed across much of the world, but also needs a moderately long-term dataset with accompanying analysis. Also the dataset needs to be updated in near-real time and have a peer-reviewed article documenting the reliability of all of these steps. This year land cover/use is not reported because the data are only updated every five years and last year's report covers the most recent data available. Lake levels, biomass, and fire disturbance ECVs were included—at least partially-monitored—for the first time this year (see Chapter 2). Other variables important for research purposes are not included as ECVs, however the GCOS list of ECVs as well as the variables presented in this report are continually reassessed as improved observing technologies emerge. Continual advancement of the number of ECVs reported herein will not be possible without increasing international efforts to make the observations of the underlying variables and provide access to these data.

A brief overview of the findings in this report is presented in the Abstract and shown in Fig. 1.1. The remainder of the report is organized starting with global scale climate variables in Chapter 2, into increasingly divided geographic regions described in chapters 3 through 7. Chapter 3 highlights the global ocean and Chapter 4 includes tropical climate phenomena such as El Niño and hurricanes. The Arctic and Antarctic respond differently through time and hence are reported in separate chapters. For a regional perspective authored largely by local government climate specialists, see Chapter 7. Seasonal patterns are encapsulated in Chapter 8.
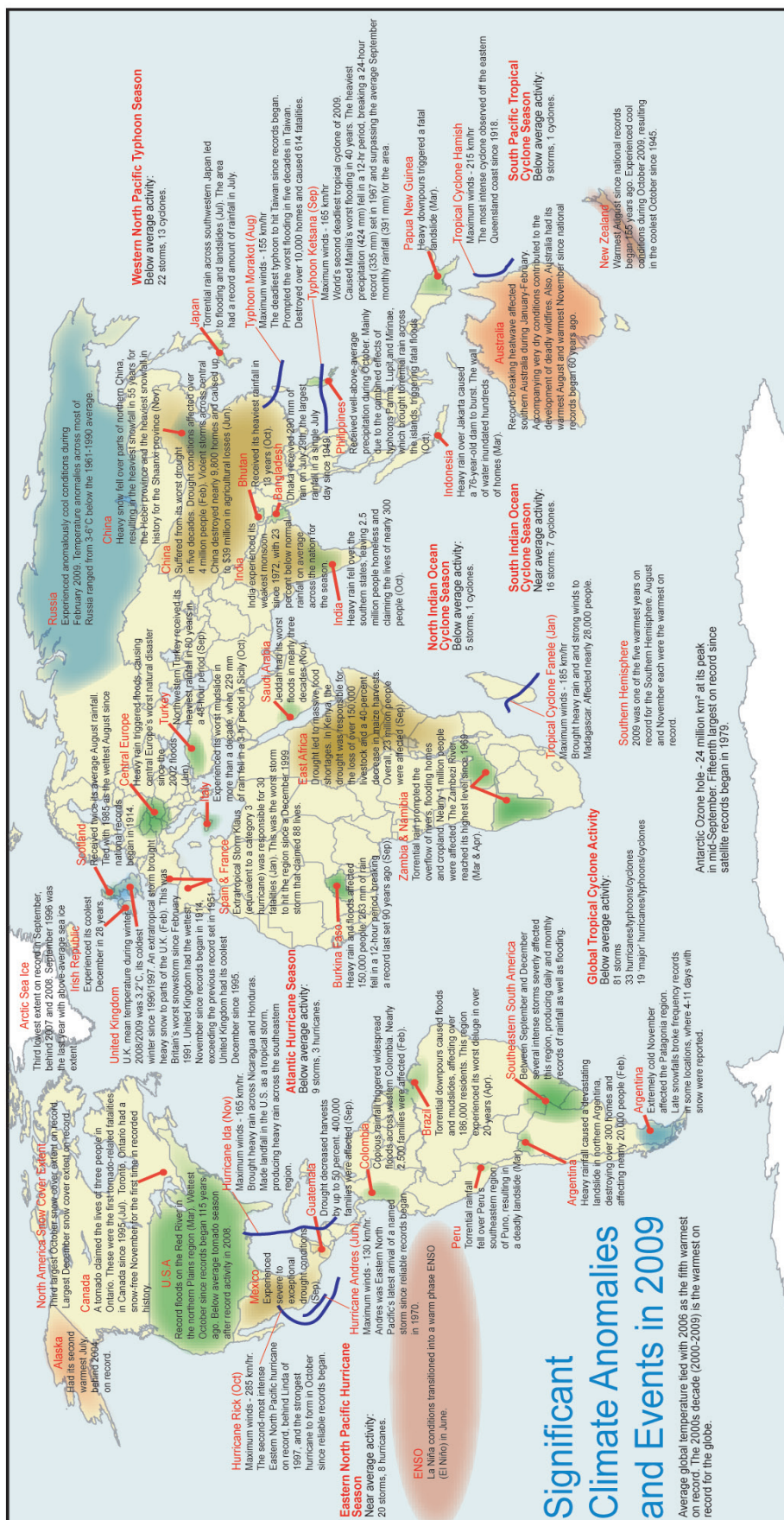
FIG. 1.1. Geographical distribution of notable climate anomalies and events occurring around the planet in 2009.

TABLE 1.1 The GCOS Essential Climate Variables (ECVs, see GCOS 2003) and their monitoring status, as reported in this and recent editions of the *State of the Climate*, are listed with the following color coding: Green indicates this ECV is being monitored on a global or near-global scale and that this report includes a section describing its changes over time; Yellow indicates the ECV is explicitly discussed in this year's *State of the Climate*, but the data are not updated globally through the year or a dataset has not yet been adequately documented in the peer-reviewed literature to prove it is an accurate indication of how this ECV has changed over time; Red indicates more work needs to be done in order to monitor this ECV. The missing ECVs in 2007 reflect the evolution and expansion of the GCOS list.

Essential Climate Variable	2007	2008	2009
Atmospheric Surface			
Air temperature	Y	Y	Y
Precipitation	Y	Y	Y
Air pressure	N	Y	Y
Surface radiation budget	N	N	N
Wind speed and direction	P	P	P
Water vapor	N	N	N
Atmospheric Upper-Air			
Earth radiation budget (including solar irradiance)	P	Y	Y
Upper-air temperature (including MSU radiances)	Y	Y	Y
Wind speed and direction	N	N	N
Water vapor	N	Y	Y
Cloud properties	P	Y	Y
Atmospheric Composition			
Carbon dioxide	Y	Y	Y
Methane	Y	Y	Y
Ozone	Y	Y	Y
[Other long-lived greenhouse gases]:	N	N	P
Nitrous oxide	Y	Y	Y
Chlorofluorocarbons	Y	Y	Y
Hydrochlorofluorocarbons	Y	Y	Y
Hydrofluorocarbons	Y	Y	Y
Sulphur hexaflurorides	Y	Y	Y
Perfluorocarbons	N	N	N
Aerosol properties.	Y	Y	Y
Ocean Surface			
Sea surface temperature	Y	Y	Y
Sea surface salinity	Y	Y	Y
Sea level	Y	Y	Y
Sea state	N	N	N
Sea ice	Y	Y	Y
Current	Y	Y	Y
Ocean color (for biological activity)	Y	Y	Y
Carbon dioxide partial pressure	P	P	P

Essential Climate Variable	2007	2008	2009
Ocean Subsurface			
Temperature	Y	Y	Y
Salinity	N	N	N
Current	P	P	P
Nutrients	N	N	N
Carbon	Y	P	P
Ocean tracers	N	N	N
Phytoplankton	N	N	N
Terrestrial			
Soil moisture and wetness	P	P	P
Surface ground temperature	N	N	N
Subsurface temperature and moisture	N	N	N
Snow and ice cover	Y	Y	Y
Permafrost	P	P	P
Glaciers and ice sheets	Y	P	P
River discharge		P	P
Water use		N	N
Ground water		N	N
Lake levels		N	Y
Albedo		N	N
Land cover (including vegetation type)[1]		P	N[1]
Fraction of absorbed photosynthetically active radiation (fAPAR)		Y	Y
Leaf area index (LAI)		N	N
Biomass		N	P
Fire disturbance		N	P

[1] The land cover data set used in the *State of the Climate* in 2008 (Di Gregorio and Jansen 2000) is updated once per five years.

2. GLOBAL CLIMATE—K. M. Willett, L. V. Alexander, and P. W. Thorne, Eds.

a. Summary—L. V. Alexander

In 2009, a transition from La Niña to El Niño dominated anomalies in many climate variables from the surface to the lower stratosphere. Averaged over the year, there was large-scale surface and tropospheric warmth and stratospheric coolness, except in the Arctic where positive annual anomalies were dominated by the largest stratospheric warming in January in the 50-year record (Plate 2.1). The ENSO transition, which occurred during the boreal summer, contributed to 2009 being ranked in the top 10 warmest years globally, about 0.1°C warmer than 2008. Global average surface temperatures during the last three decades have been progressively warmer than all earlier decades, making 2000-09 (the 2000s) the warmest decade in the instrumental record. The 2000s were also the warmest decade on record in the lower troposphere, being about 0.6°C warmer than the 1960s and 0.2°C warmer than the 1990s. The decadal warming has been particularly apparent in the mid- and high-latitude regions of the Northern Hemisphere. This chapter also includes a sidebar on the veracity of and supporting evidence for the surface temperature records following much recent discussion in the popular media. Globally averaged surface temperature anomalies are shown to be robust given the close agreement between independently-derived datasets and strong corroborative evidence across a wide range of other climate variables.

Cloud and moisture increased in the tropical Pacific although there was no distinctive ENSO signature in annual surface pressure, owing to the cancelling effect of the shift from La Niña to El Niño. Preliminary data indicate a high probability that 2009 will be the 19th consecutive year that glaciers have lost mass. Precipitation anomalies were variable but most marked was a drying over the tropical Atlantic coincident with the position of ITCZ. Greenhouse gas concentrations continued to rise in 2009, with CO_2 increasing at a rate above the 1978 to 2008 average. Ozone-depleting gas concentrations continued to decline although some halogens such as hydrochlorofluorocarbons are increasing globally. Total-column ozone concentrations are still well below pre-1980 levels but have seen a recent reduction in the rate of decline, while upper stratospheric ozone has shown continued signs of ongoing slow recovery in 2009.

This year's global chapter incorporates additional climate variables over previous years. There is not a section on land cover because there are limited annual updates to this variable. Land cover will be included in future summaries as updates become available. Advances and improvements in technology have enhanced our ability to monitor the Earth's climate using methods such as Global Positioning System Radio Occultation (see sidebar), which can be used to measure multiple meteorological parameters. Also included this year are lake levels (a proxy for precipitation changes over a catchment basin) and biomass burning (a proxy for land cover change and fire disturbance). In addition, for the first time, data from a reanalysis product have been included. This was possible through substantial recent improvements in reanalysis products. There is exciting potential to use analyses from these observing systems and combined products to enhance future global summaries.

Publicly available datasets used in this chapter are included in Table 2.1

b. Temperatures

1) Introduction of reanalysis data—P. W. Thorne

This year for the first time there are fields from a reanalysis product within the global chapter. Reanalyses consist of modern day data assimilation schemes fed with all available historical observations. They produce spatially complete fields of a whole suite of meteorological parameters—both measured parameters and derived parameters such as potential vorticity. Papers documenting reanalyses are some of the most highly cited (e.g., Kalnay et al. 1996; Uppala et al. 2005), attesting to the high utility of reanalyses for a myriad of applications. They have not been included in the global chapter of *State of the Climate* to date because of well documented concerns about the ability of early reanalysis products to characterize long-term trends. The third generation of reanalysis products include substantial improvements as each successive effort has learned from previous efforts and taken advantage of developments in the sphere of weather forecasting. The ability of these much newer reanalysis products to characterize long-term changes in at least a subset of meteorological parameters has now been documented (e.g., Simmons et al. 2010). As a first step towards their more comprehensive inclusion in future *State of the Climate* reports this year there are results from the European Centre for Medium Range Forecasts (ECMWF) ERA-40 and ERA-interim reanalyses (Simmons et al. 2010) incorporated into the three temperature sections. It is hoped that in future years these can be augmented by other third generation reanalysis products from NASA (MERRA, Bosilovich 2008), JRA-55 from the Japan Meteorologi-

Stratospheric Temperature

a)

-10.0 -7.5 -5.0 -3.0 -2.0 -1.0 -0.5 -0.25 0.0 0.25 0.5 1.0 2.0 3.0 5.0 7.5 10.0
Anomalies from 1979-1998 (degC)

Cloudiness

d)

-20. -15.0 -10.0 -5.0 -2.5 0.0 2.5 5.0 10.0 15.0 20.0
Anomalies from 1982-2009 (%)

Lower Tropospheric Temperature

b)

-10.0 -7.5 -5.0 -3.0 -2.0 -1.0 -0.5 -0.25 0.0 0.25 0.5 1.0 2.0 3.0 5.0 7.5 10.0
Anomalies from 1989-2008 (degC)

Total Column Water Vapor

e)

-7.0 -5.0 -3.0 -2.0 -1.0 -0.5 0.0 0.5 1.0 2.0 3.0 5.0 7.0
Anomalies from 1987-2009 (mm)

Surface Temperature

c)

-10.0 -7.5 -5.0 -3.0 -2.0 -1.0 -0.5 -0.25 0.0 0.25 0.5 1.0 2.0 3.0 5.0 7.5 10.0
Anomalies from 1961-1990 (degC)

Precipitation

f)

-1250 -1000 -750. -500. -250. -100. 0.0 100. 250. 500. 750. 1000 1200
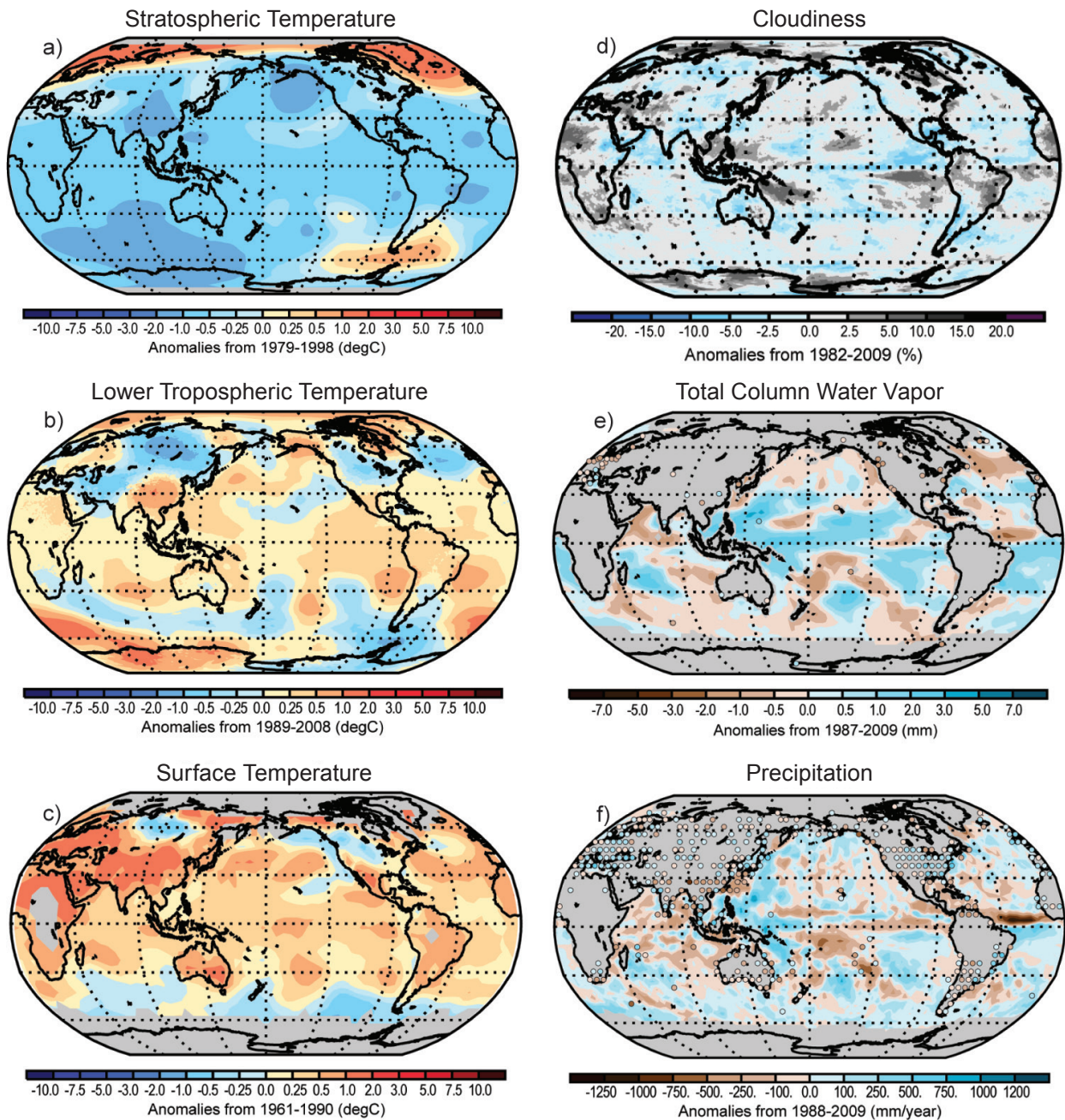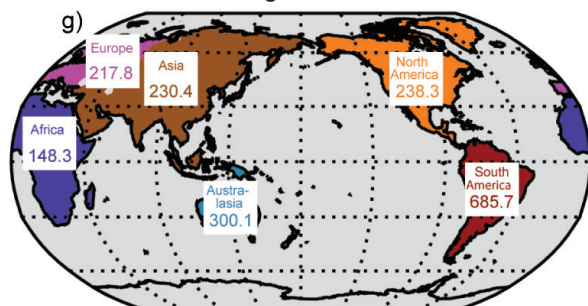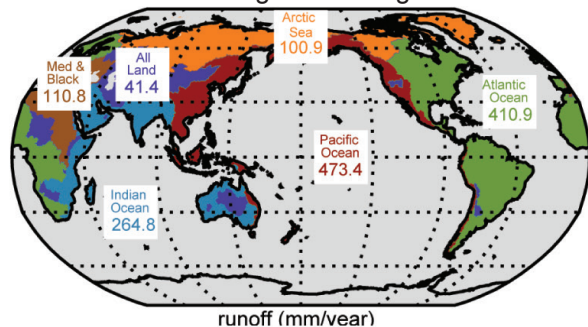Anomalies from 1988-2009 (mm/year)

PLATE 2.1. Global annual anomaly maps for those variables for which it is possible to create a meaningful 2009 anomaly estimate. Climatologies differ among variables, but spatial patterns should largely dominate over choices of climatology period. Dataset sources/names are as follows: lower stratospheric temperature (RSS MSU); lower tropospheric temperature (ERA-interim); surface temperature (NOAA/NCDC); cloudiness (PATMOS-x); total column water vapor (SSM/I over ocean, ground based GPS over land); precipitation (RSS over ocean, GHCN (gridded) over land); river discharge (authors); mean sea level pressure (HadSLP2r); wind speed (AMSR-E); ozone (GOME2); FAPAR (SeaWIFS); Biomass Burning (GEMS/MACC). See relevant section text and figures for more details.
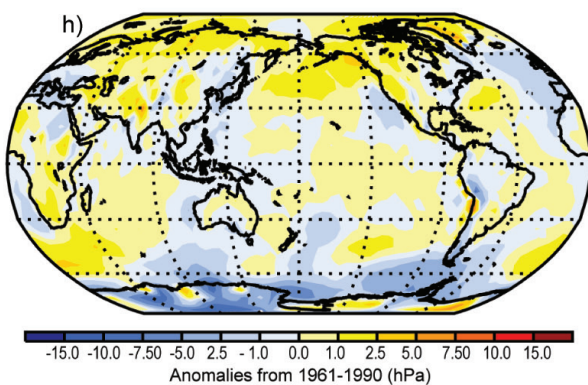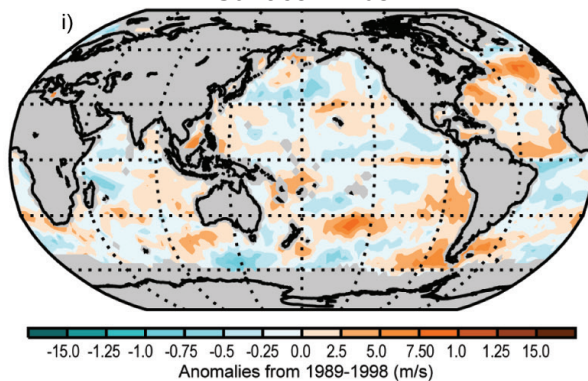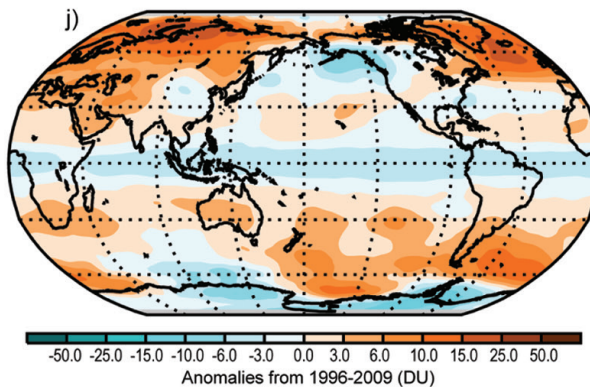
River Discharge Continent Runoff

g)

Europe 217.8
Asia 230.4
North America 238.3
Africa 148.3
Austra-lasia 300.1
South America 685.7

River Discharge Receiving Oceans

Med & Black 110.8
All Land 41.4
Arctic Sea 100.9
Atlantic Ocean 410.9
Indian Ocean 264.8
Pacific Ocean 473.4

runoff (mm/year)

Sea Level Pressure

h)

-15.0 -10.0 -7.50 -5.0 -2.5 -1.0 0.0 1.0 2.5 5.0 7.50 10.0 15.0
Anomalies from 1961–1990 (hPa)

Surface Winds

i)

-15.0 -1.25 -1.0 -0.75 -0.5 -0.25 0.0 2.5 5.0 7.50 1.0 1.25 15.0
Anomalies from 1989–1998 (m/s)

Ozone

j)

-50.0 -25.0 -15.0 -10.0 -6.0 -3.0 0.0 3.0 6.0 10.0 15.0 25.0 50.0
Anomalies from 1996–2009 (DU)

Fraction of Absorbed Photosynthetically Active Radiation

k)

-0.15 -0.10 -0.05 -0.03 -0.02 -0.01 0.00 0.01 0.02 0.03 0.05 0.10 0.15
Anomalies from 1998–2009 (FAPAR)
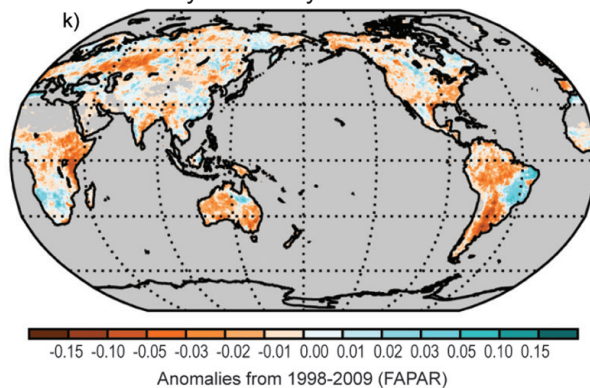
Biomass Burning (average fire radiative power)

l)

-0.0050 -0.0030 -0.0020 -0.0010 -0.0005 0.0000 0.0005 0.0010 0.0020 0.0030 0.0050
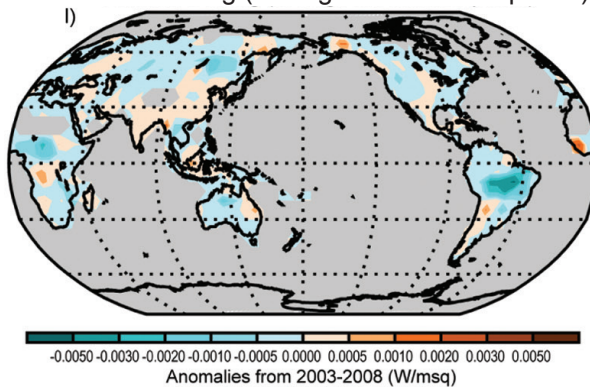Anomalies from 2003–2008 (W/msq)

TABLE 2.1. Sources of those datasets used in this chapter that are publicly available for bona fide research purposes.

Source	Datasets	Section
http://www.metoffice.gov.uk/hadobs	HadCRUT3, HadAT2, HadCRUH, HadSLP2r	2b.2; 2b.3; 2b.4; sidebar 1; 2d.1
http://data.giss.nasa.gov/gistemp	GISS surface temperature record	2b.2; sidebar1
http://www.ncdc.noaa.gov/cmb-faq/anomalies.html	NOAA/NCDC surface temperature record	2b.2; sidebar1
http://www.ecmwf.int/research/era/do/get/index	ERA reanalysis products	2b (all sections)
http://www.remss.com	Remote Sensing Systems products MSU, SSM/I, TMI, AMSR-E	2b.3; 2b.4; 2c.1; 2c.2; 2d.2; sidebar1
http://vortex.nsstc.uah.edu/public/msu/	UAH MSU records	2b.3; 2b.4; sidebar1
http://www.ncdc.noaa.gov/oa/climate/ratpac	RATPAC	2b.3; 2b.4; sidebar1
http://www.univie.ac.at/theoret-met/research	RAOBCORE 1.4, RICH	2b.3; 2b.4; sidebar1
http://www.ccrc.unsw.edu.au/staff/profiles/sherwood/rad-proj/index.html	IUK	2b.4; sidebar1
http://www.star.nesdis.noaa.gov/smcd/emb/mscat/mscat-main.htm	STAR	2b.4; sidebar1
By email to Junhong Wang	GPS-PW	2c.1
http://cosmic-io.cosmic.ucar.edu/cdaac/index.html	COSMIC	2c.1; sidebar2
http://www.ncdc.noaa.gov/oa/climate/ghcn-monthly/index.php	GHCN data (T, precipitation)	2b.2; 2c.2
http://precip.gsfc.nasa.gov	GPCP precipitation	2c.2
http://www.cpc.noaa.gov/products/global_precip/html/wpage.cmap.html	CMAP precipitation	2c.2
http://www.esrl.noaa.gov/psd/data/gridded/data.gpcc.html	GPCC precipitation	2c.2
http://climate.rutgers.edu/snowcover	Snowcover extent	2c.3
http://www.atmos.washington.edu/~ignatius/CloudMap	SOBS clouds	2c.4
http://isccp.giss.nasa.gov	ISCCP D2 clouds	2c.4
http://cimss.ssec.wisc.edu/patmosx	PATMOS-x	2c.4
http://ladsweb.nascom.nasa.gov	MODIS	2c.4
http://eosweb.larc.nasa.gov/PRODOCS/misr/level3/overview.html	MISR	2c.4
http://grdc.bafg.de http://www.gtn-h.net	Global Runoff Data Centre Global Terriestrial Network for Hydrology	2c.5

Source	Datasets	Section
http://www.pecad.fas.usda.gov/cropexplorer/global_reser-voir/index.cfm http://tethys.eaprs.cse.dmu.ac.uk/RiverLake/shared/main http://www.legos.obs-mip.fr/soa/hydrologie/hydroweb/ http://gcmd.nasa.gov/records/GCMD_GLWD.html	Lake level products	2c.6
http://www.bom.gov.au/climate/current/soi2.shtml	BoM SOI	2d.1
http://www.cpc.noaa.gov/products/precip/CWlink/daily_ao_index/ao_index.html	AO index	2d.1
http://manati.orbit.nesdis.noaa.gov/quikscat/	QuikScat	2d.2
http://science.larc.nasa.gov/ceres/	CERES data	2e
http://www.esrl.noaa.gov/gmd/ccgg/trends/	CO_2	2f.1i
http://www.cmdl.noaa.gov/odgi/	ODGI	2f.1ii
http://www.esrl.noaa.gov/gmd/aggi/	AGGI	2f.1iii
http://www.esrl.noaa.gov/gmd/hats/insitu/cats/cats_conc.html	Trace gas measures	2f.1iv
http://www.gmes-atmosphere.eu/	MACC/GEMS	2f.2; 2g.3
http://www.ndacc.org/data/data_tbl http://acdb-ext.gsfc.nasa.gov/Data_services/merged/ http://eosweb.larc.nasa.gov http://haloe.gats-inc.com http://eopi.esa.int/registration http://www.iup.uni-bremen.de/scia-arc/	Stratospheric ozone	2f.3
http://www.woudc.org/data_e.html http://acdb-ext.gsfc.nasa.gov/Data_services/merged/ http://www.iup.uni-bremen.de/gome/wfdoas/wfdoas.html	Total ozone	2f.3
http://www.geo.unizh.ch/wgms/	WGMS	2g.1
http://fapar.jrc.ec.europa.eu/	FAPAR	2g.2

cal Agency, and NCEP (CFFSR, Saha et al. 2010) and others as they complete and that these reanalyses can be incorporated for additional variables where deemed appropriate by the section authors.

2) Global surface temperatures—M. J. Menne and J. J. Kennedy

Global surface temperatures in 2009 saw a return to near-record levels as the cooling in the tropical Pacific associated with the 2007/08 La Niña event gave way to strengthening El Niño conditions in 2009 (Fig. 2.1). This led to large areas of the tropics experiencing higher-than-average temperatures towards the end of the year. According to the three major surface temperature datasets (Fig. 2.2, NASA/GISS, Hansen et al. 2001; HadCRUT3, Brohan et al. 2006; and NOAA/NCDC; Smith and Reynolds 2005, Smith et al. 2008) 2009 averaged about 0.1°C warmer than 2008, which was the coolest year since 2000. Anomalies from the 1961–90 average for 2009 were 0.50°C, 0.44°C, and 0.46°C, respectively, and 0.37°C, 0.31°C, and 0.38°C for 2008. Analyses are based on air temperature data over land and SSTs derived from ship and buoy reports with independently derived adjustments to account for changes in observing-system bias.

The three institutions use different reconstruction and interpolation techniques (Table 2.2), hence the analyses differ in some details, especially in data sparse regions and in the specifics of yearly rankings.
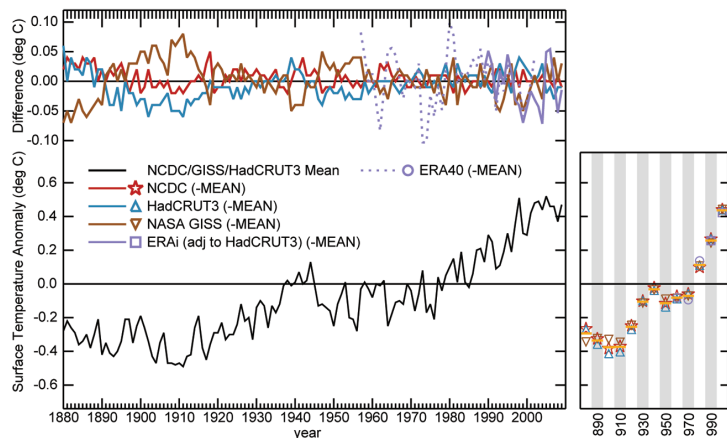
FIG. 2.2. Global surface temperature anomalies with respect to the 1961 to 1990 average. bottom: mean of the NASA/GISS, Had-CRUT3 and NOAA/NCDC analyses; and, top) difference between NASA/GISS, HadCRUT3, NOAA/NCDC, ERA-interim, ERA-40 and the mean. Decadally averaged anomalies are shown on the right-hand side where 66% of months are present along with the multi-dataset mean. ERA-interim anomalies are with respect to a 1989-2008 climatology and so have been adjusted by the difference between the ERA-interim and HadCRUT3 mean over the 1989-1998 period for consistency. Documented issues exist with ERA-40 pre-1979, especially in the Southern hemisphere and Antarctic, e.g. Simmons et al (2004). ECMWF always tell users to use caution when mixing pre-1979 data from ERA-40 into a climate analysis.

Nevertheless, the three reconstructions are in close agreement regarding the low-frequency variations in the surface temperature signal as indicated in Fig. 2.2. Higher values in the NASA/GISS analysis in recent years may be a consequence of the Hansen et al. (2001) approach to interpolating and averaging temperature anomalies across the data sparse high Arctic where positive anomalies have been particularly large during the last few years. The tendency for much above-average temperatures in the high-latitude regions of the Northern Hemisphere continued in 2009 (Plate 2.1). Above average temperatures were also prevalent across much of Europe and Asia, Mexico, Africa, and Australia whereas cooler-than-average conditions occurred across the southern oceans, central Siberia, and the region spanning southern Canada and the north central contiguous United States.

Unusual warmth was widespread throughout the year. Southern Asia and north Africa were exceptionally warm in all seasons, in contrast the northern
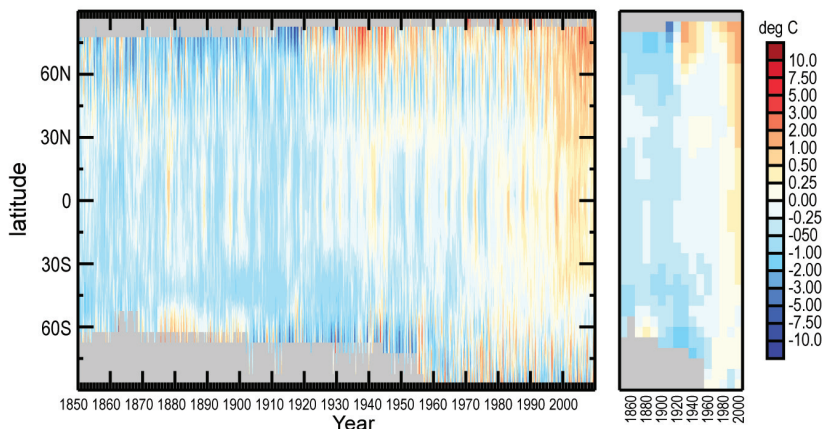

FIG. 2.1. HadCRUT3 monthly average temperature anomalies by latitude for the period 1850 to 2009. Decadally averaged anomalies are shown on the right-hand side where 66% of months are present. Grey areas indicate missing data. HadCRUT3 data have been smoothed in space and time using a 121 filter.
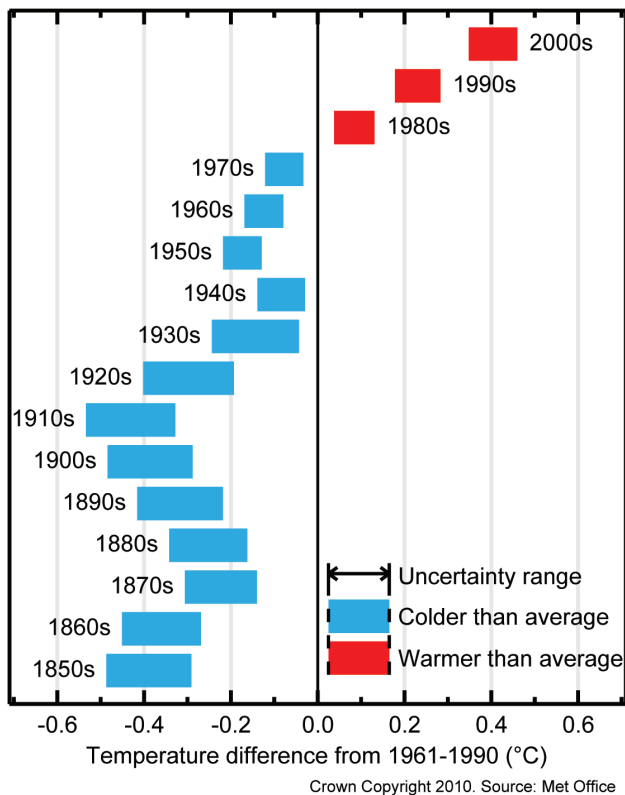
Fig. 2.3. 95% confidence range of decadal average temperatures for the HadCRUT3 temperature analysis (see Brohan et al. 2006 for the error model derivation).

U.S. and Canada were cooler than average for much of the year. In mid-December 2009 the Arctic Oscillation index turned strongly negative setting a pattern of colder-than-average temperatures over northern Eurasia and the U.S., coupled with warmer-than-average temperatures over the polar regions, southern Eurasia, and Canada that persisted throughout the winter. Nevertheless, December 2009 (and the rest of the winter season) was well above average in the North Hemisphere despite headlines about the unusual cold and snowy winter.

The uncertainties in deriving the global mean surface temperature imply that 2009 is statistically indistinguishable from the other high-ranking years shown in Fig. 2.2. Year to year variability is dominated by natural variability such as ENSO, but the effects of external climate forcings are expected to manifest themselves at decadal and longer time scales (Alley et al. 2007). Each of the last three decades was warmer than all earlier decades in the instrumental record (Fig. 2.3) and each set a new and statistically

significant record, culminating in the 2000s, which was the warmest decade of all.

3) LOWER TROPOSPHERIC TEMPERATURES—J. Christy, M. Free, C. Mears, and L. Haimberger

The 2009 global average temperature of the lower tropospheric layer (TLT, surface to ~8 km, see Fig. 2.2 in Karl et al. 2006) was approximately +0.3°C above the 1979–98 average. The first half of the year was near the decade's average but the troposphere subsequently warmed quickly in response to the developing warm phase of ENSO (Fig. 2.4). When the tropical Pacific ocean experiences these large temperature anomalies, the atmosphere above responds with similar temperature changes which, for the global average, lag the surface fluctuations by two to four months (Christy and McNider 1994). In the 31 (satellite) and 52 (radiosonde) years of records, 2009 ranked as the sixth or seventh warmest (depending upon the choice of dataset) in the lower troposphere, being around 0.2°C to 0.3°C cooler than the warmest (El Niño) year of 1998. Areas in the Northern Hemisphere midlatitudes, including central North America, north Atlantic, northern Asia, along with the Antarctic Peninsula were below the base-period average. North polar regions, south Asia, Atlantic–Indian ocean basin, and much of the tropics were on average warmer than the mean (Plate 2.1).
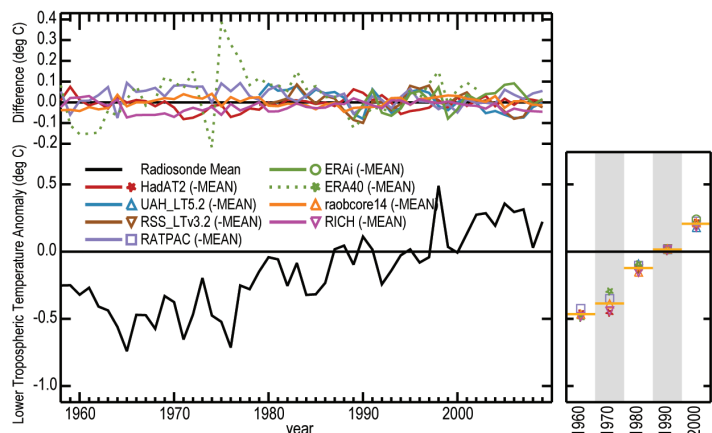

Fig. 2.4. As for Fig. 2.2 for global mean lower tropospheric temperature (1958–2009) from multiple datasets including four radiosonde datasets (HadAT2 (Thorne et al. 2005), RATPAC (Free et al. 2005), RAOBCORE and RICH (both Haimberger et al. 2008), two satellite MSU datasets (UAH (Christy et al. 2003), RSS (Mears and Wentz 2009a) and ERA-interim and ERA-40 Reanalyses (Simmons et al. 2010). Continuing research has documented procedures to account for inhomogeneities in these systems in order to provide the most confident estimates of the temperature values through time.

HOW DO WE KNOW THE WORLD HAS WARMED?—J. J. KENNEDY, P. W. THORNE, T. C. PETERSON, R. A. RUEDY, P. A. STOTT, D. E. PARKER, S. A. GOOD, H. A. TITCHNER, AND K. M. WILLETT

Although the IPCC AR4 concluded that "warming of the climate system is unequivocal," public debate over the evidence for global warming continues. However, it is often confined to a small set of reiterated disputes about Land Surface Air Temperature (LSAT) records, diverting attention from the broader evidence basis.

The methods used to derive the principal estimates of global surface temperature trends— HadCRUT3 (Brohan et al. 2006), NOAA (Smith et al. 2008), and NASA/GISS (Hansen et al. 2001)—are largely independent (Table 2.2). So, the spread of the three estimates indicates the likely degree of uncertainty in the evolution of the global mean surface temperature. It is noteworthy that independently-derived estimates of tropospheric temperature trends for the whole troposphere channel (distinct from section 2b2) from satellites differ by an order of magnitude more than do estimated surface temperature trends (Thorne et al. 2010, manuscript submitted to *Wiley Interdisciplinary Reviews: Climate Change*).

Numerous studies attest to the robustness of the global LSAT records and their nonreliance on individual stations (e.g., Jones et al. 1997; Peterson et al. 1999; Parker 2006; Parker et al. 2009; Menne et al. 2010). Evidence from recent reanalyses lends further support (Simmons et al. 2010).

The IPCC conclusion (Alley et al. 2007) that "warming of the climate system is unequivocal" does not rest solely upon LSAT records. These constitute only one line of evidence among many, for example: uptake of heat by the oceans, melting of land ice such as glaciers, and the associated rise in sea level, and increased atmospheric surface humidity (Fig. 2.5). If the land surface records were systematically flawed and the globe had not really warmed, then it would be almost impossible to explain the concurrent changes in this wide range of indicators produced by many independent groups. The observed changes in a broad range of indicators provide a self-consistent story of a warming world.
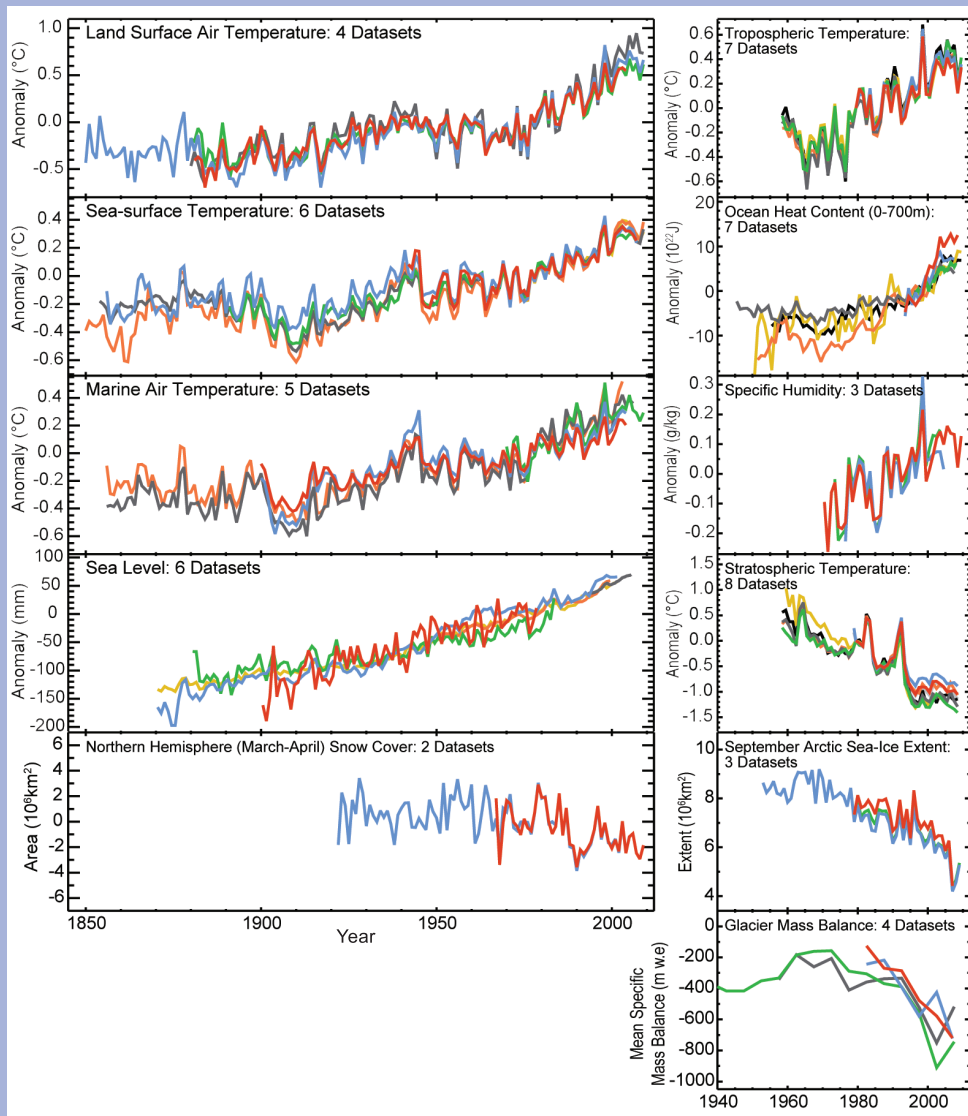

FIG. 2.5. Time series from a range of indicators that would be expected to correlate strongly with the surface record. Note that stratospheric cooling is an expected consequence of greenhouse gas increases. A version of this figure with full references is available at www.ncdc.noaa.gov/bams-state-of-the-climate/.

| **TABLE 2.2. Comparison between the HadCRUT, NOAA and NASA/GISS global surface temperature analyses.**			
	HadCRUT	**NOAA**	**NASA**
Land Surface Air Temperature			
Number of station	c. 4500	4,400	c. 6300
Sources of station data	The CRU archive containing: GHCN (over 30 sources of data, most are not regularly updated), Antarctic SCAR (Scientific Committee on Antarctic Research) data, various regional compilations, paper archives, USHCN data. Regular updates primarily from CLIMAT messages.	GHCN. Regular updates are primarily from USHCN data in the U.S. and CLIMAT messages.	GHCN, USHCN v2 adjusted, Antarctic SCAR (Scientific Committee on Antarctic Research) data.
Quality control (QC) procedures	Manual inspection; regional studies as published	Automatic QC tests based on statistics and physics (e.g., outlier tests, sequences of identical values).	Unrealistic outliers and segments of station series were eliminated after manual inspection.
Homogeneity adjustments	Visual and near-neighbor comparisons. c.20% of stations affected. Regional studies as published.	Non-climatic step changes and trends identified using USHCN v1 methods (US) and PEEP (Peterson and Easterling, 1994; Easterling and Peterson 1995) methods (remainder globe). Data adjusted to remove those artificial biases.	If there are multiple records at a given location, these are combined into one record adjusting according to the average difference during the period of overlap.
Urbanization effects	Some urban sites eliminated or adjusted by the QC and homogeneity adjustments. Uncertainty model includes a one-tailed urbanization error	Addressed by the homogeneity adjustments methodology.	Non-rural stations (defined by night-lighting in USA and by population data elsewhere) adjusted to match neighboring rural stations. Urban stations without nearby rural stations are dropped.
Ocean data			
Sources of station data	Ships, buoys from ICOADS (1850-1997) and GTS (1998 on)	Ships and buoys observations from ICOADS with updates from GTS.	HadISST1: 1870-1981. Reynolds et al. 2002: 11/1981-present
Quality control	Automatic QC tests based on statistics and physics (e.g. climatology-based outlier test, check against near neighbors)	Climatology-based removal of outliers.	HadISST1 and Reynolds are interpolated analyses with implicit QC so no GISS QC is applied.
Homogeneity adjustments	Physically based adjustments for changing types of buckets used to sample water in early 20th Century.	Statistical adjustment for the transition between buckets and engine intakes based on a relationship between SSTs and night time air temperature and global metadata for the timing of the transition.	HadISST1 and Reynolds are interpolated pre-adjusted analyses so no GISS specific homogeneity adjustment is applied.
Spatial interpolation, merging and calculating of global average			
Merging procedures	Land and ocean grid boxes merged with a weighting based on inverse error estimates for land and ocean data.	Land and ocean grid boxes with data merged with a weighting based on fraction of the grid box having land versus ocean.	After gridding, non-missing values are averaged over the zones 90S-23.6S,23.6S-0,0-23.6N,23.6N-90N; and the four means are averaged with 3:2:2:3 weighting to represent their area.
Accounting for data void regions	No infilling performed. Incomplete sampling accounted for in the uncertainty model.	Low frequency component filtered using very large grid boxes. Anomaly spatial covariance patterns guide interpolation of the high frequency component. Data sampling criteria limit how far interpolation can be made. Land and ocean data interpolated separately. Areas of sea ice are set to missing.	For each of 8000 equal area grid boxes, stations within that box or within 1200 km of the box centre are combined using the reference station method.
Calculation of global average	Average of gridbox area-weighted NH and SH values. Avoids over-weighting better sampled NH.	Area weighted analysis based on 5x5 degree grid boxes.	After gridding, non-missing values are averaged over the zones 90°S–23.6S, 23.6°S–0°, 0°–23.6°N, 23.6°N–90°N; and the four means are averaged with 3:2:2:3 weighting to represent their area.
Notes	The uncertainty model also takes into account incorrect/missing adjustments and temporal/measurement sampling errors.	The above was based on GHCN version 3 which is scheduled to be released in the spring of 2010.	Info from Hansen et al. 1999, 2001; and http://data.giss.nasa.gov/gistemp/ Code to calculate GISSTEMP is available from http://data.giss.nasa.gov/gistemp/sources/.
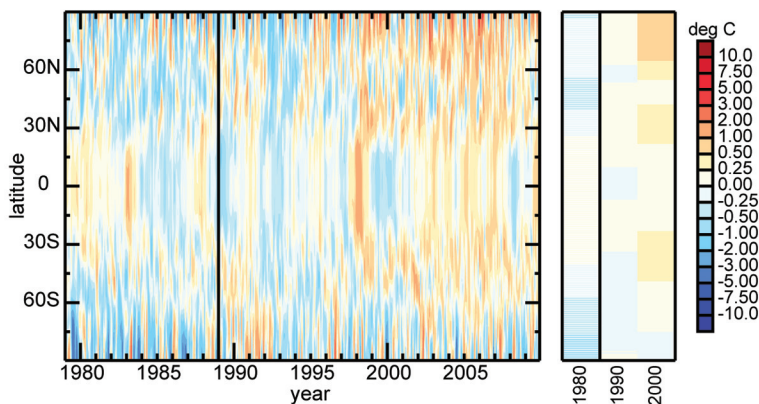
FIG. 2.6. As for Fig. 2.1 but for lower tropospheric temperature from the combined ERA-40 (1957 to 1988) and ERA-Interim (1989 to 2009) Reanalyses relative to the 1989 to 1998 base period.

The calendar decade of 2000–09 was the warmest of the last five decades. "Cool" La Niña conditions, persistent from late 1999, were evident as the decade began and reappeared in 2008. "Warm" El Niño conditions in 2003, 2005, briefly in 2007, and in the second half of 2009 were of modest magnitude compared with the significant event of 1997/98. Decades 1960–69 and 1970–79, were cooler than 2000–09 by about 0.6°C, with 1980–89 cooler by about 0.35°C and 1990–99 cooler by 0.2°C. The overall trend for both radiosondes (since 1958) and satellites (since 1979) is approximately +0.15°C per decade. Empirically the 52-year time series (Fig. 2.4) may equally plausibly be divided into three periods of relative temperature stability with transitions to warmer temperatures in 1977 (about +0.35°C) and 1998 (about +0.32°C) (e.g., Seidel and Lanzante 2004).
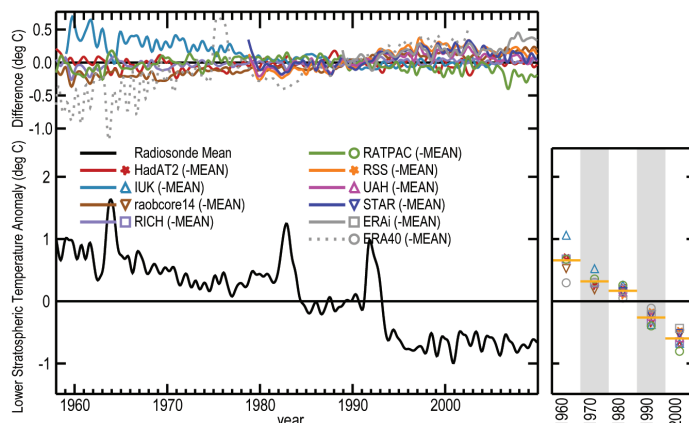

FIG. 2.7. As Fig. 2.2 but all time series are for the layer sampled by MSU channel 4 lower stratospheric temperature, spanning 10–25 km in altitude, with a peak near 18 km. References are the same as Figure 2.4 except for RSS (Mears and Wentz, 2009b) and the additional IUK radiosonde dataset (Sherwood et al. 2008) and STAR MSU record (Zou et al. 2009).

ECMWF Reanalyses (ERA-40 and ERA-interim) show that the warmest anomalies of 2000-09 were in the mid- and especially high-latitudes of the Northern Hemisphere. Similar regions in the Southern Hemisphere were not significantly different from the late 20th century (Fig. 2.6 – N.B. Choice of dataset is immaterial to the depiction of the main features as they are shown in all datasets). The Reanalyses reproduce the El Niño (warm, e.g., 1982-3, 1997-8) and La Niña (cool, e.g., 1989, 2008-9) events throughout the record. One to two year cooling periods follow volcanic eruptions in 1963 (Agung), 1982 (El Chichon) and 1991 (Mt. Pinatubo). Note the general trend toward warmer temperatures in the northern extratropics and tropics over the entire time period.

4) STRATOSPHERIC TEMPERATURES—M. Free and W. Randel

The 2009 annual average temperature of the global lower stratosphere was similar to that of the previous 15 years (Fig. 2.7), ranking 7th to 10th coolest since 1979 according to the dataset. Globally-averaged, the recent temperatures were approximately 1.5°C cooler than estimates from the late 1950s–early 1960s, when the first systematic radiosonde measurements of the lower stratosphere began. The overall cooling trend is punctuated by transient warming from three large volcanic eruptions (section 2b3), and the time series of cooling appears as step changes after these volcanic events (Seidel and Lanzante 2004; Ramaswamy et al. 2006). The volcanic warming events are mainly evident in low latitudes (Fig. 2.8).

The overall behavior of lower stratospheric temperature (TLS) shows reasonable agreement between radiosonde and satellite datasets for the post-1978 satellite period, although there are differences in detail between independent analyses of the radiosonde and satellite data (with the satellite data showing slightly less cooling than radiosondes). For the presatellite era (1958–78), there is larger disagreement and more uncertainty in trends among the different radiosonde-based datasets. For the overall record 1958–2009, the global trend from the average of the datasets is -0.33 ± 0.07°C per decade. For 1979–2009, trends range from -0.57 to -0.30°C per decade; the mean trend for all datasets shown is -0.41°C per decade.
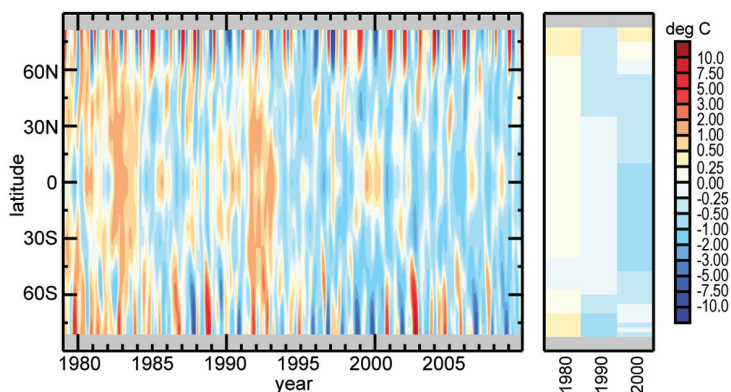
Fig. 2.8. As Fig. 2.1 but for the lower stratospheric channel estimate from RSS.

Evolution of lower stratospheric temperatures from satellite measurements (Fig. 2.8) highlights relatively constant temperatures since ~1995, modulated by the Quasi-Biennial Oscillation (QBO) in the tropics, plus large interannual variability in high-latitudes (during the respective winter–spring seasons). The QBO shifted from westerly to easterly winds in 2009, resulting in cold tropical lower stratosphere temperature anomalies in the second half of the year. The Arctic stratosphere was strongly influenced by a large stratospheric sudden warming in January 2009 (the largest in the 50-year record), resulting in rapid temperature increases of over 60°C in the polar middle and upper stratosphere (Fig. 2.9); the remainder of the Arctic winter (February–April) was relatively cold without large dynamic variability. The Antarctic polar vortex was relatively cold and undisturbed during 2009, with an ozone hole similar to other recent undisturbed years (Section 2f3).

TLS anomalies for 2009 (Plate 2.1) show large Arctic warming related to the January 2009 sudden stratospheric warming and a strong wave-1, or dipole pattern, in the zonal band around 60°S related to Antarctic changes in September–October. An increasing trend in this Antarctic pattern was noted in recent papers (Hu and Fu 2009; Lin et al. 2009).

As in previous years, changes in temperatures for altitudes above the lower stratosphere are difficult to characterize because of the relatively immature state of continuous datasets derived from the Stratospheric Sounding Unit (SSU), which ended in 2005, and the Advanced Microwave Sounding Unit (AMSU), with several different instruments operational since 1998.

c. Hydrological cycle

1) TOTAL COLUMN WATER VAPOR—C. Mears, J. Wang, S. Ho, L. Zhang, and X. Zhou

Total column water vapor (TCWV) over the world's oceans has been monitored since the first Special Sensor Microwave/Imager (SSM/I) satellite in late 1987 (Wentz 1997). In this section, we use data from the SSM/I and the Advanced Microwave Scanning Radiometer Earth Observing System (AMSR-E) instruments. Independent evaluations have found these data to be accurate enough for climate studies (Trenberth et al. 2005). Beginning in the late 1990s, ground-based GPS measurements provide a second accurate measurement of TCWV (Wang et al. 2007). Since these stations are often land based, they provide an important complement to the ocean-only SSM/I measurements. Even more recently, the Constellation Observing System for Meteorology, Ionosphere and Climate (COSMIC, see sidebar) series of satellites have begun using satellite-to-satellite radio occultation (RO) measurements to make globally distributed measurements of water vapor profiles over land and ocean. Here COSMIC TCWV is calculated from corresponding water vapor profiles.

The map of TCWV anomalies (Plate 2.1) includes data both from SSM/I (over the oceans) and from a subset of the ground-based GPS stations with continuous data from 1997 to 2009. This subset was chosen so that a meaningful anomaly estimate can be calculated—many more stations would be avail-
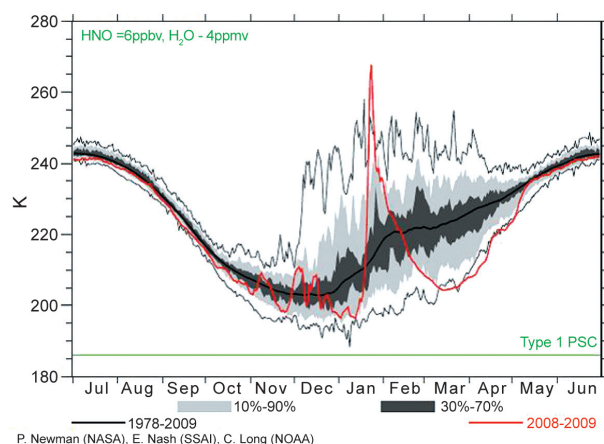

Fig. 2.9. Time series of 10 hPa temperature (red) at 80°N from CPC GFS analysis , highlighting January 2009 stratospheric sudden warming. Dark shaded areas indicate the range of the 30th to 70th percentile, light shade indicates the 10–90% range, and the light black lines indicate the maximum and minimum temperatures for the period since 1978.
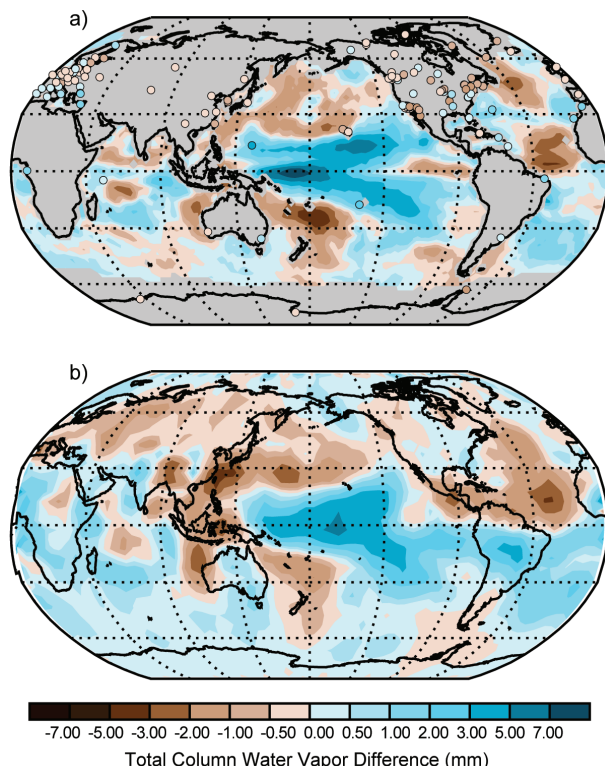
a)

b)

-7.00 -5.00 -3.00 -2.00 -1.00 -0.50 0.00 0.50 1.00 2.00 3.00 5.00 7.00
Total Column Water Vapor Difference (mm)

FIG. 2.10. Change in TCWV from 2008 to 2009. Panel (a) shows measurements from AMSR-E and ground based GPS stations, (b) from COSMIC.

able if this requirement were relaxed since the size of the network is increasing rapidly with time. There is general agreement between the SSM/I and ground-based GPS measurements at locations where overlaps occur with differences typically less than 0.5 mm. In the latter half of the year, a large wet anomaly in the tropical Pacific was associated with the onset of El Niño conditions. In contrast, most regions outside the tropics were drier than normal.

Changes in TCWV from 2008 to 2009 measured by three different measurement systems show the dramatic moistening of the tropical Pacific as the climate system shifted from strong La Niña conditions in 2008 to moderate El Niño conditions by the end of 2009 (Fig. 2.10). The COSMIC measurements show this moistening extending across the Amazon basin, a region previously unobserved.

SSM/I TCWV, from the world's ice-free oceans, shows maxima in 1987/88, 1997/98, 2002, 2006/07, and 2009 (/10), associated with ENSO events, with GPS data, only available since 1997, showing similar features
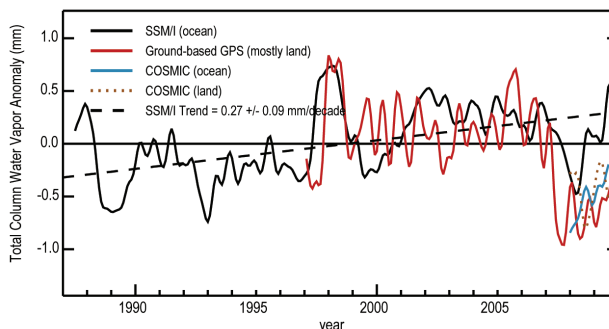

FIG. 2.11. Anomaly time series of TCWV both from SSM/I, ground based GPS, and COSMIC. Except for COSMIC, the reference period is 1997–2008. The COSMIC ocean anomalies are calculated relative to a SSM/I climatology for 1997–2008. The COSMIC land anomalies are calculated only at the locations of GPS ground stations, and are relative to a 1997–2008 ground-based GPS climatology. The timeseries have been smoothed to remove variability on time scales shorter than 6 months. A linear fit to the SSM/I data is also shown indicating an increasing trend in water vapor over the 1988–2009 period.

(Fig. 2.11). An exact match is not expected since the two measurement systems sample different regions of the globe. The COSMIC data show the sharp increase from 2008 to 2009 seen in the other two datasets. The SSM/I data show an increasing trend in TCWV (0.27 mm per decade). In the tropics this increase has been formally attributed to anthropogenic change over the 1988–2006 period (Santer et al. 2007). A Hoffmueller plot derived from SSM/I (Fig. 2.12) shows that the increase is largest in the tropics and Northern Hemisphere and relatively small in the Southern Hemisphere.
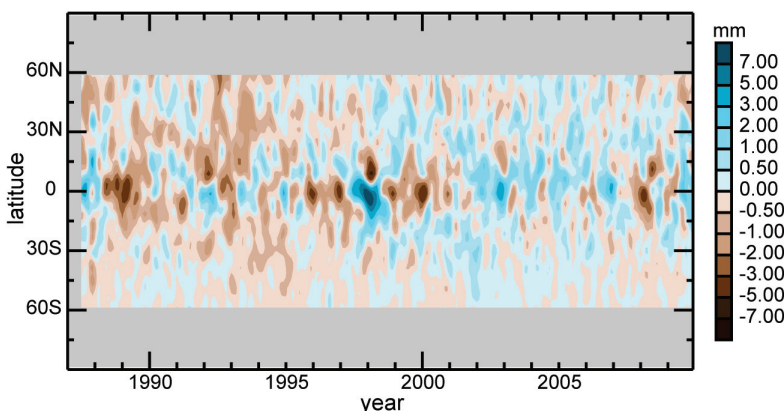

FIG. 2.12. As for Fig. 2.1 but for TCWV anomalies calculated using a reference period of 1988–2007. The data (SSM/I and AMSR-E measurements) have been smoothed in the time direction to remove variability on time scales shorter than 4 months.
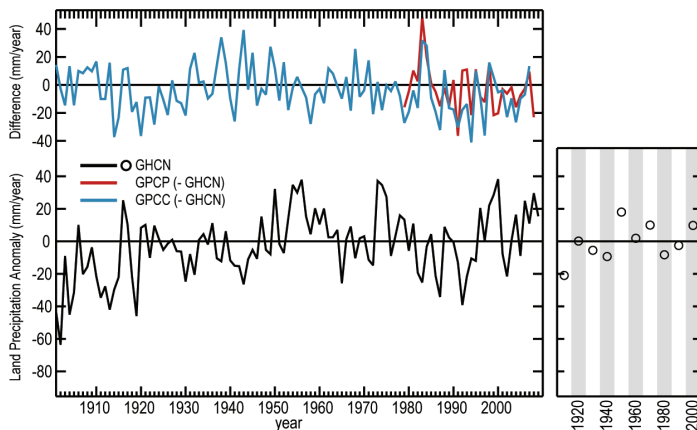
FIG. 2.13. As for Fig. 2.2 but for annual global land surface precipitation anomalies (mm) over the period 1901–2009 from the GHCN dataset relative to the 1961-1990 climatology (Vose et al. 1992). Two different historical comparisons of global land-based precipitation anomalies are also shown: beginning in 1901 using the difference between GPCC and GHCN, and beginning in 1979 using the difference between GPCP and GHCN (Schneider et al. 2008). All anomalies for the difference series were determined with respect to the 1981–2000 climatology.

2) GLOBAL PRECIPITATION—D. H. Levinson, K. A. Hilburn, J. H. Lawrimore, and M. C. Kruk

Global land precipitation estimates are derived from monthly totals of rain gauge measurements extending back at least to the beginning of the 20th century. In 2009 the positive anomaly continued an extended period of above average global precipitation covering the past five years (Fig. 2.13), and much of the period since 1996. Also shown (top curves) is the difference between global annual anomalies from three independent datasets (Global Historical Climatology Network [GHCN], Global Precipitation Climatology Centre [GPCC], and Global Precipitation Climatology Project [GPCP]). Overall, each of these datasets depict similar global anomalies on annual to interannual time scales, but some obvious differences occur on decadal timescales (e.g., during the early 1980s). Whether it is a gauge only (i.e., GHCN, GPCC) or a satellite-gauge blended product (i.e., GPCP), the gauge inventories used and the inclusion criteria applied to the analysis (i.e., percentage of data required during the base period), among other factors, lead to the observed differences in the annual anomalies over time.

Over the global oceans, precipitation records are only available for the much shorter satellite era. Remote Sensing Systems (RSS) produces inter-calibrated passive microwave

rain retrievals; which include retrievals from a total of eight microwave imagers into monthly-averaged maps at 2.5° x 2.5° resolution. For 2009, this included retrievals from TMI on TRMM, AMSR-E on Aqua, and F13 SSM/I on DMSP until it stopped functioning in late November 2009. There is substantial disagreement among three satellite-derived precipitation products over the ocean: RSS (Hilburn and Wentz 2008), Version 2.1 GPCP (Adler et al. 2003), and CMAP (Xie and Arkin 1997), especially during the first half of the time period (Fig. 2.14). RSS and GPCP trends for 1988–2008 were similar (19.5 ± 7.7 mm year^{-1} decade^{-1} and 14.8 ± 9.1 mm year^{-1} decade^{-1}, respectively; Levinson et al. 2009), but there are notable differences between the new version of GPCP and that used last year. However, in both versions there has been a relative drift compared to RSS since 2005. Based on updated analysis (Fig. 2.14), their 1988–2009 trends differ significantly and now exceed the 95% confidence interval. The RSS trend has not changed much, currently at 20.4 ± 7.1 mm year^{-1} decade^{-1}, but the GPCP trend is much lower at 2.4 ± 8.1 mm year^{-1} decade^{-1}.
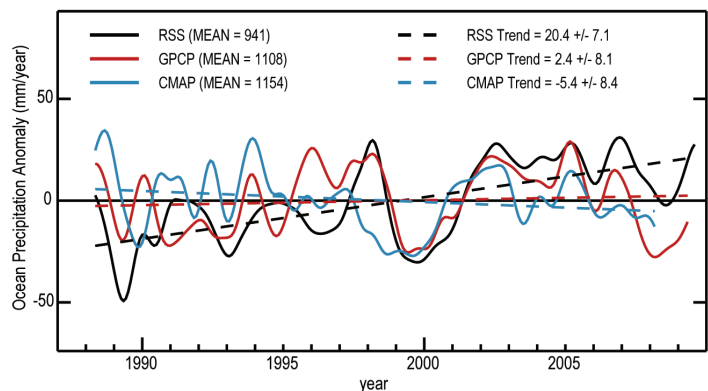

FIG. 2.14. Time series of precipitation anomalies relative to the period 1988–2009 for three datasets: RSS (black), GPCP (blue), and CMAP (red). Averages are for the global ocean equatorward of 60° latitude using a common definition of "ocean". The annual cycle has been removed and the time series have been low-pass filtered by convolution with a Gaussian distribution, with 4-month width at half-peak power. RSS data are available through all of 2009, GPCP data are available through September 2009, and CMAP data are available through July 2008. The key gives the 1988–2009 mean (in units of mm year^{-1}) and the linear trend (in units of mm year^{-1} decade^{-1}) with the 95% confidence interval. The linear trends are shown by the straight lines. The confidence interval is estimated based on deviations from the linear fit, and does not represent a particular dataset's "error".

Precipitation anomalies in 2009, over both land and ocean reflected the transition from La Niña at the end of 2008 to El Niño by late 2009. Over land, several regions experienced significant changes as a result. Long-term drought conditions in the southeastern United States persisted during the winter of 2008/09 (DJF; Fig. 2.15a), dissipated during the boreal spring (MAM; Fig. 2.15b), and were replaced by pronounced wet anomalies in the boreal fall as the El Niño developed (SON; Fig. 2.15d). Similarly, dry conditions that dominated northern Argentina for most of 2009 eventually broke later in the year as wet anomalies developed during the austral spring (SON; Fig. 2.15d). Abnormally dry conditions were also observed in southern Asia and the Indian subcontinent during the southwest monsoon (JJA; Fig. 2.15c).

During the La Niña in early 2009, a dry anomaly covered the western and central Pacific, with a wet anomaly over the far western Pacific Ocean. As the equatorial Pacific basin transitioned from La Niña to El Niño, dry anomalies over the western equatorial Pacific expanded, as wet anomalies in the far western Pacific region weakened (Plate 2.1). Dry conditions were also observed over parts of the central southern Pacific and Indian Ocean basins. The most pronounced precipitation signal over the oceans
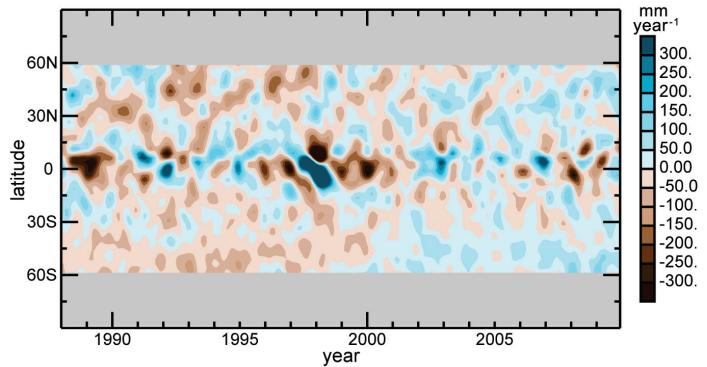

FIG. 2.16. As for Fig. 2.1 but for global ocean precipitation anomalies (with units of mm year^{-1}) as observed by the RSS monthly average dataset. The anomaly is calculated using the 1988–2009 base period by removing the latitude-dependent annual cycle.

was a dry anomaly over the tropical Atlantic along the climatological latitude of the ITCZ just north of the equator. This was in conjunction with a weaker wet anomaly just south of the equator indicating an anomalous southward excursion of the ITCZ. Precipitation anomalies over the tropical oceans were relatively weak compared to other years (Fig. 2.16). In addition, the wetter-than-normal conditions over the Southern Ocean that started in 2000 continued through 2009.

3) NORTHERN HEMISPHERE CONTINENTAL SNOW COVER EXTENT—D. A. Robinson

Annual snow cover extent (SCE) over the Northern Hemisphere (including snow over the continents and the Greenland ice sheet) was 0.4 million km^2 less than the 40-yr average; 2009 experienced the 13th least extensive cover on record (Table 2.3). The SCE in 2009 ranged from 47.1 million km^2 in January to 2.4 million km^2 in August.

2009 began with SCE in the second highest quartile over Eurasia and North America. North American extent remained within this quartile until April. However, Eurasian SCE fell into
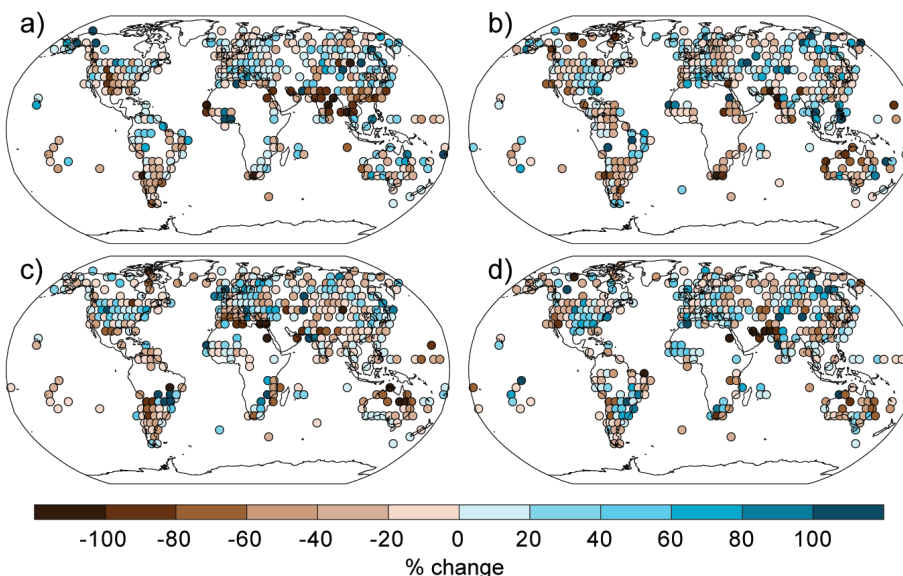

FIG. 2.15. Global precipitation anomalies (in % change) determined using the GHCN-Monthly dataset for the following 3-month seasons: (a) Dec 2008 to Feb 2009, (b) Mar to May 2009, (c) Jun to Aug 2009, and (d) Sep to Nov 2009. Seasonal anomalies were determined relative to the 1961–90 means, with at least two-thirds (66%) of the years without missing data required during the base period.

TABLE 2.3. Monthly and annual climatological information on Northern Hemisphere (NH) and continental snow extent between November 1966 and December 2009. 1968, 1969, and 1971 have 1, 5, and 3 missing months respectively, so are not included in the annual (Ann) calculations. North America (N. Am.) includes Greenland. Ranks are from most extensive (1) to least (ranges from 40 to 44 depending on the month). (Source: Rutgers Global Snow Lab.)

	Number of years with data contributing to the record	Mean snow extent (x 10^6 km^2)	Standard Deviation (x 10^6 km^2)	2009 snow extent (x 10^6 km^2)	2009 NH rank	Eurasia rank	N. Am. rank
Jan	43	46.6	1.5	47.1	14	17	16
Feb	43	45.5	1.8	44.5	34	35	16
Mar	43	40.3	1.9	39.3	29	35	20
Apr	43	30.6	1.7	29.2	33	40	12
May	43	19.6	1.7	18.0	37	38	22
Jun	42	10.2	2.0	7.1	41	41	38
Jul	40	4.2	1.2	2.7	39	40	38
Aug	41	3.1	0.7	2.4	37	39	32
Sep	41	5.3	0.9	4.3	34	38	23
Oct	42	17.9	2.6	20.7	6	10	3
Nov	44	33.6	2.0	34.4	14	5	41
Dec	44	43.2	1.8	45.9	2	7	1
Ann	40	25.0	0.9	24.6	28	29	19

the lowest quartile in February where it remained until early fall. Being the larger of the two continents, this most often placed the hemispheric landmass into the lowest quartile until fall. SCE increased rapidly across both continents in early October, with Eurasia maintaining a top 10 ranking throughout the remainder of the year. North American SCE flipped from third most extensive in October to fourth least extensive in November and then to the most extensive of the satellite era in December. This exemplifies the significant intra- and inter-seasonal variability of continental snow extent, particularly during the fall season. Hemispheric SCE in December was the second greatest of the past 44 years, doubtless linked to the extreme negative phase of the Arctic Oscillation and associated circulation anomalies (Fig. 2.29).

Late-year positive SCE anomalies resulted in the twelve-month running mean of Northern Hemisphere extent rising from its low extent of the past approximately two years and approaching the long-term mean (Fig. 2.17). Both hemispheric and Eurasian (Fig.

2.17) running means had not been as consistently low since the late 1980s and early 1990s. Meanwhile, the North American running mean remained close to the long-term mean throughout 2009.
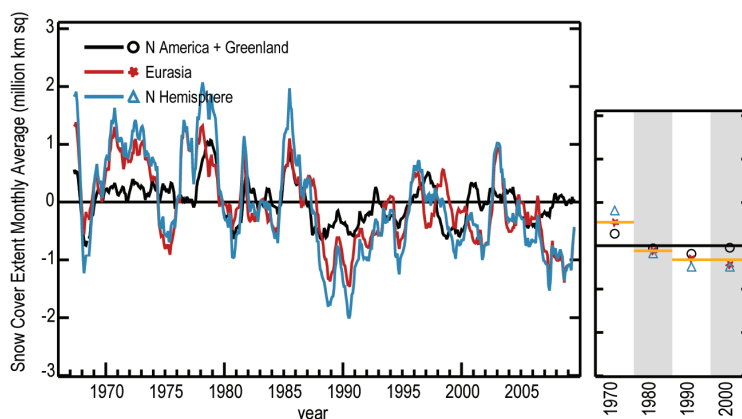

FIG. 2.17. As for Fig. 2.2 but for monthly anomalies of mean snow cover extent between November 1966 and December 2009 over Northern Hemisphere lands (including Greenland), Eurasia and N. America. Running monthly means are plotted on the seventh month of a given interval. Anomalies are calculated from NOAA snow maps. Mean hemispheric snow extent is 25.0 million km^2 for the full period of record. Monthly means for the period of record are used for nine missing months between 1968 and 1971 in order to create a continuous series of running means. Missing months fall between June and October, no winter months are missing.
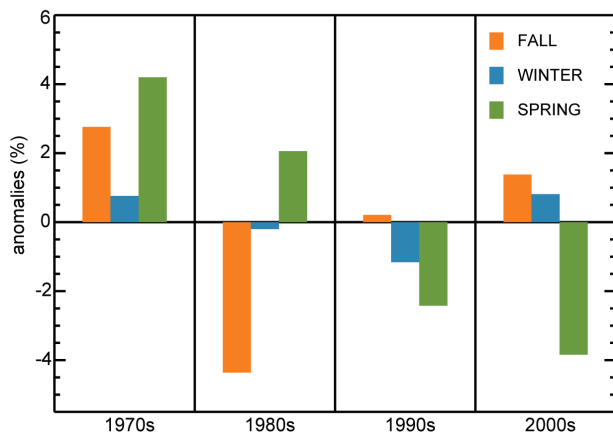
Fig. 2.18. Seasonal SCE anomalies (excluding summer) for the four decades beginning in December 1969 and ending in November 2009. Decadal percent anomalies are calculated for the 40-year interval.

Decadal snow cover extent behavior over Northern Hemisphere land regions between 1970 and 2009 was quite different between seasons (Fig. 2.18). The 1970s had the most extensive fall snow cover, with the 1980s the least extensive (approx -4% and the only decade below average). Winter SCE was almost equally above the 40-yr mean in the 1970s and 2000s, close to average in the 1980s, and below average in the 1990s. All winter decadal means were within 1.2% of average. Spring SCE steadily declined from the 1970s to 2000s, with these decades approximately +4% and -4% relative to the mean, respectively.

4) Global cloudiness—M. J. Foster, S. A. Ackerman, A. K. Heidinger, and B. C. Maddux

Global cloud anomalies in 2009 reflected the shift from weak La Niña conditions to an El Niño during boreal summer. The resulting temperature and circulation anomalies enhanced large-scale convection in the central Pacific and suppressed convection in the western Pacific near Indonesia. This generated positive cloud anomalies in the central equatorial Pacific and corresponding negative anomalies around Indonesia in the latter half of the year. Large positive annual anomalies of 10% to 15% were seen off the western coast of Peru and eastern coasts of Australia and Papua New Guinea (Plate 2.1). Since the shift to El Niño conditions did not occur until boreal summer, the magnitudes of the annual cloud anomalies were relatively small. Only small portions of the anomaly off the west coast of Peru were statistically significant at the 5% level. 2009 also saw some unusual continental cloudiness with positive cloud anomalies over large portions of northwestern Africa coupled with negative anomalies over eastern Africa (Plate

2.1), sustained throughout much of the year. Parts of Brazil also maintained positive cloud anomalies for much of 2009 and an interesting though short-lived cloudiness event occurred over the continental United States. Large positive anomalies over most of North America in October 2009 (Fig. 2.19) coincided with the wettest October since records began in 1894. Portions of the Midwest cloudiness anomalies are statistically significant at the 5% level.

Global mean monthly cloud anomalies from four different satellite cloud climatologies and surface observations (Fig. 2.20) are defined as each month minus its corresponding time series monthly mean. Differences in cloudiness estimates can in part be attributed to variations in how cloud-masking algorithms define cloud versus clear-sky thresholds. This is in addition to correcting for factors such as sensor viewing angle, pixel footprint size, spectral channels, diurnal satellite drift, and sensor calibration. The trend of cloud anomalies over the last four decades is smaller than seasonal and diurnal variability and within the range of estimated uncertainties for each product. With that in mind t-values are calculated for the slope of each month to remove seasonal effects: the surface weather observations (Fig. 2.20) data record shows a positive trend for all months while the International Satellite Cloud Climatology Project (ISCCP, Fig. 2.20) record shows a negative trend. None of the other records show significant trends. Relative to the entire Pathfinder Atmospheres Extended (PATMOS-x, Fig. 2.20) time series, 2009 was slightly cloudier-than-normal. The mean cloudiness for the year was 65.6%, 0.3% higher than the 28-year average, making 2009 the ninth cloudiest of the time
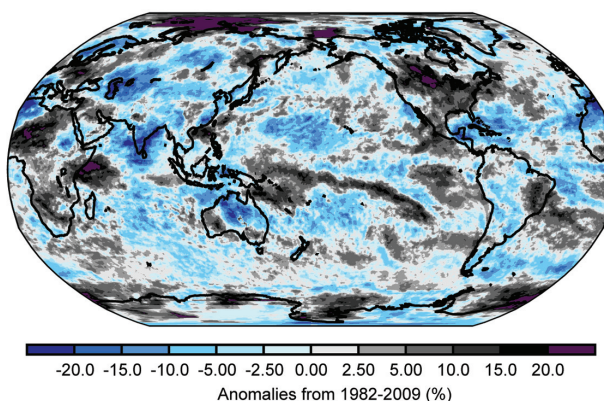

Fig. 2.19. Cloud anomaly map for October 2009 generated from the 28-year Pathfinder Atmospheres Extended (PATMOS-x, Heidinger and Pavolonis 2009) cloud climatology (1982 to present), which is derived from NOAA's Advanced Very High Resolution Radiometer (AVHRR).
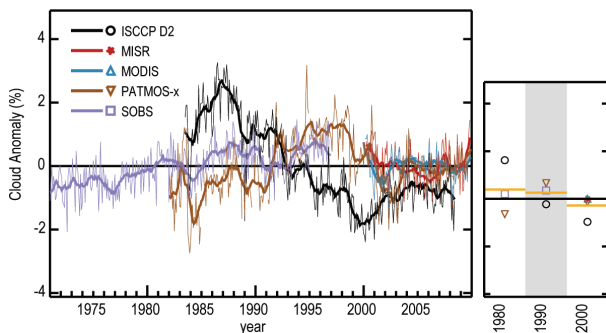
Fig. 2.20. As for Fig. 2.2 but for monthly anomalies of cloud amount from 1971 through 2009 taken from five datasets. Climatologies are derived from different instruments and cover different periods, the earliest of which are (a) surface weather observations (SOBS) from 1971 to 1996 (Hahn and Warren 2007); (b) Moderate Resolution Imaging Spectroradiometer (MODIS, Ackerman et al. 2008); (c) Multiangle Imaging Spectroradiometer (MISR, Di Girolamo et al. 2010) instruments on NASA's Terra satellite from 2000 to present (a MODIS instrument is also located on NASA's Aqua satellite and is included in the climatology); (d) International Satellite Cloud Climatology Project (ISCCP) data derived from imaging radiometers on operational weather satellites of several nations from 1983 to 2008 (and continuing); and (e) PATMOS-x described in Fig. 2.19. Thick solid lines represent average cloudiness for each dataset using a boxcar filter with a twelve-month window.

series. Nine months had higher cloudiness than the monthly mean (not significant), with only April, May, and August falling below the mean.

  5) River discharge—B. M. Fekete, R. B. Lammers, A. Mac-Donald, L. C. Bowling, and R. Lawford

Discharge gauges are efficient and relatively inexpensive, and river discharge is the most accurately measured component of the water cycle (Fekete et al. 2002; Hagemann and Dümenil 1998). While modern telecommunication technologies are readily available to share in situ observations in a timely manner, the lack of international cooperation and data sharing are the main obstacles in accessing discharge data. For this reason historical runoff analyses are always delayed by three to five years and are incomplete in important geographical areas. As few as ~300 discharge gauges, strategically located near river mouths of large rivers around the world, could monitor over 50% of the continental land mass (Fekete et al. 2002). The World Meteorological Organization is proposing to establish 265 real-time reporting discharge gauges globally (to monitor 40% of the continental land mass) as the number of operating discharge gauges has steadily declined since the mid-1980s

(Shiklomanov et al. 2002; Vörösmarty et al. 2002) at the same time as concerns about climate change effects are growing.

The only way to reconstruct recent changes in global runoff is to carry out water balance calculations using a relatively simple configuration of the Water Balance Model driven by observed air temperatures and precipitation (Vörösmarty et al. 1998; Wisser et al. 2008, 2010). Water balance calculations were carried out for the periods of 1901–2002, 1948–2007, 1986–2008, and 2003–05 using combinations of different climate forcings (due to the lack of single consistent time series from the beginning of the 20th Century to present). The overlapping periods were used to reconcile the different runoff estimates.

The reconciled runoff estimates (Fig. 2.21/Plate 2.1) reveal that the last decade (2000–09) had similar or increased river discharge in all continents and ocean catchments, except Africa and the Mediterranean/Black Sea drainage when compared to the long-term mean. 2009 appeared to return to the 20th Century global average except over Africa, the Pacific Islands, South America, and the Arctic and Pacific Oceans. Most of the continents show similar patterns except Africa, which is drying steadily and Asia, which fell below the 20th Century average in 2009.
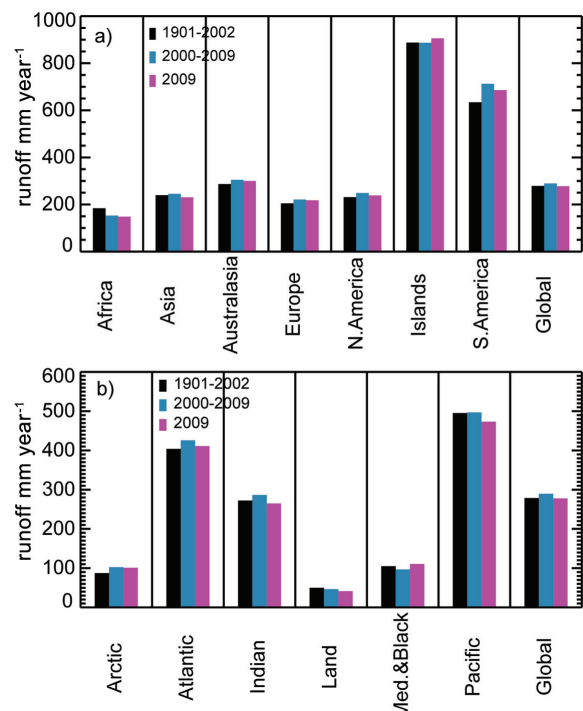

Fig. 2.21. River runoff by (a) continent and (b) receiving oceans. "Islands" refers to the Pacific Islands, "Med. & Black" refers to the Mediterranean and Black Sea drainage regions and "Land" represents the mean of all internal (endorheic) basins found on every continent.

USING SI-TRACEABLE GLOBAL POSITIONING SYSTEM RADIO OCCULTATION MEASUREMENTS FOR CLIMATE MONITORING—
S-P. HO, Y.-H. KUO, W. SCHREINER, AND X. ZHOU

Global Positioning System (GPS) Radio Occultation (RO) data are an important component of the evolving global observing system (NRC 2007; WMO 2007; GCOS 2004). GPS-RO is the only self-calibrated observing technique from space whereby its fundamental measurement is traceable to the international system of units (SI) (SI traceability; Ohring 2007). GPS receivers on low-Earth orbiting (LEO) satellites receive measurable radio frequency signals transmitted from GPS satellites; monitoring and corrections from a series of atomic clocks allows the signal timing to be traced to the SI second with a high degree of accuracy. Significant advantages of SI-traceable GPS-RO observations for climate monitoring include: (i) no satellite-to-satellite bias (Hajj et al. 2004; Ho et al. 2009a); (ii) great precision (Anthes et al. 2008; Foelsche et al. 2009; Ho et al. 2009a); and (iii) no synoptic sampling bias (cloud/precipitation effects).

Raw RO observations and precise positions and velocities of GPS and LEO satellites, can be used to derive atmospheric temperature and moisture profiles (Hajj et al. 2004; Kuo et al. 2004; Ho et al. 2009b). GPS-RO temperature can be validated by comparing temperature measurements from FORMOSAT-3/ COSMIC with high quality radiosonde measurements. With a uniform distribution of COSMIC RO data in time and space (~2500 profiles per day, Fig. 2.22), more than 10 000 collocations of Vaisala-RS92 radiosonde and COSMIC data within 2 hours and 300 km exist (Fig. 2.23). The precision of COSMIC derived temperature profiles is estimated to be better than 0.05 K from 8 km to 30 km (Ho et al. 2009a); COSMIC temperature is very close to radiosondes from 200 hPa to 20 hPa (around 12 km to 25 km). Because the quality of RO data does not vary with location and time, it is very useful for assessing systematic errors in different radiosonde sensors (e.g., He et al. 2009; Kuo et al. 2005; Elliott and Gaffen 1991; Luers and Eskridge 1998). Radiative temperature biases that vary during the day and night can be identified for different radiosonde sensor
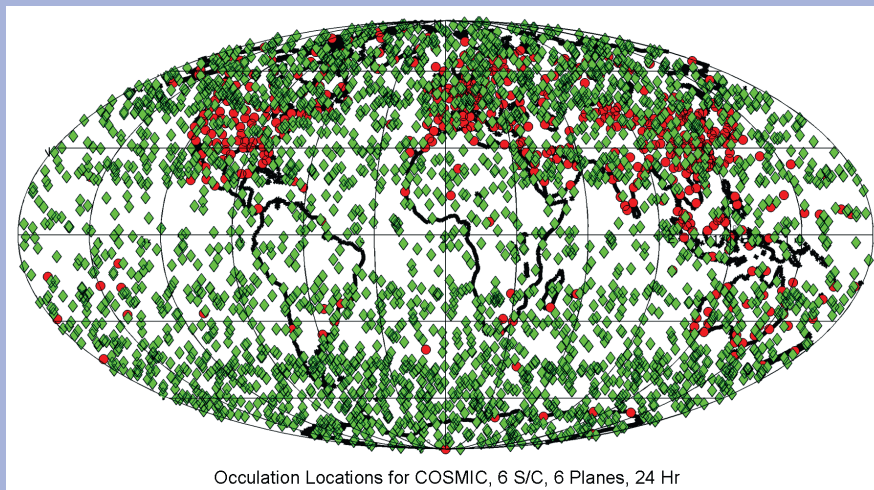
Occulation Locations for COSMIC, 6 S/C, 6 Planes, 24 Hr

FIG. 2.22. Typical operational distribution of COSMIC GPS radio occultation soundings (green dots) over a 24-hr period across the globe. Red dots are locations of operational radiosonde stations.

Mean Bias = -0.01
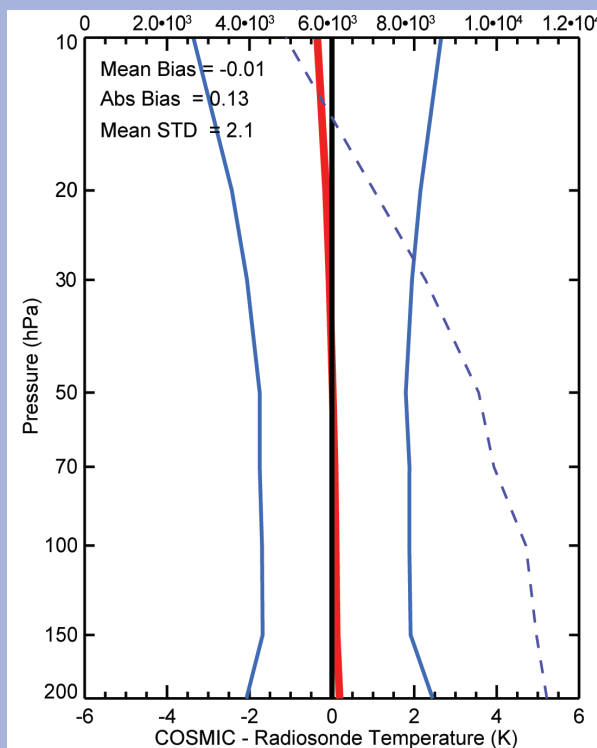Abs Bias = 0.13
Mean STD = 2.1

FIG. 2.23. Temperature comparisons between COSMIC and radiosonde Vaisala-RS92 in 2007. Mean bias, absolute mean bias and mean standard deviation are computed from 200 hPa to 10 hPa. The red line is the mean difference, the blue line is the standard deviation, and the dotted line is the sample number for RO and radiosonde pairs in that height (upper horizontal axis).

types when comparing with collocated COSMIC RO soundings (He et al. 2009).

The upper troposphere and lower stratosphere (UT/LS) is a critical region for understanding the radiative balance of the climate system and climate processes. However, due to poor vertical resolution and/or fundamental measurement uncertainty, most in situ and satellite sounder measurements of meteorological parameters in this region are not suitable for climate monitoring (Karl et al. 2006). The very high precision and vertical resolution (from ~60 m near the surface to ~1.5 km at 40 km) of GPS-RO data makes them very suitable to detect changes in UT/LS temperature (Ho et al. 2007), tropopause height, and the distribution of

Pictoral representation of GPS-RO measurement

double tropopauses (Randel et al. 2007). Because GPS-RO data are not affected by on-orbit heating and cooling of satellite components, they are very useful for identifying the time/location dependent biases of microwave sounders (Ho et al. 2009c), making them potentially useful as a climate benchmark (Ho et al. 2009a) in addition to being well suited to detect climate trends (Ho et al. 2009b; Ringer and Healy 2008).

Using refractivity data and reasonably independent temperature profiles, highly precise COSMIC water vapor profiles can be derived. Comparisons of total-column water vapor (TCWV) from COSMIC with those derived from ground-based GPS (i.e., International Global Navigation Satellite Systems—IGS, Wang et al. 2007) show that the mean global difference between IGS and COSMIC TCWV is about -0.2 mm with a standard deviation of 2.7 mm (Fig. 2.24).
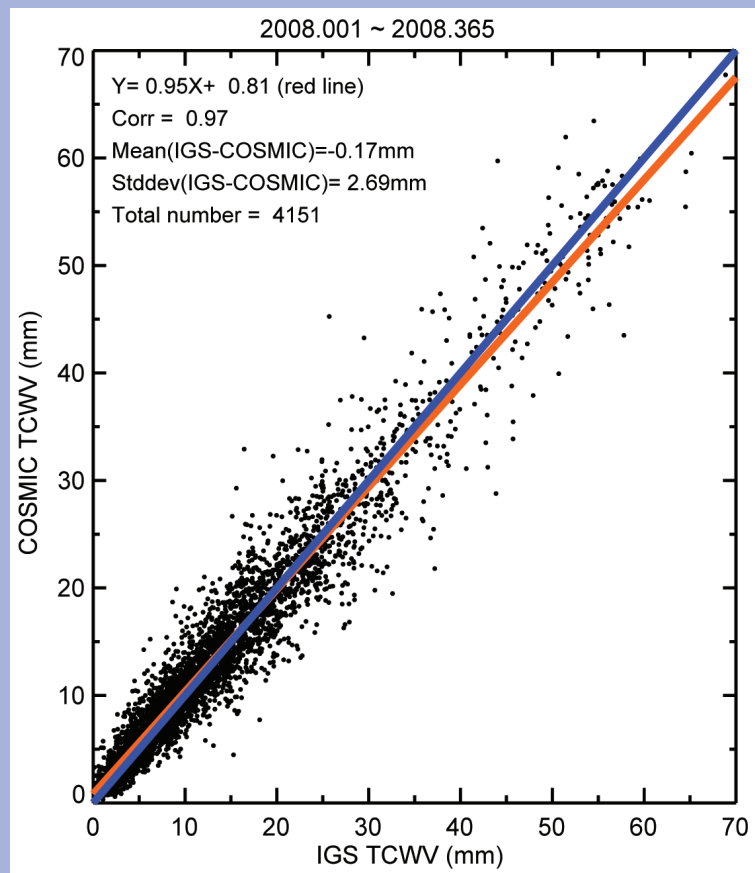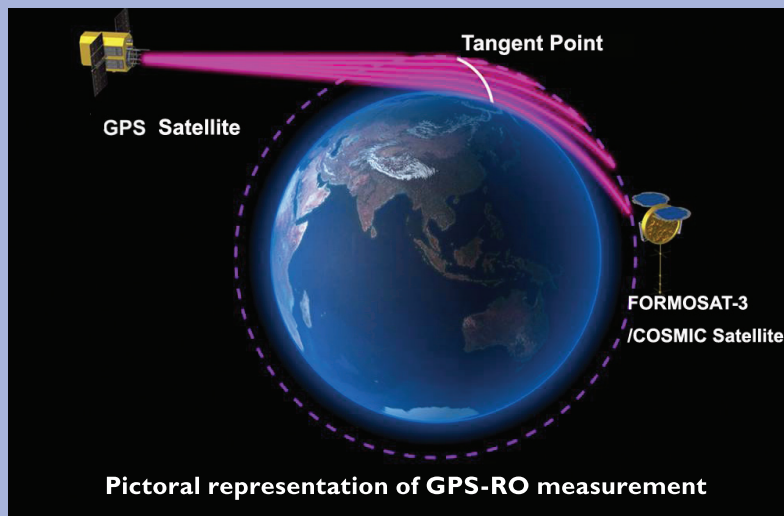

Fig. 2.24. Global comparisons of TCWV between COSMIC and those derived from ground-based GPS (i.e., IGS) for 2008.

6) Lake levels—C. Birkett

Lake volumes respond to changes in precipitation integrated over their catchment basins (Street-Perrott et al. 1986) and are indirect indicators of climatic change (Langbein 1961; Szesztay 1974). The response is particularly marked for closed lakes (having no significant surface or subsurface outflow) whose surface area, when in hydrological equilibrium, has been used in paleoclimatic studies to indicate changes in aridity. Closed lakes act as low-pass filters to variations in aridity, with a characteristic time constant of between 1 and 1000 years, depending largely on lake geomorphology (Mason et al. 1994). Historical studies of the links between climate and lake levels have concentrated on individual lakes or regions. However, both natural and anthropogenic climate effects have highlighted the need for a global approach to the systematic monitoring of lake levels (Williams 1993). For many lakes ground-based lake levels ('stage')

can be difficult to acquire, and while satellite-based imagery can reveal surface extent, there are currently no operational products.

Satellite-based lake-level products, however, are now being offered within three programs (NASA/USDA, ESA, and LEGOS; Fig. 2.25). Records are now long enough in theory to support climate monitoring. Large-lake levels are derived using several satellite radar altimeters with varying temporal (10-, 17-, 35-day) and spatial resolutions. Errors relative to ground-based gauge data can range from a few centimeters to tens of centimeters RMS (Birkett, 1995). The NASA/CNES suite of instruments offers measurements from 1992, the ESA suite from 1994. The number of lakes considered varies within each program but Fig. 2.26 shows the potential spatial distribution of all lake products within the NASA/USDA program. Location and lake type information can also be found in the databases of Birkett and Mason (1995, lakes of surface area ≥ 100 km^2) and Lehner and Döll (2004, surface areas ≥ 50 km^2).

While the NASA/USDA program provides a graphic comparison of the near-real-time water level status with respect to a short-term mean (Fig. 2.27), published research has focused more on single basin studies or regional water level variations and their links to ENSO and Indian Ocean SST anomalies (Birkett et al. 1999; Arpe et al. 2000; Mercier et al. 2002; Bergonzini et al. 2004; Zola and Bengtsson 2006; Ricko et al. 2009, manuscript submitted to *J. Climate*). Although the focus in these studies is on larger, open lakes (having significant surface or subsurface outflow), the ability of these phenomena to gain a rapid reaction in lake level regardless of anthropogenic controls shows that global and regional studies should not exclude other lake types and reservoirs.

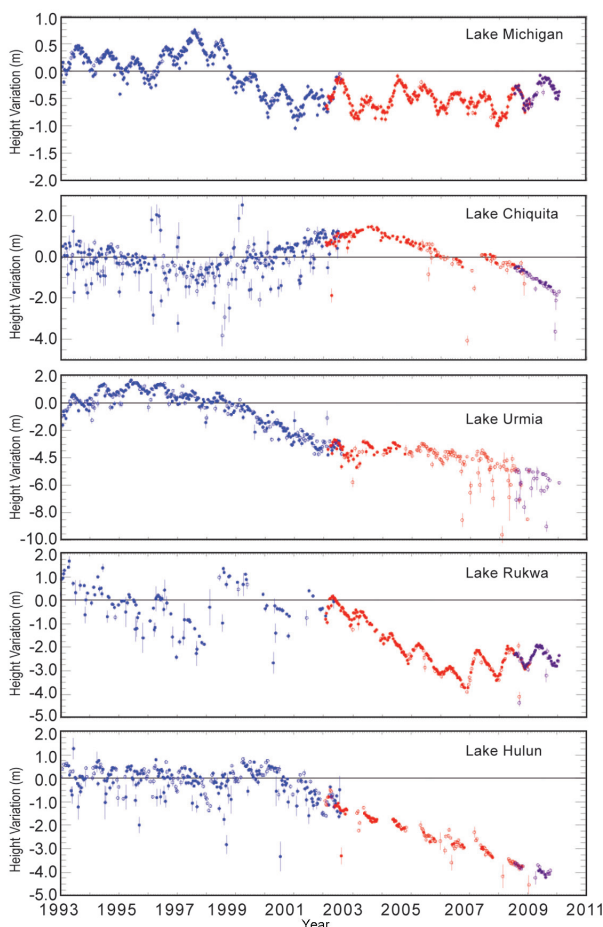**Fig. 2.25. Lake level products from the NASA/USDA/FAS. Topex/Poseidon (blue), Jason-1 (red), and Jason-2 (purple) radar altimeters. The lakes reside in the USA (Michigan), Argentina (Chiquita), Iran (Urmia), Tanzania (Rukwa), and China (Hulun).**
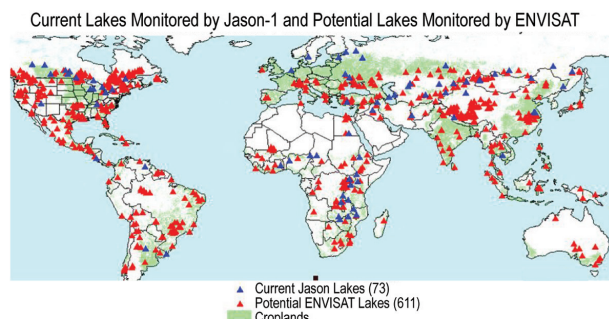

Fig. 2.26. Locations of lakes and reservoirs for which near real time lake level products are or will be available through the NASA/USDA/FAS web site.

Fig. 2.27. Map showing location of currently available NASA/USDA/FAS lake level products depicting the near real time lake level status with respect to a short-term mean (1992–2002), red (low water), navy (high water), white missing data .

d. Atmospheric circulation

1) MEAN SEA LEVEL PRESSURE—R. Allan

As highlighted in previous sections, a weak-moderate El Niño event developed mid-2009 following the collapse of La Niña early in the year. As a consequence, the annual global MSLP field showed no distinct El Niño signature (Plate 2.1).

El Niño and La Niña events can be measured by the Southern Oscillation Index (SOI), the normalized MSLP difference between Tahiti and Darwin (Allan et al. 1996). El Niños (negative SOI) and La Niñas (positive SOI) vary in magnitude, duration, and evolution, with no two events or episodes exactly the same. The SOI since 1900 is dominated by interannual to multidecadal vacillations, but very long-term trends are not evident (Fig. 2.28a). The SOI trace since 2000 highlights the shift from the La Niña of 2007/08 to the El Niño of 2009 (Fig. 2.28b). Major El Niño and La Niña events can be near-global in their influence on world weather patterns, owing to ocean-atmosphere interactions across the Indo-Pacific region with tele-
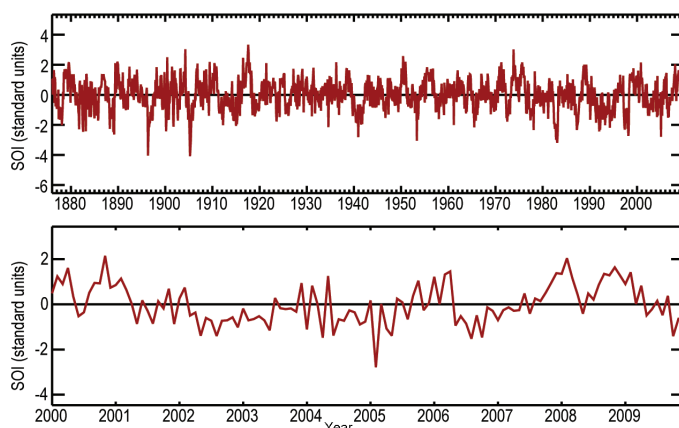
connections to higher latitudes in both hemispheres.

The other major event in 2009 was the development of an extreme negative North Atlantic Oscillation (NAO)/Arctic Oscillation (AO) phase in December 2009 that persisted through much of the 2009/10 winter. In Fig. 2.29, the December 2009 global MSLP field distinctly shows the NAO/AO influence

-15.0 -10.0 -7.50 -5.00 -2.50 -1.00 0.00 1.00 2.50 5.00 7.50 10.0 15.0
Anomalies from 1961-1990 (hPa)
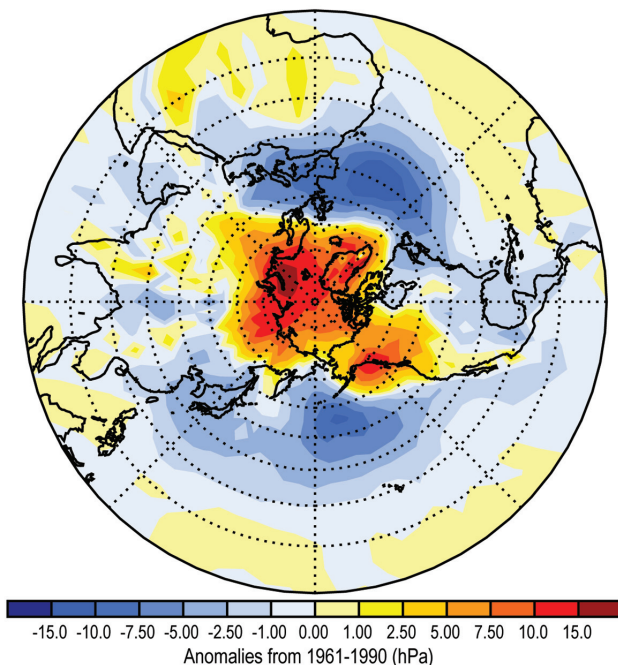
Fig. 2.29. Global MSLP anomalies (hPa) for December 2009 from HadSLP2r (Allen and Ansell, 2006).

across the North Atlantic and North Pacific with positive pressure anomalies over higher latitudes and negative anomalies over the mid-latitudes and an associated reduction in westerlies. This is further evident in Fig. 2.30a which highlights the major shift in atmospheric circulation in early December 2009 which led to record snow and cold temperatures across the UK and parts of Europe and North America. Monthly AO values since 1950 (Fig. 2.30b) indicate that the December 2009 value was the lowest December value in that record.

2) SURFACE WIND SPEED—C. Mears

Surface wind speed over the world's oceans began to be monitored continuously with

Fig. 2.28. The Australian Bureau of Meteorology SOI for (top) 1876 to 2009 and (bottom) from 2000 to 2009 relative to the 1876 to 2009 average.

FIG. 2.30. (a) The daily AO index from 31 Aug 2009 to 29 Dec 2009 is constructed by projecting the daily (00Z) 1000mb height anomali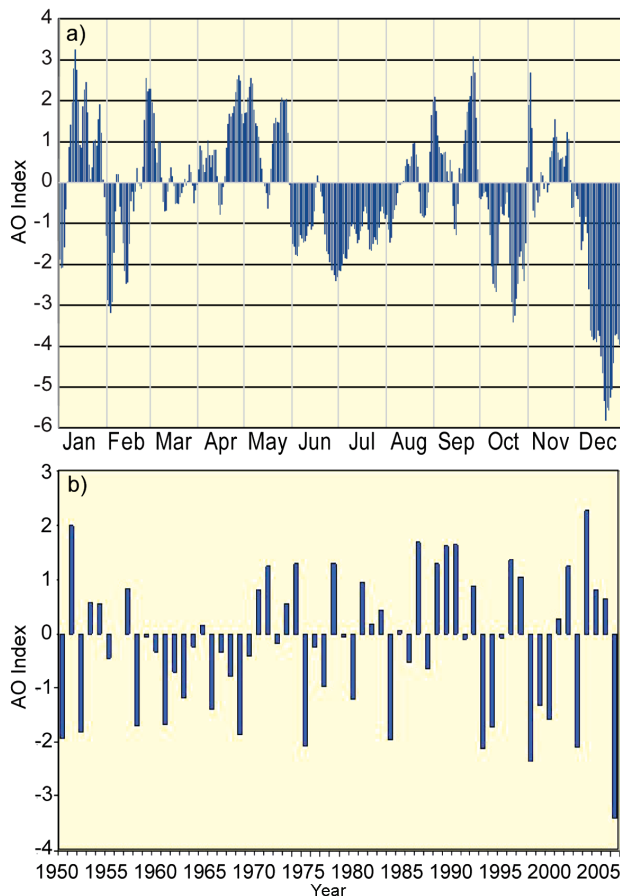es poleward of 20°N onto the loading pattern of the AO. The loading pattern is defined as the leading mode of an EOF analysis of monthly mean 700-hPa height anomalies onto the EOF mode. (b) Constructed as in (a) for monthly December values.
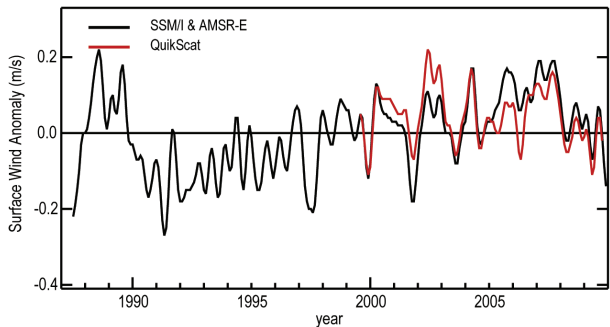

FIG. 2.31. Surface wind speed anomalies over the global ice-free oceans as measured by Remote Sensing Systems from the SSM/I and the Advanced Microwave Scanning Radiometer EOS (AMSR-E) instruments. The time series has been smoothed to remove variability on time scales shorter than 4 months. The reference period for the combined AMSR-E and SSM/I measurements is 1988–2007. For the QuikSCAT measurements the reference period is 2000–2007, with the mean adjusted to match the SSM/I anomalies for 2000–07.

2007. In 2008 and 2009, global wind speed fell slightly. Wind speeds derived from the QuikSCAT microwave scatterometer (Lungu and Callahan 2006), carried on a different satellite than the SSM/I instrument, using a different measurement technology show nearly identical results. Surface wind speed is dominated by short-term variability making it difficult to discern long-term trend behavior.

Winds in the tropics, especially the central tropical Pacific, were sharply reduced during 2009 (Fig. 2.32, Fig. 2.33), as the tropical pacific transitioned to El Niño. Positive wind anomalies in the Atlantic around 45°N coincided with a negative phase of the NAO/AO (Hurrell et al. 2003; Fig. 2.30b) during much of 2009 (Plate 2.1, Fig. 2.33).

the launch of the first Special Sensor Microwave/Imager (SSM/I) satellite in late 1987. The SSM/I instrument is a microwave radiometer that makes measurements of upwelling microwave radiation to infer the surface roughness of the worlds oceans and thus, the surface wind speed (Wentz 1997). Since the first SSM/I instrument, a number of additional microwave imaging sensors have been launched and intercalibrated to the accuracy necessary for climate studies (Wentz et al. 2007). Globally-averaged winds (Fig. 2.31) exhibited a maximum in 1988/89, followed by a minimum in 1991, and then an increasing trend in global winds from 1990 to
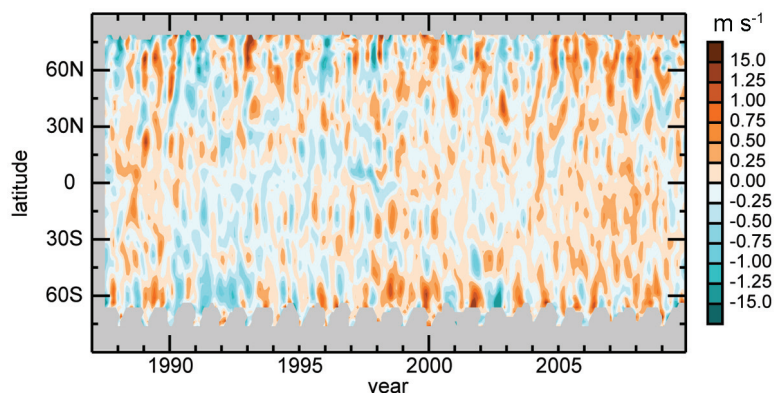

FIG. 2.32. As for Fig. 2.1 but for surface wind speed anomalies (reference period 1988–2007) over the ice-free oceans. Data have been smoothed in time to remove variability on time scales shorter than 4 months.
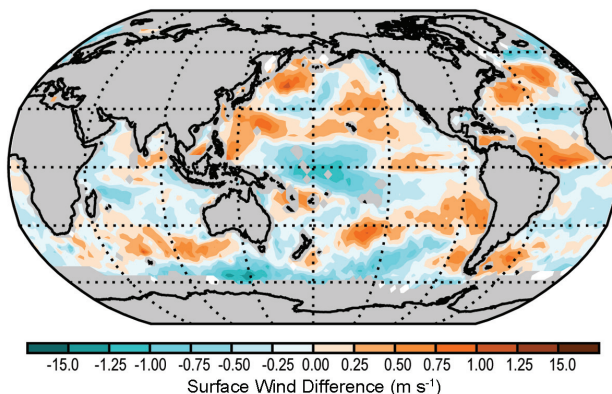
FIG. 2.33. Map of the difference in annual mean wind speed, 2009 minus 2008 calculated using data from AMSR-E.

e. Earth radiation budget at top-of-atmosphere—P. W. Stackhouse, Jr., T. Wong, N. G. Loeb, D. P. Kratz, A. C. Wilber, D. R. Doelling, and L. C. Nguyen

Preliminary analysis suggests that both the global-annual mean outgoing longwave radiation (OLR) and the reflected shortwave radiation increased slightly by ~0.1 Wm^{-2}, from 2008 to 2009 (Table 2.4). There was very little annual average change in the total solar irradiance (< 0.01 W m^{-2}) since the solar activity remained at minimum during the period. Thus, the combined longwave and shortwave changes caused a reduction of ~0.2 Wm^{-2} in total net radiation into the Earth climate system in 2009. These initial results derived from the Clouds and the Earth's Radiant Energy System (CERES; Wielicki et al. 1998) Fast Longwave and Shortwave Radiative Fluxes (FLASHFlux) dataset (Stackhouse et al. 2006; L'Ecuyer et al. 2008) may still include small instrument drift artifacts between January 2008 and December 2009. Reassessments of these results are expected in the forthcoming CERES Edition 3 instrument calibration data and after CERES FLASHFlux is upgraded to provide global gridded monthly anomaly information. Relative to the multiyear dataset average for 2001 to 2008, the 2009 global-annual mean anomaly (Table 2.4) is -0.4/0.0/+0.4 W m^{-2} for longwave/shortwave/total net radiation, respectively. These are within their corresponding 2-sigma interannual variabilities for this period.

Global monthly deseasonalized anomalies since March 2000 have been constructed by merging Earth Radiation Budget (ERB) datasets from two sources: a new CERES SSF (Single Scanning Footprint) 1x1 Degree Lite (SSF 1Deg Lite; a Top-of-Atmosphere [TOA] only version) using the Edition 2.5 instrument calibration; and CERES FLASHFlux (Fig. 2.34). TOA Fluxes from both datasets in the year 2007 were used to normalize the FLASHFlux data to SSF 1Deg Lite. The 2-sigma monthly uncertainty from the overlapped period is ±0.4/±0.9/±1.3 Wm^{-2} for the longwave/shortwave/net radiation, respectively. By mid-2009, the decrease in the OLR and the increase in the total net TOA flux continuing from late 2008 peaked and then reversed sign. Smoothed averaged TOA OLR shows a general agreement in fluctuations with a similarly smoothed Multivariate ENSO Index where the index peaked negatively in late 2008/early 2009 and reversed sign during the year. Thus, it appears that change in El Niño intensity is largely responsible for the global averaged monthly TOA variability during this time period. Linear trend analyses are not recommended due to the natural fluctuation in ERB relating to ENSO activity in the short record, large uncertainty from the data merging process, and instrument drift potential in the FLASHFlux data. A long-term homogeneous data source with in-depth instrument stability analysis is needed to reduce these uncertainties for future reassessment activity.

f. Atmospheric composition

1) ATMOSPHERIC CHEMICAL COMPOSITION—R. C. Schnell

(i) Carbon dioxide, methane, and carbon monoxide—E. J. Dlugokencky

(A) CARBON DIOXIDE (CO$_2$)

Since 1750, ~335 billion tons of carbon has been emitted into the atmosphere by human activities, about half of this since the mid-1970s (Marland et al. 2008), and emissions rates increased by > 3% from 2000–04 (Raupach et al. 2007). Atmospheric CO$_2$ has increased from about 280 ppm at the start

TABLE 2.4. Summary of the 2009 global-annual mean TOA radiative flux component (W m^{-2}) changes relative to 2008 and the 2001–2008 climatology. TOA Total Net = Incoming (SW) – Outgoing (SW+LW).

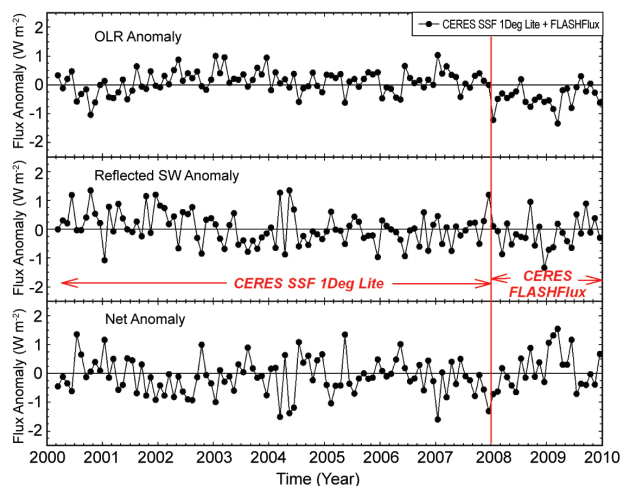|	2009 minus 2008	2009 anomaly (relative to a 2001-08 climatology)	2-sigma Interannual variability 2001 to 2008
Outgoing Longwave	0.1	-0.4	±0.6
Reflected Shortwave	0.1	0.0	±0.4
Total Net (>0 into system)	-0.2	0.4	±0.6

FIG. 2.34. Time series of global-monthly mean de-seasonalized anomalies of TOA Earth Radiation Budget for longwave (top panel), shortwave (middle panel), and net radiation (bottom panel) from March 2000 to December 2009. Anomalies are computed relative to the calendar month climatology derived for the March 2000 to December 2009 period. The vertical red line in the figure separates the portion of the time series that is constructed using the CERES SSF 1Deg Lite (3/2000 to 12/2007) and the CERES FLASHFlux (1/2008 to 12/2009) dataset, respectively. Mean differences between datasets were removed using available data from the overlap year 2007 and the combined ERB time series was anchored to the absolute value of CERES SSF 1Deg Lite before de-seasonalization (Source: The official data file name of the CERES SSF 1Deg Lite is CER_SSF1deg_month-lite and is available at http://science.larc.nasa.gov/ceres/).

of the industrial revolution to more than 380 ppm today. About half of the emitted CO_2 remains in the atmosphere after a year, and after a millennium, ~20% remains (Archer and Brovkin 2008).

The preliminary globally averaged atmospheric CO_2 mole fraction in 2009 was 386.29 ppm; 1.5 ppm more than 2008 (see Conway et al. (1994) for a description of sampling network and methods). This is slightly greater than the average rate of increase from 1979 through 2008 of 1.63 ppm yr^{-1}. Despite fossil CO_2 emissions being predominantly in the northern hemisphere, the rate of increase of atmospheric CO_2 is approximately geographically uniform (Fig. 2.35). The amplitude of the seasonal cycle varies based on exposure of air masses arriving at the sites to the terrestrial biosphere, but there are no significant differences in long-term trends.

(B) METHANE (CH₄)

After a decade of near-zero growth, atmospheric methane increased globally in 2007 and 2008 by ~7.5 ppb yr^{-1} (Rigby et al. 2008; Dlugokencky et al. 2009), mostly from emissions in the Arctic in 2007 and Tropics in 2007 and 2008. Likely drivers for increased emissions are anomalously high temperatures and precipitation in wetland regions, particularly in the Arctic during 2007. In 2009, globally averaged atmospheric CH_4 increased again (by 6.5 ppb) to 1793.9 ppb, but the main drivers of the continued increase are unclear. The current atmospheric CH_4 observing network, including in situ and remotely-sensed observations, is insufficient to determine with certainty the causes of CH_4 increases over the past three years (see Fig. 2.35).
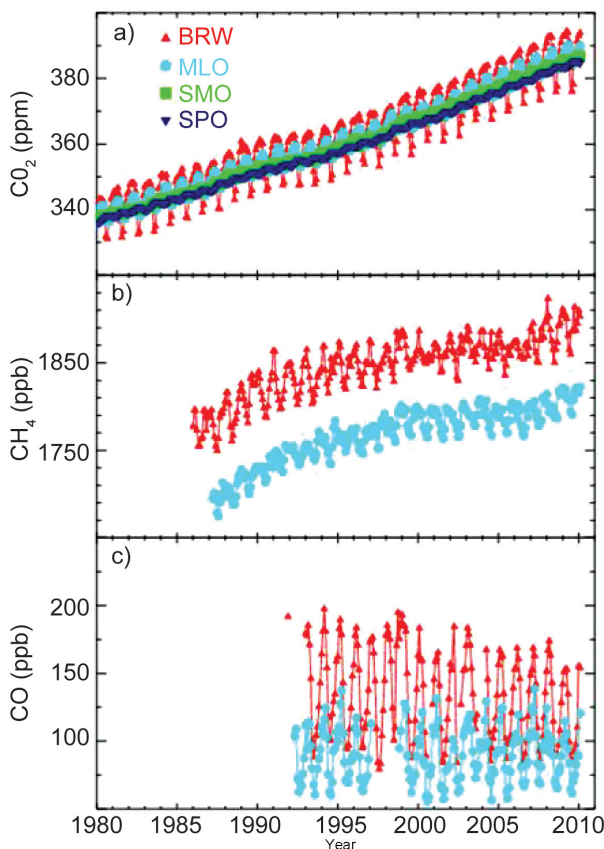
FIG. 2.35. Monthly mean mole fractions determined from NOAA/ESRL Observatories at Barrow, Alaska (BRW); Mauna Loa, Hawaii (MLO); American Samoa (SMO); and South Pole (SPO) for (a) CO₂, (b) CH₄, and (c) CO. 2009 results are preliminary. Monthly means are courtesy of Kirk Thoning (CO₂), Ed Dlugokencky (CH₄), and Paul Novelli (CO), all from NOAA/ESRL. Additional plots can be found at: http://www.esrl.noaa.gov/gmd/ccgg/iadv/ and http://www.esrl.noaa.gov/gmd/Photo_Gallery/GMD_Figures/ccgg_figures/.

(C) Carbon monoxide (CO)

There has been no long-term CO trend since ESRL measurements began in 1990 (Novelli et al. 2003), but CO anomalies occurred during 1997 to 1998, and again in 2002 to 2003. These anomalies are likely the result of tropical (Langenfelds et al. 2002) and boreal biomass burning (Kasischke et al. 2000). Since the lifetime of CO is relatively short (few months), the CO enhancements quickly disappeared. The preliminary globally averaged CO mole fraction in 2009 is 80 ppb, 15 ppb lower than 1998. ESRL's surface sampling network is less sensitive to biomass burning emissions of CO than remotely sensed CO observations, such as MOPITT (Measurements Of Pollution In The Troposphere; Pan et al. 1998), because emissions are rapidly transported away from the surface where the sampling sites are. The combination of surface measurements and MOPITT retrievals provide useful auxiliary information in determining the contribution of biomass burning to recent increases in atmospheric CH_4 (see Fig. 2.35).

(ii) Changes in atmospheric abundances of ozone-depleting gases and their replacements—S. A. Montzka and G. S. Dutton

Long-lived halocarbons affect the radiative balance of the atmosphere because they efficiently absorb terrestrial infrared (IR) radiation. Those containing bromine (Br) and chlorine (Cl) also influence the radiative atmospheric balance indirectly through their destruction of stratospheric ozone. Through amendments and adjustments to the 1987 Montreal Protocol on Substances that Deplete the Ozone Layer, the decline in mixing ratios of most of the potent ozone-depleting gases continued in 2009 (Fig. 2.36). However, mixing ratios of some halogenated gases continue to increase globally. The most rapid increases are observed for hydrochlorofluorocarbons (HCFCs) and hydrofluorocarbons (HFCs), common replacements for chlorofluorocarbons (CFCs), halons, and other ozone-depleting gases. Increases in HCFCs have recently accelerated owing to enhanced use in developing countries

(Montzka et al. 2009). Both HCFCs and HFCs are efficient absorbers of infrared radiation (Table 2.5). HCFCs contain chlorine but have smaller influence on ozone than the CFCs; HFCs do not cause ozone destruction.

The influence of halocarbon trace-gas trends on future levels of stratospheric ozone can be estimated from weighted sums of Cl and Br in long-
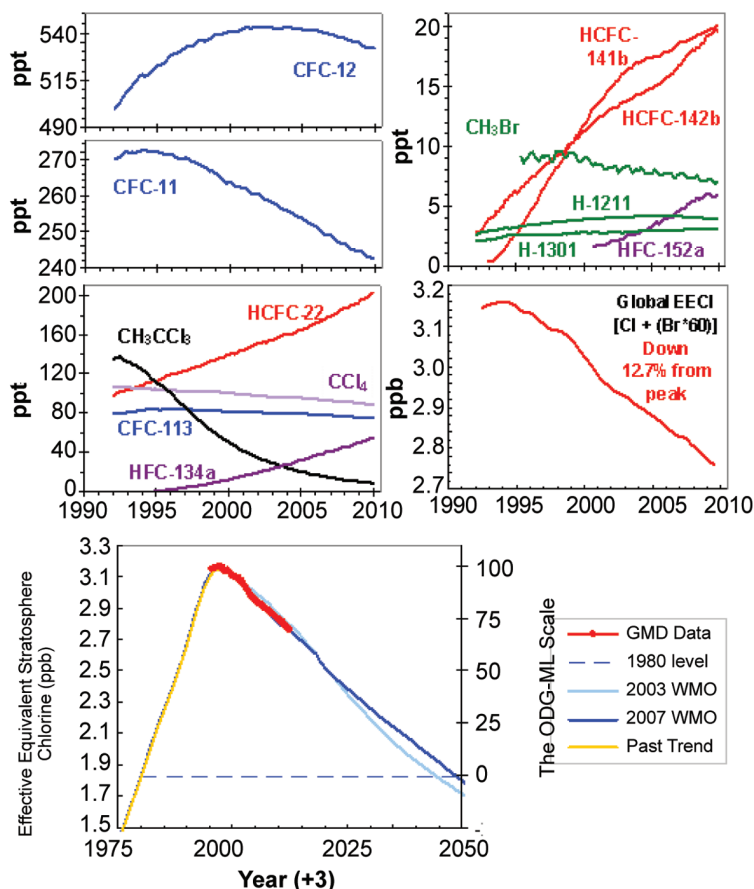
FIG. 2.36. Changes in global mean tropospheric mixing ratios (in ppt, or pmol mol⁻¹) of the most abundant CFCs, HCFCs, HFCs, chlorinated solvents, and brominated gases. The middle-right hand panel shows secular changes in atmospheric effective equivalent chlorine (EECl; in ppb or nmol mol⁻¹), which is an estimate of the ozone-depleting power of these atmospheric halocarbons. EECl is derived from observed mixing ratios of ozone depleting gases appearing in the other 4 panels, and it is derived from the sum of [Cl + (Br×60)] contained in these gases. The bottom panel shows the recent changes in Effective Equivalent Stratospheric Chlorine (EESC) observed by the NOAA/GMD global network relative to the secular changes observed in the past, including the level observed in 1980 when the ozone hole was first observed, and a projected future. The Ozone Depleting Gas Index for mid-latitudes is derived (right hand axis) from rescaling EESC. EESC is derived from EECl by simply adding 3 years to the time axis to represent the lag associated with mixing air from the troposphere to the middle stratosphere, where the ozone layer resides (Source: updates to Montzka et al. [1996, 1999].)

lived halocarbons. In the midlatitudes, this influence is expressed as effective equivalent chlorine (EECl; Fig. 2.36) and is derived from surface-based measurements. It provides an estimate of the near-future ozone-depleting power of trace gases (EESC, Fig. 2.36), when air at the Earth's surface will have become mixed into the midlatitude stratosphere. A second metric, equivalent chlorine (ECl, not shown), provides an estimate of the ozone-depleting power of trace gases in the near future for the stratosphere over the Polar Regions.

The EECl content of the lower atmosphere has declined fairly steadily since the peak in 1994 through 2009 at a mean rate of 28 ppt yr^{-1}. Despite these substantial changes, full recovery of stratospheric ozone is not expected until the middle to latter part of the 21st century owing to the long lifetime of many of these chemicals (lower panel of Fig. 2.36; Table 2.5). Progress towards EECl reductions can now be readily assessed with the NOAA Ozone-Depleting Gas Index (ODGI) (Hofmann and Montzka 2009). In 2009 the ODGI for the midlatitudes was 68.7 and the ODGI for Antarctica derived from ECl estimates was 83.5 (not shown).

(iii) The combined influence of long-lived trace gases on the radiative balance of the atmosphere.—S. A. Montzka

Long-lived trace gases have a direct and indirect influence on the energy balance of the atmosphere. The direct radiative influence of a trace gas is proportional to its atmospheric abundance and its radiative efficiency (Table 2.5). High precision measurements of the major long-lived greenhouse gases and 15 minor greenhouse gases (Table 2.5) have been used to calculate the overall change in the direct radiative climate forcing (Hofmann et al. 2006) (Fig. 2.37). By mid-2008, the increases in the abundances of all these gases amounted to an additional direct radiative forcing to the atmosphere totaling approximately 2.74 W m^{-2}, changes in the abundance of CO_2 accounting for 63% of this enhanced radiative forcing.

The NOAA Annual Greenhouse Gas Index (AGGI)(Hofmann et al. 2006) is calculated as a ratio relative to the direct radiative forcing calculated from these gases for 1990; indirect effects (e.g., arising from ozone depletion or water-vapor feedbacks) are not considered. Preliminary data indicated that the 2009 AGGI was 1.275 (Fig. 2.37) and CO_2 had accounted for about 80% of the observed increase since 1990.
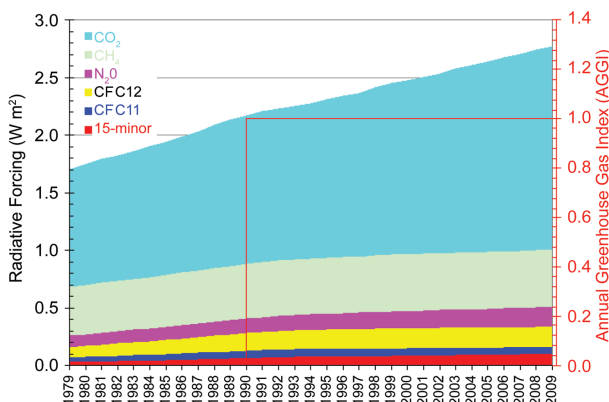

FIG. 2.37. The NOAA Annual Greenhouse Gas Index (AGGI) shows radiative forcing relative to 1750, of all the long-lived greenhouse gases indexed to 1 for the year 1990. Since 1990, radiative forcing from greenhouse gases has increased 27.5%.

(iv) Nitrous oxide (N$_2$O) and sulfur hexafluoride (SF$_6$)—J. W. Elkins and G. S. Dutton

Nitrous oxide (N$_2$O) and sulfur hexafluoride (SF$_6$) are important atmospheric trace gases with significant man-made sources. Nitrous oxide has the third strongest anthropogenic climate forcing after CO_2 and CH_4 and is considered a major greenhouse gas (Butler 2009). Atmospheric N$_2$O is also responsible for stratospheric ozone depletion by providing a source of stratospheric nitric oxide (Ravishankara et al. 2009). The 2009 mean global concentration of N$_2$O was 322.5 ± 0.1 ppb yr^{-1} (Fig. 2.38 top panel). Its mean global growth rate since 1977 is 0.733 ± 0.002 ppb but with substantial interannual variation (Fig. 2.38 bottom panel). The atmospheric N$_2$O budget is out of balance by one-third as a result of man-made emissions, primarily through emissions from nitrogen fertilizers (Crutzen et al. 2007).

Sulfur hexafluoride has one of the strongest Global Warming Potentials (GWP) of all trace gases at 23 900 times CO_2 with a 100-yr time horizon (Solomon et al. 2007) with the fifth strongest climate forcing of the 10 minor greenhouse gases (Hofmann et al. 2006). Its global average concentration for 2009 was 6.76 ± 0.07 parts-per-trillion dry by mole fraction (ppt) (Fig. 2.38 top panel) and thus its climate forcing contribution is small. The atmospheric lifetime of SF$_6$ is long (3200 yr); so, many developed countries have instituted voluntary programs with suppliers and utilities to reduce their emissions. The global atmospheric growth rate peaked at 0.32 ppt yr^{-1} in 2008 but in 2009 decreased, perhaps as a result of the recent global economic recession and voluntary efforts by countries to reduce emissions (Fig. 2.38 bottom panel).

Industrial Designation or Common Name	Chemical Formula	AGGI	ODGI	Radiative Efficiency (Wm^{-2} ppb^{-1}) *	Mean suface mixing ratio mid-2009 [change from 2008 to 2009][a]	Lifetime
TABLE 2.5. Mixing ratios, radiative efficiencies and lifetimes of chemicals considered in the AGGI.						
Carbon Dioxide	CO_2	Y	N	1.41×10^{-5}	386.3[1.5]	NA
Methane	CH_4	Y	N	3.7×10^{-4}	1.79 [6.5×10^{-3}]	9.0
Nitrous oxide	N_2O	Y	N	3.03×10^{-3}	322.5[0.6]	114
Chlorofluorocarbons						
CFC-11	CCl_3F	Y	Y	0.25	243.3[-1.8]	45
CFC-12	CCl_2F_2	Y	Y	0.32	532.6[-3.0]	100
CFC-113	CCl_2FCClF_2	Y	Y	0.30	75.9[-0.5]	85
Hydrochlorofluorocarbons						
HCFC-22	$CHClF_2$	Y	Y	0.20	198.4[8.7]	12.0
HCFC-141b	CH_3CCl_2F	Y	Y	0.14	19.8[0.6]	9.3
HCFC-142b	CH_3CClF_2	Y	Y	0.20	19.4[1.1]	17.9
Hydrofluorocarbons						
HFC-134a	CH_2FCF_3	Y	N	0.16	52.5[4.8]	14
HFC-152a	CH_3CHF_2	N	N	0.09	5.9[0.3]	1.4
Chlorocarbons						
Methyl Chloroform	CH_3CCl_3	Y	Y	0.06	9.2[-1.6]	5.0
Carbon Tetrachloride	CCl_4	Y	Y	0.13	89.4[-1.4]	26
Methyl Chloride	CH_3Cl	N	Y	0.01	542[-2]	1.0
Bromocarbons						
Methyl Bromide	CH_3Br	N	Y	0.01	7.3[-0.0-2]	0.7
Halon 1211	$CBrClF_2$	Y	Y	0.30	4.0[-0.05]	16.0
Halon 1301	$CBrF_3$	Y	Y	0.32	3.1[0.02]	65
Halon 2402	$CBrF_2CBrF$	N	Y	0.33	0.45[-0.01]	20
Fully fluorinated species						
Sulfur Hexafluoride	SF_6	Y	N	0.52	6.76[0.26]	3,200

NA = Not applicable; the lifetime of CO_2 cannot be expressed as a single number (Archer and Brovkin 2008).

* Radiative forcings and lifetimes are taken from Daniel et al. (2007) and Clerbaux and Cunnold et al. (2007).

[a] Mixing ratios are measured global surface means determined from NOAA global cooperative sampling network (Hofmann et al. 2006). Changes indicated in brackets are simply the difference between the 2009 and 2008 annual global surface mean mixing ratios. Units are ppm for CO_2, ppb for CH_4 and N_2O, and ppt for all others.

2) GLOBAL AEROSOLS—J.W. Kaiser, A. Benedetti, and J.-J. Morcrette

Atmospheric aerosols influence atmospheric radiation and cloud droplet nucleation. Inadequate understanding of these direct and indirect effects dominates uncertainty of the radiative forcing in climate projections from climate models (Alley et al. 2007). The aerosol sources are influenced by changes in land cover, wind and precipitation patterns, and human activities. Global monitoring of aerosols remains a substantial scientific challenge due to their large variability and heterogeneity in chemical composition and size. Current routine ground- and satellite-based observations of aerosols cannot provide high temporal
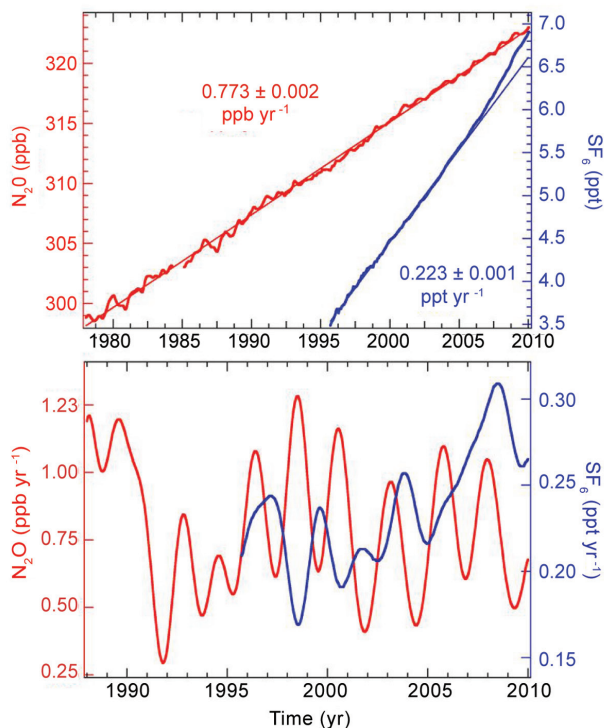
Fig. 2.38. (top) Global monthly means along with estimates for the linear growth rate of atmospheric nitrous oxide (N_2O, red) in ppb and sulfur hexafluoride (SF_6, blue) in ppt from the NOAA/ESRL halocarbon network (binomial smoothing with 3 month filter). (bottom) Instantaneous growth rate of N_2O and SF_6 of data above using a FFT smoothing algorithm (Thoning et al. 1989) with a two year filter, note the rise of the atmospheric SF_6 growth rate after 2003. Atmospheric data for N_2O prior to 1989 and for SF_6 prior to 1999 were analyzed from flasks instead of continuously operating instruments at NOAA/ESRL baseline observatories.

resolution global coverage and yield only very limited information on the chemical composition, size distribution, and vertical profiles.

The Global and regional Earth-system Monitoring using Satellite and in-situ data project (GEMS, Hollingsworth et al. 2008) has created a continuous space-time representation of the global aerosol distribution since 2003. It assimilates 550 nm aerosol optical depth (AOD) observations from Moderate Resolution Imaging Spectroradiometer (MODIS) into ECMWF's numerical weather prediction model extended to include the sources, sinks, and transport and conversion processes of several aerosol species (Benedetti et al. 2009; Morcrette et al. 2009). Monitoring Atmospheric Composition and Climate (MACC), the follow-up project of GEMS,

is currently producing real-time aerosol analyses and forecasts and a new reanalysis starting in 2003, both with improved model, emission inventories and data assimilation system. Total AOD is strongly constrained by observations over ocean but over land, the total AOD information is a mix from observations and model. Total AOD at high latitudes and the relative distribution between the aerosol species at all latitudes come largely from the model.

On a global scale, the aerosol distribution up to September 2009 appears to have been in line with previous years back to 2003 (Fig. 2.39). The largest contribution to AOD comes from organic matter, closely followed by sea salt, then dust and sulfate. Dust aerosols have a fairly regular annual cycle with a maximum in the Northern Hemisphere summer. Organic matter varies with a higher frequency and more variability, but less amplitude than dust. Sea salt and black carbon exhibit little variability.

Sea salt aerosols are associated with storms, particularly in the Southern Ocean (Fig. 2.40). Dust is lifted by strong winds from bare soils and deserts; the Sahara, with its dust outflow over the Atlantic, is most pronounced. Organic matter and black carbon are dominantly produced by biomass burning at low-latitudes and to a lesser degree in boreal forests. Even though black carbon has a relatively low AOD, as the most absorbing aerosol type, it has a large impact on atmospheric radiation. The distribution of sulfate aerosols reflects the anthropogenic emission inventory that was used in the model with rather localized sources in North America, Europe, India, and China.

3) Stratospheric ozone—M. Weber and W. Steinbrecht

The 2009 annual mean anomaly of total column ozone was generally positive (compared to the 1996 to
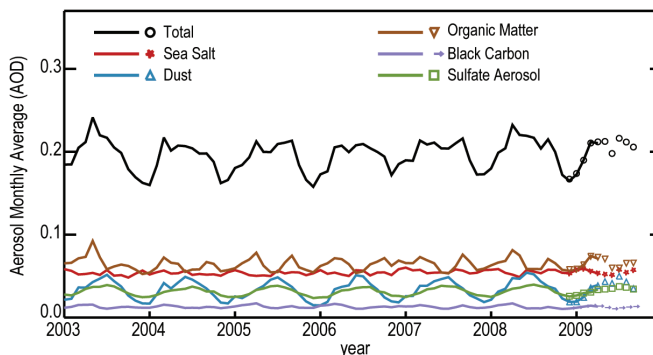

Fig. 2.39. Global, monthly average optical depth at 550 nm of total aerosols for January 2003–September 2009 and the individual contributions of sea salt, dust, organic matter, black carbon and sulfate aerosols. Lines: reanalysis. Symbols: real-time analysis/forecast.
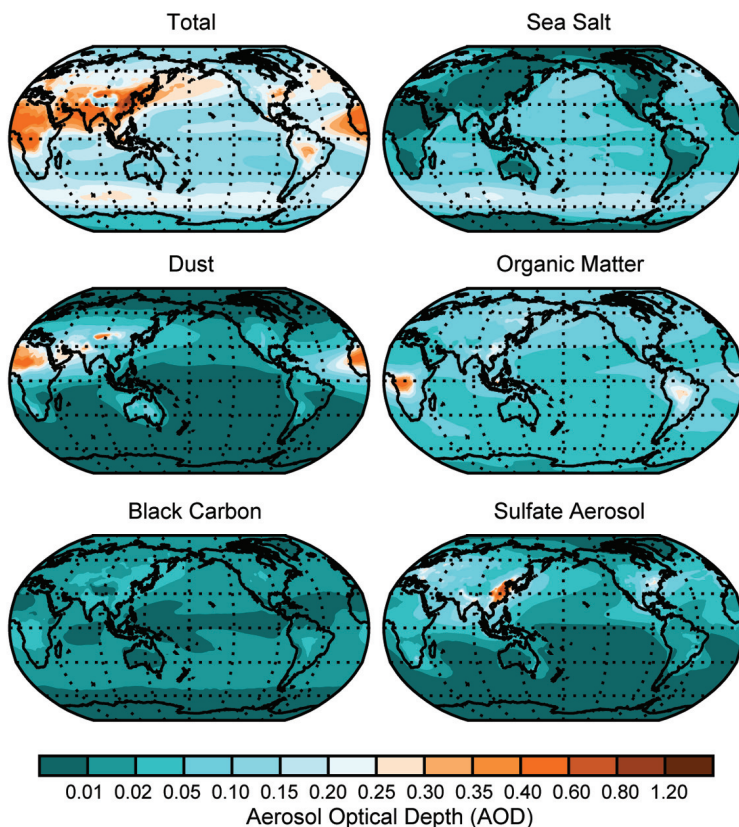
Fig. 2.40. Distribution of average optical depth at 550 nm in 2003–08 of total aerosols and the individual contributions by total, sea salt, dust, organic matter, black carbon and sulfate aerosols.

ozone is dominated by the QBO (see Section 2b4; Baldwin et al. 2001). During 2009, the QBO phase (stratospheric equatorial winds near 50 hPa) changed from west to east. This led to negative total ozone anomalies in the second half of 2009. The QBO has a periodic signature in tropical (and extratropical) total ozone (Fig. 2.41). Plate 2.1 and Fig. 2.41 show that the 2009 Antarctic ozone hole was slightly larger than the long-term mean, comparable to 2007, but not as large as in 2008, or in the record year of 2006.

The trend in the global annual mean total ozone (Fig. 2.42a) has its main contribution from changes at midlatitudes in both hemispheres (Fig. 2.42b,d), while tropical ozone (Fig. 2.42c) does not show a significant trend. The long-term decrease starting in the 1970s slowed by the mid-1990s and has since leveled off in the extratropics. The substantial minimum in the Northern Hemisphere in the mid-1990s is due to intensification of the chlorine induced ozone decline by the Mount Pinatubo volcanic eruption and by a series of unusually cold Arctic winters with reduced ozone transport and high polar ozone loss (Dhomse et al. 2006). It is expected that total ozone should recover since stratospheric halogen has levelled off and is now declining (Section 2f1ii). However, other factors, e.g., changes in the Brewer-Dobson circulation, annular modes of internal variability, or the 11-year solar cycle also contribute to decadal changes (Appenzeller et al.

2009 climatological mean) except for a narrow band in the tropics, a small region over the North Pacific, and above Antarctica (Plate 2.1). Maximum positive anomalies of up to about 20 Dobson Units (DU) occurred at northern mid- to high latitudes, from the North Atlantic to Russia. Positive anomalies were also observed at similar latitudes in the Southern Hemisphere. The largest year-to-year variability is normally observed during winter/spring in each hemisphere. In February and March 2009 positive anomalies of over 50 DU were observed over Europe and Russia and much of the north polar region. However, a region above the Aleutian peninsula, characterized by the Aleutian high, associated with a high tropopause and dynamically reduced column ozone, experienced a -25 DU anomaly. During Arctic winter an unusually large sudden stratospheric warming (SSW) event occurred in January 2009 (Fig. 2.9), contributing to a weaker than usual Arctic vortex and increased ozone transport into high latitudes (Labitzke and Kunze 2009).

Negative anomalies were observed in the tropics within a narrow 20° latitude band around the equator. Interannual modulation of tropical stratospheric
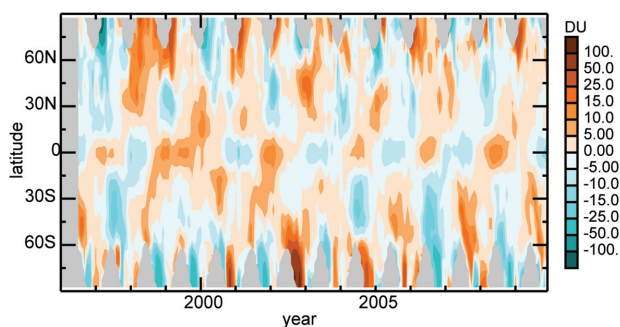

Fig. 2.41. As for Fig. 2.1 but for total ozone anomalies. Anomalies are based on the merged GOME1/SCIA-MACHY/GOME2 merged total ozone (Weber et al. 2007). Anomalies were calculated from area weighted monthly mean zonal mean data in 5° latitude steps after removing the seasonal mean from the period 1996–2009.
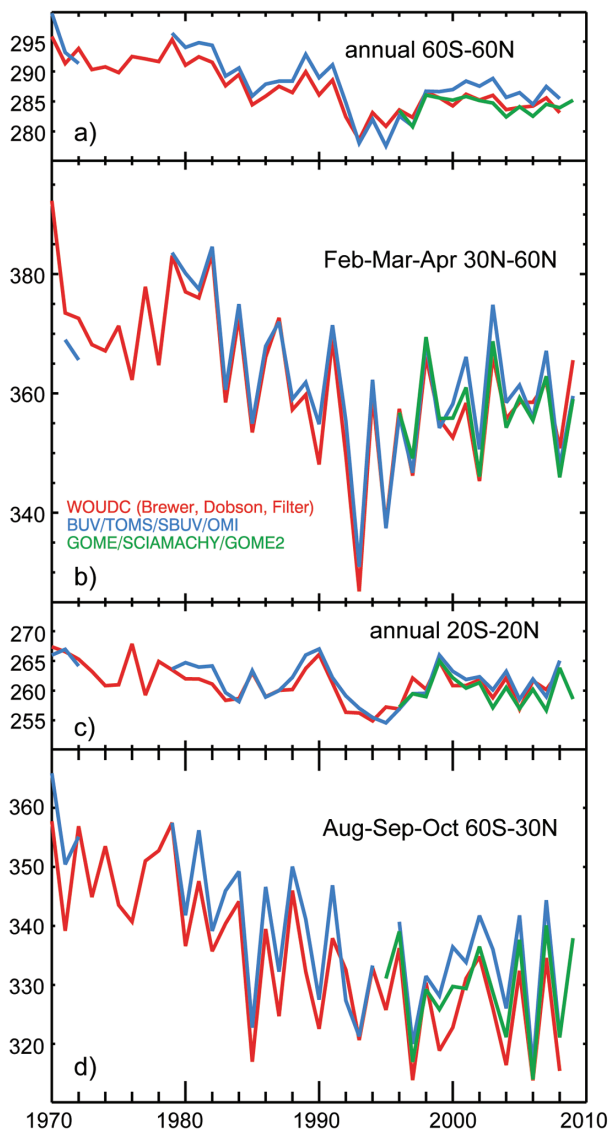
Fig. 2.42. Total ozone time series of ground-based measurements combining Brewer, Dobson, and filter spectrometer data (red, Fioletov et al. 2002), the merged BUV/SBUV/TOMS/OMI (blue, Frith et al. 2004), and GOME1/SCIAMACHY/GOME2 (green, Weber et al. 2007) merged data sets in the (a) 60°N-60°N (annual mean), (b) 30°N-60°N (FMA mean), (c) 20°S-20°N (annual mean), (d)and 60°S-90°S (ASO mean).

2001; Weber et al. 2003; Orsolini 2004; Yang et al. 2005; Dhomse et al. 2006; Stolarski and Frith 2006; Vyushin et al. 2007; Harris et al. 2008).

The upper stratospheric ozone is a better diagnostic to look for ozone recovery because chlorine induced chemical ozone changes there are larger than the changes in column ozone (Newchurch et al. 2003). Also, atmospheric transports play a lesser role. Ozone in the upper stratosphere declined substantially, by 10% to 15%, from the early 1980s to

the mid-1990s but has since levelled off (Fig. 2.43). In the last 10 years, the various records show signs of an increase (Steinbrecht et al. 2009; A. Jones et al. 2009). This long-term behavior of ozone in the upper stratosphere is in agreement with the earlier large increase and subsequent decline of the stratospheric halogen load (Fig. 2.36). Superimposed are quasi-
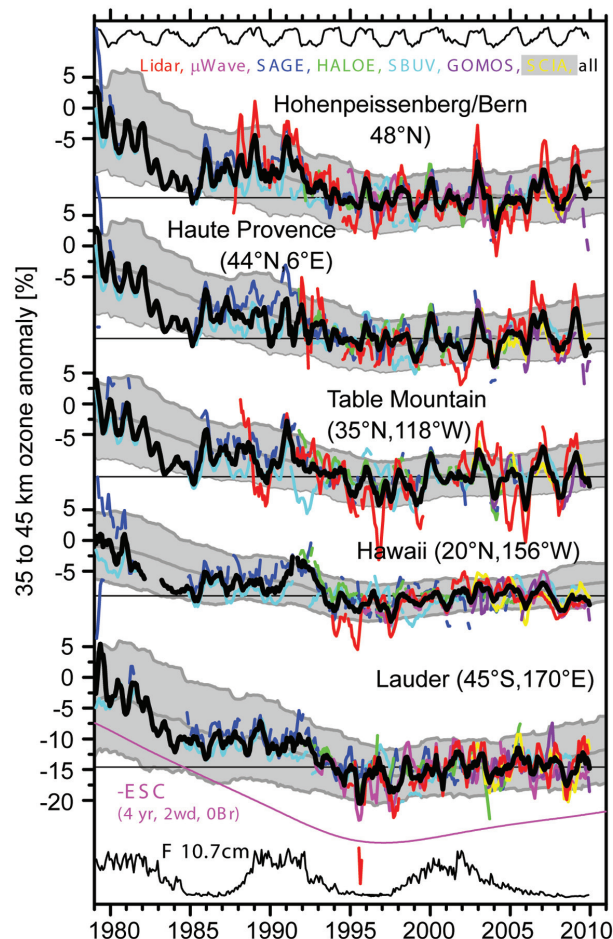
Fig. 2.43. Upper stratospheric ozone anomalies from ground-based stations (lidar, microwave radiometer) and satellite instruments (SBUV, SAGE, HALOE, GOMOS, SCIAMACHY, zonal means within ±5° latitude of the stations). Data are 5-month running mean anomalies (with the 1998 to 2008 climatology subtracted), averaged from 35 to 45 km altitude (Steinbrecht et al. 2009). Scale is shifted, so that the 1979 all instrument average (black line) is at zero. Grey underlay: Mean ±2σ standard deviation of model runs from the CCMVal initiative (Eyring et al. 2006). Black lines at top and bottom: Proxies for QBO and 11-year solar cycle, i.e. negative equatorial wind at 10 hPa (http://www.geo.fu-berlin.de/en/met/ag/strat/produkte/qbo/index.html) and solar radio flux at λ=10.7 cm (http://www.ngdc.noaa.gov/stp/SOLAR/), respectively. Pink line near bottom: Effective stratospheric chlorine (inverted, from Newman et al. 2007, age-of-air: 4±2 years).

biennial and decadal ozone variations, which follow the QBO and the 11-year solar cycle. In late 2009, the QBO phase (beginning westerly at 10 hPa, easterly at 50 hPa, see section 2b4) and the continuing solar minimum both contributed to low levels of upper-stratospheric ozone. On the whole, however, the observed long-term behavior confirms model results with an ongoing slow recovery of upper stratospheric ozone expected.

g. Land surface properties

1) Alpine glaciers and ice sheets—M. S. Pelto

The World Glacier Monitoring Service (WGMS) records of mass balance (difference between accumulation and ablation) and terminus behavior (WGMS 2009; WGMS 2008) provide global indices of alpine glacier behavior. Mass balance was negative in 2008 for the 18th consecutive year. Preliminary 2009 data from Austria, Norway, New Zealand, and the United States indicate it is highly likely that it was the 19th consecutive year of negative annual balances. The worldwide retreat of mountain glaciers is one of the clearest signals of ongoing climate change (Haeberli and Hoelzel 1995).

Alpine glaciers have been studied for more than a century (Oerlemans 1994). The retreat of their termini is a reflection of strongly negative mass balances over the last 30 years (WGMS 2007) which when combined with recent rapid retreat has led to some glaciers disappearing (Pelto 2010).

The cumulative loss of the last 30 years averaged across 30 WGMS reference glaciers is 11.6 m water equivalent (w.e.), equivalent to slicing 13 m off the top of the average glacier (Fig. 2.44). The decadal mean annual mass balance was -198 mm in the 1980's, -382 mm in the 1990's, and -624 mm for 2000–08 (Fig.

2.45). The declining trend is remarkably consistent from region to region (WGMS 2009). A glacier with a sustained negative balance will retreat. Glacier retreat primarily results in the loss of the low-elevation region of a glacier; this potentially reduces total ablation, increases mass balance, and reestablishes equilibrium. Currently, despite sustained negative mass balance and significant glacier retreat, alpine glaciers are not approaching equilibrium. If a glacier experiences significant thinning in the upper regions during this retreat this is symptomatic of not having a sufficient accumulation zone to survive the current climate (Pelto 2010; Paul et al. 2007).

Of 93 Austrian glaciers surveyed in 2009, 85 receded, 7 were stationary, and 1 advanced with a mean terminus change rate of -14.3 m, slightly higher than in 2008. Winter accumulation on Austrian glaciers was about average and summer loss was above average due to higher than normal summer temperatures. The mass balance loss was larger than the decadal mean 1998–2008; Hintereisferner -1182 mm w.e., Kesselwandferner -795 mm w.e., and Jamtalferner -953 mm w.e. (A. Fischer, personal communication).

Over Switzerland 81 of the 88 glaciers examined retreated, 2 advanced, and 5 were stable in 2009. Overall mass balance was negative (Swiss Glacier Monitoring, personal communication).

Preliminary 2009 results indicate normal accumulation and ablation for Norway (L. Andreasson, personal communication). Terminus fluctuation data from 27 glaciers indicates 22 retreating, 3 stable, and 2 advancing with average terminus change of -18 m, compared to -13 m in 2008.

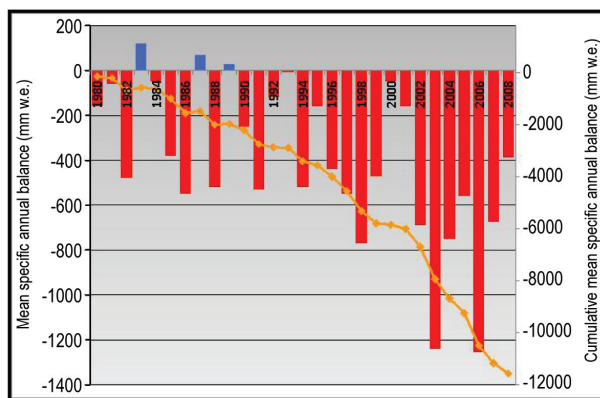In the North Cascades, Washington, (Pelto 2010) the ENSO transition led to negative mass balances

FIG. 2.44. The mean annual balance reported for the 30 reference glaciers to the WGMS (bars) and the cumulative annual balance for the reference glaciers (line).
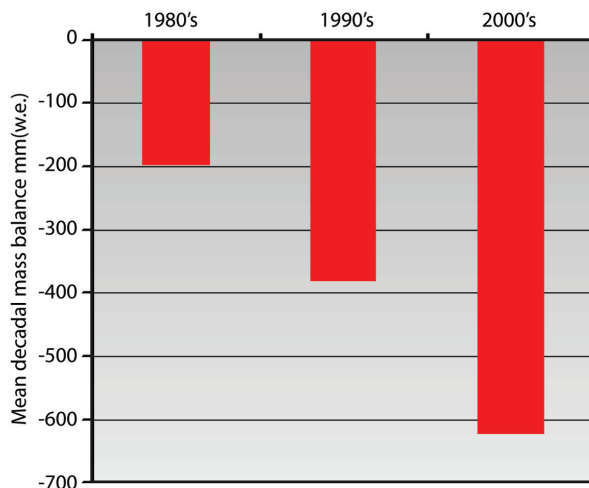

FIG. 2.45. The decadal mean cumulative specific mass balance (mm w.e.) for the 30 reference glaciers.

with all 42 glaciers observed retreating. Winter accumulation during La Niña was near normal, but summer melting as El Niño began was well above average leading to substantial negative balances on all 10 glaciers observed, averaging -1930 mm w.e.

In New Zealand, glaciers shrank between April 2008 and March 2009 owing to above normal temperatures and below normal rainfall in both winter and summer (J. Hendrikx, personal communication). On 50 glaciers surveyed the average snow line was 95 m above the equilibrium snow line elevation, the sixth highest in the 33 year record.

Negative anomalies in melting days occurred in 2009 in South and West Greenland, and positive anomalies in North and East Greenland as derived from SSM/I brightness temperatures relative to the 1979–2008 average (Tedesco et al. 2008). Melt extent was 670 000 km², slightly lower than in 2008. Surveys of Greenland marine terminating outlet glaciers from MODIS imagery (J. Box, personal communication) indicate that the 34 widest glaciers collectively lost 106.4 km² of ice extent between late summer 2008 and late summer 2009.

A 30-year minimum Antarctic snowmelt occurred during austral summer 2008/09 according to microwave satellite observations. Strong positive phases of the SOI and the Southern Hemisphere Annular Mode were recorded during the months prior to and including the 2008/09 melt season. Wilkins Ice Shelf experienced the highest number of melting days across Antarctica (90 days; Tedesco and Monaghan 2009), ending in the collapse in April 2009 of the last strip of ice connecting Wilkins Ice Shelf to Charcot Island.

2) Fraction of Absorbed Photosynthetically Active Radiation (FAPAR)— N. Gobron, W. Knorr, A. S. Belward, and B. Pinty

The state of vegetation has been monitored using monthly estimates of the FAPAR from NASA/SeaWiFS and ESA/MERIS from 1998 to 2009 (Gobron et. al. 2010, manuscript submitted to *Geophys. Res. Lett.*) FAPAR is largely controlled by Leaf Area Index (which controls attenuation of radiation) and to a lesser extent by the absorption efficiency of the vegetation elements composing the canopy and the soil background brightness (through backscattering processes). In Plate 2.1 the strongest positive anomalies for 2009, indicating favorable vegetation growing conditions, are found in eastern Brazil (Cerrado and Mid-Atlantic coastal region) and South Africa, while most of the rest of South America and east Africa exhibit the strongest negative anomalies. Persistent droughts in Southern America, East Africa, and Australia (WMO 2010) are clearly manifest in poor vegetation growth and vigor. The profound nature of the impact of these droughts is further illustrated in Fig. 2.46, which provides a seasonal breakdown. Figure 2.46 illustrates how the Southern Hemisphere contrasts sharply with the Northern Hemisphere—negative anomalies persist through all seasons in the south, while the north (especially central North America and western Europe) fluctuates between the two states. Pronounced positive anomalies of eastern Brazil are mainly due to FAPAR changes in the Southern Hemisphere winter and spring, i.e., the local dry season. The weaker positive anomaly in southern Africa and the strong negative anomaly in southeastern South America are manifest mainly during December 2008–February 2009. This period was characterized by moderate La Niña conditions. Southern Africa (South Africa, Botswana, and Namibia) exhibits statistically significant negative correlations between SOI (which is positive during La Niña) and observed precipitation, while no known significant teleconnection exists between ENSO and the South American region (van Oldenborgh and Burgers 2005).
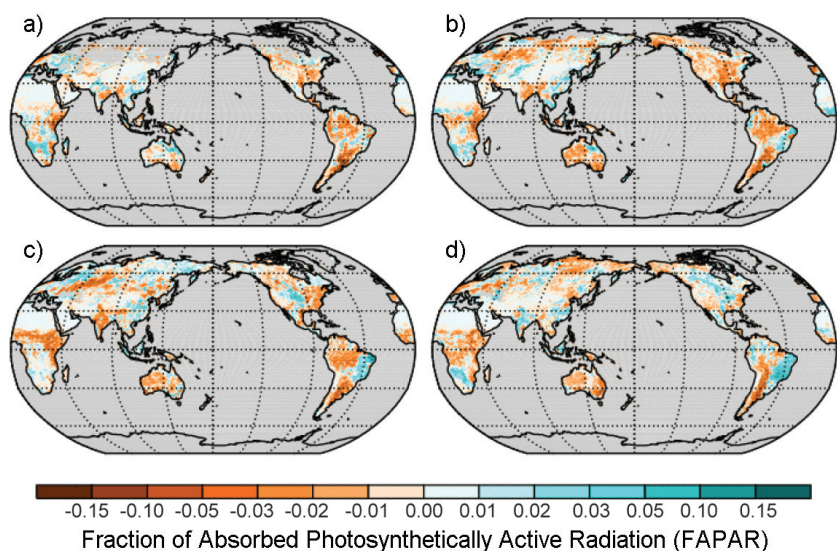

FIG. 2.46. Maps of seasonal FAPAR Anomalies in 2009. Each panel shows the anomalies averaged over the Northern Hemisphere: (a) winter (DJF); (b) spring (MAM); (c) summer (JJA); and (d) fall (SON), respectively.
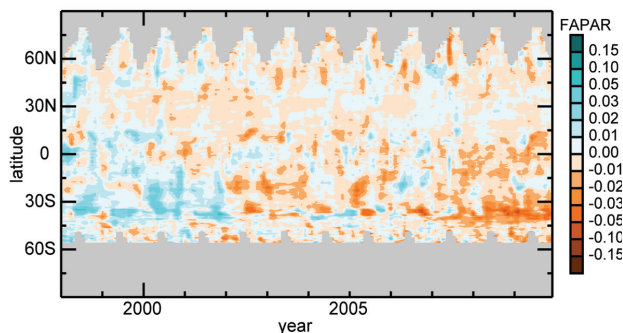
FIG. 2.47. As for Fig. 2.1 but for monthly zonal FAPAR anomalies

Figure 2.47 suggests the presence of a negative trend occurring over the latitude band 30°S to 50°S. This is apparent in the globally averaged time series (Fig. 2.48) and strong enough to yield global monthly negative anomalies for the most recent years. These negative anomalies have been continuous since 2007 reaching a minimum in May 2009. FAPAR is related to CO_2 assimilation by plants. The negative tendency since records began in 1998 indicates that the efficiency of CO_2 assimilation, at least as monitored through the FAPAR proxy of photosynthetic rate, does indeed appear to be declining (Knorr et al. 2007). Both Figs. 2.47 and 2.48 also show that this trend is not merely a result of an anomalous year in 1998. Instead, after the period of FAPAR decline in 2000–03 noted by Knorr et al. (2007), we find another period of similar decline since 2007, interrupted by only a moderate recovery during 2004–07.

3) BIOMASS BURNING—J. W. Kaiser and J. G. Goldammer

Vegetation fires (burning of live and dead biomass) and their impacts are influenced by complex interactions between biosphere, humans, and climate (e.g., Bowman et al. 2009). Size, intensity and severity of fires respond to changes of weather and climate (interannual climate variability and long-term climate change). The resulting carbon emissions, e.g., 2.0 Pg C year^{-1}–3.2 Pg C year^{-1} in 1997–2004 (van der Werf
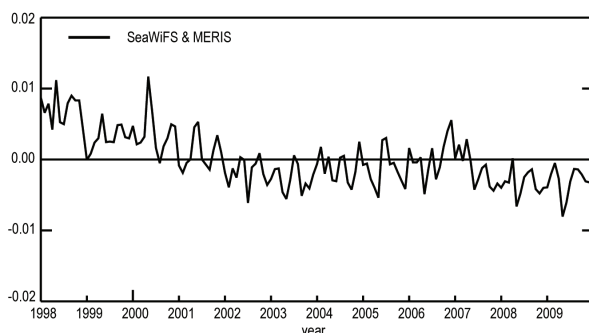
et al. 2006), can amount to almost half those from fossil fuels, i.e., 7.2 Pg C year^{-1} in 2000–05 (Alley et al. 2007). Therefore, fire must be included in any quantitative model of the global carbon cycle. In ecosystems where regular fires are part of the natural cycle, the released carbon is taken up again by regrowth. If fires result in permanent deforestation or vegetation degradation, on the other hand, carbon stocks may be depleted irreversibly (Fargione et al. 2008). The emitted carbon monoxide and ozone also significantly increase the radiative forcing, while the net effect of the resulting changes in surface albedo reduces it (Bowman et al. 2009). The indirect effect of smoke aerosols is still poorly understood.

The GEMS project and its follow-up MACC (Hollingsworth et al. 2008) derive retrospective and real-time biomass burning emissions from satellite-based observations of Fire Radiative Power (FRP). This is approximately proportional to the biomass combustion rate for open fires (Wooster et al. 2005). Figure 2.49 shows FRP averaged over 2003–08 (a) and for 2009 (b), with five-degree resolution. These are derived from the FRP products of the two MODIS sensors using a cloud cover correction at a resolution

FIG. 2.48. Monthly FAPAR anomalies at the global scale relative to the 1998 to 2009 average.
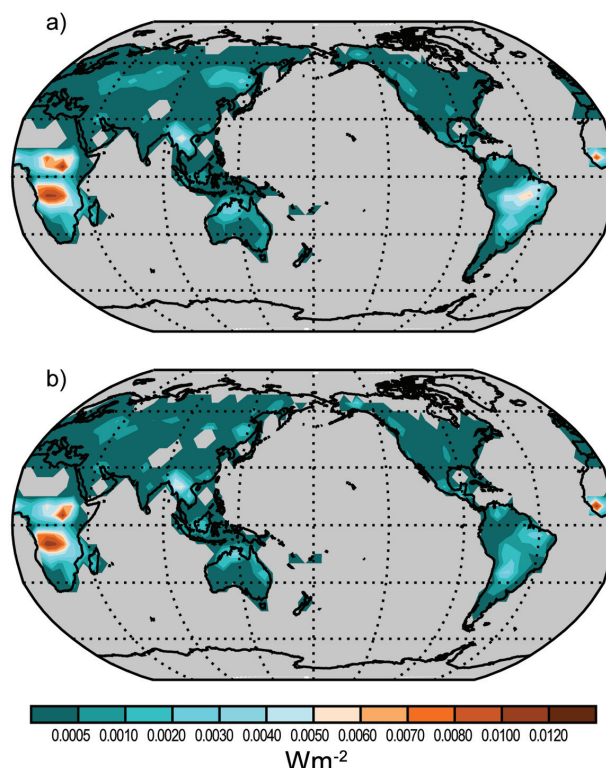
FIG. 2.49. Global fire distribution of 2003-2008 (climatology period) (a) and 2009 (b), all in terms average fire radiative power density (W m^{-2}) observed by MODIS.

of 0.1° and 5 days (Kaiser et al. 2009). Validation of the data is still ongoing.

The climatology displays the main burning seasons in Sub-Saharan and Southern Hemispheric Africa, South America, the South-East Asian peninsula, and Australia. Boreal forest fires are only of secondary importance for the global budget. Peat forest fires on South-East Asian islands and understory ground fires are expected to be underrepresented because they are not fully visible from space. Fires detected around the Persian Gulf are flares from oil production instead of biomass burning (cf. Schultz 2002).

Globally, the biomass burning rate of 2009 was the lowest in the short record. Two-thirds of the global reduction has taken place in South America, where Brazil has drastically reduced the deforestation in the Amazon basin (Fig. 2.49/Plate 2.1: see also http://www.obt.inpe.br/prodes/prodes_1988_2009.htm). On-site field exploration by the Global Fire Monitoring Center (GFMC) in the Russian Federation also revealed a significant decrease of wildfires in 2009 as compared to the early 2000s due to prevailing moist weather conditions (http://www.fire.uni-freiburg.de/GFMCnew/2009/10/1014/20091014_ru.htm). Global and regional budgets of FRP are listed in Table 2.6.

TABLE 2.6. Regional Budgets of Burnt Biomass in terms of Fire Radiative Power.

Region	Climate: average (range) [GW]	2009 [GW]	Change w.r.t. average (%)
Global	132 (125-139)	113	-14
SH Africa	35 (33-36)	34	-1
NH Africa	33 (29-35)	30	-7
C & S America	30 (23-35)	18	-39
SE Asia & Australia	19 (14-23)	18	-1
Northern Asia	11 (8-15)	8	-27
N America	5 (4-5)	4	-18
Europe	3 (2-4)	3	-1

3. GLOBAL OCEANS—J. M. Levy, Ed.

a. Overview—J. M. Levy

As the global ocean observing system matures and climatologies of essential climate variables grow more robust, observations of anomalous departures continue to shed light on the evolving behavior of the coupled ocean-atmosphere system. Calendar year 2009 was characterized by the following findings:

- Global SST exhibited several noteworthy features, including development of the 2009 El Niño in the tropical Pacific, transition of the Pacific Decadal Oscillation (PDO) from a two-year persistent negative phase to a positive phase during the fall/winter 2009, substantial cooling in the mid-latitude North Atlantic from May 2009 to December 2009, and significant warming in the tropical Indian Ocean from influences of the 2009 El Niño.

- During the latest El Niño a considerable build up of heat was observed in the upper equatorial Pacific Ocean. Global integrals of upper-ocean heat content for the last several years have reached values consistently higher than for all prior times in the record, demonstrating the dominant role of the oceans in the Earth's energy budget.

- Ocean heat fluxes played a dual role in the dynamics of large-scale SST anomalies. Heat fluxes generated SST anomalies in some regions (such as in the North Atlantic and the tropical Indian Oceans) while acting to dampen SST anomalies that had already been generated in other regions (such as in the tropical and extratropical Pacific).

- The surface of the western equatorial Pacific freshened considerably from 2008 to 2009, at least partially owing to an eastward spreading of the western equatorial fresh pool along the equator during this latest El Niño. Outside the more variable tropics, the anomalously salty surface values of salinity in climatologically drier locations and anomalously fresh values in rainier locations observed since 2004 generally persisted into 2009, suggesting an increase in the hydrological cycle consistent with climate model predictions for global warming scenarios.

- Very strong eastward surface current anomalies were seen across the equatorial Pacific, associated with the El Niño event of 2009. Such current anomalies typically lead eastern Pacific SST anomalies by several months. By the last two months of 2009, the anomalies had reached values similar to the 2002 El Niño, exceeded during the altimetry age (1993–present) only by the 1997/98 El Niño.

- Unusually low Florida Current transports were observed in May and June of 2009, a time of year that transport is typically high. This low-transport event was linked to unusually high sea level and coastal flooding along the east coast of the United States in the summer of 2009.

- Sea level variations during 2009 were strongly affected by the transition from La Niña to El Niño conditions, especially in the tropical Indo-Pacific. Globally, variations about the long-term trend also appear to have been influenced by ENSO, with a slight reduction in global mean sea level during the 2007/08 La Niña event, and a return to the long-term trend and perhaps slightly higher values during the latter part of 2009 and the current El Niño event.

- The global ocean CO_2 uptake flux for 2008, the most recent year for which analyzed data are available, is estimated to have been 1.23 Pg C yr^{-1}, which is 0.25 Pg C yr^{-1} smaller than the long-term average. This lower uptake is significant when compared to the 1σ interannual variability estimate of ±0.14 Pg C yr^{-1} for the whole 27-year record. The total global ocean inventory of anthropogenic carbon stored in the ocean interior as of 2008 is 151 Pg C. This estimate suggests a 33 Pg C increase in inventory since 1994, reflecting uptake and storage of anthropogenic CO_2 at rates of 2.0 and 2.3 ±0.6 Pg C yr^{-1} for the decades of the 1990s and 2000s, respectively.

- The downward trend in global chlorophyll observed since 1999 has continued through 2009, with current chlorophyll stocks in the central stratified oceans now approaching record lows since 1997.

b. Sea surface temperatures—Y. Xue, R. W. Reynolds, and V. Banzon

The unique features in the global SST in 2009 include (1) the development of the 2009/10 El Niño in the tropical Pacific, (2) the transition of the PDO from a 2-year persistent negative phase to a positive phase during the fall/winter 2009, (3) a significant warming in the tropical Indian Ocean, and (4) a substantial cooling in the mid-latitude North Atlan-
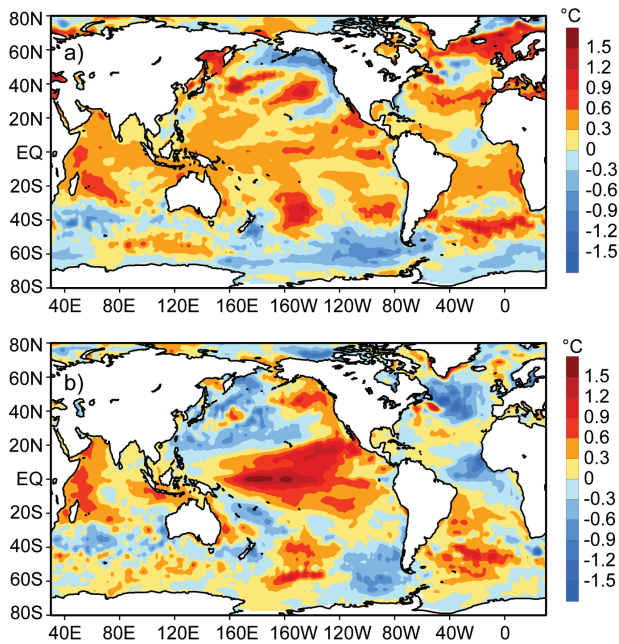
Fig. 3.1. (a) Yearly mean SSTAs in 2009 and (b) SSTA differences between 2009 and 2008. SSTs are the monthly fields interpolated from the weekly 1° OISST of Reynolds et al. (2002). All anomalies are defined as departures from the 1971–2000 climatology (Xue et al. 2003).

tic. We used the Optimal Interpolation SST version 2 (OISST v.2), which is a weekly analysis on a one-degree grid derived by combining in situ and satellite observations for the period of November 1981 to present (Reynolds et al. 2002). To put the 2009 SST in a historical perspective, we also analyzed the Extended Reconstructed SST version 3b (ERSST.v3b), which is a monthly merged land-ocean surface temperature analysis on a two-degree grid for the period of 1854 to present (Smith et al. 2008). SST anomalies (SSTA) are defined as departures from the 1971 to 2000 climatology described by Xue et al. (2003).

The yearly mean SSTA in 2009 is characterized by overall positive SSTA in all the tropical oceans, and negative SSTA south of 40°S. The 2009 SSTA has a negative PDO pattern in the North Pacific, and a tripole pattern in the North Atlantic (Fig. 3.1a). The 2009 minus 2008 SSTA differences show signatures of the development of the 2009/10 El Niño and the transition of the PDO from a negative to positive

phase (Fig. 3.1b). It also indicates a substantial warming in the tropical Indian Ocean and a cooling in the equatorial Atlantic and the mid-latitude North Atlantic.

The 2009/10 El Niño was preceded by weak La Niña conditions during the winter 2008/09 (Fig. 3.2a). The tropical Pacific returned to near-normal conditions during boreal spring (Fig. 3.2b), and transitioned into weak El Niño conditions (Niño3.4 > 0.5°C) during boreal summer (Fig. 3.2c). The June-July-August seasonal mean SSTA was about +1.2°C in the far eastern equatorial Pacific. It is noteworthy that there were two additional SSTA maxima of about +0.9°C, one in the subtropical northwestern Pacific that might be related to the positive SSTA in the central North Pacific, and another one in the northeastern Pacific near the coast of Mexico. The positive SSTA in the central-eastern equatorial Pacific strengthened rapidly in October–November 2009, and the 3-month-running mean Niño3.4 (170°W–120°W, 5°N–5°S) SST was about 1°C above-normal in September–November 2009, indicating a moderate strength of El Niño (Fig. 3.2d). At the same time, the positive SSTA in the subtropical northwestern Pacific weakened rapidly. It is interesting to note that the positive SSTA in the northeastern tropical Pacific persisted while that in the southeastern tropical Pacific dissipated quickly and switched into negative SSTA in boreal fall. The El Niño reached a peak phase during December 2009, and the SSTA pattern in January 2010 falls into the category of the central-Pacific event or Modoki event (Ashok et al. 2007) in which the larg-
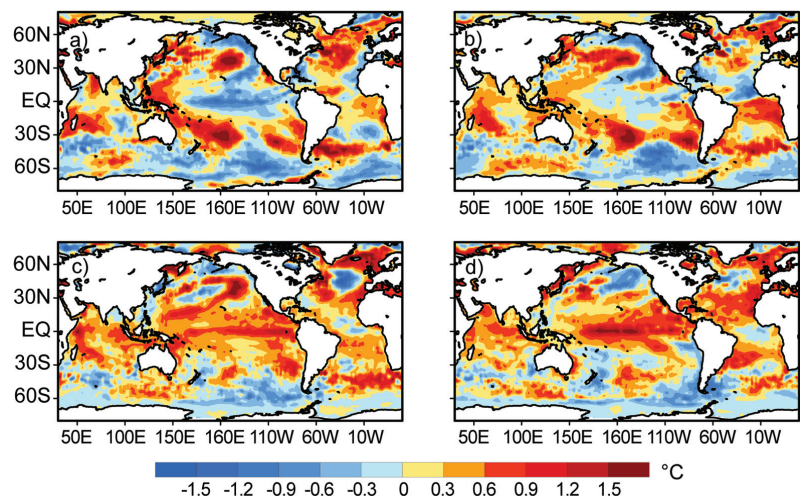

Fig. 3.2 . Seasonal mean SSTAs (°C) for (a) December 2008 to February 2009, (b) March to May 2009, (c) June to August 2009 and (d) September to November 2009. SSTs are the monthly fields interpolated from the weekly 1° OISST of Reynolds et al. (2002). All anomalies are defined as departures from the 1971–2000 climatology (Xue et al. 2003).

est warming is centered near the Dateline. Since June 2009 there have been four episodes of downwelling oceanic Kelvin waves associated with westerly wind burst events, which are believed to contribute to the maintenance and strengthening of the 2009/10 El Niño (see "Monthly Ocean Briefing" slides from the Climate Prediction Center (CPC), NCEP, at http://www.cpc.ncep.noaa.gov/products/GODAS).

The SSTA in the North Pacific was dominated by a negative PDO pattern during the winter 2008/09 and spring 2009, characterized by a horseshoe pattern of positive SSTA extending from the equatorial western Pacific to the mid-latitudes in both hemispheres and negative SSTA extending along the west coast of North America (Fig. 3.2a and Fig. 3.2b). Consistent with the negative PDO phase, upwelling along the west coast of North America was mostly above-normal during the winter 2008/09 and spring 2009 (see the CPC "Monthly Ocean Briefing" referred to above). During summer 2009, the PDO phase returned to near-normal (see the PDO index at http://jisao.washington.edu/pdo, Mantua et al. 1997) and El Niño conditions developed in the tropical Pacific (Fig. 3.2c). During fall 2009, the El Niño conditions intensified, while the PDO phase remained near-normal. Note that the PDO phase became weakly above-normal in January 2010, indicating that atmospheric teleconnections from the El Niño started to influence SST in North Pacific.

The tropical Indian Ocean SSTA increased substantially from 2008 to 2009. Figure 3.1a shows that the yearly mean SSTA in 2009 was about +0.3°C (+0.6°C) in the central-eastern (western and southwestern) tropical Indian Ocean. The 2009 minus 2008 SSTA differences indicate that SSTA increased by more than 0.6°C in the western and southeastern tropical Indian Ocean (Fig. 3.1b). As a result, 2009 became the second warmest year in the tropical Indian Ocean behind 1998 when the record warming occurred, which is seen from the basin mean yearly SSTA indices derived from ERSST.v3b for 1950–2009 (Fig. 3.3b). The increase in the tropical Indian Ocean SST is clearly associated with that in the tropical Pacific Ocean SST (Fig.

3.3c). The section in this chapter on "Global Ocean Heat Fluxes" (Yu and Weller 2007), suggests that the basin-wide warming in the tropical Indian Ocean from July to December 2009 can be largely attributed to decrease of latent and sensible heat fluxes due to weakened trade winds from influences of the 2009 El Niño. Figure 3.3c also suggests that the tropical Indian Ocean SST usually warms up significantly in the years following El Niño, e.g., in 1998, 1987, and 1983. The warming in 2009 is somewhat unusual in the sense that it occurred during the El Niño year, rather than in the year after El Niño.

The historical perspective of the 2009 SSTA has been shown separately for the (a) global ocean, (b) tropical Indian, (c) tropical Pacific, (d) North Pacific, (e) tropical Atlantic, and (f) North Atlantic in Fig. 3.3. For the global ocean, the SSTA increased from 0.15°C in 2008 to 0.25°C in 2009, and became the fourth warmest year behind 1998, 2003, and 2005, the top three warmest years since 1950 (Fig. 3.3a). The five year running mean of the yearly-mean time series of global SSTA shows that SSTs have trended downward since 2003. However, the downward trend is punctuated by the two consecutive La Niñas in 2007 and 2008, which lowered the global mean SST. For the tropical Pacific, the SSTA increased from 0.08°C in 2008 to 0.34°C in 2009, and also became the fourth warmest year behind 1997, 2004, and 2002 since 1950
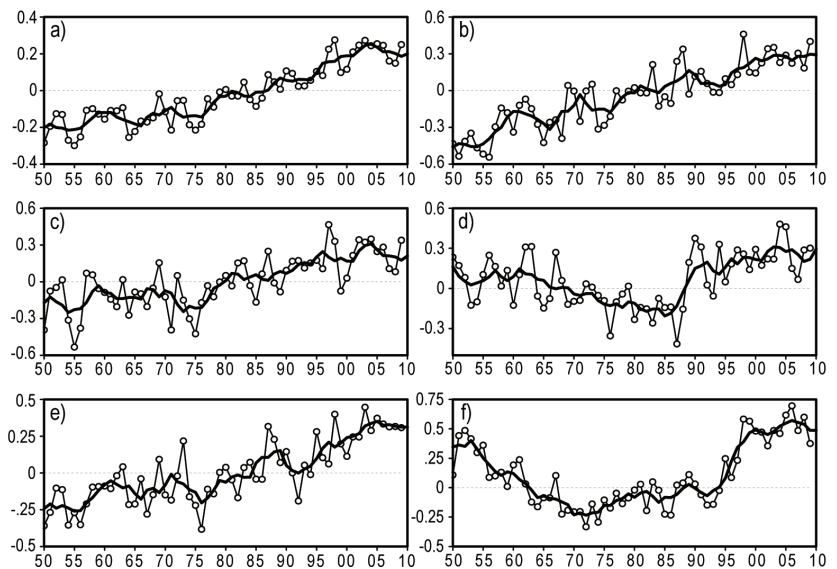
FIG. 3.3. Yearly mean SSTAs (°C) (dots) averaged in the (a) global ocean, (b) tropical Indian (30°S–30°N), (c) tropical Pacific (30°S–30°N), (d) North Pacific (120°E–110°W, 30°N–60°N), (e) tropical Atlantic (30°S–30°N), (e) North Atlantic (80°W-0°, 30°N–60°N) in 1950–2009. Black lines are the five-year running means of the yearly mean SSTAs. SSTs are the Extended Reconstructed SST version 3b of Smith et al. (2008). All anomalies are defined as departures from the 1971–2000 climatology (Xue et al. 2003).

(Fig. 3.3c). It is interesting that the tropical Atlantic SSTA peaked in 2003 and has decreased slowly since then (Fig. 3.3e). The North Pacific SST changed little from 2008 to 2009 and has been persistently above-normal since 1990 (Fig. 3.3d). The North Atlantic SSTA decreased from 0.6°C in 2008 to 0.38°C in 2009 and became the coolest year since 2002 (Fig. 3.3f).

The substantial cooling in the mid-latitude North Atlantic in 2009 is further analyzed here. In Fig. 3.4, we show the evolution of the zonal average SSTA in the North Atlantic along with the CPC North Atlantic Oscillation index and the zonal average LHF+SHF (latent and sensible heat flux) anomalies based on the Objectively Analyzed air-sea Fluxes (OAFlux)

Fig. 3.4. (a) Monthly standardized NAO index derived from monthly standardized 500-mb height anomalies obtained from the NCEP CDAS in 20°N-90°N (http://www.cpc.ncep.noaa.gov). Time-Latitude sections of (b) SSTA and (c) LHF+SHF (latent and sensible heat flux) anomalies (upward positive) averaged between 80°W and 20°W. SSTs are the monthly fields interpolated from the weekly 1° OISST of Reynolds et al. (2002), and anomalies are defined as departures from the 1971–2000 climatology (Xue et al., 2003). LHF+SHF are the Objectively Analyzed air-sea Fluxes (OAFlux) (Yu and Weller, 2007), and anomalies are defined as departures from the 1988–2008 climatology (personal communication with Dr. Lisan Yu).

project during November 2008–December 2009 (Yu and Weller 2007; http://oaflux.whoi.edu). During the early winter 2008/09, positive SSTA of about +1.5°C were present in the North Atlantic at 40°N–50°N, and SSTA of about +0.6°C in the tropical North Atlantic (TNA, hereafter) at 5°N–15°N. The two maxima of positive SSTA suddenly weakened during January 2009, which coincided with the sudden increase of LHF+SHF at 40°N–60°N and 0°–20°N. The positive LHF+SHF anomalies in the TNA persisted from January 2009 into February 2009, while those in middle-high latitudes propagated southward into the subtropics, contributing to the SST cooling in the TNA in February 2009. The middle-latitude SST further decreased and became negative in May 2009, probably forced by the positive LHF+SHF anomalies in April–May 2009. The three subsequent cooling episodes of SST that occurred during September, November, and December 2009 correspond well with the three maxima of positive LHF+SHF anomalies. The persistence of the negative SSTA from May 2009 to January 2010 can probably be attributed to the negative North Atlantic Oscillation (NAO) phases during June, July, October, and December 2009, which often cool the SST in middle latitudes and warm the SST in high latitudes and subtropics (Deser and Blackmon 1993), referred to as a negative SST dipole pattern here. The coincidence between negative NAO phases and negative SST dipole patterns seems to support the hypothesis that air-sea coupling plays a significant role in the seasonal variability of the NAO and North Atlantic SST (Czaja and Frankignoul 2002). It is also noted that the positive SSTA persisted and shifted southward, which is also consistent with the tripole SST pattern forced by the NAO. Therefore, the development of the positive SSTA in the TNA during summer can probably be attributed to the strong negative NAO during summer and the subsequent maintenance and enhancement of the TNA SST during fall/winter is likely due to the negative NAO during fall/winter.
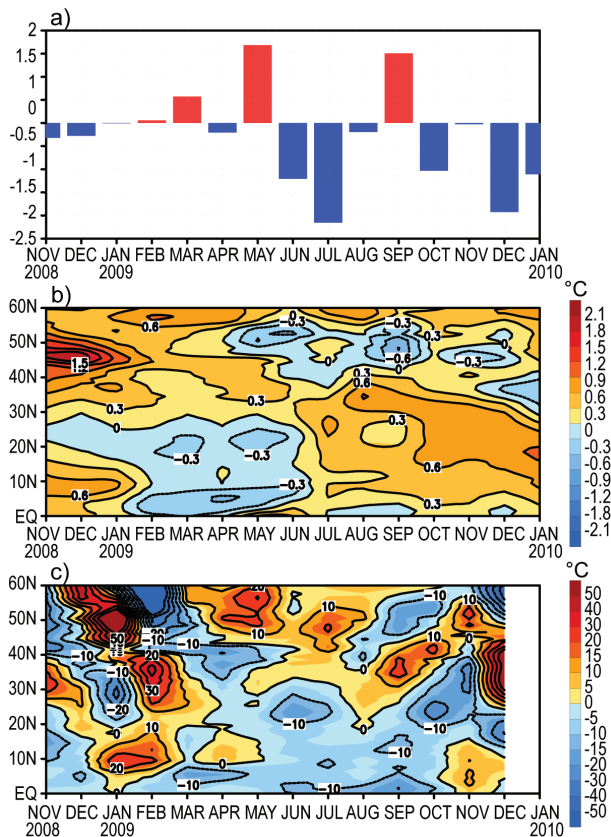
c. Ocean heat content—G. C. Johnson, J. M. Lyman, J. K. Willis, S. Levitus, T. Boyer, J. Antonov, M. D. Palmer, and S. A. Good

Storage and transport of heat in the ocean are central to aspects of climate such as El Niño (Zebiak 1989), the North Atlantic Oscillation (Curry and Mc-Cartney 2001), hurricanes (Mainelli et al. 2008), sea level rise (Domingues et al. 2008), the global energy budget (Trenberth 2009), and constraining global warming scenarios (Knutti and Tomassini 2008). The accompanying sidebar gives additional perspective.

We begin by discussing an estimate of upper-ocean (0–750 m) heat content anomaly (OHCA) for the period 1 January–31 December 2009 (Fig. 3.5a) computed from a combination of in situ ocean temperature data (World Ocean Database 2009 – Johnson et al. 2009a and Argo – Roemmich et al. 2009) and satellite altimetry data following Willis et al. (2004) but relative to a 1993–2009 baseline (the altimetry time period), hereafter the combined estimate. We also discuss changes in the combined estimate between 2009 and 2008 (Fig. 3.5b), as well as maps of the linear trend of the combined estimate from 1993–2009 and its statistical significance (Fig. 3.6). Finally, we present three different time series of global integrals of in situ only estimates of upper OHCA (Fig. 3.7).

In recent years many of the globally distributed in situ subsurface ocean temperature data are from Argo. Data from Argo floats with the potential for as yet uncorrected systematic pressure biases (http://www.argo.ucsd.edu/Acpres_drift_apex.html) have been removed from the combined estimate. In ad-

dition, annual estimates of XBT fall rate corrections have been applied for deep and shallow probe data using Table 2 of Wijffels et al. (2008) but with no XBT data used after 2005. Details of all the fields analyzed here may change after more Argo real-time data are subject to delayed-mode scientific quality control, as more data are reported, and as XBT and MBT corrections improve.

The combined estimate of OHCA in 2009 (Fig. 3.5a) shows eddy and meander variability down to the 100-km mapping scales, as does, to a greater extent, the difference of the 2009 and 2008 combined estimates (Fig. 3.5b). Strong small-scale spatial variability in OHCA fields is associated with the western boundary currents in every gyre, as well as the Antarctic Circumpolar Current (Fig. 3.5b). The difference in the combined estimates between 2009 and 2008 (Fig. 3.5b) illustrates the large year-to-year variability in ocean heat storage. Of course internal ocean dynamics, such as advection and heave, certainly play a significant role in many of these changes but for purposes of comparison only, they reach or exceed the equivalent of a 95 W m^{-2} magnitude surface flux applied over one year (~3 × 10^9 J m^{-2}). Upper OHCA, deep variability, freshwater, and mass signals all contribute to sea level anomalies. Despite this, there are many large-scale visual similarities between the combined estimate (Fig. 3.5a) and sea level (Fig. 3.22 top) fields in 2009, even relative to their differing baseline periods. This similarity shows the large contribution of heat content variations to sea level variations.

Large-scale patterns are evident in the combined estimate of OHCA for 2009 (Fig. 3.5a) and its difference from 2008 (Fig. 3.5b). The equatorial Pacific gained heat during the El Niño that commenced this year (see also Fig. 4.7) as did the off-equatorial central and eastern tropical Pacific. Despite declines in OHCA in the western tropical Pacific (excepting the Coral Sea that gained heat since 2008), OHCA there remains well above the mean. While the annual averaging period presented here is too long for detailed study of the ocean advection of heat associated with ENSO dynamics (but see Chapter 4), certainly those processes contribute to the change on the equator and perhaps those in the off-equatorial regions (Zebiak 1989).

The North Pacific shows high OHCA in its center in 2009, with low OHCA to the south, off the west coast of North America and into the eastern Bering Sea (Fig. 3.5a). This pattern is consonant with a negative Pacific Decadal Oscillation index (Mantua et al.

Fig. 3.5. (a) Combined satellite altimeter and in situ ocean temperature data estimate of upper (0–750 m) ocean heat content anomaly OHCA (10^9 J m^{-2}) for 2009 analyzed following Willis et al. (2004), but relative to a 1993–2009 baseline. (b) The difference of 2009 and 2008 combined estimates of OHCA expressed as a local surface heat flux equivalent (W m^{-2}). For panel comparisons, note that 95 W m^{-2} applied over one year results in a 3 × 10^9 J m^{-2} change of OHCA.

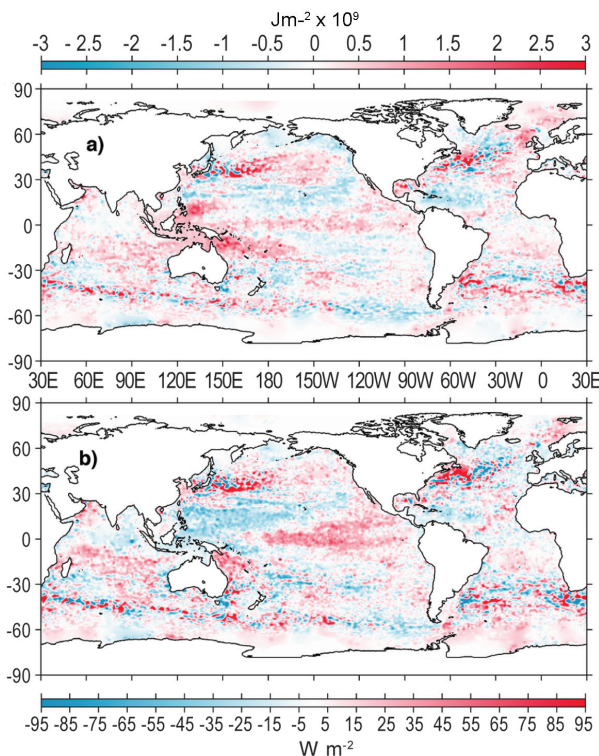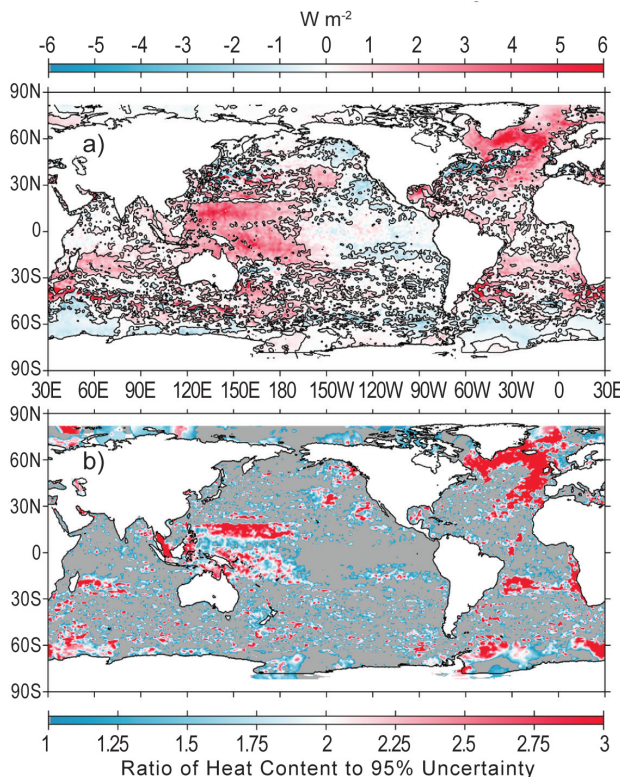**FIG. 3.6. (a) Linear trend from 1993 to 2009 of the combined satellite altimeter and in situ ocean temperature data estimate of upper (0–750 m) ocean heat content anomaly OHCA (W m^{-2}) analyzed following Willis et al. (2004). (b) Ratio of the linear trend to its 95% uncertainty estimate, with colored areas showing regions with statistically significant trends, and grey areas those without.**

1997) from late 2007 through mid 2009. The band of high OHCA along 35–50°S in the South Pacific (Fig. 3.5a) appears to have steadily migrated south from tropical latitudes since 2006 (Arguez 2007; Levinson and Lawrimore 2008; Peterson and Baringer 2009).

The Indian Ocean is mostly warmer than the baseline in 2009 (Fig. 3.5a). The northern Arabian Sea and the Indian Ocean west of the Indonesian Seas gained heat between 2008 and 2009 (Fig. 3.5b) and stand out as warmer than the rest of the region in 2009.

In the Subpolar North Atlantic, the Labrador and Irminger Seas, which cooled between 2007 and 2008 (Peterson and Baringer 2009) continued to cool between 2008 and 2009 (Fig. 3.5b), so OHCA values in these areas are now below the 1993–2009 mean (Fig. 3.5a). This change is consonant with a return of deep wintertime convection in this region during early 2008 (Våge et al. 2009) and the associated export of heat from ocean to atmosphere. The continued high OHCA values in the eastern subpolar North Atlantic (Fig. 3.5a) suggest that subtropical influences are still

strong there, consistent with anomalously salty surface conditions in that region in 2009 (Fig. 3.13a). The subtropical and tropical Atlantic in both hemispheres remains slightly warmer than the mean, with little change from 2008 to 2009.

Near the Antarctic Circumpolar Current, OHCA is highly variable (Fig. 3.5a), but appears anomalously warm around the globe, consistent with recent studies (Böning et al. 2008), except perhaps in the eastern Pacific. Western boundary current extensions in the North Pacific and both hemispheres of the Atlantic are energetic, with large year-to-year changes (Fig. 3.5b).

A few very distinct (Fig. 3.6a) and statistically significant (Fig. 3.6b) regional patterns in the Pacific
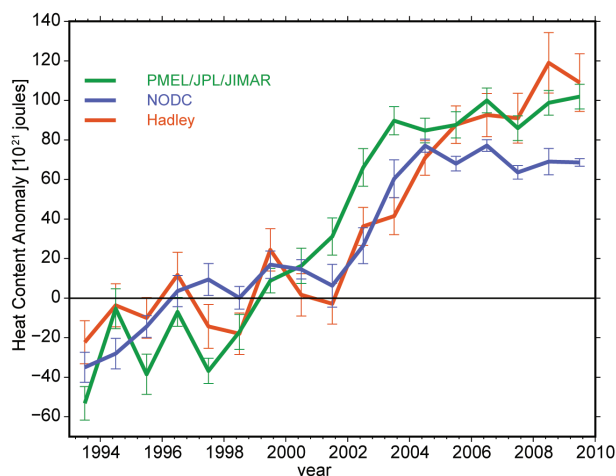
FIG. 3.7. Time series of annual average global integrals of in situ estimates of upper (0–700 m) OHCA (10^{21} J, or ZJ) for 1993–2009 with standard errors of the mean. Error estimates displayed do not contain uncertainties due to differences in climatology, treatment of the seasonal cycle, mapping methods, instrument bias corrections, or quality control. The NODC estimate follows Levitus et al. (2009). The PMEL/JIMAR estimate is a weighted integral with sampling errors (Lyman and Johnson 2008) using Argo and WOD 2009 (Johnson et al. 2009a) data relative to a 1993–2002 climatology with the Wijffels et al. (2008) Table 2 XBT bias adjustments applied and no XBT data after 2005. The Hadley estimate applies XBT bias adjustments from Table 1 of Wijffels et al. (2008) to the EN3 dataset (Ingleby and Huddleston 2007; www.metoffice.gov.uk/hadobs) relative to a 1993–2002 climatology and is computed from estimates of monthly OHCA following Palmer et al. (2007) and Palmer and Brohan (2010, manuscript submitted to *Int. J. Climatol.*) with error estimate methodology similar to Rayner et al. (2006) but adding uncertainty in the XBT bias correction. For comparison, the NODC estimate has been offset relative to its 1993–2002 mean, the climatology time period for the other estimates.

and Atlantic Ocean stand out in the 1993–2009 local linear trends of OHCA. In the Atlantic Ocean, the Labrador, Irminger, and Greenland-Iceland-Norwegian Seas have all trended warmer over the interval, reflecting a robust regional warming trend over the longer time period (Fig. 3.6a) that has not been overcome by the recent cooling there (Fig. 3.5a) in the last few years. These changes are related to variations the NAO index. In addition, the eastern portions of the Atlantic trends warmer across both hemispheres. As in the 2009 OHCA map, areas of warming appear more widespread than areas of cooling.

The statistically significant (Fig. 3.6b) 1993–2009 regional trends in the Pacific Ocean (Fig. 3.6a) are of warming in the western tropical Pacific and off-equatorial cooling in the east, consistent with general strengthening of the subtropical-tropical circulation in the past two decades (McPhaden and Zhang 2004). The statistically significant warming in the central North Pacific and cooling south of Alaska and off the west coast of North America are also consistent with an overall downward trend in the PDO index (Mantua et al. 1997) from 1993 to 2009.

Three different upper ocean estimates (0–700 m) of globally integrated in situ OHCA (Fig. 3.7) reveal a large increase in global integrals of that quantity since 1993. The interannual details of the time series differ for a variety of reasons including differences in climatology, treatment of the seasonal cycle, mapping methods, instrument bias corrections, quality control, and other factors. Most of these factors are not taken into account in the displayed uncertainties, so while the error bars shown do not always overlap among the three estimates, these estimates are not necessarily statistically different from each other because the error bars are likely unrealistically small. Even so, errors are too large to obtain reliable trends over a few years. However, the three curves all agree on a significant decadal warming of the upper ocean since 1993, accounting for a large portion of the global energy imbalance over this time period (Trenberth 2009), and the three sets of maps (not shown) from which the curves are produced show similar large-scale features.

d. Global ocean heat fluxes—L. Yu and R. A. Weller

Most of incoming solar energy absorbed by Earth is absorbed at the top ocean layer, but not all the absorbed heat is stored and transported by the oceans. Over 80% of the heat is released back to the atmosphere by two heat exchange processes at the air-sea interface: evaporation that releases latent heat and conduction, and convection that releases sensible heat. The amount of heat being exchanged is called heat flux. Latent and sensible heat fluxes from the oceans are significant energy sources for global atmo-

RECENT ADVANCES IN OUR UNDERSTANDING OF GLOBAL OCEAN HEAT CONTENT—M. D. PALMER, K. HAINES AND J. M. LYMAN

Quantifying and understanding changes in global and regional ocean heat content (OHC) are of fundamental importance to climate science. The long-term increase in OHC has an important contribution to sea level rise (Antonov et al. 2002, 2005; Domingues et al. 2008), reflects a first-order estimate of Earth's radiation balance (Levitus et al. 2005; Murphy et al. 2009), and provides a powerful constraint on model projections of future surface temperature rise (Knutti and Tomassini 2008). Here we review some of the major progress made in OHC research since publication of the IPCC Fourth Assessment Report (AR4) (Fig. 3.8).

The first major advance is the quantification of a time-varying warm bias in the expendable bathythermograph data (XBT), which constitute a large fraction of the historical subsurface temperature observations (Gouretski and Koltermann 2007). This warm bias, in combination with a small number of faulty Argo floats, was responsible for the spurious cooling seen in the AR4 results over the period 2003–05 (Fig. 3.8; Willis et al. 2007). We note that since profiling floats are still a relatively new technology, there may
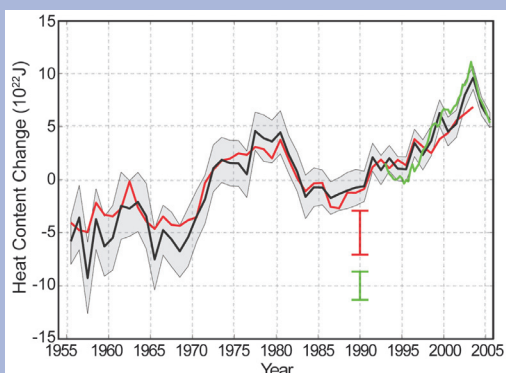
Fig. 3.8. The IPCC AR4 estimates of annual ocean heat content anomaly (10^{22} J) for the 0–700 m layer. The black curve is updated from Levitus et al. (2005), with the shading representing the 90% confidence interval. The red and green curves are updates of the analyses by Ishii et al. (2006) and Willis et al. (2004, over 0–750 m) respectively, with the error bars denoting the 90% confidence interval. Anomalies are computed relative to the 1961–90 average. Figure reproduced from Bindoff et al. (2007).

be some unresolved biases in the Argo data. Several groups have estimated XBT bias corrections and computed OHC time-series – a marked increase in OHC work since the AR4. These new XBT-corrected OHC time series (Fig. 3.9) show a reduction in the decadal variability compared to the AR4 results (Fig. 3.8), improving agreement with coupled climate model simulations (Domingues et al. 2008). However, there are still considerable differences in interannual variability among the XBT-corrected curves that require further investigation. The impact of XBT corrections on the long-term trend varies (Wijffels et al. 2008; Ishii and Kimoto 2009; Levitus et al. 2009; Gouretski and Reseghetti 2010), but all the time series show an underlying rise in OHC consistent with our understanding of anthropogenic climate change.

The limited historical ocean sampling (AchutaRao et al. 2006) has motivated a novel approach to understanding the observed changes in OHC from a more mechanistic point of view. Palmer et al. (2007) have evaluated the ocean warming signal relative to fixed isotherms. This approach seeks to separate the influence of air-sea heat flux and ocean circulation in observed OHC change by measuring the average temperature above an isotherm and isotherm depth, respectively (Palmer and Haines 2009).

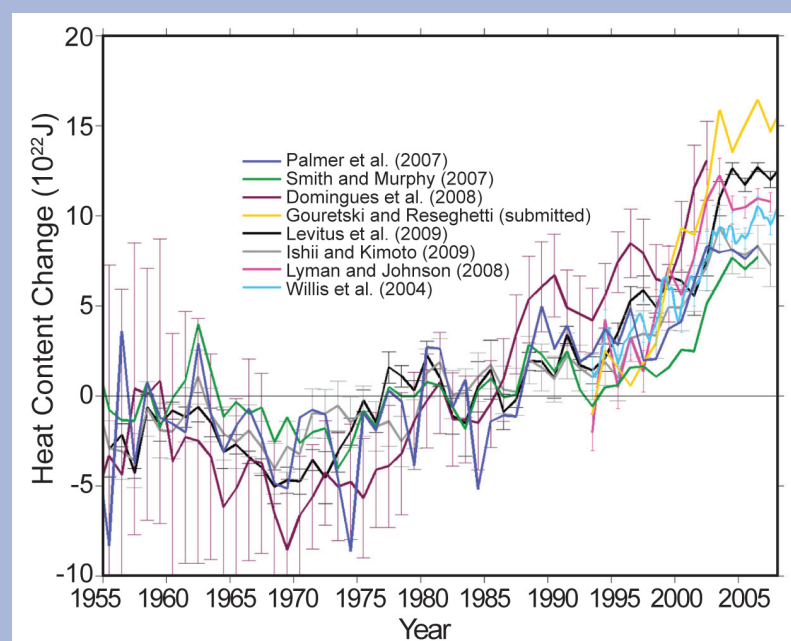**Fig. 3.9. XBT corrected estimates of annual ocean heat content anomaly (10^{22} J) for the 0–700 m layer. Differences among the time series arise from: input data; quality control procedure; gridding and infilling methodology (what assumptions are made in areas of missing data); bias correction methodology; and choice of reference climatology. Anomalies are computed relative to the 1955–2002 average. Figure reproduced from Palmer et al. (2010).**

The average temperature above isotherms is also immune to one known contributor to XBT bias, namely fall rate errors (e.g., Wijffels et al. 2008). By isolating the air-sea heat flux signal of ocean warming, the isotherm methodology has enabled the separate detection and attribution of volcanic and anthropogenic greenhouse gas forcings in the ocean temperature record for the first time (Palmer et al. 2009). However, due to the inherent spatial limitations, this method does not directly address the global energy budget.

The deployment of the Argo array of autonomous profiling floats over the last decade has revolutionized our ability to observe the deeper ocean (Roemmich et al. 2009). There are currently over 3000 active floats measuring temperature and salinity over the upper 2000 m every 10 days. Argo is already providing a uniformly sampled baseline for assessing past OHC changes (Lyman and Johnson 2008). A sustained Argo promises to give the detailed information on upper ocean warming that is critical to understanding the rates of global and regional climate change and for testing and improving climate models (Barnett et al. 2005). Argo data will also provide the key to initializing climate models to make better seasonal to decadal predictions in the future (Smith et al. 2007).

The XBT-corrected OHC curves level off after 2003 (Fig. 3.9, see also Fig 3.7). Knight et al. (2009) noted a recent slowing of observed sea surface temperature rise at around the same time. However, sea level rise has continued at around 2 mm yr^{-1} since 2003 (Leuliette and Miller 2009; see also section 3h). Recent work suggests that the reduction in ocean thermal expansion over this period was partly offset by an increase in oceanic mass gain from melting terrestrial ice (Cazanave et al. 2009). Trenberth et al. (2010, see also Trenberth and Fasullo 2010) point out that melting of ice requires at least an order of magnitude less energy per unit sea level rise than ocean thermal expansion. Assuming that the top-of-atmosphere radiation balance of approximately 0.9 W m^{-2} has remained constant in recent years, an emerging issue is "where has this excess energy gone since 2003?" Deep ocean warming may account for some of the missing energy (Johnson and Doney 2006; Johnson et al. 2007; Johnson et al. 2008a). Only with a truly global ocean observing system can we close fully the global energy and sea level budgets, so we must improve our observations of the ocean below 2000 m where Argo floats currently do not reach.

spheric circulation, and their changes on short- and long-term timescales have important implications for global weather and climate patterns (e.g., Emanuel 1986; Cayan 1992; Frankignoul et al. 1998).

Global estimates of daily ocean latent and sensible heat fluxes on one-degree spatial resolution are being routinely produced by the OAFlux project at Woods Hole Oceanographic Institution (Yu and Weller 2007). The computation of the OAFlux products uses the state-of-the-art bulk flux algorithm version 3.0 developed from the Coupled Ocean-Atmosphere Response Experiment (COARE) (Fairall et al. 2003), with input surface meteorological variables determined from an optimal blending of satellite retrievals (e.g., Special Sensor Microwave Imager (SSMI), QuikSCAT, Advanced Very High Resolution Radiometer (AVHRR), and Advanced Microwave Scanning Radiometer for EOS (AMSR-E) and the surface meteorology from reanalysis/forecast models of National Centers for Environment Prediction (NCEP) and the European Center for Medium range Weather Forecasting (ECMWF).

The global latent plus sensible heat fluxes (LHF+SHF) in 2009 (Fig. 3.10a) show that, on the annual-mean basis, the largest ocean heat losses occur over the regions that are associated with major western boundary currents (WBCs) and their extensions, such as the Kuroshio off Japan, the Gulf Stream off the United States, the Agulhas current off the African coast, the Falkland/Brazilian Current off South America, and the Eastern Australian Current. Magnitude of annual mean LHF+SHF in these regions exceeds 250 W m^{-2}, produced largely during the fall-to-winter seasons by strong winds and cold and dry air masses coming from the lands. The second largest heat loss (~180 W m^{-2}) is located over the broad subtropical southern Indian Ocean, where the large air-sea heat exchange is sustained primarily by the strong southeast trade winds in the monsoon months June–September. The spatial distribution of the mean global LHF+SHF field depicts a close relationship of LHF+SHF to SST and winds.

The 2009-minus-2008 difference plot of LHF+SHF (Fig. 3.10b) shows coordinated basin-scale variability with magnitude of change of the order of ±50 W m^{-2}. One such large-scale change occurred in the tropical Pacific Ocean in association with an evolving warm phase of the ENSO phenomenon. During an El Niño, the sea surface is anomalously warm in the central and eastern equatorial basin and anomalously cool in the western basin (Fig. 3.1). The change in SST affects the near surface humidities, because saturation specific humidity goes up with temperature, and the change in sea-air humidity contrast affects latent heat flux. Hence, latent heat increased over the warm SST anomalies in the east and reduced over the cool SST anomalies in the west. The larger latent heat released from the warmer ocean surface acts to damp the positive SST anomalies, suggesting that the ocean heat flux is a key control on the persistence and amplitude of SST anomalies. Variability of ocean heat fluxes in the tropical Pacific on ENSO time scales is a dominant interannual signal (e.g., Yu and Weller 2007), and the ocean heat flux acts as a damping mechanism that regulates the growth of ENSO SST.

ENSO has far-reaching effects on global climate, and one such example is clearly demonstrated in the tropical Indian Ocean. Positive SST anomalies started to develop in the tropical Indian Ocean (IO) north of 15°S in summer 2009 after the El Niño conditions were fully established in the Pacific. The SSTs were elevated by more than 0.5°C from July to December 2009 (Fig. 3.11a). However, the basin-wide LHF *reduced* when the sea surface was warmer (Fig. 3.11b), which is in sharp contrast to the LHF increase over the warmer eastern tropical Pacific. Weaker LHF means less heat loss at the sea surface, whose effect
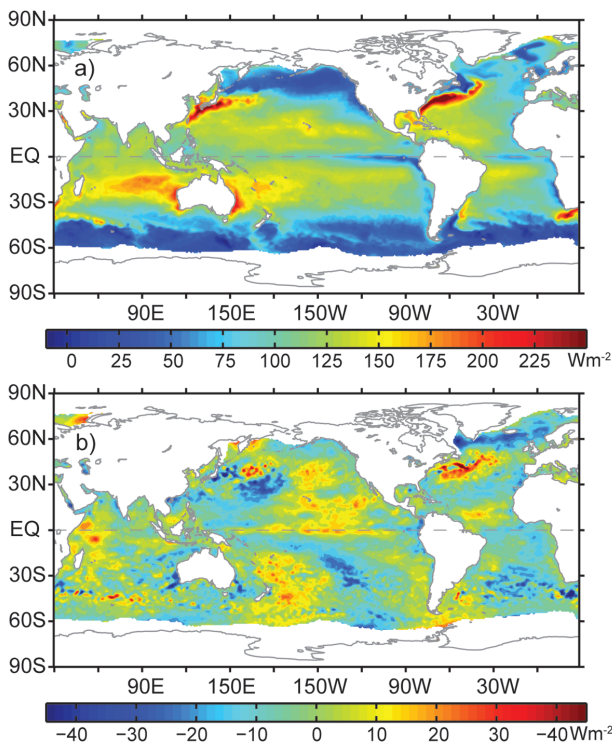

Fig. 3.10. (a) Annual mean latent plus sensible heat fluxes in 2009. The sign is defined as upward (downward) positive (negative). (b) Differences between the 2009 and 2008 annual mean latent plus sensible heat fluxes.

is to cause SST to rise if oceanic processes (e.g., mixing and advection) do not dominate. The weaker LHF was induced primarily by the weaker trade winds associated with the weakening of the Walker Circulation during El Niño, similar to the previous ENSO-induced IO warm events (Yu and Rienecker 2000). In this case, the impact of ocean heat flux was to force, not to damp, the SST anomalies.

For the Pacific Ocean, the SST 2009-minus-2008 difference map has a pattern resembling the warm phase of PDO: there is a horseshoe shaped region of negative difference anomalies surrounding a core of warmer difference anomalies to the east. The pattern suggests that the PDO phase became less negative in 2009. Indeed, the negative phase that started in September 2007 began to taper off in the first half of 2009 (http://jisao.washington.edu/pdo/PDO.latest) and since July 2009, the PDO index was mostly positive because of the El Niño event developing in the equatorial region during fall and winter 2009/10. The 2009-minus-2008 difference map of LHF+SHF (Fig. 3.10b) has a pattern in broad agreement with that of SST (Fig. 3.1), because the ocean heat flux responded to the SST anomalies and acted as damping to suppress the growth of SST anomalies.

Unlike the Pacific where the correlation between SST and LHF+SHF difference anomalies is *positive*, the correlation between the pair is *negative* in the Atlantic. For instance, the 2009 SSTs in the Atlantic were

predominantly cooler than the 2008 SSTs, except for the subtropical Atlantic between 15°N and 30°N and the high-northern latitudes. The surface warming in the subtropical region, together with the cooling to its north and south, was in apparent association with the NAO tripole structure. The tripole pattern is also evident in the LHF+SHF 2009–08 difference field, but positive (negative) LHF+SHF anomalies occurred mostly over cooler (warmer) sea surface. It is known that the NAO SST tripole is due primarily to the oceanic response to atmospheric forcing via the effects of the changes in LHF+SHF and surface wind induced Ekman currents (Cayan 1992; Deser and Blackmon 1993). The negative correlation between SST and LHF+SHF tripole in 2009 is consistent with the existing theory, indicating that the Atlantic basin-scale SST variability in 2009 was driven primarily by the atmospheric forcing: SST increases (decreases) as a result of reduced (enhanced) latent and sensible heat loss at the sea surface. This is seen clearly in Fig. 3.3 where a series of surface cooling episodes in the North Atlantic between 40–60°N can be well explained by the changes in the ocean heat flux.

The changing relationships between LHF+SHF and SST in the global oceans indicate that the ocean heat fluxes played a dual role in the dynamics of large-scale SST anomalies: they not only generated SST anomalies (such as in the North Atlantic and the tropical Indian Oceans) but also acted to damp SST anomalies that had already been generated (such as in the tropical and extratropical Pacific).

The long-term perspective of the change in 2009 LHF+SHF is shown in the annual mean time series averaged over the global oceans from 1958 to 2009 (Fig. 3.12). The 2009 LHF+SHF was slightly down from the 2008 mean (Peterson and Baringer 2009), continuing the downward trend that started around
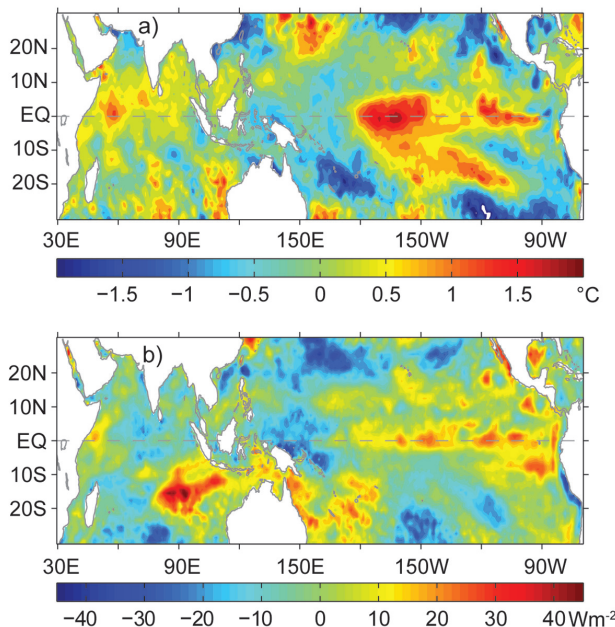

FIG. 3.11. (a) SST differences between December 2009 and July 2009 in the tropical Indo-Pacific Oceans. (b) LHF+SHF averaged over the 6 month period from July to December 2009.
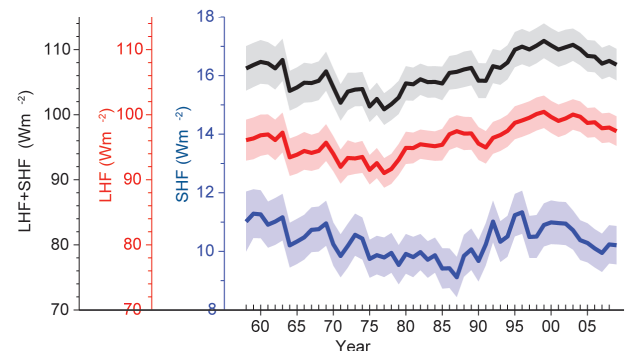

FIG. 3.12. Year-to-year variations of global averaged annual mean latent plus sensible heat flux (black curve), latent heat flux (red curve), and sensible heat flux (blue curve). The shaded areas indicate the error bars of the flux estimates at the 95% confidence level.

2000. The downward trend is driven primarily by LHF with minor positive contribution from SHF. Over the past 51 years from 1958 to 2009, the LHF+SHF time series suggests an oscillatory nature, with a low at 99 W m^{-2} in 1977 and a high at 109 W m^{-2} in 1999. The present downward trend seems to be a tendency toward reversing the upward trend that had dominated the decades of 1980s and 1990s. The accuracy of the OAFlux LHF and SHF estimates was evaluated using 105 buoys available over the global oceans (Yu et al. 2008). The averaged root-mean-square differences between OAFlux and buoy over the buoy locations are 9.6 W m^{-2} for LHF and 2.6 W m^{-2} for SHF.

e. *Sea surface salinity*—G. C. Johnson and J. M. Lyman

Ocean storage and transport of freshwater are intrinsic to aspects of global climate including the water cycle (e.g., Wijffels et al. 1992), El Niño (e.g., Maes et al. 2006), and anthropogenic climate change (e.g., Held and Soden 2006). Only since 2004 has the advent of the Argo array of profiling floats, that measures temperature and salinity year-round in the upper 2 km of the ice-free global ocean, nominally at 10-day intervals and 3°× 3° spacing (Roemmich et al. 2009), allowed an annual assessment of global ocean freshwater, and its complement, salinity. Remote sensing of Sea Surface Salinity (SSS) by two satellites is anticipated in 2010 (http://www.esa.int/esaLP/LPsmos.html; http://aquarius.gsfc.nasa.gov/).

We analyze the near-global Argo data to determine an annual average SSS anomaly for 2009 relative to a climatology and to describe how annual SSS anomalies have changed in 2009 relative to 2008, as well as assessing trends in salinity since 2004 and their statistical significance. The data, downloaded from an Argo Global Data Assembly Center in January 2010, are a mix of real-time (preliminary) and delayed mode (scientific quality-controlled) data. The estimates of SSS presented could change after all the data have been subjected to careful scientific quality control.

We subject the shallowest near-surface (< 25 m) salinity data flagged as good from each available Argo profile to a statistical check to discard outliers resulting in rejection of 8% of the profiles. After this check, we cast the remaining data as differences from a climatological mean surface salinity field from the 2001 World Ocean Atlas (WOA) based on historical data reported through 2001 (Boyer et al. 2002). We objectively map (Bretherton et al. 1976) the resulting anomalies for each year assuming a Gaussian

covariance function with 6° latitude and longitude decorrelation length scales and a noise-to-signal variance ratio of 2.2.

Climatological SSS patterns are correlated with surface freshwater flux: the sum of evaporation, precipitation, and river runoff (e.g., Béranger et al. 1999) where advection processes are not dominant. In each ocean basin, subtropical salinity maxima centered between roughly 20 and 25° in latitude are signatures of the predominance of evaporation over precipitation. Conversely, in most regions where climatological surface salinities are relatively fresh, such as the high latitudes and the ITCZs precipitation generally dominates over evaporation.

The 2009 SSS anomalies from WOA (Fig. 3.13a) reveal some large-scale patterns that also hold in 2004 through 2008 (Arguez 2007; Levinson and Lawrimore 2008; Peterson and Baringer 2009). The
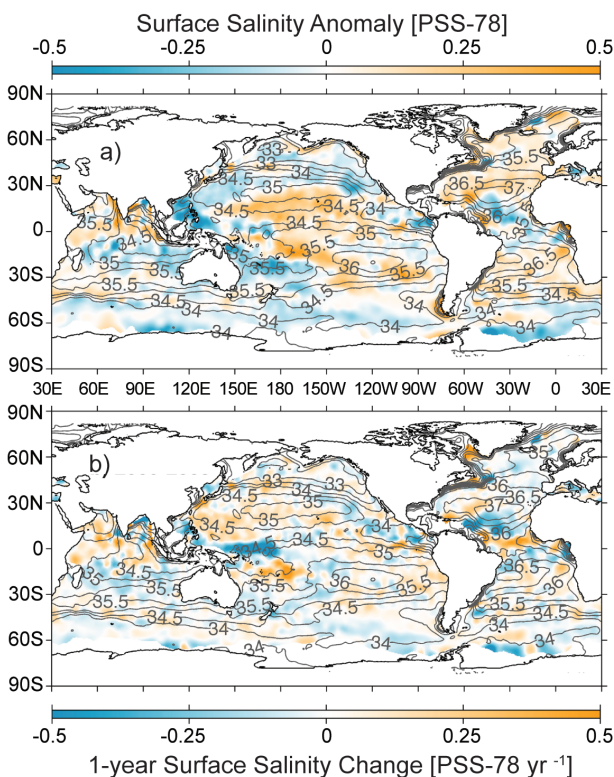
FIG. 3.13. (a) Map of the 2009 annual surface salinity anomaly estimated from Argo data [colors in PSS-78] with respect to a climatological salinity field from WOA 2001 (gray contours at 0.5 PSS-78 intervals). (b) The difference of 2009 and 2008 surface salinity maps estimated from Argo data [colors in PSS-78 yr^{-1} to allow direct comparison with (a)]. White areas are either neutral with respect to salinity anomaly or are too data-poor to map. While salinity is often reported in practical salinity units, or PSU, it is actually a dimensionless quantity reported on the 1978 Practical Salinity Scale, or PSS-78.

regions around the subtropical salinity maxima are mostly salty with respect to WOA. Most of the high-latitude climatologically fresh regions appear fresher than WOA, including most of the Antarctic Circumpolar Current near 50°S and the subpolar gyre of the North Pacific. These patterns may be consistent with an increase in the hydrological cycle (i.e., more evaporation in drier locations, and more precipitation in rainy areas), as seen in simulations of global warming. These simulations suggest this signal might be discernible over the last two decades of the twentieth century (Held and Soden 2006), consistent with the multi-year nature of these anomalies.

Nonetheless, there may be alternate explanations. It is possible that the climatology, being based on relatively sparse data distributions in many parts of the oceans, may tend to underestimate regional extrema that the well-sampled Argo array can better resolve, or that the climatology contains regional biases on seasonal or longer time-scales that are not present in the Argo data. Also, some of these patterns might be explained by interannual variability in large-scale oceanic currents or atmospheric features such as the ITCZs.

For example, in contrast to the other high-latitude areas, the subpolar North Atlantic and Nordic Seas in 2009 are anomalously salty with respect to WOA (Fig. 3.13a), as they have been since at least 2004. This salty subpolar anomaly is inconsistent with a simple increase in the strength of the hydrological cycle. However, the pattern appears mostly due to northward spread of saltier subtropical waters from the south into the northeastern North Atlantic since the mid-1990s (Holliday et al. 2008; Hakkinen and Rhines 2009). This trend towards increasing salinity in the region may have halted or even reversed recently, since salinities in the area freshened slightly from 2008 to 2009 (Fig. 3.13b) and show no large-scale significant trend since 2004 (Fig. 3.14).

Salinity in the tropics exhibits strong interannual variability owing to influences of phenomena such as the ENSO cycle (e.g., Ando and McPhaden 1997). For instance, the western equatorial Pacific fresh pool spread eastward from 2008 to 2009 (Fig. 3.13b), with the freshening in this region at least partly owing to anomalous eastward currents along the equator (Fig. 3.15) in the presence of the mean zonal salinity gradient there. In contrast, the Atlantic ITCZ became saltier. In addition, the strong fresh anomaly found south of India in the tropics in 2006 (Arguez 2007) has steadily weakened over the past few years (Levinson and Lawrimore 2008; Peterson and Baringer 2009)
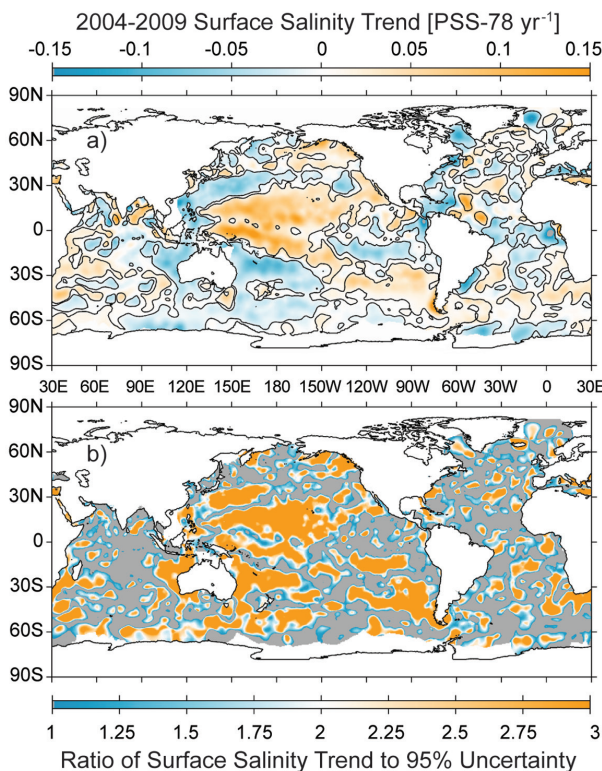
FIG. 3.14. (a) Map of local linear trends estimated from annual surface salinity anomalies for the years 2004–09 estimated from Argo data (colors in PSS-78 yr⁻¹). (b) The ratio of these trends to estimates of the 95% confidence interval, with grey regions showing areas without statistically significant trends and colors from blue to orange indicating increasing statistical significance of the trends.

and is now absent in 2009. Tropical salinity changes from 2008 to 2009 (Fig. 3.13b) show some visual similarities with changes in latent and short wave heat fluxes between the years (Fig. 3.10b), as might be expected given the relation of these parameters to evaporation.

We estimate linear trends from 2004–09 (Fig. 3.14a), since Argo coverage became near global in 2004, and the ratio of these trends to their 95% significance (Fig. 3.14b). The most striking trend patterns are in the Pacific. Saltier surface values in the western and central tropical Pacific extend into the eastern Pacific subtropics in both hemispheres. A strong freshening also occurs in the western subtropics of each hemisphere in the Pacific and the far western tropical Pacific, extending into the Indian Ocean northwest of Australia. The other large-scale patterns include freshening in the tropical Southeast Pacific and along the equatorial Atlantic.

f. Surface currents—R. Lumpkin, G. Goni, and K. Dohan

Near-surface currents are measured in situ by drogued satellite-tracked drifting buoys and by current meters on moored Autonomous Temperature Line Acquisition System (ATLAS) buoys.[1] During 2009, the drifter array ranged in size from a minimum of 778 drogued buoys to a maximum of 1149, with a median size of 937 drogued buoys (undrogued drifters continue to measure SST, but are subject to significant wind slippage; Niiler et al. 1987). The moored array included 38 buoys with current meters, all between 12°S and 21°N. These tropical moorings compose the Tropical Atmosphere Ocean (TAO; Pacific), Pilot Research Moored Array in the Tropical Atlantic (PIRATA; Atlantic) and Research Moored Array for African–Asian–Australian Monsoon Analysis and Prediction (RAMA; Indian) arrays.

Satellite-based estimates of ocean currents are produced using several methodologies, including the OSCAR (Ocean Surface Current Analyses–Real time) project, which uses satellite altimetry, winds, SST, and the Rio05 mean dynamic topography from the AVISO Ssalto/Duacs multimission altimeter gridded product (Rio and Hernandez 2004) to create one-degree resolution surface current maps averaged over the 0–30 m layer of the ocean (Bonjean and Lagerloef 2002). Anomalies are calculated with respect to the time period 1992–2007.

1) Pacific Ocean

In the equatorial Pacific, the year began with a tapering off of the westward surface current anomalies at the end of 2008 (Fig. 3.15), bringing currents back to their climatological January values, although SST anomalies remained cold until April (Fig. 4.1). By February, eastward surface current anomalies were present on the equator from 160°E to 100°W. This El Niño pattern developed and intensified through May. In June–August, this pattern weakened in the central part of the basin, and near-climatological currents (or even westerly anomalies) were seen from the dateline to 120°E. The El Niño eastward anomalies began

Fig. 3.15. Time-longitude plot of anomalous zonal equatorial currents (cm s⁻¹) from OSCAR. Black lines indicate eastward anomalies associated with propagating Kelvin waves.

redeveloping in August, in the form of eastward propagating Kelvin wave pulses that are concurrent with westerly wind anomalies (Fig. 3.15). Two major wave trains were generated at the start of October and December, resulting in strong eastward anomalies west of 140°E in October. In November through December, eastward anomalies dominated the entire equatorial band of the Pacific Ocean (Fig. 3.16).

Surface current anomalies in the equatorial Pacific typically lead SST anomalies by several months, with a magnitude that scales with the SST anomaly magnitude. Recovery to normal current conditions is also typically seen before SST returns to normal. Thus, current anomalies in this region are a valuable predictor of the evolution of SST anomalies and their related climate impacts. This leading nature can be
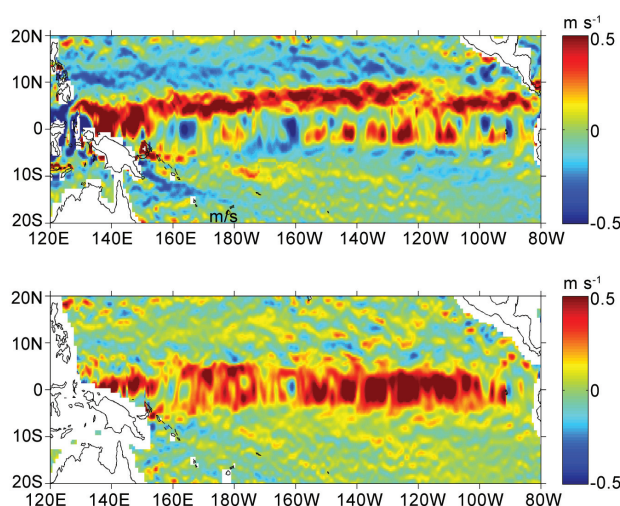
Fig 3.16. November 2009 zonal currents (top) and zonal current anomalies (bottom) in m s⁻¹, from OSCAR. Eastward anomalies exceeding 50 cm s⁻¹ dominated most of the equatorial Pacific.

---

[1] Drifter data is distributed by NOAA/AOML at http://www.aoml.noaa.gov/phod/dac/gdp.html. Moored data is distributed by NOAA/PMEL at http://www.pmel.noaa.gov/tao. OSCAR gridded currents are available at http://www.oscar.noaa.gov/ and http://podaac.jpl.nasa.gov/. AVISO gridded altimetry is produced by SSALTO/DUACS and distributed with support from CNES, at http://www.aviso.oceanobs.com/. Analyses of altimetry-derived surface currents are available at http://www.aoml.noaa.gov/phod/altimetry/cvar.

FIG 3.17. Principal empirical orthogonal functions (EOF) of surface current (SC) and of SST anomaly variations in the Tropical Pacific. (top) Amplitude time series of the EOFs normalized by their respective standard deviations. (bottom) Spatial structures of the EOFs.

seen clearly in the first principal EOF of surface current anomaly and separately of SST anomaly in the tropical Pacific basin (Fig. 3.17). By the end of 2009, the values of the normalized surface current and SST EOFs were reaching values approaching those of the 2002 El Niño, the strongest El Niño since the massive 1997–98 event.

The year ended with another strong wave pulse at the beginning of January 2010, together with a southward shift in westerly wind anomalies (Fig. 4.4), often associated with the onset of the termination of El Niño conditions (Lagerloef et al. 2003).

2) INDIAN OCEAN

The Agulhas Current in the southwestern Indian Ocean is the major western boundary current linking the Indian and South Atlantic basins. Its transport can be estimated on a monthly basis using a combination of altimetry and hydrographic climatology (see http://www.aoml.noaa.gov/phod/altimetry/cvar/index.php). In 2009, the baroclinic transport of the Agulhas decreased from a maximum seen in 2007, to ~48 Sv[2], a value similar to those of th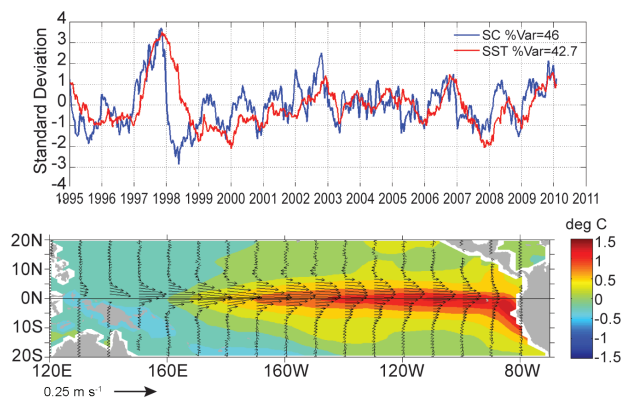e 1993–2000 period (Fig. 3.18, top). The generation of Agulhas rings, which carry Indian Ocean water into the Atlantic, decreased from the peak seen during 2007/08 (Fig. 3.18, bottom) to the more typical long-term average of ~5 rings yr^{-1}.

3) ATLANTIC OCEAN

In the tropical Atlantic, 2009, surface currents were close to climatology except during boreal spring.

---

[2] Sv is a Sverdrup or 10^6 m^3 s^{-1}, a unit commonly used for ocean volume transports.

Eastward anomalies of up to 50 cm s^{-1} occurred along the equatorial Atlantic in April through May, in response to weaker than normal Trade Winds that were also associated with anomalously cold SSTs in the northeastern Tropical Atlantic. This eastward anomaly pattern was disrupted in June–July, when westward anomalies developed east of 20°W in the Guinea Current region. By July, these currents had returned to normal climatological values.

Against the east coast of South America, the southward-flowing warm, salty Brazil Current meets the northward flowing cold, fresh Malvinas Current to create the Confluence Front.

Over the last 15 years, the location of this front has shifted to the south at a mean speed of nearly 1° latitude per decade (Goni et al. 2010, manuscript submitted to *Deep-Sea Res.*; Lumpkin and Garzoli 2010, manuscript submitted to *J. Geophys. Res.*). However, most of this shift occurred in the early part of the altimeter-derived time series; while it exhibits strong intraseasonal to seasonal fluctuations (Goni and Wainer 2001), its annual-averaged position has not changed significantly since 1998, and in 2009 it fluctuated between 37–39°S.

g. The meridional overturning circulation—M. O. Baringer, T. O. Kanzow, C. S. Meinen, S. A. Cunningham, D. Rayner, W. E. Johns, H. L. Bryden, J. J-M. Hirschi, L. M. Beal, and J. Marotzke

The meridional redistribution of mass and heat associated with the large-scale vertical circulation within the oceans is typically called the meridional overturning circulation (MOC). The most common definition of the strength of the MOC at any particular latitude is the maximum of the vertically integrated basin-wide stream function, which changes as a function of latitude and time and is influenced by many physical systems embedded within it. There are several available estimates of the steady-state global mass, fresh water, and heat transport based on the best available hydrographic data (Talley 2008; Lumpkin and Speer 2007; Ganachaud and Wunsch 2003), as well as a few local estimates of the MOC from one-time full water column hydrographic sections and western boundary arrays (e.g., McDonagh et al. 2008; Kanzow et al. 2008); however, true time-series observations of basin-wide MOC transports are logistically very challenging to collect.

Substantial progress has been made on developing a coordinated observing system to measure the MOC through the international conference called OceanObs09 held September, 2009. The conference resulted in numerous community white papers and
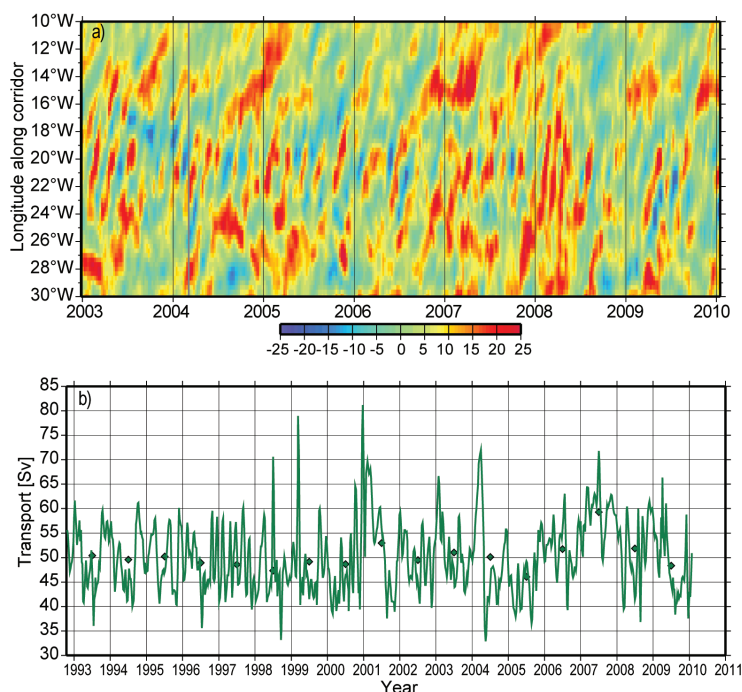
FIG. 3.18. (a) time-longitude plot of sea height anomaly (SHA) in cm along the corridor of Agulhas ring propagation into the Atlantic Ocean, showing the presence of rings as high SHA (red colors). (b) monthly transport of the Agulhas Current (solid line) and annual averages (dots).

conference summary papers aimed at synthesizing recommendations for a sustained observing system including measurements of the MOC (e.g., Cunningham et al. 2010; Rintoul et al. 2010). Presently, quantifying changes in the complex, global MOC are being inferred only from observations of one component of the MOC (e.g., a specific current or ocean layer; e.g., Kanzow et al. 2008), at discrete locations (e.g., at 26.5°N in the Atlantic; Cunningham et al. 2007; Kanzow et al. 2007; Johns et al. 2008), or from indirect measurements such as air-sea fluxes thought to force the MOC (e.g., Marsh 2000; Speer 1997), or indirect measurements thought to be influenced by changes of the MOC, such as deep property fields like temperature or salinity (e.g., Johnson et al. 2008b). A prototype for the recommended observing system has been in place since April 2004, spanning the subtropical gyre in the North Atlantic near 26.5°N, hence this note concentrates on those observations. The system is composed of UK-NERC RAPID MOC moorings, US-NSF Meridional Overturning Circulation Heat-Transport Array (MOCHA), and the US-NOAA Western Boundary Time Series program (see Kanzow et al. 2007; Kanzow et al. 2008; Cunningham et al. 2007).

The most up-to-date estimates of the MOC from the 26.5°N array include data from April 2004 to April 2008[3] (Cunningham et al. 2007; Kanzow et al. 2010, manuscript submitted to *J. Climate*). Over this time period the MOC has averaged 18.7 Sv with a high of 32.1 Sv, a low of 3.2 Sv, and a standard deviation of 4.8 Sv (using the twice daily values filtered with a 10-day cutoff as described in Cunningham et al. 2007). The data suggest no significant trend in the strength of the MOC. After four years of data, a seasonal signal is beginning to emerge (Fig. 3.19) with a low MOC in April and a high MOC in October and peak to trough range of about 7 Sv. The MOC can be divided into three components: the northward western boundary Florida Current, the wind-driven Ekman transport, and the southward "interior" transport (upper ocean geostrophic flow between the Bahamas and Africa). The seasonal cycle of the MOC appears to be largely attributable to seasonal variability in the interior rather than Ekman or Florida Current fluctuations (Kanzow et al. 2010, manuscript submitted to *J. Climate*). Of note is that all the MOC transport values estimated from five repeated CTD sections by Bryden et al. (2005) can be found within the seasonal range of the MOC time series (values ranged from 22.9 Sv in 2004 to 14.8 Sv in 1957). These results do not disprove the presence of a long-term trend in the strength of the MOC (e.g., as suggested by Bryden et al. 2005; Wunsch and Heimbach 2006), but they do suggest that a careful error analysis must be performed that includes the impact of the underlying higher-frequency variability of the MOC on trend estimates (e.g., Baehr et al. 2008; Baehr et al. 2007; Brennan et al. 2008). Other related studies of the MOC trend are, so far, contradictory with some reporting a decrease in the MOC or components of the MOC (e.g., Wunsch and Heimbach 2006; Longworth et al. 2010, unpublished manuscript) while others suggest no change or even an increase (e.g., Köhl and Stammer 2008; Zhang 2008; Olsen et al. 2008; Lumpkin et al. 2008; Schott et al. 2009). Clearly, while disagreement remains over the details of findings from any particular observing systems (e.g., Kanzow et al. 2009), agreement exists

---

[3] Observations of the strength of the MOC from the 26.5° mooring array are available only with a time-delay as the moorings are recovered over 12 to 18 month intervals.
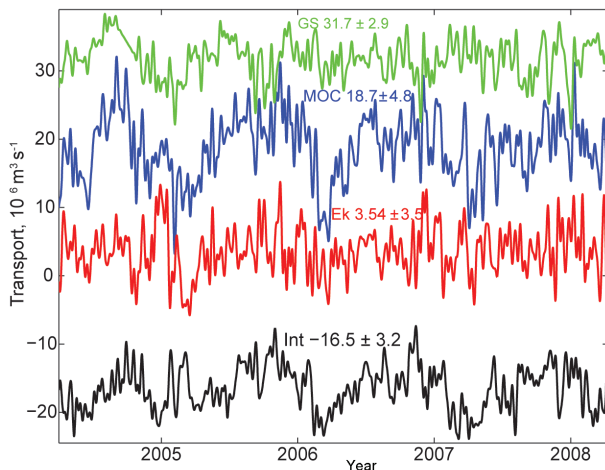
FIG. 3.19. Daily estimates of the strength of the meridional overturning circulation (MOC; blue line) and its components, the Florida Current (GS: green), wind-driven Ekman transport (Ek: red) and the geostrophic interior (Int: black), as measured by the United Kingdom's National Environmental Research Council (NERC) Rapid Climate Change Program, the National Science Foundation's Meridional Overturning and Heat transport Array, and the long-term NOAA funded Western Boundary Time Series Program. The interior volume transport estimate (accurate to 1 Sv, Cunningham et al. 2007) is based on the upper-ocean transport from April 2004 to April 2008 (see also Kanzow et al. 2009), with a 10 day low-pass filter applied to the daily transport values.

that longer time series at multiple locations, particularly of the deep transport components, is needed (e.g., Wunsch 2008).

One of the main components of the MOC estimate near 26.5°N is the Florida Current transport, the longest transport time series of an ocean circulation feature directly linked to the MOC. Near this latitude in the Atlantic the bulk of the warm upper limb of the Atlantic MOC is thought to be carried in the Florida Current through the Straits of Florida and the majority of the cold lower limb is believed to be carried to the south in the Deep Western Boundary Current (DWBC) just east of the Bahamas (e.g., Baringer and Larsen 2001; Meinen et al. 2010). Since 1982, variations in an important contributor to the upper limb of the Atlantic MOC have been monitored by measuring the Florida Current transport using a submarine cable across the Straits of Florida in combination with regular hydrographic sections. In 2009 the median transport through the Florida Straits was 31.3 ± 1.2 Sv[4], slightly lower than the 31.7 ± 2.2 Sv median transport in 2008, but well within the middle range

of mean annual values (32.2 Sv median transport of the Florida Straits from 1982 to 2008 with 50% of the annual means within +/- 2.2 Sv). There were, however, several unusual high-frequency events during the year (Fig. 3.20): anomalously low-transport (outside of two standard deviations of the daily averaged values) events during 20–22 May, 18–27 June, 14–15 November, and 21–22 December, with values as low as about 23 Sv and an unusually high transport 11–12 July, with values as high as about 38 Sv. Due to the fact that these events were relatively short-lived, it is likely they are local responses to atmospheric forcing and coastally trapped wave processes and are not particularly indicative of a climatically-important shift (e.g., Mooers et al. 2005). However, these transient fluctuations can have important environmental consequences. In the summer of 2009, the east coast of the United States experienced a high sea level event that was unusual due to it unexpected timing, large geographic scope, and coastal flooding that was not associated with any storms (Sweet et al. 2009). Sweet et al. (2009) showed that this anomalous event was related to the anomalously low Florida Current transport: a reduced Florida Current transport corresponds to a lower sea surface height gradient across the front and hence higher sea level onshore. Changes in Florida Current transport and the associated MOC have been similarly shown to affect sea level along the east coast of the United States through other studies such as Bingham and Hughes (2009) and Yin et al. (2009).
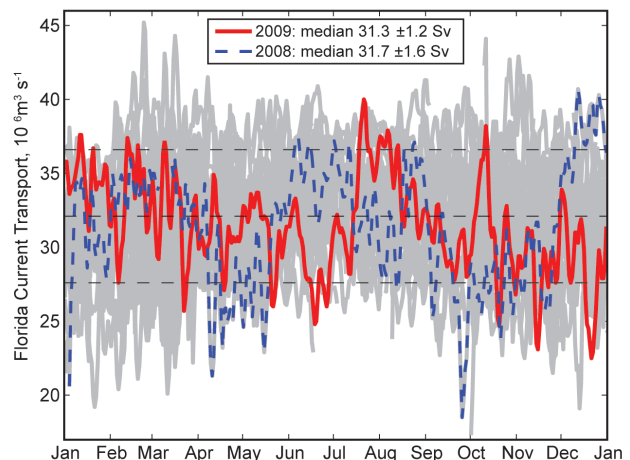
FIG. 3.20. Daily estimates of the transport of the Florida Current during 2009 (red solid line) compared to 2008 (dashed blue line). The daily values of the Florida Current transport for other years since 1982 are shown in light grey. The median transport in 2009 decreased slightly relative to 2008, and is slightly below the long-term median for the Florida Current (32.2 Sv).

---

[4] Standard error of the mean represents 95% confidence limits.

Trends in the MOC can also be determined through proxies of the MOC strength, such as paleo observations (e.g., Carlson et al. 2008), tracers (e.g., LeBel et al. 2008), and water mass characteristics (e.g., Kouketsu et al. 2009; Lohmann et al. 2008; Hawkins and Sutton 2007). For example during the past year, temperature and salinity observations in the Labrador Sea showed an abrupt return of deep convection between 2007 and 2008 (Våge et al. 2009). Yashayaev and Loder (2009) showed that the enhanced deep convection in the Labrador Sea in the winter of 2008 was the deepest since 1994 and included the largest heat loss from the ocean to the atmosphere since the mid-1990s, exceeding the long-term mean by 50%. Such anomalous local events may be a precursor to changes in the MOC strength (e.g., Lohmann et al. 2009; Bellucci et al. 2008). Large-scale changes in temperature and salinity can also provide an indication of circulation changes; for example, Kouketsu et al. (2009) and Johnson et al. (2008a) showed that deep water temperature changes are consistent with a slowing of the deep circulation.

h. Sea level variations—M. Merrifield, S. Gill, E. Leuliette, L. Miller, G. Mitchum, S. Nerem, and P. Woodworth

The dominant changes in sea level during 2009 were associated with a moderate El Niño event that peaked at the end of the year. We first describe quarterly sea level anomalies, which illustrate the sea level signature of the El Niño event, followed by the 2009 annual mean relative to a long-term mean and to the 2008 mean, which we treat as the present sea level tendency. We conclude with an update on global sea level rise and a brief description of daily sea level extremes observed at coastal and island tide gauges in 2009.

The La Niña event that developed in 2007 and persisted through 2008 was still evident during January–February–March 2009 (JFM 09) with high/low sea surface height (SSH) anomalies in the western/eastern tropical Pacific (Fig. 3.21). Positive anomalies extended throughout the Indonesian Archipelago into the tropical Indian Ocean and southward along the west coast of Australia. The La Niña weakened noticeably along the western equatorial Pacific during April–May–June 2009 (AMJ

09) with the excitation of a downwelling Kelvin wave that created positive SSH anomalies in the central and eastern equatorial Pacific. The size of the positive SSH anomalies in the western Pacific warm pool region also began to diminish during AMJ 09 presumably due to weakening trade winds to the east. The high SSH anomalies in the eastern tropical Pacific increased in amplitude during July–August–September 2009 and peaked in October–November–December 2009 (OND 09). By OND 09 the high water levels in the western equatorial Pacific had largely subsided to background levels with the exception of a branch of high water level near the South Pacific Convergence Zone. Most of these changes in equatorial sea level are associated with changes in regional ocean heat content (see section 3c.).

Averaged over the entire year, the SSH anomaly includes contributions from the weakening La Niña state and the strengthening El Niño with high water levels across the equatorial Pacific (Fig. 3.22, top panel). The low levels along the Pacific coast of North America with high levels in the central North Pacific suggest the dominance of the negative phase of the PDO. High anomalies occur along the paths of the Gulf Stream and Kuroshio extensions, suggesting either a strengthening or meridional shift of those currents. In general, sea level appears to be unusually high in the Indian Ocean relative to the 1993–2002 baseline with the exception of the mid- to high-latitude North Pacific and North Atlantic and in the
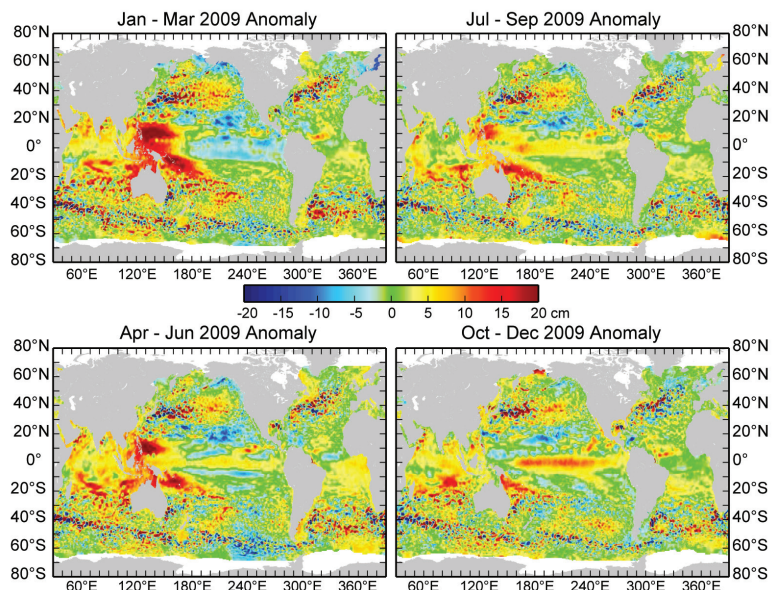

Fig. 3.21. Seasonal SSH anomalies for 2009 relative to the 1993–2007 baseline average are obtained using the multimission gridded sea surface height altimeter product produced by Ssalto/Duacs and distributed by Aviso, with support from CNES (www.aviso.oceanobs.com).
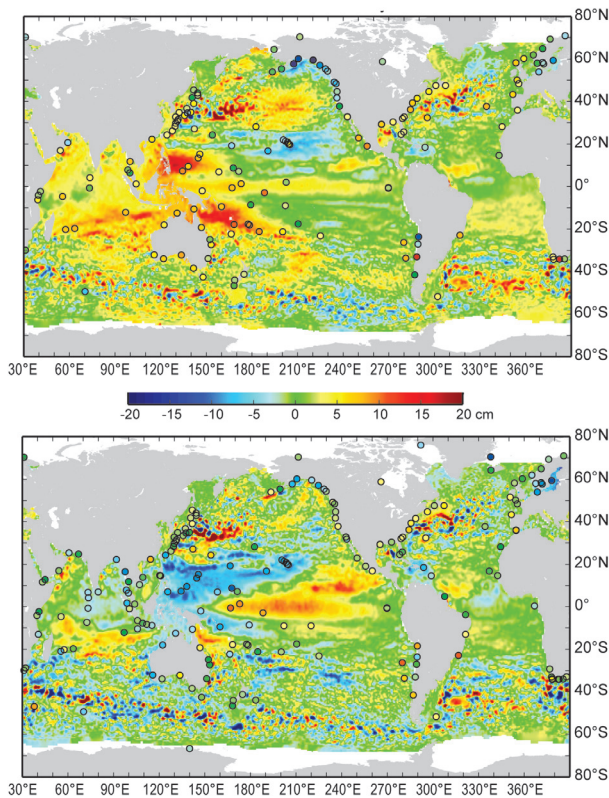
FIG. 3.22. (top) The 2009 SSH anomaly (Ssalto/Duacs product) from the 1993-2007 baseline is compared to the 2009 anomaly computed for tide gauge data (dots) obtained from the University of Hawaii Sea Level Center (http://uhslc.soest.hawaii.edu/). (bottom) The difference between 2009 and 2008 annual means.
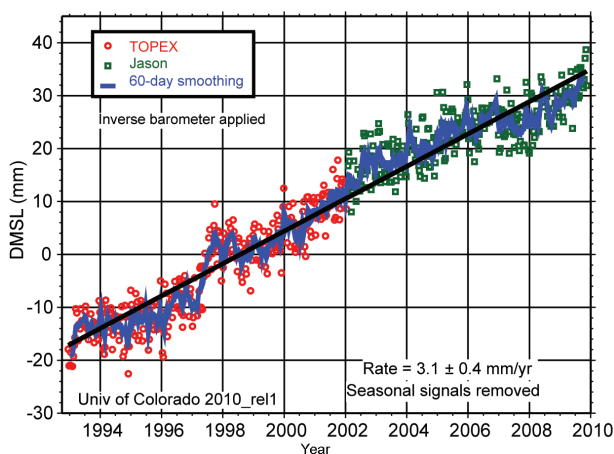

FIG. 3.23. Global mean sea level time series provided by S. Nerem, University of Colorado at Boulder. The rate does not include the global isostatic adjustment correction, which nominally adds 0.3 mm yr⁻¹ to the rate. Information on how the time series was constructed is available at http://sealevel.colorado.edu/documents.php.

southern tropical Atlantic. The coastal tide gauge and SSH levels are similar at most stations.

The SSH tendency (Fig. 3.22, bottom panel) shows the seesaw shift in water levels in the tropical Pacific caused by the El Niño event. SSH tended to drop in the Indian Ocean, except for a band south of the equator extending from Australia to Madagascar. Levels along the coast of Australia decreased from 2008 to 2009 due to the propagation of upwelling variable Kelvin waves along the coast during the El Niño event.

The rate of global mean sea level (GMSL) rise is estimated currently to be 3.1 ± 0.4 mm yr⁻¹ (3.4 mm yr⁻¹ with correction for global isostatic adjustment) (Fig. 3.23). Nerem et al. (2010, manuscript submitted to *Marine Geodesy*) and Leuliette and Scharroo (2010, manuscript submitted to *Marine Geodesy*) provide recent updates of the GMSL trend calculation. Variations in GMSL about the long-term trend tend to correlate with ENSO. This is evident as GMSL dips below the long-term trend during the 2007–08 La Niña event and returns to the long-term trend with perhaps slightly higher values during the latter part of 2009 and the current El Niño event. Because of the combination of the trend and the El Niño, GMSL levels at the end of 2009 were generally the highest over the length of the altimeter record.

Variations in GMSL due to changes in ocean density (steric sea level) and ocean mass are currently under investigation using satellite altimeters, the Argo array (measuring ocean temperature and salinity), and the Gravity Recovery and Climate Experiment (GRACE) time series (measuring ice melt and other hydrological variations). An update to the analysis of Leuliette and Miller (2009) using an additional year of steric observations from Argo profiles and ocean mass variations from the GRACE gravity mission of sea level continues to show that the sea level rise budget can be closed within the range of uncertainties (Fig. 3.24). For the period January 2004 to March 2009, total sea level rise measured by the Jason-1 and Jason-2 altimeters is 2.7 mm yr⁻¹. In areas more than 200 km from the nearest coast, the altimeter rate is 1.8 ± 1.1 mm yr⁻¹, while the combination of the steric and ocean mass components is 1.4 ± 0.6 mm yr⁻¹ or 2.3 ± 0.6 mm yr⁻¹, depending on the choice of a glacial isostatic adjustment correction.

Extreme water levels during 2009 are examined using daily averages obtained from a global set of tide gauges (Fig. 3.25). Extreme levels, taken as the average of the 2% highest daily values relative to the annual mean level (top panel), were high along the coasts of North America, Europe, South Australia, and in the
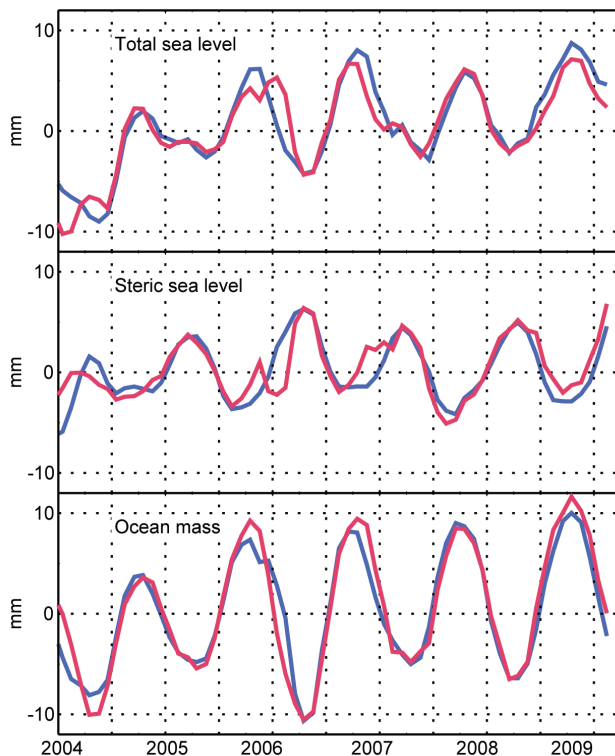
FIG. 3.24. Time series of GMSL, or total sea level, is compared with the two principal components of sea level change, upper-ocean steric change from Argo measurements, and mass change from GRACE measurements (update of Leuliette and Miller 2009). In this figure, blue lines show the observed values and red lines the inferred values from the complementary observations (e.g., the inferred steric sea level is obtained from observed total sea level minus observed ocean mass).

eastern Bay of Bengal. For time series with at least 15 years of record length, we normalize the levels by removing the mean and dividing by the standard deviation of extreme sea levels for all available years (Fig. 3.25, bottom panel). By this measure, extremes along the east coast of the United States (see Sweet et al. 2009 for a description of the summer 2009 sea level anomalies in this region), the south coast of Alaska, and at South Africa were notably higher than normal. Other areas of unusually high values include eastern and southern Australia and isolated stations in Hawaii and the South Pacific. Extremes were generally below normal along the west coast of Canada, at Chile, Scandinavia, Thailand, and at island stations in the western equatorial Pacific.

i. The global ocean carbon cycle—C. L. Sabine, R. A. Feely, R. Wanninkhof, T. Takahashi, S. Khatiwala, and G.-H. Park

1) CARBON DIOXIDE FLUXES

Global ocean surface ocean CO_2 levels are extremely variable in space and time, especially on seasonal time scales. To document the changing patterns of air-sea CO_2 exchange requires an extensive observational program. The latest global flux map, based on a compilation of approximately three million measurements collected between 1970 and 2007, provides information on the monthly patterns of air-sea fluxes during a "normal" non-El Niño year taken to be 2000 (Takahashi et al. 2009a). The number of annual surface CO_2 observations has been growing exponentially since the 1960s such that today well over one million observations are reported to data centers each year. This tremendous increase in the number of annual observations provides exciting opportunities to look at the patterns of air-sea CO_2 fluxes in greater detail to understand the seasonal to interannual variations and the mechanisms controlling them. As a compliment to Takahashi's work
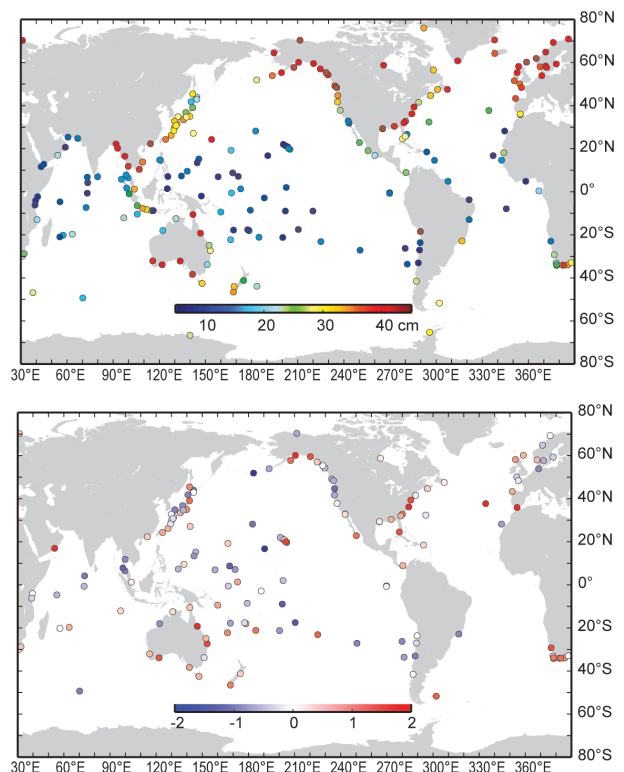

FIG. 3.25. (top) Extreme sea level variability is characterized using the average of the top 2% mean daily sea levels during 2009 relative to the annual mean at each station. (bottom) The extreme values are normalized by subtracting the mean and dividing by the standard deviation of past year extreme values for stations with at least 15-year record lengths.

to update the CO_2 climatology, there is an ongoing international effort to synthesize all the available surface CO_2 data into a quality controlled database that can be used to examine surface CO_2 variability over a range of time and space scales (SOCAT; http://www.socat.info/).

Over the last few years, we have presented annual global air-sea CO_2 flux estimates based on empirical approaches relating in situ measurements with satellite observations of wind and sea surface temperature (Sabine et al. 2008, 2009). The latest empirical approach for quantifying the air-sea CO_2 exchange utilizing in situ, climatological, and satellite data is described in Park et al. (2010, manuscript submitted to *Tellus B*). Lags in availability of quality controlled data streams including atmospheric CO_2, satellite and assimilation products preclude real-time analysis such that consistent, climate quality seasonal air-sea CO_2 flux maps are only available through 2008. The global mean air-sea CO_2 flux for the period from 1982 to 2008 gives an average contemporary net uptake of 1.48 Pg (10^{15} g) C yr^{-1}. Following the Gruber et al. (2009) assumption that the preindustrial steady state ocean was a source of 0.45 Pg C yr^{-1}, the estimated average flux equates to a net ocean anthropogenic CO_2 uptake of 1.93 Pg C yr^{-1}, consistent with the range of estimates (1.8–2.4 Pg-C yr^{-1}) recently summarized by Gruber et al. (2009).

Using the Park et al. (2010, manuscript submitted to *Tellus B*) approach the global net uptake flux for 2008 is estimated to be 1.23 Pg C yr^{-1}, 0.25 Pg C yr^{-1} smaller than the 27-year long-term average (Fig. 3.26). The uncertainty of the empirical flux estimates is difficult to evaluate as discussed in detail in Park et

al. (2006), but the 2008 uptake is significantly lower than the 1σ interannual variability estimate of ±0.14 Pg C yr^{-1} for the whole record. Compared to long-term average fluxes, 2008 generally showed less CO_2 uptake and more CO_2 release with a few notable exceptions including the high-latitude North Atlantic, the eastern subtropical North Pacific, and portions of the Southern Ocean. Greater CO_2 efflux was found in the Equatorial Pacific due to the strengthened upwelling of deep water rich in CO_2. As noted by Takahashi et al. (2009a) the 2008 flux estimates also show areas near 60°S located along the edge of the seasonal sea-ice field had less uptake of CO_2 in summer time and more release of CO_2 in winter time. Despite a band of increased CO_2 uptake in the eastern North Pacific, overall the North Pacific uptake was lower in 2008 relative to the long-term average.

Several recent publications have described regional variations in CO_2 uptake patterns, particularly in the North Atlantic and Southern Ocean, as the ocean carbon community works to distinguish secular trends from natural interannual variations (e.g., LeQuere et al. 2009; Watson et al. 2009; Metzl 2009; Lenton et al. 2009). For example, recent observations suggest a rapid decrease in the CO_2 uptake in the temperate North Atlantic. However, Thomas et al. (2008) used a general circulation model study to infer that the North Atlantic CO_2 uptake may increase again when the NAO returns to a positive state, similar to the early 1990s.

The empirical approach for evaluating the annual CO_2 flux gives an estimated interannual variability of ±0.14 Pg C yr^{-1} over the last three decades. While variability in the North Atlantic and Southern Ocean are observed in our analyses, the largest interannual variations are associated with ENSO changes. A negative correlation (R^2 ~0.68) is observed in a plot of the yearly Multivariate ENSO Index (MEI) values versus the annual global air-sea CO_2 uptake estimates for the period from 1982 to 2008 (Fig. 3.27). A negative MEI value indicates La Niña conditions and thus enhanced CO_2 outgassing in the Equatorial Pacific. In last year's report we described the CO_2 flux patterns associated with the moderate 2007 La Niña (Sabine et al. 2009). The conditions described here for 2008 reflect the second strongest La Niña conditions in the 27-year record and show an overall global ocean flux response of increased outgassing that was consistent with these conditions (Fig. 3.27).

In 2009, the ENSO switched from La Niña to El Niño conditions (chapter 4b). Interestingly, both shipboard measurements and moored CO_2 observations
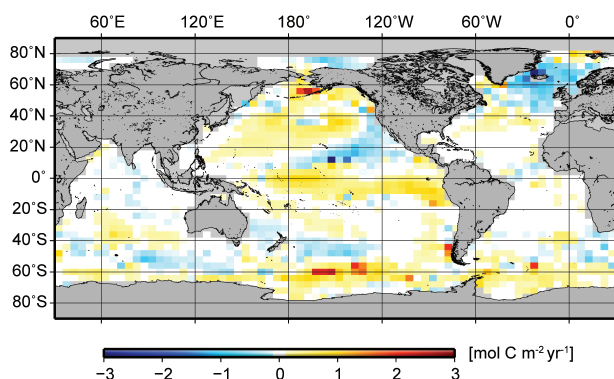

FIG. 3.26. Global distribution of air-sea CO_2 flux anomalies in 2008 compared to 27-year mean values as calculated using the Park et al. (2010, manuscript submitted to *Tellus B*) approach. Positive values indicate less uptake or more release of CO_2 by the ocean. Fluxes are not determined for the gray regions.
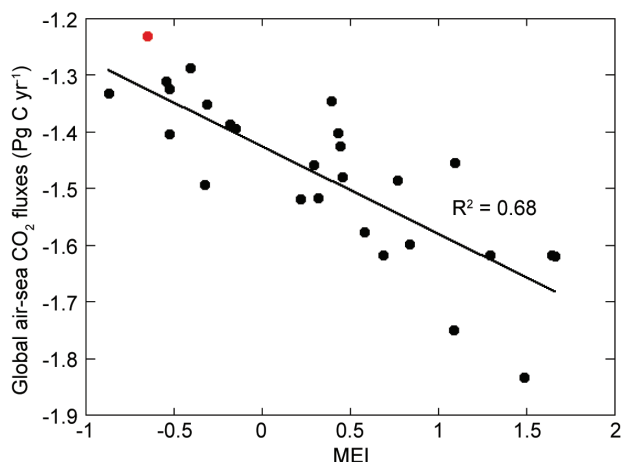
Fɪɢ. 3.27. Correlation between global air-sea CO₂ fluxes and the Multivariate ENSO Index (MEI). The red dot indicates 2008 value.

along the equator are showing a pattern of sustained CO_2 outgassing even in the presence of significant positive temperature anomalies. This switch to El Niño conditions was too recent to evaluate with the climate quality seasonal CO_2 flux maps, but preliminary estimates based on lower quality remotely sensed data are available to within three months of present (see http://cwcgom.aoml.noaa.gov/erddap/griddap/aomlcarbonfluxes.graph). These preliminary results also suggest that large-scale equatorial fluxes are not following the historical El Niño patterns.

The empirical CO_2 flux model generally agrees well with GCM models in both the timing and magnitude of the Equatorial Pacific flux anomalies associated with ENSO (Fig. 3.28). However, the correlation did not hold with the latest El Niño in 2002. The GCM model suggested a significant decrease in outgassing from the Equatorial Pacific which would be expected from the El Niño conditions, but did not seem to be reflected in the in situ observations or the empirical model (Fig. 3.28). The mechanisms responsible for the break down in correlation between the El Niño and the CO_2 during this last El Niño event are being investigated, but the pattern seems to be repeating with this current 2009/10 El Niño. It could be related to the relative roles of horizontal advection versus vertical advection when the warming is focused on the Central Pacific compared to the Eastern Pacific but the data collected during the 2009/10 event will help us to better understand these mechanisms.

2) Sᴜʙsᴜʀғᴀᴄᴇ ᴄᴀʀʙᴏɴ ɪɴᴠᴇɴᴛᴏʀʏ

In the 1990s carbon samples were collected and analyzed from approximately 95 research cruises run as part of the international World Ocean Circulation

Experiment (WOCE) and the Joint Global Ocean Flux Study (JGOFS). Based on these data, Sabine et al. (2004) estimated that the total inventory of anthropogenic CO_2 in the ocean (C_{ant}) in the year 1994 was 118 ± 19 Pg C, accounting for 48% of the CO_2 released from fossil fuel burning between 1800 and 1994. This one-time global survey, however, could not provide information on how ocean carbon inventories have evolved over time or how the storage has varied geographically over different time periods.

In 2003, the U.S. CLIVAR/CO_2 Repeat Hydrography Program began reoccupying a subset of the WOCE/JGOFS ocean survey lines. The program has identified 19 hydrographic sections distributed around the global ocean that will be reoccupied approximately every 10 years to examine changes in ocean carbon and other physical and biogeochemical tracers (http://ushydro.ucsd.edu/). This work is being conducted in collaboration with other nations that have similar repeat hydrography programs.

In 2009 a zonal line (designated as I5) across the southern Indian Ocean, nominally along 32°S, was completed as part of the U.S. CLIVAR/CO_2 Repeat Hydrography Program. The top panel of Fig. 3.29 shows a section of dissolved inorganic carbon (DIC) along I5 in 2009. Unfortunately, very few DIC measurements were made on the previous occupation of I5 by the British in 2002, but DIC can be calculated with reasonable accuracy from the total alkalinity and spectrophotometric pH measurements that were made. The calculated 2002 DIC distributions are shown in the middle panel of Fig. 3.29. The accuracy of the calculated DIC values is estimated to be ±4
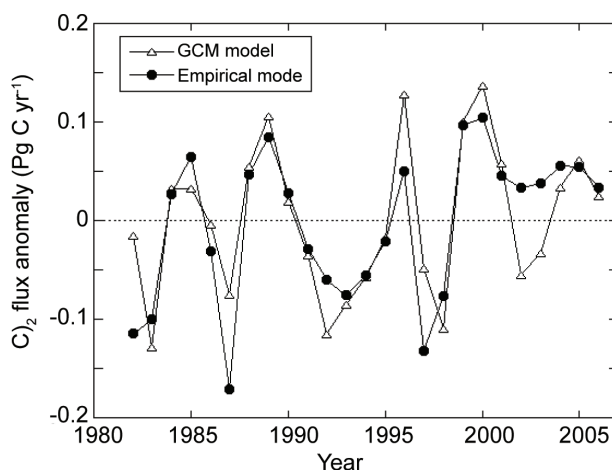

Fɪɢ. 3.28. Comparison of air-sea CO₂ flux anomalies in the Equatorial Pacific (10°S–10°N, 135°E–280°E) between the global ocean Community Climate System Model and the empirical model. Adapted from Park et al. (2010, manuscript submitted to *Tellus B*).

µmol kg^{-1} or about half of the accuracy of the directly measured values. This accuracy was confirmed by comparison with a few dozen DIC samples that were collected and analyzed from the cruise.

To the first order the DIC distributions look similar for both years, but the difference plot (Fig. 3.29, bottom) shows that DIC generally increased throughout the upper 1000 m of the water column presumably resulting primarily from the uptake of anthropogenic CO_2 from the atmosphere. The magnitude of the changes is quite patchy with variations ranging from ~ -30 to +30 µmol kg^{-1}. These changes reflect natural carbon variations as well as secular anthropogenic carbon increases.

A full global assessment of ocean DIC changes cannot be made until the resurvey of the oceans is completed in the next few years. However, a promising new approach for estimating C_{ant} accumulation in the ocean was recently published by Khatiwala et al. (2009). Their approach is based on an inverse method to estimate the ocean's transport from observed tracer distributions together with an estimate of the spatiotemporally varying air-sea CO_2 disequilibrium based on the long-term record of atmospheric CO_2 concentrations. The latter, which is also constrained by surface ocean pCO_2 data (Takahashi et al. 2009b), provides a time-varying boundary condition that can be used to compute the C_{ant} at any point in the ocean at any instant in time using the transport estimate. Khatiwala et al. have used this technique to reconstruct the spatially-resolved, time-dependent history of C_{ant} and its air-sea flux between 1765 and 2008. By taking into account the changing air-sea disequilibrium of CO_2 and the complex advective-diffusive transport of tracers in the ocean, this approach overcomes some of the main limitations and biases of previous techniques. However, it does not account for potential changes in the fundamental processes controlling the distribution of natural carbon in the ocean such as variations in large-scale circulation, ventilation, or in the biological carbon pump.

Figure 3.30 shows a map of the C_{ant} column inventory in 2008 estimated using the method of Khatiwala et al. (2009). The first order patterns are very similar to those determined from the independent approach of Sabine et al. (2004) with the largest inventories in the North Atlantic, where the formation of deep waters move C_{ant} into the ocean interior. Relatively large inventories are also associated with the subtropical convergence zone at approximately 40°S in the Southern Hemisphere. The total 2008 inventory estimated for the mapped region in Fig. 3.30 is 140 Pg C. Adding in the Arctic Ocean inventory as estimated by Tanhua et al. (2009) and the marginal seas using the same scaling function as Sabine et al. (2004) gives a total global ocean inventory of 151 Pg C. This estimate suggests a 33 Pg C increase in inventory since the Sabine et al. estimate for 1994 reflecting the continued uptake and storage of C_{ant} at rates of 2.0 and 2.3 ±0.6 Pg C yr^{-1} for the decades of the 1990s and 2000s, respectively (Khatiwala et al. 2009).

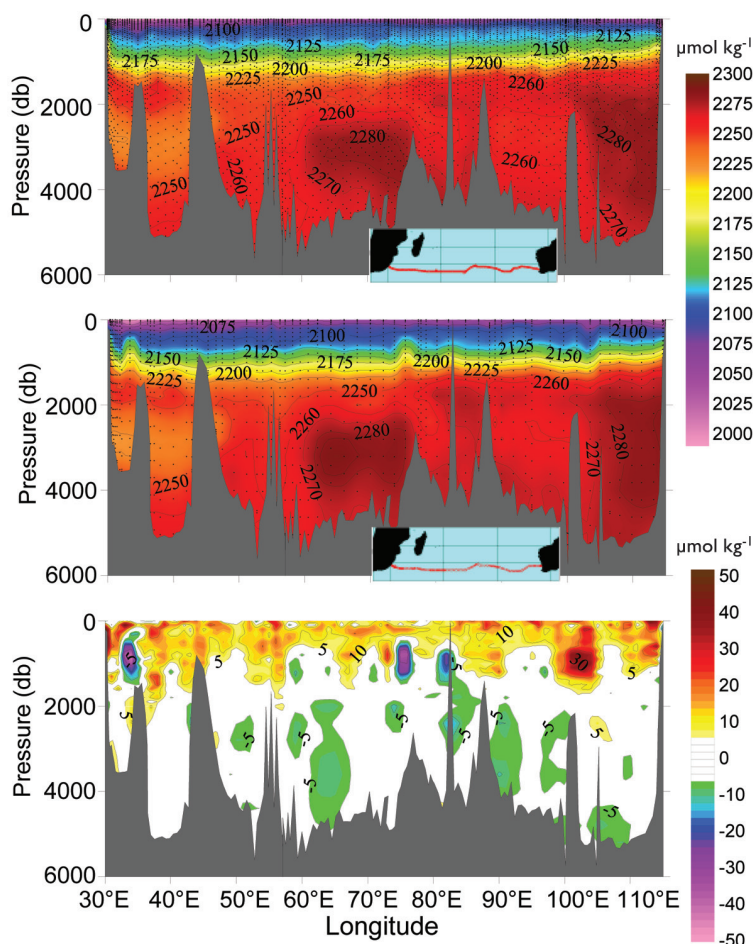**FIG. 3.29 Sections of dissolved inorganic carbon (µmol kg^{-1}) nominally along 32°S in 2009 (top) and 2002 (middle). The 2002 DIC values were calculated from total alkalinity and pH measurements (see text). Black dots show sample locations. Inset map shows cruise track in red. The bottom section shows the DIC change (µmol kg^{-1}) between the two cruises (2009 minus 2002).**
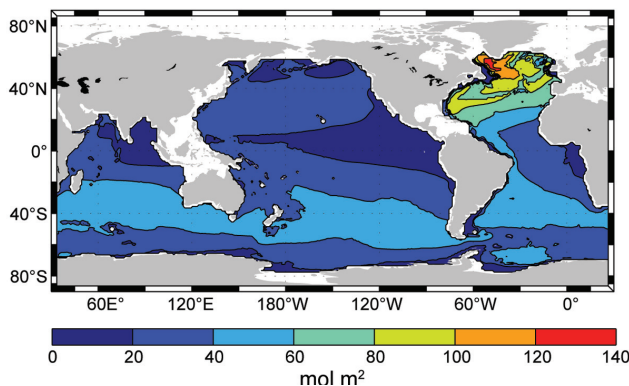
Fɪɢ. 3.30. Map of the column inventory of anthropogenic CO$_2$ in 2008. Adapted from Khatiwala et al. 2009.

One advantage of the Khatiwala estimates is the ability to examine the changes in ocean carbon storage over time. For example, these estimates suggest that the annual rate of ocean carbon storage has grown every year since the late 1700s, but the rate increased sharply in the 1950s in response to faster growth in atmospheric CO$_2$. In recent decades, however, the rate of increase in ocean carbon storage has not been able to keep pace with the atmospheric growth rate. The percentage of annual anthropogenic CO$_2$ emissions stored in the ocean in 2008 was as much as 10% smaller than the percentages of the previous decade, although significant uncertainties remain which preclude a more definitive statement. The rapid growth in emissions over the past 10 years relative to the previous decade is one important factor in the reduction in the ocean's relative uptake of anthropogenic CO$_2$ emissions. Another key factor is the decreasing ability of the seawater to store the CO$_2$ as dissolved inorganic carbon. This reduced capacity is a natural and predictable consequence of ocean carbon chemistry that, in the absence of changes in large-scale circulation or ocean biology, will become more significant with time (Egleston et al. 2010). By comparing the Khatiwala estimates at the time and location of the repeat hydrography cruises the measured ocean carbon changes can be used to validate the C$_{ant}$ estimates and monitor for changes in the natural ocean carbon cycle not constrained by the Khatiwala technique.

j. Global ocean phytoplankton—R. T. O'Malley, M. J. Behrenfeld, D. A. Siegel, and S. Maritorena

Photosynthesis by the free-floating, single-celled phytoplankton of the upper-sunlit "photic" layer of the global ocean is the overwhelmingly dominant source of organic matter fueling marine ecosystems. Phytoplankton contribute roughly half of the annual biospheric (i.e., terrestrial and aquatic) net primary production (NPP; gross photosynthesis minus plant respiration), and their photosynthetic carbon fixation is the primary conduit through which atmospheric CO$_2$ is transferred into the ocean's organic carbon pools. These tiny suspended ocean "plants" play a vital role on the Earth's biogeochemical cycles, and are the very base of the oceanic food chain. The productivity of phytoplankton depends on the availability of sunlight, macronutrients (e.g., nitrogen, phosphorous), and micronutrients (e.g., iron), and thus is sensitive to changes in these resources.

Since 1997, a continuous record of global satellite ocean color observations has been available, allowing the investigation of relationships between ocean environmental conditions and plankton ecology (e.g., McClain 2009; Behrenfeld 2010). The ecosystem property most often derived from ocean color data is surface chlorophyll concentration (Chl$_{sat}$) (Fig. 3.31a). Chl$_{sat}$ provides an estimate of phytoplankton pigment concentration throughout the upper ocean mixed layer and its variability reflects the combined influence of phytoplankton standing stock (biomass) changes and physiological responses to prevailing light and nutrient levels. Values of Chl$_{sat}$ span three orders of magnitude globally (roughly 0.03 to >30 mg m^{-3}) with a distribution closely aligned with primary ocean circulation features. Thus, high Chl$_{sat}$ is found in regions of seasonal deep mixing (e.g., North Atlantic) and upwelling (e.g., Equatorial Pacific, west coast of Africa), while low values are found in permanently stratified ocean regions, particularly the low-nutrient central ocean gyres (white contours in Fig. 3.31a).

Climate-scale analyses require both *continuity* and *consistency* in the underlying observations for correct assessments of change. Unfortunately, these attributes are not satisfied for the most recent period of satellite ocean color measurements. Starting in 2008 and after more than a decade of continuous coverage, observations from the Sea-viewing Wide-Field-of-view Sensor (SeaWiFS) became intermittent due to issues with the spacecraft and telemetry. No SeaWiFS imagery was collected for the first 88 days of 2008 and, over the whole year, only 31 of 46 possible eight-day composite images could be processed. Data gaps also exist for 2009, with only 34 valid eight-day composites available over the year. Thus, 30% of the SeaWiFS record is missing for 2008/09 and only one-third of the eight-day composites are temporally matched for the two years. This lack of continuity strongly restricts an interannual comparison. Fortunately, half of the
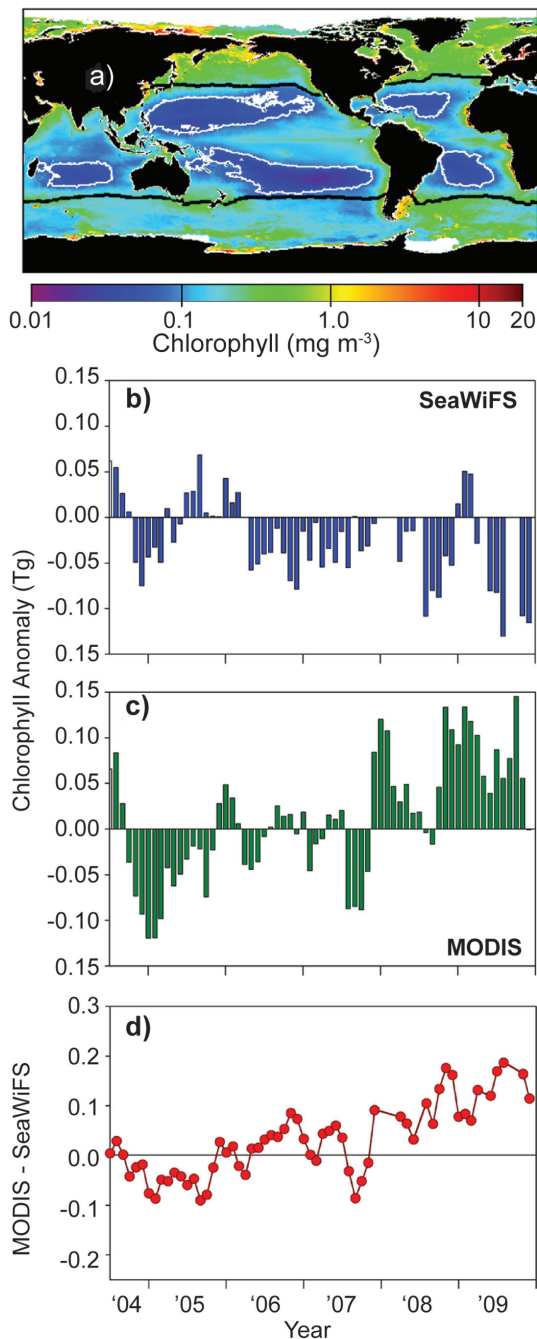
FIG. 3.31. (a) Average MODIS-*Aqua* Chl$_{sat}$ for 2009. Heavy black lines indicate where average SST=15°C, which is used herein to distinguish the permanently stratified ocean from northern and southern strongly-seasonal regions. White contours identify central ocean gyres, as defined by average Chl$_{sat}$ values of 0.07 mg m^{-3} (see also McClain et al. 2004; Polovina et al. 2008; and Henson et al. 2009). (b) Mid-2004 through 2009 monthly chlorophyll anomalies for the SeaWiFS (data from latest reprocessing: r2009.1). (c) Mid-2004 through 2009 monthly chlorophyll anomalies for the MODIS-*Aqua*. (d) MODIS-SeaWiFS anomaly difference. Data in (b), (c), and (d) are for the permanently stratified oceans (average SST>15°C).

coverage common to both years occurred at the end of the calendar year, providing two months of continuous coverage of the El Niño event developing over the latter half of 2009 (Chapter 4a).

Consistency between available U.S. ocean color datasets is also a problem. In the *State of Climate in 2008* report, we noted a relatively constant offset between the SeaWiFS Chl$_{sat}$ record and concurrent data from the MODerate resolution Imaging Spectrometer (MODIS) on the *Aqua* platform. Accordingly, we found reasonable agreement between temporal chlorophyll anomalies for the two sensors (Behrenfeld et al. 2009) [as in the current report, anomalies were calculated as the difference between an observed value for a given month and the average value for that month over a sensor's full record (e.g., 1997–2009 for the SeaWiFS)]. Unfortunately, discrepancies between Chl$_{sat}$ anomalies for the SeaWiFS (Fig. 3.31b) and MODIS-*Aqua* (Fig. 3.31c) increased during 2009, such that a simple offset correction is no longer adequate. The temporal evolution of this inter-sensor inconsistency is clearly revealed in the MODIS-SeaWiFS anomaly difference for the period 2004 to 2009 (Fig. 3.31d). While this issue of inconsistency has limited the current analysis of Chl$_{sat}$ changes to SeaWiFS data only, it is important to note that the full MODIS-*Aqua* dataset is currently being reprocessed by the NASA Ocean Biology Processing Group and preliminary comparisons between the SeaWiFS and reprocessed MODIS-*Aqua* scenes look excellent (see http://oceancolor.gsfc.nasa.gov/REPROCESSING/R2009/ for more details). Nevertheless, this experience emphasizes the critical importance of monitoring and updating ocean color sensor calibrations/algorithms and conducting periodic data reprocessing to achieve data quality levels adequate for satellite-based global climate studies.

To investigate changes in global ocean chlorophyll stocks during 2009, available SeaWiFS data were analyzed following methodologies originally described in Behrenfeld et al. (2006) and employed in our two previous *State of the Climate* reports (Behrenfeld et al. 2008b, 2009). Chl$_{sat}$ data (mg m^{-3}) were integrated to the 1% light level to calculate 'photic zone' chlorophyll concentrations (ΣChl). For analysis of chlorophyll anomaly trends, global data were binned into three broad regions: the permanently stratified ocean (approximated as those waters with annual average SST > 15°C), strongly-seasonal high-latitude northern waters (average SST < 15°C), and strongly-seasonal high-latitude southern waters (average SST < 15°C).
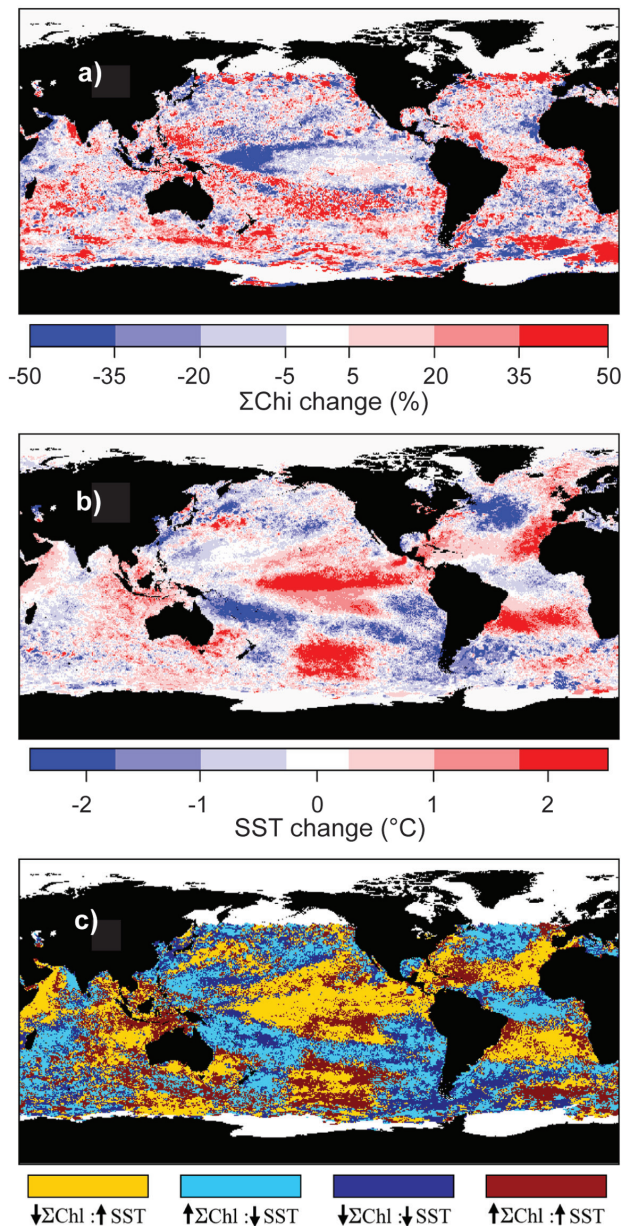
FIG. 3.32. (a) Percent change in November-December average depth-integrated chlorophyll (∑Chl) between 2009 and 2008. (b) Absolute change in November-December average SST between 2009 and 2008. (c) State-space comparison between ∑Chl and SST (from panels a and b). Yellow = increasing SST, decreasing ∑Chl. Red = increasing SST, increasing ∑Chl. Dark blue = decreasing SST, decreasing ∑Chl. Light blue = decreasing SST, increasing ∑Chl.

For each region, ∑Chl data (mg m^{-2}) were summed over surface area to give total chlorophyll stocks in units of teragrams (Tg = 10^{12} g).

Spatiotemporal variations in Chl$_{sat}$ are driven by variability in phytoplankton biomass, nutrient stress, and light acclimation (i.e., photoacclimation),

all of which are linked to physical changes within the surface mixed layer. Changes in SST provide one index of this variability in the physical environment and can be compared globally to changes in Chl$_{sat}$ (Behrenfeld et al. 2006, 2008a, 2009). The relationship between phytoplankton chlorophyll and SST changes for the 2008 to 2009 period is best illustrated over the November–December period corresponding to the strengthening of the 2009 El Niño (Fig. 3.32). For this period, expansive and spatially coherent regions are seen of increasing and decreasing ∑Chl (Fig. 3.32a). In particular, ∑Chl decreased over much of the equatorial Pacific in response to lower nutrient levels associated with reduced rates of upwelling. In contrast, significant increases in ∑Chl are found in the western tropical Pacific, the south Pacific and Indian subtropical gyres and the equatorial Atlantic Ocean (Fig. 3.32a). These changes in ∑Chl correspond to similar spatial patterns in SST changes (Fig. 3.32b), again illustrating the close link between ocean biology and their physical environment.

Overall for the stratified oceans, 63% of the pixels with increased SST for November–December 2009 also exhibited decreased in ∑Chl (yellow pixels in Fig. 3.32c). Likewise, 60% of the pixels with decreased SST corresponded to increased ∑Chl (light blue pixels in Fig. 3.32c). This dominant inverse relationship between SST changes and ∑Chl changes is consistent with surface-ocean warming (cooling) being associated with decreasing (increasing) vertical nutrient transport and increasing (decreasing) mixed-layer light levels, with light and nutrient changes driving changes in both phytoplankton cellular pigment levels and biomass.

Relationships between global chlorophyll fields and SST illustrated in Fig. 3.32 are seen at a much broader level when cast against the full 12-year Sea-WiFS record for the three regions described above. For this comparison, monthly anomalies in regional SeaWiFS chlorophyll stocks were matched to SST anomalies constructed by merging MODIS-*Aqua* SST4 data (2003–09) and AVHRR (quality 5–8) SST data (1997–2003) (regionally-integrated SST data have units of °C m^2 and are hereafter referred to as 'thermal anomalies'). Once again, an overall inverse relationship emerges at the regional scale for the full SeaWiFS record [Fig. 3.33 – note that the thermal anomaly axes are inverted (i.e., cooling at top, warming at bottom)]. Indeed, the newly reprocessed SeaWiFS data provides an even closer match between thermal anomalies and chlorophyll anomalies than previously reported (e.g., compare to Behrenfeld et al. 2009). At high-northern

latitudes, chlorophyll and thermal oscillations were relatively constrained between 1997 and 2006 and then showed significantly stronger variability (Fig. 3.33a). As in previous reports (Behrenfeld et al. 2008b, 2009), chlorophyll and thermal anomalies exhibited the largest temporal changes in the permanently stratified, lower-latitude oceans (Fig. 3.33b – note different axis scaling), with a large initial trend of increasing chlorophyll and decreasing temperature associated with the 1997–99 El Niño (Behrenfeld et al. 2006). From 1999 onward, an overall progressive decrease in chlorophyll is observed and coincident with a general increasing trend in surface-ocean temperature (Fig. 3.33b). At high-southern latitudes, temporal trends in chlorophyll and thermal anomalies are weaker (Fig. 3.33c).

While comparisons of surface chlorophyll and temperature data illustrate the strong dependencies of biology on physical forcings, it is important to recognize that the underpinnings of such relationships are correlative not causative. For each region, the full range in thermal anomalies represents an average change in SST that barely spans 1°C. The direct physiological consequences (e.g., enzymatic reaction rates) of such minute temperature changes are negligible. Thus, correlations between SST and chlorophyll anomalies emerge because SST acts as a surrogate for other environmental factors that covary with SST and directly impact phytoplankton chlorophyll levels. Two such factors are nutrient supply and mixed-layer light levels. In general, surface-layer warming is associated with stronger surface-layer stratification and shallower mixing depths, which in turn increase average mixed-layer phytoplankton light exposure and can hamper vertical nutrient exchange (Behrenfeld et al. 2005; Siegel et al. 2005). Decreased nutrient availability suppresses phytoplankton cellular chlorophyll levels and can diminish phytoplankton biomass. Likewise, acclimation to enhanced mixed-layer light exposure entails reductions in cellular chlorophyll. Changes in seasonal surface mixing cycles can also influence chlorophyll levels by altering predator-prey interactions and thereby phytoplankton biomass and species composition (Behrenfeld 2010). Thus, it is the correlation between SST and the summed expression of these, and other, direct forcings that gives rise to inverse chlorophyll–SST relationships. It is essential that these *functional* relationships be carefully considered when interpreting observed global changes in satellite chlorophyll fields and when projecting observed changes to longer time-scale trends.
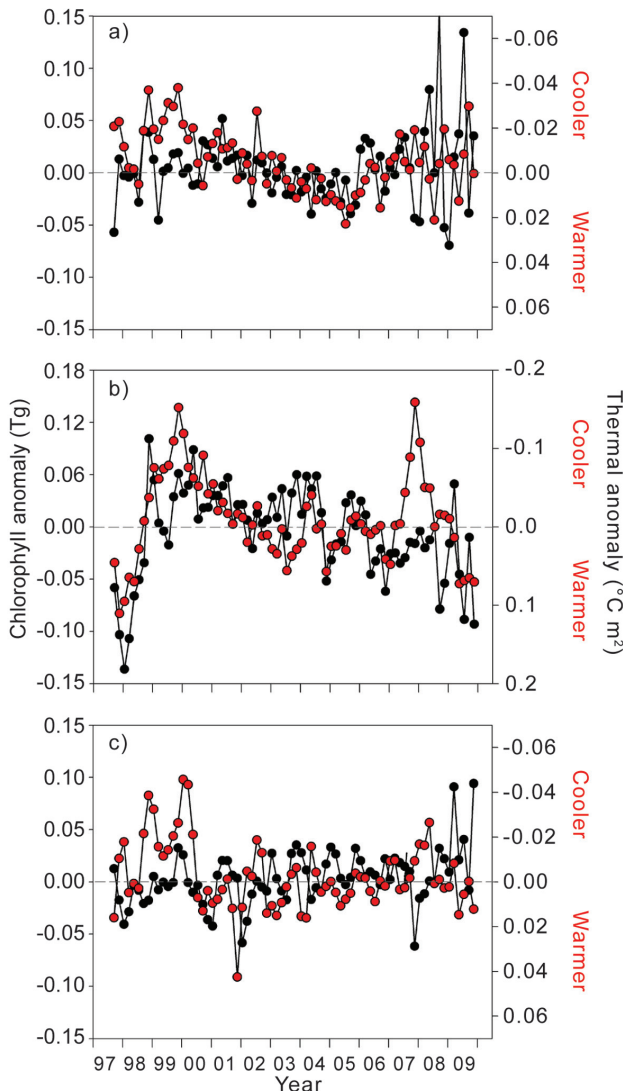
FIG. 3.33. Twelve-year record of monthly SeaWiFS chlorophyll anomalies (black symbols, left axis, Tg) and monthly AVHRR/MODIS thermal anomalies (red symbols, right axis, °C m² x10¹⁵). (a) Northern waters with average SST < 15°C. (b) Permanently stratified waters with average SST > 15°C. (c) Southern waters with average SST < 15°C. See Fig. 3.31a for location of each region. Horizontal dashed line in each panel = 0. Thermal anomaly axes (right) are inverted to illustrate the general inverse relationship with chlorophyll anomalies and thermal anomalies. Note that the use of thermal anomalies in this figure differs from Behrenfeld et al. 2008b and 2009. This change was made to preserve identical processing with the chlorophyll signal.

4. THE TROPICS—H. J. Diamond, Ed.

a. Overview—H. J. Diamond

The year was characterized by a transition from waning La Niña conditions to a building El Niño, which developed in June and then strengthened to what NOAA's Climate Prediction Center (CPC) considers to be a strong episode. By December, SSTs were more than 2.0°C above average over large parts of the central and eastern equatorial Pacific from 175°W to 90°W.

Overall global tropical cyclone (TC) activity during 2009 was the lowest since 2006, with six of the seven main hurricane basins (the exception is the Eastern North Pacific) experiencing near-normal or somewhat below normal TC activity. The El Niño contributed to what is only the second below-normal hurricane season for the Atlantic basin since 1995 and at the same time contributed to a sharp increase in TC activity in the Eastern North Pacific basin which comprises both the eastern and central Pacific sub-regions. With the passage of the remnants of Hurricane Felicia that resulted in some significant rainfall and flooding, the state of Hawaii experienced its first TC since Hurricane Iniki in 1992.

The Atlantic ITCZ was prominently featured in the news, as strong convective activity associated with it was cited as one possible factor in the tragic downing of Air France Flight 447 some 300 miles off the coast of Brazil in early June. In the Indian Ocean, the 2009 season had a neutral to weak Indian Ocean Dipole (IOD) signal after an unprecedented three-consecutive positive IOD signals from 2006 to 2008.

This tropics chapter consists of six sections: (1) ENSO and the Tropical Pacific; (2) Tropical Intraseasonal Activity; (3) TC activity for the 2009 season in seven basins: the North Atlantic, Eastern North Pacific, Western North Pacific, North Indian and South Indian Oceans, Southwest Pacific, and Australia; (4) ITCZ behavior in the Pacific and Atlantic basins; (5) the IOD; and (6) a section on TC Heat Potential, previously in the Oceans chapter, helps summarize the section for TCs from an ocean heat perspective.

b. ENSO and the tropical Pacific—M. Halpert, G. D. Bell, and M. L'Heureux

1) Oceanic conditions

ENSO is a coupled ocean-atmosphere phenomenon centered in the equatorial Pacific Ocean. ENSO features two opposing phases, El Niño and La Niña, which are responsible for considerable interannual climate variability in the global tropics and the mid-to-high latitudes. NOAA defines these ENSO phases

using the Niño 3.4 index, which reflects area-averaged SST anomalies in the east-central equatorial Pacific between 5°N and 5°S and 170°W and 120°W. El Niño occurs when the three-month running mean value of the Niño 3.4 index (called the Oceanic Niño Index—ONI) is greater than or equal to +0.5°C; La Niña occurs when the ONI is less than or equal to −0.5°C.

Both La Niña and El Niño occurred during 2009, with La Niña continuing during January–March (JFM) and El Niño prevailing from June through the end of the year (Fig. 4.1). December–February (DJF) in the 2008/09 season represented the second consecutive DJF period with La Niña conditions. During JFM, the weekly Niño 3.4 index ranged from −0.5°C to −1.1°C (Fig. 4.1). La Niña ended abruptly in early April as SST anomalies increased rapidly, with anomalous warming continuing during April–June, leading to the development of El Niño in late June. El Niño remained weak through September. Rapid strengthening during October followed and the Niño 3.4 index more than doubled to +1.5°C. Additional strengthening occurred during November and December, with the Niño 3.4 index averaging +1.8°C during December. The ONI value for October–December (OND) reached +1.5°C, which the NOAA's CPC considers to be a strong episode.

The anomalous seasonally-averaged surface and sub-surface temperature patterns associated with ENSO during 2009 are summarized in Figs. 4.2 and 4.3, respectively. During DJF, the equatorial cold tongue in the eastern Pacific Ocean was very well-defined and extended westward to the international date line (Fig. 4.2a). This feature was also stronger than average, with negative SST anomalies of −1°C evident in parts of the central and eastern Pacific (Fig. 4.2b). The pattern of sub-surface temperature anomalies during the period reflected an increased slope of the thermocline (thick black line) with positive sub-surface temperature anomalies and a deeper-than-normal thermocline in the western Pacific and negative anomalies and a shallower-than-normal
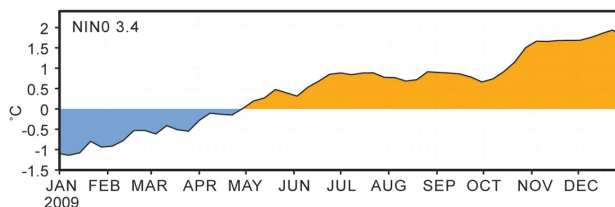

FIG. 4.1. Time series of weekly SST anomalies (°C) in the Niño-3.4 region (5°N–5°S, 170°–120°W). Anomalies are departures from the 1971–2000 weekly adjusted OI climatology of Smith and Reynolds (1998).
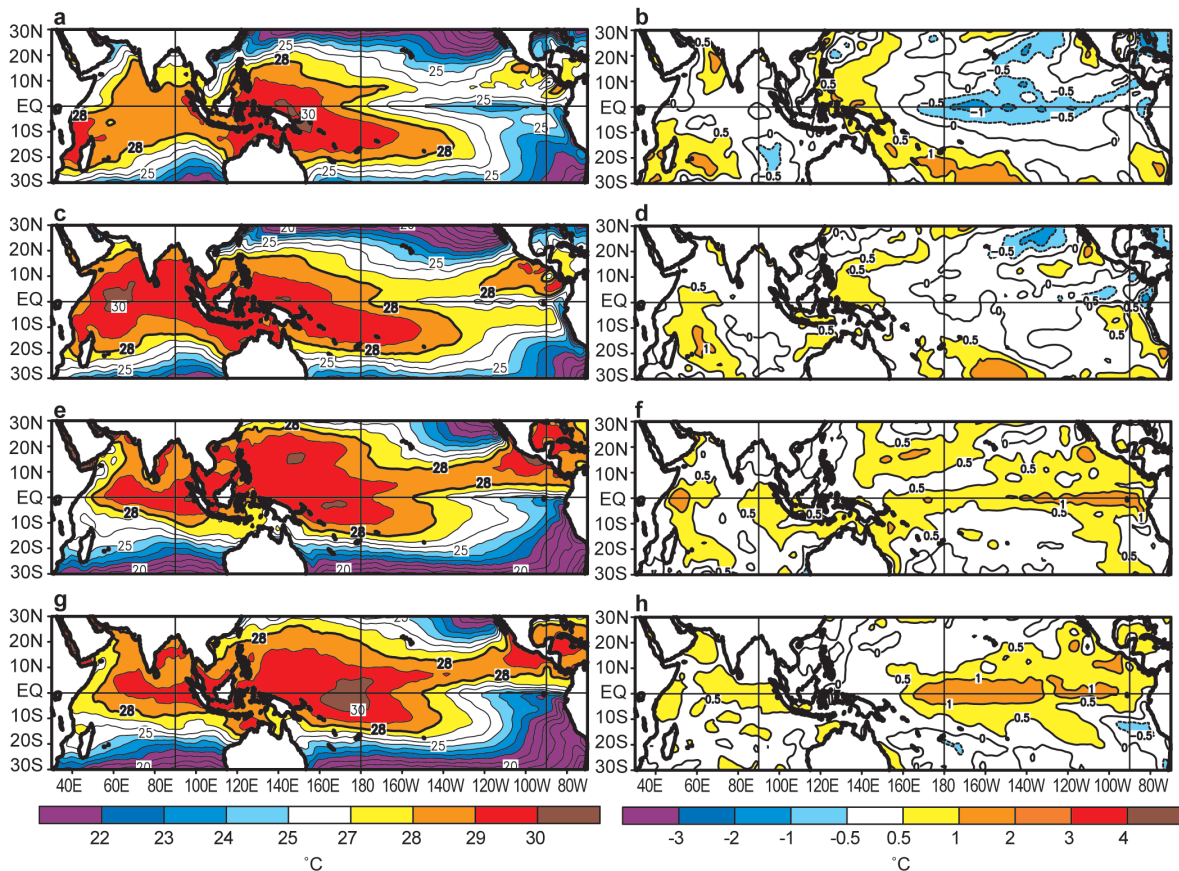
FIG 4.2. Seasonal SST (left) and anomaly (right) for (a), (b) DJF 2008/09, (c), (d) MAM 2009, (e), (f) JJA 2009 and (g), (h) SON 2009. Contour interval is 1°C, with the 0.5°C anomaly contour included. Anomalies are departures from the 1971–2000 seasonal adjusted OI climatology of Smith and Reynolds (1998).

thermocline in the east-central and eastern Pacific (Fig. 4.3a). These conditions are consistent with La Niña.

During March–May (MAM), surface (Figs. 4.2c, 4.2d) and subsurface ocean temperatures (Fig. 4.3b) returned to near-average across the eastern equatorial Pacific. Beginning in April, periodic westerly wind bursts over the western Pacific initiated equatorial oceanic Kelvin waves (section 4c, Fig. 4.7). During both June–August (JJA) and September–November (SON) (Figs. 4.3c, 4.3d) these Kelvin waves were associated with a deepening of the oceanic thermocline in the central and eastern Pacific and with a corresponding increase in subsurface ocean temperatures. At the same time, positive SST anomalies developed across the central and eastern part of the basin as El Niño developed and strengthened (Figs. 4.2f, 4.2h). Within the Niño 3.4 region, the dramatic increase in SSTs during October and early November was also associated with a strong oceanic Kelvin wave. By December 2009, SSTs were more than 2.0°C above average over large parts of the equatorial Pacific be-

tween 175°W and 90°W, with the warmest total SSTs (> 30°C) centered near the international date line.

2) ATMOSPHERIC CIRCULATION

Although La Niña was short-lived and modest in amplitude, its impacts on the patterns of tropical convection and atmospheric winds were pronounced (Fig. 4.4). For example, convection during DJF 2008/09 was suppressed over the central and west-central equatorial Pacific (brown shading) and enhanced over Indonesia and the far western Pacific (green shading). This pattern reflected a westward retraction of the equatorial convection toward the western Pacific and a disappearance of convection from the central Pacific. These conditions, combined with equatorial low-level easterly wind anomalies (Fig. 4.4a) and upper-level westerly wind anomalies (Fig. 4.4b), were associated with an enhanced Walker circulation typical of La Niña. Additional La Niña impacts were seen in the subtropics of both hemispheres, where upper-level cyclonic anomalies flanked the region of suppressed convection over the central Pacific.
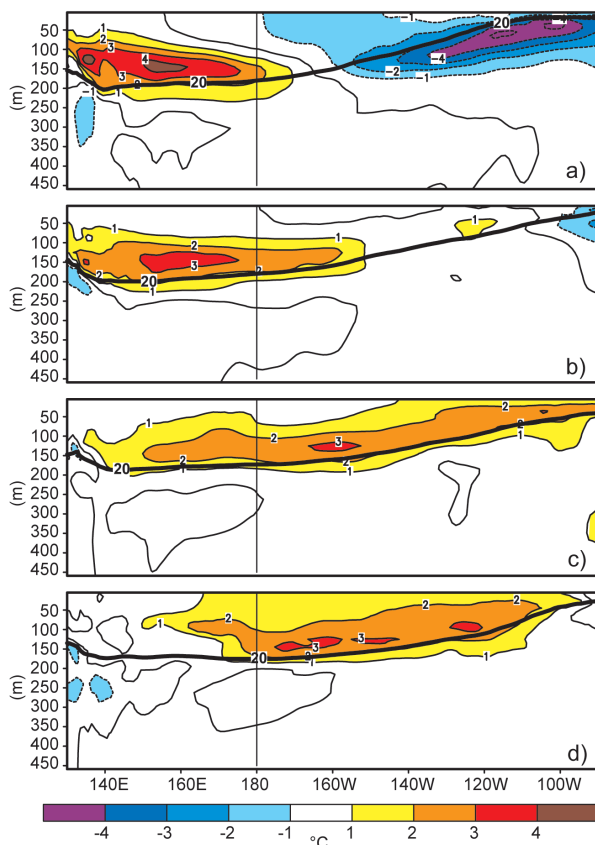
FIG. 4.4. (a) Anomalous 850-hPa wind vector and speed (m s⁻¹) and anomalous OLR (shaded, W m⁻²) during DJF 2008/09 and (b) anomalous 200-hPa wind vector and speed (m s⁻¹) and anomalous OLR (shaded, W m⁻²) during DJF 2008/09. Anomalies are departures from the 1979–95 period monthly means.

FIG 4.3. Equatorial depth-longitude section of ocean temperature anomalies (°C) averaged between 5°N and 5°S during (a) DJF 2008/09, (b) MAM 2009, (c) JJA 2008, and d) SON 2008. The 20°C isotherm (thick solid line) approximates the center of the oceanic thermocline. The data are derived from an analysis system that assimilates oceanic observations into an oceanic GCM (Behringer et al. 1998). Anomalies are departures from the 1971–2000 period monthly means.

FIG. 4.5. Anomalous 200-hPa streamfunction (shading, x 10⁶ m² s⁻¹) and wind vectors (m s⁻¹) during (a) JJA 2009 and (b) OND 2009. Anomalous ridges are indicated by positive values (red) in the NH and negative values (blue) in the SH. Anomalous troughs are indicated by negative values in the NH and positive values in the SH. Vector scale is to right of color bar. Anomalies are departures from the 1971–2000 period monthly means.

This anomaly pattern featured a retraction of the mean subtropical ridges in both hemispheres toward the western Pacific. In the Northern Hemisphere, it also reflected a westward retraction of the East Asian jet stream and below-average jet stream winds east of the date line. These conditions dissipated during MAM as La Niña ended.

El Niño developed during JJA and produced discernible impacts on the upper-level circulation (Fig. 4.5a) in a manner consistent with past episodes (Chelliah and Bell 2004). Prominent features of El Niño during this period included an anomalous zonal wave-1 pattern of 200-hPa streamfunction anomalies in the subtropics of both hemispheres. This pattern featured weak anticyclonic circulation anomalies over the central Pacific Ocean in both hemispheres and relatively stronger cyclonic anomalies extending eastward from the Americas to Australasia. Associated

with this pattern, westerly wind anomalies between 30°S and 40°S reflected a strengthening and eastward extension of the mean wintertime jet stream over the South Pacific Ocean. Similar anomaly patterns were also evident during August–October (ASO), which led to a suppression of hurricane activity across the Atlantic basin (see section 4d2) and to stronger hurricane seasons in both the central (see sidebar article) and eastern Pacific (see section 4d3) sub-basins.

El Niño impacts on the 200-hPa circulation were especially pronounced during OND (Fig. 4.5b), with well-defined anticyclonic anomalies evident in the subtropics of both hemispheres over the central equatorial Pacific. In the Northern Hemisphere, strong westerly wind anomalies over the North Pacific between 20°N and 30°N reflected a pronounced eastward extension of the East Asian jet stream and an eastward shift of the mean jet exit region toward the eastern Pacific. North of the jet, the typical El Niño-related pattern of cyclonic anomalies was also evident. Along with these impacts, the extratropical anomaly patterns during both October and December also reflected record negative phases of the Arctic Oscillation (AO).

3) ENSO TEMPERATURE AND PRECIPITATION IMPACTS

During DJF 2008/09 La Niña impacted global precipitation patterns in a manner consistent with past cold episodes (Ropelewski and Halpert 1989). These impacts included suppressed convection across the central equatorial Pacific and above-average rainfall across much of the Maritime Continent (Indonesia, Philippines, Malaysia, and Borneo), which extended to the northernmost portions of Australia (Fig. 4.4a). In addition, above-average rainfall was observed in northeastern Brazil. Similar anomalies were also observed during DJF 2007–08 in association with La Niña (L'Heureux et al. 2009).

In the United States, La Niña contributed to drier than average conditions across the South during DJF 2008/09 and to increased precipitation in the northern Rockies and the Ohio and Tennessee Valleys. Temperatures over the United States were also generally consistent with La Niña, with below-average temperatures across the northern part of the country and above-average temperatures across parts of the South.

By the end of the year, the patterns of precipitation typically associated with El Niño (Ropelewski and Halpert 1987) were observed over parts of the world. These included above-average precipitation in the central equatorial Pacific and southeastern South America and below-average precipitation in parts of Indonesia and the Amazon Basin. Enhanced storminess and precipitation were observed across the southeastern United States in association with the anomalous East Asian jet stream.

c. Tropical intraseasonal activity—J. Gottschalck and G. D. Bell

The MJO (Madden and Julian 1971, 1972, 1994) is a leading climate mode of tropical convective variability that occurs on intraseasonal time scales.

The convective anomalies associated with the MJO often have the same spatial scale as ENSO, but differ in that they exhibit a distinct eastward propagation and generally traverse the globe in 30–60 days. The MJO can strongly affect the tropical and extratropical atmospheric circulation patterns and sometimes produces ENSO-like anomalies (Mo and Kousky 1993; Kousky and Kayano 1994; Kayano and Kousky 1999). The MJO is often quite variable in any given year, with periods of moderate-to-strong activity sometimes followed by little or no activity. Overall, the MJO tends to be most active during neutral and weak ENSO periods and is often absent during strong El Niño events (Hendon et al. 1999; Zhang and Gottschalck 2002; Zhang 2005).

The MJO is seen by continuous propagation of 200-hPa velocity potential anomalies around the globe. A time-longitude section of this parameter shows four periods during 2009 with MJO activity
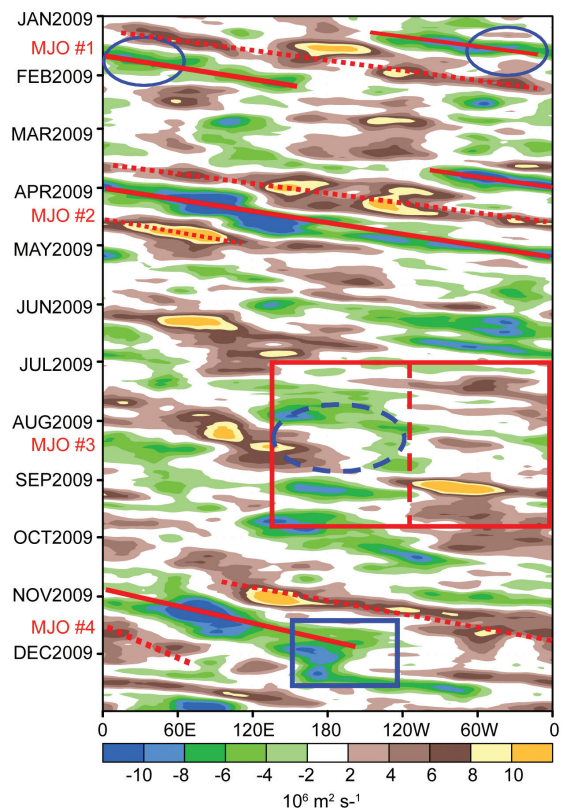
FIG. 4.6. Time-longitude section for 2009 of anomalous 200-hPa velocity potential (x 10⁶ m² s⁻¹) averaged between 5°N-5°S. For each day, the average anomaly for the previous 120 days is removed prior to plotting. Green (brown) shading highlights likely areas of anomalous divergence and rising motion (convergence and sinking motion). Red lines highlight the main MJO episodes. Anomalies are departures from the 1971–2000 base period daily means.

(Fig. 4.6). These include four MJO periods depicted in Fig 4.6 as follows: (1) moderate activity during January (labeled MJO #1), (2) strong activity from mid-March to early May (MJO #2) (3) intraseasonal variability during July and August which partly reflected the MJO (MJO #3) and (4) strong activity from late October to mid-December (MJO #4).

During the first half of January, a combination of the MJO and background La Niña conditions produced enhanced rainfall across Indonesia (indicated by negative velocity potential anomalies and anomalous upper-level divergence) and a stronger than normal South Pacific Convergence Zone (SPCZ) (not shown). During the remainder of January, very wet conditions were observed across portions of equatorial South America and Africa as this upper-level divergence shifted eastward (blue circles on Fig. 4.6). During April even stronger MJO activity produced anomalous upper-level divergence and increased tropical rainfall from the Indian Ocean across Indonesia into the western Pacific.

From late July to mid-August, several forms of intraseasonal variability [including a faster propagating atmospheric Kelvin wave (Wheeler and Kiladis 1999; Wheeler and Weickmann 2001) and the MJO] contributed to an eastward shift of positive velocity potential anomalies and anomalous upper-level convergence from Indonesia to the central Pacific Ocean (Fig. 4.6, dashed blue circle). This shift acted to increase tropical activity in the Atlantic basin during an otherwise below average season, as demonstrated by development of TCs Ana, Bill, and Claudette (see section 4d2). This observation is consistent with past studies showing that conditions are more favorable for tropical development in the Atlantic basin when upper-level convergence prevails over the western Pacific Ocean to near the international date line and upper-level divergence dominates the western hemisphere (Mo 2000; Maloney and Hartmann 2000). A similar anomaly pattern during late October and early November was more clearly linked to strong MJO activity, which offset the El Niño signal and allowed for a rare late-season hurricane (Ida) to form over the Caribbean Sea; Ida was the only storm of the season to form in the Caribbean.

Opposite patterns of anomalous velocity potential were evident during both July and September (red boxes in Fig. 4.6). During September, these conditions were associated with El Niño, and contributed to a significant increase in vertical wind shear over the Atlantic basin (Fig. 4.16b) and to suppressed Atlantic hurricane activity.

The strong MJO activity during late October through early December also produced extratropical impacts. As the MJO shifted eastward across the western and central Pacific, the associated anomalous upper-level divergence and enhanced convection became superimposed upon the El Niño signal (Fig. 4.6, blue box) and acted to strengthen and extend eastward the East Asian jet stream. During mid-December, this jet stream undercut a persistent and strong upper-level ridge over western North America, allowing very wet and stormy conditions to affect California.

Between August and December, significant intraseasonal variability was also evident across the Pacific Ocean in association with three equatorial oceanic Kelvin waves (Fig. 4.7). The first two of these waves were initiated in early August and mid-September, in response to westerly wind events operating on a faster time scale than that of the MJO. The second wave traversed the eastern Pacific Ocean during late October and November and produced exceptionally large increases in anomalous oceanic heat content. This wave also contributed to the rapid increase in SSTs in the Niño 3.4 region during late October (Fig.
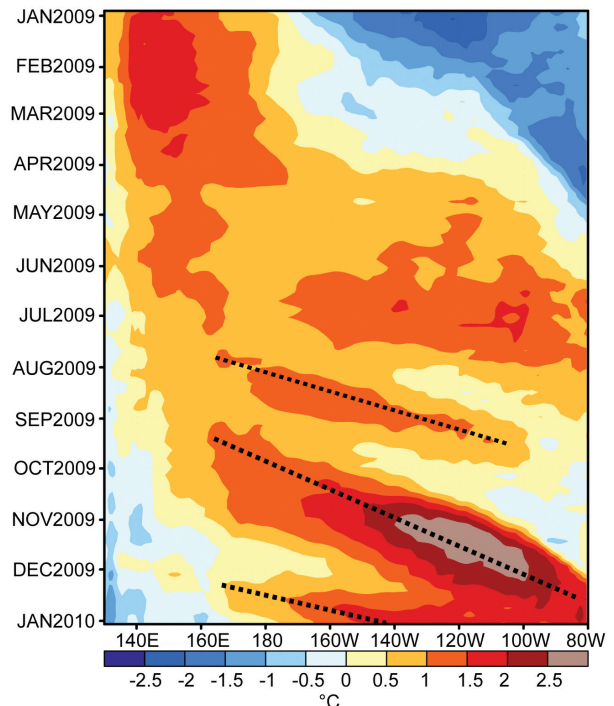

FIG. 4.7. Time-longitude section for 2009 of the anomalous upper ocean (0-300 m) heat content (°C) averaged between 5°N-5°S. Blue (yellow/red) shading indicates below (above) average heat content. The downwelling phases (dotted lines) of equatorial oceanic Kelvin waves are indicated. Anomalies are departures from the 1982–2004 base period pentad means.

4.1) and to large SST increases along the west coast of equatorial South America in early December. The third major Kelvin wave of the year was initiated over the western Pacific during December. This wave was triggered by a westerly wind burst linked to the MJO and reinforced the anomalously warm sub-surface waters in the central Pacific.

d. Tropical cyclones

1) Overview—H. J. Diamond

Global tallying of TC numbers is always challenging, and involves more than simply adding up basin totals, as some storms cross basin boundaries, some of the basins overlap, and multiple agencies are involved in tracking and forecasting TCs. Averaged across all seven TC basins, the 2009 season (2008/09 in the Southern Hemisphere) saw a below normal (1981–2000 base) number of tropical or named storms (NS) [≥ 34 kt] and a below-average number of hurricanes/typhoons/cyclones (HTC) [≥ 64 kt] and major HTCs [≥ 96 kt]. Globally, 90 NSs[1] developed during 2009 (7 below average) and 42 became HTCs (13 below average). Of these, 16 (compared to 26 in 2006, 18 in 2007, and 20 in 2008) attained major/intense status (global average is 25.4). Globally, the 2009 season was the least active since 2006.

From the standpoint of TC numbers, the 2009 season was above average in only one basin, the Eastern North Pacific which comprises both the eastern and central Pacific hurricane sub-regions. The season was below average in the North Atlantic Ocean and near to slightly below average in the remaining five basins, which are the Western North Pacific, the North Indian Ocean, the South Indian Ocean, the Southwest Pacific, and the Australian region

El Niño's emergence in June led to only the second below-normal Atlantic hurricane season (along with 1997) since 1995. El Niño also contributed to a sharp increase in hurricane activity across the central and eastern North Pacific. The re-emergence of above-normal activity in the Central Pacific sub-basin is highlighted in the chapter's sidebar article.

Despite a well below average Accumulated Cyclone Energy (ACE) Index value in the North Indian Ocean, the three systems that did make landfall ranked among the wettest ever observed in India and Bangladesh. For the Southwest Pacific the season had its

latest start since 2001, with its first NS delayed until late January. Nonetheless, 2009 was that basin's most active season since 2006.

2) Atlantic basin—G. D. Bell, E. S. Blake, T. B. Kimberlain, C. W. Landsea, R. J. Pasch, J. Schemm, and S. B. Goldenberg

(i) Seasonal activity

The 2009 Atlantic hurricane season produced nine NSs, of which three became hurricanes (Hs) and two became major hurricanes (MHs). The 1950–2000 averages are 11 NSs, 6 Hs, and 2 MHs. The reduced activity during 2009 reflected fewer, shorter-lived, and generally weaker storms compared to most seasons since the high-activity era for Atlantic hurricanes began in 1995 (Goldenberg et al. 2001). As a result, the ACE index (Bell et al. 2000) for 2009 was 60% of the median (Fig. 4.8), and approximately one-third of the seasonal average since 1995 (which is 165% of the long-term median). Based on NOAA's classification[2], 2009 was only the second (along with 1997) below-normal Atlantic hurricane season since 1995.

One NS (Claudette in the Florida Panhandle) made landfall in the United States during 2009, and Ida brought tropical storm force winds to the northern U.S. Gulf Coast before becoming extratropical prior to making landfall. Only one NS (Ida) formed in the Caribbean Sea, making landfall as a hurricane in Nicaragua before weakening to a tropical depression (TD) while crossing southeastern Honduras. Tropical Storm[3] (TS) Erika passed through the northern Caribbean Islands while weakening, and H Bill brushed Nova Scotia and Newfoundland (Cangialosi and Avila 2010).

This represents a sharp decrease in the number of landfalling NSs compared to 2008, when the nations in and surrounding the Caribbean Sea were severely impacted by four NSs and four Hs, and the continental United States was struck by three NSs and three Hs.

(ii) SSTs

For the August–October (ASO) climatological peak months of the Atlantic hurricane season, SSTs were above average throughout the Main Development Region (MDR), defined as the Caribbean Sea and tropical Atlantic Ocean between 9.5°N and 21.5°N (Shapiro and Goldenberg 1998). The largest SST departures (+0.5°C to +1.0°C) were found across

---

[1] It should be noted that in the Western North Pacific there were an additional nine unnamed tropical depressions recorded by the Japan Meteorological Agency not included in this total.

[2] See http://www.cpc.noaa.gov/products/outlooks/background_information.shtml
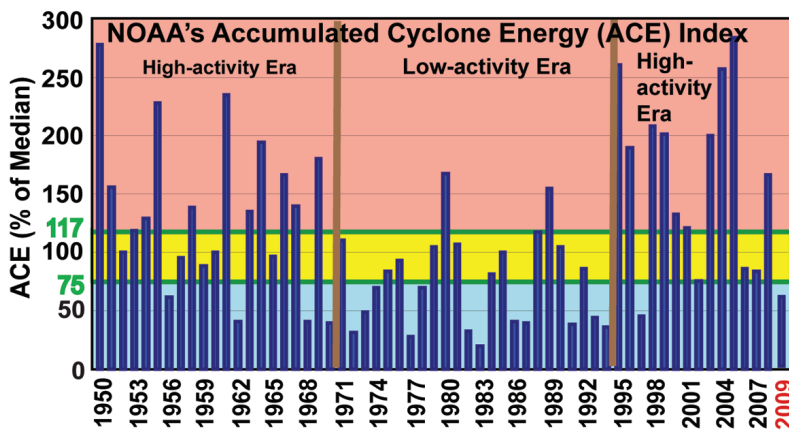
[3] A TS is equivalent to an NS

Fig. 4.8. NOAA's ACE index expressed as percent of the 1950-2000 median value (87.5×10^4 kt^2). ACE is a wind energy index that measures the combined strength and duration of the NSs. ACE is calculated by summing the squares of the 6-hr maximum sustained wind speed (kts) for all periods while the named storm has at least TS strength. Pink, yellow, and blue shadings correspond to NOAA classifications for above-, near-, and below-normal seasons, respectively. Brown lines separate high- and low-activity eras.

the south-central and eastern MDR (Fig. 4.9a). The ASO area-averaged departure for the entire MDR was +0.50°C, which is tied for seventh warmest since 1950 (Fig. 4.9b).

This warmth reflects three main factors: (1) the warm phase of the Atlantic Multidecadal Oscillation (AMO) (Enfield and Mestas-Nuñez 1999), which accompanied the 1995 transition to the active Atlantic phase of the tropical multidecadal signal (Bell and Chelliah 2006); (2) reduced mixing and reduced evaporation from the ocean surface in association with weaker northeasterly trade winds (anomalous southwesterly flow) across most of the tropical Atlantic portion of the MDR (Fig. 4.10a); and (3) long-term trend (Santer et al. 2006). The reduced Atlantic hurricane activity during 2009, despite this anomalous warmth, is consistent with previous findings indicating that local atmospheric circulation anomalies, rather than local SST anomalies, are the dominant contributor to seasonal fluctuations in Atlantic hurricane activity (Shapiro and Goldenberg 1998; Bell and Chelliah 2006; Bell et al. 2006).

(iii) Atmospheric circulation

A mixed set of atmospheric conditions, some favorable and some unfavorable to TC activity, prevailed during ASO. Favorable conditions included westerly wind anomalies at 1000-hPa and below average sea level pressure over large portions of the MDR (Fig. 4.10a). The core of the

African Easterly Jet (AEJ) was also shifted approximately 5° lat north of normal (black arrow, Fig. 4.10b), meaning the bulk of the African easterly wave energy (Reed et al. 1977) was often centered well within the MDR in an area of increased cyclonic shear (orange shading). This jet configuration favors stronger easterly waves and provides a cyclonic rotation to their embedded convective cells (Bell and Chelliah 2006).

Unfavorable conditions included exceptionally strong vertical wind shear (blue shading, Fig. 4.11) and anomalous upper-level convergence (Fig. 4.12) over the Caribbean Sea. These conditions were linked to an anomalously strong and persistent Tropical Upper Tropospheric Trough (TUTT, blue shading in Fig. 4.10c) over the Caribbean Sea. This TUTT produced a combination of anomalous upper-level westerly winds and low-level easterly winds (Fig 4.13a) which increases the vertical wind shear. The TUTT also suppressed the normal rising motion so

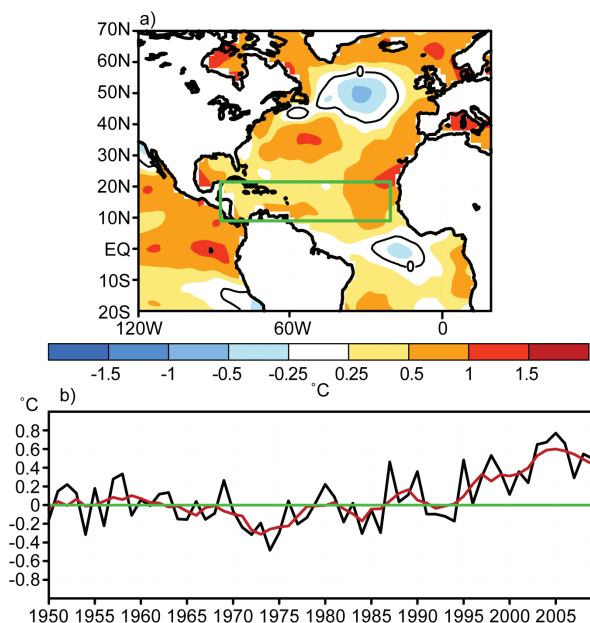**Fig. 4.9. (a)** SST anomalies (°C) during Aug–Oct 2009. **(b)** Consecutive Aug–Oct area-averaged SST anomalies in the MDR. Red line shows the corresponding 5-yr running mean. Green box in a) denotes the MDR, which spans 9.5°N-21.5°N and 20.0°W-87.5°W. Anomalies are departures from the 1971–2000 monthly means.
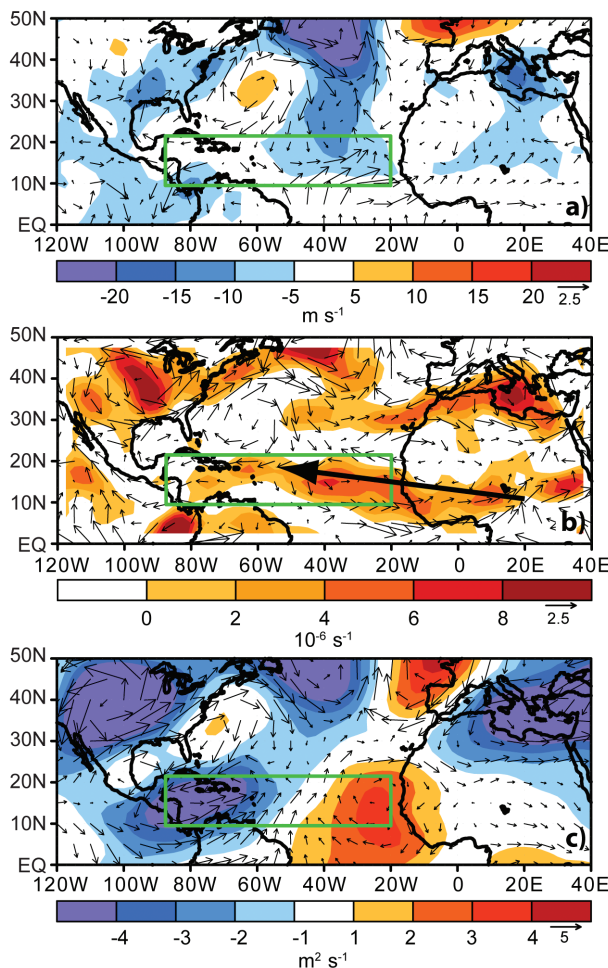
FIG. 4.10. Aug–Oct 2009: (a) 1000-hPa anomalous height (shading, m) and vector wind (m s⁻¹),(b) 700-hPa anomalous cyclonic relative vorticity (shading, x 10⁻⁶ s⁻¹) and vector wind, with thick arrow indicating the AEJ axis. (c) 200-hPa anomalous streamfunction (shading, x 10⁶ m² s⁻¹) and vector wind. Green boxes denote the MDR. Vector scales are located right of color bars. Anomalies are departures from the 1971–2000 period monthly means.
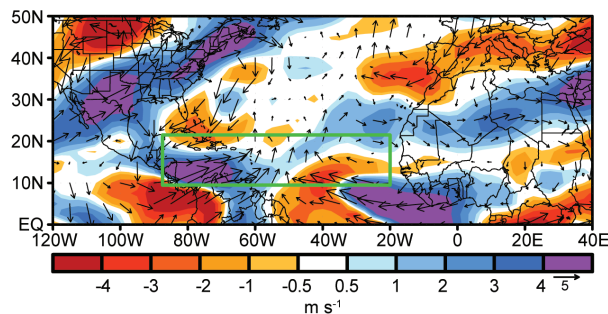
FIG. 4.11. Aug–Oct 2009: Anomalous 200-850 hPa vertical wind shear magnitude (m s⁻¹) and vectors. Green box denotes the MDR. Vector scale is located right of color bar. Anomalies are departures from the 1971–2000 period monthly means.

that only weak ascent prevailed throughout the MDR (Fig. 4.13b). In addition to suppressing the overall hurricane season strength, these conditions acted to decrease sharply the number of landfalling NSs in 2009 compared to 2008.

(iv) Links to global climate patterns

The regional atmospheric conditions and Atlantic TC activity during 2009 largely reflected two competing climate factors: El Niño and the ongoing active Atlantic phase of the tropical multidecadal signal (Bell et al. 2009). Across the tropical Pacific Ocean, the 200-hPa velocity potential and divergent wind anomalies during ASO (Fig. 4.12) were consistent with El Niño, as was an overall zonal wave-1 pattern of 200-hPa streamfunction anomalies in the subtropics of both hemispheres (Fig. 4.14). This pattern reflected enhanced subtropical ridges over the Pacific
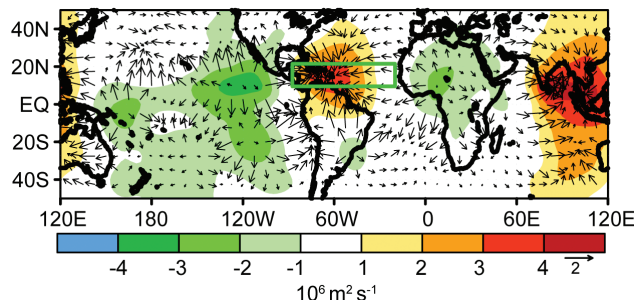
FIG. 4.12. Aug-Oct 2009: 200-hPa anomalous velocity potential (shading, x 10⁶ m² s⁻¹) and divergent wind vectors (m s⁻¹). Vector scale is located right of color bar. Anomalies are departures from the 1971–2000 period monthly means.
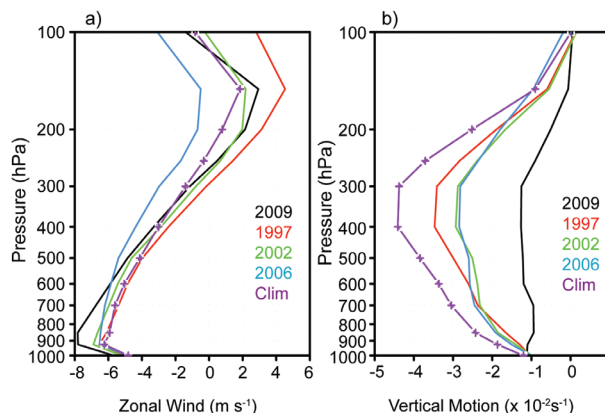
FIG. 4.13. Area-averaged conditions in the MDR during ASO for recent El Niño years: (a) total zonal wind (m s⁻¹), with negative (positive) values indicating easterly (westerly) winds and (b) total vertical motion (x 10⁻² s⁻¹), with negative (positive) values indicating rising (sinking) motion. Climatology (Clim) is the 1971–2000 base period means.
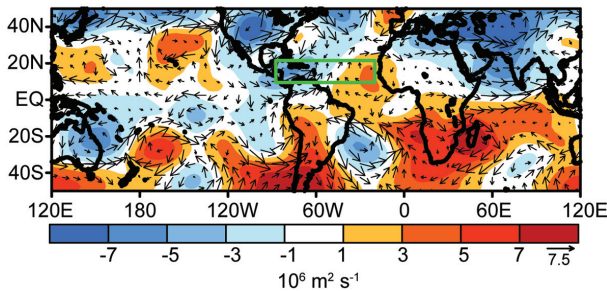
FIG. 4.14. ASO 2009: Anomalous 200-hPa streamfunction (shading, x 10⁶ m² s⁻¹) and wind vectors (m s⁻¹). Anomalous ridges are indicated by positive values (red) in the NH and negative values (blue) in the SH. Anomalous troughs are indicated by negative values in the NH and positive values in the SH. Vector scale is located right of color bar. Anomalies are departures from the 1971–2000 period monthly means.

Ocean in both hemispheres, and weaker than average subtropical ridges throughout the remainder of the global subtropics.

Over the Caribbean Sea, regional aspects of this El Niño signal included the enhanced TUTT, stronger than average westerly winds at 200-hPa, increased vertical wind shear, and anomalous sinking motion, all of which overwhelmed the ongoing multidecadal signal and suppressed the 2009 Atlantic hurricane season. These conditions are opposite to those observed during 2008, when the combination of the high-activity era and La Niña contributed to an above normal Atlantic hurricane season (Bell et al. 2009).

(v) Conditions associated with the ongoing high-activity era in the tropical Atlantic

During the current high-activity era for Atlantic hurricanes, which began in 1995, two-thirds (10 of 15) of Atlantic hurricane seasons have been above normal, and only two have been below normal (Fig. 4.8). This elevated activity contrasts with the preceding low-activity era 1971–94, when one-half of the seasons were below normal and only three were above normal. During 1995–present, four of the five seasons not classified as above normal (1997, 2002, 2006, and 2009) can be linked to El Niño.

The transition to the current high-activity era was associated with a phase change in the tropical multidecadal signal, which reflects the leading modes of tropical convective rainfall variability and Atlantic SSTs occurring on multidecadal time scales (Bell and Chelliah 2006; Bell et al. 2007). This signal highlights the convectively-driven nature of the atmospheric anomalies across the central and eastern MDR, and links them to an east-west oscillation in anomalous

convection between western Africa (Landsea and Gray 1992; Goldenberg and Shapiro 1996) and the Amazon Basin.

The combination of an enhanced West African monsoon and suppressed convection in the Amazon Basin was seen again during ASO (Fig. 4.12) and is known to be associated with an inter-related set of atmospheric anomalies typical of active hurricane seasons (Landsea et al. 1998; Bell et al. 1999, 2000, 2004, 2006, 2009; Goldenberg et al. 2001; Bell and Chelliah 2006; Kossin and Vimont 2007). These anomalies include enhanced low-level inflow into the West African monsoon region (Fig. 4.10a) and enhanced upper-level divergent outflow from that region (Fig. 4.12). They also include stronger upper-level ridges over both the eastern MDR and across the subtropical South Atlantic as seen in 2009 (Fig. 4.14), along with a stronger tropical easterly jet at 200 hPa.

Accompanying these conditions, the vertical wind shear (Fig. 4.15a) and 700-hPa zonal winds (Fig. 4.15b) in critical parts of the MDR have been much weaker since 1995 compared to the preceding low-activity era, and the 700-hPa relative vorticity has been cyclonic
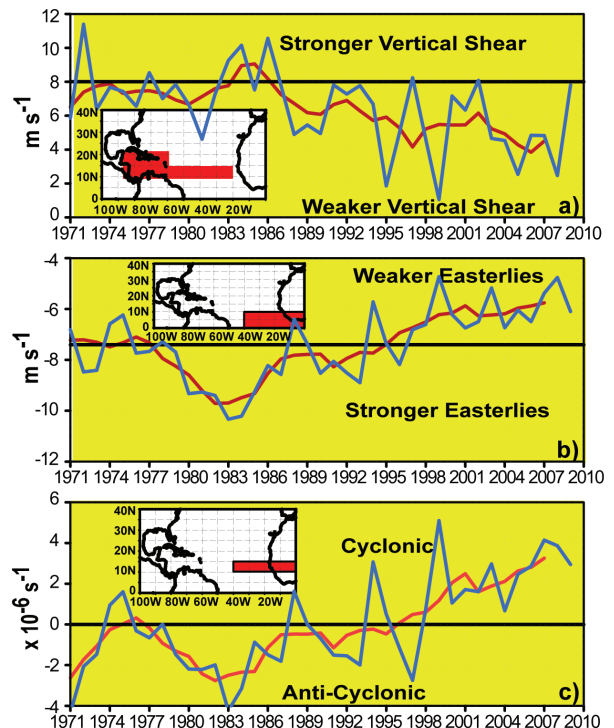

FIG. 4.15. Time series showing consecutive ASO values of area-averaged (a) 200-850 hPa vertical shear of the zonal wind (m s⁻¹), (b) 700-hPa zonal wind (m s⁻¹) and (c) 700-Pa relative vorticity (x 10⁻⁶ s⁻¹). Blue curve shows unsmoothed values, and red curve shows a 5-pt running mean of the time series. Averaging regions are shown in the insets.

rather than anticyclonic across the southern MDR (Fig. 4.15c). These latter two features were again present during ASO and are consistent with the more conducive AEJ described above.

As discussed by Bell and Chelliah (2006) and Bell et al. (2009), the above combination of conditions means that tropical storms can develop within the MDR from amplifying African easterly waves moving within the region of below-average pressure and increased cyclonic shear along the equatorward flank of the AEJ. In the absence of El Niño, these waves are also embedded within an extended region of weak vertical wind shear, which enables further intensification as they move westward over progressively warmer SSTs.

(vi) Intraseasonal variability in Atlantic hurricane activity

During 2009 intraseasonal variability in Atlantic hurricane activity resulted from a combination of the MJO and an atmospheric equatorial Kelvin wave (see section 4c). For example, six NSs including both MHs formed during 11 August to 7 September, and the third H of the season did not form until early November. During these more active periods, the MJO contributed to anomalous upper-level convergence over the central equatorial Pacific (Fig. 4.6). In mid-

August an atmospheric Kelvin wave also contributed to this anomalous upper-level convergence. These conditions resulted in a more conducive pattern of vertical wind shear across the tropical Atlantic (Fig. 4.16a) similar to that described (Mo 2000). In contrast, only two NSs formed during most of September and October, a period when El Niño dominated the 200-hPa divergence signal (Fig. 4.12). Particularly impressive is the exceptionally strong vertical wind shear during September across most of the MDR (Fig. 4.16b).

3) Eastern North Pacific (ENP) basin—D. H. Levinson, E. J. Gibney, J. Weyman, and M. C. Kruk

(i) Seasonal activity

The ENP basin is officially split into two separate regions for the issuance of warnings and advisories by NOAA's National Weather Service (NWS). NOAA's National Hurricane Center (NHC) in Miami, FL is responsible for issuing warnings in the eastern part of the basin that extends from the Pacific Coast of North America to 140°W, while NOAA's Central Pacific Hurricane Center (CPHC) in Honolulu, HI is responsible for issuing warnings in the Central North Pacific region between 140°W and the international date line. In this section analysis summarizing the tropical cyclone activity in both these warning areas will be presented using combined statistics, along with information specifically addressing the observed activity and impacts in the Central North Pacific (CNP) region.

The ENP hurricane season officially spans from 15 May to 30 November, although storms can develop outside of the official season, especially during El Niño enhanced hurricane seasons[4]. Hurricane and tropical storm activity in the eastern area of the basin typically peaks in September, while in the Central Pacific TC activity reaches its seasonal peak normally in August (Blake et al. 2009). Figure 4.17 shows the tracks of all of the observed TCs in the ENP and CNP in 2009. TC activity in the ENP started later than normal this past year, with the development of two systems in June (TD 01E during 10–18 June, and H Andres during 21–24 June), which was the first time since 1999 that no named storms formed during May. For the season as a whole, the number of NSs and MHs that developed were both slightly above their long-term means, while the number of Hs was
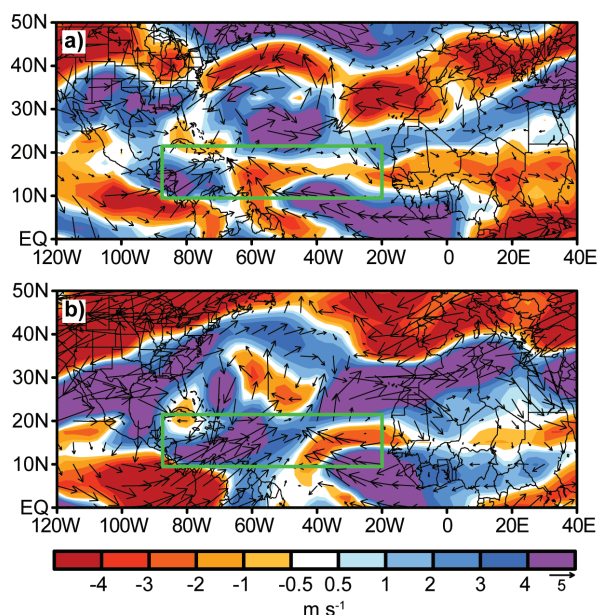
Fig. 4.16. Anomalous 200–850 hPa vertical wind shear magnitude (m s⁻¹) and vectors during (a) August 2009 and (b) September 2009. Green boxes denote the Main Development Region (MDR). Vector scale is located right of color bar. Anomalies are departures from the 1971–2000 period monthly means.

---

[4] TS Paka was the last TC to occur in December in the ENP basin when it developed in the Central Pacific region during 2–6 December1997.
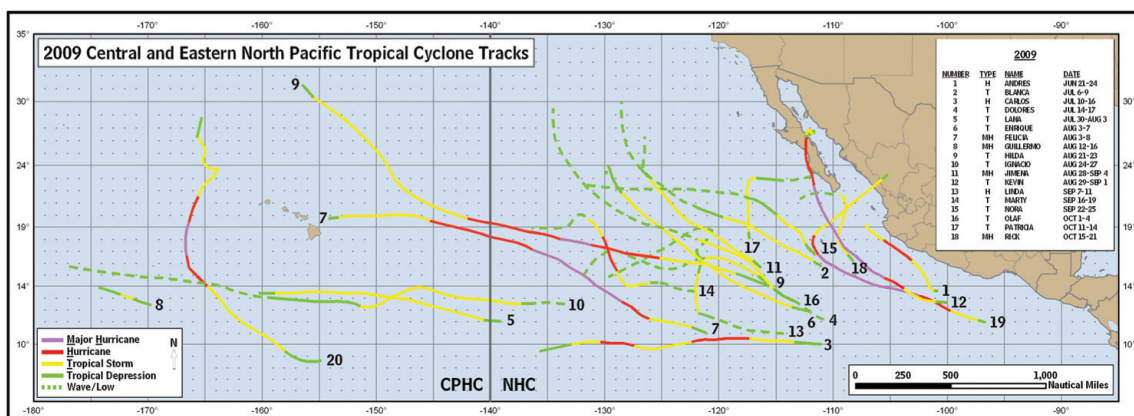
FIG. 4.17. The tracks of all TCs that occurred in the ENP and CNP basins (Source: NOAA's NHC and CPHC). Tracks are color-coded by intensity (wave/low, tropical depression, tropical storm, hurricane, major hurricane). Also shown is the delineation of the forecast area of responsibility at 140°W longitude between NOAA's NHC and CPHC.

near-normal. Primarily due to the development of an El Niño warm event during the boreal summer and early autumn in the equatorial Pacific in 2009, the hurricane season was above average in the ENP basin, with 20 NSs, 9 Hs, and 5 MHs (Fig. 4.18a). These values are at or above the 1971–2005 averages for the basin (16.2 NSs, 9.1 Hs, and 4.3 MHs).

Despite the overall above average activity in 2009 in terms of storm counts, the ACE Index (Bell et al. 2000; Bell and Chelliah 2006) was near-normal for the basin with a seasonal total of 106.1×10^4 kt^2, which was slightly below the 1971–2005 mean (126.3×10^4 kt^2), but higher than occurred during the previous two seasons (Fig. 4.18b).

A total of seven TCs were observed in the CNP region in 2009, three of which developed in the region and were officially named by the CPHC (TS Lana, TS Maka, and H Neki)[5], while three others propagated into the region from the east (Fig. 4.17) crossing the warning area boundary of 140°W (MH Felicia, MH Guillermo, and TS Hilda). Three TCs reached hurricane strength in the CNP warning area, one of which developed into a major hurricane (Neki). This was the largest number of TCs in the CNP since 1997, and well above the 1971–2005 average of 4–5 TCs[6]. The enhanced activity in the CNP was also likely a result of the influence of the El Niño warm event that developed during the hurricane season, which generated more TC activity west of 140°W (see sidebar).
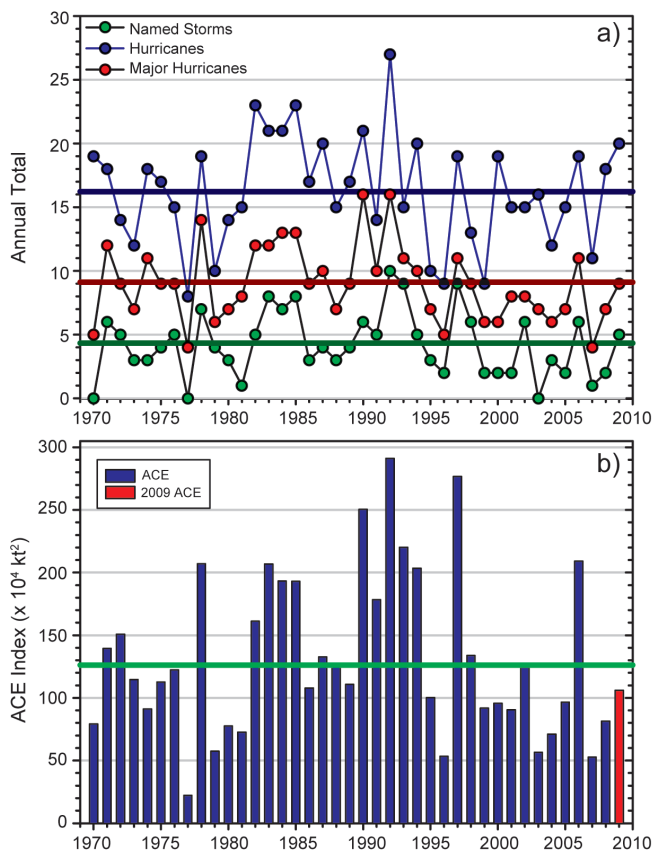
FIG. 4.18. Seasonal TC statistics for the ENP basin over the period 1970–2009: (a) number of NS, H, and MH and (b) the ACE Index (x 10^4 kt^2) with the seasonal total for 2009 highlighted in red. All time series shown include the corresponding 1971–2005 base period means for each parameter. (Source: International Best Track Archive for Climate Stewardship [IBTrACS].)

---

[5] A non-named TD (02C) was also noted during this period.

[6] NOAA's CPHC includes TDs in their climatological statistics for the CNP basin.

Since 1995, the number of NSs in the ENP basin has been near average, fluctuating about the long-term mean (Fig. 4.18a). However, the numbers of Hs and MHs have been generally below normal in most seasons, with above normal activity having occurred in only three seasons. NOAA has identified 9 of the 15 seasons in the ENP as being below normal during 1995–2009, with only the El Niño–influenced seasons of 1997 and 2006 producing above normal activity as measured by the ACE index. In contrast, enhanced activity was observed during the preceding 1970–94 period, which had 6 of 25 (24%) below normal seasons and 9 of 25 (36%) above normal seasons, as measured by the ACE index.

(ii) Environmental influences on the 2009 season

Seasonal TC activity (both frequency and intensity) in the ENP basin is influenced by several large-scale environmental factors in the basin, including SSTs, the vertical shear of the horizontal wind, the phase of the ENSO phenomenon in the equatorial Pacific, as well as the phase of the Quasi-Biennial Oscillation (QBO) in the near-equatorial lower stratosphere (Gray 1984; Shapiro 1989; Whitney and Hobgood 1997; Hobgood 2003). ENSO is known to strongly modulate both the SSTs and vertical wind shear on interannual time scales in the ENP basin (Whitney and Hobgood 1997). However, multidecadal fluctuations in ENP hurricane activity are less well understood but do show a strong inverse relationship to the phase of the tropical multidecadal mode and Atlantic hurricane activity (Bell and Chelliah 2006; Wang and Lee 2010).

Previous studies have documented that the occurrence of an El Niño typically favors an above-normal hurricane season, while La Niña (and neutral) conditions typically favor a below-normal hurricane season in the ENP (Irwin and Davis 1999; Frank and Young 2007; and Camargo et al. 2008). These ENSO impacts are modulated by the multidecadal signal, with the combination of a La Niña occurrence during an inactive hurricane era greatly increasing the probability of a below-normal season. During 2009, the transition from an ENSO neutral phase to an El Niño during the climatological peak of the hurricane season (ASO) resulted in above average SSTs (weekly and monthly SST anomalies of +0.4°C to +1.5°C) in the MDR[7].

Another significant environmental factor that likely enhanced the above-normal hurricane season in 2009 was anomalously below-average vertical wind shear between 200 hPa and 850 hPa in the MDR during the latter half of the hurricane season (Fig 4.19a). During the first half of the hurricane season (JJA), the wind shear anomalies were above average (exceeding 9–12 m s^{-1}), which suppressed tropical-cyclogenesis and inhibited intensification. Conditions changed considerably during the latter half of the season, when negative wind shear anomalies of 9–12 m s^{-1} were observed during SON (Fig. 4.19b). It is likely that the significantly weaker-than-normal shear late in the season enhanced TC intensification and as a result 2009 had an above average number of MHs in the ENP. The late season formation of MH Rick (15–21 October), which reached a maximum intensity of 155 kt Category (Cat-) 5 and was the second strongest ENP hurricane in the historical record (behind MH Linda in 1997, which had a peak intensity of 160 kt), as well as the development of MH Neki in the Central Pacific (18–26 October), were both indications of the weak wind shear during the peak months of the hurricane season.
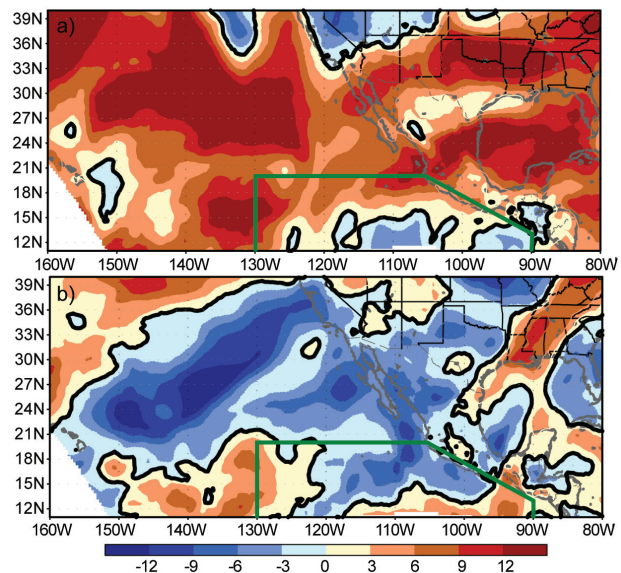
Fig. 4.19. The 200–850 hPa vertical wind shear anomalies (m s^{-1}) averaged over the following two periods in 2009: (a) June–August (JJA) and (b) September–November (SON), with anomalies determined relative to the 1979–2004 base period mean. The main development region for ENP hurricanes is the area delineated by the green polygon in both maps. (Source: North American Regional Reanalysis [NARR] dataset, provided by the NOAA National Operational Model Archive and Distribution System.)

---

[7] The MDR in the ENP covers the region delineated by the green boxes in Fig. 4.19 a-b; between10°N and 20°N and 90°Wand 130°W.

Several previous studies have shown statistically significant correlations between hurricane activity and the phase of the QBO (Gray 1984; Shapiro 1989; Whitney and Hobgood 1997). In the ENP basin, TCs have been shown to attain a higher intensity when the QBO is in its westerly phase, but there is also a corresponding decrease in the observed seasonal frequency (Whitney and Hobgood 1997). In June 2009, the phase of the QBO was westerly, as indicated by the zonally-averaged U-component winds at both 30-hPa and 50-hPa obtained from the NOAA CPC Climate Data Assimilation System (CDAS) dataset. In July, the zonal mean winds at 30-hPa shifted to easterly and remained from an easterly component for the remainder of the 2009 hurricane season. In contrast, the zonal winds at 50 hPa (not shown) remained from a westerly component for the entire hurricane season in the ENP. The effect of this split signal related to the phase of the QBO on the frequency and intensity of TC activity in the ENP is unclear. However, using data covering the 1963–1993 hurricane seasons, Whitney and Hobgood (1997) found that there are slightly fewer TCs over the ENP when the QBO is in its westerly phase, although these storms attained a slightly higher maximum intensity. Therefore, it is possible that the intensity of hurricanes in the ENP basin during the 2009 season may have been ehanced by the westerly phase of the QBO (based on the zonally-averaged wind at 50 hPa), as five major hurricanes formed during the season, which was the highest total since the 2006 season.

(iii) TC Impacts

Three TCs made landfall along the Pacific Coast of Mexico during the season (Cat-1[8] H Andres, Cat-2 H Jimena, and TS Rick). In comparison with climatology, the 2009 season was well above the 1951–2000 average of 1.34 landfalling TCs (Jauregui 2003). Along the Pacific Coast of Mexico, H Andres attained minimal hurricane strength (Cat-1 intensity) as it moved parallel to the coast in late June. Damage along Mexico's southwestern coast was minimal; however, heavy rains from Andres and its precursor disturbance flooded homes in a portion of Acapulco and resulted in the evacuation of about 200 people. Preliminary damage reports suggested that Andres was responsible for one fatality in Mexico.

Strong winds and heavy rainfall from H Jimena caused devastation as the storm crossed the Baja peninsula on 2–4 September, officially making landfall with sustained winds of 85 kt (Cat-2). Strong winds and heavy rains associated with Jimena caused widespread damage on the central and southern Baja California peninsula. The cities of Ciudad Constitución, Mulege, and Loreto were reported to be hard hit, as well as many of the smaller towns near the track of the storm's center. One fatality was reported—a drowning due to flash flooding in Mulege, Baja California del Sur—and 75% of homes were damaged in Puerto San Carlos. Severe damage also occurred to the agricultural sector. Approximately 400 hectares of citrus was lost and 80 hectares of greenhouses were destroyed by the storm. Total losses to the sector have been estimated to be at least $37.3 million (U.S.), with damages to infrastructure estimated at $12.5 million (U.S.).

On 21 October, TS Rick made landfall near Mazatlan with estimated maximum sustained winds of 50 kt, which was significantly weaker than the 155 kt the storm had reached at peak intensity. Preliminary reports suggested that Rick was responsible for two deaths in Mexico.

In the CNP, Felicia reached a maximum intensity of 120 kt (Cat-4) before it weakened significantly as it moved into the Central Pacific sub-basin and affected the main islands of Hawaii as a tropical depression in mid-August. Impacts from Felicia included heavy rainfall and localized flash flooding.

In October, the northwestern Hawaiian Islands were directly affected by MH Neki (Fig. 4.17, storm number 20), which caused the evacuations of researchers and scientists via a NOAA ship and a Coast Guard C-130 aircraft. Neki developed as a weak TC near 12°N, 130°W and slowly moved westward with little change in intensity. As it turned northwestward near 160°W, the system intensified, reaching a peak intensity of 105 kt (Cat-3). As its northern movement slowed, the storm crossed the archipelago near French Frigate Shoals and Necker Island as a strong TS (maximum sustained winds of 50–55 kt).

4) WESTERN NORTH PACIFIC (WNP) BASIN—S. J. Camargo

The 2009 season featured 28 TCs (including TDs) forming in the WNP. There were two (TS Maka and TD 02C) TCs which formed in the Central Pacific and crossed into the WNP. Of these 30 active TCs in the WNP, according to the Japan Meteorological Agency, nine additional TDs occurred in 2009. One of these TDs was named by the Philippine Atmospheric,

---

[8] Saffir-Simpson categories are used in this chapter, except for the Southwest Pacific and Australian regions which use the Australian system (see footnote in that section).

Geophysical and Astronomical Services Administration (PAGASA), which also named two other TDs (Bising and Crising) in the 2009 typhoon (TY) season. Twenty-five reached TS intensity (three of which were not named), 14 became TYs, and 5 reached super-typhoon (STY) intensity. In Fig. 4.20a the number of TSs, TYs, and STYs per year is shown for the period 1945–2009. The TC data used here is from the Joint

Typhoon Warning Center (JTWC) best-track dataset for 1945–2008, and preliminary operational data for 2009, for the TCs forming in the WNP. Preliminary data for the storms forming in the Central Pacific region is from CPHC. Climatology is defined using the period 1971–2000.

The 2009 WNP TC season (see Fig. 4.20) started in May, with TYs Kujira and Chan-Hom. These were
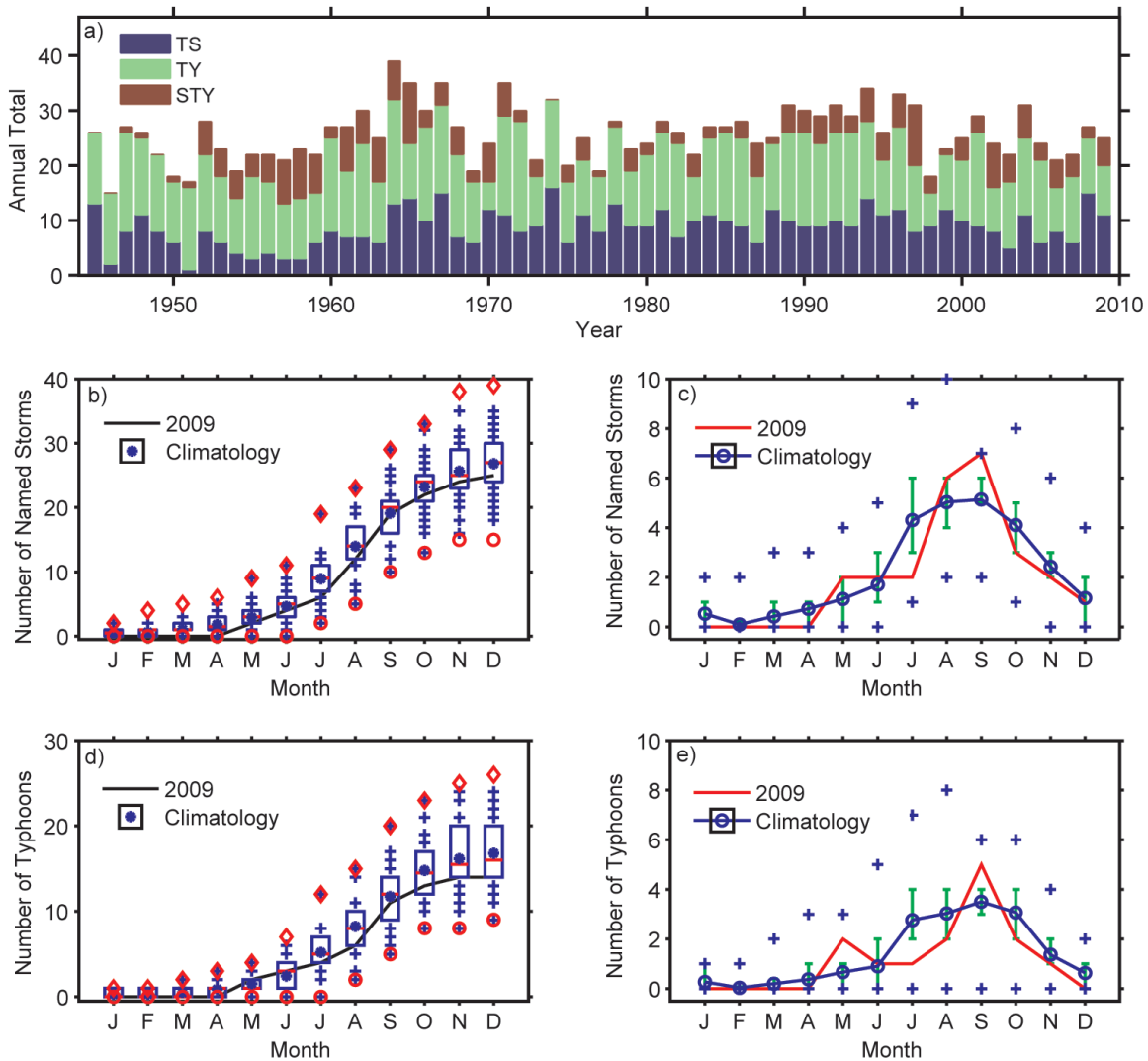
FIG. 4.20. (a) Number of TCs for the period 1945–2009. (b) Cumulative number of NSs per month: 2009 (black line), and climatology (1971–2000) shown as box plots [interquartile range: box, median: red line, mean: blue asterisk, values in the top or bottom quartile: blue crosses, high (low) records in the 1945–2008 period: red diamonds (circles)]. (c) Number of NSs per month in 2009 (black curve), mean climatological number of NS per month (blue curve), the blue plus signs denote the maximum and minimum monthly historical values (1945–2009) and green error bars show the interquartile range for each month. In the case of no error bars, the upper and/or lower percentiles coincide with the median. (d) Cumulative number of TYs: 2009 (black line), and climatology (1971–2000) shown as box plots. (e) Number of TY per month in 2009 (black curve), mean climatological number of TY per month (blue curve), the blue plus signs denote the maximum and minimum monthly historical values (1945–2009) and green error bars show the interquartile range for each month. (Source: 1945–2008 JTWC best-track dataset, 2009 JTWC preliminary operational track data.)

followed by TY Linfa and TS Nangka in June. July TC activity was below-normal, with only two TCs reaching TS intensity, TS Soudelor and TY Molave. On average for the month of July there are four NSs that develop, of which three reach TY intensity. In August, the TC activity was higher than in July, with three TSs (Goni, Etau, and Krovanh) and two TYs (Morakot and Vamco) forming in the WNP. In addition, two Central Pacific TCs, TS Maka and TD 02C crossed into the region. The most active month in TC genesis numbers was September, with one TD (Mujigae), two TSs (Dujuan and 18W), two TYs (Koppu and Ketsana), and three STYs (Choi-Wan, Parma and Melor) forming in the WNP. The seven NSs and three STYs that occurred in September tied the previous historical record of the number of NSs and STYs in that month. The TC activity in October was slightly below-average, with one TS (Nepartak), one TY (Mirinae), and one STY (Lupit) occurring in the basin. The last STY (Nida) of the 2009 season formed in November, along with two TDs (24W and 27W) and one non-named TS (25W). The season finished with the formation of TS 28W in early December.

The total number of TCs (30), NSs (25), and TYs (14) in 2009 were all below the median but equal to or above the 25th percentile of the climatological distributions (median: 30.5 TCs, 27 NSs, and 16 TYs, 25th percentile: 27 TCs, 24 NSs, and 14 TYs). The cumulative distributions of NSs (Fig. 4.20b) and TYs (Fig. 4.20c) show a slow season start, with the activity increasing in May, below-normal activity in July and August, and the high activity in September leading to slightly-below normal values for the season as a whole for NS and TY numbers. In contrast, the number of STYs in 2009 (five) was in the top quartile of the climatological distribution.

The ACE in the WNP (Fig. 4.21) reflects well the activity and number of TCs. The ACE value for the 2009 season was very near the climatological median (Fig. 4.21a), only slightly above the median, due to the very low value of ACE in July, which was not totally compensated by the high October and November ACE values. The May ACE was in the top quartile of climatology and the November ACE was very close to the 75th percentile of the climatology. July and October were complementary months, with the July ACE value being the 5th lowest and the October ACE being the 5th highest value in the historical record for the respective months. The ACE values of the two strongest storms in 2009, STYs Melor and Nida are in the top 5th percentile of the historical record and the climatological distribution. Ninety percent of the

ACE in November is due to STY Nida, while 64% of the September ACE is due to STY Choi-Wan, and 37% of the October ACE is due to STY Melor.

There were 129 days with TCs and 122 days with NSs in 2009 in the WNP, both in the bottom quartile of the climatological distribution (medians 161.5 and 144.25 days, respectively). From these, there were 110 days with typhoons, slightly below the climatological median of 120.4 days. There were 22.25 days with intense TYs (categories 3–5), above the climatological median of 19.4 days. Climatologically, 74% (11%) of the TC days consist of days with (intense) TYs. In 2009 these ratios were much higher, 85.3% and 17.25%, respectively, pointing to a more frequent occurrence of intense and STYs in the 2009 TC season. The median lifetime of NSs in 2009 was 6.5 days, below the median lifetime of 8 days for all years. From the 25 NSs, 17 had a duration below the median,
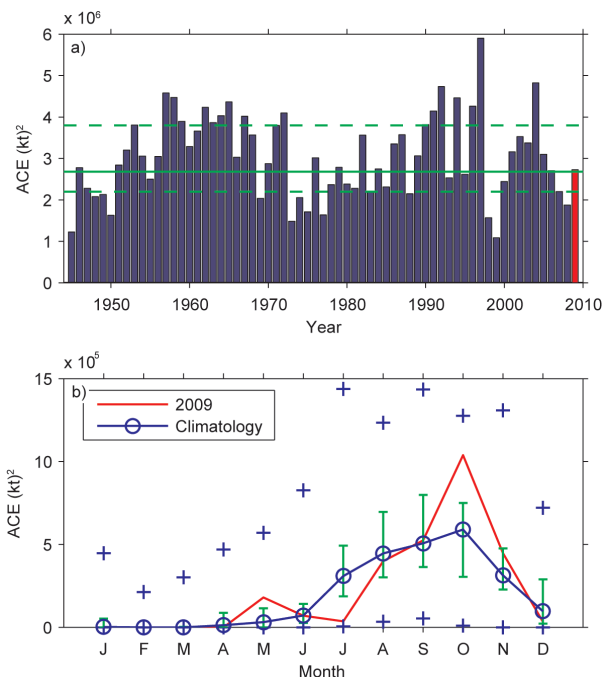
FIG. 4.21. (a) ACE Index per year in the Western North Pacific for the years 1945–2009. The solid green line indicates the median for the years 1971–2000 climatology, and the dashed green lines show the 25th and 75th percentiles. (b) ACE index per month in 2009 (red line) and the median in the years 1971–2000 (blue line), where the green error bars indicate the 25th and 75th percentiles. In the case of no error bars, the upper and/or lower percentiles coincide with the median. The blue plus signs (+) denote the maximum and minimum values during the period 1945–2009. (Source: 1945–2008 JTWC best-track dataset, 2009 JTWC preliminary operational track data.)

with 11 of those in the bottom quartile of the distribution. Only three TCs had a duration in the top quartile of the distribution, i.e., with lifetimes larger than 11.25 days, namely STYs Nida (11.75 days), Lupit (12.75 days), and Parma (17 days). STY Parma's very long lifetime of 17 days is in the top 2 percentile of the historical record.

The El Niño event in 2009 occurred in three phases. From June to September, it was a weak event and then ramped up in October to a moderate event. In December it was declared a strong event. There is a known relationship between WNP ACE and ENSO, with high values of ACE usually occurring in El Niño years, when the TCs tend to be long-lived and more intense (Wang and Chan 2002; Camargo and Sobel 2005; Camargo et al. 2007b). The 2009 ACE reflects the time evolution and strength of the El Niño event in 2009. In the early TC season, while ENSO was still weak, low (July) or average values of ACE occurred. Once the ENSO event became stronger, the ACE values also increased, especially in October and November, due to the occurrence of the five super-typhoons in the late September to November period. The 2009 median lifetime was below normal, and with exception of TY Chan-Hom, all the storms that had an above-normal lifetime occurred after late September, when the El Niño became a moderate to strong event. There was a flurry of TC activity in late September, when the MJO was active in the region, right before the ramp-up of the El Niño event. This would be in agreement with the hypothesis, discussed in Sobel and Camargo (2005), that TYs could help strengthen El Niño events.

Emanuel's genesis potential index (GPI) (Camargo et al. 2007a) shows (Fig. 4.22) clearly the shift in the environmental conditions from the early (JJA) to the late (SON) season to more typical El Niño-like conditions. While the GPI anomalies for JJA do differ from the El Niño JJA composite pattern, the SON anomalies are very similar to the El Niño SON composite.

The mean genesis location (15.2°N, 140.5°E) in 2009 was shifted northwest of the climatological mean genesis positions (12.9°N, 143.5°E). While the mean track position (20.2°N, 134.9°E) is shifted slightly northward of the climatological mean (19.0°N, 134.2°E). These shifts are not consistent with the typical El Niño events, which tend to have a southeastward shift (Chan 1985; Chia and Ropelewski 2002). The late season (September to December) mean
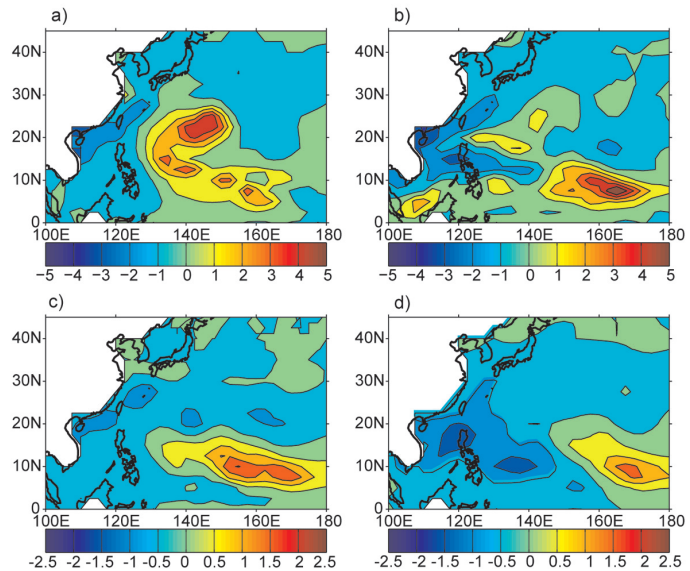
Fig. 4.22. Genesis potential index (Camargo et al. 2007b) anomalies for (a) JJA 2009; (b) SON 2009. El Niño genesis potential index anomaly composites (c) JJA; (d) SON. (Source: atmospheric variables - NCEP Reanalysis data, Kalnay et al. 1996; SST - Smith and Reynolds 2005.)

genesis position (14.2°N, 145.4°E) is more consistent with the typical shift in El Niño events.

Fourteen WNP TCs made landfall during 2009, which is just below the 1951–2000 median of 15[9]. Six systems made landfall as a TD (median is three), seven made landfall as TS (median is six), one struck as TY (median is four), and none as an STY (median is zero).

TY Morakot was a particularly catastrophic event for Taiwan, leaving 461 people dead and 192 others missing (most of whom were feared dead) with roughly $3.3 billion (U.S.) in damages. The storm produced record setting rainfall of 2777 mm, surpassing the previous record of 1736 mm set by TY Herb in 1996. The extreme amount of rain triggered enormous mudslides and severe flooding throughout southern Taiwan. One mudslide buried the entire town of Xiaolin killing an estimated 500 people in that village alone. The slow moving storm also caused widespread damage in China, leaving eight people dead and causing $1.4 billion (U.S.) in damages. Nearly 2000 homes were destroyed in the country and 136 000 more were reported to have sustained damage. The storm also caused severe flooding in the northern Philippines that killed 26 people.

---

[9] Here we consider only one landfall per TC. If a TC makes more than one landfall, the landfall event with the highest wind speed is considered.

The Philippines were severely affected by the 2009 TY season. The PAGASA-named depressions in January, February, and May brought heavy rains and flooding in the eastern Philippines, mudslides on Cebu Island, and heavy rains with flooding in the western Philippines. These were followed by typhoons Kujira and Chan-Hom in May, which caused severe damage to crops, livestock, and infrastructure, as well as deaths in the country. In June, TSs Linfa, Nangka and Soudelor also affected the Philippines. More destruction and deaths were caused by TS Goni in July. In September, the Philippines were again affected by TYs Koppu, Ketsana, and Parma, the second bringing a record rainfall amount in Manila, while the latter made three landfalls in the Philippines. In October, TY Mirinae crossed the Philippines, and in November TD Urduja brought landslides to the southern part of Luzon.

5) Indian Ocean basins

(i) North Indian Ocean (NIO)—M. C. Kruk and K. L. Gleason

The NIO TC season typically extends from April to December, with two peaks in activity during May–June and November when the monsoon trough is positioned over tropical waters in the basin. TCs in the NIO basin normally develop over the Arabian Sea and Bay of Bengal between latitudes 8°N and 15°N. These systems are usually short-lived and relatively weak and often quickly move into the Indian subcontinent. However, strong and "severe cyclonic storms"[10] can develop with winds exceeding 130 kt (Neumann et al. 1993).

The 2009 TC season produced five NSs, one cyclone (CYC), and no major cyclones (MCYC) (Fig. 4.23a). These values are near the 1981–2005 averages of 4.6 NSs, 1.4 CYCs, and 0.5 MCYCs. The season produced an ACE index value of 6.0 x 10^4 kt^2, which is far below the 1981–2005 mean of 16 x 10^4 kt^2 (Fig. 4.23b). There is generally a reduction in tropical cyclone activity, especially in the Bay of Bengal, during the warm phase of ENSO (Singh et al. 2000), which the globe was transitioning to during the boreal summer 2009.

During 2009, the monsoon trough set in relatively early (23 May). However, from 24 to 25 May, CYC Aila developed with peak winds of 65 kt in the Bay of Bengal and disrupted the normal northward ad-

FIG 4.23. Annual TC statistics for the NIO over the period of 1970-2009: (a) number of NSs, CYCs, and MCYCs, and (b) the estimated annual ACE Index (x 10^4 kt^2) for all tropical cyclones during which they were at least tropical storm or greater intensities (Bell et al. 2000). The 1981–2005 base period means are included in both (a) and (b). Note that the ACE Index is estimated due to a lack of consistent 6-hr-sustained winds for every storm.

vancement of the monsoon. This resulted in severe drought conditions across the typical rainy areas of Jharkhand, Uttar Pradesh, and Himachal Pradesh. However, by 3 July, the monsoonal position had returned to near-normal (Fig. 4.24).

Despite the below normal rainfall from the monsoon trough, three NSs that made landfall in 2009 ranked among the wettest ever observed in India and Bangladesh. In India, CYC Aila killed 149 people and stranded tens of thousands of others because of the massive flooding that resulted. The eastern state of Meghalaya received 270 mm total rainfall from 25 to 26 May. In Bangladesh, CYC Aila resulted in 179 deaths from flooding and isolated over 400 000 people as numerous villages were submerged from floodwaters. Total rainfall from CYC Aila exceeded 130 mm near Chittagong, Bangladesh. This rainfall was particularly devastating, as it followed on the heels of NS Bijli (14–17 April), which produced an estimated

---

[10] The Bangladesh Supercyclone of 1970 produced perhaps the greatest human death toll (300 000 persons) on record, primarily from storm surge flooding of low-lying deltas (Holland 1993).
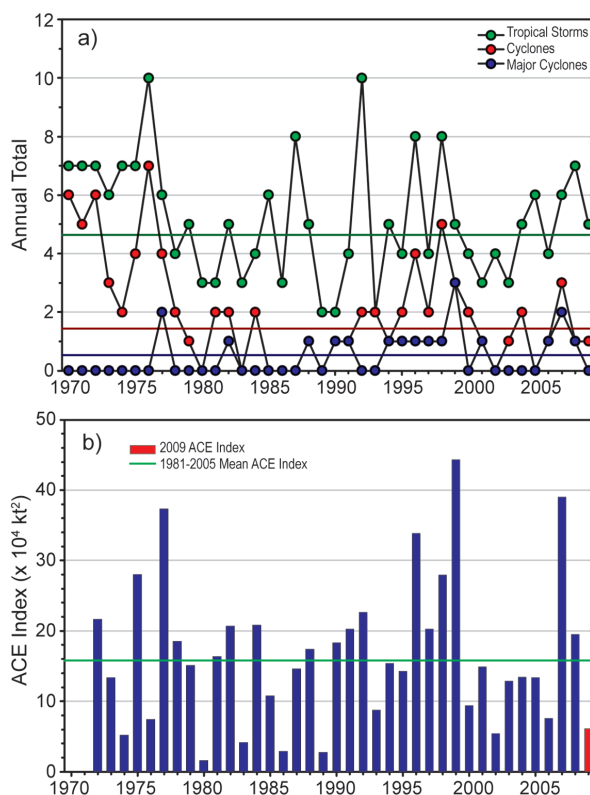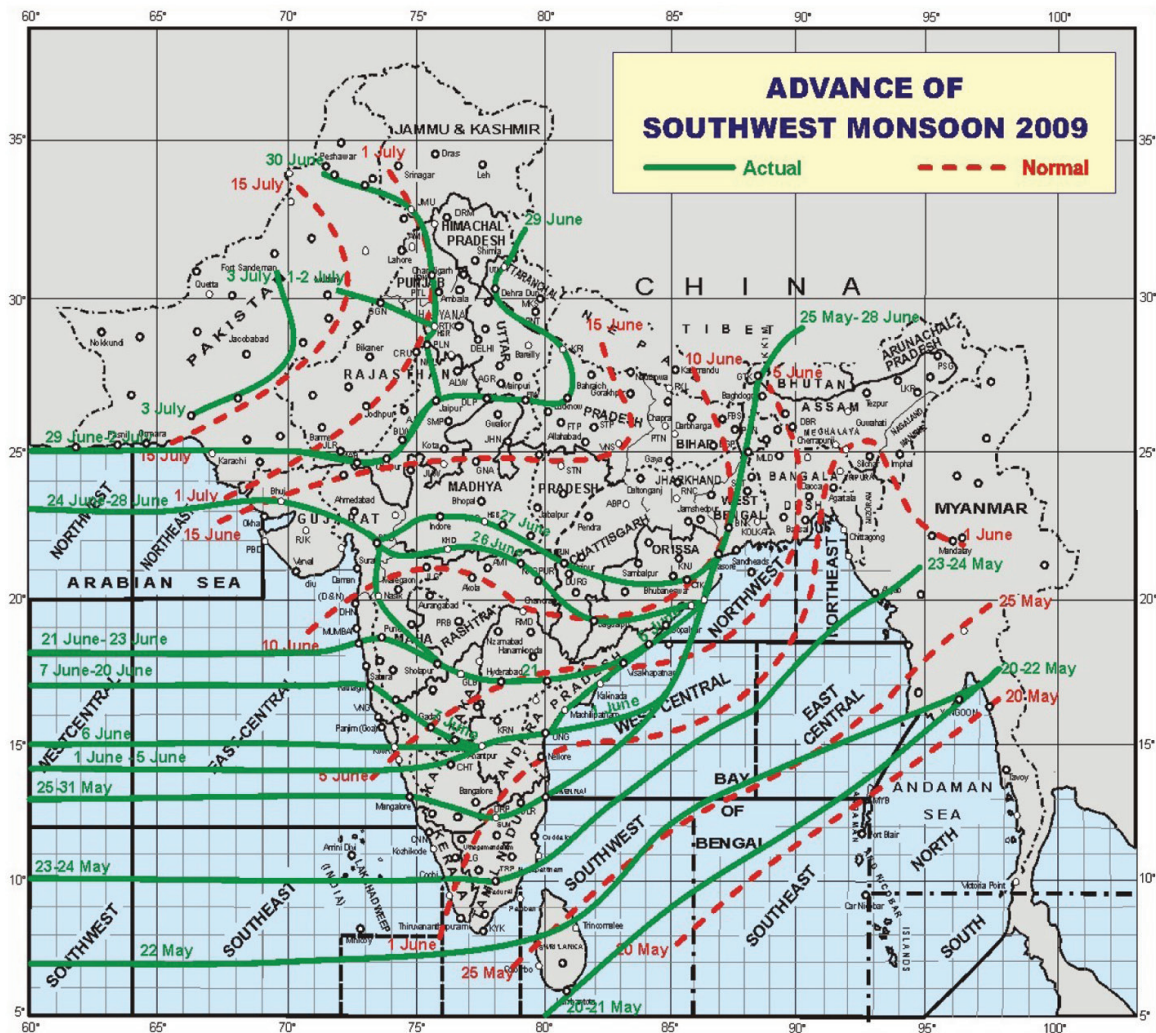
Fɪɢ 4.24. The average position of the monsoon trough by date during 2009. (Image source: India Meteorological Department.)

129 mm of rainfall over Bangladesh, according to the Tropical Rainfall Measuring Mission (TRMM), with maximum rainfall rates exceeding 50 mm hr^{-1}.

Finally, from 9 to 11 November, NS Phyan developed just southwest of Sri Lanka and moved steadily north-northwest and then northeast until making landfall along the eastern coast of India near Maharashtra. NS Phyan produced extremely heavy rainfall of 820 mm over Tamil Nadu with peak winds near 50 kt. This total rainfall ranks second only to CYC Nisha, which produced 1000 mm across the same region from 25 to 29 November 2008.

(ii) South Indian Ocean (SIO)—K. L. Gleason and M. C. Kruk

The SIO basin extends south of the equator from the African coastline to 105°E[11], with most CYCs developing south of 10°S. The SIO TC season extends from July to June encompassing equal portions of two calendar years (e.g., the 2009 season is comprised of storms from July to December 2008 and January to June 2009). The peak activity typically occurs from December to April when the ITCZ is located in the Southern Hemisphere and is migrating toward the equator. Historically, the vast majority of the landfalling CYCs in the SIO impact Madagascar, Mozambique, and the Mascarene Islands, including Mauritius and Réunion.

---

[11]In order to generate consistent basin statistics, the SIO basin boundary overlaps with the Australian Bureau of Meteorology's operational warning area from 90°E to 105°E.

The historical SIO TC data is probably the least reliable of all the TC basins (Atkinson 1971; Neumann et al. 1993), primarily due to a lack of historical record keeping by individual countries and no centralized monitoring agency; however, the historical dataset for the region has been updated (Knapp et al. 2010). The historical data are noticeably deficient before reliable satellite data were operationally implemented in the region beginning about 1983.

The 2008/09 season produced 13 NSs and near-average numbers of CYCs (5) and MCYCs (3) (Fig. 4.25a). The 1981/2005 averages are 11.8 NSs, 6.4 CYCs, and 3 MCYCs. However, the 2008/09 ACE index (~70 x 10^4 kt^2) was below the 1981/2005 average (Fig. 4.25b). With the exception of the 2001–02 season, no other season since the mid-1990s has produced an above average seasonal ACE in the SIO basin.

The strongest CY during the season was MCYC Gael, which developed in the central Indian Ocean during the first few days of February 2009. As it moved southwestward, the center of circulation remained north of the Mauritius and Reunion Islands and slowly became more organized amidst the warm SSTs and weak upper-level wind shear and was declared a tropical cyclone on 3 February by JTWC. Gael quickly intensified just north and west of Reunion and became a MCYC on 6 February. Gael began to curve to the south and then east, missing a direct strike to Madagascar, and the storm remained at sea as it continued along a southeasterly direction and eventually dissipated. MCYC Gael reached peak strength of 120 kt and was responsible for two fatalities on Reunion Island.

The strongest landfalling storm of the season formed in the Mozambique Channel in mid-January 2009 and remained quasi-stationary as it became better organized. By 18 January, Fanele became a tropical cyclone and intensified rapidly into a MCYC on 20 January with sustained winds of 100 kt. MCYC Fanele made landfall on the west coast of Madagascar on 21 January in the Menabe Region southwest of Morondava. Weakened severely by the interaction with the land, Fanele entered the Indian Ocean as a tropical depression and regained some strength before becoming extratropical. At least eight fatalities were reported as a result of MYC Fanele. Fanele's landfall occurred just two days after TS Eric brushed the eastern coast of Madagascar. The two CYCs impacted more than 50 000 people and left thousands homeless.
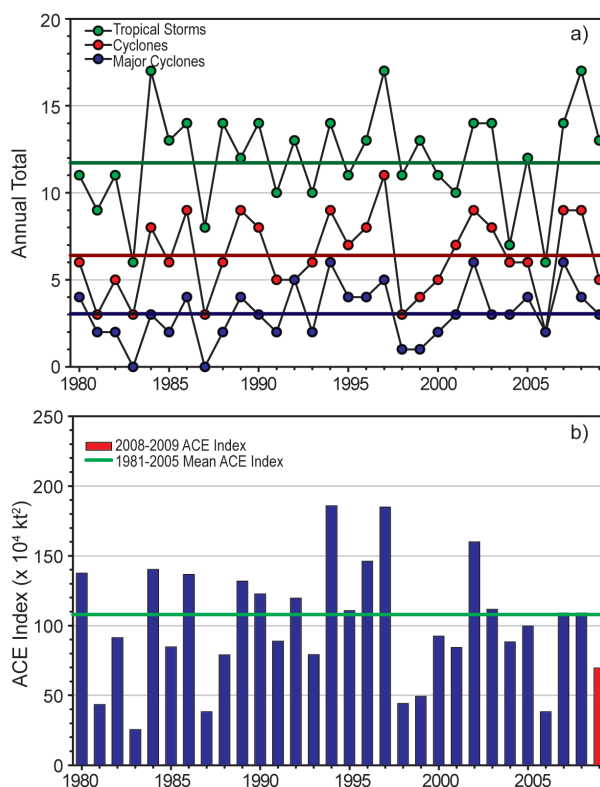
Fig. 4.25. Annual TC statistics, with long-term mean, for the SIO over the period of 1970–2009: (a) number of NSs, CYCs, and MCYCs, and (b) the estimated annual ACE Index (x 10^4 kt^2) for all tropical cyclones during which they were at least tropical storm or greater intensities (Bell et al. 2000). The 1981–2005 base period means are included in both (a) and (b). Note that the ACE Index is estimated due to a lack of consistent 6-hr-sustained winds for every storm.

6) SOUTHWEST PACIFIC BASIN—A. M. Lorrey, S. McGree, and J. Renwick

Eight TCs occurred in the Southwest Pacific during the 2008/09 season, which was one less than the long-term average (1969/70 to 2007/08). This was the most active TC season for the region since 2005/06. The first TC formed on 28 January, which was the latest start to the Southwest Pacific TC season since 2000/01. Four systems developed into TCs west of the international date line and four TCs formed east of it. Peak activity occurred in March (four TCs), and December and February were unusually quiet. Only one TC reached hurricane intensity (sustained wind speeds of at least 64 kt). TC Hettie was the first to form in the southwest Pacific during the 2008/09 season and developed on 28 January to the southeast of Fiji. This system brought southerly winds and heavy rain to the central district of Fiji on 28–29 January before dissipating on 30 January.

Early on 30 January, a tropical low formed in the Coral Sea region and intensified into TC Ellie, a Cat-1 storm, on 1 February. TC Ellie reached peak winds of 43 kt and made landfall in Australia on 2 February. Torrential rain from the dying end of this storm flooded parts of Northern Queensland and caused damages estimated at $110 million (AUS). TC Innes was the third to form in the southwest Pacific and initiated on 13 February as a tropical depression east of Fiji. On 17 February, after passing over Vanuatu and moving toward New Caledonia, Innes was upgraded to a TC. No significant impacts or loss of life were reported from this system. Subsequently, on ex-tropical transition, the dying remains of TC Innes merged with a low pressure system to the east of Australia that generated significant rainfall in northern New Zealand.

Four TCs affected the southwest Pacific region during March. TC Hamish formed off the Australian coast in the Coral Sea on 5 March. TC Joni followed on 11 March, and formed near the Southern Cook Islands and attained a maximum intensity of 55 kt. Damage in the Southern Cooks from TC Joni was minimal. TC Ken then formed between Niue and the Southern Cook Islands on 17 March, attained a maximum intensity of 50 kt, and did not affect land areas. TC Jasper entered the southwest Pacific from the Coral Sea on 24 March with storm intensity and later passed through New Caledonia's waters, with no significant damage reported. Only one TC (Lin) formed in the basin during April. TC Lin formed on 4 April east of Fiji and passed over Tongatapu on 5 April. Sustained winds for Lin were estimated at 55 kt with gusts up to 80 kt closer to the storm's center.

7) AUSTRALIAN REGION BASIN—B. C. Trewin

The 2008/09 TC season was near normal in the broader Australian basin (areas south of the Equator and between 90°E and 160°E[12], which includes Australian, Papua New Guinea, and Indonesian areas of responsibility). The season produced 10 TCs, equal to the long-term average. There were four TCs in the eastern sector[13] of the Australian region during 2008/09, five TCs in the western sector (one of which formed in the northern sector before moving west), and one in the northern sector. There were four landfalls during the season.

The most intense TC of the season was Hamish, which tracked south-east, parallel to the Queensland coast, from 5 to 11 March. It reached its maximum intensity on 7 March while near 19°S, 150°E (approximately 200 km offshore from Bowen), with estimated maximum gusts of 160 kt, maximum sustained winds of 115 kt, and a minimum central pressure of 925 hPa, making it the most intense cyclone observed[14] in the vicinity of the Queensland coast since 1918. It remained at Cat-4 or 5 intensity[15] for three days. While Hamish posed a substantial potential threat to the Queensland coast, it did not make landfall or approach the coast closely enough to cause any significant damage on land. However, two lives were lost at sea, and damage to a ship from the associated large waves resulted in a serious oil slick and coastal pollution in the Brisbane area.

Four TCs made landfall during the season, the strongest being Cat-2. None caused significant damage through wind or storm surge, but all were associated with flooding. Billy made landfall near Wyndham, Western Australia on 20 December as a Cat-2 system, causing minor tree damage and widespread flooding through the Kimberley region. The system later reintensified as it moved back over the ocean and ultimately peaked at Cat-4 intensity (maximum gusts 135 kt, maximum sustained winds 95 kt, minimum central pressure 950 hPa) on 24 December, when north of Port Hedland and moving away from the coast.

Two short-lived Cat-1 systems affected Queensland early in 2009. Charlotte made landfall near the Gilbert River Mouth, on the east coast of the Gulf of Carpentaria, on 12 January, while Ellie made landfall north of Cardwell, on the east coast, on 1 February. Both moved over areas that were already experiencing flooding and hence exacerbated conditions. The Herbert River catchment was severely affected, particularly around Ingham, which received 1481 mm of rain from 25 January to 9 February, including 949 mm from 30 January to 4 February. The heaviest daily total associated with the system was 497 mm at Hawkins Creek, northwest of Ingham.

---

[12]The Australian Bureau of Meteorology's warning area overlaps both the southern Indian Ocean and Southwest Pacific.

[13] The western sector covers areas between 90°E and 125°E. The eastern sector covers areas east of the eastern Australian coast to 160°E, as well as the eastern half of the Gulf of Carpentaria. The northern sector covers areas from 125°E to the western half of the Gulf of Carpentaria.

---

[14] Note that it is likely that the intensity of many cyclones was underestimated prior to the use of satellite data from the 1970s.

[15]See http://www.bom.gov.au/weather/cyclone/faq/index.shtml for a definition of Australian TC categories.
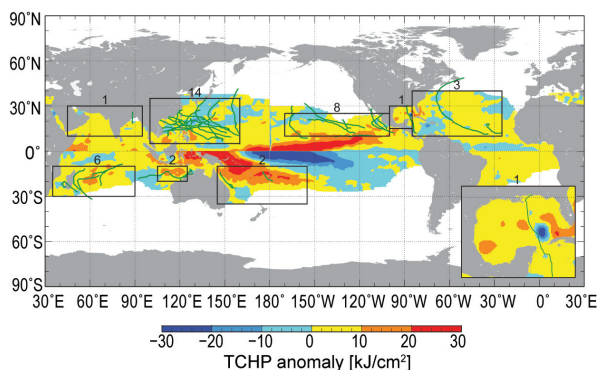
FIG. 4.26. Global anomalies of TCHP corresponding to 2009 computed as described in the text. The boxes indicate the seven regions where TCs occur: from left to right, Southwest Indian, North Indian, West Pacific, Southeast Indian, South Pacific, East Pacific, and North Atlantic (shown as Gulf of Mexico and tropical Atlantic separately). The green lines indicate the trajectories of all tropical cyclones reaching at least Cat- 1 (1-minute average maximum wind ≥119 km hr⁻¹) and above during November 2008–December 2009 in the Southern Hemisphere and 2009 in the Northern Hemisphere. The numbers above each box correspond to the number of Cat- 1 and above cyclones that travel within each box. The Gulf of Mexico conditions during June–November 2009 are shown in detail in the insert shown in the lower right corner.

The fourth landfalling system of the season was Dominic, a Cat- 2 system (maximum gusts 75 kt, maximum sustained winds 55 kt, minimum central pressure 976 hPa) which made landfall near Onslow, Western Australia on 27 January. As for the Queensland systems, the principal impact was flooding, with daily rainfall totals of 243 mm at Thevenard Island and 238 mm at Onslow Airport. Of those TCs that did not make landfall, the most intense was Ilsa, which peaked at Cat- 3 intensity (maximum gusts 125 kt, maximum sustained winds 90 kt, minimum central pressure 958 hPa) on 19 March when more than 1000 km off the Western Australian coast, near 16°S, 107°E.

e. TC heat potential (TCHP)—G. J. Goni, J. A. Knaff, and I-I Lin

TCHP is discussed here for the seven TC basins previously documented as a way to summarize that activity from a slightly different perspective. The TCHP, defined here as the ocean heat content contained between the sea surface and the depth of the 26°C isotherm, has been shown to be more closely linked than SST to intensity changes (Shay et al. 2000; Goni and Trinanes, 2003; Lin et al.,

2008, 2009), provided that atmospheric conditions are also favorable. The TCHP shows high spatial and temporal variability associated with oceanic mesoscale features that can be globally detected with satellite altimetry TCHP (Goni et al. 2009). In general, the real-time forecast of TC intensity is highly dependent on track forecasts and many of the errors introduced in the track forecast are translated into the intensity forecast (Mainelli, et al. 2008). Clearly, areas with high values of TCHP may be important only when TCs travel over them.

To examine the interannual variability of TCHP with respect to TCs, TCHP anomalies are computed during the months of TC activity in each hemisphere: June through November 2009 in the Northern Hemisphere and from November 2008 through April 2009 in the Southern Hemisphere. Anomalies are defined as departures from the mean TCHP calculated during the same months for the period 1993 to 2009. These anomalies show large variability within and among the TC basins (Fig. 4.26).

The WNP basin exhibits the anomalies from the El Niño conditions, which have been in place in the equatorial Pacific Ocean since June 2009. Similar to the conditions during 2008, the South Pacific basin showed mostly positive anomalies. The NIO basin exhibited positive values in the Bay of Bengal and in the Arabian Sea. The Gulf of Mexico (Figs. 4.26, 4.27) showed mostly positive values except for a small region of negative values, which was probably due to a different location of the Loop Current. The tropical Atlantic exhibited mostly positive values, which is also observed in sea height and SST fields (http://www.aoml.noaa.gov/phod/regsatprod/atln/index.php).

The ENP season was very active although the first named storm of the season did not develop until late in June, being the latest start of the ENP
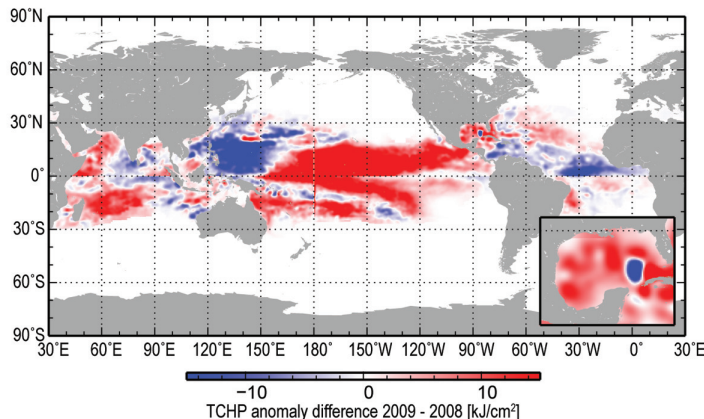

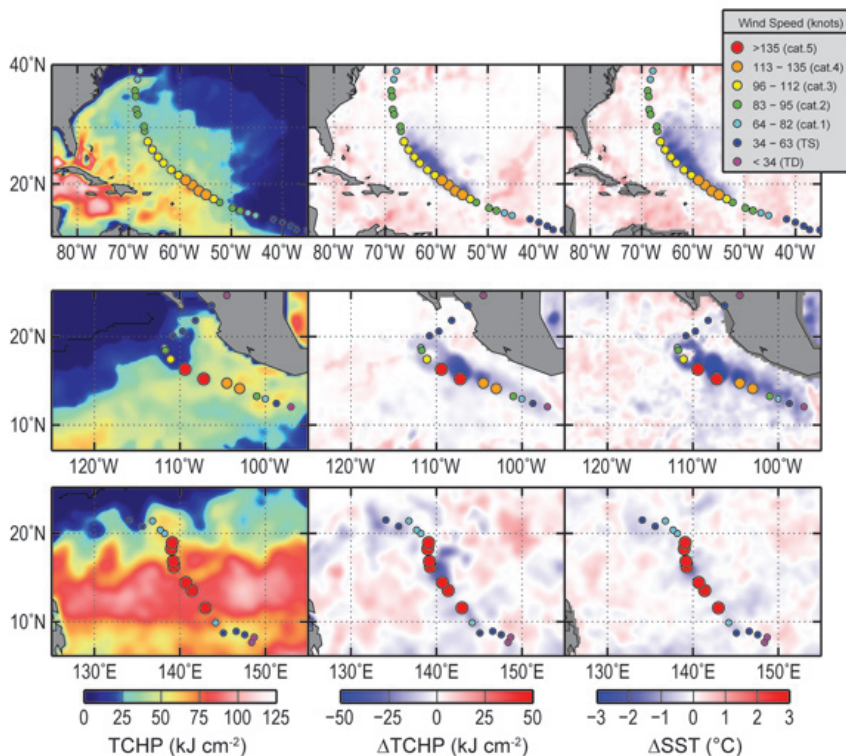**FIG. 4.27. Differences between the TCHP fields in 2009 and 2008.**

Fig. 4.28. (Left) TCHP, and surface cooling given by the difference between post- and pre-storm values of (center) tropical cyclone heat potential and (right) sea surface temperature, for (from top to bottom) Hs Bill and Rick, and TY Nida.

(Figs. 4.26 and 4.27), this was only a small decrease compared to typical TCHP values (Lin et al. 2008). In the WNP, especially between the 10°N and 20°N latitudinal belt, the TCHP values are typically around 100–160 kJ cm^{-2} (Lin et al. 2008). Therefore, even with a 10–15 kJ cm^{-2} decrease, the resultant TCHP in 2009 was still around 85–140 kJ cm^{-2} (Lin et al. 2008), sufficient to keep the TY's self-induced ocean cooling negative feedback small during the intensification (Lin et al. 2009).

TY Nida was a Cat- 1 storm on 24 November and intensified into a Cat- 5 STY on 25 November, reaching peak winds of 160 kt, according to the preliminary JTWC best tracks. The track of this TY travelled from a region of high (~50 kJ cm^{-2}) TCHP values to over a region of extremely high (above 100 kJ cm^{-2}) values. The strength of this TY is also independently revealed by its large 10-minute sustained winds of 115 kt estimated at the same time in the final best track produced by RSMC Tokyo, the greatest intensity since TY Jangmi in 2008. However, the cooling produced by this TY was only of approximately 1°C, probably because of the very deep warm and stable surface layer (Fig. 4.28).

f. Intertropical Convergence Zones (ITCZ)
1) PACIFIC—A. B. Mullan

There are two prominent convergence zones in the Pacific: the ITCZ in the Northern Hemisphere, lying approximately parallel to the Equator with a slight poleward tilt on its eastern end and varying in position from around 5°N–7°N in February–May to 7°N–10°N in August–November; and the SPCZ, which extends diagonally from around the Solomon Islands (10°S, 160°E) to near 30°S, 140°W and is most active in the November–April half-year. A southern branch of the ITCZ can also occur but is only apparent in the January–May period and is strongest in La Niña years.

Figure 4.29 shows 20°N to 30°S transects of quarterly rainfall in the Pacific, as derived from the 0.25

hurricane season in 40 years. H Rick reached Cat-5 in mid-October, and became the first Cat-5 ENP H since Kenna in 2002 and the second strongest ENP hurricane on record, behind Linda in 1997. H Rick intensified from Cat- 2 (85 kt, 975 hPa) to Cat- 5 (150 kt, 914 hPa) in one day. Six hours later Rick reached a maximum intensity of 155 kt just off the southern coast of Mexico (Fig. 4.28). This rapid rate of intensification occurred while traveling over a region of very high TCHP (above 70 kJ cm^{-2}) and in a favorable atmospheric environment. This TC weakened as quickly as it intensified under the influence of strong upper-level southwesterly wind associated with an amplified short-wave trough (Cangialosi and Avila 2010).

The WNP TY season was calmer than average in the early part of the season (June–August) but became very active during the later part of the season (September to November). During these three months, five Cat- 4 and 5 TYs developed, as compared to two in 2008. This happened despite the general cooling tendency of TCHP due to El Niño (Figs. 4.26 and 4.27) in the western Pacific in 2009. Although the TCHP in the western Pacific decreased by about 10–15 kJ cm^{-2} with respect to the average conditions and to 2008

FIG. 4.29. Rainfall rate (mm/day) from TRMM 0.25 degree analysis for the four quarters of 2009. The separate panels for each quarter show the 2009 rainfall cross-section between 20°N and 30°S (solid line) and the 1999–2008 climatology (dotted line), separately for four 30° sectors from 150°E–180° to 120°W–90°W.

ENSO-neutral conditions continued through much of the second quarter of 2009, with the Pacific convergence zones mostly near their normal position and intensity. During this season, the SPCZ tends to contract so that by June only the far western end near Papua New Guinea is active; conversely, the ITCZ strengthens on its eastern end from 150°W eastward. In the western Pacific (150°E–180°), the ITCZ was weaker on its northern edge and resulted in persistent very dry conditions in the northern atolls of the Marshall Islands (PEAC 2009; Fig. 4.29 top right panel).

degree resolution NASA TRMM rainfall data (3B-43 product, Huffman et al. 2007). The convergence zones are clearly evident in the transects over progressive 30-degree longitude bands across the Pacific, where the 2009 positions can be compared with the short 10-year climatology 1999–2008. TRMM data are also available for 1998; this year was omitted from the climatology due to the extremely unusual position of the convection on that year, although in fact the only noticeable effect of including 1998 would be to increase the rainfall along the equator east of the international date line during the first quarter of the year.

La Niña conditions strengthened at the end of 2008, and during the first quarter of 2009 the convergence zones reflected typical La Niña characteristics, with the ITCZ and SPCZ both poleward of their climatological positions and suppressed convection evident near the international date line (Fig. 4.29 and the top panel of Fig. 4.30). Many islands of the southwest Pacific (Vanuatu, New Caledonia, Fiji, Tonga, Samoa, and Southern Cooks) experienced above normal rainfall during this season, with January being particularly wet in Fiji where many new rainfall records were set (ICU 2009). In February, the southern ITCZ appeared and remained prominent for the following two months until ENSO-neutral conditions were established.

El Niño conditions had established themselves by July but were initially weak. During the second half of 2009, the ITCZ east of the Dateline tended to be

FIG. 4.30. Average rainfall rate from TRMM 0.25 degree analysis for January–March 2009 (top) and October–December 2010 (bottom), as a percentage of the 1999–2008 climatology.

FIG. 4.31. (a) Atlantic ITCZ position inferred from outgoing longwave radiation during May 2009. The colored thin lines indicate the approximate position for the six pentads of May 2009. The black thick line indicates the Atlantic ITCZ climatological position. The SST anomalies (Reynolds et al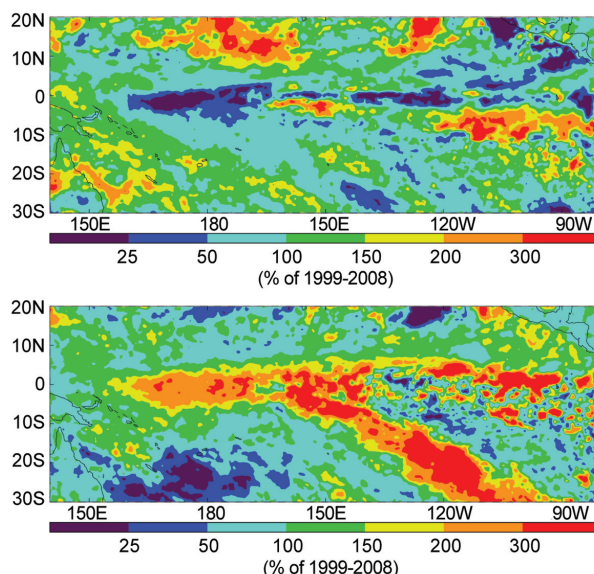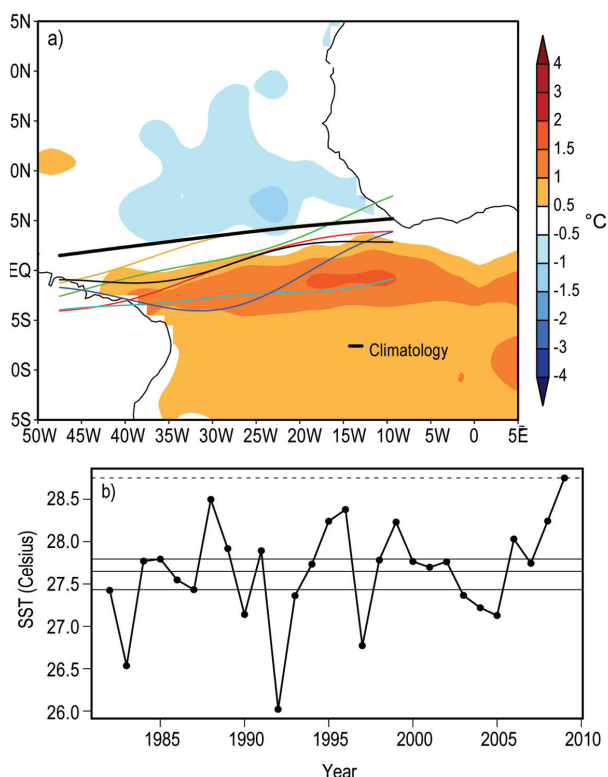. 2002) for May 2009 based on the 1982-2009 climatology are shaded. (b) SST time series averaged over the Atlantic warm pool (5°W to 30°W, 0°S to 5°S) for the period 1982–2009. The solid horizontal central line indicates the climatological mean. The other solid horizontal lines represent the upper and lower terciles. The dashed horizontal line puts the May 2009 record value in climate perspective.

equatorward of its normal position and often more intense (Fig. 4.29). In the OND quarter the SPCZ typically reintensifies, but this year the SPCZ was weak, with suppressed convection in the central portion of the southwest Pacific. Rainfall in the islands was very variable, but a number of islands (New Caledonia, Vanuatu, Fiji, Tonga, and French Polynesia) experienced some months of very low rainfall during this period. By contrast, enhanced convection occurred along the Equator west of the Dateline (Western Kiribati). Fig. 4.30 summarizes this typical El Niño rainfall pattern; the increased rainfall along a line from 5°S, 150°W to 20°S, 120°W appears very significant, but this band of stronger convection is at the very northeast edge of the SPCZ and the rainfall amounts are not very large.

For 2009 as a whole, the TRMM data suggests rainfall was between 50% and 150% of normal over most of the equatorial and tropical Pacific (except in the far eastern sector south of the Equator), reflecting the influence of opposite ENSO phases during the year.

2) ATLANTIC—A. B. Pezza and C. A. S. Coelho
(i)Description

The Atlantic ITCZ is a well-organized convective band that oscillates approximately between 5°N–12°N during July–November and 5°N–5°S during January–May (Waliser and Gautier 1993; Nobre and Shukla 1996). As equatorial Kelvin waves can modulate its interannual variability, ENSO is also known to influence it on a seasonal scale (Münnich and Neelin 2005). In 2009, the Atlantic ITCZ was influenced by ENSO and the Atlantic SST gradient between the Northern and the Southern Hemisphere. A transition occurred from a weak La Niña (January–March) to El Niño towards the end of the year, but the dynamic signature in the Atlantic was also very marked with a strong SST gradient towards the Southern Hemisphere during the first half of the year (warmer towards the south, Fig. 4.31a) changing into a reversed gradient pattern in the second half. As a result the ITCZ reached its southernmost position and maximum intensification in April and May, rapidly migrating back to the north from mid-June. The maximum intensification in May was accompanied by outbursts of severe convection facilitated by the ITCZ migrating into the core of the 'Atlantic warm pool' with SSTs of the order of 30°C (Fig. 4.31b) and high values of CAPE producing positive rainfall anomalies over a large area of northeastern South America and adjacent ocean near the equator (Fig. 4.32a and b).

(ii) Air France 447 disaster: did the Atlantic warm pool play a role?

These formations are not rare but are within the variability of an enhanced pattern intrinsic to years of very active ITCZ. It was unfortunate that a routine commercial flight between Rio de Janeiro and Paris starting its trip on the evening of 31 May (Brazilian time) crossed overnight an area of strong cumulus towers (cold tops) under development at about 3°N (Fig. 4.33), crashing into the ocean at about 0200 UTC on 1 June. The accident made headlines internationally and raised the question as to whether it is safe to fly over the ITCZ during very active periods. We note that there is no definite proof of causality

FIG. 4.33. NOAA GOES-10 infrared satellite photo with enhanced color scheme depicting the approximate time of the crash of Air France flight 447 from Rio de Janeiro to Paris on the morning of 1 June. The red circle near the equator indicates the likely position where the crash occurred.

FIG. 4.32. TRMM (a) mean and (b) anomalous precipitation rate (mm hr⁻¹) for May 2009. The anomaly was based on the climatology for the period 1982–2008.

between the behavior of the ITCZ and the plane crash, but evidence suggests that the weather was an influencing factor. The enhancement observed in May 2009 was a partial thermodynamic response to the large warm pool directly underneath the ITCZ coupled with the dynamic synergy of an already low static stability in the large scale due to the suppressed Kelvin wave propagation from the Pacific during a southern summer of weak La Niña, which would have established anticyclonic conditions over the area. The SST averaged over the Atlantic warm pool in May was the highest on record for the period from 1982 to 2009, suggesting a connection with the unusual enhancement observed (Fig. 4.31b).

g. Indian Ocean Dipole (IOD)—J. J. Luo

The IOD is an internal air-sea coupled climate mode in the tropical Indian Ocean (IO). It can be driven by the tropical Pacific ENSO or sometimes occur independently (Luo et al. 2008, 2010). Positive IOD features anomalous SST cooling in the eastern IO and weak warming in the west during boreal summer and fall and vice versa for negative IOD. Associated with its strong nonlinearity, positive IOD is usually more intensive and predictable than negative

FIG. 4.34. (a) Monthly anomalies of SST (°C, solid lines) and precipitation (mm day⁻¹, dashed lines) in the eastern (IODE, 90°E–110°E, 10°S–0°, blue lines) and western pole (IODW, 50°E–70°E, 10°S–10°N, red lines) of IOD. (b) As in (a), but for the IOD index (measured by the SST difference between IODW and IODE) and surface zonal wind anomaly (m s⁻¹) in the central equatorial IO (70°E–90°E, 5°S–5°N). The anomalies were calculated relative to the climatology over the period 1982–2008. These are based on the NCEP optimum interpolation SST (www.emc.ncep.noaa.gov/research/cmb/sst_analysis/), NCEP CPC CAMS_OPI precipitation (http://iridl.ideo.columbia.edu), and NCEP atmospheric reanalysis data.

IOD. Following the three unprecedented consecutive positive IODs during 2006–08, SST anomalies in the tropical IO during June to November 2009 reflected a neutral-to-weak negative IOD condition (Fig. 4.34). SSTs in the eastern and western tropical IO were warmer than normal since April–May 2009, presumably due to more solar radiation reaching the sea surface associated with the dry conditions there (Fig. 4.34a). The nearly in-phase relationship between SST and rainfall anomalies in the western and eastern poles of IOD during 2005–08 was broken in 2009; SST anomalies in the two poles during 2009 appear to be driven by the atmosphere rather than a forcing of the convection anomalies. Correspondingly, zonal surface wind anomalies in the central equatorial IO showed no or less relationship with the west–east SST gradient during 2009 (Fig. 4.34b). In contrast to the pronounced low-frequent variations and well-coupled conditions during 2005–08, the wind anomalies in 2009 were characterized by high-frequency fluctuations in response to active intraseasonal oscillations despite a tendency of strengthening easterly anomalies associated with the evolution of La Niña to El Niño in the Pacific. By adjusting the equatorial Walker circulation, ENSO evolution may largely influence the tropical IO climate, particularly in cases when the IO internal air-sea coupled processes are weak. The 2008/09 La Niña event caused more rainfall over the equatorial eastern IO and Maritime Continent during DJF; this cooled the local SSTs and induced westerly wind anomalies in the central-eastern equatorial IO (Fig. 4.35a). The westerly winds drove down-welling equatorial Kelvin waves and deepened the oceanic thermocline in the eastern IO and along the west coast of Sumatra-Java (Fig. 4.36a). An IO basin-wide cooling condition, frequently observed several months after La Niña peak, was however, not well developed in early 2009 (Figs. 4.35a and 4.35b). Warmer SSTs occupied the southwestern IO, northeastern Arabian Sea and Bay of Bengal; this appears to be associated with deeper-than-normal thermocline in these areas (Figs. 4.36a and 4.36b).

During March–May, warmer SST anomalies started to develop in the western equatorial IO owing to less cloud condition there (Fig. 4.35b). This is related to the La Niña influence and completely decoupled from the local cold subsurface signal (Fig. 4.36b). The cold subsurface signal in the western IO during December 2008 to May 2009 reflected as eastward-propagating equatorial upwelling Kelvin waves and raised the thermocline in the eastern IO (Fig. 4.36c). Meanwhile, the original warm subsurface signal in the
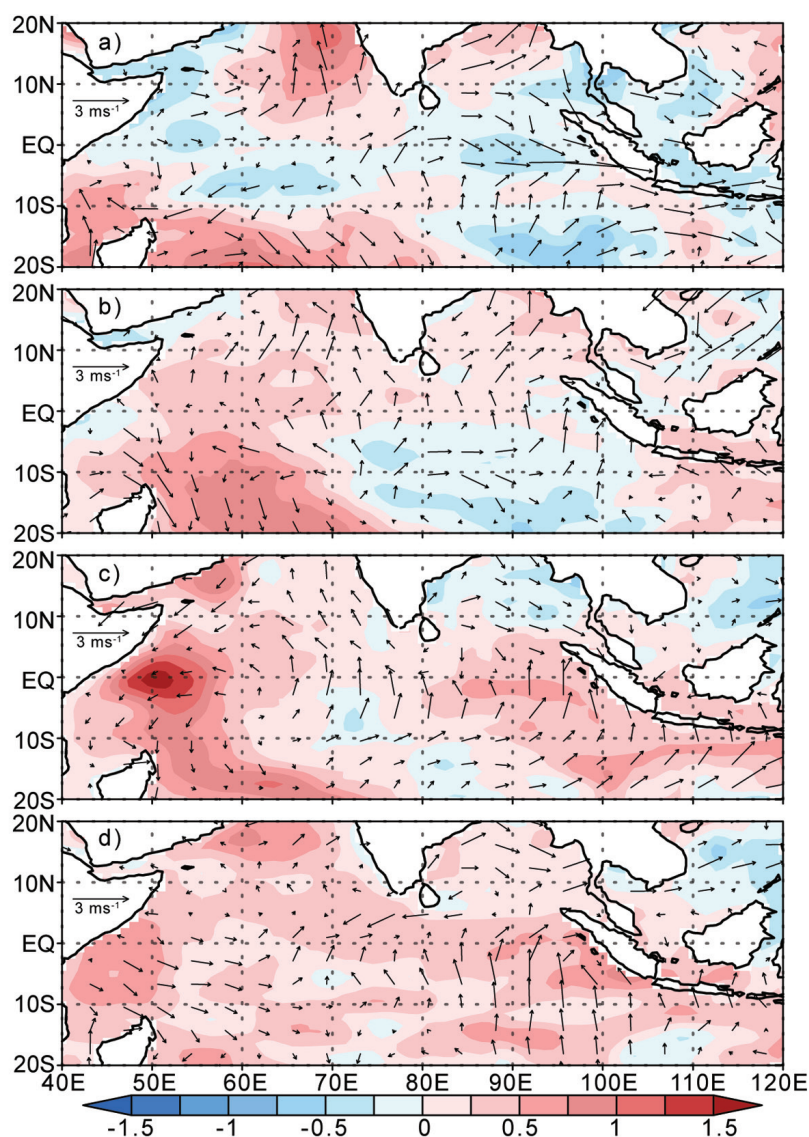

Fig. 4.35. SST and surface wind anomalies during (a) Dec–Feb 2008–09, (b) Mar–May 2009, (c) Jun–Aug 2009, and d) Sep–Nov 2009.

The CNP, between 140°W and the international date line, is best described as a "sub-basin" of the ENP; no other analog exists in the other global TC basins. On average the CNP experiences four to five TCs per season (Blake et al. 2009). These are typically systems that have propagated westward from the ENP basin where they originally developed in the monsoon

FIG. 4.37. Annual TC activity in the CNP, 1971–2009, with seasonal totals of: TCs including TDs (brown), NSs (green), Hs (purple), and MHs (yellow diamonds). Circles at top denote the ENSO phase (El Niño: red, La Niña: blue) for each TC season.

trough west of Mexico and Central America. However, every few years the CNP becomes more active for tropical cyclogenesis and storm formation occurs in situ within the sub-basin, well outside of the Main Development Region of the ENP. Therefore, the CNP is an unusual and transient region of TC activity, where the atmospheric and oceanic conditions can be termed "enhanced" or "quiescent" based on large-scale synoptic patterns typically associated with the ENSO phase (Chu and Wang 1997; Chu and Clark 1999; Chu 2002). The 2009 TC season was one such year when the CNP was in an enhanced phase, as seven TCs were officially tracked by NOAA's CPHC, with four of these systems developing within the sub-basin.

The rarity of TC activity in the CNP has been known for a long time (e.g., Wann 1974; Chu and Wang 1997; Chu and Clark 1999), but improved monitoring due to satellite coverage since the late 1960s has allowed for a more complete picture of the historical variations of activity in the sub-basin. Figure 4.37 shows the time series of TC activity in the CNP in terms of all TC types (including TDs) since 1971. It is clear from Fig. 4.37 that the sub-basin experiences pronounced interannual and interdecadal variability in the frequency of TC occur-

rences. Also plotted in Fig. 4.37 are the ENSO phases during July–October when the majority of TC activity occurs in the CNP. Since 1971, most of the enhanced TC seasons have occurred in conjunction with El Niño warm events, although there have been several notable exceptions, such as in 1978, 1985, and 1992.

The CNP sub-basin also exhibits longer-term, multidecadal periods of enhanced and diminished TC activity similar to the ENP basin as a whole (and inverse to the North Atlantic; Wang and Lee 2010). Previous studies identified epochs of lower activity and higher activity associated with changes in the large-scale atmospheric and oceanic conditions, especially during the peak H season (July–September). Specifically, the period 1982–1994 is clearly an active epoch, one with warmer SSTs, lower mean sea level pressures, anomalously stronger low-level cyclonic vorticity, reduced vertical wind shear, and increased precipitable water content across the region (Chu and Clark 1999; Chu 2002). Despite the current quiescent period that began in 1995, enhanced TC activity has occurred in conjunction with El Niño events, which is an obvious concern for the Hawaiian Islands due to the increased probability of TCs developing and impacting the islands (Chu and Wang 1997; Chu and Wang 1998). With the development of an El Niño during the boreal summer, the 2009 season was clearly a more active one. Of note was the formation of MH Neki (Fig. 4.38) that reached Cat-3 intensity (peak winds of 105 kt), and was the first MH to develop in the sub-basin since 2006 (also an El Niño year). Therefore, the CNP sub-basin reemerged in 2009, which was the most active season in the region since the influence of the strong El Niño in 1997.

FIG. 4.38. Merged METOP-A/AVHRR image on 21 Oct as MH Neki was located southwest of the Hawaiian archipelago. Maximum sustained winds were about 105 kt (Cat-3) at this image time (2000 UTC), which was during the period of peak intensity for the storm.

eastern IO reflected as a pair of westward-propagating downwelling Rossby waves and reached the west during JJA; this contributed to the rapid enhancement of the surface warming in the western equatorial IO (Fig. 4.35c). An off-equatorial warm Rossby wave at 10°S also propagated slowly westward from ~73°E to ~53°E during the period from December 2008 to November 2009 (Fig. 4.36). However, it appears to have had little contribution to the western IO SST warming from March to November. Forced by more solar radiation associated with the less cloud condition, SSTs in the eastern IO became warmer than normal during June–August despite the local cold subsurface signal (Figs. 4.35c and 4.36c). The warmer SSTs generated a local wind convergence and deepened the thermo-

cline in the eastern IO which in turn helped to intensify the surface warming (Figs. 4.35d and 4.36d). This led to a weak negative IOD index during September–November, in contrast to what has been often observed during El Niño developing years. The weak negative IOD condition may have caused more rainfall in the eastern IO and Maritime Continent and reduced the short rains in eastern Africa during the boreal fall season, which is counter to the remote influence of the developing El Niño. It is also possible that the eastern IO SST warming might have hampered the El Niño development during 2009 (Luo et al. 2010).
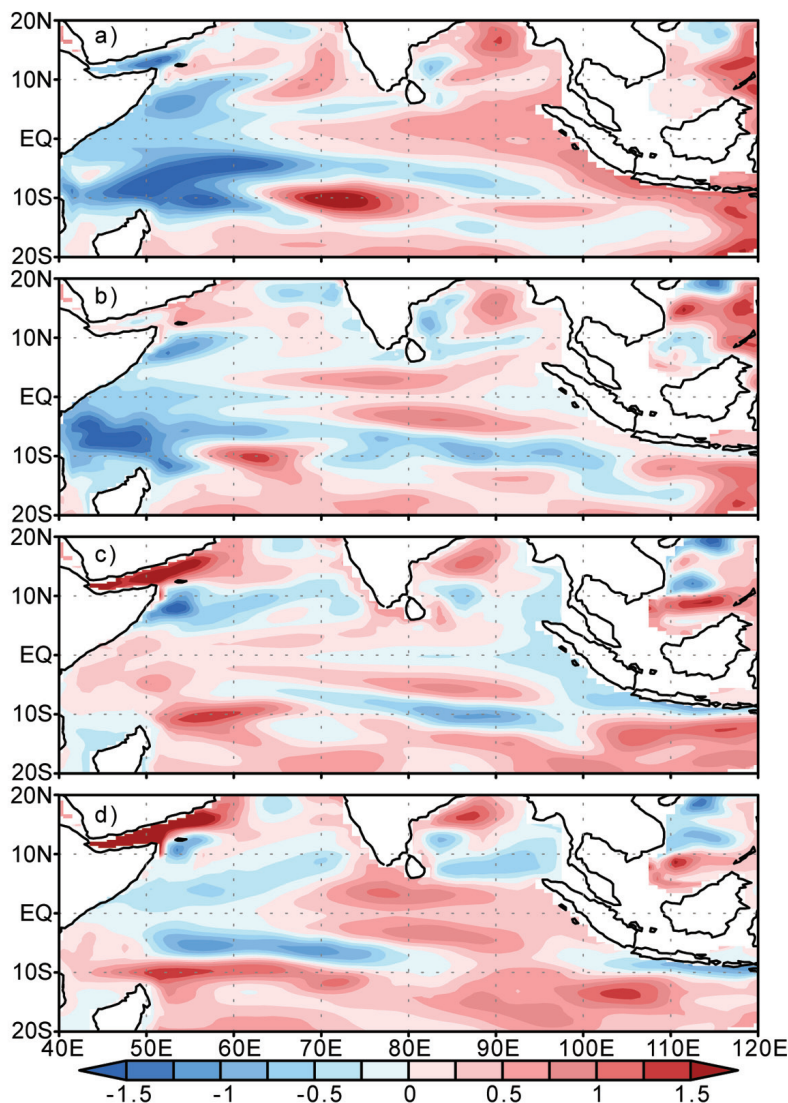
Fig. 4.36. As in Fig. 4.35, but for the upper 300-m mean ocean temperature anomalies based on the NCEP ocean reanalysis (available at www.cpc.ncep.noaa.gov/products/GODAS/).

5. THE ARCTIC—J. Richter-Menge, Ed.

a. Overview—J. Richter-Menge

The permanent presence of sea ice, ice sheets and continuous permafrost are defining features of the polar regions. The Arctic is further distinguished because it sustains a human population in a harsh environment. In this chapter we highlight observations that indicate changes and trends in the state of the physical components of the Arctic system, including the atmosphere, ocean, sea ice cover, land, and Greenland. In 2009 there continued to be widespread evidence of the impact of a general, Arctic-wide warming trend in surface air temperatures over land, evident since the mid-1960s. Significant regional and temporal variability was also widely apparent, tempering the dramatic evidence of warming reported in recent years (e.g., a record positive surface air temperature anomaly in 2008, record summer sea ice minimum extent in 2007, and record ocean surface temperature anomalies in 2007).

Surface temperature anomalies (relative to a 1961–90 reference period) highlight the major feature of current Arctic conditions: an Arctic amplification of temperature anomaly of a factor of two or more, relative to more southerly latitudes. Below normal precipitation (with reference to the 1971–2000 base period) led the Greenland ice sheet surface mass balance in 2009 to be 25% to 50% less positive than normal, despite below-normal melting and runoff across much of the ice sheet below ~1800 m altitude. The 34 widest marine-terminating glaciers in Greenland lost 101 km^2 ice area in 2009, within a remarkably linear (R =−0.99) annual loss rate of –106 km^2 over the past decade. The 2008/09 Arctic snow-cover season marked a continuation of relatively shorter snow seasons, due primarily to an early disappearance of snow cover in spring. Observations show a general increase in permafrost temperatures during the last several decades in Alaska, northwest Canada, Siberia, and Northern Europe. Changes in the timing of tundra green up and senescence are also occurring, with earlier green up in the High Arctic and a shift to a longer green season in fall in the Low Arctic. The 2009 summer minimum sea ice extent was the third-lowest recorded since 1979. Surface ocean temperatures remained relatively warm and surface water was much fresher than in the 1970s.

Linkages between the various elements of the Arctic systems continue to emerge. For instance, tendencies in the magnitude and distribution of upper ocean temperatures are observed to be strongly dependent on changes in the characteristics (e.g.,

pace and location) of the summer sea ice retreat and their effect on local atmospheric warming. The heat accumulated in the surface and near-surface layers of the ocean during the summer is then released back to the atmosphere in the following autumn, impacting temperatures in the lower troposphere. The coupling between the atmosphere, ocean, and sea ice has also impacted the overall characteristics of the Arctic sea ice cover, which is now dominated by relatively thin seasonal ice. The effects of the retreating sea ice also influence the temperature and vegetation of adjacent lands. Temporal analyses generally show that, within a specific region, periods of lower sea ice concentration are correlated with warmer land surface temperatures and an increase in the amount of live green vegetation in the summer. In the Eurasian river drainage basins, the correlation between river discharge and sea ice extent, over the period 1979–2008, is greater than the correlation between precipitation and runoff.

b. Atmosphere—J. Overland, M. Wang, and J. Walsh

The annual mean temperature for 2009 over Arctic land areas was cooler than in recent years, although the average temperature for the last decade remained the warmest in the record beginning in 1900 (Fig. 5.1). The 2009 average was dominated by very cold temperatures in Eurasia in February (the coldest of the decade) and December, while the remainder of the Arctic remained warm (Fig. 5.2). The spatial distribution of annual temperature anomalies for 2009 has a
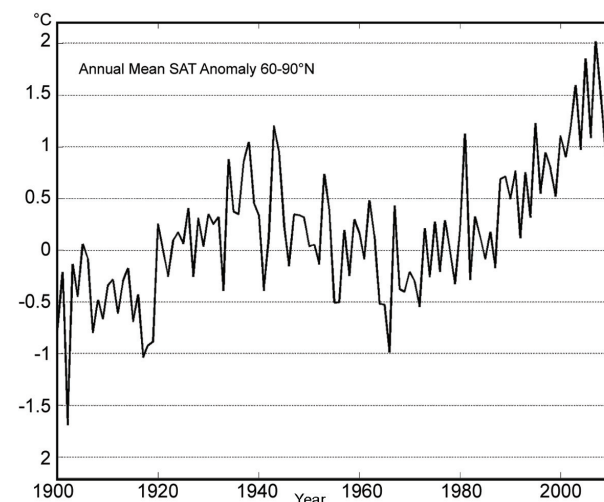
FIG. 5.1. Arctic-wide annual average surface air temperature anomalies relative to the 1961–90 mean, based on land stations north of 60°N from the CRUTEM 3v dataset, available online at www.cru.uea.ac.uk/cru/data/temperature/. Note this curve does not include marine observations.

NCEP/NCAR Reanalysis
1000mb air (C) Composite Anomaly 1968-1998 climo
NOAA/ESRL Physical Science Division

Feb 2009
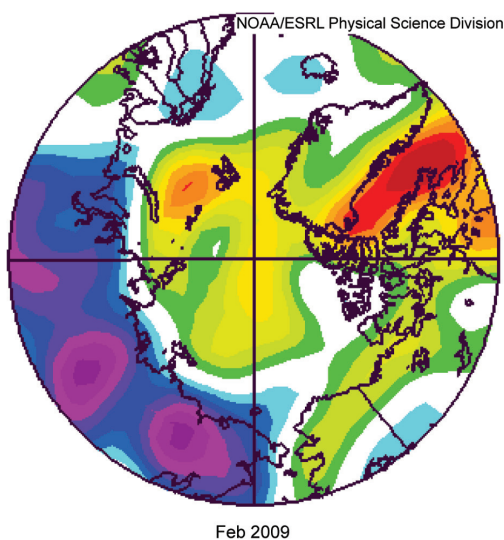
Fig. 5.2. Near-surface (1000 mb) air temperature in °C anomalies for February 2009. Anomalies are relative to the 1968–96 mean, according to the NCEP–NCAR reanalysis through the NOAA /Earth Systems Research Laboratory, generated online at www.cdc.noaa.gov.

NCEP/NCAR Reanalysis
1000mb air (C) Composite Anomaly 1968-1995 climo
NOAA/ESRL Physical Science Division

Jan to Dec: 2009
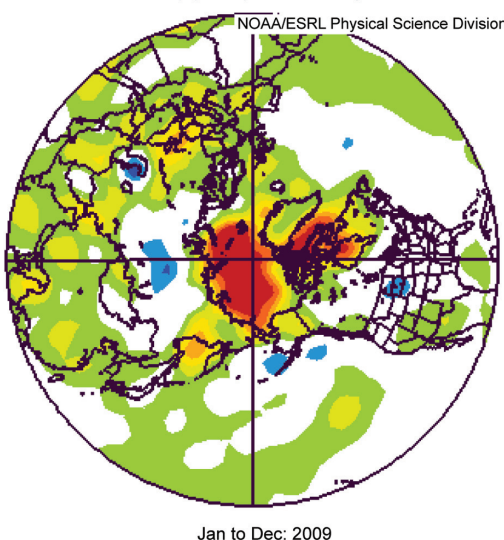
Fig. 5.3. Near-surface (1000 mb) annual air temperature in °C anomalies for 2009 over the northern hemisphere relative to 1968–96 mean according to the NCEP–NCAR reanalysis through the NOAA / Earth Systems Research Laboratory, generated online at www.cdc.noaa.gov. Arctic amplification of air temperature anomalies are a factor of two or more relative to lower latitudes.

pattern with values greater than 2.0°C throughout the Arctic, relative to a 1968–96 reference period (Fig. 5.3). These anomalies show the major feature of current Arctic conditions: a factor of two (or more) amplification of temperature relative to lower latitudes.

As noted in the Arctic sea ice section, September 2009 had the third minimum sea ice extent relative to the period when observations began in 1979. Although 2009 did not have a record sea ice minimum

NCEP/NCAR Reanalysis
850mb air (C) Composite Anomaly 1968-1995 climo
NOAA/ESRL Physical Science Division

Oct 2009

Fig. 5.4. Lower tropospheric (850 hPa) air temperature in °C anomalies for October 2009 relative to the 1968–96 mean according to the NCEP–NCAR reanalysis through the NOAA /Earth Systems Research Laboratory, generated online at www.cdc.noaa.gov.

in September, there were still extensive regions of open water in the Chukchi, East Siberian Laptev, and Kara Seas (see sea ice section below, Fig. 5.11), which allowed extra solar and longwave radiation to be absorbed by the ocean (see ocean section below, Fig. 5.5). This heat can be released back to the atmosphere the following autumn. This release of heat impacted temperatures in the lower troposphere (Fig. 5.4) with consequences for regional and far field wind patterns through horizontal gradients in the 500–1000 hPa thickness fields (Overland and Wang 2010).

The year 2009 ended with record-setting negative values for the Arctic Oscillation (AO) index, a condition favoring meridional (north-south) atmospheric flow. Thus, December 2009 and early 2010 exhibited extremes in both warm and cold temperatures with record-setting snow across lower latitudes. Northern Eurasia (north of 50° latitude to the Arctic coast)

and North America (south of 55° latitude) were particularly cold (monthly anomalies of −2°C to −10°C). Arctic regions had anomalies of +4°C to +12°C. While individual weather events cannot be directly linked to larger scale climate changes, recent data analysis and modeling suggest a link between loss of sea ice and a shift to an increased impact from the Arctic on midlatitude climate (Francis et al. 2009; Honda et al. 2009).

c. Ocean—A. Proshutinsky, M.-L. Timmermans, I. Ashik, A. Beszczynska-Moeller, E. Carmack, I. Frolov, R. Krishfield, F. McLaughlin, J. Morison, I. Polyakov, K. Shimada, V. Sokolov, M. Steele, J. Toole, and R. Woodgate

1) Circulation

In 2009, the annual wind-driven ocean circulation regime can be characterized as cyclonic (counterclockwise), with a Beaufort Gyre that is significantly reduced in strength and a Transpolar drift that is effectively nonexistent (Fig. 5.5). This is the first time that an annual cyclonic circulation regime has been observed in the Arctic since 1997. The anticyclonic circulation regime that persisted through 2008 lasted at least 12 years instead of the typical 5–8 year pattern [as reported in Proshutinsky and Johnson (1997), who analyzed statistics of Arctic circulation regimes between 1948 and 1989]. The climatological seasonal cycle of the Arctic has anticyclonic ice and ocean circulation prevailing in winter and cyclonic
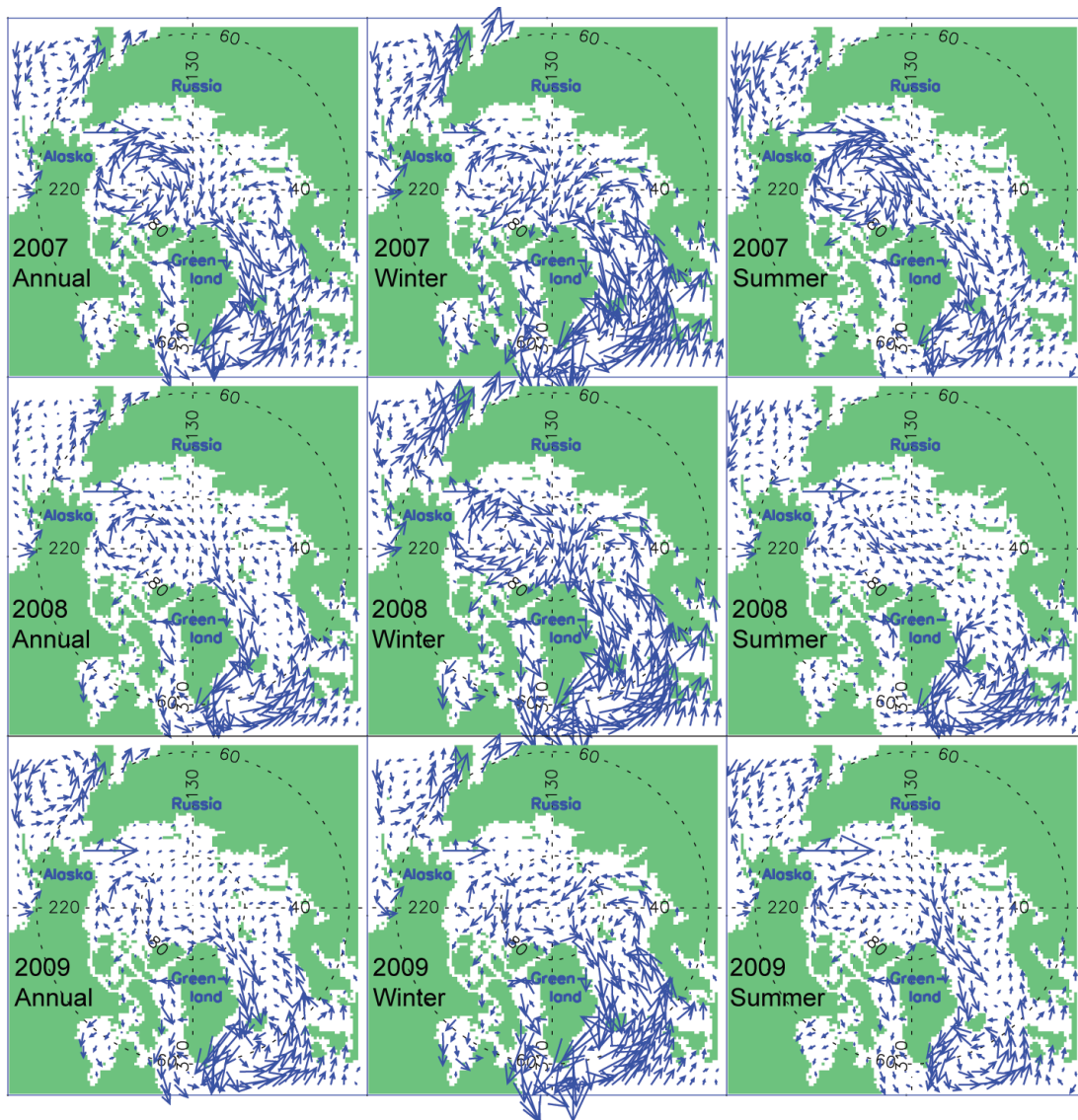
Fig. 5.5. Simulated circulation patterns of the upper-ocean wind-driven circulation in 2007 (top), 2008 (middle) and 2009 (bottom). Annual, winter, and summer circulations are shown in the left, center, and right panels, respectively.

FIG. 5.6. Satellite-derived summer (JAS) SST anomalies (Reynolds et al. 2002) in 2007 (left), 2008 (middle), and 2009 (right) relative to the summer mean over 1982–2006. Also shown is the Sep mean ice edge (thick blue line).

circulation in summer. Since 2007, this seasonality has changed dramatically. In 2007, both summer and winter circulations were very strongly anticyclonic (Fig. 5.5, top panels) and resul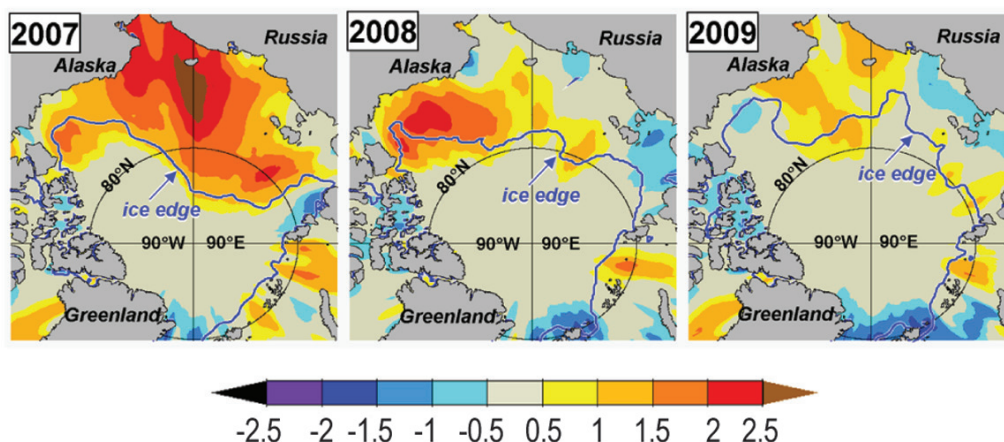ted in the unprecedented reduction of the Arctic Ocean summer sea ice cover. In 2008, the winter circulation was anticyclonic but the summer circulation was unusual with a well-pronounced Beaufort Gyre and a cyclonic circulation cell north of the Laptev Sea (Fig. 5.5, middle panels). In 2009 (Fig. 5.5, bottom panels), the circulation reversed relative to climatology in both winter and summer: it was anticyclonic in summer (instead of cyclonic) and cyclonic in winter (instead of anticyclonic). These wind-driven conditions significantly influenced the characteristics of the sea ice cover, oceanic currents, ocean freshwater and heat content observed during 2007–09.

2) WATER TEMPERATURE AND SALINITY

Maximum upper ocean temperatures in summer 2009 continued to decline since the historical extreme in summer 2007 (Fig. 5.6). This tendency is strongly linked to changes in the characteristics (e.g., pace and location) of the summer sea ice retreat and their effect on local atmospheric warming (Steele et al. 2010, manuscript submitted to *J. Geophys. Res.*). Surface warming and sea ice reduction in the Canada Basin has also been accompanied by the widespread appearance of a near-surface temperature maximum at 25–35 m depth due to penetrating solar radiation (Jackson et al. 2010). As described in the Arctic atmosphere section, the heat accumulated in the surface and near-surface layers of the ocean can be released back into the atmosphere in the fall—a cycle that is likely to influence sea ice conditions in the future.

Surface-layer waters in the Arctic Ocean in 2009 remained much fresher than in the 1970s (Timokhov and Tanis 1997, 1998). In the Beaufort Gyre, freshwater content in 2009 (Fig. 5.7) was comparable to the 2008 freshwater conditions, with the exception of the southwest corner of the Canada Basin. In this region, the freshwater accumulation was increased relative to 2008 by approximately 0.4 km^3 under enhanced Ekman pumping and sea ice melt in this region. In total, during 2003–09 the Beaufort Gyre (Proshutinsky et al. 2009) has accumulated approximately 5000 km^3 of freshwater (from 17 300 km^3 in 2003 to 22 300 km^3 in 2009), which is 5800 km^3 larger than climatology of the 1970s (Timokhov and Tanis 1997, 1998).

Hydrographic surveys conducted in 2007–09 summer (Fig. 5.7) in the Canada Basin indicate that in 2007 and 2008 there were two shallow temperature maximums in the upper Pacific water layer. However, in 2009, the heat content in this layer was reduced.

Atlantic Water layer maximum temperature anomalies for 2007–09 (Fig. 5.8) were calculated relative to the 1970s (Timokhov and Tanis 1997, 1998; Polyakov and Timokhov 1994). The 2007–09 Atlantic Water layer data were derived from ship-based and Ice-Tethered Profiler (ITP) instruments. In 2007–09, the temperature anomalies were generally higher on the Eurasian side of the Lomonosov Ridge, reaching a maximum of up to 1.5°C along the Eurasian Basin boundaries. Warming was less pronounced in the Canada Basin. There was little to no temperature anomaly (<0.1°C) at the southeast boundary of the Canada Basin or in the basin boundary regions adjacent to Greenland and the Canadian Archipelago. Negative (cooling) temperature anomalies were detected in the vicinity of Nares Strait. Considering 2009 data alone, the warming pattern remained similar with the major difference being that maximum temperature anomalies along the Eurasian Basin boundaries were lower (<1.0°C).

Fig. 5.8. 2007–09 Atlantic water layer temperature maximum anomalies relative to climatology of Timokhov and Tanis (1997, 1998).
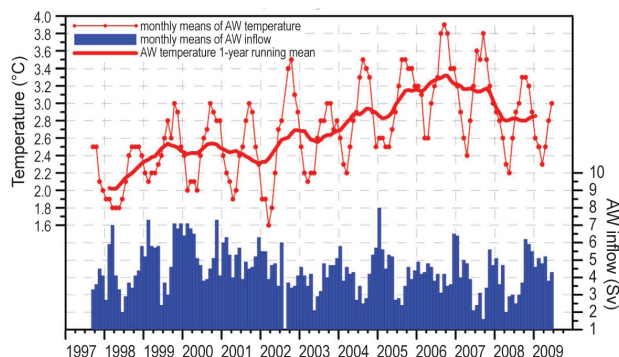
Fig. 5.9. Mean temperature of Atlantic water (AW, defined with TAW >1°C) and the AW volume inflow in the West Spitsbergen Current, northern Fram Strait measured by the array of moorings at 78°50'N.

Fig. 5.7. Summer heat (1 × 10¹⁰ J m⁻²) (left) and freshwater (m) content (right) in the 1970s, 2007, 2008, and 2009. The top two panels show heat and freshwater content in the Arctic Ocean based on 1970s climatology (Timokhov and Tanis 1997, 1998). The bottom six panels show heat and freshwater content in the Beaufort Gyre based on hydrographic surveys (black dots depict locations of hydrographic stations). For reference, this region is outlined in black in the top panel of each column. The heat content is calculated relative to water temperature freezing point in the upper 1000m ocean layer. The freshwater content is calculated relative to a reference salinity of 34.8.

The characteristics of the Atlantic Water layer discussed above are regulated by the Atlantic water parameters in the Fram Strait (Fig. 5.9), where the Atlantic water inflows to the Arctic Ocean. After reaching a maximum in 2006, the temperature of Atlantic water in Fram Strait decreased until 2008. In 2009, Atlantic water temperature and salinity in the northern Fram Strait started to rise again, returning to their long-term means. The late winter of 2008 and early spring of 2009 were also characterized by a higher Atlantic water volume inflow with the West Spitsbergen Current as compared to 2005–07 (Fig. 5.9).

The Bering Strait is another important gateway to the Arctic Ocean. Preliminary analysis of mooring data from the Bering Strait does not suggest a repeat

of the very high heat fluxes from 2007 (Woodgate et al. 2010). Temperatures in 2008 were generally cooler than in 2007, reaching only 2°C–3°C in near-bottom temperature, compared to 4°C–5°C in 2007. Similarly, by the time of mooring turnaround in 2009, water temperatures were about a degree colder than the same month (August) in 2007. These cooler temperatures are more in agreement with temperatures of 2000–06 in the strait.

An interesting change in ocean geochemistry was observed in the Canada Basin in 2008 and 2009. The input of sea ice meltwater, in combination with CO_2 uptake and global ocean acidification, caused the surface waters of the Canada Basin to become corrosive to calcifying organisms in the upper layer in 2008 (Yamamoto-Kawai et al. 2009). This is the first deep basin observation of aragonite undersaturation in surface waters. In 2009 the areal extent of surface waters unsaturated in aragonite, a form of calcium carbonate produced by marine organisms, increased. The increased stratification and decrease in upper-layer nutrient concentrations has also resulted in an increase in the number of picoplankton and a decrease in nanoplankton. Shifts such as these may alter the food web in the future (Li et al. 2009).

3) Sea level

Fig. 5.10 shows sea level (SL) time series from nine coastal stations in the Siberian Seas, having representative records for the period of 1954–2009 (Arctic and Antarctic Research Institute data archives). In 2009, the SL along the Siberian coastline has significantly decreased relative to 2008. This caused a slight reduction in the estimated rate of SL rise for the nine stations over the period, to 2.57 ± 0.45 mm yr^{-1} (after correction for glacial isostatic adjustment, GIA). The changing SL rise tendency may be due to the substantial change in the wind-driven ocean circulation regime (less anticyclonic, as de-
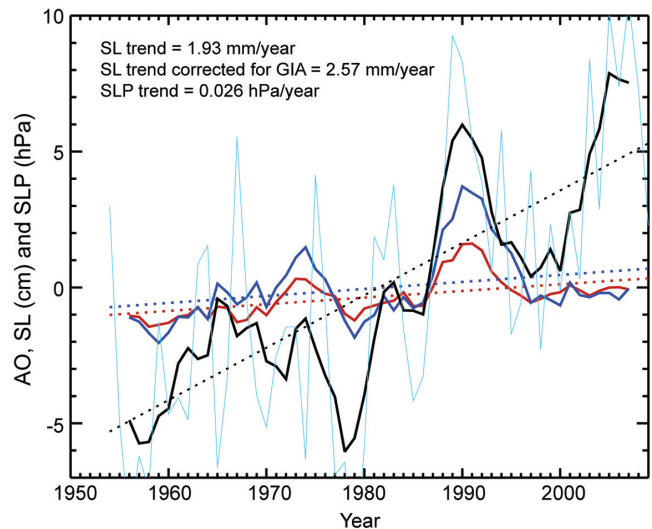
FIG. 5.10. Five-year running mean time series of: the annual mean sea level at nine tide gauge stations located along the Kara, Laptev, east Siberian, and Chukchi Seas' coastlines (black line); anomalies of the annual mean Arctic Oscillation (AO) Index multiplied by 3 (red line); sea surface atmospheric pressure at the North Pole (from NCAR–NCEP reanalysis data) multiplied by -1 (dark blue line); annual sea level variability (light blue line). Dotted lines depict estimated trends for SL, AO, and SLP.

scribed in section 5c1) and/or due to steric effects associated with the reduction of surface ocean warming and freshening rates (section 5c2). Ocean cooling and salinification both result in sea level decrease.
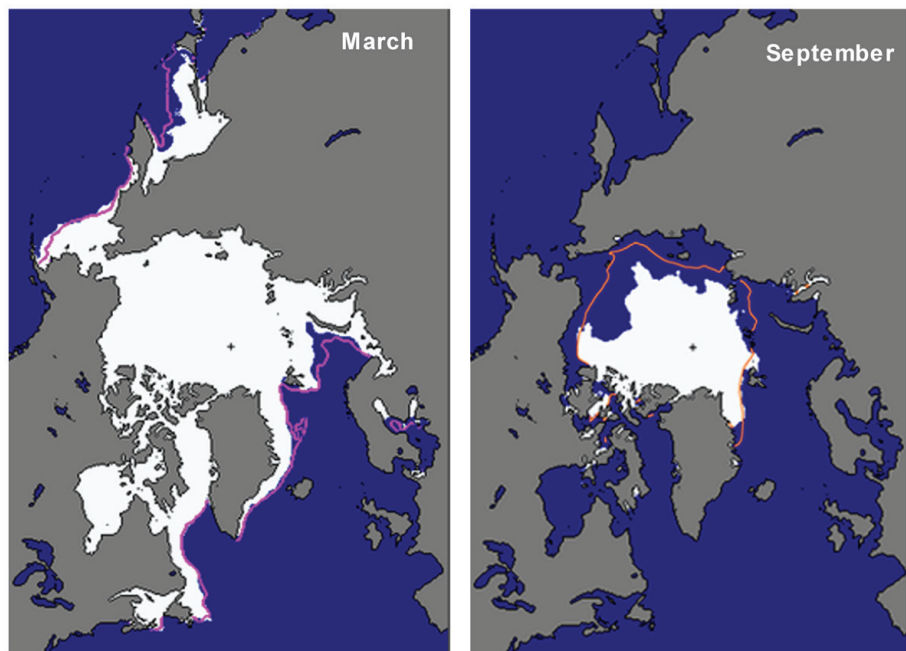
FIG. 5.11. Sea ice extent in March 2009 (left) and September 2009 (right), illustrating the respective winter maximum and summer minimum extents. The magenta line indicates the median maximum and minimum extent of the ice cover, for the period 1979–2000. (Source: National Snow and Ice Data Center.)

d. Sea ice cover—D. Perovich, R. Kwok, W. Meier, S. Nghiem, and J. Richter-Menge

1) Sea ice extent

Sea ice extent is the primary parameter for summarizing the state of the Arctic sea ice cover. Microwave satellites have routinely and accurately monitored the extent since 1979. There are two periods that define the annual cycle and thus are of particular interest: March, at the end of winter when the ice is at its maximum extent, and September, when it reaches its annual minimum. Ice coverage maps for March 2009 and September 2009 are presented in Fig. 5.11, with the magenta line denoting the median ice extent for the period 1979–2000.

The March 2009 maximum ice extent was 15.2 million km^2, the same as in 2008 and only 4% less that the 1979–2000 average of 15.8 million km^2. On 12 September 2009 sea ice extent reached a 2009 minimum of 5.1 million km^2. The 2009 summer minimum is the third-lowest recorded since 1979. It was 0.6 km^2 greater than 2008 and 1.0 km^2 above the record low in 2007 (an increase of 25% compared to 2007). Surface air temperatures through the 2009 summer were relatively cooler, particularly in the Chukchi and Beaufort seas. Winds in 2009 also tended to disperse the ice pack over a larger region. While the 2009 minimum extent was an increase over the two previous years, it was still 1.6 million km^2 (~10%) below the 1979 to 2000 average minimum. By December 2009 the ice extent had increased to 12.5 million km^2, the fourth lowest December extent on record. This relatively slow recovery was due in part to a strongly negative Arctic Oscillation in the fall, an atmospheric circulation pattern that promotes meridional flow and relatively warm air temperatures in the Arctic.

The time series of the anomalies in sea ice extent in March and September for the period 1979–2009
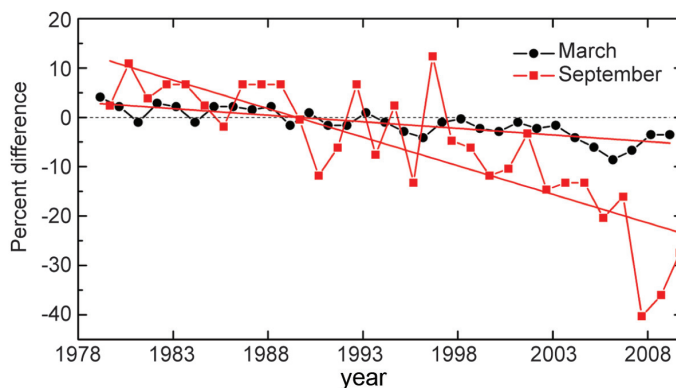
Fig. 5.12. Time series of the percent difference in ice extent in March (the month of ice extent maximum) and September (the month of ice extent minimum) relative to the mean values for the period 1979–2000. Based on a least squares linear regression for the period 1979–2009, the rate of decrease for the March and September ice extents is –2.5% and –8.9% per decade, respectively.

are plotted in Fig. 5.12. The anomalies are computed with respect to the average from 1979 to 2000. The large interannual variability in September ice extent is evident. Both winter and summer ice extent exhibit a negative trend, with values of -2.5% per decade for March and -8.9% per decade for September over the period 1979–2009.

2) Sea ice age and thickness

The age of the sea ice is another key descriptor of the state of the sea ice cover, since older ice tends to be thicker and more resilient than younger ice. A simple two-stage approach classifies sea ice into first year and multiyear ice. First-year is ice that has not yet survived a summer melt season, while multiyear ice has survived at least one summer and can be several years old. Satellite derived maps of ice age for March of 2007, 2008, and 2009 are presented in Fig. 5.13.

In the past decade, the extent of multiyear sea ice rapidly reduced at a rate of 1.5×106 km^6 per decade, triple the reduction rate during the three previous decades (1970–2000). Springtime multiyear ice extent was the lowest in 2008 in the QuikSCAT data record since 2000 (Nghiem et al. 2007). QuikSCAT results in March 2009 showed a multiyear ice extent of 3.0 ± 0.2 million km^2. This was 0.3 million km^2 larger
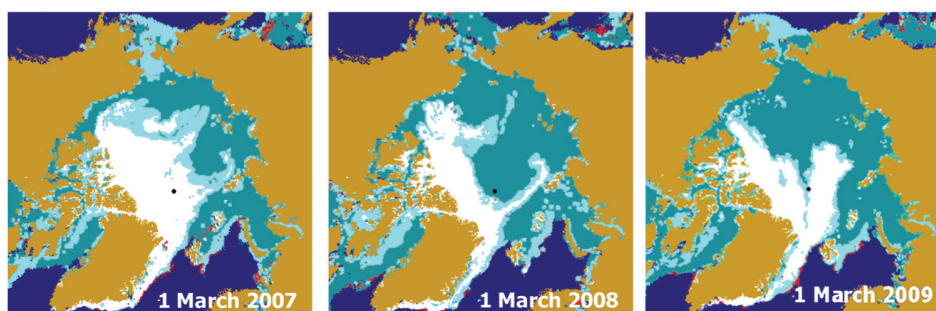
Fig. 5.13. Arctic sea ice distribution in March of 2007, 2008, and 2009. Multiyear ice is in white, mixed ice aqua, first-year ice teal, and ice with melting surface red. Dark blue is for open water and brown for land. Figure courtesy of Son Nghiem.
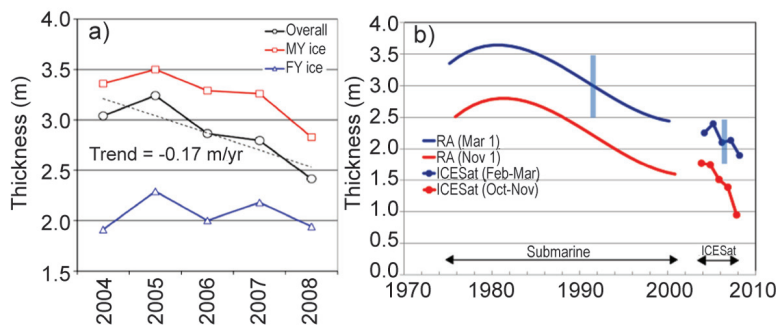
Fig. 5.14. (a) Winter Arctic Ocean sea ice thickness from ICESat (2004–08). The black line shows the average thickness of the ice cover while the red and blue lines show the average thickness in regions with predominantly multiyear and first-year ice, respectively. (b) Interannual changes in winter and summer ice thickness from the submarine and ICESat campaigns within the data release area for a period of more than 30 years. The data release area covers approximately 38% of the Arctic Ocean. Blue error bars show the uncertainties in the submarine and ICESat datasets (Kwok et al. 2009).

(11% increase) than the multiyear ice extent on the same date in 2008, even though the total sea ice extent was similar in the spring of 2008 and 2009. While the multiyear ice extent was similar in March 2008 and 2009, its distribution was quite different. More specifically, in 2008 there was a significant amount of multiyear ice in the Beaufort Sea and in 2009 there was a large amount of multiyear ice in the central Arctic Ocean.

Changes in ice age also have implications for the average ice thickness (Haas et al. 2008; Kwok 2007; Maslanik et al. 2007; Giles et al. 2008). Recent estimates of Arctic Ocean sea ice thickness from satellite altimetry show a remarkable overall thinning of ~0.6 m between 2004 and 2008 (Fig. 5.14a). Since the average thickness of the thinner first-year ice in midwinter (~2 m) did not exhibit a downward trend (blue line in Fig. 5.14a), the declines in total volume and average thickness (black line in Fig. 5.14a)

are explained almost entirely by thinning and loss of multiyear sea ice due to melting and ice export. The total multiyear ice volume in the winter experienced a net loss of more than 40% in the four years since 2005 while the first year ice cover gained volume due to increased overall coverage of the Arctic Ocean. These changes have resulted in seasonal ice becoming the dominant Arctic sea ice type, both in terms of area coverage and of volume. In 2008, seasonal ice covered more than two-thirds of the Arctic Ocean.

In Fig. 5.14b the recent satellite estimates (ICESat) are compared with the longer historical record of declassified sonar measurements from U.S. Navy submarines (Kwok et al. 2009; Rothrock et al. 2008). Multiple regression of the submarine data was used to separate interannual changes, the annual cycle, and spatial changes. Within the submarine data release area (covering ~38% of the Arctic Ocean), the overall mean winter thickness of 3.6m in 1980 can be compared to a 1.9 m mean during the last winter of the ICESat record in 2008, a decrease of 1.7 m in thickness. This combined submarine and satellite record shows a long-term trend of sea ice thinning over submarine and ICESat records that span three decades.
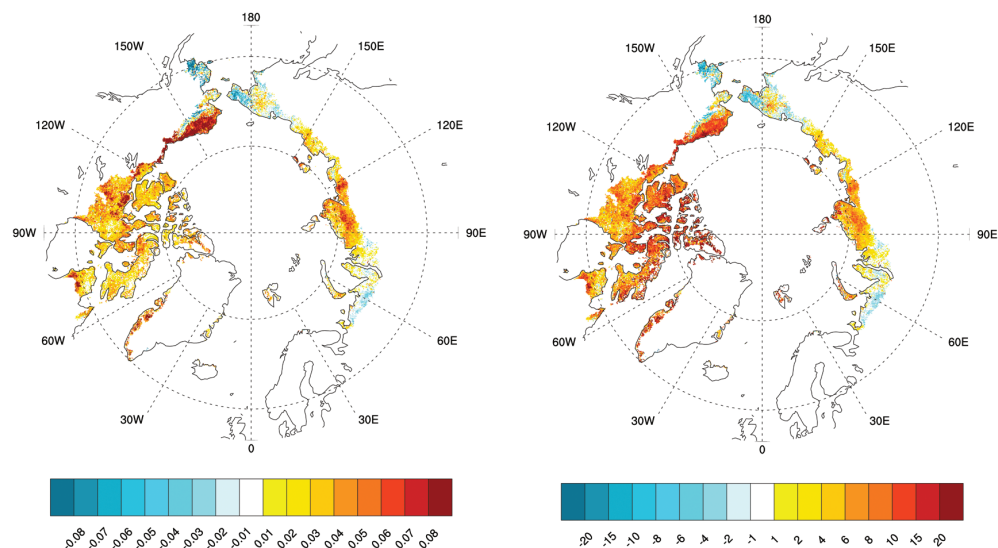
Fig. 5.15. Magnitude (unitless, left) and percentage (right) change of maximum NDVI from 1982 to 2008 for the circumpolar arctic tundra region. Colors show changes only within the area north of the Arctic tree line. Color scales are not linear (Bhatt et al. 2009, manuscript submitted to *Earth Interactions*).

e. Land

1) Vegetation—D. A. Walker, U. S. Bhatt, J. C. Comiso, H. E. Epstein, W. A. Gould, G. H. R. Henry, G. J. Jia, S. V. Kokelj, T. C. Lantz, J. A. Mercado-Díaz, J. E. Pinzon, M. K. Raynolds, G. R. Shaver, C. J. Tucker, C. E. Tweedie, and P. J. Webber

The summer greenness of Arctic tundra vegetation as measured using the maximum Normalized Difference Vegetation Index (MaxNDVI) has generally increased during the period 1982–2008 (Fig. 5.15). Changes in MaxNDVI are much greater in North America (9% increase) than Eurasia (2%). Coherent temporal relationships between near coastal sea ice, summer tundra land surface temperatures, and vegetation productivity have been demonstrated using Advanced Very High Resolution Radiometer (AVHRR)-derived 3g NDVI data (Pinzon et al. 2009, manuscript submitted to *EOS, Trans. Amer. Geophys. Union*; Bhatt et al. 2009, manuscript submitted to *Earth Interactions*). Absolute MaxNDVI changes are by far the greatest in the northern Alaska/Beaufort Sea area (0.09 AVHRR NDVI units), whereas the percentage changes have been highest in the Baffin Bay, Beaufort Sea, Canadian Archipelago, and Davis Strait areas (10–15% changes) (Fig. 5.15). The changes in NDVI are positively and significantly correlated with changes in summer Arctic land surface temperatures. Yearly variations in summer land temperatures are strongly and negatively correlated with yearly variations in the summer coastal sea ice (Bhatt et al. 2009, manuscript submitted to *Earth Interactions*). These observations support model projections that the Arctic land surfaces should warm as a result of the reduced summer extent of sea ice (Bhatt et al. 2008; Lawrence et al. 2008) and furthermore indicate that tundra ecosystems are responding to the increased summer warmth. Changes in the timing of tundra green up and senescence are also occurring. Green up is earlier in the cold sparsely vegetated high latitudes, whereas a shift to a longer green season is occurring during the fall in the more continuously vegetated southern Arctic (Jia et al. 2009). These changes are evident through the analysis of NOAA AVHRR satellite data in the Canadian Arctic for the period 1982–2003.

The greening trends observed in the satellite data are now supported by quantitative, long-term in situ vegetation measurements from the International Tundra Experiment (ITEX) and the Back to the Future (BTF) projects. As in the satellite measurements, the most evident changes appear to be occurring first in the sparsely vegetated areas of the far North. A study of plots at Alexandra Fiord, Ellesmere Island,

is the first to demonstrate significant changes in above and below ground biomass over the last 25–30 years (Hill and Henry 2010; Hudson and Henry 2009) (Fig. 5.16). In addition, there has been a change in the relative abundance of species with an increase in the dominant species over this same time period. The changes in the tundra plant communities are most likely in response to the increase in temperature over the past 35 years of between 0.6°C– 1.0°C per decade, with the strongest increases seen in the winter temperatures. The increases in biomass also correspond with longer growing seasons, with extensions into the late summer and with deeper active layers (depth of summer soil thawing). In another far-north Canada study, repeat photographs of permanent vegetation study plots 46 years after their initial installation near the Lewis Glacier, Baffin Island, document rapid vegetation changes along the margins of large retreating glaciers (Johnson et al. 2009b; P. J. Webber and C. E. Tweedie 2009, personal communication).

Further south, in the more lush tundra near Toolik Lake, a detailed analysis of a 20-year record (1989–2008) of tundra vegetation structure and composition from a set of 156 permanent monitoring plots indicates a general increase in above ground biomass (Gould and Mercado-Díaz 2008). Over the last two decades the relative abundance of vascular vegetation increased by 16%, while the relative abundance of nonvascular vegetation decreased by 18%. The canopy height, as well as the extent and complexity of the canopy have been increasing over time with the amount of horizontal surface having multiple strata increasing from about 60% to 80%.
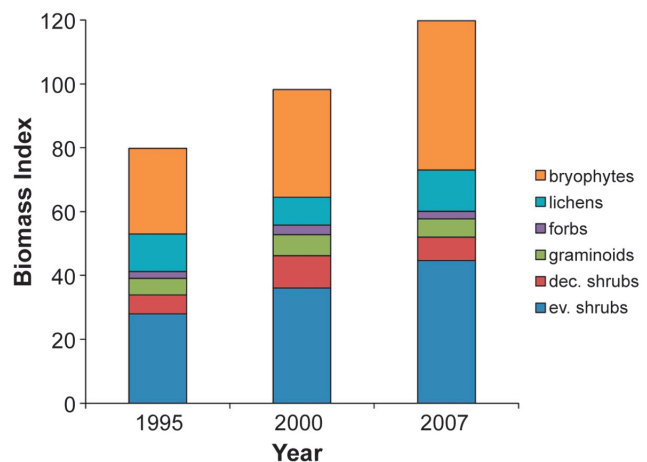

Fig. 5.16. Above ground biomass index by plant functional type for 18 permanent vegetation plots at Alexandra Fiord, Ellesmere Island, Canada, in 1995, 2000, and 2007. Values were the mean number of living tissue hits per plot using the point intercept method. Total live vegetation, bryophytes, and evergreen shrubs increased significantly over the period at p = 0.05. (Hudson and Henry 2009).

The frequencies of landslides, thermokarst features (irregular land surfaces formed in permafrost regions by melting ground ice), and fires have been noted in several areas of the Arctic (B. Jones et al. 2009; Kokelj et al. 2009; Lantz 2008; Lantz and Kokelj 2008; Walker et al. 2009; Leibman and Kizyakov 2007; Ukraientseva 2008). Warmer soil temperatures, melting permafrost, more abundant water, and increased nutrients on these features result in their pronounced greening.

In late summer 2007, the Anaktuvuk River fire near the University of Alaska's Toolik Lake Field Station burned almost 1000 km². It is the largest known fire to occur in northern Alaska and offered an opportunity for detailed analysis of the changes to the tundra energy and nutrient balance (Liljedahl et al. 2007) and spectral properties (Rocha and Shaver 2009). The burning itself released ~1.9 million metric tons of carbon to the atmosphere, which was about 30% of the carbon stock within the vegetation and active layer of this area (M. C. Mack, unpublished data).

2) PERMAFROST—V. Romanovsky, N. Oberman, D. Drozdov, G. Malkova, A. Kholodov, S. Marchenko

Observations show a general increase in permafrost temperatures during the last several decades in
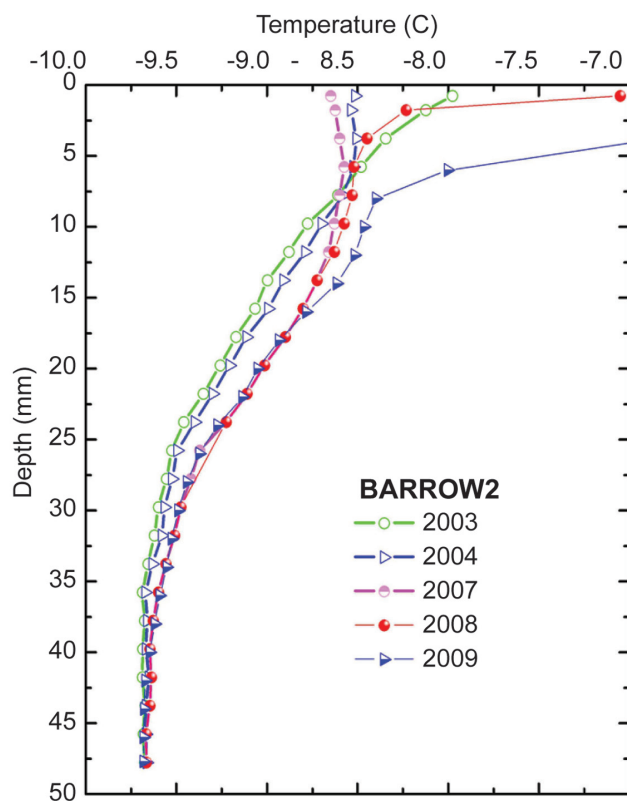
FIG. 5.17. Changes in permafrost temperature at different depths at the Barrow, Alaska, Permafrost Observatory in 2002–09.

Alaska (Romanovsky et al. 2002; Romanovsky et al. 2007; Osterkamp 2008), northwest Canada (Couture et al. 2003; Smith et al. 2005), Siberia (Oberman and Mazhitova 2001; Oberman 2008; Drozdov et al. 2008; Romanovsky et al. 2008), and Northern Europe (Isaksen et al. 2000; Harris and Haeberli 2003).

Most of the permafrost observatories in Alaska show a substantial warming during the 1980s and 1990s. The detailed characteristic of the warming varies between locations but is typically from 0.5°C to 2°C at the depth of zero seasonal temperature variations in permafrost (Osterkamp 2008). However, during the last nine years, the permafrost temperature has been relatively stable on the North Slope of Alaska. There was even a slight decrease in the Alaskan Interior during the last three years. Only coastal sites in Alaska still show continuous warming, especially during the last three to four years (Fig. 5.17).

Permafrost temperature has increased by 1°C to 2°C in northern Russia during the last 30 to 35 years. A common feature for Alaskan and Russian sites is more significant warming in relatively cold permafrost than in warm permafrost in the same geographical area. An especially noticeable permafrost temperature increase in the Russian Arctic was observed during the last three years—the mean annual permafrost temperature at 15m depth increased by more than 0.35°C in the Tiksi area and by 0.3°C at 10m depth in the European North of Russia.

The last 30 years of increasing permafrost temperatures have resulted in the thawing of permafrost in areas of discontinuous permafrost in Russia (Oberman 2008). This is evidenced by changes in the depth and number of taliks (a layer of year-round unfrozen ground that lies in permafrost), especially in sandy and sandy loam sediments compared to clay. A massive development of new closed taliks in some areas of the continuous permafrost zone, as a result of increased snow cover and warming permafrost, was responsible for the observed northward movement of the boundary between continuous and discontinuous permafrost by several tens of kilometers (Oberman and Shesler 2009).

3) RIVER DISCHARGE—A. Shiklomanov

Annual river discharge to the Arctic Ocean from the major Eurasian rivers in 2008 was 2078 km³ (Fig. 5.18). In general, river discharge shows an increasing trend over 1936–2008 with an average rate of annual change of 2.9 ± 0.4 km³ yr⁻¹. An especially intensive increase in river discharge to the ocean was observed during the last 20 years when the sea ice extent in the
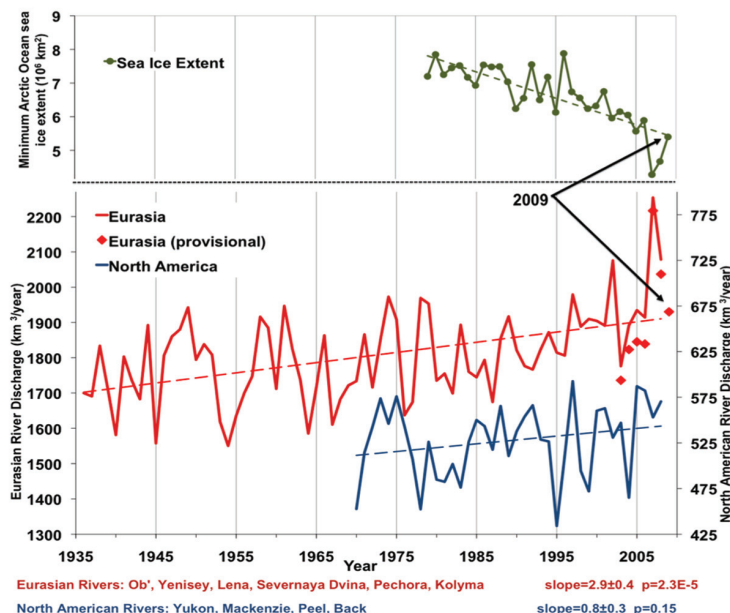
FIG. 5.18. Total annual river discharge to the Arctic Ocean from the six largest rivers in the Eurasian Arctic for the observational period 1936–2008 (updated from Peterson et al. 2002) (red line) and from the four large North American pan-Arctic rivers over 1970–2008 (blue line). The least squares linear trend lines are shown as dashed lines. Provisional estimates of annual discharge for the six major Eurasian Arctic rivers, based on near-real-time data from http://RIMS.unh.edu, are shown as red diamonds. Upper green line shows the September (minimum) sea ice extent in the Arctic Ocean over 1979–2009 from NSIDC (http://nsidc.org/data).

Arctic Ocean began decreasing. Interestingly, the correlation between Eurasian river discharge and sea ice extent over 1979–2008 is r = -0.72, or greater than the correlation between precipitation (Willmott et al. 1996) and runoff in these Eurasian drainage basins (r = 0.54). This suggests that both rivers and sea ice were responding to changes in large-scale hemispheric climate patterns (Shiklomanov and Lammers 2009). There is also an increasing tendency in river discharge to the Arctic Ocean from North America (Fig. 5.18) (Shiklomanov and Shiklomanov 2003; Rawlins et al. 2010). The mean annual discharge to the ocean over 2000–08 from the four large North American Arctic rivers was 6% (31 km³) greater than the long-term mean from 1970–99.

Official river discharge data are usually processed and published with some delay. This gap is related to discharge calculation techniques that take into account diverse flow conditions and ambiguous relationships between measured water stage (water level) and estimated river discharge. Cold regions with long periods of ice cover present the most difficult conditions for reliable discharge estimates in near–real time (Shiklomanov et al. 2006). However,

in cooperation with Russian partners, we developed a method to estimate river discharge from the most important Russian monitoring sites in near–real time using provisional stage measurements and river ice data (http://RIMS.unh.edu). Provisional estimates for the 2009 annual river discharge to the Arctic Ocean from the six Eurasian rivers was greater than the long-term mean over 1936–2008 but much smaller than discharge in 2007 and 2008 (Fig. 5.18). Taking into account that the provisional estimates over 2003–07 show a tendency to underestimate the annual observed values within an error of ± 2–4%, we anticipate the total discharge of six largest Eurasian rivers in 2009 being in the range 1930–1970 km³.

4) TERRESTRIAL SNOW—C. Derksen, R. Brown, and L. Wang

The 2008/09 Arctic snow cover season marked a continuation of the shorter snow seasons (due primarily to an early disappearance of snow cover in spring) observed during the last two decades following a rapid reduction in snow cover duration (SCD) that occurred in the 1980s.

Characterizing Arctic snow cover with conventional observations is a challenge because the station network is sparse, biased to coastal locations (particularly in North America), and the measurements themselves are uncertain. For instance, point snow depth measurements are subject to local scale wind drifting or scour and may not represent the prevailing regional conditions. Even when they do, the large distances between stations does not allow for meaningful spatial interpolation (i.e., kriging), and coastal stations do not represent vast inland areas. Because of these limitations, both satellite measurements and modeling approaches are necessary to characterize the various parameters related to Arctic snow cover, including snow cover extent (SCE), snow water equivalent (SWE), SCD, and snowmelt timing/duration.

For the 2008/09 snow season, analysis of the NOAA snow extent data record derived primarily from optical satellite imagery (http://climate.rutgers.edu/snowcover/) showed a shorter-than-normal snow cover season across a large portion of eastern Siberia, with strong negative anomalies in the North American sector confined to the Canadian
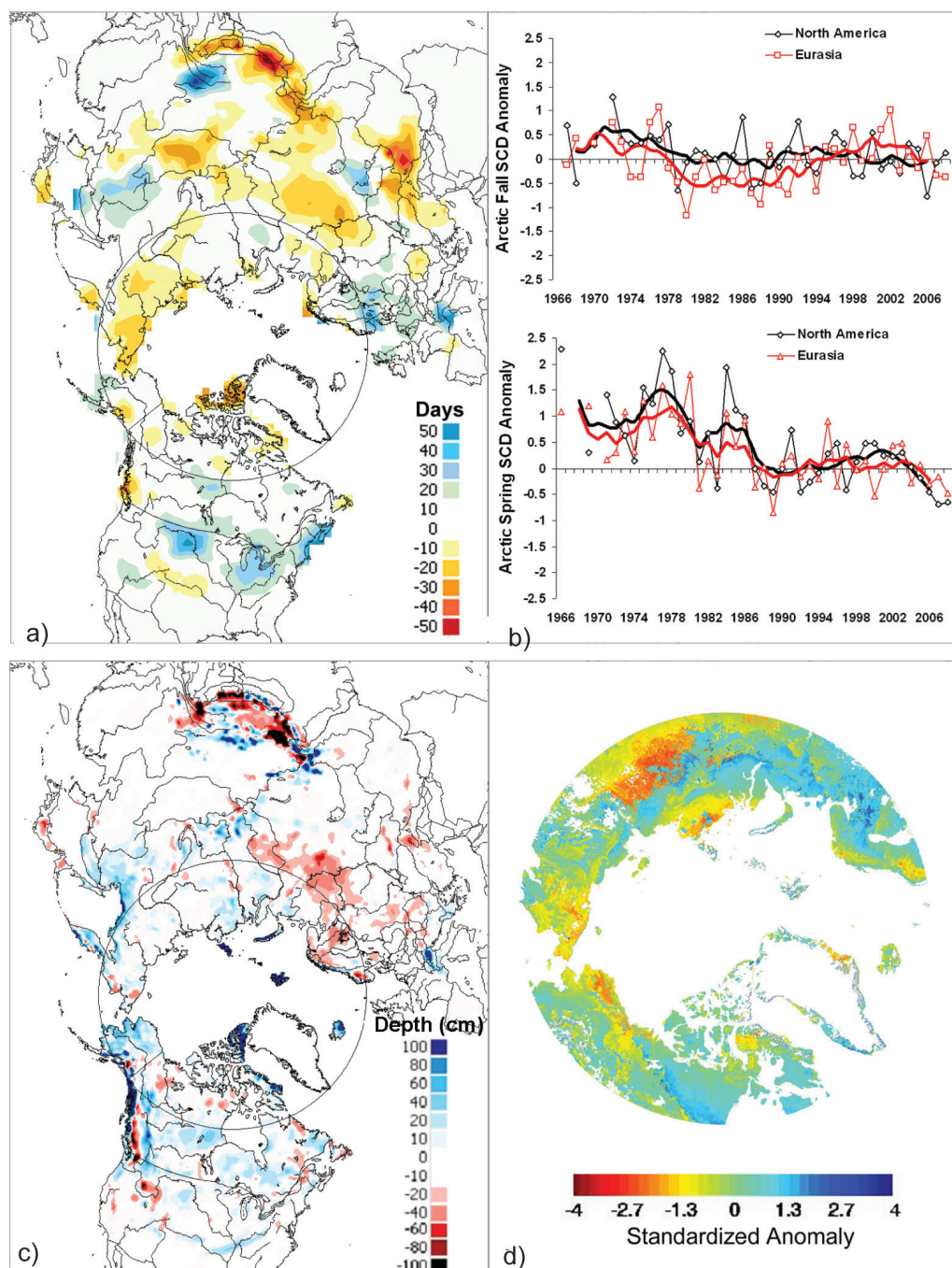
Fig. 5.19. (a) Snow cover duration (SCD) departures (with respect to 1988–2007) for the 2008/09 snow year and (b) Arctic seasonal SCD anomaly time series (with respect to 1988–2007) from the NOAA record for the first (fall) and second (spring) halves of the snow season. Solid lines denote 5-yr moving average; negative number means shorter snow season than normal. (c) Maximum seasonal snow depth anomaly for 2008/09 (with respect to 1998/99–2007/08) from the Canadian Meteorological Centre snow depth analysis. (d) Terrestrial snowmelt onset anomalies for 2009 (with respect to 2000–09) from QuikSCAT data derived using the algorithm of Wang et al. (2008).

Arctic Islands (Fig. 5.19a). The period 1988–2007 was selected as the historical reference period for these anomaly calculations to place the anomalies in the context of more recent snow cover condi-

tions following a rapid reduction in hemispheric snow cover during the 1980s. When standardized SCD anomalies were calculated for NOAA grid cells north of 60°N and averaged for North America and Eurasia,

negative SCD anomalies were evident across Eurasia in the fall and the entire Arctic in spring (Fig. 5.19b). The shorter-than-average snow season in 2008/09 occurred in spite of slightly deeper-than-average snow depth (relative to the 1998–2009 average) in many parts of the Arctic (Fig. 5.19c), as identified by the daily global snow depth analysis (produced by combining the available ground observations with a snow model) from the Canadian Meteorological Centre (CMC, Brasnett 1999). Snowmelt onset anomalies determined from the QuikSCAT record (2000–09) derived with the algorithm of Wang et al. (2008) show that the initial timing of snowmelt in 2009 was near normal, or slightly later than normal across large regions of western Siberia, northern Europe, and the Canadian tundra (Fig. 5.19d). Collectively, these datasets suggest that although the snowpack was not anomalously shallow, and melt was initiated near the average time, the melt was of sufficient intensity to rapidly remove the snowpack across large regions of the Arctic. These observations are consistent with an intensification of snow-related high-latitude hydrological processes as discussed in Dery et al. (2009).

5) Glaciers outside Greenland—M. Sharp and G. Wolken (with data contributions from D. Burgess, J. G. Cogley, A. Arendt, and S. Luthcke)

Mountain glaciers and ice caps are a major contributor to global sea level change (Meier et al. 2007). In the Arctic ice masses of these types cover an area of over 400 000 km^2, representing 55% of the global glaciers and ice caps (excluding the ice sheets that cover Greenland and Antarctica). Although many of these glaciers lose mass by iceberg calving as well as by surface melt and runoff (Blaszczyk et al. 2009), the surface net mass balance (the difference between annual snow accumulation and annual runoff) is widely used as a measure of glacier response to climate variability and change. As measurements for the 2008/09 balance year are not yet available, we summarize measurements for 2007/08. These are available for 20 glaciers in Alaska (three), Arctic Canada (four), Iceland (nine) and Svalbard (four). Sixteen of the glaciers had a negative annual balance and four had a positive balance (two in Alaska and

two in Svalbard). In addition, satellite gravimetry measurements reveal a regional annual net balance of -9 ± 20 Gt yr^{-1} for Gulf of Alaska glaciers. Here, two glaciers located close to the coast had positive annual balances, reflecting heavy winter snowfall in winter 2007/08, while Gulkana Glacier in the Alaska Range had a slightly negative annual balance. In Arctic Canada, annual net balances were among the three most negative balances recorded in the 43–48 year record, likely due to the very warm summer in 2008, extending the period of very negative balances that began in 1987. The annual balances recorded in Iceland were slightly more negative than average (16–17 years of record), while those in Svalbard were more positive than average (20–42 years of record).

Summer (JJA 2009) air temperature data (700 hPa level) and winter (September 2008–May 2009) precipitation data from the NCEP/NCAR Reanalysis provide indications of climatic conditions over the major glaciated regions of the Arctic in the 2008/09 mass balance year (Fig. 5.20; Table 5.1). Winter precipitation anomalies were positive (relative to the 1948–2008 mean) in Iceland and over the Alaska panhandle and adjacent areas to the north, and negative in southwest Alaska and southwest Svalbard. Summer temperature anomalies were strongly positive over southern Alaska, the Canadian Arctic and Svalbard, and very negative over Novaya Zemlya and Severnaya Zemlya.

Melt season duration, and the dates of melt onset and freeze-up, on Arctic glaciers and ice caps were determined from 2009 backscatter time-series measured by the SeaWinds scatterometer on QuikScat (Fig. 5.21; Table 5.1). In Arctic Canada, melt duration anomalies (relative to the 2000–04 average) were positive on all ice caps in the Queen Elizabeth Islands, with the largest anomalies occurring on the
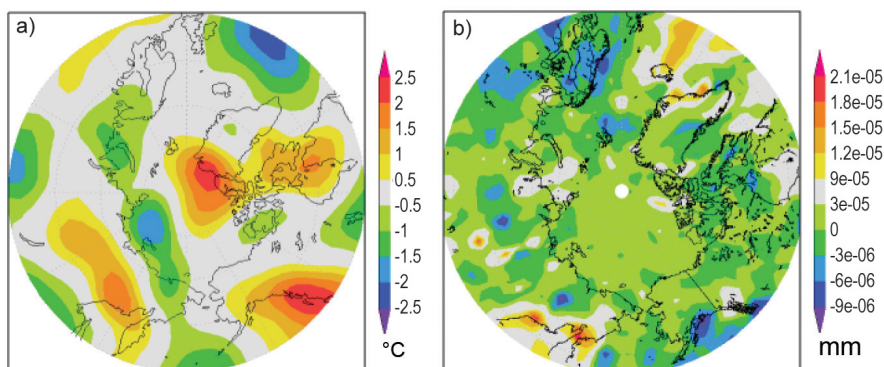
Fig. 5.20. Anomalies in (a) summer (JJA) 2009 air temperature (°C) at 700 hPa, and (b) winter (September 2008–May 2009) precipitation (mm) in the NCEP/NCAR Reanalysis relative to a 1948–2008 climatology.

Region	Sub-Region	Latitude (N)	Longitude (E)	JJA 700hPa T Anomaly	2008 Rank	Sep-May Ppt Anomaly	2008 Rank	Melt Onset Anomaly	Freeze-up Anomaly	Melt Duration Anomaly
				(°C)	(/62)	(mm)	(/61)	days	days	days
Arctic Canda	N. Ellesemere Island	80.6 - 83.1	267.7 - 294.1	2.05	3	14.0	10	12.5	9.5	7.0
	Axel Heiberg Island	78.4 - 80.6	265.5 - 271.5	1.60	7	2/	4	6.2	5.7	9.0
	Agassiz Ice Cap	79.2 - 81.1	278.9 - 290.4	1.66	8	5.5	19	19.2	14.6	5.4
	Prince of Wales Icefield	77.3 - 79.1	278 - 284.9	1.16	11	10.6	13	7.3	5.7	3.8
	Sydkap	76.5 - 77.1	270.7 - 275.8	1.20	11	-39.2	49	4.5	3.8	2.0
	Manson Icefield	76.2 - 77.2	278.7 - 282.1	1.15	11	-51.7	51	-1.2	0.5	2.9
	Devon Ice Cap	74.5 - 75.8	273.4 - 280.3	0.90	16	-8	32	1.4	-2.0	4.7
	North Baffin	68 - 74	278 - 295	1.02	11	-0.9	25	1.1	-28.5	-9.9
	South Baffin	65 - 68	290 - 300	1.06	9	20.4	18	3.9	-12.6	-4.9
Eurasian Arctic	Severnaya Zemlya	76.25 - 81.25	88.75 - 111.25	-0.91	52	45.6	9	-2.3	29.3	-1.0
	Novaya Zemlya	68.75 - 78.75	48.75 - 71.25	-0.94	50	34.1	15	19.65	-12.9	-8.4
	Franz Josef Land	80 - 83	45 - 65	0.10	30	30.1	14	4.7	-8.9	-4.2
	Svalbard	76.25 - 81.25	8.75 - 31.25	0.46	18	-49.2	47	4.5	3.8	2.0
	Iceland	63 - 66	338 - 346	-0.09	37	258.6	3	2.7	14.6	-1.2
Alaska	SW Alaska	60 - 65	210 - 220	391.77	2	29.1	25	-10.7	3.0	0.1
	SE Alaska	55 - 60	220 - 230	1.92	3	167.4	9	*	*	*

northernmost ice caps (N Ellesemere, Agassiz, and Axel Heiberg) despite later-than-average melt onset dates. Melt duration anomalies were also positive on Svalbard and slightly positive in southwest Alaska, mainly due to both early melt onset and late freeze-up in the eastern Alaska Range. Melt duration anomalies were strongly negative on north and south Baffin Island, due to very negative (early) freeze-up anomalies,
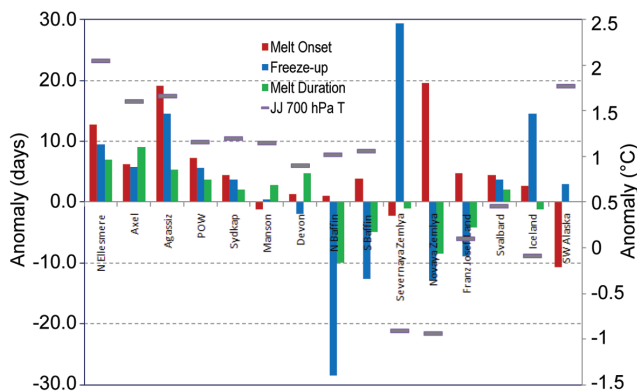
FIG. 5.21. Anomalies (relative to 2000–2004 climatology) in melt season duration and the dates of melt onset and freeze-up on Arctic glaciers and ice caps (outside of Greenland) derived from SeaWinds scatterometer on QuikScat, and anomalies in summer (JJA) 2009 air temperature (°C) at 700 hPa in the NCEP/NCAR Reanalysis relative to a 1948–2008 climatology. Melt onset and freeze-up dates define the first and last days on which melt occurred during the year. As there can be cold periods during the summer when melt ceases, the melt duration can be less than the number of days between the onset and freeze-up dates.

and on Novaya Zemlya, due to both very positive (late) melt onset and negative (early) freeze-up anomalies. Melt duration anomalies were also negative on Iceland and Franz Josef Land, and slightly negative on Severnaya Zemlya despite exceptionally positive (late) freeze-up anomalies.

By comparing 2009 summer temperature, winter precipitation, and melt season anomaly patterns with both the anomaly patterns and measured mass balances for 2007/08, we predict another very negative mass balance year in Arctic Canada (but probably not as negative as 2007/08), and annual balances more negative than in 2007/08 in Alaska, Svalbard and Franz Josef Land, and more positive than in 2007/08 in Iceland, Novaya Zemlya and Severnaya Zemlya.

f. Greenland—J. E. Box, I. Bhattacharya, J. Cappelen, D. Decker, X. Fettweis, K. Jezek, T. Mote, and M. Tedesco

1) COASTAL SURFACE AIR TEMPERATURES

Warmer-than-normal winter and summer air temperatures prevailed along the northwest Greenland coast in 2009, compared to the 1971–2000 average, according to surface air temperature data recorded at operational meteorological stations (Table 5.2). Summer air temperatures at Thule AFB/Pituffik were the warmest on record since 1961. Aasiaat summer temperatures were second warmest on record since 1950. At stations

with records beginning in 1873, the only outstanding anomaly was summer at Upernavik ranking second warmest. In contrast, autumn surface temperatures anomalies along west Greenland were relatively cool.

2) UPPER-AIR TEMPERATURES

Seasonally-averaged 2009 upper-air temperature data, available from twice-daily balloon sounds at the Integrated Global Radiosonde Archive (http://www.ncdc.noaa.gov/oa/climate/igra/) (Durre et al. 2006), indicate a pattern of warm atmospheric anomalies below ~5 km (Fig. 5.22). This is consistent with a warming trend prevailing since reliable records began in 1964 and especially since the mid-1980s (Box and Cohen 2006). A number of sites were outstanding. These included Danmarkshavn and Illoqqortoormiut, with record-setting warm anomalies in the winter in the lower stratospheric between 50 and 200 hPa, and Aasiaat, where the summer was the warmest on record since 1964 at 1000 hPa. The averaged total column (1000 hPa–20 hPa) temperatures in winter ranged between the fourth and second warmest on
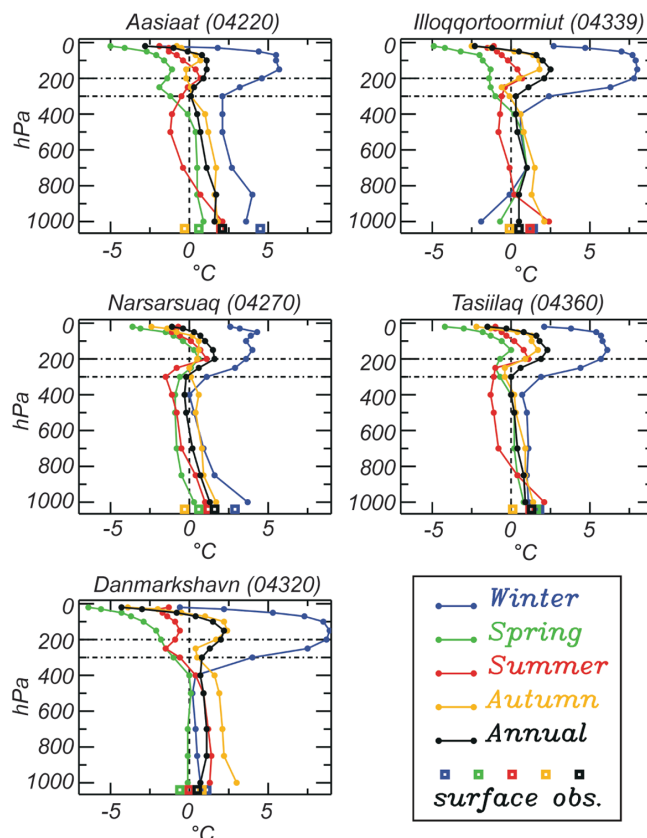
FIG. 5.22. Upper-air and surface seasonal and annual mean temperature anomalies in 2009, with respect to the 1971–2000 average. The station WMO ID number is indicated beside the location name. See Table 5.2 for site coordinates.

Table 5.2. 2009 Greenland station surface air temperature anomalies by season, relative to 1971–2000.					
Station (Region) **Latitude, Longitude, time range**	**Winter**	**Spring**	**Summer**	**Autumn**	**Annual**
Thule AFB/Pituffik, 76.5 N. 68.8 W, 1961-2009	**3.7**	1.0	**2.6***	-1.4	**1.6**
Upernavik (NW), 72.8N, 56.2 W 1958-2009	**5.1**	1.0	**2.7**	0.9	**2.3**
Aasiaat (W), 68.7N 52.8, 1958-2009	**4.5**	0.6	**2.0**	0.3	2.1
Nuuk (SW), 64.2 N, 43.2 W, 1958-2009	2.3	0.1	1.1	**-0.6**	1.1
Prins Christian Sund (S), 60.0 N, 43.2 W, 1958-2009	1.4	0.6	0.7	0.4	1.0
Tasiilaq (SE) 65.6 N, 22.0 W, 1958-2009	1.8	1.6	**1.2**	0.1	**1.3**
Illoqqortoormiut (E), 70.4 N, 22.0 W, 1958-2009	1.4	0.1	1.2	-0.1	0.5
Danmarkshavn (NE), 76.8N 18.8 W, 1958-2009	1.1	0.6	0.0	0.8	0.5

*Anomalies are in °C, with respect to the 1971–2000 base period. Bold values indicate values that meet or exceed 1 standard deviation from the mean. Underlined values exceed 2 standard deviations from the mean. The * symbol indicates a record setting year. The winter value takes December from the previous year.

sive-than-average melt during the remainder of July. August was near normal. Late June corresponded to periods of temperatures at 850 hPa averaging 1°C–3°C below normal over most of the ice sheet in the North American Regional Reanalysis, while 850 hPa temperatures were above normal during July across the northern half of the ice sheet. Passive (SMMR and SSM/I, 1979–2009) and active

record among the sampling sites. In the spring, these sites were among the second/third coolest, making the annual total column mean temperature near normal. Surface air temperature anomalies (Table 5.2) are broadly consistent with the lowest level of the upper-air observations. The main exception is a consistent pattern of surface observations indicating a cool autumn season, while the lowest upper-air level (1000 hPa) indicates warming.

3) Atmospheric circulation anomalies

Persistent 500 hPa geopotential height anomalies drew more warm air than normal across northern Greenland (Fig. 5.23, see also Fig. 5.3). The pattern was very similar to that of 2008 (Fettweis et al. 2010). Consistent with the geopotential height anomaly, passive microwave satellite data indicate a higher number of melting days than normal at the north of the ice sheet and along the eastern margin.

4) Surface melt extent and duration

Passive microwave measures of melt extent (Mote 2007) indicate that the seasonally-averaged melt extent (JJA) in 2009 was near the 1979–2009 average and was also the lowest since 1996 (Fig. 5.24). There was less-extensive-than-average melt from mid-June through the first week of July and much more exten-

Fig. 5.23. The geopotential height and wind anomalies for JJA 2009 (referenced to the 1960–2009 mean) at 500 hPa from the NCEP/NCAR Reanalysis. Areas where geopotential height anomalies were at least twice the 1960–2009 standard deviation are hatched. The blue arrows represent wind vector anomalies, with scale indicated by the blue arrow below the plot
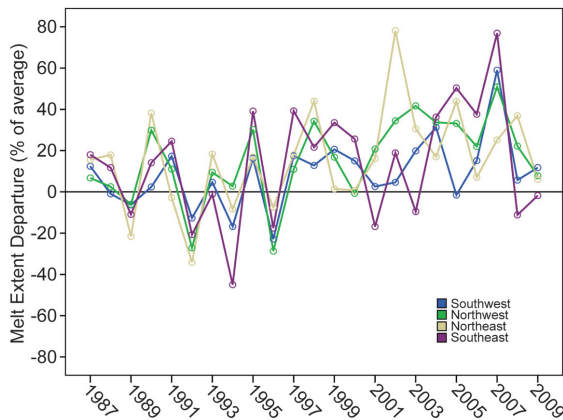
FIG. 5.24. Time series of Greenland regional melt extent anomalies derived from passive microwave remote sensing, after Mote (2007).
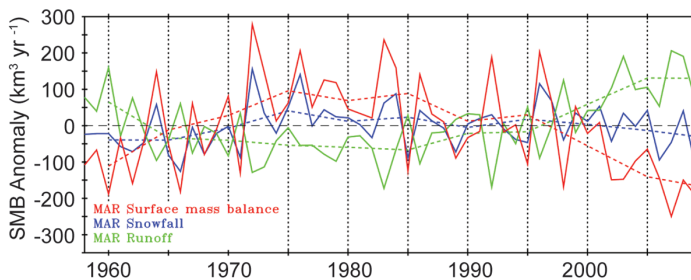
FIG. 5.25. Time series of surface mass balance component anomalies simulated by the regional climate MAR model (Fettweis et al. 2010).
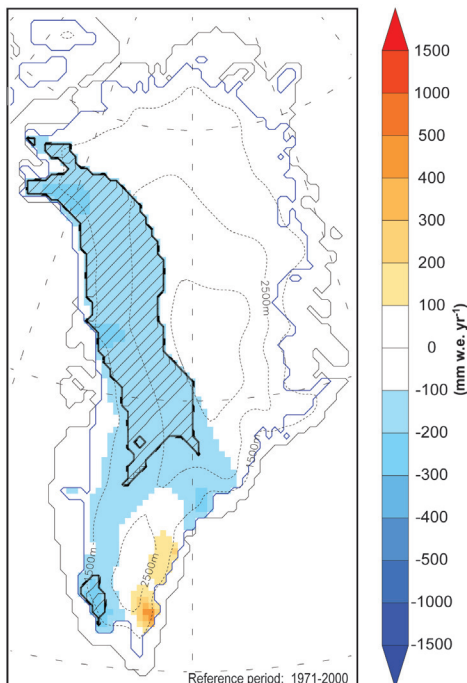
FIG. 5.26. Year 2009 snowfall anomalies (mm w.e. yr⁻¹) simulated by the regional climate MAR model (Fettweis et al. 2010). Hatched areas indicate an anomaly that is twice or more the 1971–2000 standard deviation.

(QuikSCAT, 2000–09) microwave remote sensing indicate substantially less melt duration in areas below ~1800 m elevation compared to recent years of high melt duration. More melting than normal is evident above ~800 m elevation in the north and eastern ice sheet.

5) PRECIPITATION AND SURFACE MASS BALANCE

The balance between ice mass gain from snowfall and the loss from meltwater runoff is positive for any healthy ice mass. The 2009 surface mass balance anomaly was 25% to 50% less positive than normal (Fig. 5.25). This condition usually reflects a heavy melt year. However, in 2009 melt was below-normal (Table 5.3). The source of the relatively low surface mass balance was the below normal snow accumulation for Greenland, especially evident along the western slope (Fig. 5.26). For the ice sheet as a whole snowfall was 25% (150 Gt) below normal, resulting in below normal mass input to the ice sheet. The temperature and precipitation anomalies are very likely the result of regional circulation anomalies that deserve more attention.

6) NORTH WATER POLYNYA

Nares Strait, separating Greenland from Ellesmere Island is host to the largest recurring polynya (a persistent area of open water surrounded by sea ice) in the Arctic. This "North Water" polynya is formed by some combination of ocean heat and winds. Ecologically, the North Water is known to be a wildlife "bonanza" for marine mammals, including narwhal and beluga whales. Strong winds and large atmosphere-to-surface temperature contrast result in tremendous ocean-to-atmosphere heat transfer, frazil ice, and saline deep water production. The sea ice consolidated into land-fast ice 500 km north of its typical position (Fig. 5.27) in the Lincoln Sea, far enough outside of the mouth of Nares St. that the normal strong winds that funnel through the strait (Samelson et al. 2006; Samelson and Barber 2008) allowed an "ice bridge" to persist all winter and into summer 2009. Nares Strait remained unconsolidated the entire 2008/09 winter. On 7 July 2009, the ice bridge collapsed allowing the normal flow of Arctic Ocean pack ice into the strait that makes ship navigation normally difficult, even for ice breakers. Summer (JJA)-averaged MODIS-derived (MOD28 4.88 km) sea surface temperatures were nearly 2°C warmer in Kane Basin than the 2000–07 average. Passive microwave sea ice concentration indicates

TABLE 5.3. Greenland ice sheet surface mass balance anomalies, after Fettweis et al. (2010).				
2009 anomaly referenced to	Toptal SMB (Gt)	Total Snowfall (Gt))	Total Runoff (Gt)	JJA Air Temperature (°C)
1971–2000	-280	-150	110	0.72
1991–2000	-230	-140	84	0.52
2001–2009	-85	-100	-37	-0.71

an unprecedented low sea ice concentration in Nares Strait during summer 2009, relative to the 1979–2009 average. AMSR-E 12.5 km passive microwave sea ice concentrations were 20% below the 2002–07 base average north of Smith Sound.

7) Outlet glaciers

Daily surveys of Greenland ice sheet marine-terminating outlet glaciers from cloud-free Moderate Resolution Imaging Spectroradiometer (MODIS) visible imagery (http://bprc.osu.edu/MODIS/) indicate that the 34 widest glaciers collectively lost 101 km² of marine-terminating ice between the end of summer 2008 and the end of summer 2009. Twenty-three of

thirty-four of the glaciers retreated in 2009 relative to their end of summer 2008 position. The total net effective length change of these glaciers was -1.2 km. The largest area changes included a 32 km² loss along the 110 km wide Humboldt Glacier; a 31 km² loss at the calving front of another north Greenland outlet, the Zachariæ Isstrøm; and 15 km² ice loss at the Midgard glacier. This marked a continuation of a highly linear (R = -0.99) deglaciation trend (-104 km² yr⁻¹, Fig. 5.28) of the past 10 summers when MODIS data are available. The cumulative area change from end of summer 2000 to 2009 is -967 km², an area loss equivalent to 11 times the area of Manhattan Island.
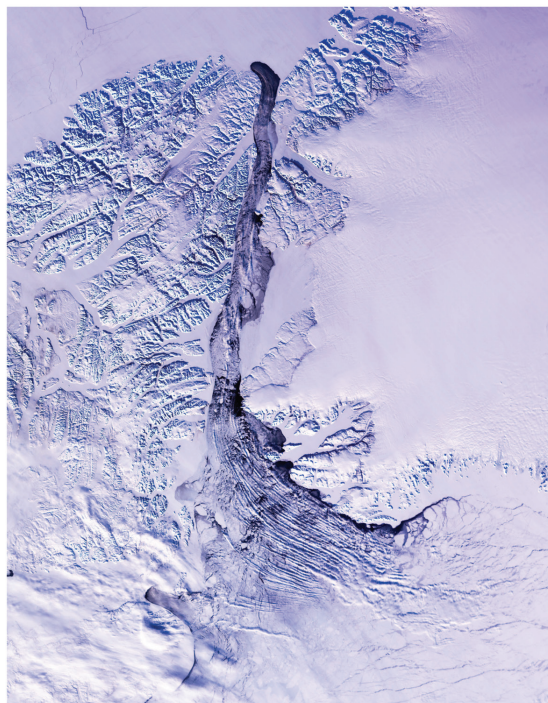
FIG. 5.27. Satellite view of the Nares Strait polynya between Arctic Canada and northwest Greenland. Note the wind-driven "sea smoke" cloud streaks, that is, ice fog condensate from the much warmer ocean surface.
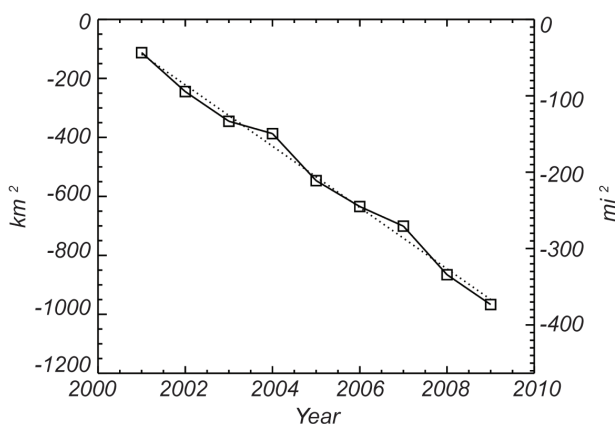
FIG. 5.28. Cumulative annual area changes for 34 of the widest Greenland ice sheet marine-terminating outlets.

6. ANTARCTICA

a. Overview—R. L. Fogt

The calendar year 2009 was relatively calm, climatologically speaking, for much of Antarctica, especially compared to the past two years which included ice shelf collapses juxtaposed with record-high sea ice extent. However, the total ice sheet melt during austral summer 2008/09 was the lowest of the 30-yr satellite record with no melt detected on the Ronne-Filchner and Ross Ice shelves, among other regions. In 2009, the polar atmosphere temperatures were persistently above average in the mid-to-lower troposphere during the winter. The latter half of the year was marked with short-lived anomalies lasting about one month. Nonetheless, the tropical El Niño event in late 2009 did influence Antarctica, particularly through ridging in the South Pacific. In turn, this created anomalous meridional temperature advection patterns that subsequently led to regional sea ice extent and concentration anomalies and decreased precipitation to the west of the Antarctic Peninsula.

With the close of 2009 also comes the end of the first decade of the 21st Century. Although Antarctic climate records are much shorter than the rest of the globe, there were still many interesting and noteworthy occurrences during this last decade. A few of these are highlighted in Fig. 6.1, which shows annual and seasonal averages of the decadal mean temperature anomalies at Faraday/Vernadsky and Marambio, situated on the Western and Eastern Antarctic Peninsula, respectively, and the decadal mean Southern Hemisphere Annular Mode (SAM) index anomalies. Notable Antarctic climate events of the last decade include:

- Observations indicate continued rapid warming of the Antarctic Peninsula. The warming on the western Peninsula is most marked during austral winter (June–August; Fig. 6.1a) while the warming on the eastern Peninsula is most marked during austral summer (December–February; Fig. 6.1b). The Peninsula warming trends are approximately five times larger than the global mean warming and are likely associated with anthropogenic greenhouse gas increases (Gillett et al. 2008).
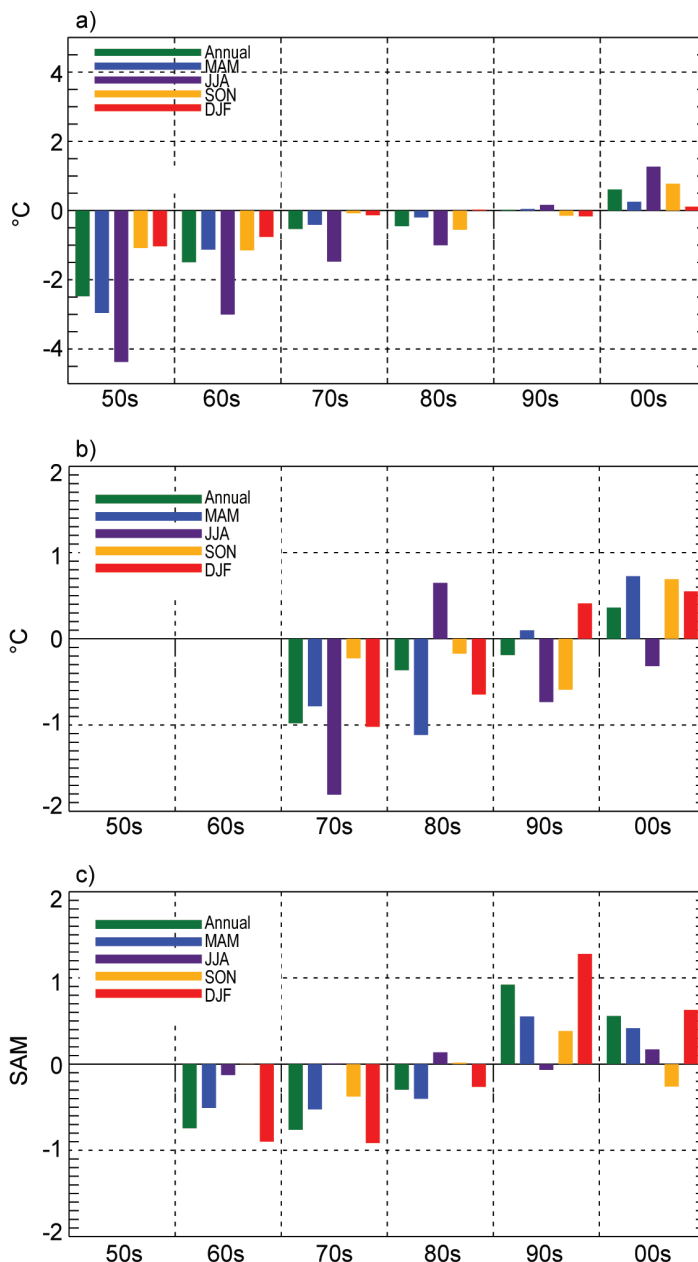
FIG. 6.1. Decadal averages of the seasonal and annual mean anomalies for (a) temperature at Faraday/Vernadsky, (b) temperature at Marambio, and (c) SAM index (http://www.antarctica.ac.uk/met/gjma/sam.html). See Fig. 6.4a for locations of stations used in 6.1a–b.

- Based on a statistical temperature reconstruction, West Antarctica has been warming at a rate of 0.1°C decade[-1] over the last 50 years (Steig et al. 2009).
- Based on surface observations, interior and coastal East Antarctica have remained stable during the last decade, with no significant warming or cooling trend (Turner et al. 2005).

- Significant ice loss has occurred along the Antarctic Peninsula and West Antarctica in the last decade. In 2002, the Larsen B Ice Shelf on the east side of the Peninsula disintegrated, likely due to the regional warming (see above) (Marshall et al. 2006). In 2008/09, part of the Wilkins Ice Shelf on the west side of the Peninsula collapsed, more likely due to influences other than regional warming (Scambos et al. 2009). More recently, ice loss has been reported in the Pine Island Bay region of West Antarctica (Rignot 2002), due perhaps to oceanic influences (Payne et al. 2007).

- All-time positive records of continent-averaged sea ice extent were reached in December 2007, and March–April 2008, in conjunction with a small but significant increase in overall sea ice extent over the last 30 years (Fogt et al. 2009a). Embedded in this signal are large regional departures: during the last three decades there was an anomalous decrease in sea ice in the Amundsen/Bellingshausen Seas, especially in winter, and an anomalous increase in sea ice extent in the Ross Sea sector.

- The 2008/09 Antarctic-wide austral summer snowmelt was the lowest in the 30-yr history (Tedesco and Monaghan 2009).

- Many of the climate impacts can be related back to changes in the overlying atmospheric circulation and, in particular, the average positive phase of the SAM. Figure 6.1c shows that although the SAM weakened somewhat during the 2000/09 decade, it still remained positive on average (compared to the 1979–2008 mean) during all seasons except austral spring. It is widely accepted that the strong positive phase of the SAM in austral summer can be traced back to stratospheric ozone depletion and greenhouse gas increases (Fogt et al. 2009b; Arblaster and Meehl 2006; Shindell and Schmidt 2004; Thompson and Solomon 2002).

- The Antarctic ozone hole reached its maximum area (27.7 million km^2) on 24 September 2006, larger than the North American continent. Due
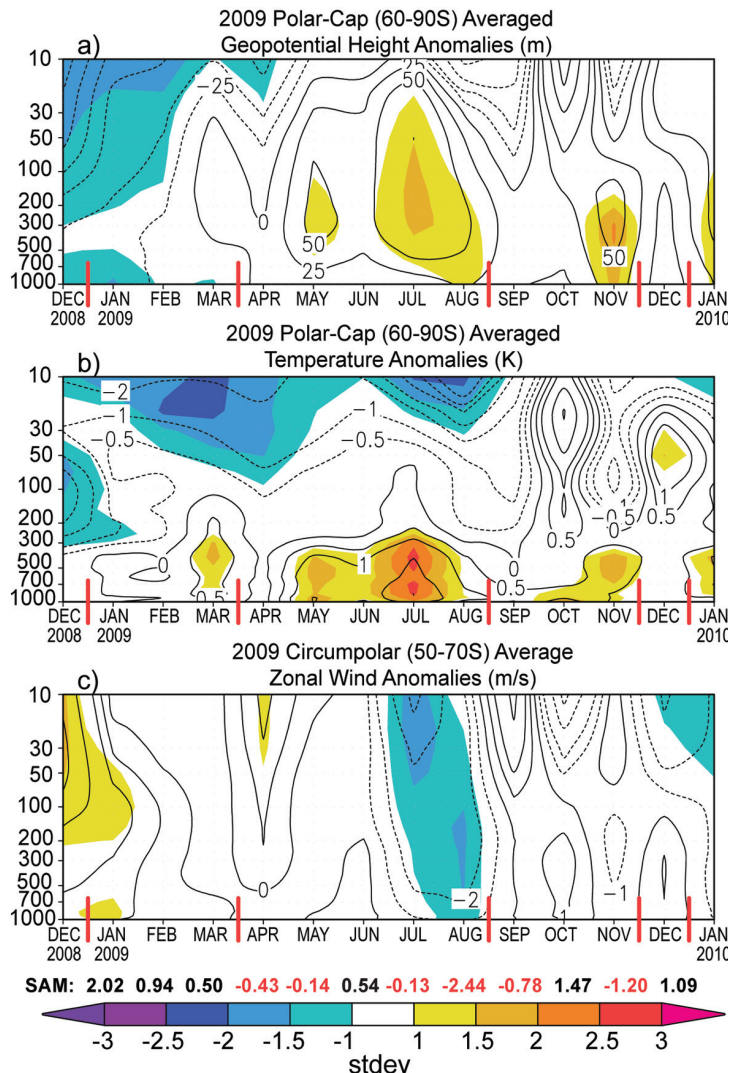
FIG. 6.2. Zonally-averaged climate parameter anomalies for the southern polar region in 2009 relative to the 1979–2008 period: (a) polar cap averaged geopotential height anomalies (m); (b) averaged temperature anomalies (K); (c) averaged wind anomalies (m s^{-1}). Absolute anomaly values are contoured, and the panels are shaded according to how many standard deviations the anomalies are from the 1979–2008 mean (color bar at bottom for scale). Red vertical bars indicate the four separate periods shown as spatial climate anomalies for 2009 in Fig. 6.3. Primary contour interval is 50 m in (a), 1 K in (b), and 2 m s^{-1} in (c), with additional contours at ± 25 m, ± 0.5 K, ± 1 m s^{-1} in (a), (b), and (c), respectively. Values for the SAM index are shown along the bottom in black and red. (Source: NCEP–NCAR reanalysis.)

to large interannual variability, it is unclear yet whether or not the ozone hole has begun a slow recovery process.

Many of these impressive conditions during the last decade, and projections for the Antarctic climate over the next 100 years, are described in more detail in the Scientific Committee on Antarctic Research

(SCAR) report 'Antarctic Climate Change and the Environment,' which was released in November 2009. This report not only parallels the climate discussion on the following pages, but also includes paleoclimatic changes, oceanic changes, and changes in the marine/terrestrial biosphere.

b. Atmospheric circulation—R. L. Fogt and S. Barreira

Antarctic large-scale circulation anomalies during 2009 based on the NCEP–NCAR reanalysis are examined throughout the troposphere–stratosphere (Fig. 6.2) and at the surface (Fig. 6.3). Because the high southern latitude reanalysis data quality improves drastically at the start of the modern satellite era (Bromwich and Fogt 2004; Bromwich et al. 2007), reanalysis data is used starting in 1979. Dividing the circulation anomalies into groups was particularly challenging for 2009, as many of the anomalies were weak and only lasted for a short time, especially during the latter half of the year. Nonetheless, both Figs. 6.2 and 6.3 indicate that the beginning of the year was dominated by below-average heights/pressures from the surface up to 10 hPa, accompanied by weakly positive circumpolar zonal wind anomalies and positive tropospheric temperature anomalies. The positive surface temperature anomalies were most marked in East Antarctica (Fig. 6.3b), and there was a notable negative surface pressure anomaly in the South Pacific Ocean during January–March (> 2 standard deviations below the 1979–2008 mean). The clockwise circulation about this low pressure anomaly increased warm-air advection to the Peninsula, making the temperatures higher there during the early part of the year (Fig. 6.3b). Furthermore, both the northeastern Weddell and Bellingshausen Seas were free of sea ice during January and February, which is consistent with the circulation and temperature anomalies presented in Figs. 6.3a,b.

From April to August, comprising most of the polar winter, the above-average temperatures are seen throughout the Antarctic troposphere with positive pressure/height anomalies over the continent. This pattern was most marked in July, when temperature anomalies were > 2°C (from the surface up to 500 hPa; Figs. 6.2b and 6.3d) and more than two standard deviations above the 1979–2008 mean. Further, the positive height anomalies during this time period are matched with anomalously weak circumpolar zonal winds. Note, however, that the (SAM) index reached its lowest value for 2009 (-2.44) one month later, in August. Here the SAM magnitude is defined using the Marshall (2003) index, which is based on mean
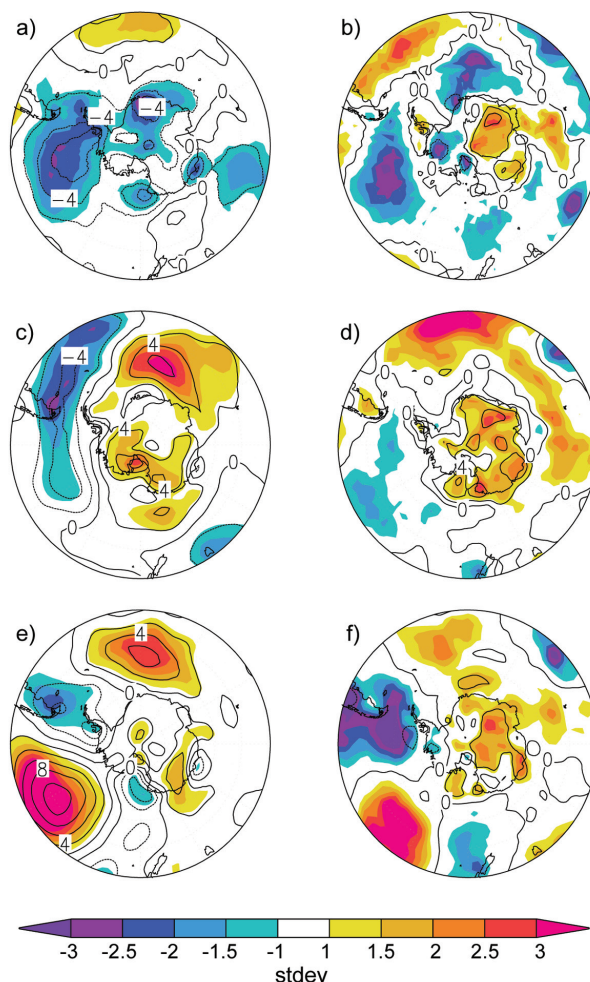
FIG. 6.3. (left) Surface pressure anomalies and (right) surface temperature anomaly contours relative to 1979–2008 climatology for (a,b) January–March 2009, (c,d) April–August 2009, and (e,f) September–December 2009. The shaded regions correspond to the number of standard deviations the anomalies are from the 1979–2008 mean, as in Fig. 6.2. (Source: NCEP–NCAR reanalysis.)

sea level pressure anomalies. Although the overall circulation anomalies were most marked in July, there was a one-month delay in timing of peak magnitude at the surface, clearly seen in the downward anomaly propagation from July–August in both geopotential height and circumpolar zonal winds (Fig. 6.2).

The above average near-surface temperatures continued through austral spring (September–November, Fig. 6.2b). During the end of the year the SAM index was relatively weak and nonstationary, altering between negative and positive states. Examining the spatial surface pressure anomalies (Fig. 6.3e) reveals that the circulation pattern during the end of the year shows a distinct wave train from the Pacific to Atlantic sectors, resembling the Pacific

South American Pattern (Karoly 1989). Further, the spatial temperature anomalies from 180°W–0° in Fig. 6.3f are readily explained by the ensuing meridional temperature advection changes resulting from the anomalous circulation. Of these, most notable was the strong positive pressure anomaly (>2.5 standard deviations) in the South Pacific, characteristic during El Niño events (Turner 2004). This circulation anomaly made the temperatures in the South America–Antarctic Peninsula region below average (> 2.5 standard deviations) and the central South Pacific above average (> 2.5 standard deviations) during the latter half of the year.

c. Surface manned and automatic weather station observations—S. Colwell, L. M. Keller, and M. A. Lazzara

The circulation anomalies are further examined and confirmed here using direct measurements of temperature, wind, and pressure at several manned and automatic weather stations across Antarctica. Fig. 6.4a displays the location of these stations. Two representative manned stations are displayed in Figs. 6.4b,c, and two automatic stations are displayed in Figs. 6.4d,e. A Google Earth file displaying the time series for each station described in this section can be found at: http://www.antarctica.ac.uk/met/momu/BAMS/anomalies.kml. The base period for calculating the anomalies was 1979–2008 for the manned stations and 1980–2008 for the automatic weather stations.

The temperatures in the northern part of the Antarctic Peninsula were below average for most of the year, with June, July, and August being especially cold at Bellingshausen and Marambio (Fig. 6.4c), although not breaking records. Further south on the Peninsula at Rothera station, the temperatures were slightly higher than average for most of the year. In the Weddell Sea region, the temperatures at Halley and Neumayer remained fairly close to the long-term average for most of the year, except for August, which was 3.5°C colder than average and October which was 4°C warmer than average. The pressures in

August were much higher than average at Marambio (Fig. 6.4c; +14.8 hPa), Bellingshausen (+11.4 hPa), Rothera (+12.4 hPa) and Halley (+9.9 hPa), due to high pressure anomalies over the Weddell Sea (i.e., Fig. 6.3c).

Around the coast of East Antarctica the temperatures at Mawson, Davis, and Casey were generally higher than the long-term averages, although these stations experienced below-average temperatures at
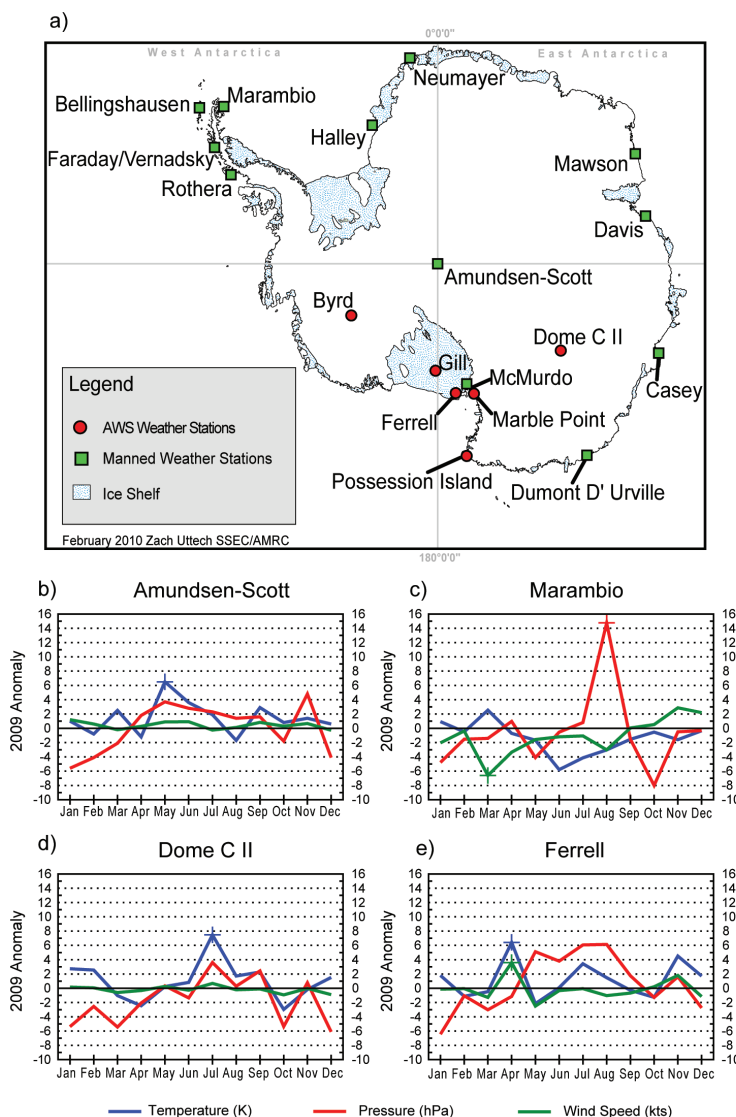
FIG. 6.4. (a) Locations of automatic and manned Antarctic weather stations described in Chapter 6. (b)–(e) 2009 Antarctic climate anomalies at four representative stations (two manned, and two automated). Monthly mean anomalies for temperature (K), MSLP (hPa), and wind speed (m s^{-1}) are shown, with plus signs (+) denoting all-time record anomalies for a given month at each station. Climatological station data starts in 1957 for Amundsen-Scott, 1970 for Marambio (1983 for Marambio wind speeds), and 1980/81 for the AWS records. The base period for calculating the anomalies was 1979–2008 (1980–2008 for the AWS records).

these stations in April, August, and December. At the South Pole Amundsen Scott station (Fig. 6.4b) they recorded its warmest ever May temperature of -51.4°C, which was 2.0°C higher than the previous warmest value in 1981. They also recorded their highest annual mean temperature of -47.9°C, which was 0.1°C warmer than the previous warmest year of 2002.

Records from automatic weather stations on the Ross Ice Shelf, West Antarctica, and the Polar Plateau were also analyzed. On the Ross Ice Shelf both Gill and Ferrell (Fig. 6.4e) reported record-high mean temperatures and record mean high wind speeds for April 2009, where Gill was around 10.0°C higher than the long-term April mean and Ferrell was 6.4°C higher. Marble Point, near the Ross Sea and McMurdo Station, reported a record high mean wind speed for April. In West Antarctica, Byrd station reported above-average temperatures in July, August, November, and December, as well as higher-than-normal pressure for April, July, August, and November, but no records were set. On the Polar Plateau, Dome C II (Fig. 6.4d) had a record high monthly mean temperature in July (7.5°C above the long-term mean). Possession Island, near Cape Adare at the northwest corner of the Ross Sea, also had a record high mean temperature for July (-17.0°C), and record high mean pressures for May and August (8.3 and 6.3 hPa respectively higher than normal), as reflected in Figs. 6.3c,d.

d. Surface mass balance—
D. H. Bromwich and S.-H. Wang

Earlier studies (e.g., Bromwich et al. 2004; van den Broeke et al. 2006) suggest that precipitation-minus-evaporation/sublimation (P-E) closely approximates the surface mass balance over most of Antarctica, with precipitation being the dominant term at regional and larger scales. Precipitation and evaporation fields from the Japanese Reanalysis (JRA; Onogi et al. 2007) were examined to assess Antarctic snow

accumulation behavior for 2009. The evaporation in JRA was calculated from the surface latent heat flux variable. In comparison to other long-term global reanalyses (e.g., NCEP1 and NCEP2), JRA has higher model resolution, both horizontally and vertically, greater observational usage, and a more advanced model configuration (Onogi et al. 2007).

Figure 6.5 shows the JRA annual anomalies of P-E and mean sea level pressure (MSLP) for 2008 (Figs. 6.5b,d) and 2009 (Figs. 6.5a,c) to demonstrate the similarities and major differences between these years. In general, the annual anomalies over the high interior of the continent are small (within ± 50 mm yr^{-1}) in both years, consistent with the low amount of snow accumulation in this region. Most coastal regions in 2009 display much bigger P-E anomalies than during the previous year. The most negative P-E anomalies in 2009 can be observed to the west of the Antarctic Peninsula, in contrast to large positive anomalies over the Peninsula in 2008. In both years, the annual P-E anomalies are consistent with the mean atmospheric circulation implied by the MSLP anomalies (Figs. 6.5c,d). In 2008, a strong negative MSLP anomaly was observed in the Amundsen/Bellingshausen Seas (105°W, along with secondary negative MSLP
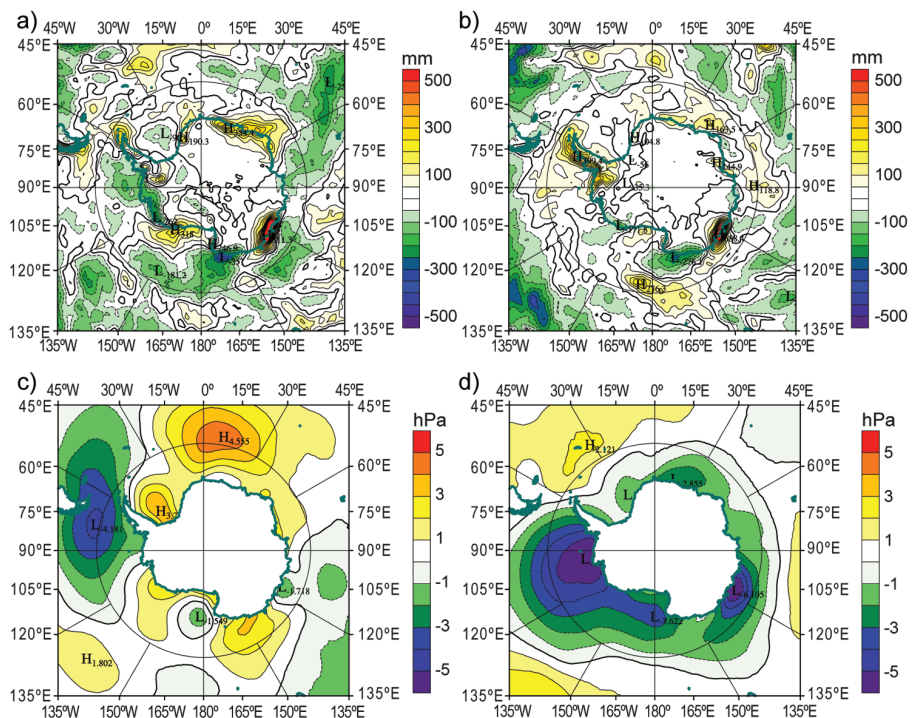
Fig. 6.5. Japanese Reanalysis annual precipitation minus evaporation (P-E) and annual mean sea level pressure anomalies: (a) 2009 P-E anomalies, departure from the 1979–2008 mean; (b) 2008 P-E anomalies, departure from the 1979–2007 mean; (c) 2009 annual mean sea level pressure anomalies; and (d) 2008 annual mean sea level pressure anomalies.

anomalies observed in the Ross Sea and along the Antarctic coast between 100°E to 140°E [Fig. 6.5d]). These circulation anomalies produced three P-E anomaly features along the Antarctic coast in 2008 (Fig. 6.5b): positive anomalies over the Ross Ice Shelf and near Casey station (110°E) and a negative center over the Balleny Islands (165°E). In 2009, a strong negative pressure anomaly center was observed near the Drake Passage (Fig. 6.5c). The circulation about this low pressure in 2009 produced stronger offshore flow and less precipitation to the west of the Antarctic Peninsula, leading to the P-E minimum along coastal West Antarctica (Fig. 6.5a). Further, 2009 was also marked with a positive MSLP anomaly center at 15°E (Fig. 6.5c). This pressure anomaly brought more moisture from the ocean into the region along the coast between 0° to 60°E, where the 2009 annual

positive P-E anomalies have increased to more than double the 2008 values.

The austral spring (SON) and autumn (MAM) P-E anomalies (not shown) have the largest impact on 2009 annual P-E anomalies. The SON anomalies contribute nearly 40% of the annual P-E coastal values. A strong negative MSLP anomaly in SON 2008 from 120°E eastward to a dominant center near 100°W has been replaced by a strong positive center at 125°W, nearly a 20-hPa change (i.e., Fig. 6.3e). This indicates less-than-normal storm activity during the 2009 SON season that results in the change to the west of the Antarctic Peninsula from large positive to large negative P-E anomalies.
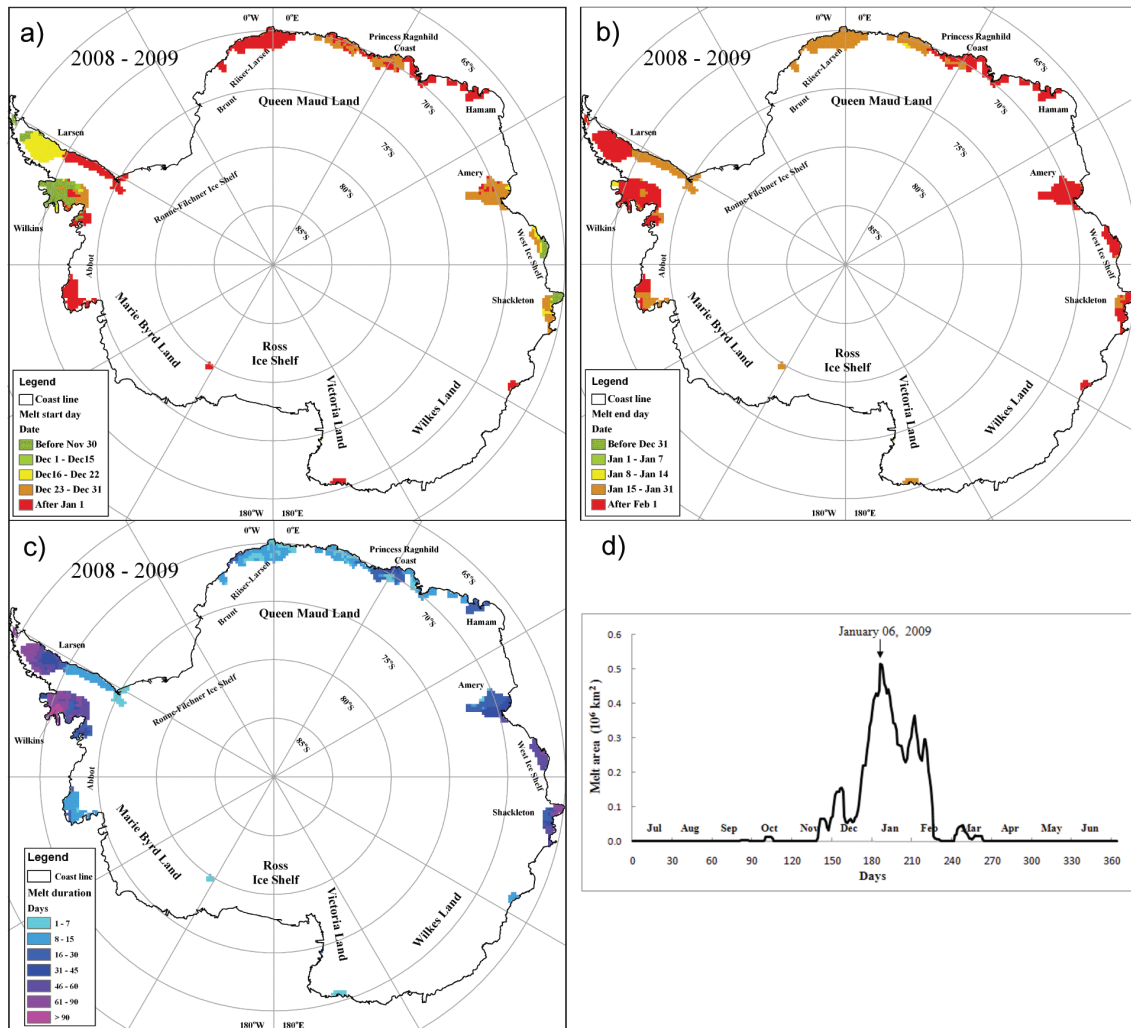
FIG. 6.6. Surface snow melt (a) onset date, (b) end date, (c) duration, and (d) melt area for the austral summer 2008/09 melt season.

e. 2008–2009 Seasonal melt extent and duration—L. Wang, K. C. Jezek, and H. Liu

Summer surface snow melt on the Antarctic Ice Sheet during 2008/09 was estimated using 19-GHz horizontal-polarization channel SSM/I data. We applied a wavelet transform-based edge detection method (Liu et al. 2005) to the daily time series of brightness temperatures for individual SSM/I grid cells to detect and track the surface melt occurrences. Surface melt extent and duration maps are shown in Fig. 6.6. The total melt extent is 681 900 km^2, which includes all areas with at least one day of surface melting during the 2008/09 austral summer. The melt extent covers only 4.9% of the continent, which is considerably smaller than the average melt percentage (about 9.3%) over the past 27 years (Liu et al. 2006). The integrated melt index (the summation over the continent of the product of melt duration times the pixel area) during 2008/09 is 20 533 000 day km^2. Both melt extent and melt index for the entire ice sheet are smaller than the last year (800 000 km^2 for melt extent and 24 354 000 day km^2 for melt index), consistent with the decreasing trend of the past six years. Melt extent and melt index for the austral summer 2008/09 are record lows for the period of passive microwave satellite observations that began in 1978 (Tedesco and Monaghan 2009).

The Antarctic Peninsula, Amery Ice Shelf, West Ice Shelf, and Shackleton Ice Shelf (see Fig. 6.6a for locations) have relatively longer melt durations than other regions. Abbot Ice Shelf and the small ice shelves in Queen Maud Land have melt durations of less than two weeks. No surface melt was detected on the Ronne-Filchner Ice Shelf, Ross Ice Shelf, Victoria Land, or on Wilkes Land (Fig. 6.6). The surface melt onset date and end date varies spatially, as shown in Figs. 6.6b,c. Surface melt events primarily took place in January (Fig. 6.6d).

f. Sea ice extent and concentration—R. A. Massom, P. Reid, S. Stammerjohn, and S. Barreira

After a maximum in zonally-averaged sea ice extent (based on the satellite passive microwave record) in December 2008 (monthly average of 11.2 x 10^6 km^2, or ~1.0 x 10^6 km^2 above the long-term mean for 1979–2008), anomalies in January 2009 were generally well above average (~0.8 x 106 km^2) but dipped dramatically to be slightly below average in February. For much of the rest of the year, overall sea ice extent and area were above average or close to average, with seasonal peaks in April (extent +1.0 x 10^6 km^2) and late September (+0.5 x 10^6 km^2). Starting in October,

however, there was a decrease in zonally-averaged extent that lasted through mid-December 2009.

Embedded in the zonally-averaged sea ice extent are again strong regional contrasts in the sea ice record, in accordance with recent observations (e.g., Comiso and Nishio 2008; Stammerjohn et al. 2008). In many regions, and especially during early 2009, regional sea ice extent anomalies were generally consistent with long-term (30-year) regional trends (Fig. 6.7a): negative in the Bellingshausen Sea and western Weddell Sea (January through June/July), the W Pacific sector from ~90°E–120°E (February–December) and in the eastern Ross Sea (January–March); positive in the central-eastern Weddell Sea (January–June/July) and the western and central Ross Sea (January–June and January–October, respectively); and a largely neutral/mixed signal over much of the Indian Ocean sector (January–April), the W Pacific sector from 120°E–145°E (throughout the year), and the Amundsen Sea (January–May).

Not all regional sea ice extent anomalies were consistent with long-term (30-year) regional trends. Most notable was the regional departure from long-term trends that began in October 2009 that was associated with a distinct hemispheric wave-3 pattern in that month. Distinct sea ice extent anomalies occurred in two regions due to the presence of a high pressure anomaly centered on 120°W (reflected in Fig. 6.3e): positive in the Bellingshausen-Amundsen Seas (BAS) region and negative in the eastern Ross Sea (Fig. 6.7c). Similarly, a negative sea ice extent anomaly developed in the western Ross Sea, caused by a low MSLP/storm center west of the high pressure center (Fig. 6.3e). This coincides with the development (from October onwards) of a warm pool of SSTs in the central South Pacific that persisted through December. From October, departures in regional sea ice extent are up to 3.4 standard deviations away from the (untrended) mean and are in distinct contrast to the long-term regional trends. This is particularly evident by comparing the areas of the BAS-NW Weddell Sea and Ross Sea sectors for April (similar to the trend, Fig. 6.7e) and November (opposite to the trends, Figs. 6.7b,c).Other less obvious departures from the long-term mean were the large negative and positive anomalies that persisted in the NW and central-NE Weddell Sea (CNEWS) from January through July that subsequently advected eastwards with the surface waters of the Weddell Gyre (Venegas and Drinkwater 2001; Fig. 6.7a). This resulted in a switch to a strong negative anomaly in CNEWS accompanied by a strong positive anomaly from ~0°–60°E (inconsistent with

a)

b) April   c) Nov.

Ice concentration, %

d) Duration   e) Trend

Shorter   Anomaly, days   Longer
<-60   -30   0   30   >60

<-4   -2   0   2   >4
                Trend, days/yr
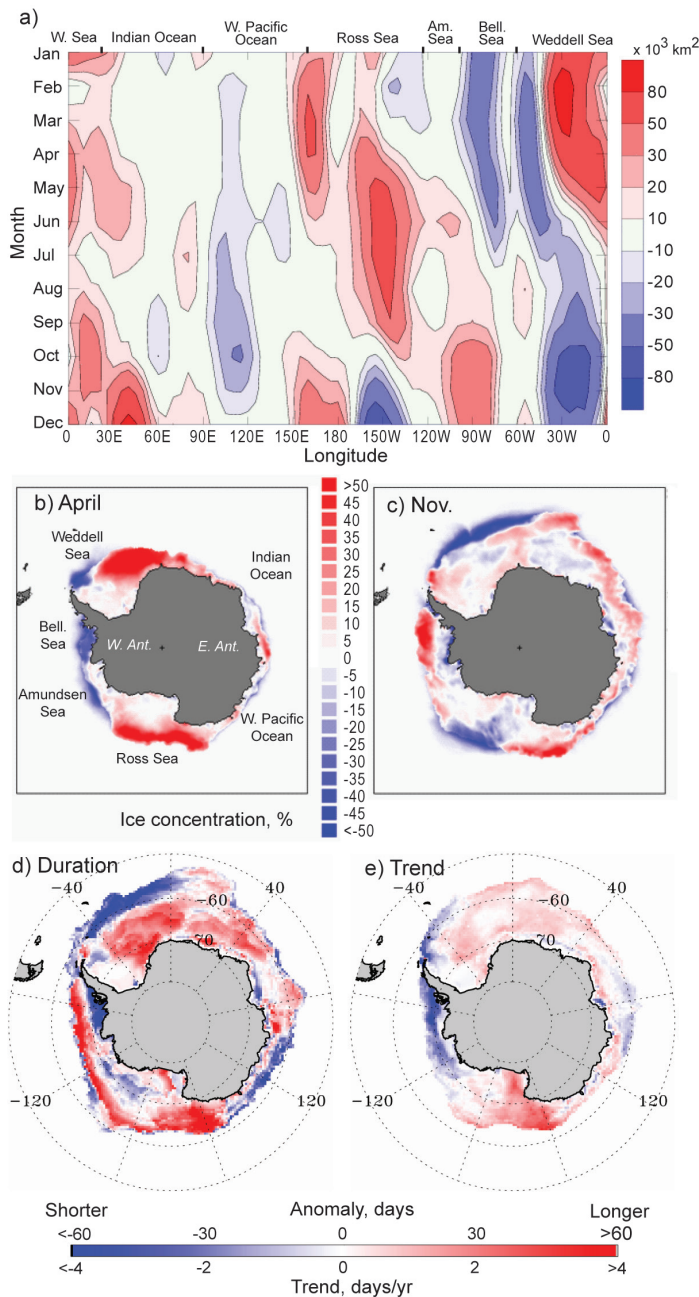
FIG. 6.7. (a) Hovmöller diagram of daily satellite-derived sea ice extent anomalies for 2009 (2009 minus the 1979–2008 long-term mean, in 10³ km²); (b) and (c) sea ice concentration anomaly maps for April and November 2009, respectively, derived versus the monthly means for 1979–2000 (total anomalies of 1.0 and 0.1 2 x 10⁶ km², respectively) (courtesy NSIDC; Fetterer et al. 2009); (d) sea ice duration anomaly for 2009, and (e) duration trend (1979–2007). For (d) and (e), see Stammerjohn et al. (2008) for a description of techniques (using daily satellite passive-microwave data). Note that the data used in (d) and (e) are from three different sources: i) 1979–2007 (GSFC Bootstrap dataset, V2); ii) 2008 (F13 Bootstrap daily data); and iii) 2009/10 (NASA Near-Real-Time Sea Ice dataset). However, discrepancies introduced by this factor lead to an uncertainty (difference) level that is well below the magnitude of the large changes/anomalies.

the long-term trend) for the remainder of the year, while the NW Weddell Sea and Bellingshausen Sea switched to positive/near-neutral anomalies. A progressive eastward advection/propagation is also noted in positive anomalies from the W Ross Sea to the Amundsen Sea. This propagation may be consistent with sea ice drift data (under investigation) and, for the Ross-Amundsen Seas, consistent with Assmann et al. (2005).

Consistent with the monthly sea ice extent anomalies (Fig. 6.7a), the ice-edge advance anomalies (not shown) further highlight the late-autumn advance in the Bellingshausen, Western Weddell, and outer central Weddell Sea regions, as well as in East Antarctica between 100°E and 140°E. In contrast, early sea ice advance anomalies are found in most of the Ross Sea and the inner pack ice zone of the Weddell Sea. In further contrast, the ice edge retreat anomalies (also not shown) generally tell a different regional sea ice anomaly story. For example, they show late retreat almost everywhere but in the eastern Ross Sea, the outer pack ice of the Weddell Sea, and the inshore region of the southern Bellingshausen Sea. Thus, as a result, the ice season duration anomaly (Fig. 6.7d) shows a longer ice season in most areas except in East Antarctica (between 100°E and 140°E), the outer western Weddell Sea, and the inshore region in the Bellingshausen Sea.

As highlighted by the sea ice extent anomalies (Fig. 6.7a), the most striking seasonal changes include a switch from late sea ice advance and low sea ice concentration anomalies (blue, Fig. 6.7b) to late sea ice retreat and high sea ice concentration anomalies (red, Fig. 6.7c) in most of the Bellingshausen Sea. This stands in contrast to the switch from early sea ice advance to early sea ice retreat in the western Amundsen/eastern Ross Sea (~140°W–160°W). This seasonal flip in the sign of regional ice anomalies in the high-latitude South Pacific is, however, consistent with moderate La Niña/+SAM conditions prevailing during late 2008/early 2009 versus moderate El Niño/-SAM conditions prevailing late in 2009 (e.g., Stammerjohn et al. 2008; Fogt and Bromwich 2006). Nonetheless, the 2009

positive ice-season duration anomalies for most of the BAS region are in contrast to the strong long-term negative trend in that region, whereas the negative duration anomalies in the outer western Weddell Sea and in East Antarctica (100°E–140°E) are in contrast to the weak but positive trend in those regions (Fig. 6.7e). These negative duration anomalies are however consistent with the eastward "propagation" of ice extent anomalies in the regions in 2009, as described earlier (see Fig. 6.7a). In these regions, i.e., the outer Bellingshausen and western Weddell Seas and East Antarctica, the 2009 anomalies are >2 standard deviations above/below the long-term mean.

g. Ozone depletion—P. A. Newman, E. R. Nash, C. S. Long, M. C. Pitts, B. Johnson, and M. L. Santee

The 2009 Antarctic ozone hole was comparable in size to previous ozone holes. The area of the hole was approximately 22.9 million km², about the same size as 2007 and smaller than the 2006 record of 27.7 million km². While 2009 was smaller than many recent sizable ozone holes, it is still much larger than values observed prior to 1990. The large area of the ozone hole is consistent with severe depletion caused by the continued high levels of chlorine and bromine in the Antarctic stratosphere. At present, we estimate that ozone depleting substances (ODSs) have only decreased by about 4.3% from the peak levels in the 2000–02 period.

Figure 6.8a displays the average area of the Antarctic ozone hole from 1979 to 2009. The average is calculated by: 1) summing the area of the daily values from the Total Ozone Mapping Spectrometer (TOMS) and Aura Ozone Monitoring Instrument (OMI) observations where total ozone values are less than 220 Dobson Units

and then 2) averaging the daily estimates from 21–30 September. Using daily SBUV total ozone from the NOAA polar orbiter satellites, the 2009 Antarctic ozone hole was estimated to be the 10th largest on record.

The total ozone values over Antarctica steadily decreased from July to early October 2009. Aura OMI observations showed ozone values of about 236 Dobson Units in July and a low value of 94 Dobson Units on 26 September 2009. Balloon-borne ozonesonde observations from NOAA/ESRL at the South Pole also showed similar behavior. On 25 September, total ozone estimated from the sonde was 98 Dobson Units. The ozonesonde profiles in Fig. 6.8b show that the large losses occurred in the lower stratosphere by late September, with a near complete loss of ozone in the 15–20 km layer on Sep. 29.

The temperature variability of the Antarctic stratosphere modulates the severity of the ozone hole from year to year. Colder-than-average Antarctic temperatures result in larger and deeper ozone holes, while
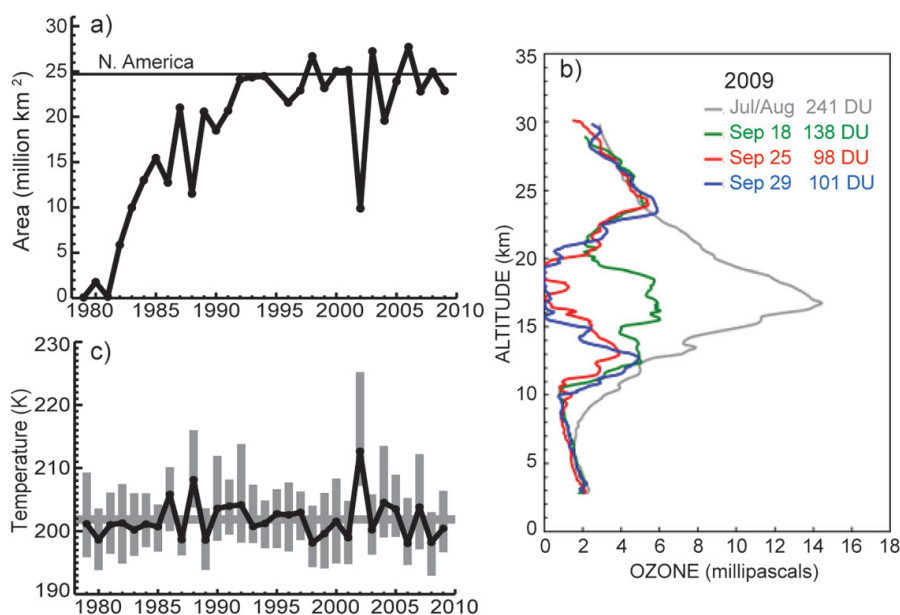
FIG. 6.8. (a) Ozone hole area versus year from 1979 to 2009. The area is determined by first calculating the area enclosed by the 220 Dobson Unit value over the SH for each day from 21 to 30 September, and then averaging these 10 days. The area of the North American continent is indicated by the horizontal bar (24.71 million km2). (b) Four selected profiles of altitude vs ozone partial pressure (millipascals) measured by ozonesondes at South Pole Station. These 2009 profiles show the pre-ozone hole average in July and August (241 Dobson Units), a mid-September profile and the minimum values of 98 and 101 DU measured at the end of September. (c) Temperature versus year at 50 hPa from 60°S to 75°S during September. The vertical bars represent the range of values from the individual days of September. The September average over the 1979 to 2009 period is indicated by the horizontal line.

warmer temperatures lead to weaker ozone holes. Fig. 6.8c shows the temperature average (NCEP/DOE reanalysis 2) for September at 50 hPa averaged from 60°S–75°S (edge of the polar vortex). The 2009 September period was near the 31-year average. The cold temperatures in the Antarctic vortex enable the formation of polar stratosphere clouds (PSCs), and these PSCs lead to the activation of reactive chlorine that rapidly destroys ozone as the sun rises over Antarctica.

A fundamental process behind the formation of the ozone hole is the conversion of chlorine molecules from the nonreactive forms (HCl and ClONO2) into ozone reactive forms on the surfaces of PSCs. This reactive chlorine then leads to rapid ozone destruction. The Calipso satellite provides an extremely high-resolution estimate of PSC structure over Antarctica using lidar technology. Calipso observations show that, in terms of season-integrated totals, the 2009 season PSC volume was much less than the record 2006 season and was virtually zero by late September (update from Pitts et al. 2009). The Microwave Limb Sounder (MLS) on the NASA Aura satellite provides information on the chlorine monoxide (ClO) levels inside the Antarctic vortex. In 2009, the chlorine activation was quite high (consistent with high levels of inorganic chlorine from man-made chlorine containing compounds such as chlorofluorocarbons), but less intense, extensive, and persistent than in the last few years.

The Antarctic stratosphere is warmed by the return of sunlight at the end of the polar winter and by large-scale weather systems (planetary-scale waves) that form in the troposphere and move upward into the stratosphere. During the 2009 Antarctic winter and spring, these planetary-scale wave systems were near average for the August–September period. Because the wave levels were near average in 2009, the September Antarctic stratospheric temperatures were also near average as can be seen in Fig. 6.8c.

The 2009 ozone hole was relatively short-lived, with low ozone values disappearing by the end of November. Strong wave forcing in early October and in November caused a dynamically driven warming of the polar stratosphere. By late November into December 2009, lower stratospheric temperatures had risen above average (i.e., Fig. 6.2b) with an accompanying increase of ozone. The ozone hole had virtually disappeared by late November.

7. REGIONAL CLIMATES

a. Introduction—A. B. Watkins and L. A. Vincent

This chapter provides a regional perspective of the global climate in 2009, with a focus on extreme or unusual events. Analyses are provided for continents, nations and most broad geographic regions. Where possible, information for the year is placed into a historical context using anomalies, percentages (relative to 1961-90, unless otherwise noted) or rankings. Authors for most regions are local scientists and hence, unless otherwise noted, data is made available by their affiliated agency. While this chapter covers the climate of 2009, information from the previous year may be included in order to accurately cover relevant climate events (e.g., descriptions of the austral summer and boreal winter seasons typically include data from December 2008).

Extreme warmth was experienced across large areas of South America, southern Asia, Australia and New Zealand, while severe cold snaps were reported in the United Kingdom, China and the Russian Federation. Drought affected large parts of southern North America, the Caribbean, South America and Asia while heavy rainfall and floods impacted Canada, the United States, Amazonia and southern South America, many countries along the east and west coasts of Africa, and the United Kingdom.

Descriptions of the background atmospheric state to local anomalies are found in Chapter 2. Similarly, descriptions of tropical cyclones may be found in Chapter 4. Seasonal summaries of temperature and precipitation are found in Chapter 8, and a global summary map is provided in Fig. 1.1.

b. North America

1) CANADA—R. Whitewood and D. Phillips

The year 2009 was another warm year in Canada (relative to 1951–80). It was also a drier-than-normal year after experiencing seven consecutive wet years.

(i) Temperature

The national mean temperature for 2009 was 0.8°C above normal (Fig. 7.1), which ties 1988 as the fourteenth warmest year since nationwide records began in 1948. The warmest year was 1998 (+2.5°C), and 1972 (-1.8°C) remains the coolest. Much of Canada's above-normal temperatures occurred in the North, where temperatures were more than 2°C above normal (Fig. 7.2a). Overall, the rest of the country saw normal temperatures with the exception of southern Saskatchewan which experienced temperatures that were more than 1°C cooler than normal. The national
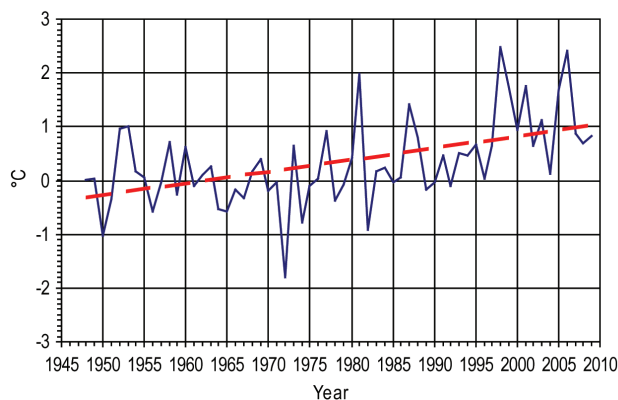
FIG. 7.1. Annual mean temperature anomalies for Canada, 1948–2009. The reference period is 1951–80. (Source: Environment Canada.)

annual mean temperature shows a linear increase of 1.4°C over the 62-year period (Fig. 7.1).

In comparing the decades, it is clear that the 2000s was the warmest decade out of the six that are available for this national study, with an average temperature of 1.1°C above normal. In order, from warmest to coolest, the remaining decades are: 1990s (+0.7°C); 1980s (+0.4°C); 1950s (+0.1°C); 1960s (0.0°C); and 1970s (-0.2°C).

Seasonally, three of the four seasons were warmer than normal. Winter was 0.3°C above normal (33rd warmest); spring was 0.4°C cooler than normal (14th coolest); summer was 0.4°C above normal (27th warmest); and autumn experienced the greatest above normal temperatures of the four seasons, 1.7°C above normal (third warmest autumn on record).

(ii) Precipitation

Overall, Canada experienced a drier-than-normal year in 2009 (2.6% below normal) and it ranked as the 10th driest year out of the 62-year period of record. Fig. 7.2b shows the south experienced most of the dry conditions. Regions that were more than 20% drier than normal were: British Columbia's west coast, eastern British Columbia, most of Alberta, small regions of Saskatchewan and Ontario, and Baffin Island. There were also regions that were at least 20% wetter than normal, including: southern Northwest Territories; central Nunavut; small areas of Manitoba, Ontario, and Quebec; and the Atlantic provinces. Since the 1970s, precipitation across Canada has tended to be higher than the 1951–80 average. The wettest year on record, for the 62-year period of record, occurred in 2005 (13.4% above normal), and the driest was 1956 (7.3% below normal).

Comparing precipitation by decades, the 1980s was the wettest decade at 4.2% above normal. The remain-
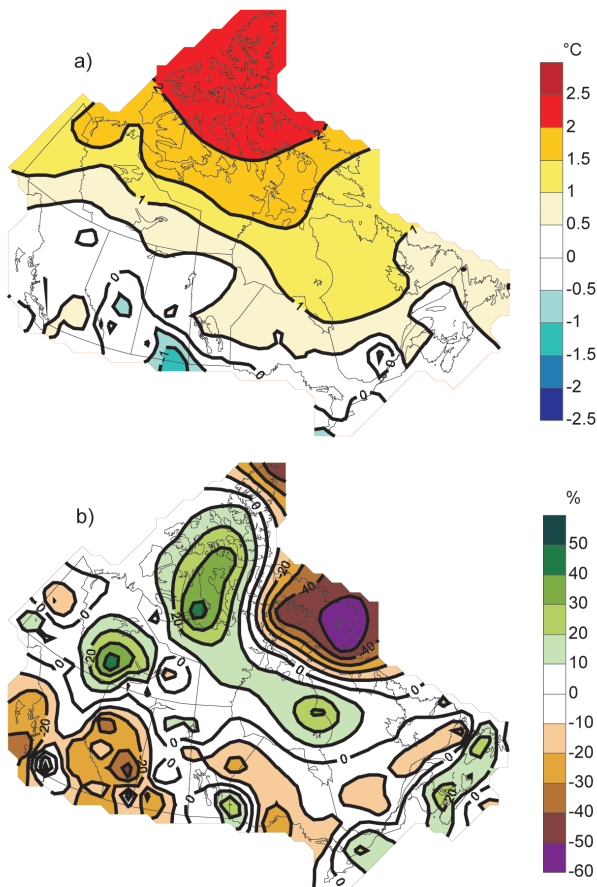
Fig. 7.2. (a) Annual mean temperature anomalies (°C) for Canada (based on 1951–80) for 2009 and (b) annual precipitation anomalies (% of 1951–80) for 2009. (Source: Environment Canada.)

ing decades in order from wettest to driest are: 1990s (+3.2%); 1970s (+2.5%); 2000s (+2.2%); 1960s (-0.8%); and 1950s (-3.0%).

Nationally, precipitation for each of the four seasons in 2009 was close to normal. Winter was right on normal with 0.0% (26th wettest); spring was the season with the greatest below-average amount of precipitation with -2.8% (22nd driest); the season with the greatest above-normal precipitation was summer with +2.2% (30th wettest); and autumn was -1.2% (21st autumn driest on record).

(iii) Notable events

It was a particularly intense fire season for British Columbia, which saw 3200 fires this year. Of those, 100 were considered significant with nearly half prompting evacuation orders. Wildfires scorched 68 000 hectares of land across the province—almost seven times more than the previous year's fire season. Costs of direct fire fighting were enormous, close to $400 million CAN or six times that budgeted, sur-

passing the most expensive season on record in 2003.

It was a long and deadly tornado season for Ontario, beginning on 25 April and ending on 28 September, claiming four lives. Ontario witnessed 29 tornadoes in 2009, which tied the record for the most tornadoes in one year, set in 2006. On average, the province sees 11 tornadoes each year. Three lives were lost during the 9 July F2 tornado in northwestern Ontario, an area where tornadoes are relatively rare. The fourth life was lost during the 20 August supercell storm when a boy was killed at a day camp. By the end of the day this storm system had produced at least 18 tornadoes—a record number of tornadoes in one day for Canada—and caused an estimated $100 million CAN in damage from Windsor through North Bay.

Manitoba's Red River recorded its second highest spring flooding in nearly 100 years. North of Winnipeg at Breezy Point and St. Clements, ice jamming caused the worst flood of the century, forcing full-scale evacuations. The ice jamming and flooding were caused by a number of factors, including: a wet autumn, heavy snow accumulation during the winter, a cool spring slowing snow melt, and a sharp change in temperature in mid-April that weakened the river ice which broke into large chunks later to jam down river. At the height of the flood, nearly 3000 people left their homes—more than half from First Nations communities. Near Morris, the metres-wide Red River grew to 16 km across, submerging rich farmland and highways. Total flood claims exceeded $40 million CAN with 500 homes damaged or destroyed.

Agriculture producers in Alberta and Saskatchewan faced one of the most challenging growing seasons in years with drought, cold, floods, and hail. Parts of the Prairies experienced their driest spring in 50 years and their coldest in 35 years. Cool weather delayed crop development by three to four weeks, and with the risk of frost continuing into July, producers never caught up even when killing cold and the first snows came much later than usual in mid-October. A dozen counties and municipal districts in Alberta declared a state of drought emergency or disaster.

Arctic ice continued to be a concern in 2009. In Canadian waters, sea ice extent was similar to that of 2008, but its spatial distribution was different. According to the Canadian Ice Service, greater-than-normal concentrations of ice occurred in the southeastern Beaufort Sea under prevailing northerly winds that carried some of the multiyear pack ice southwards. In the central and western parts of the Northwest Passage, thicker and more extensive ice led to delays in navigability of the southern route,

FIG. 7.3. Annual mean temperature for the contiguous United States, 1895–2009. (Source: NOAA/NCDC.)

while the northern route did not become truly navigable at all. By contrast, both routes were navigable in the summers of 2007 and 2008. Close to 80% of the Arctic sea ice was new, weaker, salty, and less than a year old. Further, old, durable multiyear ice was slowly thinning, more broken-up, and moving faster, which all contributed to melting earlier in the season. More information on Arctic sea ice can be found in Chapter 5.
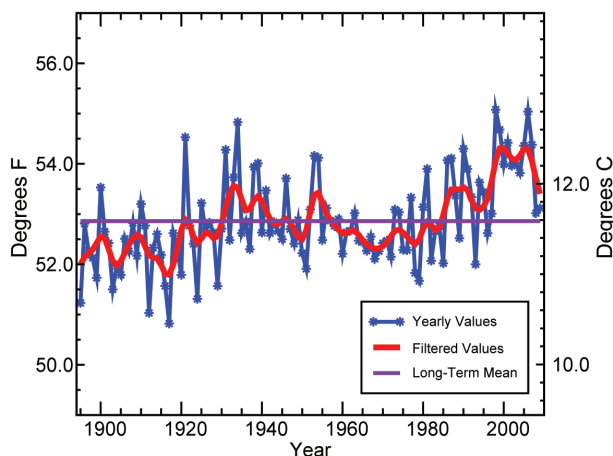
Just before midnight on 2 August, a powerful storm moved out of the Rocky foothills and tracked southeastward across the province with wind and hail that left a devastating path of destruction to city and country. The main hail zone hit the extreme northeastern portion of Calgary. Inside the city, hail diameters reached baseball size and wind speeds peaked at 107 km hr^{-1}. In its wake, the storm left downed trees, broken windows and a swath of damage, knocking out power to several thousand customers. In some places, hail measured 10 cm deep. Canadian insurers estimated industry loss estimates at $500 million CAN, which made it the second or third largest catastrophic event in Canadian history. The massive hailstorm decimated over 600 000 ha of Alberta cropland spurring 1500 hail crop damage claims. In total, two-thirds of the year's hail crop losses occurred as a result of the long weekend storm.

2) UNITED STATES—C. Fenimore, J. Crouch, R. R. Heim Jr., and J. Blunden

Based on preliminary data, 2009 was the second consecutive year the nationally averaged temperature was 11.7°C, which is 0.1°C above the long-term (1895–2009) average. The year was characterized by extreme fluctuations in the weather pattern. The average temperature for the contiguous United States the

first half of the year (January–June) was in the top tercile (25th warmest), while the average temperature during the last half of the year (July–December) was in the bottom tercile (37th coolest).

Below-average temperature anomalies in the central United States were associated with above-average precipitation anomalies. Overall, 2009 was the 18th wettest on record for the contiguous United States. Regionally, much-above-normal precipitation fell in the lower and middle Mississippi Valley, parts of the Southeast, and the middle third of the Atlantic Coast. The western third of the United States averaged below-normal precipitation for the year.

(i) Temperature

For the contiguous United States, the 2009 temperature very nearly tied 2008, which was the coolest since 2000 (Fig. 7.3). The spatial pattern consisted of cool anomalies in the northern and central U.S. Plains and Midwest, with warm anomalies in the Southwest and Florida (Fig. 7.4a). A persistent cool anomaly was entrenched in the U.S. Plains and Upper Midwest during the summer and fall periods. The decade long (2000–09) average annual temperature was 0.7°C above the twentieth century average. Over the past 30 years, the average temperature has increased at a rate of 0.4°C per decade.

As with most winter seasons, December 2008–February 2009 featured regional variations in temperature but the overall average for the contiguous United States was "near-normal," or within the middle third of historic winter temperatures. The warm anomalies strengthened in the spring (March–May), making it the 29th-warmest spring of the 115-year record. The warmer-than-average temperatures that were seen in the South and Southwest regions during the winter shifted to the West and Southwest regions during the spring.

The contiguous United States experienced its 44th coolest summer (June–August). A recurring upper-level trough in the Central United States was associated with cool Canadian air, bringing below-normal temperatures to the central and northern Plains, Midwest, and Great Lakes areas. The cool anomalies peaked in July, when six states (Ohio, Indiana, Illinois, Iowa, Pennsylvania, and West Virginia) experienced record cool temperatures for the month. It is noteworthy that an El Niño emerged during early summer 2009. Preliminary attribution exercises performed by NOAA scientists indicated that cooler-than-normal temperatures in the central United States during summer and early autumn are
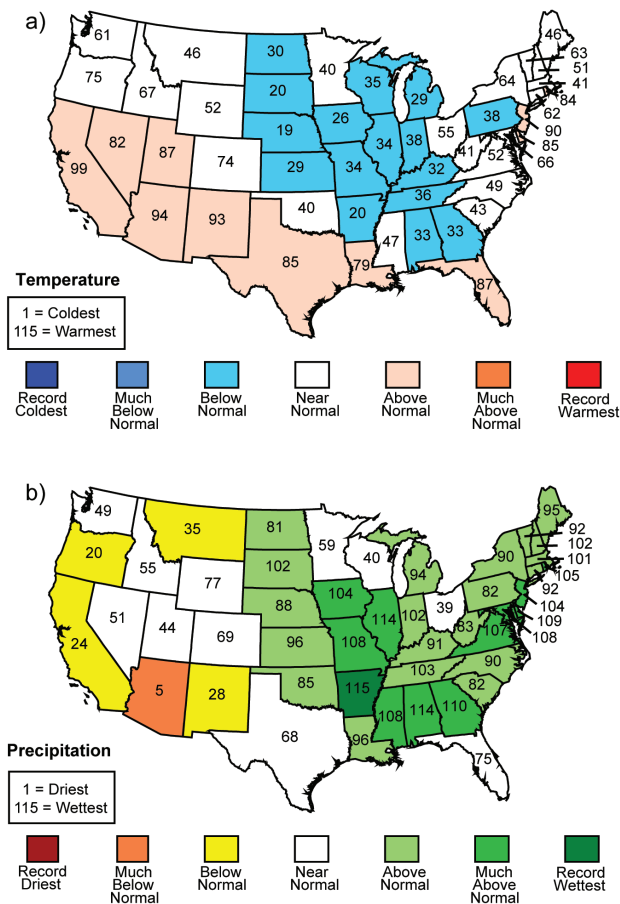
Fig. 7.4. Statewide ranks of (a) 2009 temperatures and (b) 2009 precipitation. A rank of 115 represents the warmest/wettest year since 1895. Much above-normal temperature/precipitation is defined as occurring in the top 10% of recorded years, which corresponds to a rank of 105–115. Above-normal temperature/ precipitation is defined as occurring in the warmest/ wettest third of recorded years (ranks 78–103). Much below-normal temperature/precipitation is likewise the bottom 10% of coolest/driest years since 1895, and below normal is defined as the remaining coolest/driest third of the distribution. (Source: NOAA/NCDC.)

not inconsistent with expectations during a developing El Niño episode (see sidebar).

Fall 2009 was a season of extremes for the contiguous United States. While September was about 0.8°C above the long-term average, October was marked by an active weather pattern that reinforced unseasonably cool air behind a series of cold fronts, creating an average temperature that was 2.0°C below the long-term average and ranked the nation as the fourth coolest October on record. During this month, 43 of the lower 48 states averaged temperatures that were below normal. Florida was the only state with an above-normal temperature for October. The fol-

lowing month was something of a mirror image, becoming the third warmest November on record, 2.2°C above the long-term average. Overall, the nationally-averaged temperature for the three-month autumn period was above-normal, ranking as the 34th warmest on record.

The average annual temperature for Alaska in 2009 was 0.5°C below the 1971–2000 long-term average. This represents the second consecutive annual period in which Alaska has experienced cooler-than-normal temperatures. Seasonal anomalies contrasted the contiguous United States, with both winter and spring temperatures below average. The summer and fall seasons were warmer-than-normal as 500 mb height anomalies increased.

(ii) Precipitation and snowpack

Average precipitation for the contiguous United States in 2009 was 64 mm above the long-term average of 740 mm. Precipitation across the United States in 2009 was characterized by persistent wetness in the Midwest and Southeast, while precipitation in the West, Northwest, and Southwest was below average (Fig. 7.4b). Arkansas observed its wettest year on record with four months of top three precipitation ranks (May, wettest; July, third wettest; September, second wettest; October, wettest). The unrelenting weather pattern also contributed to the second wettest annual period in Alabama and Illinois. More than half of the contiguous United States received above-normal precipitation for the year. Conversely, the lack of monsoonal moisture in the Southwest contributed to Arizona's fifth driest annual period. The decadal trend of the contiguous United States continued its above-normal precipitation streak with the past decade (2000–09) averaging 18 mm above the 20th century average and precipitation over the past four decades averaging 27 mm above the 20th century average.

It was the 22nd driest winter (December 2008–February 2009) for the contiguous United States in the 1895–2009 record. Texas recorded its driest winter period, while North Dakota experienced its wettest winter on record. The contrasts in rankings were the result of an active upper-level pattern that shuttled systems rapidly across the northern-tier states, while bypassing the deeper south. Conversely, the contiguous United States experienced its 18th wettest spring (March–May). Relatively slow-moving storm systems and surface fronts across the southern United States led to above-normal precipitation averages across the southeastern United States. Georgia experienced

its second wettest such period. Several other states experienced a spring period that saw above-average precipitation: Florida and Illinois (fifth wettest each), Alabama (seventh), and Arkansas (ninth). In March, record flooding occurred in parts of Minnesota and North Dakota along the Red River. The flooding was preconditioned by copious winter precipitation coupled with persistent precipitation-producing storms in the spring. Record-high flows were recorded along the Red River with peak levels exceeding the 500-year return interval.

Summer (June–August) precipitation was variable in 2009, which is typical for the season, but overall near normal, ranking 54th wettest out of 115 years. Regionally, the Northeast had its second-wettest summer on record, continuing a string of abnormally wet summer periods. Deficient monsoonal rains in the Southwest contributed to Arizona's third-driest summer. Precipitation averages in Georgia and South Carolina were also much below normal. Conversely, Massachusetts experienced its wettest summer and it was Maine's third-wettest such period.

It was the 11th wettest autumn (September–November) on record for the contiguous United States. Anomalously wet conditions in October led to a record wet month for the nation as a whole. The nationwide precipitation of 105.4 mm was nearly double the long-term average of 53.6 mm. Persistent precipitation during September and October made Arkansas' autumn precipitation its greatest ever. Nine other states were much above normal in terms of precipitation for the autumn season. Interestingly, these high precipitation anomalies occurred despite only two tropical cyclones (Tropical Storms Claudette in August and Ida in November) making landfall during the Atlantic Hurricane season. The variable climatic extremes continued in November when the upper-level jet retreated to the north, contributing to a nationally-averaged precipitation that ranked 18th driest, continuing the run of below-normal November precipitation in the contiguous United States. The summer and fall months were drier than average in much of Alaska.

During winter 2008/09, snowpack levels were below- to near-normal for the Cascade Mountains and the Northern Rockies in Idaho, Montana, western Wyoming, and Utah. The Olympic Mountains and Okanagan Highlands of Washington had snow levels less than 50% of normal. The Sierra Nevada also experienced below-normal snowpack for the season. Conversely, the central and southern Rockies in Colorado, New Mexico, and northern Arizona

had above-normal snowpack totals by the end of the season. Alaska snowpack was generally above normal, with the exception of the northern and southern coastal regions of the state.

March brought several large snowstorms that broke daily and monthly snow records across the center of the country. Statewide records for 24-hr snowfall accumulations were observed in Texas (64 cm), Oklahoma (66 cm), and Kansas (76 cm). Seasonal snowfall records were measured in International Falls, Minnesota, with 318 cm and Spokane, Washington, with 248 cm of snowfall.

The beginning of the 2009/10 snow season brought below-normal snowpack to the western United States, including much of Alaska, while Arizona and New Mexico observed above-normal snowpack. The low snowfall amounts contributed to ongoing drought in California. October and December were particularly snowy across the contiguous United States, with both months setting new snowfall extent records. October was North Platte, Nebraska's snowiest month on record with 77 cm, while December brought record snowfall to the Northeast corridor and the Plains, including Philadelphia, Pennsylvania; Washington, D.C.; and Oklahoma City, Oklahoma.

(iii) Droughts and wildfires

Widespread precipitation extremes occurred during 2009, with large areas (20–25%) of the country very dry (monthly precipitation total in the bottom tenth percentile of the historical record) during January, February, and November and large areas very wet (top tenth percentile) during May, June, October, and December. The dryness exacerbated areas of drought during early 2009 while the abundant precipitation brought drought recovery during the later months. The year began with 19.2% of the contiguous United States experiencing moderate to exceptional drought, as defined by the U.S. Drought Monitor (USDM). That percentage increased to 26.6% by late March before decreasing during the summer and fall, ending the year at 12.4%, which was among the lowest values in the ten-year USDM record. Based on the 110-year Palmer Drought Severity Index (PDSI) record, 2009 capped a decade of expansive drought, with the 2000–09 decade ranking as the third biggest drought decade in the last 110 years.

The drought epicenters during 2009 were southern Texas, the southern Appalachians, California, and Hawaii. Severe agricultural impacts were felt, especially in Texas and Hawaii. Low streams, reservoirs and stock ponds, and depleted soil moisture combined

to ravage agricultural (pasture, range, and crop) lands in Texas early in the growing season. Heavy irrigation of crops was required across much of Hawaii amidst low soil moisture and irrigation restrictions in some areas.

Beneficial rains beginning in September brought drought relief to southern Texas, but not before these areas turned in their driest September–August 12-month period in the 1895–2009 record. The PDSI plummeted to the extreme drought category by early summer, but it did not pass the levels of the record 1950s drought for southern Texas, both in terms of intensity or duration. An analysis of post oak tree-ring chronologies from 1652–1995 indicates that southern Texas has experienced a dozen individual years prior to the 20th century which had very low

January–June precipitation similar to the lowest values of the past 110 years. The 1950s drought likely was matched and possibly exceeded by one that occurred during 1711–17.

Parts of the Southeast began 2009 with lingering moderate to extreme drought, but by the beginning of summer, drought in the Southeast was mostly gone. Parts of the Upper Mississippi Valley and adjacent western Great Lakes have been in some level of dryness or drought for most of the last seven years, with moderate to severe drought lingering at year's end. Northwest Wisconsin had the driest 12-month October–September period on record in 2009 (October 2008–September 2009).

Parts of the West, especially California, have suffered through three years of drought. Northern

STRONG SEASONALITY IN 2009 U.S. TEMPERATURES—NOAA CSI TEAM—M.P. HOERLING

What Happened?

Headlines regarding U.S. surface temperatures for 2009 should read "Strong Monthly and Seasonal Variability". This climate variability story is all too easily obscured by the mundane outcome that annually-averaged temperatures were just slightly above their 20th century average (+0.2°C). As illustrated in Fig. 7.5 (left panels), the year began (JFM) with much-above-normal temperatures (i.e., in the top quintile of the 115-yr record) over the Central and Southern Great Plains and the Desert Southwest, flanked to the north and east by below-normal temperatures. A southward expansion of cold conditions occurred across much of the Great Plains in the spring (AMJ). By the summer (JAS), much-below-normal temperatures shifted eastward, and a swath from the eastern Plains thru the upper Ohio Valley succumbed to record-breaking low July averaged temperatures. Meanwhile, the western third of the United States remained very warm during the summer, and September was the warmest month on record for California and Nevada. But that latter warmth too came to an abrupt end, with the West and Rockies experiencing much below temperatures during the fall (OND) that also engulfed the western Plains (notwithstanding a brief interlude of high temperatures during November). By all measures, a wild rollercoaster ride for U.S. temperatures through 2009!

Why did it happen?

Can any reason be given for this strong seasonality? Such seasonal extremes most certainly were not the result of human-induced climate change. It is known that the U.S. tem-

perature impact of greenhouse gas (GHG) and aerosol forcing, as estimated from the climate models of the IPCC Fourth Assessment, is comparatively uniform across the seasons. Thus, the observed rapid swings between much-below- and much-above-normal temperatures in 2009 were unlikely a symptom of anthropogenic forcing. Natural processes of climate variability were instead more likely the dominant cause.

In the far-away reaches of the equatorial Pacific, a no-less dramatic seasonal reversal in SST conditions was taking place during 2009. La Niña conditions that developed in late 2008 persisted through March 2009. A swift transition occurred in early spring, leading to El Niño SST conditions by July. This El Niño increased to moderate intensity by October 2009. The impact of tropical east Pacific SST forcing on U.S. seasonal climate is well known, and the question we ask here is which, if any features of U.S. temperature seasonality may have resulted from the seasonal reversal in SST forcing. Six different global climate models were subjected to the monthly variability in observed 2009 global SSTs. The resulting ensemble-averaged seasonally varying U.S. temperature response (260 simulations in total) is shown in the right side plots of Fig. 7.5. Several qualitative aspects of the observed seasonality appear linked to fluctuations in the oceans. Notably, a warm JFM over much of the Great Plains gave way to cold conditions during JAS in the simulations. Likewise, the early winter warm conditions in the southern Plains and Gulf Coast were replaced by cold conditions in fall in the simulations. These simulated features are broadly consistent with the seasonality observed, and they

California began the year with moderate to extreme drought. Conditions improved throughout the year, but the state ended 2009 with areas of moderate to severe drought remaining. An analysis of blue oak tree-ring chronologies from the coast ranges of California revealed as many as seven three-year drought events in the 1332–1900 period which were more severe than the driest three-year drought events of the 20th to early 21st centuries.

The United States had a near-normal wildfire season for 2009, similar to 2008. The first half of the year was marked by above-average number of fires and acreage burned, primarily in the western and central regions of the country where ongoing drought had increased fire danger. The second half of the year was generally cool and wet for the nation and was associated with below-average fire activity. For the year as a whole, nearly 77 500 fires burned over 2 million hectares. Despite the near-normal season, the Station Fire in California burned an estimated 64 983 hectares, marking the largest recorded fire in Los Angeles County history and California's tenth largest fire since 1933.

(iv) Tornadoes

Across the United States, 2009 was a below-average year for tornadoes. As of February 2010, confirmed tornado reports and estimates for the end of 2009 indicated that there were 1150 tornadoes from January–December, which is below the 10-year (1999–2008) average of 1291 and the fifth lowest (sixth highest) total of the decade. The number of strong-to-violent

FIG. 7.5. Seasonally averaged surface temperature departures (relative to 1971–2000) during 2009 based on NCDC climate division data (left panels), and climate simulations forced with observed monthly varying global sea surface temperature and sea ice conditions during 2009 (right panels). The simulations consist of 6 different models and a total ensemble size of 260 members conducted for 2009. (Source: NOAA/ESRL.)

are mostly consistent with the known U.S. impacts of La Niña (during winter) and El Niño (during summer and fall).

By no means are all the seasonal features of 2009 U.S. temperatures interpretable as resulting from ocean forcing. In particular, the spatial scale and intensity of the observed cold summer conditions is considerably greater than the simulated SST-induced coolness. Likewise, the very cold conditions over the western United States during fall were apparently unrelated to that region's sensitivity to the SST forcings. These conditions are assumed to have resulted from purely atmospheric-driven variability. An important research task remains to ascertain how likely the cold summer and fall conditions were given both the state of global SSTs and anthropogenic GHG forcing in 2009.

tornadoes (rated EF3–EF5) reported in 2009 was 21, which is also below average.

There were 21 tornado fatalities in 2009, associated with nine tornadoes, which is the second lowest in the 1950–2009 record. The most deadly tornado of the year occurred in Oklahoma on 10 February, when an EF4 killed eight people. This was the state's first February EF4, and the deadliest February tornado in Oklahoma history. February was also the most deadly month of the year with a total of nine fatalities.

Louisiana and Alabama had their busiest tornado year of the decade, while the typically active states of Texas and Kansas had their second slowest. The largest outbreak of the year occurred on 9–10 April when 117 tornadoes were reported from Texas to North Carolina. A total of five tornado-related deaths were reported—three in Arkansas and two in Tennessee. There were also 221 straight-line damaging wind reports and 435 severe hail reports associated with the outbreak. According to preliminary data, November tied as the second quietest November since 1950 with only two tornado reports. In the past, November has been a fairly active month for tornadoes in the southeastern United States.

3) México—V. Davydova-Belitskaya and F. Romero-Cruz

México experienced warmer-than-normal temperatures in 2009 and on average it was 10% drier than normal. México's National Meteorological Service (SMN) reported a national precipitation average of 681.9 mm, compared with a historical average of 759.6 mm (1971–2000). The nationwide annual mean temperature was 22.5°C, which was 1.0°C above the long-term climate average. Extreme weather caused several deaths and millions of dollars in damages to the agricultural and water sectors.

(i) Temperature

In general, México registered an annual temperature anomaly in a range from -1.0°C to +1.0°C, which is considered a normal variation. With the exception of the Baja California Peninsula, northwestern, northern, northeastern, and western regions, as well as the Yucatan Peninsula, the anomalies were between 1.0°C and 2.0°C above normal (Fig. 7.6a). Annual mean temperature for the country as a whole was 22.5°C, with an anomaly of 1.0°C above normal. However, spatial and temporal variations were observed. During the winter, spring, and summer, anomalies from +1.0°C to +4.0°C were found in the northern, northwestern, western, and central regions of the country as well as in the Yucatan Peninsula. Recovering from the

rainy season, at the end of August and beginning of September temperatures quickly decreased to normal in most of these regions, with the exception of the Yucatan Peninsula and the southeastern regions, where anomalies between 1.0°C and 2.0°C above normal remained.

By the end of November and during December, unusually low temperatures prevailed in the northwestern, northern, western, and central regions of México; in the states of the northern Gulf coast; and in the Sierra Madre Oriental and the Eje Neovolcanico regions. The anomalies were as much as 4.0°C below normal. This behavior was related to intense humidity from the tropical Pacific and its interaction with cold fronts; these conditions resulted in cloudier-than-normal skies, which led to low diurnal temperatures in most of the country.

(ii) Precipitation

The rain pattern was variable during the year and across the country, but was generally very dry (Fig. 7.6b). The year began much drier than normal in the winter and spring, but it changed to normal precipitation in the beginning of the rainy season (May–June).
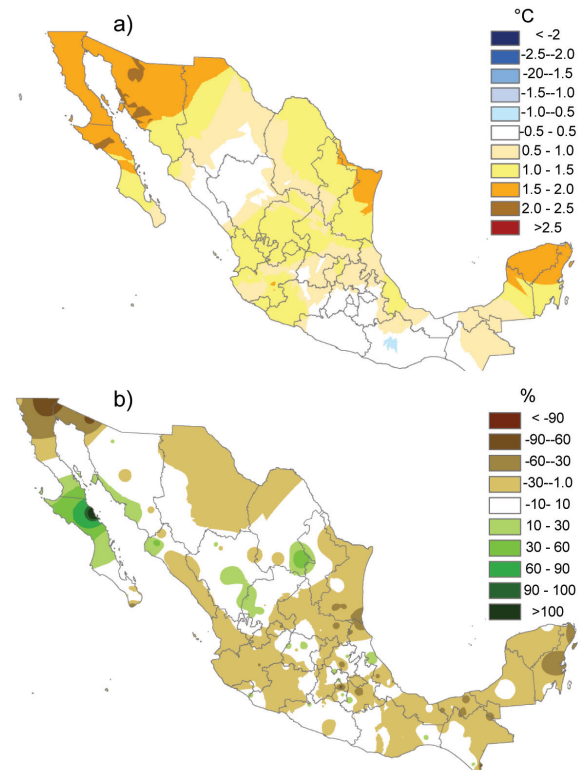
FIG. 7.6. (a) Annual mean temperature anomalies (°C) for Mexico (based on 1971–2000) for 2009 and (b) annual total precipitation anomalies (% of 1971–2000) for 2009. (Source: National Meteorological Service of México.)

The first drought occurred in March and April and produced some impacts in the southern and southeastern states of the country. Thousands of livestock and hundreds of thousands of dollars U.S. were lost by the end of April, seriously impacting the economy of Tabasco. The development of the rainy season during May and June allowed the scheduled farming activities in most of the country; however, a new drought developed as a consequence of the fast appearance of El Niño. This drought episode hit agricultural, cattle, and water sectors in most of México.

Precipitation statistics ranked July 2009 as the driest since 1941 at a national level. Due to the devastating impacts, some farmer organizations in the central region of the country declared the event as the worst drought in 70 years.

Precipitation recovered in the western, central, and southern areas of México in the beginning of September, with an exceptionally wet autumn. However, the total annual precipitation reported by the National Meteorological Service was below normal (Fig. 7.6b). The largest negative annual anomalies were registered in Distrito Federal (-47.7%), Nayarit (-24.7%), Tabasco (-23.6%), Yucatan (-22.7%), Quintana Roo (-22.4%), Aguascalientes (-22.2%), Sinaloa (-20.0%), Estado de México (-19.8%), Jalisco (-18.4%), Michoacán (-18.3%), Veracruz (-16.8%), Morelos (-14.9%), Chiapas (-14.5%), Queretaro (-12.4%), and Chihuahua (-11.8%). Only

five of the 32 states of Mexico reported rainfall above normal: Baja California Sur (+69.6%), Baja California (+26.6%), Hidalgo (+11.3%), Zacatecas (+6.7%), and Sonora (+4.5%).

(iii) Wildfires

According the National Forest Commission (CONAFOR) reports less than 10 000 wildfires were observed during 2009 in the country. Most were registered during the period from February through July. The states with the highest occurrence of fires were México, Distrito Federal, Michoacán, Chihuahua, Puebla, Jalisco, Chiapas, Tlaxcala, Hidalgo, and Baja California. Those with the highest affected areas were Baja California, Quintana Roo, Coahuila, Yucatán, Oaxaca, Zacatecas, Chiapas, Michoacán, Guerrero, and Chihuahua.

c. Central America and the Caribbean
   1) Central America—J. A. Amador, E. J. Alfaro, H. G. Hidalgo, E. R. Rivera, and B. Calderon

For this region, seven stations from the following five countries were analyzed: Belize, Honduras, Costa Rica, Panama, and Guatemala.

(i) Temperature

Most stations located on the Pacific coast show, for 2009, very little surface temperature departures from
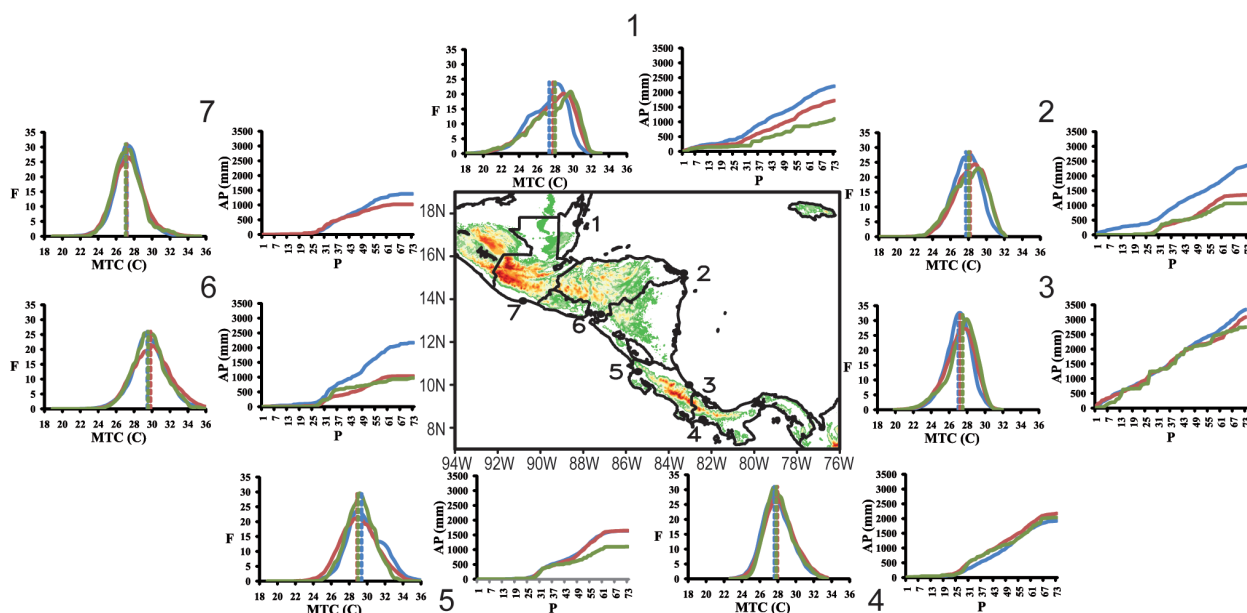
FIG. 7.7. Central America showing the location of selected stations: 1. Phillip Goldson Int. Airport, Belize; 2. Puerto Lempira, Honduras; 3. Puerto Limon, Costa Rica; 4. David, Panama; 5. Liberia, Costa Rica; 6. Choluteca, Honduras; and 7. San Jose, Guatemala. For each station, surface temperature frequency is shown on the left and accumulated pentad precipitation on the right. Blue represents climatology for the base period 1971–2000, red the 2000–09 decade and green 2009. Note that San Jose does not show 2009 precipitation data due to large amount of missing data. (Source: NOAA/NCDC.)

their climatology or from their 2000–09 averages (Fig. 7.7). Stations located on the Caribbean side present a shift toward the right in their frequency distribution, implying a warmer year than normal. Distribution for the 2000–2009 decade confirms, in general, a warmer decade than normal.

(ii) Precipitation

The year was generally drier-than-normal for three of the seven stations analyzed: Phillip Goldson A. (Belize), Puerto Lempira (Honduras), and Liberia (Costa Rica). None of these sites show dry conditions exceeding the 95% confidence level with respect to the mean. In terms of the starting and ending dates (SD and ED) of the rainy season, there is a general tendency for 2009 being a year with late SDs when compared to both the baseline period and 2000–09 average. Also, the 2009 rainy season had an early ED for Liberia, compared to the averages for 1971–2000 and 2000–09, while Choluteca shows an early ED compared to 1971–2000 but a late ED compared to 2000–09. David behaves in an opposite way to Choluteca. These variabilities suggest more local than regional physical mechanisms controlling precipitation.

The number of five-day rainy events (pentads) during 2009 was lower than average in six of the seven stations analyzed. The exception was Puerto Limon (Costa Rica). Conversely, the 2009 number of dry pentads was higher than normal for four of the seven stations analyzed (Phillip Goldson, Puerto Lempira, Liberia, and San Jose), while Choluteca and David were lower than normal and Puerto Limon was about average. The interquartile range (IQR, a measure of variability for the pentad data) was about average in all stations, except for San Jose. Finally, the number of wet outliers was lower than normal for San Jose, Lempira, Choluteca, David, and Liberia; slightly less than average for Belize; and above average in Limon. Most below-normal precipitation in the Pacific slope of Central America can be associated with a warm ENSO condition for the second half of the year and stronger-than-normal winds associated with the Intra-Americas Seas (IAS) low-level jet. A cold or near-neutral ENSO condition during northern winter 2009 did not reflect in relevant departures from normal conditions in the region.

(iii) Tropical cyclone activity

Tropical cyclone activity in the Caribbean was below normal during 2009. There were two named storms in this region (nine in the Atlantic) and one hurricane (three in the Atlantic). No strong hurri-canes (category > 2) were observed in this region (two in the Atlantic). Typical values (given by the median) in the Caribbean during the last four decades are four named storms, two hurricanes and one strong hurricane. As a consequence of this decrease in tropical cyclone formation, Central America experienced reduced societal impacts caused by hurricanes. Of special interest for the region was Hurricane Ida. This storm originated over the Caribbean Sea on 4 November, and moved ashore over Nicaragua the following day. After reemerging over the Caribbean, the storm gradually grew stronger as it moved northward.

(iv) Notable events

According to the Costa Rican National Meteorological Institute, 16 easterly cold waves were observed between June and October. There were 12 cold outbreaks in the Caribbean Sea during 2009, in contrast to the observed typical value of 16 events per year (relative to 1975–2001). In El Salvador, deadly floods and landslides, associated in part with Hurricane Ida, claimed 192 lives. The National Electricity Board of Costa Rica (ICE in Spanish) reported an additional investment of more than $5 million U.S. to produce thermal electricity. This additional production of thermal energy was necessary due to the drier-than-normal year.

2) The Caribbean—C. Fonseca Rivera, B. Lapinel Pedroso, R. Pérez Suárez, A. Carrión Romero, A. León Lee, V. Cutié Cancino, I. González García, T. S. Stephenson, M. A. Taylor, J. M. Spence, and S. Rossi

Countries considered in this region include: Cuba, Jamaica, Puerto Rico, and the U.S. Virgin Islands.

(i) Temperature

For Cuba, 2009 was characterized by mean temperatures above the long-term average (1971–2000), resulting once again in a warm year. The annual mean of 25.9°C ranks 2009 as the 10th warmest year since 1951 (Fig. 7.8a). This behavior was strongly influenced by an increase in extreme temperatures and high values reported in the summer. It highlights July, August, and September as the warmest since 1970. Also October 2009, where the values were 1°C above normal, was the warmest October since 1970.

For Jamaica, slightly-above-normal temperatures were recorded for some coastal stations. This was observed against negative sea surface temperature anomalies around Jamaica for the first half of the year with a shift to positive anomalies for the latter half of the year.

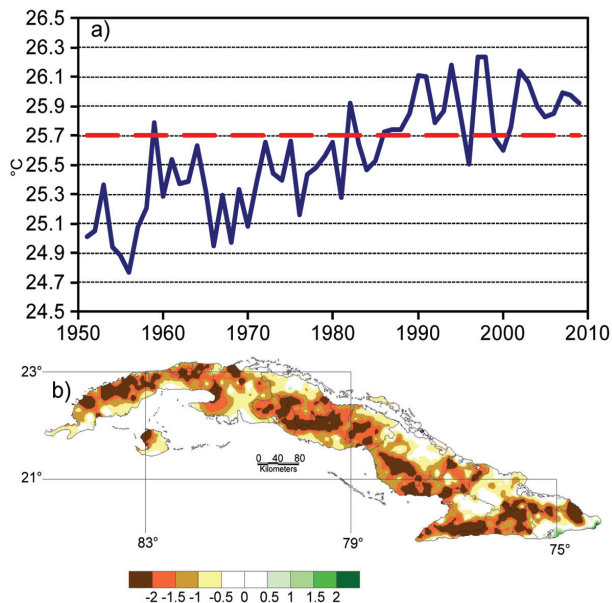**Fig. 7.8. (a) Annual mean temperature for Cuba, 1951–2009 and (b) annual precipitation anomalies, represented as Standardized Precipitation Index (based on 1971–2000) for 2009. (Source: Institute of Meteorology of Cuba.)**

Temperatures across Puerto Rico ranged from 7.2°C in Adjuntas, which was recorded on both 28 February and 23 March, to 36.1°C in Ponce, which occurred on 30 July and 10 August. By the end of the year, 2009 ranked as the 4th warmest year since record began at the Luis Muñoz Marin International Airport in 1956 (the daily mean temperature was 27.4°C versus the 30-year normal of 26.6°C). Temperatures across the U.S. Virgin Islands ranged from 15°C at Beth Upper New Works near Christiansted on Saint Croix (recorded on 14 and 28 January), to 34.4°C, also at Beth Upper New Works (on 20 July). The annual mean temperatures at the Cyril E. King Airport on Saint Thomas, and at the Christiansted Airport on Saint Croix, were both 27.2°C in 2009; these values ranked near their long-term average of 27.2°C and 27.6°C, respectively.

(ii) Precipitation

For Cuba, the annual total rainfall for 2009 was below average (Fig. 7.8b). The deficit amounts of rain which affected the three regions of Cuba were 24% below the mean, resulting in the 2nd driest year since 1961. At the end of dry season (November 2008–April 2009) which usually represents 25% of the annual total, only an accumulated value of 18% was observed. The western region ranked as one of the 10 lowest since 1961. Also, the rainy season (May–October 2009) finished with marked deficits in the country, accumulat-

ing only 60% of the annual total, and ranked 4th driest for the same period.

For Jamaica, the average annual rainfall for 2009 was below normal. This manifested as below-average rainfall for nine months, particularly during the latter half of the year (Fig. 7.9). Barring these, near-normal rainfall amounts were recorded in January while above-normal values were measured during February and May. February, a usually dry month, received 128 mm of rainfall which represented the 13th wettest February on record. The primary cause during that month was the frontal systems and troughs, and the northeastern parishes received much of this rainfall. Also noteworthy were the rainfall amounts recorded for July (57 mm) and October (168 mm), which respectively represented the second and seventh driest monthly totals on record. All 14 parishes experienced below-normal rainfall in July. For October, only two parishes recorded above-normal rainfall. The rainfall deficit experienced during the Caribbean rainfall season (June–November) was related to the appearance and subsequent persistence of El Niño conditions since June 2009. The El Niño contributed to increased vertical wind shear in the main development region over the tropical Atlantic and appeared to have offset the effect of the ongoing multidecadal signal. There were no hurricanes impacting Jamaica.

In Puerto Rico, just before the hurricane season began, the presence of several persistent upper-level lows across the southwestern Atlantic, contributed to wetter-than-normal precipitation during April through June (this wet start to the year can been seen in the blue shading in Fig. 7.10). By the end of the year, cooperative weather stations indicated that Puerto Rico experienced another near-normal year, receiving 97% of its normal rainfall; however, precipitation varied from 55% to 113% across the U.S. Virgin Islands in 2009.
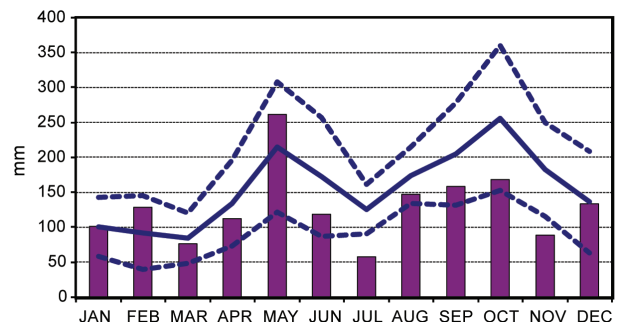

Fig. 7.9. Monthly Jamaican rainfall for 2009 (bars), climatology (black), and one standard deviation from climatology (dashed). The reference period is 1961–90. (Source: Meteorological Service of Jamaica.)
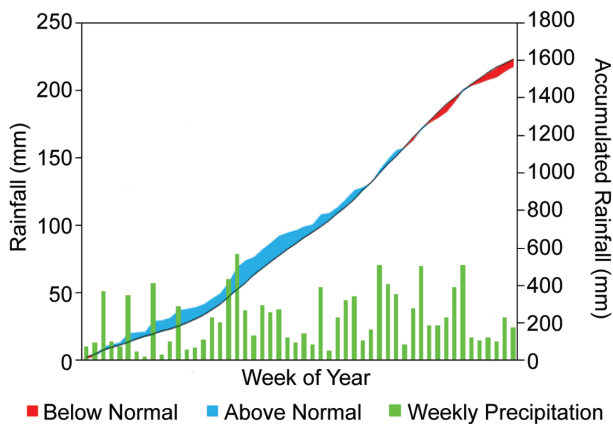
FIG. 7.10. Weekly mean rainfall for Puerto Rico, based on over 50 cooperative weather stations, with accumulative rainfall displayed on the right hand axis of chart. Year to date surpluses and deficits displayed with blue and red shading respectively. (Source: NOAA/NWS.)

(iii) Notable events

A significant drought started in Cuba during the dry season (November 2008–April 2009). This event affected large areas in the western and central regions. Later, the drought continued across the country and during the rainy season (May–October 2009), which was extremely dry. At the end of 2009, nearly 60% of the country showed moderate to severe dry conditions. This event is consistent with the increasing trend observed in the anticyclone influence on the area in recent decades accompanied by persistent and severe drought.

Meteorological drought conditions persisted in Jamaica from January to November 2009 for 3 of the 14 parishes, interrupted only by May rains. The parishes affected were Clarendon, St. Thomas, and St. Mary.

In Puerto Rico, on 15 November, record flooding was observed along the Rio Piedras in San Juan—the river crested at an all time high of 7.2 meters—resulting in major flooding across the interior portions of the San Juan metro area. This rainfall event contributed to the 308 mm of rain that accumulated at the Luis Muñoz Marin International Airport during November, making it the wettest month since April 2005. However, the year's heaviest 24-hr rainfall came on Christmas Eve, when the remnants of a cold front moved across Puerto Rico dropping 229 mm of precipitation across the municipality of Aibonito, located in the eastern interior of the island. This rainfall event led to significant flash flooding and mudslides, including the destruction of dozens of homes in the municipality of Aibonito, which prompted the governor of Puerto Rico to declare an emergency zone for the affected areas after the event.

d. South America

The 2009 annual mean temperature was generally near normal to above normal across South America (Fig. 7.11a). Significant positive anomalies were mainly observed in Venezuela, Peru, Brazil, Bolivia, Paraguay, and Argentina. Overall, the annual total precipitation was near normal to below normal except for some small regions in northern and southern Brazil. The main negative anomalies were found in Venezuela, Brazil, Chile, and Argentina (Fig. 7.11b).

1) NORTHERN SOUTH AMERICA AND THE TROPICAL ANDES—R. Martinez, A. Mascarenhas, E. Jaimes, G. Leon, A. Quintero, and G. Carrasco

Countries considered in this section include: Venezuela, Colombia, Ecuador, Peru, and Bolivia.

(i) Temperature

The temperature and precipitation behaviors were mainly associated with the ENSO evolution during the second half of the year. The 2009 annual mean temperature anomaly was near +1°C in Venezuela. In Colombia, the temperature was near normal during the first half of the year while a gradual increase was observed during the second half of the year with anomalies between +1°C and +3°C almost everywhere across the country. The stronger anomalies were found in September and December when historical maximum temperature records were registered. In Ecuador, the mean temperature was above normal in the first quarter of the year except for the central and northern Ecuadorian Andes. In Peru, the annual mean temperature was mainly near normal with an anomaly near +1°C in the east; however, several frosts occurred in the southern and central Andes zones in August and September.

(ii) Precipitation

In Venezuela, dry conditions were predominant during 2009. During the dry season (February–March), the rainfall deficit was near -60 mm. This deficit increased during May–June (start of the rainy season) when it reached between -140 mm to -180 mm, especially over Portuguesa, Guárico, Apure, and Monagas states. The dry conditions affected rice and corn crops in these areas. From August to October, precipitation deficit fluctuated between -140 mm and -220 mm over the center and south zones extending to the Andean region and continuing to December. The main impact of this deficit was evident in the agriculture and energy sectors. Seventy percent of the national energy production comes from El Guri
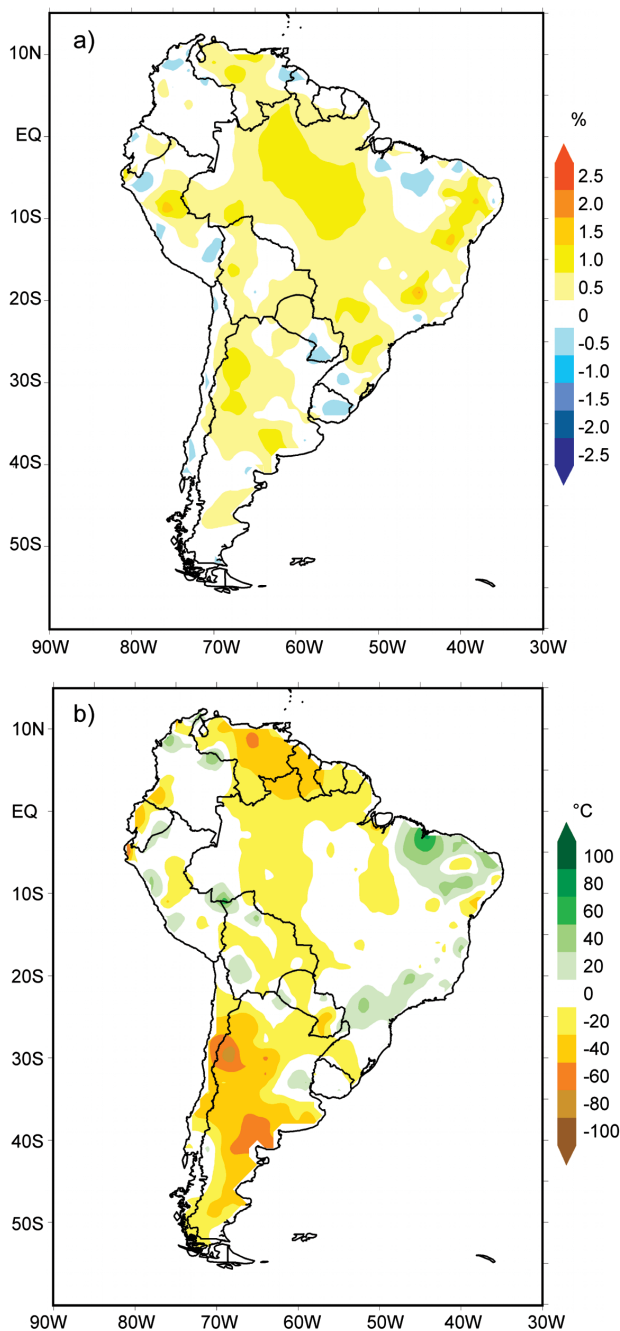
FIG. 7.11. (a) Annual mean temperature anomalies for South America (based on 1971–2000) for 2009 and (b) annual precipitation anomalies (% relative to 1971–2000) for 2009. Sources: National Meteorological Services of Argentina, Brazil, Bolivia, Chile, Colombia, Ecuador, Paraguay, Peru, Uruguay and Venezuela. Data compilation and processing by CIIFEN 2009.

Hydroelectric Plant (Caroní River Basin in Bolivar State). The reservoir was severely affected by the precipitation deficit with an 11 m below-average water level, leading to an electric power restriction at the national level.

In Colombia, positive precipitation anomalies between +40% and +70% were predominant across the country from January to March, especially in the Andean region. When the Tropical Pacific sea surface temperature switched from neutral to warm conditions, precipitation anomalies became negative. Negative anomalies between -40% and -70% were observed in the last quarter of 2009 over the Caribbean, Andean, and Pacific regions.

In Ecuador, negative anomalies were registered from January to May in the coastal and Andean zones. The deficit reached 60% of the normal value. During the second half of the year, the rainfall deficit was generalized over the entire country. Severe restrictions were imposed on the use of hydro energy during November and December.

In Peru, the precipitation anomalies were mostly negative during the first quarter of the year, especially in the southern zone where they reached -60% to -100%. In contrast, in April–June, precipitation anomalies became positive, registering up to 100% in the northern and central Amazonia and causing some floods. The possible cause of these rainfalls could be the typical moisture flux coming from the north. This humidity continued in July–August but with minor intensity. The southern region of Peru registered snow and hail storms which paralyzed transportation in this area. In September–October, negative precipitation anomalies down to -80% were registered in northern and central Amazonia, while negative anomalies down to -100% were observed in the southwest of the country. This caused a deficit in the water level of the Titicaca Lake (Puno).

In Bolivia, negative precipitation anomalies were also found in January–February in several regions: the Altiplano (-16%), the Valleys (-62%), the eastern Llanos-Santa Cruz (-64%), and the Bolivian Chaco (-71%). This condition persisted from April to October in the Valleys, Beni, and Chaco regions. In northern La Paz, negative anomalies of -49% were observed during the last quarter of 2009. In contrast, Pando in northern Bolivia observed positive precipitation anomalies all year; December was the rainiest month with +58%. Precipitation anomalies from +25% to +50% were also observed during February–March in the eastern Llanos-Santa Cruz while in the Altiplano, anomalies between +58% and +84% were registered in November–December.

(iii) Notable events
In Venezuela, one of the reported extreme events was the occurrence of a small tornado in San Cris-

tobal which damaged public services and basic infrastructure in the city. These events have become more frequent in Venezuela during the last years.

In 2009, several extreme events occurred in Peru. On 11 April and 14 April, precipitation exceeded the monthly means in Jauja, Huayao, and Tarma. On 12 July, 25 cm of snow was observed in Tumayhuarapa and Pampachiri (Andahuaylas, Southern Highlands of Apurímac). On the first days of November, nine hours of continuous rainfall with winds of 50 km hr^{-1} were reported in Nauta-Iquitos (Northern Amazonia).

2) Tropical South America east of the Andes—J. A. Marengo, J. Ronchail, J. Baez, and L. M. Alves

Countries considered in this section include: Brazil, east Bolivia, Paraguay, and north Argentina.

La Niña-like conditions were present in early 2009, followed by the development of El Niño patterns starting in June 2009. During June–September, sea surface temperatures were generally about 1°C warmer than the long-term average across the central and eastern equatorial Pacific. Considering the summertime mean of the 2000–09 decade for the tropical region east of the Andes, this decade showed less rainfall (about 200 mm below normal) as compared to 1980–90 (about 350 mm above than normal), while air temperatures were 0.5°C to 2°C warmer. The annual mean temperature and total rainfall anomalies are presented in Figs. 7.11a and 7.11b, respectively.

(i) Temperature

Most of tropical South America east of the Andes experienced a warm 2009 austral summer, with maximum temperatures 3°C to 4°C warmer than normal in the South American monsoon area in southeastern Brazil and in the coastal region of northeast Brazil. Likewise, warm summer conditions (1°C to 2°C above normal) were observed in central and eastern Amazonia and eastern Paraguay. In April, mean temperatures were about 3°C–4°C above normal over western Paraguay and northern Argentina, with maximum temperatures reaching 5°C higher than normal in Paraguay. Average temperatures during May were about 2°C above normal in central Amazonia, northern Paraguay and eastern Bolivia.

In June, cooler-than-normal conditions (anomalies of -0.5°C to -1°C) were observed in southern and southeastern Brazil, and some sectors of western Amazonia, due to an episode of cold air intrusion. Maximum/minimum temperatures in southern Brazil were 2°C–3°C cooler than normal, and frost was reported in the elevated regions of southern Brazil.

The cooling was also observed in Paraguay, where minimum and maximum temperatures were about 4°C and 1°C below normal, respectively.

In July, cold temperature anomalies were detected in eastern Amazonia, northeast Brazil, southern Paraguay, and northern Argentina. Minimum temperatures were 3°C colder than normal in southern Brazil and in some regions of southeastern Brazil and western Amazonia and 4°C colder than normal in southern Paraguay. This cooling was due to a cold front penetration during late July. In the city of São Joaquim, state of Santa Catarina in southern Brazil, temperature reached -6.2°C on 24 July. Cold temperature anomalies also persisted over southern Paraguay. On the other hand, warm temperature anomalies (1°C–3°C) were detected in central and southeastern Brazil and over the Amazon region.

In August, most of tropical South America east of the Andes was about 1°C–2°C warmer than normal. In September, the eastern coast of northeast Brazil was about 3°C warmer than normal, while the rest of the tropical region was 1°C–2°C warmer than normal.

October temperatures across most of tropical South America were 1°C above normal, with the largest warming over Amazonia and southeastern Brazil. In November, temperatures were warmer than normal in southern and southeastern Brazil and western Amazonia. The largest warming was detected over northern Paraguay where the mean temperatures were 4°C–5°C warmer than normal. In December, temperatures in most of tropical South America east of the Andes were 1°C–2°C warmer than normal, especially over northern and eastern Amazonia and southeastern Brazil. In some regions of southeastern Brazil, temperatures were 4°C warmer than normal during the second week of December.

(ii) Precipitation

Most of the austral summer and fall months were characterized by episodes of intense rainfall and floods in large cities such as Sao Paulo and Rio de Janeiro, as well as in most of tropical South America, north of 5°S. This was due to the presence of the South Atlantic Convergence Zone (SACZ). Northwestern Amazonia observed more than 200 mm above normal. This intense rainfall was the main cause of the record high levels of the Rio Negro River in Manaus in July (see sidebar), the highest level in 107 years of measurements. Northeast Brazil was also severely affected by heavy rainfall and flooding in April and May, otherwise the dry season was predominant in that region.

EXTREME RAINFALL AND THE FLOOD OF THE CENTURY IN AMAZONIA 2009—JOSE. A. MARENGO

During the austral summer and winter 2009, the Amazon basin, drained by the Amazon River and its tributaries, was hit by heavy flooding. This year the water level rose higher and stayed longer than it has in several decades. According to national and international press, almost 376 000 people were left homeless and 40 died because of the floods. The communities living on the river banks and on the urban areas of cities like Manaus suffered the impacts of the rising waters, and the floods affected the exotic wildlife and the endangered species. Damages were estimated on the order of $200 million U.S. in the Brazilian state of Amazonas.

FIG. 7.12. (a) December 2008 to February 2009 rainfall anomalies and (b) February to May 2009 rainfall anomalies (% relative to 1961–90). (Source: CPTEC/INPE.)

During the summer (December 2008–February 2009), above normal rainfall was found in the entire Amazon region (Fig. 7.12a), reaching 100% above normal in northern and western Amazonia, where the basin of the Rio Negro is located. Brazil's Center for Weather Forecasts and Climate Studies reported large rainfall anomalies during January and February 2009. During late summer and fall (Fig. 7.12b), rainfall in northern and central Amazonia was between 25% and 50% above normal, and the largest rainfall anomalies (up to +100%) were detected in the border region of eastern Amazonia and northeast Brazil. In central Amazonia, rainfall in April, May, and June was between normal and above normal. In the city of Manaus, during the first 15 days of June 2009 it rained almost 30 mm above the climatology for that month (117 mm).

According to the measurements of the State University of Manaus (UEA), the heavy rainfall of January–February in northwest Amazonia led to high water levels of the Solimões River at Tabatinga in March–April. The water levels reached 12.5 m, compared to the long-term climatology of 11.8 m. The water levels of the Rio Negro at Manaus and the Amazonas at Obidos reached high values a few months after. The level of Rio Negro at Manaus reached maximum values between May and July. The measurements at Manaus site reflected the contribution of the Rio Negro and, to some degree, the Rio Solimões that extend over Amazonia. It takes about four to five months for rain falling on the upper basin of the Rio Negro in northwest Amazonia to travel downstream to the Manaus gauge site. Therefore, the anomalously high levels measured during June and July were due to the intense rainfall that fell

during January and February over northwestern Amazonia and, to a lesser degree, to the intense rainfall in May and June over central Amazonia, where the rainfall takes one month or less to reach the gauge site at Manaus.

Historically, according to the Brazilian Geological Survey, the floods in Amazonia in 2009 show the highest levels in the history. In July, the level of the Rio Negro in Manaus reached 29.75 m, a new record high since the beginning of data collection in 1903. The five previous records observed in Manaus were: 29.69 m (1953; Fig. 7.13), 29.61m (1976), 29.42 m (1989), 29.35 m (1922), and 29.17 m (1908). Levels of the Amazon River at Óbidos and the Tapajos River at Santarem also showed records highs. Furthermore, the levels of the Amazonas, Marañón, Napo, and Corrientes Rivers in the Peruvian Amazon also experienced record level/discharge highs, according to the meteorological service of Peru (SENAMHI).
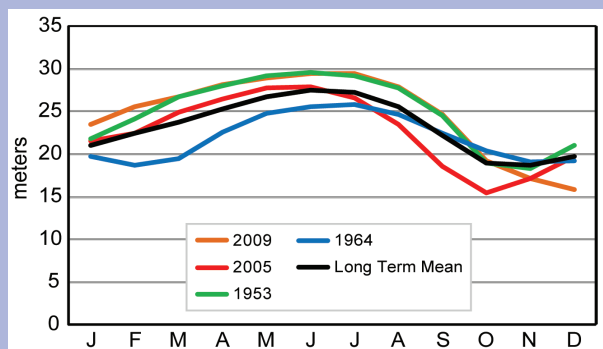
FIG. 7.13. Monthly mean water level of the Rio Negro in Manaus, Brazil, for some extreme years: dry (1964, 2005), wet (1953, 2009), compared to the 1903–86 average. (Source: CPTEC/INPE.)

During the austral fall, northeastern Brazil, Amazon region, and northern Bolivia observed normal rainfall. The largest anomalies were observed on the border between eastern Amazonia and northeast Brazil, with rainfall anomalies greater than 100 mm per month until June, which normally marks the beginning of the dry season. The ITCZ was intense. In some places in the Amazon, rainfall was 300 mm above normal. In the Peruvian Amazonia, the river levels were about 1 m–2 m above normal. In northeast Brazil, 49 deaths occurred as a consequence of floods. More than 408 000 were left homeless and damages to highways and irrigation structures were reported. In May, eight people died because of the breaking of a small dam in the state of Piauí in Northeast Brazil, and 600 families were forced to leave their houses. The estimated losses due to the floods in Brazil until July were about $800 million U.S. On the other hand, during April, a severe drought was reported in Paraguay, with negative precipitation anomalies around -160 mm in the south of the country. This represents a new historical record minimum precipitation for that month.

During the spring (September–November), when the rainy season normally starts, anomalously wet conditions were reported in most of southeastern South America, causing floods in Paraguay, where thousands of people were forced to evacuate along the Paraná River. The anomalously wet conditions detected over most of this region affected the harvest of rice and other vegetables.

In November, while extremely large rainfall anomalies were detected over Uruguay, southern Brazil, southern Paraguay, and northern Argentina, dry conditions were reported on the coast of Ecuador and the South American monsoon region. In the same region, the last two weeks of November were characterized by dry weather and relative humidity of about 15%. In December, very wet conditions (rainfalls of 100 mm–150 mm above normal) were reported in southeastern Brazil and northern Paraguay. Intense rainfall and landslides in the city of Angra dos Reis, Rio de Janeiro, killed 53 people on New Year's Eve, and intense rainfall episodes were detected in most of southeastern South America in December. From 31 December 2009 to 1 January 2010, the total rainfall was 275 mm in Angra dos Reis. The cities of Cochabamba, Chuquisaca, Tarija, and Santa Cruz in Bolivia were affected by floods, forcing more than 10 000 families into food insecurity. During the last three months of 2009, rainfall was below normal in Northeast Brazil.

3) SOUTHERN SOUTH AMERICA—M. Bidegain, M. Skansi, O. Penalba, J. Quintana, and P. Aceituno

Countries considered in the section are Chile, Argentina and Uruguay. The annual mean temperature and total rainfall anomalies for Southern South America are in Figs. 7.11a and 7.11b, respectively.

(i) Temperature

In Argentina and Uruguay, above-normal temperature was observed during austral autumn (MAM), with mean anomalies ranging from +0.5°C to +1.5°C. Anomalies from +2.0°C to +3.0°C in west-central Argentina during these months led to the warmest austral autumn over the past five decades. In contrast, the austral winter (JJA) brought cold conditions. For instance, the mean temperature in July was more than 3°C below normal in northeastern Argentina, southern Paraguay, northern Uruguay, and southern Brazil. July 2009 was the second coldest July of the past 50 years (after July 2007) for many locations in Uruguay and Argentina. In August, monthly mean temperature anomalies greater than +1.7°C were reported in northern Argentina and Uruguay, and anomalies greater than +1.4°C were found in November. During the spring (SON), positive anomalies were observed in the north and northwest of Argentina, where record high values were registered with respect to the last 50 years. In contrast, negative temperature anomalies on the order of -2°C characterized the climate of the Patagonia region during this season although the annual mean temperature remained from +0.5°C to +1°C above the climatological mean.

In Chile, very large anomalies, both positive and negative, characterized the temperature regime during 2009. The daily maximum temperatures during the austral summer were well above the climatological average, with mean anomalies of +2.3/+3.0 standard deviations for January/March, defining new records since 1914 at Santiago (33°S) and since 1961 for the region between 33°S and 37°S (Fig. 7.14). This behavior, associated with an anomalously intense subtropical anticyclone in the SE Pacific, persisted in the fall when anomalies close to +3.0°C were reported for the April mean daily maximum temperature in this region. In contrast, the 2009 austral spring (SON) was the coldest in the past 50 years in the region south of 37°S due to a large frequency of incursions of cold air masses from higher latitudes. This was particularly extreme during November, when anomalies from -2°C to -4°C were reported for the mean daily maximum temperature at stations between 35°S and 53°S, damaging the fruit ripening process in central Chile.
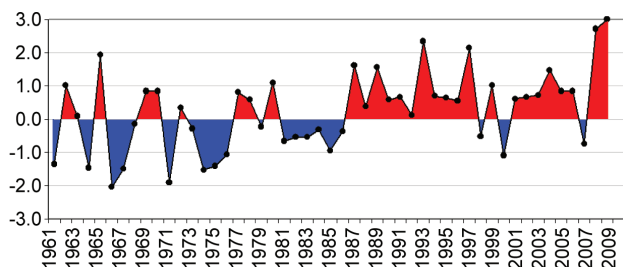
FIG. 7.14. Composite for standardized mean anomaly of daily maximum temperature along the subtropical west side of South America (Central Chile) for January–March, based on measurements at Santiago (33.5°S), Curicó (35.0°S) and Chillán (36.6°S). Standardization was done using 1971–2000. (Source: Dirección Meteorológica de Chile.)

(ii) Precipitation

During the first half of 2009, the exceptionally low precipitation in southeastern South America was driven by a La Niña episode, which began during the last quarter of 2007 and prevailed through 2008. La Niña gradually weakened during the first half of 2009. The positive SST anomalies that returned to the tropical Pacific Ocean by the middle of the year favored strong positive rainfall anomalies in southeastern South America during October–December 2009.

Large parts of eastern Argentina, Uruguay, Paraguay, and southern Brazil experienced a prolonged and intense drought during the first half of 2009, which caused severe damage to many socioeconomic sectors (agriculture, cattle farming, and hydro power generation). These conditions exacerbated the severe water shortage for the summer crops (soybean, maize, and rice) and pastures.

In particular, in Uruguay the mean rainfall deficit reached -20% during January– June, with values of -39% reported for the stations of Salto and Melo. In northern and northeastern Uruguay, rainfall returned to normal conditions in September. Exceptionally wet conditions followed in November, when monthly rainfall reached 613 mm in Artigas and 540 mm in Rivera (more than four times the monthly average) (DNM 2009). This heavy precipitation explains the fact that, although all months from January to August were drier than normal, the year ended with a positive rainfall anomaly of +31% in Uruguay.

In Argentina, the cumulative rainfall during 2009 was predominantly below the 1961–90 average. Deficits larger than -40% were observed in the Cuyo region, northeast of Patagonia, southeast of La Pampa, and north of Cordoba. In some cases the annual rainfall was the lowest since 1961. For example, the 369.1 mm measured at Pilar beat the previous record of 514.8 mm in 1962. Regarding anomalous wet conditions, above-average rains were registered in the northeast and east portion of the country (Iguazú +142% and +Gualeguaychú 149%) and also in the extreme northwestern territory and southern Patagonia (Bariloche +130%).

As in Uruguay, rains were markedly deficient in almost all the Argentinean territory until spring, giving continuity to an extremely dry period that had persisted since 2008, with important consequences for agriculture and livestock, water resources, and even some towns that had no water for consumption.

In spite of the El Niño conditions that persisted in the equatorial Pacific since May 2009, winter (JJA) rainfall in central Chile was near the climatological average, although it was characterized by a considerable intraseasonal variability at the monthly scale with May, July, and September being anomalously dry and June and August being anomalously wet. On the other hand, large-scale circulation anomalies linked to El Niño contributed to rainfall anomalies above +40% that were observed in the region 39°S to 46°S during the spring (SON).

(iii) Notable events in Argentina

The severe rainfall deficit of 2008 continued during almost all of 2009, mainly in the humid pampa and the west-central region. This reduction of rainfall not only affected the agriculture and cattle ranching, but also the lagoons and lakes.

On 2 February, a severe storm with heavy rains, high winds, and hail killed a dozen of people in the city of Rosario (second largest city in Argentina). On 8 February, local intense rain events generated landslides in Tartagal, Salta Province, northwestern Argentina, with 500 people evacuated and two deaths.

Between 21 and 23 July, a snowfall episode affected almost half the country, reaching an unusual intensity in some areas (south of Buenos Aires, La Pampa, and the eastern portion of Rio Negro).

During August, intense and persistent rainfall and snowfall episodes affected the western part of Mendoza and the provinces of Neuquén, Chubut, and Rio Negro (western and northwestern Patagonia Cuyo). During the same month, significant fires hit central Argentina (Cordoba and San Luis). A combination of lack of rainfall, high temperatures and strong winds made it difficult to control them.

During the night of 7 September, a category F4 Tornado hit the district of San Pedro, leaving 10 people dead and 17 severely injured.

Portions of northern Uruguay, southern Brazil and northeastern Argentina experienced significant positive precipitation anomalies during November (Fig. 7.15). Northern and western Uruguay, Rio Grande do Sul (state in Brazil), and Entre Rios (province in Argentina) felt the impacts of the flooding that affected all cities along the lower basin of Rio Uruguay River. Estimates indicated that more than 5000 people were evacuated from Uruguay alone.

November 2009 was the wettest November in the last 30 years, since the Salto Grande dam was built (Fig. 7.16). Overall, more than 350 mm of rain felt in the region between 25°S-35°S and 50°W-60°W. The monthly average is 150 mm, but in some places the record exceeded 600 mm.

The National Institute of Meteorology of Brazil (INMET) and the National Institute for Space Research (INPE) reported that the November precipitation surpassed 400 mm at 19 meteorological stations of Rio Grande do Sul State, and average rainfall in all states was about 300 mm above normal. In Sao Luiz Gonzaga, the rainfall was 640 mm while the historical monthly average was 154 mm, a record for November since observations began in 1912.

FIG. 7.15. November 2009 rainfall (mm) in Southeastern South America. (Source: CPTEC/INPE.)
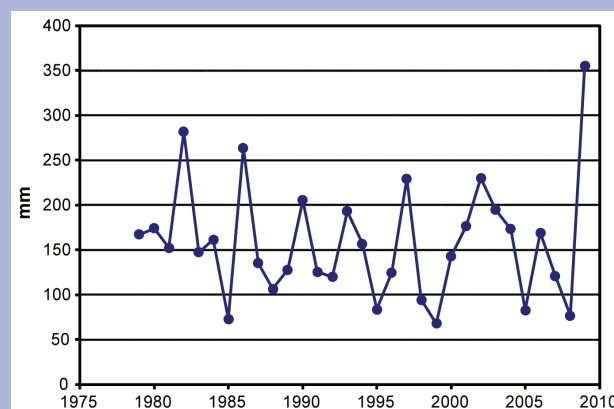
FIG. 7.16. November mean rainfall for Southeastern South America, 1979–2009. (Source: GPCP.)

In November, there were exceptional rains in eastern Argentina, causing flooding and high levels of the Parana and Uruguay rivers. In many cities located over Rio Uruguay, people were evacuated (more than 5000 in Uruguay and 15 000 in Argentina. Excesses as large as 200% of normal rainfall and associated floods affected the southern and northern part of the Buenos Aires province (Gualeguaychú +334.8%, Laboulaye +246.8%, Junin +210.7%.), with the precipitation registered at Gualeguaychú (430 mm) and Laboulaye (377 mm) being the largest since 1940. San Antonio de Areco in the northern part of the province of Buenos Aires was the city with the most damage and evacuees.

e. Africa

1) NORTHERN AFRICA—K. Kabidi, A. Sayouri, S. Rachid, S. M. Attaher, and M. A. Medany

Countries considered in this region include: Morocco, Algeria, Tunisia, and Egypt.

(i) Temperature

In northwest Africa (Morocco, Algeria, and Tunisia), the annual mean temperature was mainly above normal in 2009, with the anomalies between +0.4°C and +2.5°C. Winter and autumn were exceptionally cold over the region with monthly mean minimum temperatures 0.1°C to 3°C below normal. January anomalies of -2.0°C and -2.2°C were found in Algeria and Morocco, respectively. Spring temperature
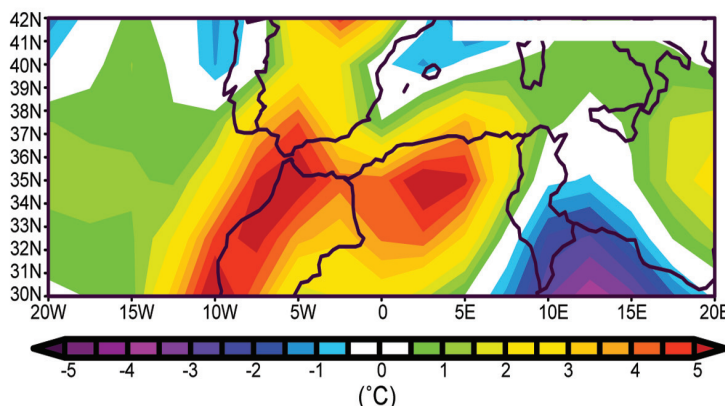
FIG. 7.17. Daily maximum temperature anomalies (°C) on July 21st 2009 for northwest Africa (based on 1968–96). (Source: NOAA/ESRL.)

reached 1.5°C above average over most parts of Morocco; the temperature ranged from 7°C in the north to 23°C in the south. During the summer, exceptional heat waves occurred. The monthly mean temperatures exceeded the normal; for example, the anomaly was +2.4°C in Tetouan in July. On 21 July, the daily maximum temperature reached between 47°C and 50°C in the Saharien City, Maskara in Algeria, Agadir, Tiznit, and Tan Tan in Morocco (Fig. 7.17).

In Egypt, 2009 can be described as a year with more stable and moderate weather than the previous years, with less temperature fluctuations and extreme events. For the 2000–09 decade, the annual mean temperature of Egypt remained above the normal by about 1.1°C. Fig. 7.18 shows a continued increasing trend from 1975. Only two years were below the average, 1982 and 1983. The warmest and second warmest years were 2008 and 2005 with anomalies of +1.9 and +1.7°C, respectively.
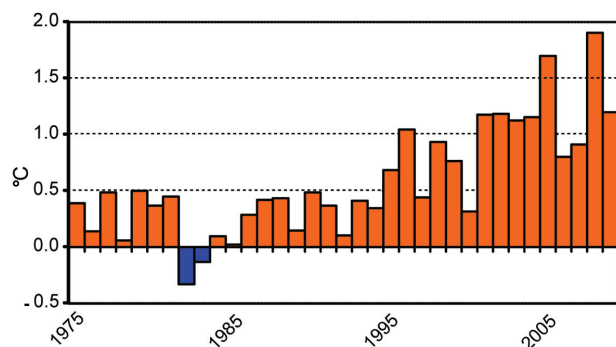
(ii) Precipitation

In northwest Africa, **annual 2009 pre**cipitation was near normal to above normal. Large positive deviations also occurred in some regions and seasons, especially during the winter 2008/09 and the beginning of winter 2009/10, where rainfall was between 45% and 280% of average for most locations. Precipitation records during December 2009 represented 31% of the annual total. Many weather stations in Morocco, Algeria, and Tunisia reported rainfall exceeding 150 mm in less than 24 hours. Heavy storms that occurred from 20 to 25 December produced heavy rains causing floods. Rainfall amounts up to 200 mm in 48 hours were recorded, especially in the extreme north of Morocco. For example, Chefchaouen City recorded 834.9 mm in December for which the monthly normal is 265.4 mm (calculated from 1994 to 2000). The fall was variable spatially and temporally, but overall it was wetter than normal; October and November were considerably below average but September total rainfall exceeded the monthly mean by more than +800% in some areas of Morocco (for example in Rabat). In Tunisia, more than 90 mm was recorded in less than four hours at Zarzis, Gribis, and Souihel during the same month. Spring and summer were characterized by reduced rainfall activity over most of northwest Africa reaching more than 90% deficit, especially in August due to anticyclonic conditions.

In Egypt, the annual number of rainy days and the annual total precipitation for 2009 were near the historical average (based on 1961–90). The relative humidity was also around the historical average, with a variation range of ±5%.

(iii) Notable events

The year 2009 was characterized by heavy rainfall events, especially during winter, that affected Algeria, Tunisia, and Morocco. These events caused important infrastructure damages and human life loss in many cities and villages when many daily rainfall records for September and December were broken. Record wind speeds also occurred; for example, 140 km hr^{-1} in Khouribga City in May and 115 km hr^{-1} in Tangier in December. Several forest fires occurred in July and August, especially when the daily temperature exceeded 50°C for some locations in Algeria and 49°C in Morocco.

FIG. 7.18. Annual mean temperature anomalies (based on 1961–90) for Egypt, 1975–2009. (Source: Egyptian Meteorological Authority.)

2) Western Africa—L.N. Njau and W.M. Thiaw

Western Africa is the region which extends from the Guinea coast and Côte d'Ivoire to Chad and the Central African Republic. The year was characterized by above-normal rainfall in the extreme western region, while dry conditions were found in the Côte d'Ivoire and Gabon areas.

(i) Temperature

January 2009 temperature anomalies (based on 1971–2000) were above normal with anomalies greater than 3°C in eastern Niger, western Chad, and part of northern Nigeria. The positive temperature anomalies continued in February, with anomalies greater than +3°C covering most of Niger, eastern Mali, northern Burkina Faso, and all of northern Nigeria. From March to June, the positive temperature anomalies decreased and became near normal in July, August and September. In October, the temperature once again became much above normal with anomalies reaching above +3.5°C over northern Niger. In November and December, the positive temperature anomalies continued over most of Western Africa. At Bilma, located in northern Niger, monthly mean temperatures were above normal for every month of the year (Figure 7.19). Negative temperature anomalies were almost nonexistent in the region, except in January when significant negative anomalies (less than -1.5°C) were observed over south Mauritania, western Mali, northern Guinea and Senegal.

(ii) Precipitation

In Western Africa, the rainfall anomalies (based on 1971–2000) showed significant deficits in April and May over Guinea, Liberia, southwest Côte d'Ivoire, and south Mali. In contrast, excessive rainfall was recorded over southeast Ghana, south Togo, southwest Benin, and parts of the central African countries. In June, rainfall deficits were observed over Guinea while heavy rains and floods hit most of the coastal settlements in the subregion.

In July, the Sahel rainfall increased with peaks ranging from150 mm–300 mm over western Senegal, the Gambia, and Guinea Bissau. The eastern Gulf of Guinea and northwestern part of the central African countries had a rainfall increase, with peaks ranging from 300 mm–400 mm over Nigeria and Cameroon.

In August, the peak rainfall for the Sahel ranged from 300 mm–400 mm over Burkina Faso, southern Mali, and southern Chad, intensifying to about 700 mm over Senegal and the Gambia and resulting in flooding. The southern Gulf of Guinea had a rainfall deficit. Above-normal rainfall was observed over the central African countries with peaks ranging from 300 mm–500 mm, intensifying to about 600 mm over Guinea Bissau, Guinea, and Sierra Leone.

In September, the rainfall in the Sahel generally decreased, but high accumulations ranging from 250 mm–500 mm were observed over central Burkina Faso, southern Mali, and Senegal. The Gulf of Guinea countries observed, similarly, a general decrease in rainfall, but observed high amounts of about 400 mm over Guinea Bissau, Guinea, and Nigeria spreading over parts of the central African countries.

Compared to the base period 1971–2000, July, August, and September 2009 had significant positive rainfall anomalies with severe rainfall deficits over most of the Gulf of Guinea countries and central African countries (Fig. 7.20). Positive rainfall anomalies were found in September with the maximum amount observed over south Mauritania, Senegal, Gambia, and central and western Mali.

(iii) Notable events

According to UN Integrated Regional Information Networks (IRIN) 9 October report, more than 60 schools in Senegal were flooded due to the heavy rains in July, August, and September. The spokesperson for Senegal's Interior Ministry confirmed a $4.5 million U.S. emergency plan to pump out the water from flooded zones, rid standing water of mosquito larvae, and provide free health services at medical posts set up in affected areas.

3) Eastern Africa—C. Oludhe, L. Ogallo, P. Ambenje, Z. Athery, and W. Gitau

The Great Horn of Africa (GHA) region can be divided into three main sectors. The northern sector

Fig. 7.19. Monthly mean temperature in 2009 and 1961–90 average for Bilma, Niger. (Source: African Centre of Meteorological Applications for Development.)
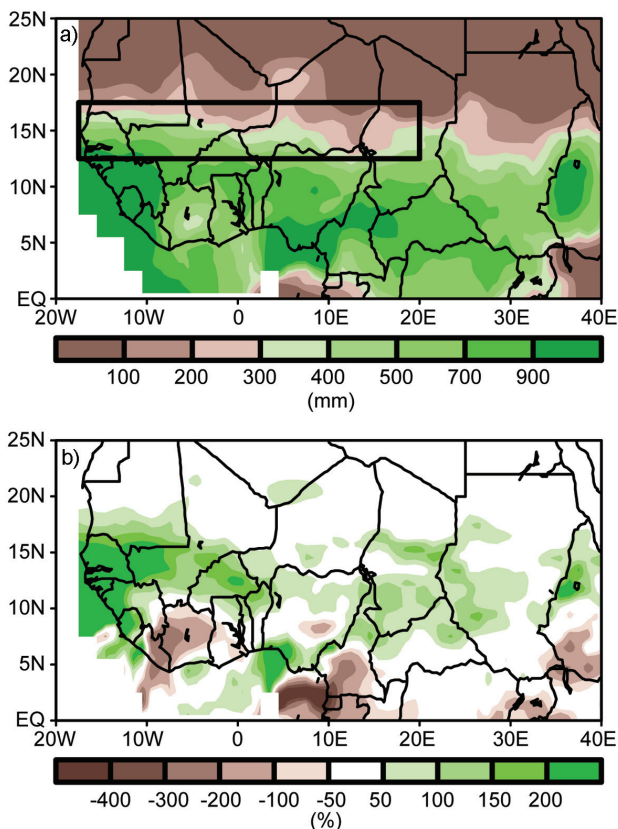
FIG. 7.20. (a) July to September 2009 rainfall (mm) for Western and Central Africa and (b) July to September 2009 anomalies (expressed as percentage of 1971–2000.) (Source: NOAA/NCEP.)

covers Sudan, Ethiopia, Eritrea, Djibouti, and northern Somalia; the equatorial sector includes Uganda, Kenya, Burundi, Rwanda, southern Somalia, and northern Tanzania; and the southern sector refers to central and southern Tanzania. The base period is 1961–90.

(i) Temperature

Overall, the temperature was warmer than average over most of the GHA. In June, the minimum temperatures were warmer than normal over western and northern Sudan; localized parts of western, central, and southern Ethiopia; coastal parts of Kenya; and eastern Tanzania. They were cooler than average only over a smaller area including central Somalia and southeastern Ethiopia. During the same month, the maximum temperatures followed a similar pattern; however, the below-average area was larger, extending to south Somalia and eastern Kenya. The patterns of above-average maximum and minimum temperatures in western and central GHA and of below-average maximum and minimum temperatures in the east were generally found throughout the year.

(ii) Precipitation

December to February marks the main rainfall season over the southern sector and the hottest season over the equatorial sector. During December 2008–February 2009, most of the northern and equatorial sectors received less than 75% of their long-term average (Fig. 7.21a). Isolated small areas over southern
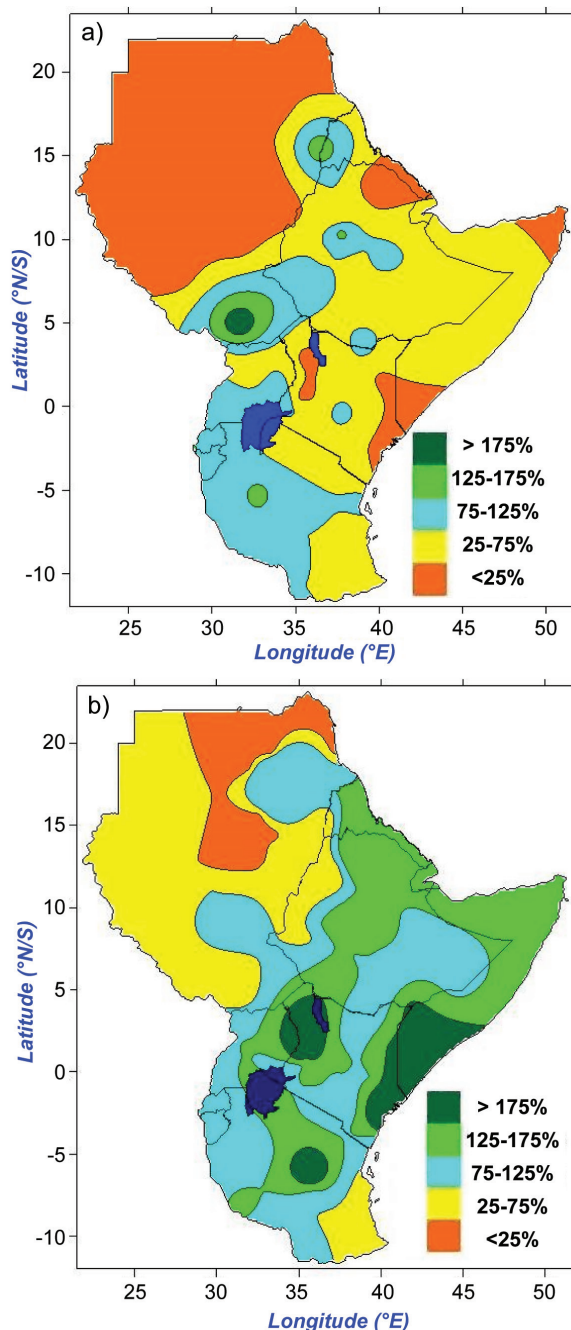
FIG. 7.21. (a) December 2008 to February 2009 rainfall anomalies and (b) October to December 2009 rainfall anomalies (expressed as percentage of 1961–90) for the Great Horn of Africa. (Source: ICPAC, 2009.)

and eastern Sudan, western and central Ethiopia, western Eritrea, central Kenya, and central Tanzania received more than 75% for the period.

March to May (MAM) is the main rainfall season over the equatorial sector. The onset of the MAM 2009 seasonal rainfall was rather late and the ending early. The western areas of both southern and equatorial sectors received 75%–125% of their long-term average. The rest of the GHA received less than 75% of their long-term average. The poor rainfall distribution resulted in crop failure and loss of livestock and wildlife due to drought conditions.

June to August is the main rainfall season over the northern sector and also the coldest period over the equatorial sector. The western parts of the equatorial sector received substantive rainfall over this period. The northern sector and northern parts of the equatorial sector received less than 75% of their long-term average. Localized areas over northern Uganda, northern and central Ethiopia, and central Sudan received near-normal precipitation.

September to December marks the second rainfall season (short rainfall season) over the equatorial sector. GHA, especially the equatorial sector, has one of the strongest climatic signals of ENSO events in terms of rainfall. The onset of ENSO for the short rainfall season was timely. However, over several locations, the distribution was not uniform with prolonged periods of dryness immediately followed by the onset of the rainfall season. Much of the GHA received between 75% and 125% of their long-term average, with eastern and northwestern Kenya, southern parts of Somalia, and central Tanzania receiving more than 175% of their long-term average (Fig. 7.21b). Episodic rainfall events towards the end of the period resulted in localized flooding in several parts of the central equatorial sector.

Fig. 7.22 compares the cumulative 10-day rainfall totals for 2009 with their long-term average. Neghelle, in southern Ethiopia, represents northern sector; Dagoretti, in central Kenya, represents equatorial sector; and Kigoma, in western Tanzania, represents the southern sector. The figure shows the rainfall deficit in the northern and equatorial sectors and adequate rainfall in the southern sector. The rainfall deficits resulted in cumulative climate stress which had both direct and indirect impacts on the climate-
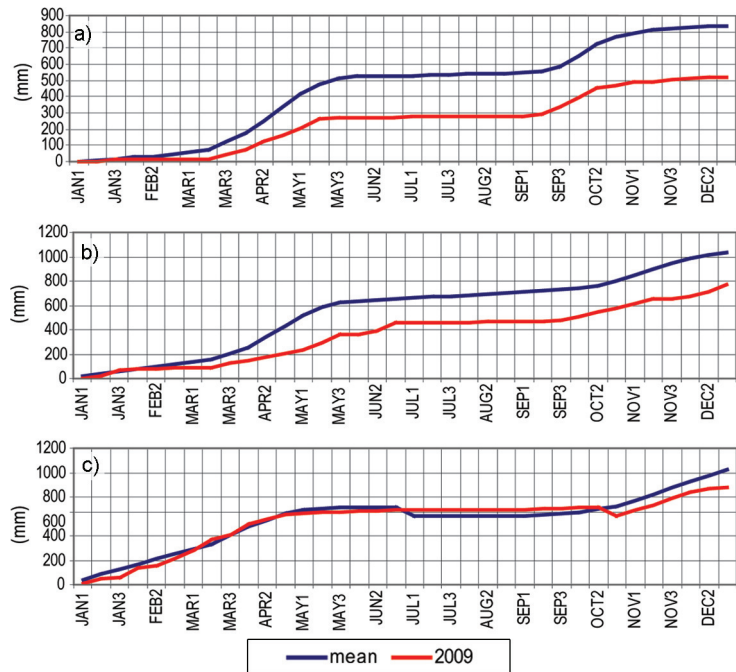
FIG. 7.22. Cumulative rainfall for (a) Neghelle, Ethiopia, (b) Dagoretti, Kenya and (c) Kigoma, Tanzania. (Source: ICPAC, 2009.)

dependent sectors. Such impacts that were observed in 2009 include loss of livestock due to inadequate pastures, crop failure resulting in food insecurity, scarcity of the water resources resulting in rationing of hydropower and limited water for domestic and industrial uses, poor health resulting from malnutrition, and contamination of the water sources among other socioeconomic challenges.

4) SOUTHERN AFRICA—A. Kruger, C. McBride, A. Mhanda, J. Banda, and W. M. Thiaw

This region includes the countries south of 15°S with more focus on South Africa and Zimbabwe.

(i) Temperature

For South Africa, the annual mean temperature anomalies for 2009, based on 27 climatological stations, was about 0.4°C above the reference period (1961–90). This made 2009 the 15th warmest year since 1961. Fig. 7.23 shows that the past 13 years were all above normal. For Zimbabwe, the temperatures were near normal with no records broken throughout the year.

(ii) Precipitation

The mean rainfall of South Africa is temporally and spatially very diverse. The main features are the fairly regular decrease in rainfall from east to west and also the marked influence of orographic features
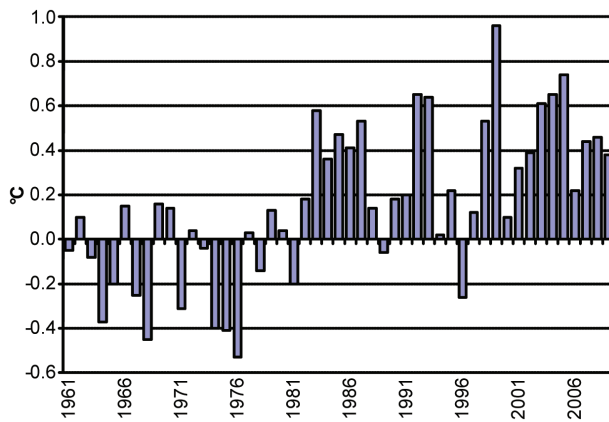
Fig. 7.23. Annual mean temperature anomalies (based on 1961–90) average over 27 stations in South Africa, 1961–2009. (Source: South African Weather Service.)

on the rainfall. The latter is most pronounced over the northeastern escarpment, the area around the northern border with Lesotho, and the southwestern and southern Cape. The average annual rainfall over the coastal plateau of the southwestern Cape is about 400 mm but in the mountains it ranges to more than 2000 mm in some locations. Although it is clear that there is a relationship between rainfall and elevation, other factors such as distance from the sea, rain-bearing winds, and type of rainfall (convective or frontal) also play a role.

The 2009 rainfall anomalies (Fig. 7.24) reflected the mean rainfall pattern, as most places in South Africa measured 75%–150% of the 1961–90 average. The most notable exception was the south and southeastern coast and adjacent interior, which received mainly less than 75% of its annual mean.
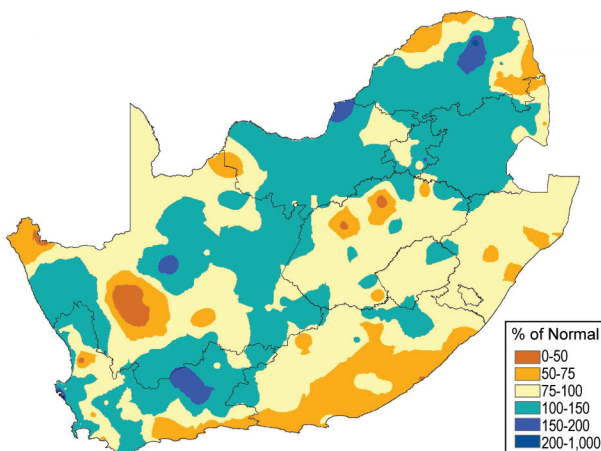
Fig. 7.24. Rainfall anomalies (expressed as percentage of 1961–90) for South Africa for 2009. (Source: South African Weather Service.)

For Zimbabwe, the rainfall season, from November 2008–March 2009, was characterized by normal to above-normal rainfall in most parts of the country. Rainfall amounts were generally moderate with no outstanding daily totals. The last two weeks of the season were very dry across the whole country. Overall, the December 2008–February 2009 rainfall anomalies for Southern Africa were near normal (Fig. 7.25).

(iii) Notable events

On 2 January, 45 families were left homeless when a storm accompanied by strong winds destroyed areas of Taung in the northwest. Villages that were affected include
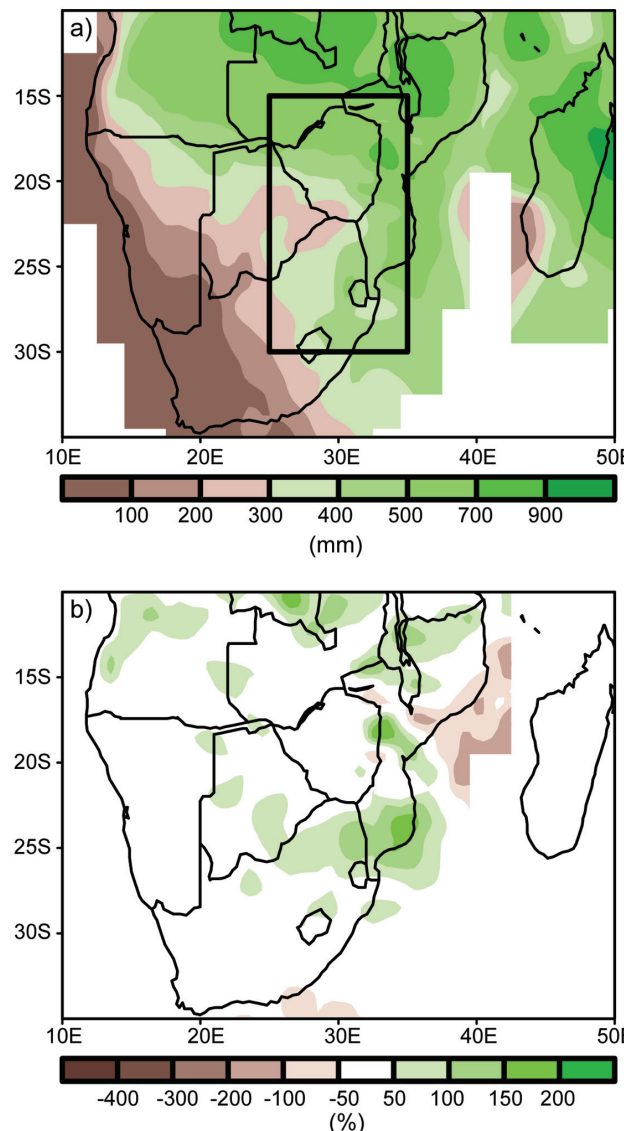
Fig. 7.25. (a) December 2008 to February 2009 rainfall (mm) for Southern Africa and (b) December 2008 to February 2009 anomalies (expressed as percentage of 1971–2000). (Source: NOAA/NCEP.)

Vergenoeg, Molelema, Kokomeng, and Longaneng. The storm left more than 500 people homeless and disaster management had to provide the affected families with blankets, mattresses, food parcels, and tents. The damage was estimated at more than R2 million ($264 000 U.S.).

A man died in his sleep when his mud hut collapsed on him during heavy rains at Mohlabaneng village in the Limpopo Province on 5 January, and 123 villagers were injured when their houses collapsed. Three hundred houses were destroyed and more than 1500 people were left homeless in the storm. The affected villages include Jamela, Mohlabaneng, Phaphadi, and Shawela.

Heavy rain that fell over the northern coastal areas of KwaZulu-Natal during the weekend of 7 March claimed the lives of at least five people and flooded hundreds of houses. KwaDukuza was also left without water after their water pumps and the pumps of the reservoir at Gledhow (which are used in emergency situations) were washed away. All rivers in the KwaDukuza area burst their banks causing extensive damage to houses in all 20 wards of the municipality.

Nearly 500 houses, affecting more than 1700 people in 28 informal settlements in Cape Town, were flooded during the weekend of the 16–17 May when the first of the annual Cape winter storms with intermittent rain and strong winds hit the Western Cape. Swells of about nine meters also occurred along the coastal regions.

Thousands were left homeless after heavy rains on 12 July caused flooding in the Western Cape, while rock- and mudslides caused damage to the infrastructure. The Lourens River in Strand and the Liesbeek River outside Cape Town burst their banks adding to the flooding problem. The Cape Flats seemed to be worst hit with people from 20 informal settlements having to be housed in community halls. About 9000 people from 2500 shacks were left homeless but there were no injuries reported. In Grabouw, 143 people had to leave their flooded homes while about 19 families from Jamestown and about 25 families near Cloetesville in Stellenbosch had to be evacuated because of rising flood waters.

Kimberley was hit by two heavy storms on 3–4 November causing extensive damage to houses, cars, and businesses; uprooting trees; ripping off roofs; and flooding several streets. The storms struck across the Northern Cape, including areas of Barkly West, Kuruman, and Longlands. Hundreds of houses were flooded in Galeshewe and some were completely washed away as water ripped through the low-lying areas of these informal settlements. An ecological disaster occurred at the swamped Kamfers Dam outside Kimberley where the third breeding season of the small flamingos started about a month earlier. Hundreds of both chicks and eggs were lost. This is one of four breeding spots in Africa and one of six in the world.

Hundreds of families were left homeless after heavy rains accompanied by golf ball-sized hail and strong winds affected Newcastle in northern KwaZulu-Natal on 11 December. Another storm hit the area seven days earlier and left 300 homes flattened. Six hundred families were left homeless after roofs were blown away, trees uprooted, and livestock destroyed in a damage estimated at millions of rands (hundreds of thousands of U.S. dollars). The municipality provided the victims with tents and food parcels. There were no injuries or deaths reported in both the storms.

5) WESTERN INDIAN OCEAN COUNTRIES—L. A. Vincent, E. Aguilar, M. Saindou, A. F. Hassane, G. Jumaux, D. Schueller, P. Booneeady, R. Virasami, L. Y. A. Randriamarolaza, S. Andrianiafinirina, V. Amelie, and B. Montfraix

The analysis for the Western Indian Ocean countries is included for the first time in the *State of the Climate* report. This region is made of many islands grouped into five countries, namely République des Comoros, République de Madagascar, Republic of Mauritius, La Reunion (France), and République des Seychelles. Overall, the 2009 land surface temperature was well above normal (relative to 1971–2000) at most locations (Fig. 7.26a), while precipitation was generally near or slightly below normal (Fig. 7.26b).

(i) Temperature
In Comoros, the 2009 temperature was above normal every month with the exception of April when it was slightly below normal; the annual anomaly was +0.4°C. For Madagascar, the monthly mean temperatures were also near normal to above normal resulting in an above-normal annual mean temperature across the country (Fig. 7.27a). The highest monthly anomaly was +2°C observed in the northwest in October. The April temperature was also slightly below normal with a departure of -1.1°C in the south highlands. For the Republic of Mauritius, the 2009 temperature was above the 1971–2000 average by 1.0°C for Mauritius, 0.8°C for Agalega, and 0.6°C for Rodrigues islands. Every month stayed above normal at these locations except for Rodrigues when the temperatures were slightly below normal from July to September. For
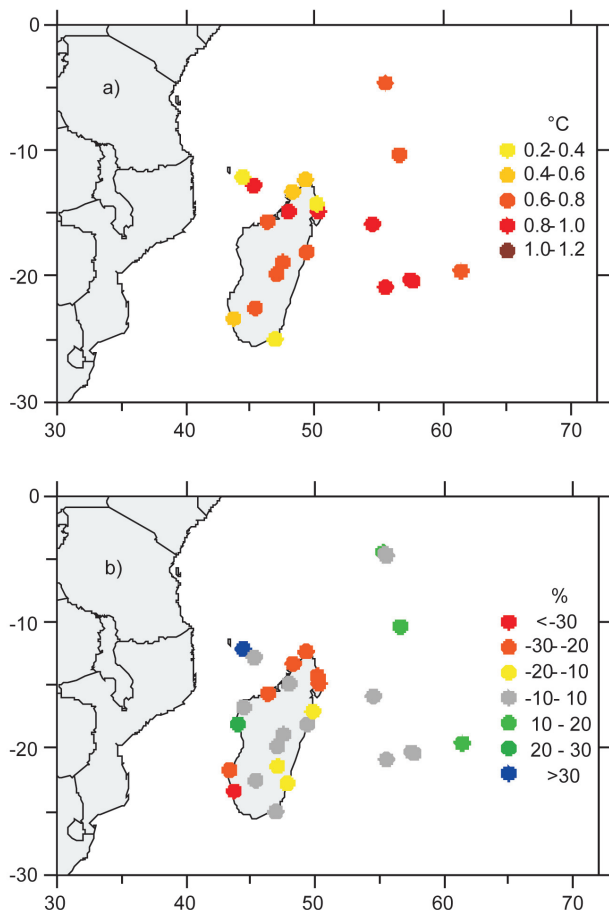
Fɪɢ. 7.26. (a) Annual mean temperature anomalies (°C; based on 1971–2000) and (b) annual precipitation anomalies (% of 1971–2000) for the countries of the Western Indian Ocean for 2009. (Source: Météo Nationale Comorienne, Service Météorologique de Madagascar, Météo-France, Mauritius Meteorological Services and Seychelles National Meteorological Services.)
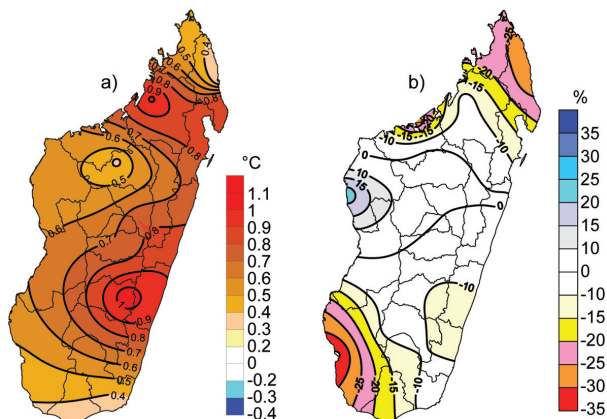
Fɪɢ. 7.27. (a) Annual mean temperature anomalies (°C; based on 1971–2000) and (b) annual precipitation anomalies (% of 1971–90) in Madagascar for 2009. (Source: Service Météorologique de Madagascar.)
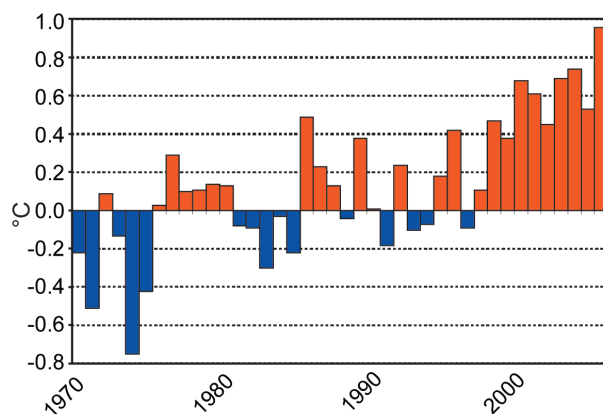
Fɪɢ. 7.28. Annual mean temperature anomalies for La Reunion (average of 10 stations observations), 1970–2009. (Source: Météo-France.)

La Reunion, 2009 was the warmest year since 1970 (Fig. 7.28) with an anomaly of +0.95°C (+0.84°C for minimum temperature and +1.07°C for maximum). Fig. 7.28 shows that the temperature has been above the 1971–2000 average for 10 consecutive years, with 8 of the warmest 10 years occurring in the last decade. For Seychelles, above-normal temperatures occurred every month with the exception of February. The annual anomaly was +0.6°C.

(ii) Precipitation

For Comoros, the 2009 annual total anomaly was +41.2% even though rainfall was below normal for nine months. April was very wet, as more than 1700 mm of rain was observed in 23 days. For Madagascar, the annual total was mainly near normal while some small regions in the north and south had below-normal precipitation (Fig. 7.27b). The accumulated annual rain over Mauritius, Agalega, and Rodrigues islands was near normal or slightly above normal. However, October 2009 was the wettest October on record in Mauritius with 250% of the long-term average (1971–2000). For La Reunion, the annual anomaly was +10% over the island (13th wettest year since 1970) although a contrast of -19% in the west to +53% in the southeast was observed. April was also a very wet month in La Reunion. The annual total precipitation was generally near normal for Seychelles.

(iii) Notable events

April 2009 was marked by significant heavy rainfall in Comoros, Madagascar, Agalega (part of Republic of Mauritius), and La Reunion. This was due to Tropical Storm Jade, which appeared on 5 April. Wind gusts of 170 km hr^{-1} were observed on the east coast of Madagascar and heavy precipitation led to

several floods. More than 100 houses were flooded in southeast La Reunion.

Heavy precipitation was also observed in July in Comoros and Seychelles. Although it brought landslides and flooding in Seychelles, the rain was a relief for the country since it was experiencing very dry conditions and government-imposed restrictions on water use. The increase in precipitation was associated with an easterly wave which brought more than 150 mm of rain over a time period of 12 hours. This type of weather is rare in Seychelles.

f. Europe

1) Overview—A. Obregón, P. Bissolli, J. J. Kennedy, and D. E Parker

Widespread anomalous warmth affected much of continental Europe in 2009. The annual-average land surface air temperature anomaly from the CRUTEM3 dataset (Brohan et al. 2006), relative to 1961–90, was +1.05[1]±0.07°C for the European region (35°N–75°N, 10°W–30°E). This ranked 2009 as between the third and tenth warmest year since 1850, with a nominal ranking of seventh. Notably, 2000–09 was the warmest decade on record for Europe, with an anomaly of +1.0±0.12°C, significantly warmer than previous decades (1990s: +0.58±0.11, 1980s: +0.06±0.10).

The highest temperature anomalies of 2009 were recorded in the Mediterranean countries, Eastern and parts of Central Europe, Fennoscandia (Norway, Sweden, Finland) and the Arctic region (including Iceland and Greenland), all with annual mean temperature anomalies in the range from +1°C to +2°C (Fig. 7.29). Svalbard (Arctic Norway), which has recorded the highest anomalies in greater Europe in recent years, again exceeded +2°C.

Total precipitation for the year 2009 (Fig. 7.30; Schneider et al. 2008) was above average over most of Eastern and Southeastern Europe, Ireland, northern and southern parts of the UK, Iceland, and in parts of Fennoscandia. It was particularly wet in Austria, where new record annual precipitation totals were set in several places, and in Belarus. Drier-than-average conditions occurred over the Low Countries (Neth-

erlands, Belgium, and Luxembourg), western parts of Germany, much of France and central parts of England, where totals were 80%–100% of normal. Some smaller parts of Iberia, southern France, Scandinavia, Russia, the Middle East, and Greenland received rainfall totals below 80% of the long-term average over the year 2009.

The year commenced with below-average 500-hPa heights over Southern Europe and large positive anomalies over Fennoscandia and Russia (Fig. 7.31, DJF). This large-scale circulation mode is similar to the Eastern Atlantic/Western Russia pattern (Barn-

Fig. 7.29. Annual mean anomalies of surface air temperature in Europe and over the North Atlantic, 2009 (°C, 1961–90 base period), CRUTEM3 data updated from Brohan et al. 2006. (Source: UK Met Office.)
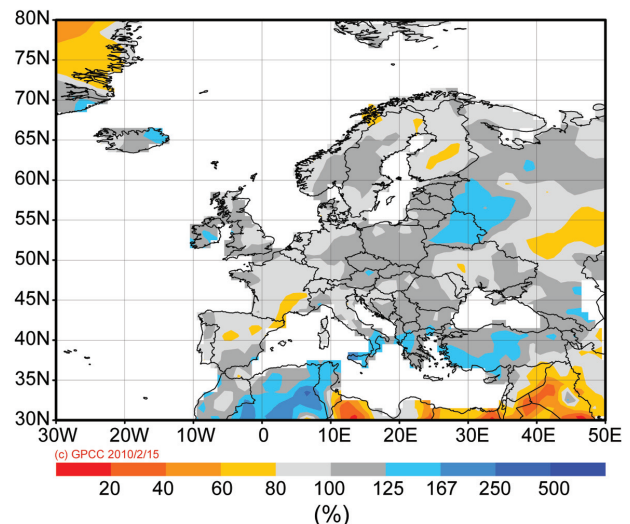
Fig. 7.30. European precipitation totals (% of normal, 1951–2000 base) for 2009. (Source: Global Precipitation Climatology Centre [GPCC], Schneider et al. 2008.)

---

[1] The standard reference period used for European averages is 1961–90 for temperature and 1951–2000 for precipitation, unless otherwise expressly identified.
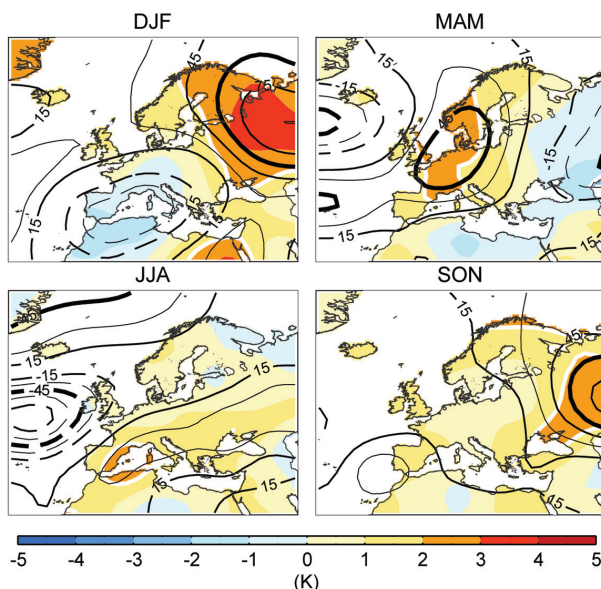
FIG. 7.31. Seasonal anomalies (1961–90 reference) of 500 hPa geopotential height (contour, gpm) and 850 hPa temperature (shading, K) using data from the NCEP/NCAR reanalysis. (DJF) winter (Dec 2008–Feb 2009), (MAM) spring (Mar–May 2009), (JJA) summer (Jun–Aug 2009) and (SON) autumn (Sep–Nov 2009). Black (white) thick lines highlight those geopotential height (temperature) contours with all the encircled grid points having absolute anomalies above their 1-sigma level of the base period.

ston and Livezey 1987). As a consequence, western and southwestern parts of Europe were significantly colder than normal (Fig. 7.32a), with monthly mean anomalies during January as low as -3°C in France and parts of Germany. Southern and Southeastern Europe experienced above-average precipitation (Fig. 7.33, DJF) and increased winter storm activity. In contrast, mild temperatures prevailed over Eastern Europe during winter 2008/09 with peak anomalies > +4°C in northwest Russia and Finland. Spring was very warm, particularly in Western and Central Europe (Fig. 7.32b), largely due to an anomalous ridge of high pressure which remained dominant throughout the season (Fig. 7.31, MAM). Temperature anomalies peaked during April, when they exceeded +5°C in places in Germany, Austria, and the Czech Republic (Fig. 7.34). Mean temperature records for April were broken in several locations.

Summer was also warmer than normal over Europe, though with smaller anomalies than spring (Fig. 32c). This was largely the result of a dipole pattern of near- to below-average 500-hPa height anomalies over the Atlantic and

Fennoscandia, and above-average 500-hPa heights over the Mediterranean and Southern Europe (Fig. 7.31, JJA). Consequently, above-average precipitation was observed across Northwestern Europe and Fennoscandia (Fig. 7.33, JJA), and above-average temperatures were observed across Southern Europe with anomalies exceeding +2°C in southern France and Spain (Fig. 7.32c). A heat wave affected Italy in July, with temperatures locally reaching 45°C, while Iberia also experienced several heat waves during the summer. Some stations in Norway reported new daily maximum temperature records. Western and Central Europe were affected by severe thunderstorms, accompanied by heavy rain and hail, causing local flooding.

Autumn temperatures were well above average across Europe, particularly in the central and eastern regions (Fig. 7.32d). Precipitation showed extreme temporal and spatial variation during autumn (Fig. 7.33, SON). Positive 500-hPa height anomalies across Northern Europe and a broad trough across Southern Europe during September (Fig. 7.31, SON) were associated with above-average temperatures across much of Europe and western Russia. Southern Europe and the Mediterranean experienced very high precipitation totals (Fig. 7.33, SON). October precipitation was exceptionally high in Eastern and Southeastern Europe, and October temperatures were low in Scandinavia and Northeastern Europe. During November, an extensive flow of marine air into the European continent resulted in generally above-average temperatures with the largest departures in Fennoscandia
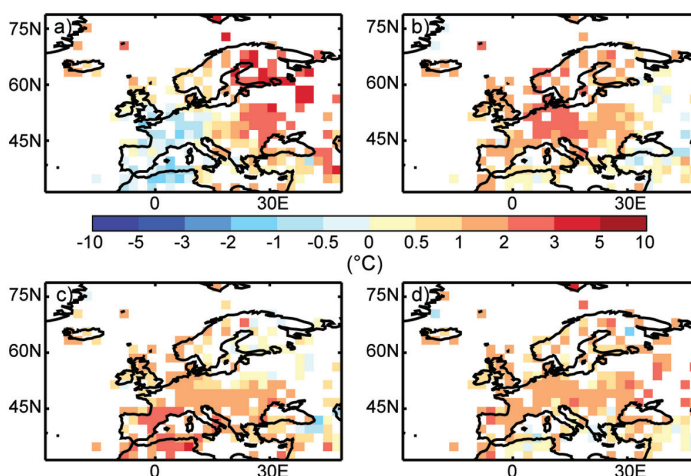
FIG. 7.32. European land surface air temperature anomalies (°C, 1961–90 base period), CRUTEM3 updated from Brohan et al. 2006. (a) December 2008 to February 2009; (b) March to May 2009; (c) June to August 2009; (d) September to November 2009.

DJF MAM

JJA SON

| 0 | 20 | 40 | 60 | 80 | 100 | 120 | 140 | 160 | 180 | 200 |
Percent
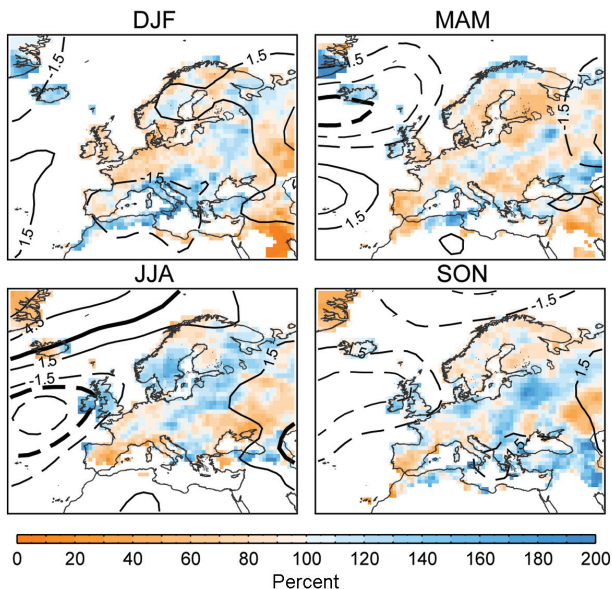
FIG. 7.33. Seasonal anomalies, with respect to the 1961-90 mean, of sea level pressure (hPa) from NCAR/NCEP reanalyses. Colored shading represents the percentage of accumulated seasonal precipitation compared with the 1951–2000 climatology from the seasonal GPCC precipitation data set (only values above 15 mm per season are represented). Thick black lines highlight those sea level pressure anomalies which are greater than one standard deviation above the mean.

and western Russia, where temperature anomalies exceeded +3°C. Increased cyclonicity led to well-above-average November precipitation, particularly in the northern half of Europe with new records set across Ireland and the UK.

The end of the year was characterized by an extremely negative phase of the Arctic Oscillation (AO) with high pressures dominating the higher latitudes of the Northern Hemisphere, affecting the weather in Europe. The AO Index in December 2009 was -3.4, the lowest value observed for that month in 60 years (Fig. 2.30b in Section 2d), with extremely negative values in the second half of the month. Most of Europe was under the influence of a strong high pressure system over the Arctic and Scandinavia that favored intense advection of cold polar air far into the middle latitudes (Trigo et al. 2004). The negative North American Oscillation index in December also contributed to a starkly contrasting temperature pattern over Europe. While Southeastern Europe and parts of the polar region (Greenland, Iceland, Svalbard) experienced mild temperatures—Greenland

was 7°C warmer than average—colder-than-average conditions prevailed over the northern half of Europe with heavy snowfall in places. The Scandinavian high pressure also caused a dry December in Northern Europe, while most of the rest of Europe, particularly the South, experienced a very wet end of the year.

2) CENTRAL AND WESTERN EUROPE—A. Obregón, P. Bissolli, J. J. Kennedy, and D.E. Parker

Countries considered in this section include: Ireland, the United Kingdom, the Netherlands, Belgium, Luxembourg, France, Germany, Switzerland, Austria, Poland, Czech Republic, Slovakia, and Hungary.

(i) Temperature

Annual mean temperatures in Central Europe were 1°C–2°C above the 1961–90 average throughout most of the region (Fig. 7.29). Over Western Europe, anomalies were mostly below +1°C.

Winter 2008/09 was the coldest in the UK since 1996/97. In France, it was the third coldest winter in 20 years. Severe cold waves during January and February brought temperatures below -25°C to Germany and Poland. The lowest recorded daily minimum temperature in 2009 in Poland was -28.2°C in the southwest of the country on 7 January. A private weather service station in Saxony, eastern Germany, recorded -29.1°C on the same day. In contrast, winter was warmer than average in the easternmost regions (Poland, Czech Republic, Slovakia, Austria, and Hungary; Fig. 7.32a).

Spring temperatures were well above average, mainly due to an exceptionally warm April (Fig. 7.34). Belgium and Switzerland each reported their second warmest spring on record. April was the second warmest on record for De Bilt in the Netherlands

Data basis: CLIMAT and ship observations
Last update: 12 May 2009

Dev. in K
> 4
3 - 4
2 - 3
1 - 2
0 - 1
-1 - 0
-2 - -1
-3 - -2
-4 - -3
< 4

FIG. 7.34. Monthly mean anomalies of surface air temperature across Europe and over the North Atlantic, April 2009 (1961–90 base period) based on CLIMAT and ship observations. [Source: Deutscher Wetterdienst (DWD).]

(1706–2009), and new national records were set for mean anomalies in Hungary (+4.2°C) and Germany (+4.5°C; 1901–2009).

Summer temperatures were generally above average (Fig. 7.32c), most notably in southern France and Switzerland where anomalies were more than +2°C. A significant heat wave affected Western Europe during July, while a heat wave in France from 15–20 August resulted in temperatures above 36°C in the North and 40°C in the South.

Monthly mean temperatures for November were among the three warmest in the last century across the United Kingdom, Netherlands, Belgium, France, and Germany. In southern Germany, maximum temperatures of around 20°C were reached as a result of foehn winds; such high temperatures are unusual during November.

December was cold especially in the UK and Ireland but also in northern Central Europe and on both sides of the Alps, with anomalies below -1°C. This was mainly due to a long cold spell in the second half of the month.

(ii) Precipitation

Annual precipitation amounts were normal or above normal in Central Europe (Fig. 7.30), though some regions in southern France received only 70–80% of their normal totals. T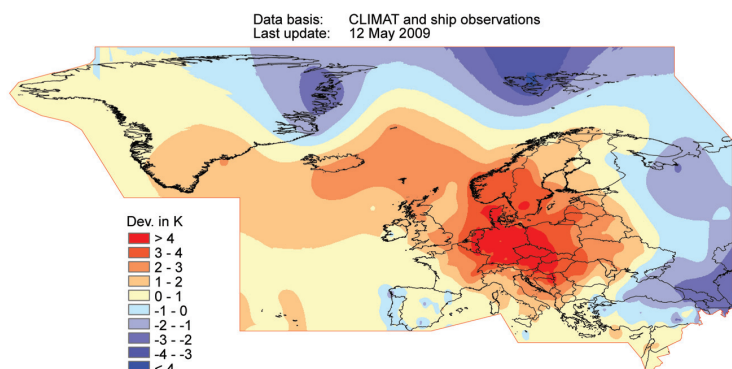he United Kingdom and Ireland experienced a wet year. Valentia Observatory in Ireland reported its highest annual rainfall total since records began in 1866.

Winter was mainly dry throughout Central and Western Europe (around 60%–80% of normal, Fig. 7.33, DJF), but with heavy snowfall in some areas particularly during February. In February and March, heavy snowfall in parts of the northern Alpine region resulted in peak snow depths of over four meters.

It was the driest spring since 1997 in England and Wales, while March was exceptionally wet in eastern Central Europe; the Czech Republic reported almost double its average March rainfall. April was very dry in eastern Central Europe. Hungary recorded only 23% of its average 1971–2000 April rainfall, while Poland experienced rainfall in the 10th percentile of its 1961–90 distribution.

England and Wales had their wettest July on record, while western Scotland had its wettest August since records began in 1910. This was the third consecutive wet summer in the UK and Ireland (Fig. 33, JJA). In Switzerland, the city of Lugano reported its highest July precipitation (397 mm) since records began in 1864, mainly due to two large thunderstorms

during the middle of the month. In contrast, dry conditions in August and September prevailed over Western and Central Europe.

November was the wettest in recorded history across the UK and most of Ireland. The Alps had received intense snowfalls by the end of November. December again was a wet month in most of Western and Central Europe but very dry in Ireland and Scotland.

(iii) Notable events

A severe North Atlantic storm with strong winds up to 174 km hr^{-1} affected the UK and Ireland on 17 January. Another Atlantic storm, with gusts of hurricane force, affected Western Europe on 23–24 January. Southern Ireland saw heavy rain with severe flooding on 29–30 January.

Unusual snow events affected Western Europe at the beginning of the year. On 6–7 January, a Mediterranean storm dropped 20 cm–40 cm of snow across southeastern France for the first time since 1987. At the beginning of February, the United Kingdom experienced its most widespread snowfalls since 1991, resulting in peak snow depths of up to 30 cm. London received its heaviest snowfalls in 18 years. In the Alpine region, the snows lasted until the end of February even at low elevations, which was unusual, especially south of the Alps.

Various episodes of heavy rainfall occurred during summer. On 6 June and 16–17 July, the United Kingdom experienced daily totals of more than 90 mm. Likewise, heavy precipitation, flooding, and mudslides affected Central Europe on 21 June. On 2 July, Dublin was affected by flooding after torrential rainfall. A severe storm on 23 July affected Germany, Poland, and the Czech Republic.

Autumn also had some noteworthy heavy rain events with flooding. On 3 September in northeast Scotland, daily totals exceeded 120 mm. Parts of Aberdeen city centre were flooded with disruptions to roads and rail services. A frontal system moving across the Atlantic Ocean caused record precipitation and widespread flooding in northwestern England on 18–20 November (see sidebar). Central Europe experienced gusts of hurricane force on 23–24 November.

A severe cold spell and heavy snowfall 15–22 December affected most of the region. Temperatures below -20°C were reported in Germany and France. The Netherlands experienced unusually heavy snowfall, with snow depths up to 30 cm. Cold and snowy conditions continued into 2010.

Exceptionally prolonged and heavy rainfall on 18–20 November led to severe flooding across the Lake District in Cumbria (northwest England). Parts of the high ground received more than 400 mm in 72 hours. Seathwaite in Borrowdale recorded 316.4 mm in 24 hours, approaching its November average of 364.3 mm and setting a new UK record for any 24-hr period. The flooding problems were made worse by saturated ground conditions following wet weather earlier in the month. Many rivers in the Lake District exceeded their previous maximum flows by a wide margin and exceptionally high flows were also reported across north Wales and southern Scotland. Several road bridges collapsed or were damaged, and some 1500 properties were flooded, many in the town of Cockermouth. Cumbria last experienced serious flooding on 8 January 2005, when Carlisle was badly flooded by the River Eden.
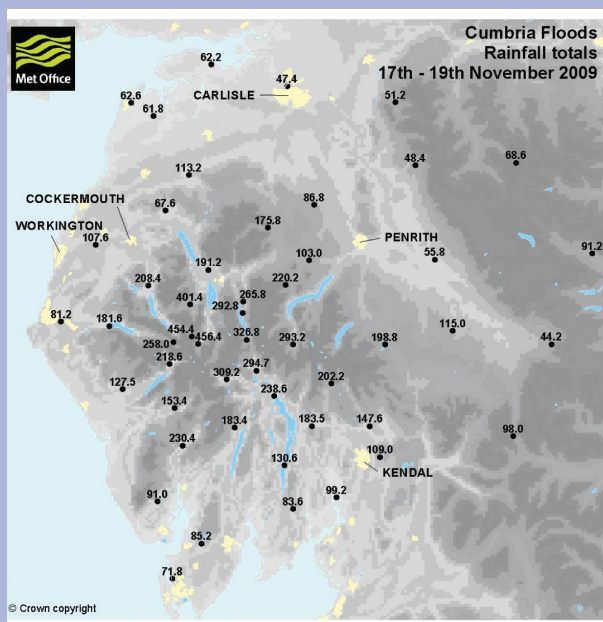
FIG. 7.35. Rainfall across northwest England from 0900 UTC on 17th to 0900 on 20th November 2009.

3) THE NORDIC AND BALTIC COUNTRIES—C. Achberger, S. Hellstrom, J. Cappelen, S. Saku, K.A. Iden, T. Jonsson, A. Obregón, P. Bissolli, J.J. Kennedy, and D.E. Parker

Countries considered in this section include: Iceland, Norway, Denmark, Sweden, Finland, Estonia, Latvia, and Lithuania.

(i) Temperature

Mean annual temperatures in the Nordic Countries were above normal, with annual temperature anomalies ranging from +0.5°C to +1.5°C, except in the Arctic where they were higher. The highest positive anomalies were recorded in Svalbard, with mean temperatures 2°C–3°C above the 1961–90 average. In Iceland, Reykjavik reported its tenth warmest year since measurements commenced in 1870, while Denmark recorded its eighth warmest year since records began in 1874 with an anomaly of +1.1°C. Norway recorded a mean annual temperature anomaly of +1.0°C, ranking 19th since records began in 1900, with all seasons recording above-average mean temperatures. Throughout the Baltic countries, annual temperature anomalies also were around +1°C (Fig. 7.29).

A very mild winter 2008/09 prevailed everywhere except in the western Nordic countries, though February was cold over most of Fennoscandia. The highest departures, exceeding +4°C, were observed on Svalbard and in Finland (Fig. 7.32a). Anomalies in Denmark were +1°C, which was less than in 2007 and 2008 when anomalies exceeded +4°C.

Spring was exceptionally warm throughout most of the region (Fig. 7.32b). April was exceptionally warm (Fig. 7.34), with Denmark setting a new record mean temperature of 9.4°C, some 3.7°C above normal. In Norway, it was the third mildest April since 1900, with several stations in the South setting new monthly mean temperature records. In Sweden, April average temperatures were generally 1°C–4°C warmer than normal, and there were locations with monthly mean temperatures above 10°C, which has never occurred in Sweden during April since records began in 1860. The April mean temperature in Gothenburg was 10.4°C, beating former nationwide records. In contrast, April was the only month of the year with below-average temperatures on Svalbard (-3.7°C anomaly). In Longyearbyen, 22 April saw the coldest April temperature (-19.5°C) since 1993.

Summer and autumn were at least slightly warmer than normal across much of the Nordic and Baltic region (Fig 7.32c,d), particularly during August. However, the beginning of June and July was exceptionally

cold in southern and central Finland. Except for the Arctic, October was a cold month throughout Northern Europe with anomalies below -2°C in some areas.

The end of the year was exceptionally mild in the Arctic region, with anomalies at Svalbard airport of +8.4°C for November and +10.9°C for December. The rest of the region (with the exception of northern Finland and Iceland) experienced a colder-than-normal December with monthly mean anomalies below -1°C.

(ii) Precipitation

Total annual precipitation was generally near normal over the Nordic countries during 2009 (Fig. 7.30). While large parts of Sweden and areas in Denmark recorded rainfall above their 1961–90 average, only eastern Iceland received in excess of 125% of their 1951–2000 normal totals. Annual precipitation was below 80% of normal over northern Greenland and parts of northern Scandinavia.

Winter in Denmark was characterized by well-below-average precipitation, recording only 66% of its average total for the season (Fig. 7.33, DJF). In contrast, in Östersund, Sweden, a snow depth of 81 cm during February was the highest monthly depth recorded since March 1988.

Spring precipitation was more than 20% below normal in parts of Sweden and Denmark, southern Finland and across the Baltic countries. April was particularly dry in southeastern Sweden (in places the driest since 1974), with the region recording less than 5% of its 1961–90 average rainfall. In some locations, no measurable April precipitation was reported; the last month without any measurable precipitation in parts of Sweden was August 2002. It was also dry in the Baltic countries. In contrast, May was the second wettest on record in northern Norway, resulting in a nationwide mean rainfall value that was 165% of its 1961–90 average.

Summer was very wet over most of the region (Fig. 7.33, JJA). Rainfall in Denmark and Sweden was 15% above the 1961–90 long-term average. On 11–12 June, Sjælland in the eastern part of Denmark received more than double its monthly-normal rain within these two days. One station on Sjælland recorded 160 mm for the event. Likewise, Lithuania was significantly wet in June and July, while for many places in Norway and Sweden July was among the wettest since records began in 1900. Some areas of Sweden recorded up to 350% of their average July totals. Conversely, July and August were very dry in western Greenland; the station of Nuuk recorded its second driest July since 1890 with a total of only 1.4 mm. For Iceland, the first part of the summer (particularly June and July) was very dry in the southern and western part of the island. The summer was the driest for the capital, Reykjavik, since 1889. Similarly, the western part of Iceland suffered from the dry conditions. October was significantly wet in the Baltic countries, with 150% of the 1961–90 average in Latvia and Lithuania. November was wetter than average in southern Scandinavia and Denmark, where the 90th percentile of the 1961–90 distribution was exceeded. A new November record of 27 precipitation days was registered for Denmark as a whole.

December precipitation in Latvia was 140% of the 1961–90 normal. In Estonia, snow depths of 43 cm at the end of December set a new record snow depth for this month. In contrast, parts of the Norwegian west coast received < 40% of their December precipitation normal 1961–90 (some areas < 15%) owing to the infrequency of westerly airflow.

In Iceland, the number of days in 2009 when the ground was covered by snow was much lower than the 1961–90 normal (e.g., 40 days in Reykjavik compared to a normal of 65 days).

(iii) Notable events

The Nordic Region was hit by a number of significant and relatively rare summer storms that locally caused damage and even casualties.

A supercell thunderstorm hit the southern part of central Finland on 28 June. Storm downbursts caused extensive forest damage. Furthermore, extremely large hailstones with diameters up to 8 cm damaged buildings and cars.

On 30–31 July, an intense low pressure system formed over southern Norway generating very strong winds in Denmark, southern Sweden, and southern Norway. Wind speeds up to 101 km hr^{-1} were measured locally along the Danish and Swedish west coast. One ship sank outside the Swedish west coast causing the deaths of six people and a bulk freighter grounded in southern Norway causing an oil spill across a wide area.

In the middle of November, Denmark was again hit by a strong storm with wind gusts up to hurricane force (132.5 km hr^{-1}). A low-pressure system formed locally over the North Sea developing its full strength when passing Denmark on 18 November. The strong winds considerably raised the sea level along the Danish west coast, uprooted trees, and caused minor damage to buildings.

4) IBERIA—R.M. Trigo, D. Barriopedro, C.C. Gouveia, A. Obregón, P. Bissolli, J.J. Kennedy, and D.E. Parker

Countries considered in this section include: Portugal and Spain.

(i) Temperature

The Iberian Peninsula registered significantly above-average temperatures for 2009 (Fig. 7.29). The annual mean anomalies for Iberia generally ranged between +1°C and +2°C, with higher values in the East. Large parts of the West recorded anomalies of between 0°C and +1°C. The year started with a negative anomaly for the winter (-0.72°C), followed by a warmer-than-average spring (+1.57°C), a particularly warm summer (+1.88°C), and a relatively warm fall (+1.26°C, Fig. 7.31). Several cold spells affected Iberia in January and February. Snowfall occurred even in low-altitude coastal regions of Portugal, which is an unusual phenomenon there, and new records in the number of snow days in Spain were reached for January, e.g., in León (14 days, highest since 1938, about 800 m elevation) and Ávila (11 days, highest for about 20 years, 1100 m elevation). The following seasons were generally characterized by high values of 500-hPa geopotential height, with maximum anomalies located north of Iberia (spring) and over eastern (summer) and western (autumn) Iberia.

It was the third warmest year in Spain since 1961 (anomaly +1.25°C relative to 1971–2000). The largest anomalies were observed in the central and southern regions, and in the northwestern Iberian Peninsula. The lowest deviations were restricted to the Balearic Islands. Temperature departures in Portugal were highest in the North (+0.9°C, 1971–2000 base) but generally lower than those anomalies in Spain (+0.5°C averaged over whole mainland Portugal). The warmest months of 2009 in Spain (relative to normal) were May, June, October, and November, when mean temperatures were more than 2°C above average. Overall, in Portugal the warmest months (relative to normal) were March, May, and October.

Winter 2008/09 temperatures were slightly below the long-term average. In contrast, much of the rest of the year was exceptionally warm (Fig. 7.32). Temperature anomalies in spring exceeded +2°C in the central Peninsula, while summer brought record mean temperatures (for the last 50 years) to many stations in Catalonia and to northern and central parts of the Peninsula. The summer and autumn anomalies for Spain including the Balearic Islands were +1.9°C and +1.7°C, respectively, making both seasons the third warmest on record. In November, some stations in southern and eastern Spain reported record-breaking monthly mean temperatures at stations with long histories (e.g., Valencia, with observations dating back 141 years.)

(ii) Precipitation

Iberia experienced, on average, near-normal conditions during 2009, with only local sectors of central and southern Iberia receiving less than 80% of the climatological average (Fig. 7.30). Dry episodes are relatively common in Iberia and, regarding the duration and intensity of dry periods in this context, 2009 can be classified as a moderately dry year, particularly when compared with exceptional dry years such as 2005. Nevertheless, all seasons recorded lower-than-average precipitation for the aggregated area of Iberia (Fig. 7.33), particularly spring, summer, and autumn, but December 2009 was an exceptionally wet month.

May was especially dry (40% of normal), with some stations in northeastern Spain recording new historical minima (as low as 1.1 mm) in a series of up to 130 years. June showed a remarkable dipole pattern over Iberia. While the eastern half of the Peninsula, particularly the Mediterranean coast, was dry, Galicia and much of Portugal were quite wet, with the impact even discernible in the summer (JJA) average (Fig. 7.33, JJA). Rainfall anomalies exceeded 150% along the Atlantic coast. Monthly mean anomalies for June in Lisbon reached nearly 300% (59 mm), although June is a relatively dry month and hence moderate values of precipitation can result in a large percentage anomaly.

Averaged across Iberia, autumn seasonal mean deficits were similar to spring and summer; though some regions, like the southern Mediterranean coast, were much wetter than normal. The year closed with considerably wetter-than-average conditions in much of Iberia during December 2009. In southeast Spain, December precipitation was more than twice normal.

(iii) Notable events

On 24 January, an exceptional storm hit northern Spain with strongest gusts reaching 190 km hr^{-1}. It was the worst storm in this region since 1999 (see sidebar).

On 27–29 September, heavy precipitation was recorded at a number of locations on the Spanish southeastern coast. Although such convective episodes are typical for that time of the year, the event of 27–29 September significantly contributed to the very high monthly totals, which broke records at some locations in southeastern Iberia (e.g., Alicante with 309 mm; records commenced in 1939) and the Balearic Islands (e.g., Palma, with 222 mm; series commenced in 1951).

EXCEPTIONAL STORM STRIKES NORTHERN IBERIA AND SOUTHERN FRANCE

An exceptional North Atlantic storm swept through northern Iberia and southern France on 23–24 January 2009. The storm (labeled Klaus by the German Weather Services, DWD) developed off Bermuda on 20 January and crossed the Atlantic, reaching the Bay of Biscay in the early hours of the 23rd, where it deepened further (Liberato et al. manuscript submitted to *Weather*). The strongest winds induced by Klaus were felt in northern Spain, including the large populated cities of Santander, Bilbao, and Barcelona (Fig. 36). But it was in southern France (namely in the cities of Bordeaux, Narbonne, and Perpignan) that the wind gusts surpassed many previous records. The highest level of wind warning possible was issued by Meteo France, though sadly at least 20 fatalities occurred that were a direct consequence of the storm. More than one million homes suffered power cuts as trees and power lines were downed, while road and rail links were blocked and airports closed. Klaus was considered the most damaging wind storm to affect northern Iberia, southern France, and the western Mediterranean since the storm Martin in late December 1999, which killed 88 people and uprooted millions of trees (Liberato et al. manuscript submitted to *Weather*).
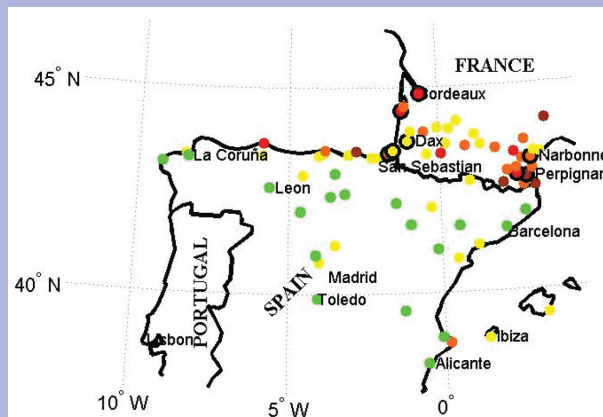
FIG. 7.36. Maximum wind gusts recorded in Spain and southern France (on either 23 or 24 January 2009). Green (100–120 km hr⁻¹), yellow (120–140 km hr⁻¹), orange (140–160 km hr⁻¹), red (160–180 km hr⁻¹), and brown (180–200 km hr⁻¹). Stations which set new wind gust records are highlighted with a solid circle around the color circle.

5) MEDITERRANEAN, ITALIAN, AND BALKAN PENINSULAS—A. Obregón, P. Bissolli, J. J. Kennedy, D. E. Parker, and S. Sensoy

Countries considered in this section include: Italy, Malta, Slovenia, Croatia, Serbia, Montenegro, Bosnia and Herzegovina, Albania, Macedonia, Greece, Bulgaria, and Turkey.

(i) Temperature

Much of Southeastern Europe was 1°C–2°C warmer than average during 2009 (Fig. 7.29), exceeding anomalies of +2°C over eastern Slovenia and +2.5°C in northeastern Italy and western Slovenia. Throughout Croatia, very high annual temperatures prevailed, exceeding the 98th percentile of the 1961–90 distribution over most regions. In Zagreb, it tied with 2008 as the third warmest year since 1862. In Turkey, the 2009 mean temperature was 0.9°C above the 1971–2000 average.

Winter temperatures were near normal over most of the region (Fig. 7.32a). Negative anomalies were observed over the western Mediterranean, Sicily, Sardinia, and in parts of Italy. The largest positive anomalies were recorded in Bulgaria and Montene-gro, where many locations in the East recorded their warmest winter on record.

Spring and summer were exceptionally warm except in Turkey, which was colder than normal (Fig. 7.32b,c). April was particularly warm in Serbia and Croatia (Fig. 7.34). May was the third warmest in the last two centuries in Italy, mainly due to a heat wave at the end of the month. Another very strong heat wave in July brought temperatures of 40°C–45°C to various places in Italy. The official peak value was 45.0°C in Decimomannu, Sardinia, a new local record. In Mostar (Bosnia and Herzegovina), it was the warmest summer on record. September was particularly warm in Turkey, with maximum and minimum temperature records broken in a number of locations.

In Italy, December was a month of strong contrasts. A cold spell between 18–23 December saw a number of records broken in northern Italy, with temperatures falling below -15°C in a number of locations. Only days later, on 25–30 December record high temperatures were recorded across central and southern Italy, with temperatures exceeding 25°C. In Bulgaria, several stations registered record high temperatures on Christmas Day (e.g., 21.2°C in Vratsa). December mean temperature was well above normal

in Turkey and also in Macedonia, which recorded monthly mean anomalies of greater than +4°C in places.

(ii) Precipitation

The year brought well-above-average precipitation over most of the southwestern Balkan Peninsula and southern Italy, exceeding 125% of normal in most places (Fig. 7.30). In Croatia, rainfall was significantly below average in the East, while on the southern Adriatic coast precipitation was above the long-term mean. Some places in Turkey recorded 150% of their annual average.

Winter brought wetter-than-normal conditions over most of Italy and the Balkan Peninsula, with the exception of Bulgaria (Fig. 7.33, DJF). January rainfall was particularly high, with maxima in Greece and on the Adriatic coast of the Balkan Peninsula. Luqa Airport on Malta received its highest monthly rainfall total in 85 years (247 mm).

The northern Balkan Peninsula experienced drier-than-normal conditions during spring, while wetter conditions occurred in the South. March precipitation in Athens was twice the normal. The eastern Balkan Peninsula had a very dry April, but places in northern Italy registered their second wettest April in 75 years or more, resulting in the flooding of the Po River.

It was generally wet during June. Monthly average totals were exceeded by more than 25% with the exception of northern Italy, southern Greece and western Turkey, which were all very dry. July and August were mostly dry.

Abundant rainfall occurred in southern Italy and Sardinia in September and October, whereas drier-than-average conditions occurred in Tuscany and northeastern Italy. Autumn was also very wet in the southern and eastern parts of the Balkan Peninsula (Fig. 7.33, SON). September brought exceptional rainfall totals to Athens (48 mm or 480% of 1961–90 average). Serbia and northern parts of Bulgaria were very wet during October.

December was also generally wetter than average across the region. Several stations in northern Italy recorded their wettest or second wettest December in nearly 90 years, mainly due to an intense precipitation event around Christmas. An exceptional local 24-hr precipitation record was set in Makrinitsa in central Greece, where 417.2 mm fell on 10 December. This corresponds to nearly half of the total rainfall for 2009 at this station. Other locations also received exceptional precipitation on that day, resulting in significant flooding and widespread damage.

(iii) Notable events

An outbreak of cold air from Eastern Europe brought abundant snowfall over northern Italy from 3–10 January. Temperatures dropped below 0°C in many places. On 7 January, a snow depth of 26 cm was reported in Milan.

On 24 February, exceptionally heavy rainfall in Malta led to the cancellation of the National Carnival grand finale. A heavy storm over the western Mediterranean with gusts up to hurricane force, heavy rain, snowfall, and high seas followed on 4–6 March due to a cut-off cyclone.

From 20–22 June, an Atlantic disturbance affected most of Italy with heavy rainfall and strong winds. Daily precipitation on 21 June set new records at four locations which had 58 years of record.

On 7–12 September, torrential rains and flooding affected northwestern Turkey, with the heaviest rainfall in 80 years. Istanbul received 67 mm of rain within one hour on 9 September.

A violent storm crossed southern Italy on 15–17 September, flooding the city of Palermo (Sicily). On 2 October, a storm dropped 70 mm of rain within six hours in Messina, Sicily. Civil protection measurement stations recorded up to 300 mm of precipitation at mountainous sites, resulting in Italy's worst mudslides in more than a decade.

Abundant snowfalls occurred from 18–20 December over northern parts of Italy, with depths up to 30 cm. Subsequent warming and continuous rainfall resulted in rapid snowmelt causing extensive flooding in Tuscany just before Christmas.

6) Eastern Europe—A. Obregón, P. Bissolli, J. J. Kennedy, and D. E. Parker

Countries considered in this chapter include: European Russia, Belarus, Ukraine, Moldova, and Romania.

(i) Temperature

Annual temperature anomalies over Eastern Europe ranged between +1°C and +2°C (Fig. 29), with only northern parts of European Russia recording anomalies below +1°C. Parts of Romania exceeded anomalies of +2°C. Moldova experienced its second warmest year in history, beaten only by 2007.

Unlike most of Western Europe, Eastern European countries experienced well-above-average temperatures during winter 2008/09 with anomalies surpassing +2°C (Fig. 7.32a).

Spring temperature anomalies exceeded +1°C in western parts of Belarus, Ukraine, and Romania (Fig.

7.32b). April was particularly mild, although there was a 10 to 20 day frost period in the Ukraine, notably in eastern parts of the country. April was colder than normal in European Russia (Fig. 7.34).

Temperature anomalies reached +3°C in the Ukraine during June and July, with a highest daily maximum temperature for the region of 40°C. Summer temperature anomalies exceeded +1°C in Romania and Moldova, while anomalies in European Russia (+0.5°C) and Belarus were closer to normal.

Autumn was characterized by the extremely mild months of September and November throughout Eastern Europe, with temperatures generally above the 90th percentile of the 1961–90 distribution. These months contributed to a seasonal anomaly of over +1°C in Romania, Moldova, Belarus, western parts of Ukraine, and northern parts of European Russia, while the eastern Ukraine and southern European Russia had anomalies in excess of +2°C (Fig. 7.32d).

December temperatures in Belarus differed greatly during the month. The beginning of the month was anomalously warm, with temperatures ranging from 5°C–10°C above average. On 2 December, several locations set new records for this day including Minsk, where temperatures reached 9.3°C, and Moscow (8.1°C), while in Moldova, it was the warmest night for a 2 December in the past 65 years. However the warmest day in Moscow in December 2009 was on the 6th, with 9.4°C. Remarkably, this value was measured in the early morning and was a local record high for December. In sharp contrast, temperatures plunged below -15°C in the middle of December in many parts of Belarus, with temperatures falling as low as -27°C. The city of Perm in European Russia (in the lowlands near the Ural Mountains) experienced temperatures as low as -41.4°C on 16 December, which was a new local record.

(ii) Precipitation

Precipitation totals in 2009 were generally close to or above average for most of Eastern Europe (Fig. 7.30). Only a few places in the Ukraine and central European Russia reported a rainfall deficit, recording 60%–80% of average. Annual precipitation in the north of European Russia exceeded 125% locally.

Winter 2008/09 brought near-normal precipitation (Fig. 7.33, DJF) to the region; only a few scattered locations in Eastern Europe received considerably above-average seasonal totals. It was dry, however, in eastern parts of European Russia, with some areas receiving less than 40% of their normal precipitation.

Spring was dry in Moldova, with areas receiving only 50%–75% of their average rainfall for the season. Similarly, parts of Romania and Ukraine were also dry. April was particularly dry in the western regions. In Moldova, only 11.5 mm (26% of normal) of rainfall was recorded, making April the second driest in 60 years, second only to April 1974 (9mm). April was also drier than average in the Ukraine and Russia, where many stations reported monthly rainfall amounts below the 10th percentile.

Summer was unusually wet in Belarus (second wettest since 1936), mainly due to well-above-average precipitation during June and July. Minsk reported a new record of monthly precipitation in June (187 mm, more than twice normal). However, August had only about half of the normal precipitation totals in Belarus.

Autumn precipitation was well above average over northern European Russia and Belarus, as well as in western parts of Romania and Ukraine (Fig. 7.33, SON), with October being particularly wet. Belarus received more than twice its normal rainfall and in Romania precipitation exceeded 150% of normal in most places, with some areas exceeding 200%. In contrast, autumn was dry in Moldova and in central parts of Ukraine.

There was a heavy snowfall in Moscow at the end of December, when 19 cm fell within 24 hours. A new record daily snowfall of 31 cm was set in Kyiv, beating the previous record by 3 cm. Ukraine saw heavy snow storms in the first half of December.

7) Middle East—A. Obregón, P. Bissolli, J. J. Kennedy, and D. E. Parker

Countries considered in this section include: Israel, Cyprus, Jordan, Lebanon, Syria, western Kazakhstan, Armenia, Georgia, and Azerbaijan.

(i) Temperature

Warmer-than-average conditions prevailed throughout the region during 2009. The largest anomalies were experienced in Israel, Cyprus, and the western parts of Syria and Kazakhstan, with values generally ranging between +1°C and +2°C (Fig. 7.29).

The largest positive temperature anomalies in winter 2008/09 were in the Caucasian countries (i.e., Armenia, Georgia, Azerbaijan) and Israel. On 9 February, temperatures above 30°C were recorded in parts of Israel, while between 13–16 February temperatures reached 20°C in southern Armenia. While spring and summer temperatures were well above average in Jordan, Syria, Israel, and Cyprus,

temperatures in western Kazakhstan, Armenia, Georgia, and Azerbaijan were cooler than average. June 2008 and 2009 were the two warmest Junes in the last 40–50 years in Israel, due to several Sharav (hot winds from the Arabian Desert) events. Autumn temperature anomalies exceeded +1°C in Georgia and Azerbaijan and up to +2°C in western Kazakhstan. Israel experienced a very hot October with a monthly mean anomaly exceeding +3°C (1981–2000 base), primarily due to a six-day heat wave between 15–20 October, with successive days above 35°C in many places. December was unusually warm over the whole Middle East (+2°C anomaly or more), most notably during the second half of the month.

(ii) Precipitation

Southern parts of Israel, Jordan, and parts of Syria received less than 80% of their annual rainfall average (Fig. 7.30). Anomalies below 40% of normal were restricted to southern and eastern parts of Jordan. For the sixth year in succession, Israel's 2008/09 rainfall season delivered below-average rainfalls, with resulting water shortages and deteriorating quality of ground water reservoirs. In contrast, Georgia and Armenia recorded 100%–125% of normal, while annual precipitation in western Syria, Lebanon, and Cyprus was in the range of normal to slightly below normal, bringing to an end a three-year drought period in Cyprus.

In western Kazakhstan, the first half of the year featured a contrasting temporal pattern of rainfall. Winter was particularly dry with areas receiving less than 40% of average precipitation, while spring rainfall was significantly above average, exceeding 160% of normal in places. In the rest of the region, winter and spring precipitation were generally below average (Fig. 7.33, DJF, MAM). Israel had very little rainfall in January, less than 20% of the monthly long-term average, making it one of the driest in the 70-year measurement history; yet, February was the third rainiest in 70 years. Summer was unusually wet in Armenia. Rainfall, sometimes heavy, was reported almost every day during July–September. Autumn was generally very wet across the Middle East (Fig. 7.33, SON), particularly in the Caucasian countries and Syria. In September, the monthly rainfall in Cyprus was eight times higher than normal. Israel also had very heavy rainfall during September and October, marking an early start to the 2009/10 rainy season. In December, Cyprus once again experienced heavy precipitation, with a hailstorm on the 16th resulting in a monthly total of almost 150% of the normal.

(iii) Notable events

Severe rainfall was recorded in northern Israel on 27–28 February. Precipitation amounts of 100 mm–180 mm over 48 hours caused flooding and extensive damage to agriculture. This event also affected Cyprus, with flooding in a number of places.

Severe drought conditions, which began in 2006, affected eastern Syria during August. Thousands of Syrian farming families were forced to migrate to cities after two years of drought and failed crops. However, high September rainfall brought an end to this drought period.

Accompanied by heavy precipitation and hailstorms, a tornado affected several areas in Cyprus on 18 September causing injuries and significant damage. Tornadoes of lower intensity along with large hail on 19 September affected areas around Nicosia.

g. Asia

1) Russia—O. N. Bulygina, N. N. Korshunova, and V. N. Razuvaev.

i) Temperature

The year 2009 was warm in Russia, with the mean annual air temperature, averaged over the Russian territory, 0.6°C above the 1961–90 average (Fig 7.37). This anomaly was substantially smaller than those recorded in the two previous years, when anomalies were close to +2°C.

During January, a large warm region formed in northeastern Siberia, with mean monthly air temperature anomalies exceeding +10°C in the southeastern Siberian Taimyr Peninsula. As a result, frequent snowfalls, with winds as strong as 108 km hr^{-1} and poor visibility (down to as little as 50 meters) occurred in the southern areas of the peninsula. It was also very warm in northern Western Siberia, as well as in northwestern European Russia. Simultaneously, in the first 10 days of the month, severe frosts (-35°C
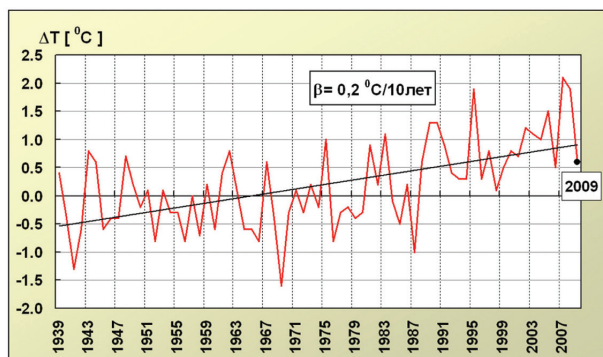
Fig. 7.37. Anomalies of annual mean air temperature averaged over the Russian territory for the period 1939–2009 (base period: 1961–90).

to -44°C) persisted in southern Western Siberia and in the Irkutsk Region, with lowest minima of -49°C and observed frost fogs. Extreme cold weather was also recorded in the far eastern regions of Chukotka, the Magadan Region, and northern Kamchatka, with temperatures as low as -50°C. As a result, the mean monthly air temperature in these regions was 8°C–10°C below normal.

February was warm over most of European Russia but cold over Asian Russia. In European Russia, the warmest weather was observed in the northwestern and southern areas, where mean monthly air temperatures were 4°C–5°C above normal. As for the Asian territories, the first and second 10-day periods were the coldest, with mean daily air temperatures in the Tomsk Region 10°C–20°C below normal. In early February, severe frosts persisted in Taimyr and Evenkia, with temperatures as low as -50°C to -58°C.

During March, record-breaking low air temperatures were recorded in the Krasnoyarsk Territory, Transbaikalia, western Yakutia, and the Amur Region. Over much of the rest of the country it was very warm. Throughout March, record-breaking maximum daily temperatures were registered at meteorological stations in the Krasnodar Territory, Bashkiria, southern Ural, the Central Volga Region, southern Western Siberia, Kolyma, and the northern Khabarovsk Territory.

April was cold over European Russia, while in contrast the whole of Asian Russia recorded positive temperature anomalies (Fig. 7.38). In the latter half of the month, record-breaking cold weather spread into central Russia and southern areas of European Russia. New record daily minima were set in Tambov, Kursk, Lipetsk, Krasnodar, Mineralnye Vody, Sochi, and Makhachkala. At some meteorological stations, extreme low daily air temperatures (below the fifth percentile of all the April minimum temperatures from 1961 to 1990) persisted for more than 10 days (Fig. 7.38b). In Eastern Siberia, anomalies of mean monthly air temperature exceeded 6°C in Evenkia and southern Taimyr. In the first and third 10-day periods of the month, new record maximum temperatures were set at stations in the region (see the inset in Fig. 7.38). Extremely high temperatures (above the 95th percentile of all April maximum temperatures from 1961 to 1990) were observed for more than 10 days (Fig. 7.38a). Over the Far East territories, mean
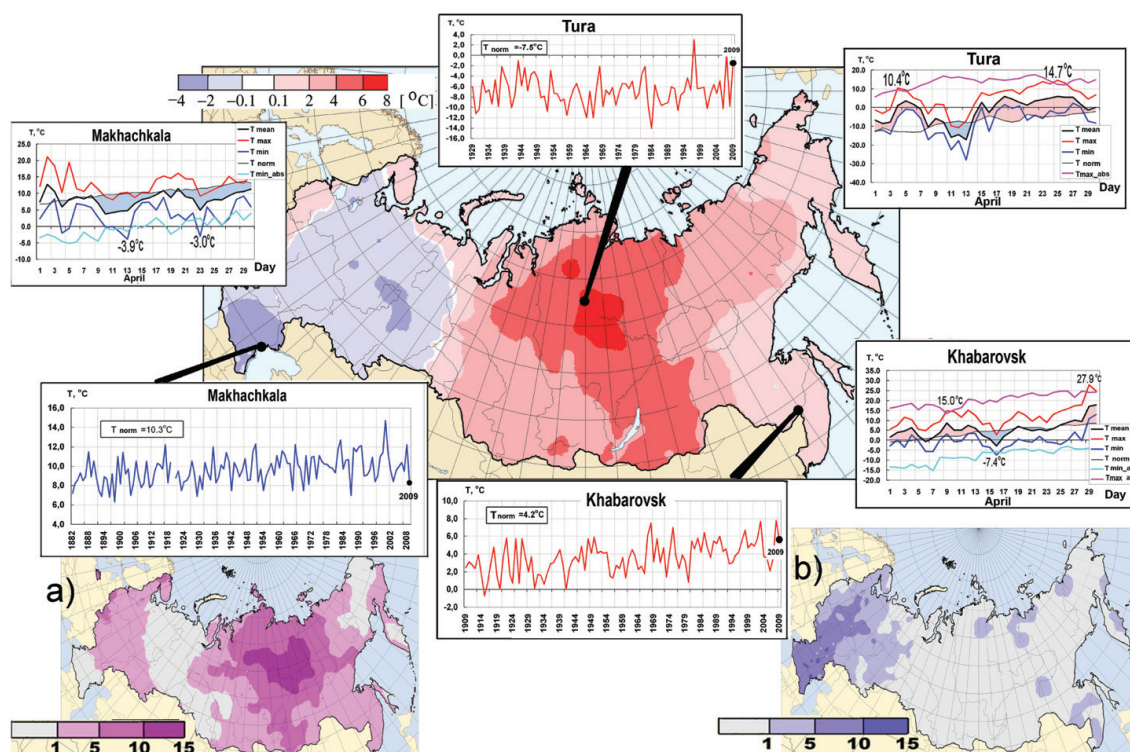
FIG. 7.38. Air temperature anomalies in April 2009. Insets show mean April air temperatures and mean daily air temperatures in April 2009 at meteorological stations Khabarovsk, Makhachkala and Tura; (a) Number of days with high temperature extremes in April 2009; (b) Number of days with low temperature extremes in April 2009.

monthly temperature anomalies exceeded +5°C in northwestern Yakutia. In the southern Far East, heat waves and cold snaps alternated several times throughout the month, with both record monthly maxima and minima temperatures being set. In early April, record-breaking maximum daily air temperatures occurred in the Khabarovsk Territory, Maritime Territory, and Amur Region. Another record-breaking heat wave came to the southern Khabarovsk Territory and the Maritime Territory late in April. In the Khabarovsk Territory, extremely low air temperatures were recorded in between these heat waves in mid-April. In some areas of the Territory, record values of minimum daily temperatures were broken.

In some contrast, May saw mean monthly air temperatures close to normal over most of the Russian territory. The largest positive anomalies (up to +6°C) were found in the northern Far East (Kolyma and Chukotka). In the Maritime Territory, temperatures were, at times, as warm as they were during summer (30°C–34°C). Maximum temperature records were exceeded in Vladivostok, Blagoveshchensk, and Yuzhno-Sakhalinsk.

June was very warm in southern European Russia. On 25 June, new temperature records were set in five cities of the region. Above-normal temperatures were also recorded in Yakutia and the northern Far East. In Oimyakon, the mean monthly temperature anomaly exceeded +6°C. New record-breaking maximum daily temperatures were recorded in Yakutia, Chukotka, and the Magadan Region. In Kamchatka, as early as the beginning of June, air temperatures exceeded 20°C. Such warm temperatures so early had never been noted in the history of meteorological observations in this region. In July, temperatures were close to normal over Russia as a whole; however, arctic air penetrated into Western Siberia and eastern European Russia, contributing to extremely low temperatures. In contrast, southern European Russia was hot in July, with air temperatures reaching record levels (40°C–42°C) in the Volgograd and Astrakhan regions.

Although August temperatures were largely close to normal, cold weather dominated central and southern European Russia, with some southern areas experiencing their coldest August in more than 30 years. New daily air temperature minima were registered in many cities of the region (e.g., Kotlas, Pskov, Saratov, Volgograd, Krasnodar, Stavropol, Mineralnye Vody). In contrast, September, under the influence of the Azores anticyclone, proved to be abnormally warm in European Russia, the Ural region, and Western

Siberia. New record temperature maxima were set in the same cities.

October was very warm and largely dry in southern and eastern European Russia, Ural, Western Siberia, and northern Eastern Siberia. In Eastern Siberia, maximum positive mean monthly air temperature anomalies of more than +10°C were recorded on the Arctic islands.

November was warm in European Russia, with mean monthly air temperatures being 2°C–3°C above normal. In the north of Eastern Siberia (Taimyr and the Arctic islands), mean monthly air temperatures were 4°C–10°C above normal, although on the last days of November, Taimyr experienced severe frosts (-35°C to -40°C). In contrast, December air temperatures were below normal over much of the Russian territory (Fig. 7.39). Very cold weather was observed in northern and northeastern European Russia and in Ural, with mean daily air temperatures being up to 30°C below normal. Arctic air penetrated into the Upper Volga and Central Volga areas. In the city of Kazan, minimum temperatures were the lowest since records began in 1872. On 16 and 17 December, record minimum temperatures were recorded in the city of Perm, with -41.4°C and -38.4°C, respectively. The center of the cold area was over Western Siberia, where mean monthly air temperature anomalies reached -9°C to -11°C.

ii) Rainfall

Precipitation over Russia was generally near normal (80%–120%) for the year. Above-normal precipitation (120%–140%) was recorded in the northwestern areas of European Russia and in areas of southern Siberia and the Far East.

During January, the areas of extreme cold in far eastern Russia also experienced large precipitation deficits, recording only 2%–20% of their monthly average. In contrast, across the southern Far East, active cyclogenesis caused heavy snowfalls. At meteorological station Ternei, the snowfall recorded over only two days was the equivalent of 185 mm of precipitation, approximately 1200% of the January average.

In March, precipitation in the Okhotsk area was up to 600% of normal, breaking March records at a number of stations. Transportation between the city of Okhotsk and other cities of the Khabarovsk Territory was brought to a standstill for a week, and snow buried some houses. In contrast, during April, Transbaikalia recorded above-average temperatures and a significant precipitation deficit (6%–30% of normal), resulting in greatly increased fire risk.
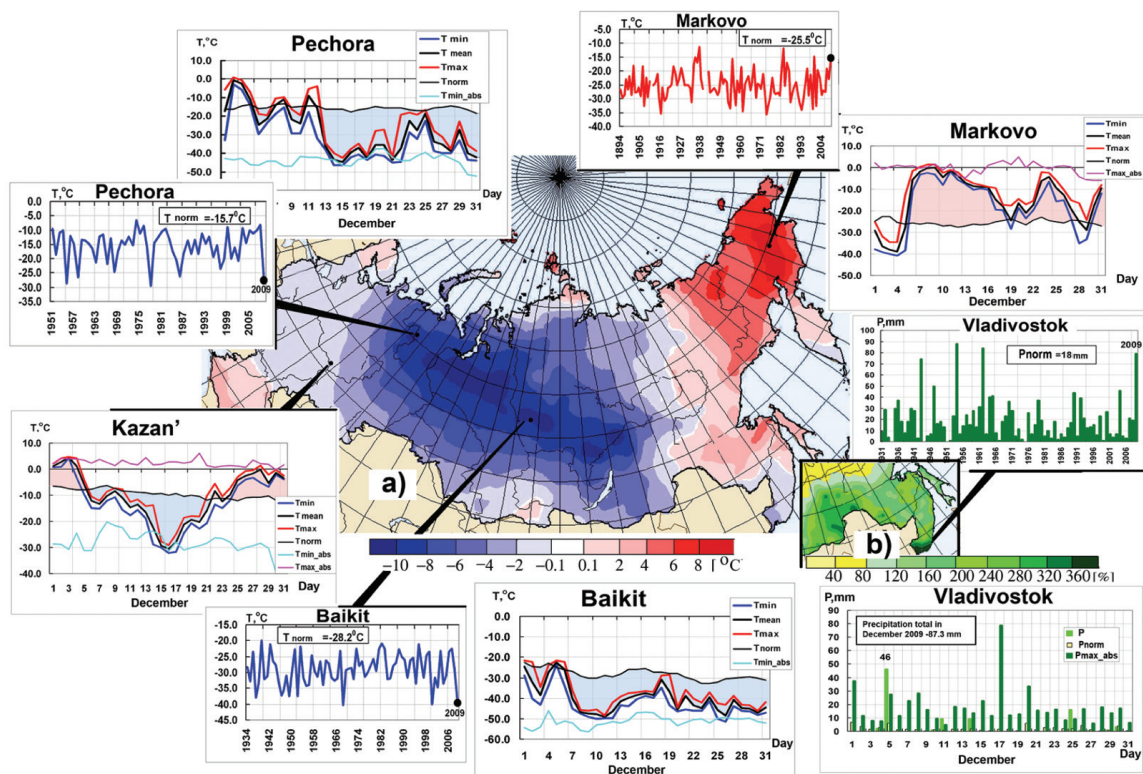
Fɪɢ. 7.39. Weather conditions in December 2009 (a) Air temperature anomalies. Insets show the series of mean monthly and mean daily air temperatures in December 2009 at meteorological stations Pechora, Baikit, Markovo, and Kazan; (b) Percentage of monthly mean precipitation in the southern Far East. Insets show the series of monthly and daily precipitation totals in December 2009 at meteorological station Vladivostok.

June saw large precipitation anomalies in southern Eastern Siberia and the southern Far East. In Sakhalin and the Maritime Territory where peak rainfall occurs in the latter half of summer with the monsoon, rainfall peaked in early June, with southern Sakhalin and the Ternei area of the Maritime Territory flooded due to frequent rains. Monthly precipitation was two to three times the average, with most of the rainfall occurring in just a few days, resulting in flooding. Such high early season rainfalls have never been observed before.

Autumn was particularly wet over parts of eastern Russia. In Northern Caucasia, September was very rainy in the Krasnodar and Stavropol Territories and the Chechen Republic. Particularly heavy rains were recorded in Dagestan on 20–21 September, causing mud flows, river floods, and significant economic damage. October was also very rainy on the coast of the Sea of Okhotsk. Ayan, for example, received more than five times its monthly average rainfall. Typhoon Melor brought heavy rainfall and hurricane-strength winds (up to 144 km hr⁻¹) to the Southern

Kuril Islands. During November, precipitation was significantly above normal in Dagestan for the second month running. Makhachkala, for example, received more than 500% of its normal November rainfall, with avalanches in mountain regions.

In December, the Kemerovo Region and the Republic of Altai received more than double their monthly normal rainfall. In Chukotka, very warm conditions (anomalies between +9°C and +10°C) were accompanied by rainfall that was twice the long-term average. Even more precipitation fell in the southern Khabarovsk Territory and the Maritime Territory, where some meteorological stations recorded 400%–600% of their monthly mean. Vladivostok received 87.3 mm for the month against an average of only 18 mm, with more than half the precipitation (46 mm) falling on 5 December (Fig. 7.39 b).

(iii) Notable events

In early January, ice slush buildup occurred at Sochi (Black Sea coast), with a maximum depth of 96 mm, while 38 avalanches, with volumes as large

as 30 m³ to 200 m³, occurred in Northern Caucasia on 7 January. An additional 52 avalanches occurred in the same region on 24–25 March.

During May, the Krasnodar Territory received 107 mm of rainfall in six hours on the 11th, while on 29 May the Astrakhan Region received 141 mm of precipitation in five hours.

On 4 June, large hail (50 mm–70 mm in diameter) fell in southern European Russia (Krasnodar Territory), while numerous mud flows caused by heavy rains occurred in Dagestan (Northern Caucasia) on 18–19 June. In contrast, July brought 142 forest fires over an area of more than 105 000 ha in the Magadan Region. August again brought heavy rain and floods to the rivers Detrin, Ola, Arman, and Kolyma (30–31 August, Magadan Region), while heavy rainfall in the Upper Volga region (Republic of Mordovia) on 8 August saw 80 mm fall in only 48 minutes. Heavy rainfall also fell on 21 September in Makhachkala (Republic of Dagestan), when they received 100.2 mm of precipitation in just three hours.

2) East Asia—K. Osawa, P. Zhang, Y. Zhu, and H. Na

Countries considered in this section include: China, Korea, Japan, and Mongolia.

In the first half of 2009, anticyclonic anomalies in the upper troposphere were dominant over China, a pattern which is consistent with the La Niña event early in the year. During the boreal summer, the subtropical jet stream became stationary, with a ridge over China and a trough over the Korean Peninsula, significantly affecting conditions over the region. Likewise, a trough became dominant over Mongolia and China during November and December.

Over most of East Asia, the annual mean surface air temperature during 2009 was near or above normal, with the notable exception of northeastern China (Fig.7.40). Temperatures for most of East Asia were significantly above normal during February, May, and June, while significantly-below-normal temperatures were observed over eastern China and Mongolia during November and December.

Annual precipitation totals were above normal on the Pacific side of northern Japan, eastern to central China, and Hai Nan
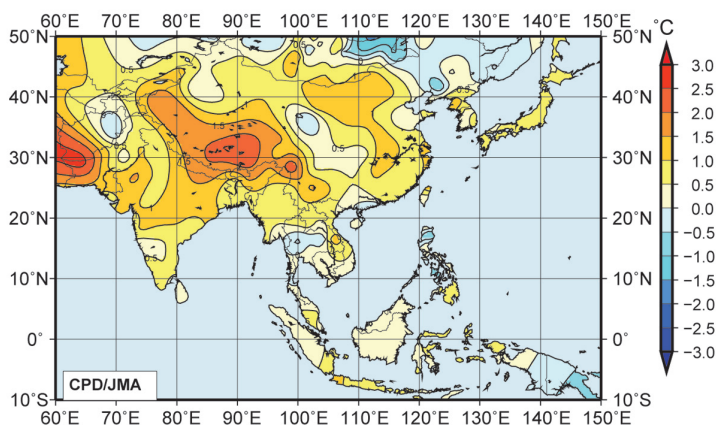
Fig. 7.40. Annual mean temperature anomalies (°C; 1971–2000 base period) over East Asia in 2009. (Source: Japan Meteorological Agency.)

Island. In contrast, precipitation was below normal on the Pacific side of western Japan, in Okinawa/Amami, over southern and western China, and around Mongolia (Fig. 7.41). In August, Typhoon Morakot caused significant damage to parts of the Taiwan province of China, resulting in over 600 fatalities.

(i) Temperature

The mean temperature over China for 2009 was 9.8°C, 1.0°C above the 1971–2000 normal, the fourth warmest year since records began in 1951 and the 13th above average year since 1997. Annual mean temperatures for 2009 were above normal over most of China, with temperatures 1°C–2°C above normal in west and central east China. In contrast, some parts of the northeast and southern areas of South China recorded below-average temperatures for the year. Temperatures over China were above normal (based
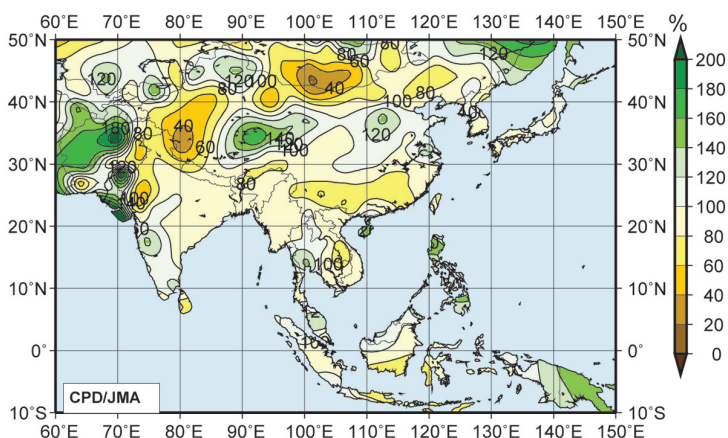

Fig. 7.41. Annual precipitation ratio as percentage of normal (1971–2000 base period) over East Asia in 2009. (Source: Japan Meteorological Agency.)

on the 1971–2000 climatology) for all seasons, with anomalies of 1.7°C, 1.3°C, 0.6°C, and 0.6°C for winter, spring, summer, and autumn, respectively. The winter 2008/09 mean temperature was the third warmest, and the spring value second warmest, since 1951.

The average surface temperature over Japan (averaged over 17 observatories confirmed as being relatively unaffected by urbanization) in 2009 was 0.56°C above the 1971–2000 average, making 2009 the seventh warmest year since 1898. Area-averaged annual mean temperature anomalies were +0.6°C in northern Japan, +0.7°C in eastern Japan, +0.6°C in western Japan, and +0.5°C in Okinawa/Amami.

(ii) Precipitation

The average annual precipitation over China was 574.0 mm, 38.8 mm below normal, making 2009 the fourth driest year since 1951 and the driest year since 1987. While spring precipitation was near normal, the seasonal totals for winter, summer, and autumn were all below average. Autumn precipitation was the driest in the last 10 years. As a result of the dry year, China suffered severe drought during 2009. In late 2008 and early 2009, serious autumn and winter rainfall deficiencies affected the northern wheat growing areas. From April to May, severe spring drought impacted Heilongjiang and northeastern Inner Mongolia. From late June to early November, severe summer and autumn drought occurred in Liaoning, Jilin, and southeastern Inner Mongolia. Similarly, from August to early November, severe autumn drought impacted Hunan, Jiangxi, Guizhou, Yunnan, Guangxi, and Guangdong, resulting in water levels in parts of the Gan and Xiangjiang rivers being the lowest recorded in the past 50 years. During the summer, the precipitation in eastern China was near to below normal, while precipitation was about 30% below normal in the southern part of Northeast China and the middle part of Inner Mongolia.

In Japan, annual precipitation was significantly above normal on the Pacific side of northern Japan. Conversely, rainfall was below normal on the Pacific side of western Japan and Okinawa/Amami, but near normal in other areas. Several tropical cyclones, and the lingering Bai-u front along the Japanese archipelago (consistent with the weak northward expansion of the North Pacific High), brought unusually wet and cloudy conditions to western and northern Japan during July 2009. A new record for monthly total precipitation for July was set on the Pacific side of northern Japan (209% of the 1971–2000 normal), and correspondingly, the Sea of Japan side of the

country experienced its lowest monthly sunshine duration since 1946. Some crop damage and a rise in vegetable prices were reported in association with this unsettled weather. The active Bai-u front also caused disastrous flooding in western Japan in July 2009.

(iii) Notable events

Over the western North Pacific and the South China Sea, 22 named tropical cyclones (TCs) formed in 2009, 13 of which reached typhoon intensity. This total is less than the 30-year (1971–2000) average frequency of 26.7. Although the formation of the first named TC in 2009 was relatively late, the total number of cyclones (21) that formed from May to October was similar to the 30-year average frequency of 21.3. Morakot swept across the Taiwan Province and caused more than 400 deaths and severe damage to agriculture and infrastructure.

In spring 2009, China was affected by seven dust and sand events (five dust storms, two blowing sand), which was significantly less than 2000–08 average of 13.3 events. The average number of dust days across all recording stations in northern China was 0.9 days (4.7 days less than normal of 1971–2000), ranking the least since 1954.

The Republic of Korea was affected by a total of 10 dust events during 2009, with the strongest occurring on 25 December and lasting for two days. The average number of dust days over the 28 recording stations was 7.7 days in 2009, which was twice the normal (3.8 days) but slightly less than the most recent 10 years, which averaged 9.2 days. The number of dust days in spring 2009 was 2.5 days, which was slightly below normal (3.6 days) and one-third of the recent 10-year average (7.5 days). The year was notable in that 60% of all dust events appeared during the autumn and winter seasons.

In Japan, the number of days on which any meteorological station in Japan observed a Kosa (yellow sand/aeolian dust event) in 2009 was 22, which was near normal (20.2 days). The annual cumulative number of Kosa observations in 2009 was 251, which was above normal (163.0 days). Kosa was observed in October and December for the first time in last 17 years and 16 years, respectively.

Asian summer monsoon activity was generally suppressed throughout the season, except in the western North Pacific monsoon region. At the north periphery of the upper Tibetan High, the subtropical jet stream was stronger than normal.

The South China Sea (SCS) summer monsoon (SCSM) broke out in the 6th pentad of May and with-

drew in the 3rd pentad of October. The intensity index of the SCSM was -0.35, near normal. From the 6th pentad of May to the 2nd pentad of August, the SCSM was stronger than normal, while after mid-August it became weaker than normal (Fig. 7.42). At the end of September, the warm and wet air swiftly retreated south of 25°N, and hence by the third pentad of October the summer monsoon had withdrawn from the SCS.

3) SOUTH ASIA—M.Rajeevan, A. K.Srivastava, and J. Revadekar

Countries considered in this section include: Bangladesh, India, Pakistan, and Sri Lanka.

(i) Temperatures

During 2009, South Asia experienced notably warmer-than-normal conditions. January and February were characterized by unusually high temperatures. Prolonged breaks during the summer monsoon season also resulted in above-average temperatures, with many stations reporting their highest temperatures on record. Similarly, during the winter season, many parts of India and Pakistan experienced mean temperatures 3°C–5°C above their 1961–90 normal.

The annual mean temperature for India was +0.91°C above average, making 2009 the warmest year since nationwide records commenced in 1901 (Fig 7.43). This superceded the previous five warmest years on record, notably 2002 (+0.71°C), 2006 (+0.60°C), 2003 (+0.56°C), 2007 (+0.55°C), and 2004 (+0.51°C). January (+1.43°C) and August (+1.00°C) mean monthly anomalies were also the highest since 1901, while the anomalies for February, September, and December were all second highest since records began. The recent decade (2001–09) was the warmest decade on record over India with decadal mean temperature of 0.59°C.

FIG 7.43. Annual mean temperature anomalies (with respect to 1961–90 normal) averaged over India for the period 1901–2009. The smoothed time series (9-point binomial filter) is shown as a continuous line.

(ii) Precipitation

The summer monsoon season (June–September) contributes 60%–90% of the annual rainfall over major portions of South Asia. In 2009, South Asia experienced one of its worst droughts since records began in 1875.

For India, the long-term average (LTA) value of the summer monsoon rainfall, calculated using all data from 1941 to 1990, is 890 mm. For 2009, the summer monsoon seasonal rainfall over India was only 78% of its LTA value, marking 2009 as the driest monsoon season since 1972 (76% of LTA). During the season, most parts of the country experienced large rainfall deficiencies (Fig. 7.44). The onset phase of monsoon 2009 was characterized by an early onset (23 May) over the southern parts of India. However, the formation and northward movement of tropical cyclone Aila over the Bay of Bengal and the persistent intrusion of dry air into the South Asian region due to eastward moving mid-latitude troughs disrupted the northward progress of the monsoon. The slow progress of the monsoon resulted in a record rainfall deficiency (47% below normal) for June over the country. Rainfall activity during July was near normal with monthly rainfall of 96% of the LTA. However, rainfall activity was again suppressed both in August (73% of LTA) and September (80% of LTA), making the 2009 summer monsoon season the second most deficient season since records began in 1875.

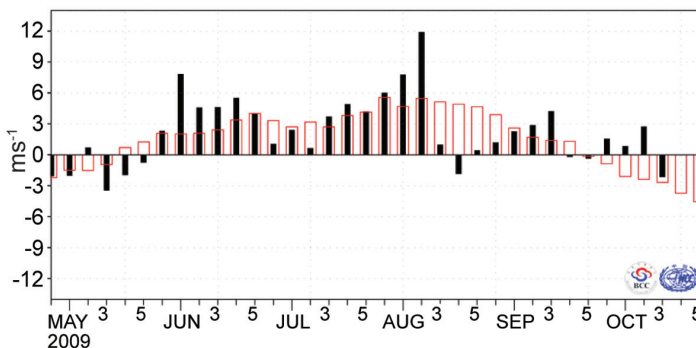During the season, of the 36 meteorological subdivisions, only three received

FIG 7.42. Variation of pentad zonal wind index over the monitoring region (10°N–20°N, 110°E–120°E). Red open bars are climatology (Unit: m s⁻¹) (Source: China Meteorological Administration.)
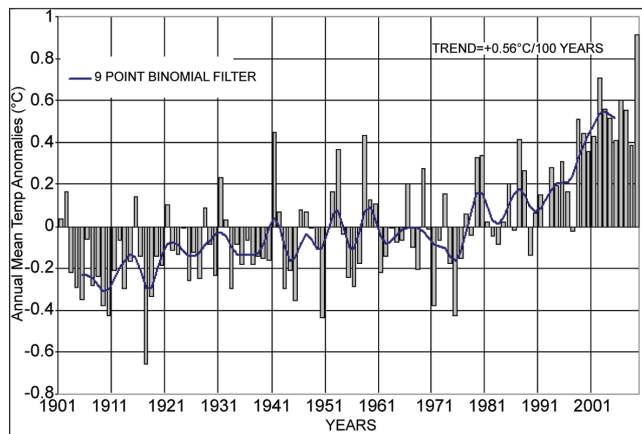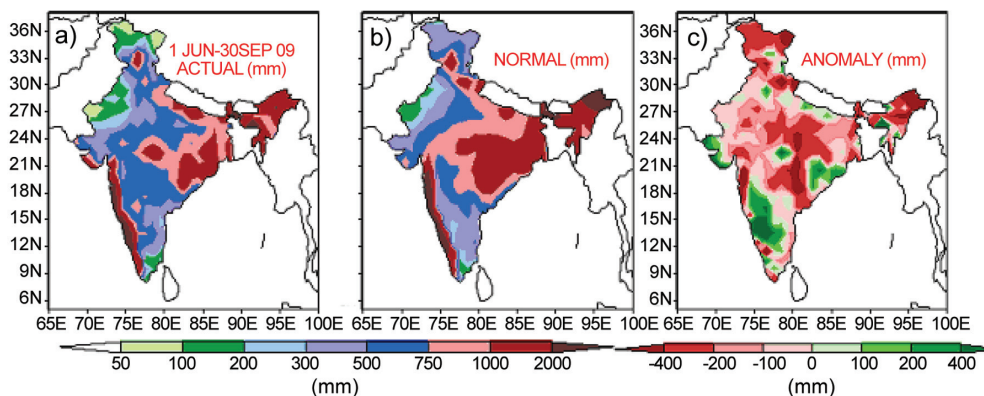
FIG. 7.44. Monsoonal (Jun–Sep) rainfall over India in 2009. (a) actual, (b) normal (base period) and, (c) anomalies (with respect to base period.)

excess rainfall, while 11 subdivisions received normal rainfall and the remaining 22 subdivisions received deficient rainfall. Out of 516 meteorological districts for which rainfall data were available, 59% of districts received 80% or less of their LTA. The 2009 summer monsoon was also characterized by strong intraseasonal variability (Fig. 7.45). Consistent with the observed decreasing trend in the frequency of monsoon depressions over the Indian Ocean, only four short-lived depressions formed during the season, against the long-term average of seven.

Over India, rainfall activity during the winter and pre-monsoon seasons was also below average. In 2009, the annual rainfall over the country was the most deficient (20% below normal) since records began in 1875, surpassing the previous record set in 1972. During the winter, rainfall over the country was 46% below normal, while during the pre-monsoon season (March–May), rainfall deficiency was 32%. While no drought had occurred over South Asia in the previous decade (1991–2000), the recent decade (2001–09) witnessed three major droughts in 2002, 2004, and 2009.

During the 2009 summer monsoon season, Pakistan also experienced one of its worst droughts. The area-weighted summer monsoon rainfall over Pakistan was 26% below its LTA. Most parts of the country, with the exception of Karachi and Hyderabad (southwest Sindh), experienced large rainfall deficiencies during the season. As a result, the 2009 monsoon season rainfall was the third lowest in the most recent decade (2001–09), after 2002 (54% deficiency) and 2004 (38%). Rainfall in July, August, and September was 9%, 41%, and 37% below normal, respectively.

The observed drought over the region had several possible causes. These include the El Niño-Modoki (warming over the Central Pacific; Ratnam et. al 2010), unusually warm equatorial Indian Ocean sea surface temperatures (Francis and Gadgil 2010), and the formation of an anomalous blocking high over west Asia with the associated descent of dry air into the Indian region (Krishnamurti et al. 2010).

The northeast monsoon (NEM) sets in over southern peninsular India during October and over Sri Lanka in late November. The NEM contributes 30% to 50% of the annual rainfall over southern peninsular India and Sri Lanka as a whole. The 2009 NEM seasonal rainfall over south peninsular India was above normal (110% of LTA), consistent with the observed relationship with El Niño. During the first week of November, heavy rainfall caused significant flooding and landslides in the southern Indian state of Tamil Nadu, sadly leading to the deaths of about 75 people. Above-normal rainfall was also reported over Sri Lanka during the season.

(iii) Notable events

Heat wave/hot day conditions prevailed over parts of central and peninsular India during the first three weeks of March; over the northern parts of the country on many days during April; and over northern, central, and peninsular parts of the country during the second half of May. There were approximately 150
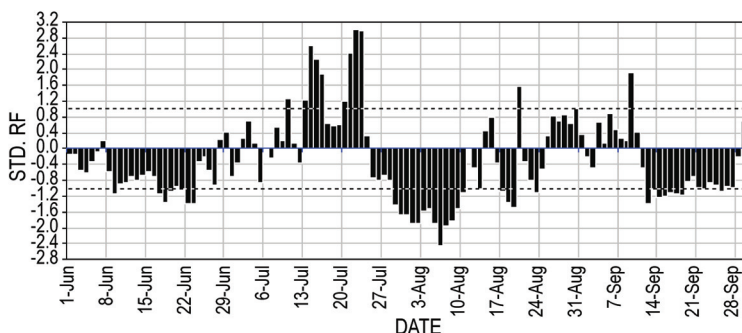
FIG. 7.45. Daily standardized rainfall time series averaged over the monsoon region of India (1 June to 30 September 2009).

S.No.	Station	New Record	Date	Previous Record	Date	Year	Data Period

TABLE 7.1. Record 24-hr rainfall (mm) in South Asia during 2009.

S.No.	Station	New Record	Date	Previous Record	Date	Year	Data Period
Month: June 2009
1	Bangalore	89.6	11	76	9	1996	1901-2009
Month: July 2009
2	Porbandar	444.3	16	252.6	16	1969	1961-2009
3	Veraval	503.8	16	361.7	23	1996	1901-2009
4	Naliya	301.3	25	273.9	21	1992	1958-2009
5	Dahanu	439.1	16	431.0	1	1956	1951-2009
6	Raipur	275.2	14	228.7	2	1970	1901-2006
7	Kozhikode	282.2	17	279.3	11	1997	1901-2000
Month: September 2009
8	Narsingpur	286	9	271.3	15	1999	1962-2009
Month: October 2009
9	Jalpaigure	258.2	8	244.3	1	1909	1901-2009
10	Panjim	256.8	3	178.3	6	1929	1901-2009
11	Kurnool	185.9	1	147.6	17	2001	1901-2009
12	Karwar	434.0	3	190.2	13	2002	1901-2009

deaths due to heat waves in May, mainly in Andhra Pradesh.

Tropical Cyclone Aila developed as a tropical depression on 23 May in the North Indian Ocean and made landfall near the India-Bangladesh border on 25 May as a severe cyclonic storm. The storm not only affected residents but also affected the ecosystem of the Sundarbans. Dhaka, the capital city of Bangladesh, received 290 mm of rain on 29 July, the greatest rainfall in a single July day since 1949.

On 16 July, northern parts of the west coast of India received exceptionally heavy rainfall, with many stations reporting record heavy rainfall, causing large-scale flooding. On 16 July, Veraval, a coastal town in Gujarat, recorded 500 mm of rainfall in just 24 hours. During the first week of October, the southern states of Karnataka and Andhra Pradesh received their heaviest rainfall in more than 60 years, leading to one of their worst floods on record. At least 286 people were killed and 2.5 million were left homeless following the torrential downpours and subsequent flooding. Government officials reported total damages in the range of $6.7 billion U.S. On 3 October, the city of Panjim on the west coast of Goa, recorded 256.8 mm of rainfall in 24 hours, the heaviest October rainfall on record for Panjim (Table 7.1)

4) SOUTHWEST ASIA

(i) Iraq—M. Rogers

Iraq, in 2009, experienced temperatures higher than the 1961–90 average across most areas and the extension of the drought which has led to falling river levels in the Tigris and Euphrates. Rainfall was generally lower than the 1949–90 average, which had a massive impact upon wheat, rice, and barley production within the country.

(A) TEMPERATURE

Averaged over the year, temperatures for Iraq were 1°C–2°C above the 1961–90 normal, although some areas in the west of the country recorded temperatures up to 1°C below average.

Mean winter temperatures were slightly above average during December 2008 and January 2009 but were around 3°C higher than average during February. For the winter as a whole, temperatures were near normal in the south but 1°C–2°C higher than normal further north. Spring temperatures were generally average during March and April but in most areas were 2°C–3°C above normal during May. The exception was in the western desert, where temperatures were below average (around 3°C below at Ar Rutbah).

Summer temperatures were 1°C–3°C above average. Again, the exception was western Iraq, with below-average temperatures (1.5°C at Ar Rutbah). The northwesterly Shamal winds dominated conditions, bringing occasional dust storms. Similarly, September–October temperatures were generally 1°C–2°C above normal, except in the West where they were near average. The year ended with temperatures 2°C–3°C above the December average.

(B) RAINFALL

Rainfall over Iraq was generally less than 60% of the 1949–90 average, with significantly lower falls recorded in some regions (Fig. 7.46).

The winter period, Iraq's wet season, was much drier than normal with most locations receiving less than 30% of their normal winter rainfall. Baghdad only recorded around 8% of its average rainfall. Rainfall in spring was also well below average, with Mosul receiving just 52% of their normal spring total and Baghdad just 36%.

However, an unsettled period of weather during September and October led to above-average rainfall in many places. Both Mosul and Baghdad recorded rainfall totals 10% higher than average during autumn, even though November was drier than normal. Mosul received over 200% of the normal rainfall during October. The rainfall in December at Mosul was just over 20% higher than expected but further south it was again drier than normal.

(C) NOTABLE EVENTS

Due to the dry conditions lifted dust occurred more frequently across the year and fog occurred less.

(ii) Iran—F. Rahimzadeh and M. Khoshkam
(A) TEMPERATURE

Maximum, minimum, and mean temperature anomalies for Iran were mixed during 2009 (Table 7.2). Winter was generally much warmer than the 1989–2008 average, with temperatures around 3°C above normal and local anomalies of up to +4°C. During spring, while the northern part of the country experienced temperatures up to 2.8°C below average, the southern and western parts of Iran recorded mean temperatures up to 3°C above average (Fig. 7.47). For summer, temperatures were generally 0°C–2°C above

FIG. 7.46. 2009 Rainfall percentage of 1949–90 normal. (Source: U.S. Air Force, 14th Weather Squadron.)
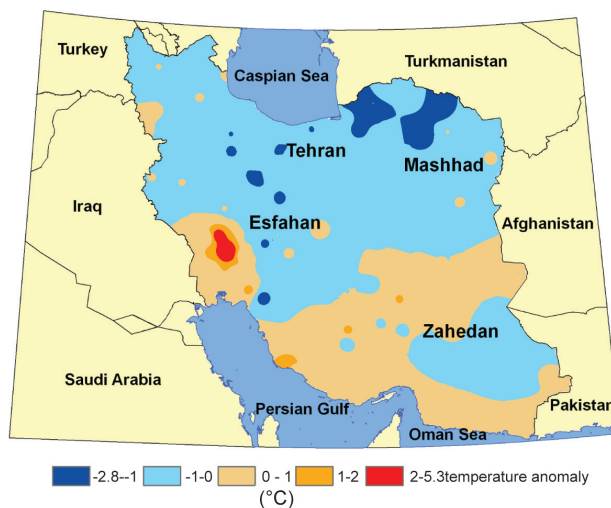

FIG. 7.47. Spring mean temperature anomaly (°C; base period 1989–2008) for Iran. (Source: Islamic Republic of Iran Meteorological Organization.)

normal; however, in the northwest of the country, average temperatures were up to 3°C below average. The largest anomalies were recorded in Dogonbadan and Amol (southeast Iran), with temperatures 3°C and 2°C below normal, respectively. Temperatures during autumn were generally warmer than average across the whole country, with anomalies around +2°C; although small areas in the South and Southeast recorded anomalies between +3 and +5°C. Only a small area of cooler-than-average conditions was confined to parts of the northwest.

(B) RAINFALL

Iran was wetter than its 1989–2008 average during spring and autumn 2009 (Table 7.2), with spring, autumn, and summer receiving more rainfall in 2009 than they received during the previous year. During winter, areas with near- to above-average rainfall were confined to some parts of the Northeast (Golestan Province), the Southeast, and small areas in the Northwest of the country. At Gonbad, in Golestan province, rainfall was up to 400% of the long-term average. The largest total of 435 mm was observed in Koohrang in the Zagross mountain area. Elsewhere conditions were very dry, with precipitation at most 30% of the long-term mean. In contrast to the previous year, precipitation was generally above average during spring (Fig. 7.48). Over more than three-quarters of the country, precipitation was at least 140%, peaking over 170%, of the long-term mean. Highest totals were recorded in Bandar Abbas, which received around 300% of its normal spring rainfall.

During the summer, most of the western half of the country received above-average precipitation, while southeastern parts of the country recorded below-normal rainfall. Although rainfall totals of up to 350 mm were recorded in Astara, some areas in the South, Central, East, and Southeast received no measurable rainfall at all.
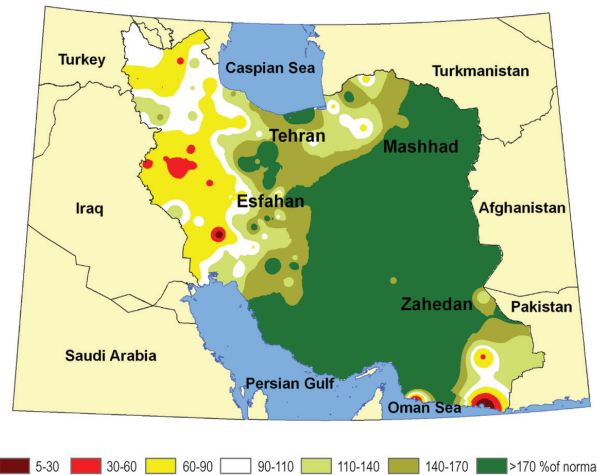
FIG. 7.48. Spring precipitation (percentage of the 1989–2008 normal) for Iran. (Source: Islamic Republic of Iran Meteorological Organization.)

During autumn, most parts of the country, except for areas in the southern half, the Northeast, and some parts of the Northwest, received up to 110% of their long-term rainfall. Highest rainfall was recorded in Zagross, in the Alborz mountain area.

(C) NOTABLE EVENTS

Significant dust storms were reported during winter, spring, and summer, spreading out over large parts of the southern half of Iran. Unusually, these conditions extended into other parts of the country, including the Southwest and central areas, during summer.

h. Oceania

1) AUSTRALIA—B. C. Trewin and A. B. Watkins

Australia experienced its second warmest year on record in 2009, featuring three exceptional and widespread heat waves. It was the warmest year on record for the states of South Australia and New South

TABLE 7.2. Seasonal amount of precipitation and temperature over Iran 2009					
parameter	Season	Winter	Spring	Summer	Autumn
Precipitation	Average (mm)	62.6	81.0	11.5	85.5
	Respect to (%) long term	42%	36%	6%	37%
	Range from-to (mm)	0 to 435	5 to 395	0 to 350	2 to 702
Temperature	Respect to long term	0 to 3	-2 to -5.3	-2 to 3	0 to 5
	Range from-to (C°)	-5.5 to 22.5	5 to 34	15 to 39	2 to 23

Wales. The warmth was particularly marked in the second half of the year, coinciding with a transition from La Niña to El Niño conditions. Nationally-averaged rainfall was close to normal, with a very wet summer in many tropical areas being followed by generally drier-than-normal conditions from March to November.

(i) Temperature

Australia had its second warmest year on record in 2009 with a national anomaly of +0.90°C, only behind the +1.06°C record mean temperature anomaly observed in 2005. Both maximum and minimum temperatures were well above normal, with anomalies of +1.04°C (third highest) and +0.76°C (fifth highest), respectively. South Australia (mean temperature anomaly +1.26°C) and New South Wales (+1.32°C) each had their warmest year ever, breaking records set in 2007, while Victoria (+1.02°C) ranked second behind 2007.

Maximum temperatures were generally above normal almost throughout the country (Fig. 7.49). Anomalies exceeded +1°C over most of mainland Australia south of the tropics except for southern Western Australia. The largest anomalies, mostly between +1.5°C and +2°C, were in inland areas of New South Wales and southern Queensland, as well as in an area straddling the Western Australia–Northern Territory border west of Alice Springs.

Minimum temperatures were also above normal through most of Australia (Fig. 7.50), although they were below normal in most tropical areas of Queensland, as well as in scattered patches through Western Australia and the northern half of the Northern Territory. The largest anomalies (+1°C and +1.5°C), were in the southern and central inland, covering most of South Australia north of Port Au-

gusta, New South Wales west of the Great Dividing Range, southwestern Queensland, and the southern Northern Territory.

Early in the year there were marked temperature contrasts between northern and southern Australia. January and February were much cooler than normal in most of the tropics as a result of the very active wet season. Maximum temperatures were at least 2°C below normal for the period over much of tropical Queensland and the eastern Northern Territory, reaching up to 6°C below normal near Cloncurry. In contrast, temperatures were 2°C–3°C above normal in much of southern Australia, during a period which included the major heat wave of late January and early February (see sidebar).

After being only slightly above normal (anomaly +0.28°C) for the first five months of the year, temperatures became sharply above normal from June onwards. The winter–spring (June–November) period (anomaly +1.22°C) was Australia's warmest on record by more than 0.3°C, as was the second half of the year (anomaly +1.22°C). Both August and November contained major heat waves, resulting in both months being the warmest on record for Australia (see sidebar).

The year 2009 also ended Australia's warmest decade since temperature records began in 1910, with a mean temperature 0.48°C above the 1961–90 average.

(ii) Precipitation

Rainfall averaged over Australia for the year was 458 mm (2% below normal), ranking 63rd highest since records began in 1900. Annual rainfall was above normal over most of the northern tropics and in Tasmania but was near or below normal over most of the southern and central mainland.
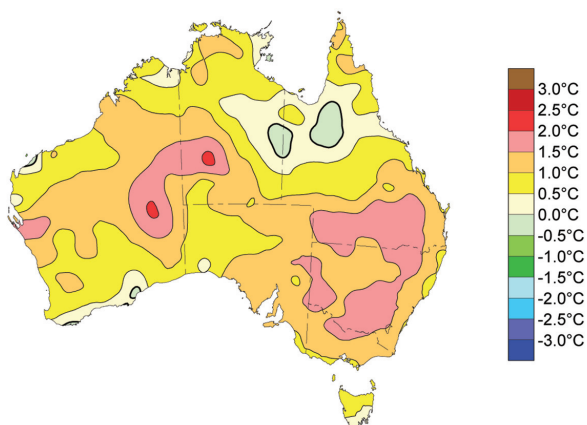

Fig. 7.49. Australian mean annual maximum temperature anomalies (base period 1961–90) for 2009.
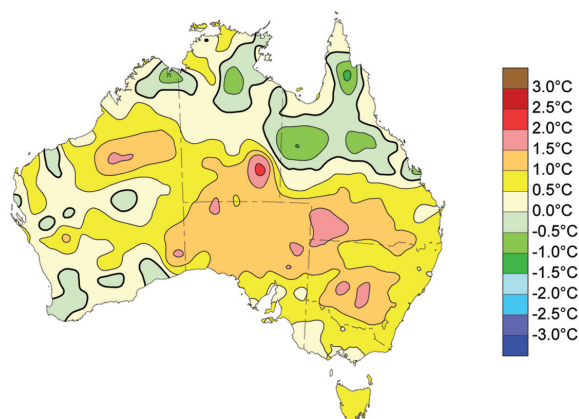

Fig. 7.50. Australian mean annual minimum temperature anomalies (base period 1961–90) for 2009.

The most significant area of above-normal rainfall was in northern Queensland (Fig 7.51), where most of the region between about 17°S and 21°S had annual rainfall in the highest decile with some areas around Mount Isa experiencing their wettest year on record. Smaller areas in the highest decile were scattered through tropical Western Australia, the Northern Territory, the West Kimberley region, the northern coast of New South Wales, and in southeastern Tasmania around Hobart.

The two most significant dry areas were in central Australia and on the southeast coast. Annual rainfall was in the lowest decile along the southeast coast and the adjacent inland region between Wollongong and Melbourne and in much of the southern Northern Territory. In northeastern South Australia, Moomba only had 11 mm from January to mid-November. There were smaller areas in the lowest decile in inland southeast Queensland and along the southern half of Western Australia's west coast (including Perth).

The bulk of the tropical rainfall fell in January and early February, with northern Queensland wet-season rainfall being the highest since 1990/91. Conditions through most northern and central areas became much drier from March onwards, and a number of locations in northwestern Queensland and the central Northern Territory had no rain between early April and late November. Wet conditions returned in December as a result of Tropical Cyclone Laurence.

The January–May period was dry across much of southern Australia, especially Victoria and southwest Western Australia, where it ranked as the third- and fifth-driest on record, respectively. Kalbarri (Western Australia) did not record its first rain of 2009 until 20 May. Rainfall returned to more normal levels from June onwards, leading to a good winter cropping season in many areas. Nevertheless, annual rainfall was 19% below normal for Victoria and 15% below normal for the Murray–Darling Basin, continuing the long-term droughts in these regions which commenced in 1997 and 2001, respectively.

Tasmania had an extremely wet winter and early spring, with June–September rainfall the second highest on record. Despite dry conditions early and late in the year, these rains were sufficient for the state's annual rainfall to be 8% above normal.

(iii) Notable events

There were three exceptional heat waves in Australia during 2009, all of which saw records broken by large margins over wide areas. The first occurred in late January and early February, affecting southeast-
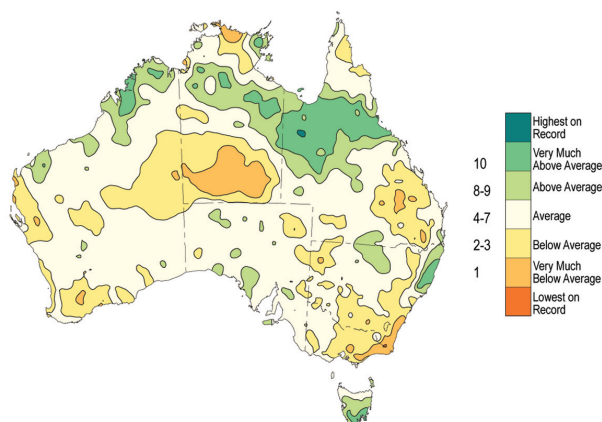
Fig 7.51. Australian annual rainfall deciles (since 1900) for 2009.

ern Australia, and was accompanied by widespread loss of life resulting from extreme heat and bushfires. Major heat waves also occurred in August in much of tropical and subtropical eastern Australia and in November in most of the Southeast (see sidebar) The heavy tropical rains early in the year resulted in widespread flooding, especially in Queensland. Floods persisted for several weeks on many rivers in northwestern Queensland. Floodwaters from the Georgina River eventually led to a partial filling of Lake Eyre. Further east, there was major flooding on a number of coastal rivers in coastal Queensland. The worst impacts were in the vicinity of Ingham, which received 949 mm of rainfall in a six day period, 30 January–4 February.

A section of the northern New South Wales coast centered on Coffs Harbour was subject to repeated flooding with five significant events during the year. The most widespread, in late May, extended north to the Clarence River catchment and parts of southeast Queensland. Property damage was mostly minor, but there was one death in the Coffs Harbour area and the town of Yamba was isolated for nine days.

At the end of the year, tropical cyclone Laurence made landfall at category 5 intensity, between Broome and Port Hedland after an earlier landfall east of Derby. Moisture from its remnants fed into an inland trough and resulted in flooding in parts of northern inland New South Wales during the last week of December.

Dust storms affected eastern Australia on a number of occasions in late September and early October. The most significant, on 22–23 September, reduced visibility to below 200 meters over a vast area, including the cities of Sydney, Brisbane, and Canberra. This is believed to be the most extensive dust storm of such intensity since at least the 1940s.

The most significant severe thunderstorms of the year affected northern Tasmania on 15 April, with some property damage and widespread power outages. A tornado passed directly over an automatic weather station at Scottsdale, with a gust of 194 km hr^{-1} recorded.

(iv) Significant statistics
- Mean annual maximum temperature anomaly: +1.04°C
- Mean annual minimum temperature anomaly: +0.76°C
- Mean annual rainfall anomaly: -3%
- Highest annual mean temperature: 29.4°C, Wyndham (Western Australia)
- Lowest annual mean temperature: 4.9°C, Mount Wellington (Tasmania)
- Highest annual total rainfall: 7440 mm, Bellenden Ker (Top Station) (Queensland)
- Highest temperature: 49.0°C, Emu Creek (Western Australia), 10 January
- Lowest temperature: -14.9°C, Charlotte Pass (New South Wales), 16 July

AUSTRALIA'S THREE GREAT HEAT WAVES OF 2009

Australia experienced three exceptional heat waves during 2009, with records broken by huge margins and with major loss of life through both extreme heat and bushfires.

January/February-The first heat wave affected southeastern Australia on 27 January–8 February. Between 27 January and 31 January, the state capitals Adelaide and Melbourne had four and three consecutive days, respectively, above 43°C, both of which were records. Large areas of southern Victoria and Tasmania set all-time records. A new state record for Tasmania was set with 42.2°C at Scamander on the 30th. Extreme day and nighttime heat (including a record high minimum of 33.9°C at Adelaide on the 29th) caused severe heat stress, with 374 excess deaths occurring in Victoria. Extreme heat returned to South Australia on 6 February and to Victoria and New South Wales on the 7th (Fig. 7.52), with an all-time record of 46.4°C at Melbourne and a Victorian state record of 48.8°C at Hopetoun. Of 35 long-term stations in Victoria, 24 set all-time records; six others set February records. The accompanying strong, dry northwesterly winds fanned bushfires which claimed 173 lives, mostly in areas northeast of Melbourne.

August-Forty-nine percent of the continent, including most of Queensland and the Northern Territory, experienced its highest August mean maximum temperature on record, resulting in a new all-time record national maximum temperature anomaly of +3.20°C. Extreme heat occurred on 14–16 August, 21–25 August, and 29–30 August. A New South Wales August record of 37.8°C was set on the 24th at Mungindi, while a new Queensland record of 38.5°C was set on the 29th at Bedourie. Site records were broken by extremely large margins with numerous long-term stations setting August records by more than 4°C. Daily maximum temperature records were set over 25% of Australia, including 55% of Queensland.
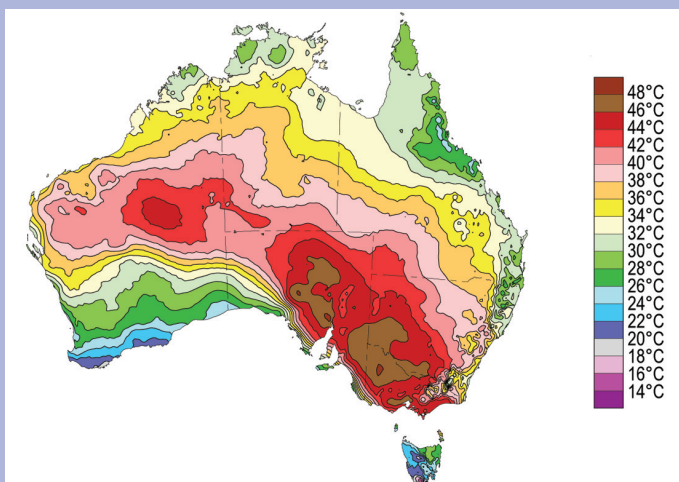
Fig. 7.52. Maximum temperatures on 7 February 2009.

November-Persistent heat occurred across much of southeast Australia. All-time duration records were set in South Australia at Port Lincoln (eight consecutive days above 30°C) and Murray Bridge (six consecutive days above 40°C); these were particularly extraordinary as extended heat waves in southern Australia have been almost entirely confined to the second half of summer and early autumn. Adelaide's eight consecutive days above 35°C was double its previous November record. Daily record high temperatures for November occurred over 41% of New South Wales, including a state November record of 46.8°C at Wanaaring on the 20th. The mean monthly temperature anomaly for New South Wales was +4.61°C, the largest recorded for any Australian state, with Victoria (+4.36°C) also breaking the previous record. (In Victoria, only one December has been hotter than November 2009). Eighty long-term stations had their largest monthly maximum temperature anomaly on record for any month, and Cowra's anomaly of +7.9°C was the largest recorded at any Australian station since 1914.

- Highest one-day rainfall: 510 mm, Urunga (New South Wales), 1 April
- Highest wind speed (measured): 211 km hr^{-1}, Mandora (Western Australia), 21 December

2) New Zealand—G. M. Griffiths

New Zealand's climate for 2009 was characterized by frequent seesaws in extreme temperature. Heat waves occurred in January and the start of February; May was the coldest on record; August was the warmest August since records began; and October had its lowest temperatures since 1945. During individual months (notably September and November), daily maximum and minimum temperatures frequently broke long-standing records, with extremely cold temperatures often occurring within a week or so of record hot events. The decade 2000–09 was the warmest in the instrumental record for New Zealand.

(i) Temperature

The New Zealand national average temperature[2] for 2009 was 12.42°C, 0.16°C below the 1971–2000 normal (Fig. 7.53), consistent with the prevailing southwesterlies over the country during the year. Temperatures were generally within 0.5°C of the long-term average over most of the country. The exceptions were parts of Auckland, Waikato, Manawatu, southern Hawkes Bay, Wairarapa, Wellington, Marlborough, inland Canterbury, and eastern Otago, where annual temperatures were 0.5°C–1.0°C below average.

The year was notable for two remarkably warm months (January and August) and a very warm spell in early February. Heat waves were experienced over the country 7–12 February, when northwesterlies transported some of the record-breaking Australian heat to New Zealand. Temperatures of 34°C or more occurred in many locations on each day in this period. Many new records of extreme high monthly maximum temperatures were established in January, February, and August. In contrast, New Zealand also experienced four extremely cold months (March, May, June, and October), and an extended frosty period across many parts of the country on 16–26 June. Many record-low monthly minimum temperatures were
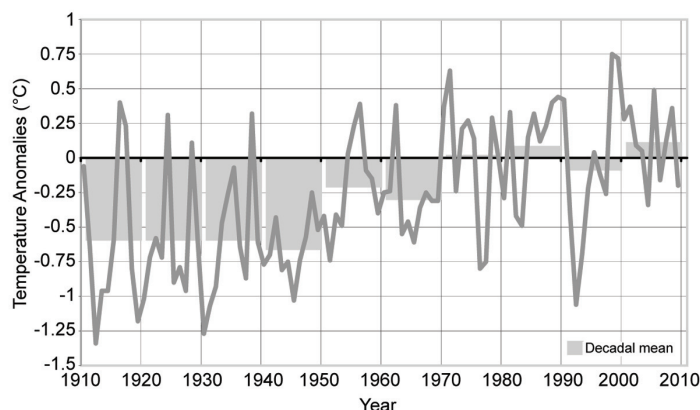
Fig. 7.53. Annual and decadal mean temperature anomalies for New Zealand based upon a seven-station series. Base period: 1971–2000.

established in these four months, as well as numerous record-low daily minimum temperatures.

The decade 2000–09 was the warmest in the instrumental record for New Zealand, with a 10-year average temperature of 12.69°C, 0.11°C above the long-term normal, just surpassing the previously warmest decade (the 1980s).

(ii) Precipitation

Annual rainfall for 2009 was below normal (50%–80% of normal) for parts of Auckland, the central North Island, and eastern areas of both islands (northern Hawkes Bay, southern Wairarapa, north Canterbury, inland south Canterbury, and central Otago). Taupo, in the central North Island, recorded its driest year since records began in 1949 (712 mm). Elsewhere, annual rainfall was near normal.

The year 2009 was unusually snowy in New Zealand, with an extended snow season that started in April and finished in October. Numerous and heavy snowfall events, and the record warmth of August, contributed to a high-risk avalanche season in the Southern Alps in August and September. Major snowfall events to low levels, which were widespread, were observed on 31 May, 16 June, 2–5 July, and 4–6 October, resulting in significant community impacts. The exceptionally heavy snow event on 4–5 October affected Hawkes Bay and the Central North Island and was estimated to be the worst in October since 1967, stranding hundreds of travelers, closing roads, and resulting in heavy lambing losses. Snowfall was also observed in Taranaki, Waikato, and Rotorua on the 6th, for the first time in about 30 years.

The most unusual precipitation event of the year was a coating of red Australian dust, sometimes 2

---

[2] http://www.niwa.co.nz/news-and-publications/news/all/nz-temperature-rise-clear/seven-station-series-temperature-data

mm thick, which fell on parts of Northland, Auckland, Waikato, Bay of Plenty, and Taranaki on 25 September.

(iii) Notable events

At the start of 2009, soil moisture levels were below normal for much of the North Island (except Gisborne and northern Manawatu), as well as in the Tasman District, northern Westland, north and south Canterbury, and south Otago. However, rainfall in late February returned soil moisture levels to near-normal status across much of the country. For regions in the north and east of the North Island, and eastern South Island (Northland, Auckland, Coromandel, Bay of Plenty, central North Island, Gisborne, Hawkes Bay, Otago, Canterbury, the Kaikoura coast), severe soil moisture deficits had again developed by the end of the year, following an extremely windy and dry November and December period. Northland was particularly affected. The geographical pattern of significant soil moisture deficits in northern and eastern areas seen at the end of 2009 is a typical impact of El Niño conditions for New Zealand.

There were 15 flooding events in New Zealand in 2009, slightly less than 2008. Major flooding occurred on 27 April on the West Coast. On that day, Mt. Cook recorded 341 mm of rainfall (its highest April one-day total since records began in 1928), and torrential rain fell in Greymouth, where roads became impassable and homes were evacuated. Trampers were stranded in the Mueller Hut in Aoraki Mt. Cook National Park, and about 120 people were evacuated from the Milford Track by helicopter. Heavy rains also caused flooding on 16–20 May in the Canterbury and Otago regions, when the Rangitata River burst its banks. On 29 June, heavy rain resulted in landslips and road closures in the Manawatu–Wanganui region. Heavy rainfall in the Gisborne District on 29 and 30 June led to flooding, evacuations, landslips, and the declaration of a Civil Defence Emergency.

(iv) Significant statistics
- Highest annual mean temperature: 15.8°C, Whangarei (Northland)
- Lowest annual mean temperature: 7.3°C, Mt. Ruapehu (central North Island)
- Highest annual rainfall total: 10 956 mm, Cropp River in the Hokitika River catchment (West Coast)
- Highest one-day rainfall: 341 mm, Mount Cook, 27 April

- Highest recorded air temperature: 38.0°C, Culverden (Canterbury), 8 February (Also highest February maximum temperature ever recorded at this location)
- Lowest recorded air temperature: -11.7 °C, Middlemarch (Central Otago), 19 July
- Highest recorded wind gust: 184 km hr^{-1}, Southwest Cape, Stewart Island, 4 November

3) Southwest Pacific—A. Peltier and L. Tahani

Countries considered in this section include: American Samoa, Cook Islands, Fiji, French Polynesia, Kiribati, Nauru, New Caledonia, Niue, Papua New Guinea, Samoa, Solomon Islands, Tokelau, Tonga, Tuvalu, and Vanuatu.

(i) Temperatures

Temperatures were below the 1971–2000 average at numerous stations in the equatorial Pacific during the austral summer, the result of the weakening La Niña event in the tropical Pacific. In contrast, an extended region of above-average air temperature encompassed northern Papua New Guinea, New Caledonia, Vanuatu, Fiji, Tonga, Southern Cook Island, and the Austral Islands with anomalies up to +1.8°C south of Rapa (150°W).

With the development of El Niño in the austral winter, the temperature pattern reversed, with above-average air temperatures near the equator and relatively low temperatures over New Caledonia, Vanuatu, and Fiji. In general, temperatures were above normal in 2009 (Fig. 7.54; Table 7.3), largely due to the early-year La Niña being relatively weak compared to the subsequent moderate 2009/10 El Niño.

(ii) Rainfall

Annual rainfall exceeded 120% of the 1979–95 mean over parts of New Caledonia and Vanuatu (Fig. 7.55; Table 7.4). Below-normal precipitation (< 80%)
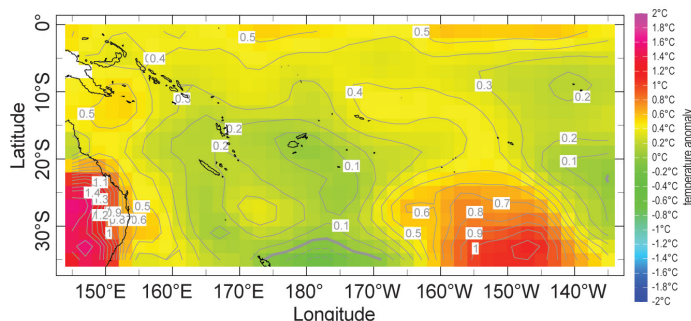

FIG. 7.54. Air temperature anomaly (1971–2000 base period) for the Southwest Pacific. (Source: NOAA NCEP CPC CAMS.)

TABLE 7.3. Average temperature anomaly (°C relative to 1971–2000 base period) for 2009 recorded by Pacific Islands Met Services. (Source: NOAA/NCEP CPC CAMS.)

Station	Island	2009 Anomaly
Peokoa Airport (Santo)	Vanuatu	+0.4
Noumea	New Caledonia	+0.6
Rotuma	Fiji	+0.1
Nadi Airport	Fiji	+0.2
Hihifo	Wallis	+0.6
Rarotonga	Cook Islands	-0.3
Tahiti-Faaa	Societ Islands	+1.4
Takaroa	Tuamotu Island	+0.5
Rapa	Austral Island	+0.9
Norfolk Island Aero	Australia	+0.3

parts of Vanuatu, New Caledonia, and Fiji, southwest of its normal position. Concurrently, a zone of suppressed deep convection was present near Western Kiribati and south of the equator, extending east through Nauru and Eastern Kiribati. From June to October, the SPCZ stagnated southwest of its normal position and contracted toward Northern Papua New Guinea. Enhanced convection was largely absent from the region during the austral winter, while the area of suppressed convection contracted towards the central part of the Southwest Pacific, near Tokelau. During November and early December, above-average convective anomalies along a southwest-displaced SPCZ were seen near northern Vanuatu, northern Queensland, and the eastern edge of Papua New Guinea, before becoming established eastward across Western Kiribati, Fiji, Tonga, Austral Islands, and the Pitcairn Islands as El Niño conditions took hold. Suppressed convection was observed during November in the central part of the Southwest Pacific near Fiji and Samoa, before extending towards the northern Cook Islands and French Polynesia during December.

(iii) Notable events

From January to March, under the influence of La Niña conditions, stronger-than-usual easterly surface winds prevailed along the equator across the Kiribati archipelago. From May until the end of the year, the trade winds weakened and hence westerly wind anomalies covered large portions of the equatorial Pacific, with the exception of some areas near the date line.

Fourteen synoptic-scale low-pressure systems formed in the Southwest Pacific in 2009. In January, record-breaking rainfall was recorded in Viti Levu

was recorded over Gambier and Tuamotu islands and along the equator across western Kiribati, Tuvalu, Tokelau, and eastern Kiribati. For the second year in a row, Tarawa and Banaba islands were particularly affected by significant drought conditions during the first six months of the year, highlighted by a number of record-low rainfall totals. Rainfall from January to April was above average over the Solomon Islands, Vanuatu, New Caledonia, Fiji, Tonga, Niue, and the Southern Cook Islands, while rainfall deficits were significant along the equator and over French Polynesia.

The rainfall pattern observed over the Southwest Pacific was heavily influenced by the state of ENSO. During the first three months of 2009 convection was suppressed along the equator from west of Nauru across Western Kiribati to the date line, while the South Pacific Convergence Zone (SPCZ) was further south and west of its mean location, extending from Papua New Guinea and northeastern Queensland to the New Caledonia archipelago (165°E). This La Niña dipole was less intense, and the area of maximum convective activity was not as spread out as during 2008, when the La Niña event resulted in the SPCZ expanding as far southeast as the Southern Cook Islands (160°W). In April 2009, the SPCZ shifted eastward, contributing to enhanced convective activity from Wallis and Futuna (175°W) to the Austral Islands (150°W). In May, the SPCZ weakened significantly, stalling over
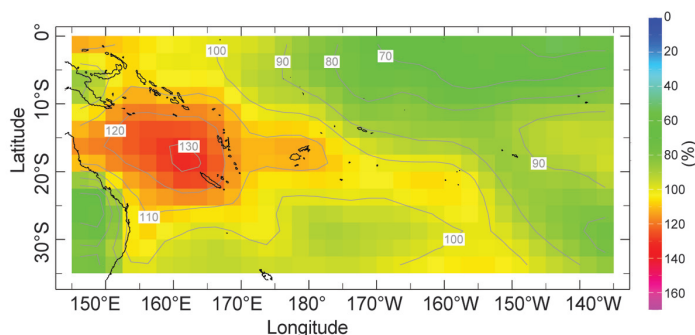

FIG. 7.55. Percentage of mean annual rainfall for 2009 (1979–95 base period) for the Southwest Pacific. (Source: NOAA NCEP CPC CAMS.)

and Vanua Levu islands (Fiji) as a consequence of a hovering monsoonal trough, an enhanced South Pacific Convergence Zone (SPCZ), two tropical depressions, and Tropical Cyclone Hettie. A total of 14 stations recorded at least 700 mm of rainfall during January, seven of them collecting more than 1000 mm. Overall, 75% of rain gauges in the Western, Central, and Eastern Divisions of Fiji recorded 200% of their average January rainfall. The related flooding is considered to be the country's worst in over 75 years, claiming 12 lives and causing substantial damages to agricultural crops, road, electricity, and water infrastructure.

In December, category 2 Tropical Cyclone Mick lashed the islands of Yasawa and Viti Levu, Fiji. On 14 December, sustained wind speeds of up to 81.3 km hr⁻¹ and gusts that reached 107.2 km hr⁻¹ were recorded at Nausori Airport near Suva. Five deaths and severe damage to crops and livestock were reported.

Typical of La Niña conditions, positive sea surface temperature anomalies were present around Vanuatu, New Caledonia, west and south of Fiji, and southern French Polynesia early in the year. From April to June, SSTs cooled in the Southwest Pacific, while positive anomalies developed in the western equatorial Pacific after May. In October, the warm anomalies in the western Pacific dissipated and warm anomalies developed south of French Polynesia. In December, a large area of positive anomalies, with the central region exceeding +3°C, existed from 160°W–90°W and 30°S–65°S.

Positive sea level anomalies existed in the Southwest Pacific in January from Papua New Guinea southeast to the Southern Cook Islands. Anomalies just east of Papua New Guinea exceeded +25 cm, while monthly mean sea levels at Fiji and Tonga were the highest on record. Monthly mean sea level at Fiji for February was, for a second month in a row, the highest on record. Tropical Cyclone Lin brought elevated sea levels to Tonga on 4 April 2009. Sea level at the height of the storm was 0.5 m higher than the predicted tide. Positive anomalies developed in the Southwest Pacific in May and extended almost to Rapa Island. In June, positive anomalies in the Southwest Pacific contracted both in area and magnitude but then expanded in July in the Southwest Pacific to the Southern Cook Islands. By September, the area with positive anomalies in

TABLE 7.4. Annual rainfall for 2009 reported by Pacific Islands Met Services

Station	Island	2009 Rainfall	Annual Mean (1979–95)	Percent of Mean
Peokoa Airport (Santo)	Vanuatu	3003	2452	122%
Koumac	New Caledonia	1529	995	415%
Noumea	New Caledonia	1129	1074	105%
Tarawa	Kiribati	2272	2302	99%
Rotuma	Fiji	3851	3515	110%
Nabouwalu	Fiji	3676	2130	173%
Nadi Airport	Fiji	2799	1708	164%
Vunisea	Fiji	2358	2047	115%
Hihifo	Wallis	2819	3218	88%
Maopopo	Futuna	4861	3206	152%
Apia	Samoa	2331	2770	84%
Papo Pago	American Samoa	3479	3003	116%
Rarotonga	Cook Islands	1657	1829	91%
Atuona	Marquesas Islands	1356	1677	81%
Tahiti-Faaa	society islands	1396	1690	83%
Takaroa	Tuamotu Island	1129	1592	71%
Rikitea	Gambier Islands	1728	1994	87%
Tubuia	Austral Islands	1777	1843	96%
Rapa	Austral Island	2865	2560	112%
Lord Howe Island Aero	Austral	1194	1483	81%
Norfolk Island Aero	Australia	901	1302	69%

the Southwest Pacific had contracted to between Australia and the Tonga and the maximum anomaly was just above +15 cm. Further weakening occurred in October in the southwest Pacific. Monthly mean sea levels were the highest on record in October at Kiribati and the highest since 2001 at Nauru.

4) NORTHWEST PACIFIC, MICRONESIA—C. Guard and M. A. Lander

Countries considered in this section include: the Commonwealth of the Northern Mariana Islands, the Federated States of Micronesia, the Marshall Islands, Palau, and the U.S.-affiliated Islands of Micronesia.

This assessment covers the area from the date line west to 130°E, between the equator and 20°N. It includes the U.S.-affiliated Islands of Micronesia, but excludes the western islands of Kiribati. The climate of the region is strongly influenced by ENSO. The first few months of 2009 began as La Niña, switching to El Niño by the boreal summer, becoming moderate to strong by December. After two years with virtually no tropical cyclone activity in Micronesia, the monsoon trough and tropical cyclone genesis regions shifted eastward, typical of their response to El Niño ocean patterns. In August two super typhoons impacted some of the Micronesian islands. The high sea levels characteristic of 2008 began to fall by September 2009 in response to El Niño. This process continued for the remainder of the year as oceanic heat content was transported eastward toward South America.

(i) Temperature

Average monthly maximum temperatures from January through June generally mirrored those conditions expected during moderate La Niña conditions and the transition to ENSO-neutral conditions. Average monthly maximum temperatures from January through June were generally typical of those expected during moderate El Niño events (Table 7.3). Average maximum temperature values at Yap were 0.53°C below normal (cooler and cloudier) for the first six months and 0.65°C above normal (warmer and clearer) for the latter half of the year as cloud systems developed farther eastward. Likewise, Pohnpei experienced January–June anomalies of +0.08°C

and July–December anomalies of +.0.55°C, suggesting clearer and warmer conditions. Still farther east, maximum temperature anomalies at Kosrae for January–June anomalies were -0.74°C, reflecting both enhanced cloudiness from the boreal spring trade wind trough and enhanced cooling due to evaporation from the strong trade winds. The July–December temperature anomaly was -0.65°C, as the near-equatorial trough became established and produced persistent cloudy conditions. At the eastern end of the region, Majuro in the southern Republic of the Marshall Islands (RMI), had near-normal January–June average maximum temperature anomalies of +0.18°C and relatively normal July–December anomalies of +0.04°C. Average minimum temperatures in the RMI were generally warmer than normal during the year, reflecting warmer-than-normal SSTs in the region.

(ii) Precipitation

Precipitation at the major island stations during 2009 was fairly typical of La Niña conditions early in the year and El Niño conditions during the second half of the year (Fig. 7.56; Table 7.5). In the first half of the year, the western half of the basin was wetter than normal, while most of the islands east of 155°E were drier than average. However, the stronger-than-normal and converging northeast and southeast trade winds typical of La Niña events allowed the trade wind trough to become well developed, keeping the western North Pacific islands between 3°N–6°N wet during the first half of the year. The trough axis typically passes very close to Kosrae, which had 2577.1 mm or 108% of normal rainfall during the first half of 2009. Generally throughout Micronesia, rainfall for
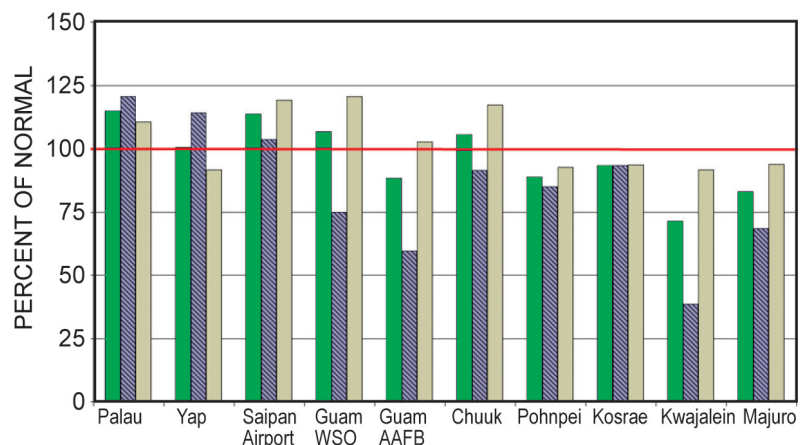

FIG. 7.56. Rainfall as a percent of normal for selected Micronesian islands for January through June (solid green), July through December (hatched blue), and for January through December 2009 (solid tan). The percent of normal is determined from the NCDC 1971–2000 base period.

TABLE 7.5. Maximum temperature anomalies and rainfall anomalies for selected Micronesian locations for January through June 2009 (Jan–Jun) and for July through December 2009 (Jul–Dec). "N" is the normal rainfall taken from the NCDC 1971–2000 base period. Locations (lat and lon) are approximate.

Location	Max Temp		Rainfall							
	Jan-Jun	Jul-Dec	Jan-Jun			Jul-Dec			Jan-Dec	
	°C	°C	N mm	2009 mm	%	N mm	2009 mm	%	2009 mm	%
Saipan 15°N 146°E	NA	NA	414.8	502.9	212	1293.1	1521.0	118	2023.9	120
Guam 13°N 145°E	+0.25	-0.13	612.1	525.0	86	1555.5	1942.1	126	2467.1	114
Yap 9°N 138°E	-0.53	+0.65	1168.9	1356.9	116	1818.6	1707.4	94	3064.3	103
Palau 7°N 134°E	+0.01	-0.64	1724.7	2020.1	117	2043.9	2300.2	113	4320.3	115
Chuuk 7°N 152°E	-0.21	-0.54	1538.0	1427.5	93	1864.9	2169.9	116	3597.4	106
Pohnpei 7°N 158°E	+0.08	+0.55	2277.6	1941.8	85	2411.5	2318.3	96	4260.1	91
Kosrae 5°N 163°E	+0.40	+0.22	2387.3	2577.3	108	2128.8	2313.5	109	4890.8	109
Majuro 7°N 171°E	+0.18	+0.04	1455.4	970.3	67	1888.7	1796.8	95	2767.1	82
Kwajalein 9°N 168°E	+0.03	+0.06	959.6	381.0	40	1590.5	1468.9	92	1849.9	73

the first six months, for the last six months, and for the entire year of 2009 fell between 75% and 125% of average. Only the eastern-most part of Micronesia fell outside this bracket, with extremely dry conditions experienced at Kwajalein (40% of average) and very dry conditions at Majuro (67% of average) during the first half of the year. Rainfall in the RMI increased to near-normal levels (95% at Majuro and 92% at Kwajalein) during the second half of the year as the monsoon trough pushed eastward. For the year as a whole, locations west of 155°E were wetter than normal and areas east of that longitude were drier. The annual rainfall for the major islands in Micronesia ranged from a high of 4890.1 mm (108%) at Kosrae to a low of 1849.9 mm (73%) at Kwajalein in the RMI. Palau at the western edge of the area had 4320.3 mm or 115% of normal, while Majuro at the eastern edge of the area had 2767.1 mm, 83% of normal for the year. In the center of Micronesia, Chuuk had 116% of its normal rainfall during the second half of the year and 106% for the entire year. Table 7.5 shows the annual

rainfall amount and percent of normal for the major Micronesian islands.

(iii) Notable events
The high sea levels that prevailed in 2007, 2008, and early 2009 finally began to fall by midyear as El Niño conditions reduced the easterly wind stress that caused water to mound up in the west of the basin. In the first three months of the year, coastal flooding and inundation affected many of the low islands from the Marshall Islands in the East to Palau in the West. From January through March 2009, sea levels averaged 15 cm–25 cm above their normal monthly averages, but during full and new moon phases, the high-tide levels were sometimes as high as 80 cm–110 cm above their normal monthly averages. The high astronomical tides coupled with the effect of La Niña and the long-term rising trend in sea level caused considerable coastal inundation in Chuuk State and in the Marshall Islands, contaminating drinking water and destroying crops. Weakened trade winds, starting

in April, triggered Kelvin waves which depressed the thermocline east of the dateline, resulting in higher ocean heat content and thus elevated sea level toward the Central and South American coasts. Correspondingly, this reduced ocean volume in the equatorial western Pacific, causing sea levels there to fall.

Tropical cyclone activity in 2009 across Micronesia increased considerably from 2008 (see chapter 4), as the El Niño conditions caused tropical cyclone genesis to occur farther to the east into central Micronesia. Super typhoons Choi-wan and Melor were the most notable, with Choi-wan devastating Alamagan Island (17.60°N, 145.85°E) in the Northern Mariana Islands and forcing the post-storm evacuation of the 14 residents.

Fig. 8.2. Dec 2008–Feb 2009 (top) Northern Hemisphere and (bottom) Southern Hemisphere 500hPa geopotential heights (9-dam contour interval) and anomalies (shading) determined from the 1979–2000 base period means.

Fig. 8.1. Dec 2008–Feb 2009 (top) surface temperature anomalies (°C) and (bottom) precipitation percentiles based on a gamma distribution fit to the 1979–2000 base period. Temperature anomalies (1971–2000 base period) are based on station data over land and sea surface temperature data over water. Precipitation data were obtained from the CAMS-OPI data set that is a combination of rain gauge observations and satellite-derived estimates (Janowiak and Xie 1999). Analysis was omitted in data-sparse regions (white areas).

FIG. 8.4. Mar–May 2009 (top) Northern Hemisphere and (bottom) Southern Hemisphere 500hPa geopotential heights (9-dam contour interval) and anomalies (shading) determined from the 1979–2000 base period means.

FIG. 8.3. Mar–May 2009 (top) surface temperature anomalies (°C) and (bottom) precipitation percentiles based on a gamma distribution fit to the 1979–2000 base period. Temperature anomalies (1971–2000 base period) are based on station data over land and sea surface temperature data over water. Precipitation data were obtained from the CAMS-OPI data set that is a combination of rain gauge observations and satellite-derived estimates (Janowiak and Xie 1999). Analysis was omitted in data-sparse regions (white areas).
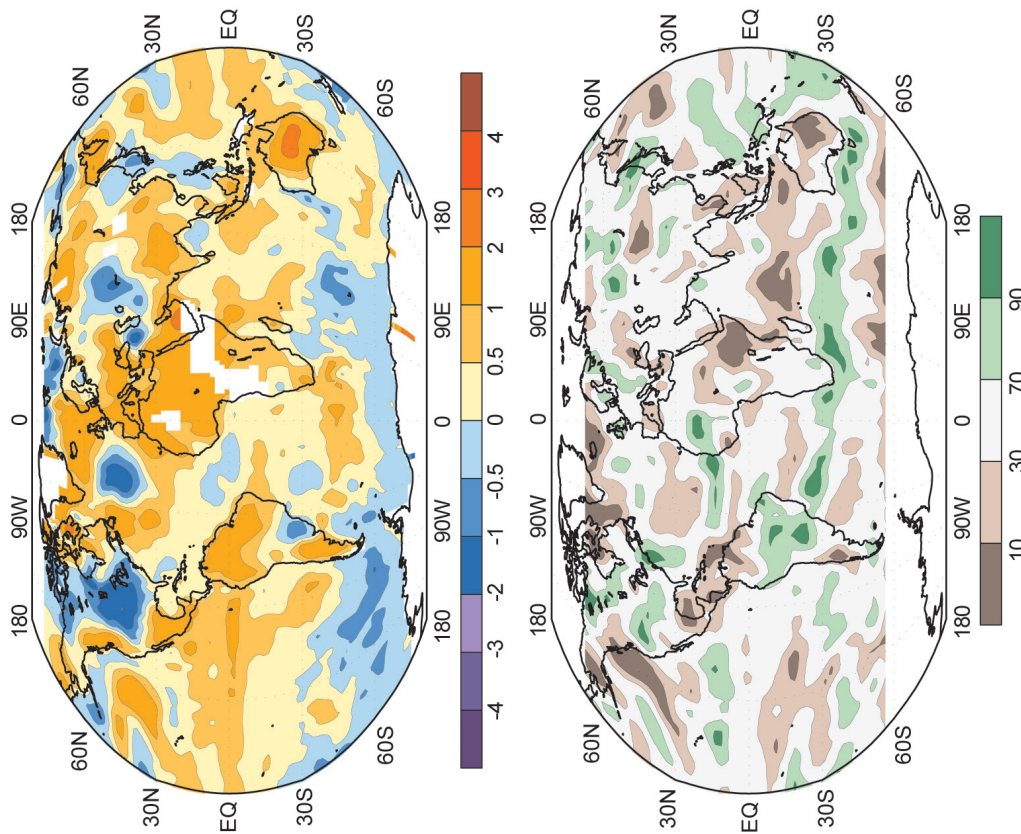
Fig. 8.5. Jun–Aug 2009 (top) surface temperature anomalies (°C) and (bottom) precipitation percentiles based on a gamma distribution fit to the 1979–2000 base period. Temperature anomalies (1971–2000 base period) are based on station data over land and sea surface temperature data over water. Precipitation data were obtained from the CAMS-OPI data set that is a combination of rain gauge observations and satellite-derived estimates (Janowiak and Xie 1999). Analysis was omitted in data-sparse regions (white areas).
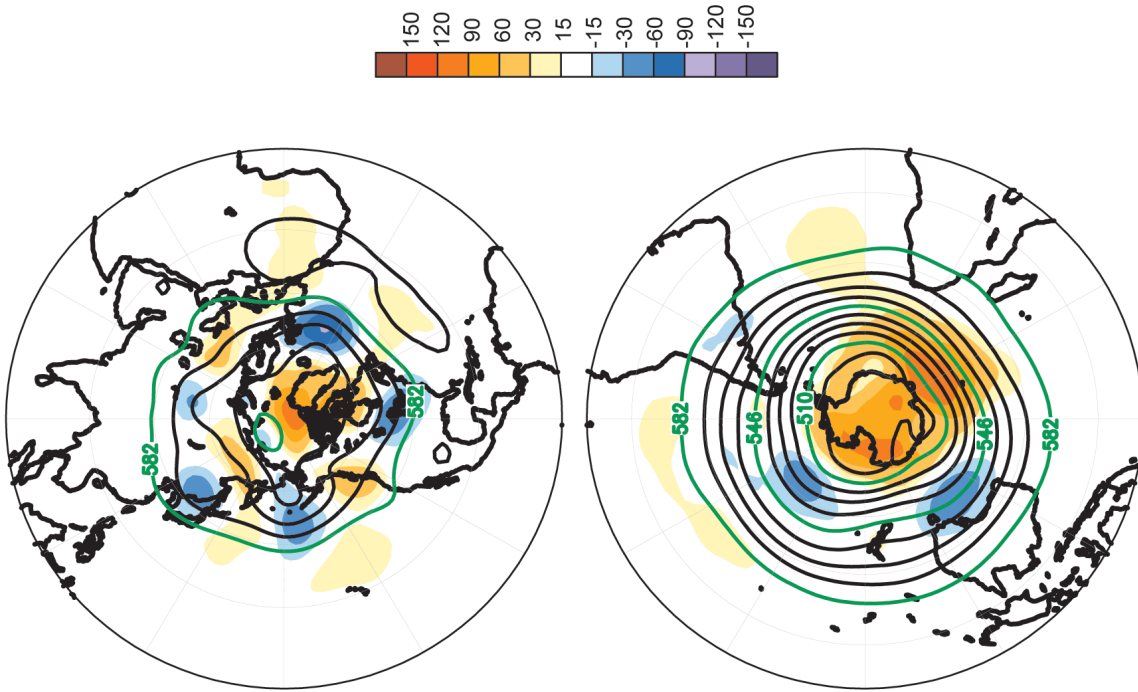
Fig. 8.6. Jun–Aug 2009 (top) Northern Hemisphere and (bottom) Southern Hemisphere 500hPa geopotential heights (9-dam contour interval) and anomalies (shading) determined from the 1979–2000 base period means.
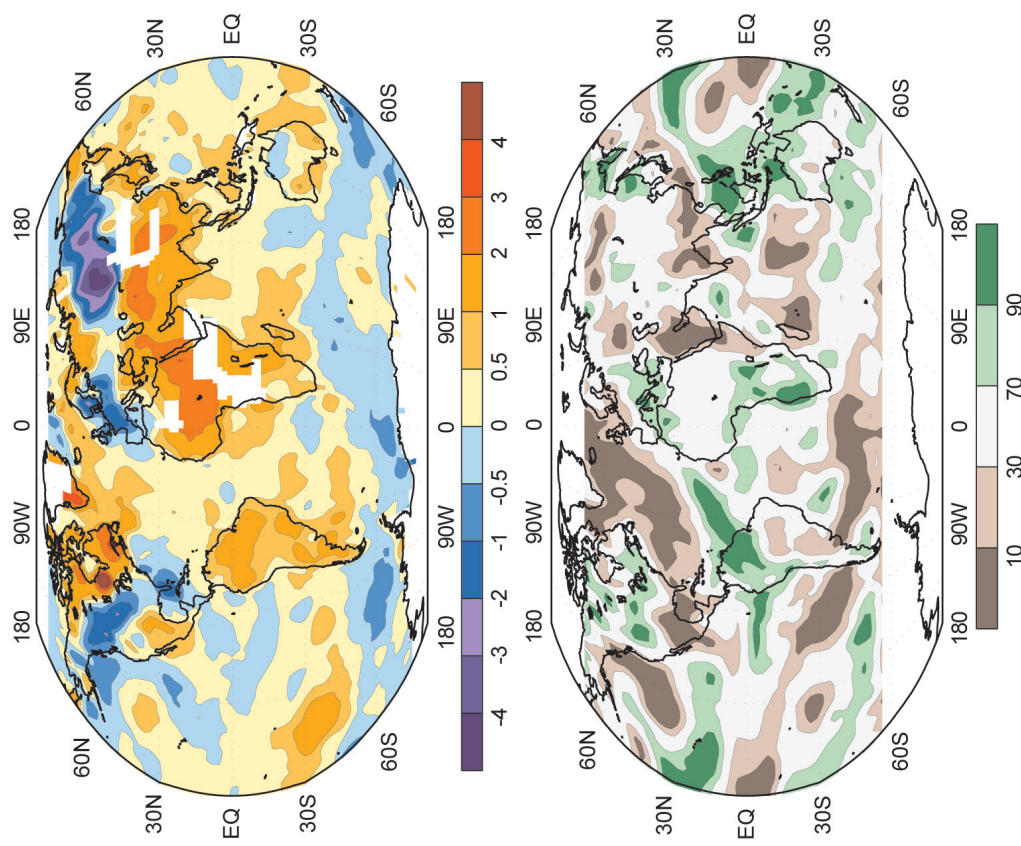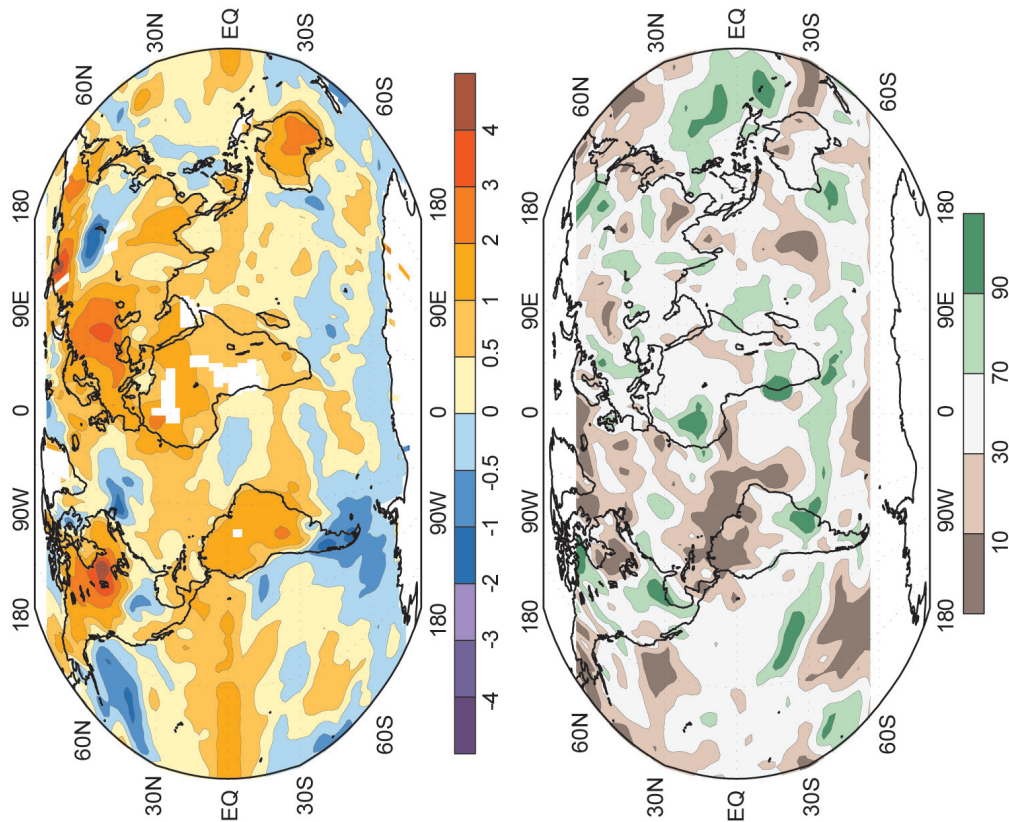
Fig. 8.7. Sep–Nov 2009 (top) surface temperature anomalies (°C) and (bottom) precipitation percentiles based on a gamma distribution fit to the 1979–2000 base period. Temperature anomalies (1971–2000 base period) are based on station data over land and sea surface temperature data over water. Precipitation data were obtained from the CAMS-OPI data set that is a combination of rain gauge observations and satellite-derived estimates (Janowiak and Xie 1999). Analysis was omitted in data-sparse regions (white areas).
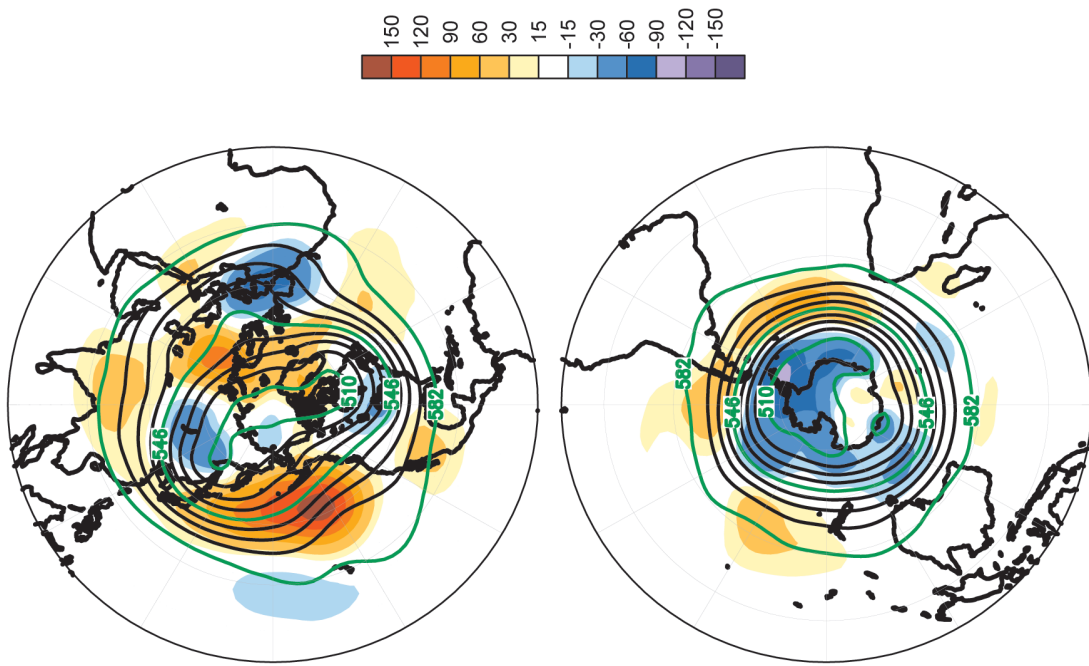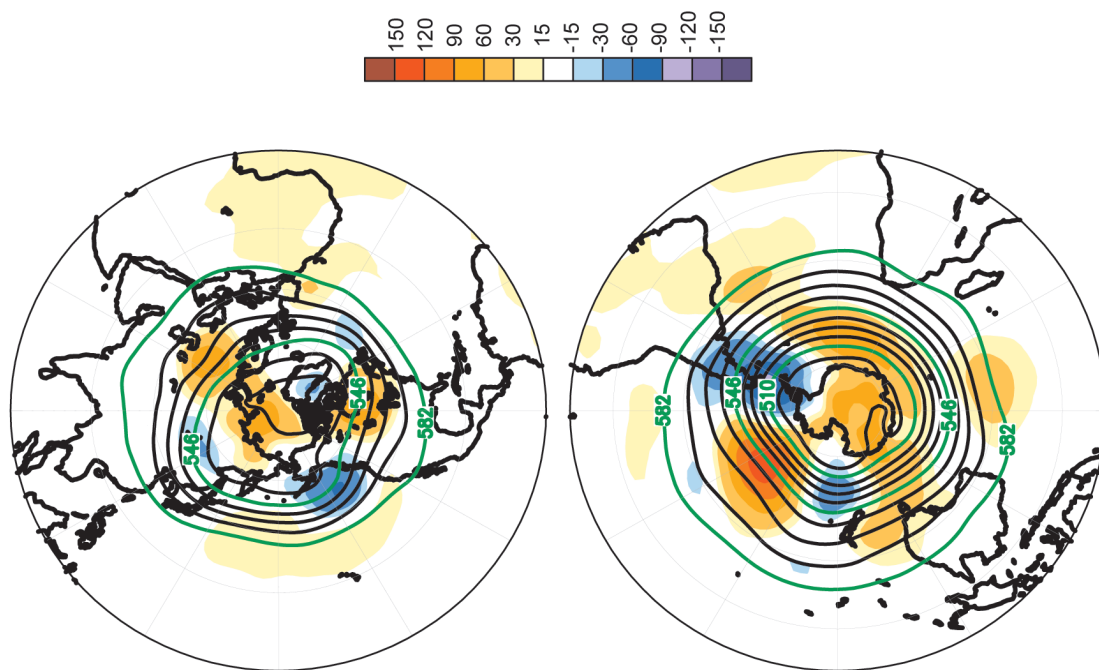

Fig. 8.8. Sep–Nov 2009 (top) Northern Hemisphere and (bottom) Southern Hemisphere 500hPa geopotential heights (9-dam contour interval) and anomalies (shading) determined from the 1979–2000 base period means.
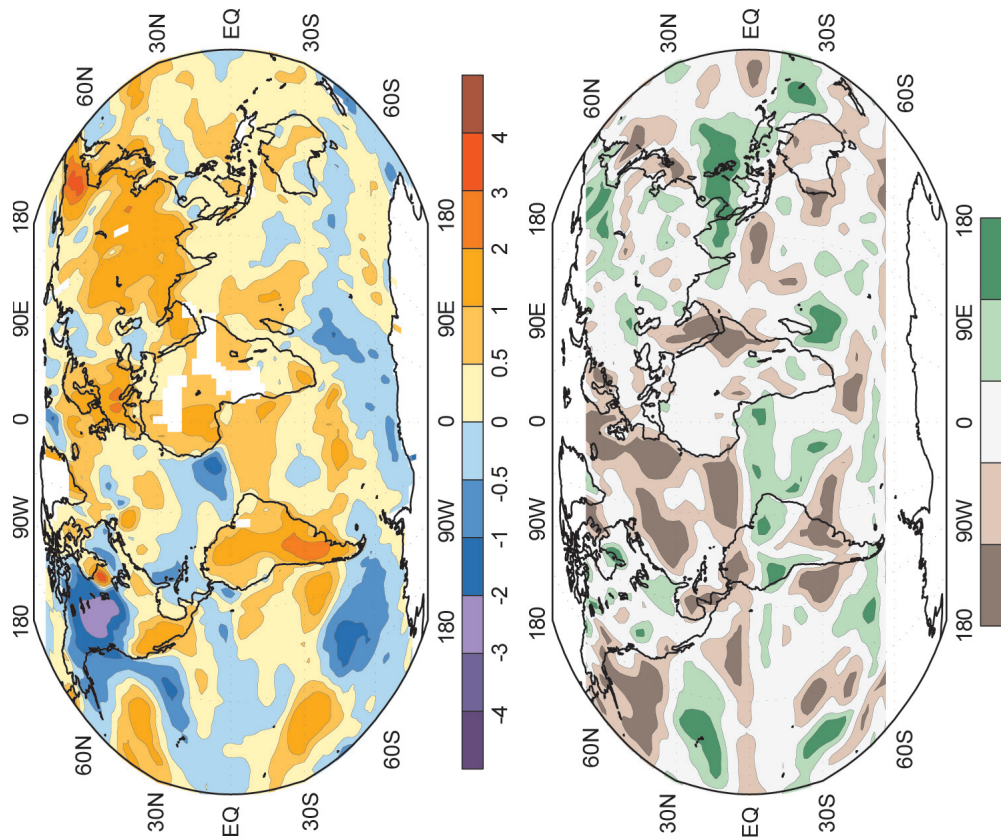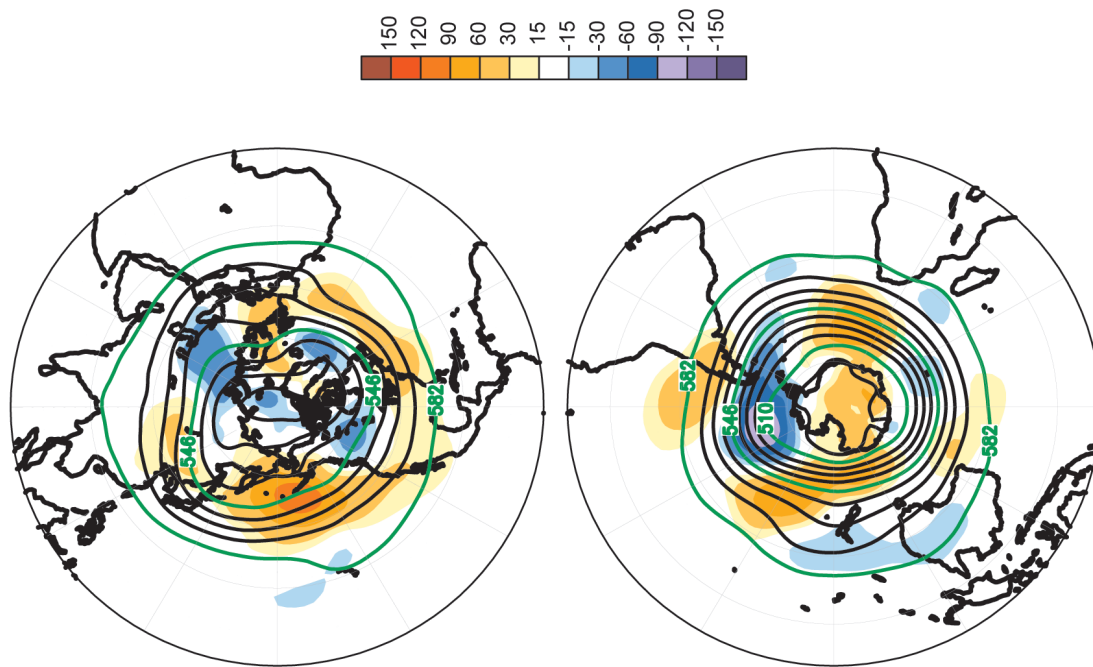
ACKNOWLEDGMENTS

The data found in various sections of the report are attributable to the home offices of the respective authors, unless otherwise noted. Further details on the datasets used are available from the following sources:

- All the global data sources used in Chapter 2 are listed in Table 2.6;
- "Monthly Ocean Briefing" slides from the Climate Prediction Center, at http://www.cpc.ncep.noaa.gov/products/GODAS;
- PDO index at http://jisao.washington.edu/pdo (Mantua et al. 1997);
- The Extended Reconstructed SST and Optimal Interpolation SST analysis products can be found at http://lwf.ncdc.noaa.gov/oa/climate/research/sst/sst.php;
- Objectively Analyzed air-sea Fluxes (OAFlux) project (http://oaflux.whoi.edu) at Woods Hole Oceanographic Institution (Yu and Weller 2007);
- Ocean drifter data is distributed by NOAA/AOML at http://www.aoml.noaa.gov/phod/dac/gdp.html;
- Moored ocean data is distributed by NOAA/PMEL at http://www.pmel.noaa.gov/tao;
- OSCAR gridded currents are available at http://www.oscar.noaa.gov/ and http://podaac.jpl.nasa.gov/;
- AVISO gridded altimetry is produced by SSALTO/DUACS and distributed with support from CNES, at http://www.aviso.oceanobs.com/;
- Analyses of altimetry-derived surface currents are available at http://www.aoml.noaa.gov/phod/altimetry/cvar;
- Atlantic Meridional Overturning Circulation estimates from the Rapid-MOC/MOCHA/WBTS program are available at http://www.noc.soton.ac.uk/rapidmoc//rapid_data/rapid_transports.html;
- The Florida Current Transport time series is available through the NOAA Western Boundary Time Series Program at http://www.aoml.noaa.gov/phod/floridacurrent/data_access.php;
- U.S. CLIVAR/CO2 Repeat Hydrography Program at http://ushydro.ucsd.edu/;

- NOAA Hurricane classification at http://www.cpc.noaa.gov/products/outlooks/background_information.shtml;
- Tropical Cyclone Heat Potential and related products at http://www.aoml.noaa.gov/phod/regsatprod/atln/index.php;
- Global ocean surface ocean CO_2 levels from SOCAT at http://www.socat.info/ and http://cwcgom.aoml.noaa.gov/erddap/griddap/aomlcarbonfluxes.graph;
- Sea-viewing Wide-Field-of-view Sensor (SeaWiFS) Ocean Color at http://oceancolor.gsfc.nasa.gov/REPROCESSING/R2009/;
- NOAA snow extent data record derived from optical satellite imagery at http://climate.rutgers.edu/snowcover/;
- Integrated Global Radiosonde Archive at http://www.ncdc.noaa.gov/oa/climate/igra/;
- Daily surveys of Greenland ice sheet marine terminating outlet glaciers from cloud free Moderate Resolution Imaging Spectroradiometer (MODIS) visible imagery at http://bprc.osu.edu/MODIS/;
- The ozone depletion analysis is based upon data from the NASA Aura satellites, in particular, the Koninklijk Nederlands Meteorologisch Instituut OMI and the Jet Propulsion Laboratory Microwave Limb Sounder;
- PSC information was obtained from the NASA Langley Research Center Calipso instrument;
- NOAA/NCEP provided analyses of satellite and balloon stratospheric temperature observations;
- Sea ice data were obtained from the NASA Earth Observing System Distributed Active Archive Center at the U.S. National Snow and Ice Data Center, University of Colorado, Boulder at http://www.nsidc.org;
- Arctic surface air temperature CRUTEM 3v dataset, at www.cru.uea.ac.uk/cru/data/temperature/; and
- Some information and figures for Chapter 7 was compiled using the IRI Data library at http://iridl.ldeo.columbia.edu/.

APPENDIX: ACRONYMS

A	Anticyclonic days
AAO	Atlantic Oscillation
ACC	Antarctic Circumpolar Current
ACE	NOAA's Accumulated Cyclone Energy Index
AEJ	African Easterly Jet
AGCM	Atmospheric general circulation model
AGGI	NOAA's Annual Greenhouse Gas Index
AMIP	Atmospheric Model Intercomparison Project
AMJ	April–May–June
AMO	Atlantic Multidecadal Oscillation
AMSR-E	Advanced Microwave Scanning Radiometer for Earth Observing System
AMSU	Advanced Microwave Sounding Unit
ANEEL	Agência Nacional de Energia Eléctrica
AO	Arctic Oscillation
AOD	Aerosol optical depth
AOML	Atlantic Oceanographic and Meteorological Laboratory
AR4	Fourth Assessment Report
ASAR	Advanced Synthetic Aperture Radar
ASO	August–September–October
ASTER	Advanced Spaceborne Thermal Emission and Reflection Radiometer
ATLAS	Autonomous Temperature Line Acquisition System
AVHRR	Advanced Very High Resolution Radiometer
AVISO	Archiving, Validating, and Interpretation of Satellite Oceanographic data
BC	British Columbia
BGOS	Beaufort Gyre Observing System
BI	Balleny Islands
Br	Bromine
C	Cyclonic days
CALIPSO	Cloud-Aerosol Lidar and Infrared Pathfinder Satellite Observation
CAMS	Climate Anomaly Monitoring System
CAPE	Convective Available Potential Energy
CERES	Clouds and the Earth's Radiant Energy System

CFC	Chlorofluorocarbon		EOF	Empirical orthogonal function

CFC | Chlorofluorocarbon
CFC-11 | Trichlorofluoromethane
CFC-12 | Dichlorodifluoromethane
CH_4 | Methane
Chl_{sat} | Surface-layer chlorophyll concentration
CIIFEN | International Research Center on El Niño
Cl | Chlorine
CLIVAR | Climate Variability and Predictability
CMA | China Meteorology Administration
CMAP | Climate Prediction Center (CPC) Merged Analysis of Precipitation
CMC | Canadian Meteorological Centre
CMIP | Coupled Model Intercomparison Project
CNES | Centre National d'Etudes Spatiales
CO | Carbon monoxide
CO_2 | Carbon dioxide
CONAFOR | National Forestry Commission, Mexico
CPC | Climate Prediction Center
CPHC | NOAA's Central Pacific Hurricane Center
CPTEC | Center for Weather Forecasting and Climate Studies
CRU | Climate Research Unit
CSI | NOAA Climate Scene Investigation
CTD | Conductivity, Temperature, Depth
CYC | Cyclone
DIC | Dissolved inorganic carbon
DISC | Data and Information Services Center
DJF | December–January–February
DMSP | Defense Meteorological Satellite Program
DOE | Department of Energy
DU | Dobson units
DWBC | Deep western boundary current
DWD | Deutscher Wetterdienst
EBAF | Energy Balanced and Filled
ECl | Equivalent chlorine
ECMWF | European Centre for Medium-Range Weather Forecasts
ECV | Essential Climate Variable
EECl | Effective equivalent chlorine
EESC | Effective equivalent stratospheric chlorine
EKE | Eddy kinetic energy
ENP | Eastern North Pacific (basin)
ENSO | El Niño–Southern Oscillation

EOF | Empirical orthogonal function
EOS | Earth Observatory System
ERB | Earth Radiation Budget
ERBE | Earth Radiation Budget Experiment
ERSST, v3b | Extended Reconstructed Sea Surface Temperature, version 3b
ESA | European Space Agency
ESRL | Earth System Research Laboratory
EU | European Union
FAO | Food and Agriculture Organization
FAPAR | Fraction of Absorbed Photosynthetically Active Radiation
FLASHflux | Fast Longwave and Shortwave Radiative Fluxes
FWC | freshwater content
GCM | General circulation model
GCOS | Global Climate Observing System
GEOSECS | Geochemical Ocean Section Study
GHA | Greater Horn of Africa
GHCN | Global Historical Climatology Network
GIA | Glacial isostatic adjustment
GIMMS | Global Inventory Modeling and Mapping Strides
GISS | NASA's Goddard Institute of Space Studies
GMD | Global Monitoring Division
GMSL | global mean sea level
GOME | Global Ozone Monitoring Experiment
GPCC | Global Precipitation Climatology Centre
GPCP | Global Precipitation Climatology Project
GPI | Genesis potential index
GRACE | Gravity Recovery and Climate Experiment
GRDC | Global Runoff Data Centre
Gt | gigaton
GTSPP | Global Temperature and Salinity Profile Project
H | Hurricane
HadAT | Hadley Centre's radiosonde temperature product
HadCRUT3 | Hadley Centre/CRU gridded monthly temperatures dataset
HadGEM1 | Hadley Centre global model
HCFC | Hydrochlorofluorocarbon
HFC | Hydrofluorocarbon
HIRS-W | High Resolution Infrared Sounder

hPa	Hectopascal (1 mb)	MM5	Fifth-generation Pennsylvania State
ICPAC	IGAD Climate Prediction and		University–National Center for
	Applications Centre		Atmospheric Research Mesoscale
IGY	International Geophysical Year		Model
INPE	National Institute for Space	MOC	Meridional overturning current
	Research, Brazil	MOCHA	Meridional Overturning
INSTAAR	Institute of Arctic and Alpine		Circulation Heat Transport Array
	Research	MODIS	Moderate Resolution Imaging
IO	Indian Ocean		Specroradiometer
IOD	Indian Ocean dipole	MOPITT	Measurements of Pollution in the
IODE	eastern pole of the Indian Ocean		Troposphere
	Dipole	MSLP	mean sea level pressure
IPCC	Intergovernmental Panel on	MSU	Microwave Sounding Unit
	Climate Change	MTSAT	Multifunctional Transport
IPCC AR4	IPCC Fourth Assessment report		Satellites
	(published in 2007)	N_2O	Nitrous oxide
IR	Infrared	NAM	Northern annular mode
IRIMO	Islamic Republic of Iran	NAMOS	Nansen and Amundsen Basin
	Meteorological Organization		Observational System
ISCCP	International Satellite Cloud	NAO	North Atlantic Oscillation
	Climatology Project	NARR	North American Regional
ITCZ	Intertropical convergence zone		Reanalysis
IUK	iterative universal Kriging	NASA	National Aeronautics and Space
JAS	July–August–September		Administration
JASO	July–August–September–October	NCAR	National Center for Atmospheric
JFM	January–February–March		Research
JGOFS	Joint Global Ocean Flux Study	NCDC	National Climatic Data Center
JJA	June–July–August	NCEP	National Center for Environmental
JMA	Japanese Meteorological Agency		Prediction
JPL	Jet Propulsion Laboratory	NDVI	Normalized difference vegetation
JRA	Japanese Reanalysis		index
JTWC	U.S. Navy's Joint Typhoon Warning	NEM	Northeast monsoon
	Center	NERC	National Environmental Research
KNMI	Royal Netherlands Meteorological		Council
	Institute	NH	Northern Hemisphere
LaRC	Langley Research Center	NHC	National Hurricane Center
LHF	Latent heat flux	NIFC	National Interagency Fire Center
MAM	March–April–May	NIO	Northern Indian Ocean
MBT	mechanical bathythermograph	NOAA	National Oceanic and Atmospheric
MCYC	Major cyclone		Administration
MDR	Main Development Region	NOMADS	National Operational Model
MEI	Multivariate ENSO Index		Archive and Distribution System
MERIS	Medium Resolution Imaging	NPEO	North Pole Environmental
	Spectrometer		Observatory
MH	Major hurricane	NPP	Net primary production
MISR	Multiangle Imaging	NRTSI	Near Real-Time SSM/I Plar
	SpectroRadiometer		Gridded Sea Ice Concentrations
MJO	Madden–Julian oscillation	NS	Named storm
MLO	Mauna Loa Observatory	NSIDC	National Snow and Ice Data Center
MLS	Microwave Limb Sounder	NSW	New South Wales, Australia
		NWS	National Weather Service
		O_3	Ozone

OAFlux	Objectively Analyzed Air–Sea Fluxes		SCIAMACHY	Scanning Imaging Absorption Spectrometer for Atmospheric Chartography
ODGI	Ozone Depleting Gas Index		SCS	South China Sea
OH	Hydroxide anion		SD	snow depth
OHCA	Ocean Heat Content Anomaly		SeaWiFS	Sea-viewing Wide Field of View
OI	Optimal interpolation		SF_6	Sulfur hexafluoride
OISST, v2	Optimal Interpolation SST, version 2		SH	Southern Hemisphere
OLR	Outgoing longwave radiation		SHF	Sensible heat flux
OMI	Ozone Monitoring Instrument		ΣChl	Photic zone chlorophyll
ONI	Oceanic Niño Index		SIO	Southern Indian Ocean
OPI	OLR precipitation index		SL	Sea level
OSCAR	Ocean Surface Current Analysis–Real Time		SLP	Sea level pressure
PATMOS (-x)	Pathfinder Atmospheres (Extended Product)		SMMR	Scanning Multichannel Microwave Radiometer
pCO_2	Carbon dioxide partial pressure		SOBS	surface weather observations
PDO	Pacific decadal oscillation		SOI	Southern Oscillation index
Pg	Petagram (1015 g)		SON	September–October–November
PIRATA	Pilot Research Array in the Tropical Atlantic		SPCZ	South Pacific convergence zone
PMEL	Pacific Marine Environmental Laboratory		SPOT	VGT satellite
			SRES	Special Report on Emissions Scenarios
PNG	Papau New Guinea		SSALTO/DUACS	Segment Sol Multimission Altimetry and Orbitography/Developing Use of Altimetry for Climate Studies
PO.DDAC	Physical Oceanography Distributed Active Archive Center			
ppb	Parts per billion			
ppbv	Parts per billion by volume		SSM/I	Special Sensor Microwave Imager
ppm	Parts per million		SSS	Sea surface salinity
ppt	Parts per trillion		SST	Sea surface temperature
PSC	Polar stratospheric cloud		SSTA	Sea surface temperature anomaly
PSS	Practical salinity scale		SSU	Stratosphere Sounding Units
PT	total precipitation		STAR	Center for Satellite Applications and Research
QBO	Quasi-biennial oscillation		STY	Supertyphoon
QuikSCAT	Quick Scatterometer		Sv	Sverdrups (1 Sv $\equiv 10^6$ m^3 s^{-1})
RAMA	Research Moored Array for African-Asian-Australian Monsoon Analysis Prediction		SWI	Summer warmth index
			SWP	Southwest Pacific
			TAO	Tropical Atmosphere Ocean
RAOBCORE	Radiosonde Observation Correction		TATL	Tropical Atlantic
RATPAC	Radiosonde Atmospheric Temperature Products for Assessing Climate		TC	Tropical cyclone
			TCHP	Tropical cyclone heat potential
			TCWV	Total Column Water Vapor
RICH	Radiosonde Innovation Composite Homogenization		TD	Tropical depression
			TI-NDVI	time-integrated NDVI
RSMC	Regional Specialized Meteorological Center Tokyo		TLT	temperature of the lower troposphere
RSS	Remote Sensing Systems		TMI	Tropical Rainfall Measuring Mission Microwave Imager
SAM	Southern annular mode			
SAT	surface air temperature		TOA	top of atmosphere
SBUV	Solar Backscatter Ultraviolet		TOMS	Total Ozone Mapping Spectrometer
SCD	snow covered duration		TRMM	Tropical Rainfall Measuring Mission
SCE	snow cover extent			
			TS	Tropical storm

TSP	Thermal state of permafrost
TW	trade winds
TY	Typhoon
UAH	University of Alabama Huntsville
USD	U.S. Dollars
USGS	U.S. Geological Survey
VasClimO	Variability Analysis of Surface Climate Observations
VOCALS	VAMOS (Variability of the American Monsoon Systems) Ocean–Cloud–Atmosphere–Land Study
WBC	Western boundary current
WGMS	World Glacier Monitoring Service
WHOI	Woods Hole Oceanographic Institute
WMO	World Meteorological Organization
WNP	western North Pacific (basin)
WOA	*World Ocean Atlas*
WOCE	World Ocean Circulation Experiment
WPO	west Pacific Ocean
XBT	Expendable bathythermograph

REFERENCES

AchutaRao, K. M., B. D. Santer, P. J. Gleckler, K. E. Taylor, D. W. Pierce, T. P. Barnett, and T. M. L. Wigley, 2006: Variability of ocean heat uptake: Reconciling observations and models. *J. Geophys. Res.*, **111**, C05019, doi:10.1029/2005JC003136.

Ackerman, S. A., R. E. Holz, R. Frey, E. W. Eloranta, B. C. Maddux, and M. McGill, 2008: Cloud detection with MODIS. Part II: Validation. *J. Atmos. Oceanic Technol.*, **25**, 1073–1086.

Adler, R. F., and Coauthors, 2003: The Version 2 Global Precipitation Climatology Project (GPCP) monthly precipitation analysis (1979-present). *J. Hydrometeor.*, **4**, 1147–1167.

Allan, R. J., and T. J. Ansell, 2006: A new globally complete monthly historical sea level pressure data set (HadSLP2): 1850–2004. *J. Climate*, **19**, 5816–5842.

——, J. A. Lindesay, and D. E. Parker, 1996: *El Niño Southern Oscillation and Climatic Variability.* CSIRO Publications, Melbourne, Australia, 405 pp.

Alley, R. B., and Coauthors, 2007: Summary for policymakers. *Climate Change 2007: The Physical Science Basis*, S. Solomon et al., Eds., Cambridge University Press, 1-18.

Ando, K., and M. J. McPhaden, 1997: Variability of surface layer hydrography in the tropical Pacific Ocean. *J. Geophys. Res.*, **102** (C10), 23 064–23 078.

Anthes, R. A., and Coauthors, 2008: The COSMIC/FORMOSAT-3 Mission: Early results. *Bull. Amer. Meteor. Sci.* **89**, 313–333.

Antonov, J. I., S. Levitus, and T. P. Boyer, 2002: Steric sea level variations during 1957-1994: Importance of salinity. *J. Geophys. Res.*, **107** (C12), 8013, doi:10.1029/2001JC000964.

——, ——, and ——, 2005: Thermosteric sea level rise, 1955-2003. *Geophys. Res. Lett.*, **32**, L12602, doi:10.1029/2005GL023112.

Appenzeller, C., A. K. Weiss, and J. Staehelin, 2000: North Atlantic Oscillation modulates total ozone winter trends. *Geophys. Res. Lett.*, **27**, 1131–1134.

Arblaster, J. M., and G. A. Meehl, 2006: Contributions of external forcings to southern annular mode trends. *J. Climate*, **19**, 2896–2905.

Archer, D., and V. Brovkin, 2008: Millennial atmospheric lifetime of anthropogenic CO_2. *Climatic Change*, **90**, 283–297.

Arguez, A., Ed., 2007: State of the climate in 2006. *Bull. Amer. Meteor. Soc.*, **88** (6), S1–S135.

Arpe, K., L. Bengtsson, G. S. Golitsyn, I. I. Mokhov, V. A. Semenov, and P. V. Sporyshev, 2000: Connection between Caspian sea level variability and ENSO. *Geophys. Res. Lett.*, **27**, 2693–2696.

Ashok, K., S. K. Behera, S. A. Rao, H. Weng, and T. Yamagata, 2007: El Niño Modoki and its possible teleconnection. *J. Geophys. Res.* **112**, C11007, doi:10.1029/2006JC003798.

Assmann, K. M., H. H. Hellmer, and S. S. Jacobs, 2005: Amundsen Sea ice production and transport. *J. Geophys. Res.* **110**, doi: 10.1029/2004JC002797.

Atkinson, G. D., 1971: Forecasters' guide to tropical meteorology. U.S. Air Force Tech. Rep. 240, 360 pp.

Avila, L. A., 2010: Tropical cyclone report: Hurricane Bill (AL032009), 15-24 August 2009. Tropical Cyclone Rep. AL 032009, 17 pp. [Available online at http://www.nhc.noaa.gov/pdf/TCR-AL032009_Bill.pdf.]

Baehr, J., H. Haak, S. Alderson, S. A. Cunningham, J. H. Jungclaus, and J. Marotzke, 2007: Timely detection of changes in the meridional overturning circulation at 26ºN in the Atlantic. *J. Climate*, **20**, 5827–5841.

——, K. Keller, and J. Marotzke, 2008: Detecting potential changes in the meridional overturning circulation at 26ºN in the Atlantic. *Climatic Change*, **91**, 11–27.

Baldwin, M. P. and Coauthors, 2001: The Quasi-Biennial Oscillation. *Rev. Geophys.*, **39**, 179–229.

Baringer, M. O., and J. Larsen, 2001: Sixteen years of Florida Current transport at 27ºN. *Geophys. Res. Lett.*, **28**, 3179–3182.

Barnett, T. P., D. W. Pierce, K. M. AchutaRao, P. J. Gleckler, B. D. Santer, J. M. Gregory and W. M. Washington, 2005: Penetration of human-induced warming into the world's oceans. *Science*, **309**, 284–287.

Barnston, A. G., and R. E. Livezey, 1987: Classification, seasonality and persistence of low-frequency atmospheric circulation patterns. *Mon. Wea. Rev.*, **115**, 1083–1126.

Behrenfeld, M. J., 2010: Abandoning Sverdrup's critical depth hypothesis on phytoplankton blooms. *Ecology*, **91**, 977–989.

——, E. Boss, D. A. Siegel, and D. M. Shea, 2005: Carbon-based ocean productivity and phytoplankton physiology from space. *Global Biogeochem. Cycles*, **19**, GB1006, doi:10.1029/2004GB002299.

——, and Coauthors, 2006: Climate-driven trends in contemporary ocean productivity. *Nature*, **444**, 752–755.

——, K. H. Halsey, and A. J. Milligan, 2008a: Evolved physiological responses of phytoplankton to their integrated growth environment. *Philos. Trans. Roy. Soc.*, **B363**, 2687–2703.

——, D. A. Siegel, and R. T. O'Malley, 2008b: Global ocean phytoplankton and productivity [in "State of the Climate in 2007"]. *Bull. Amer. Meteor. Soc.*, **89** (7), S56–S61.

——, ——, ——, and S. Maritorena, 2009: Global ocean phytoplankton and productivity [in "State of the Climate in 2008"]. *Bull. Amer. Meteor. Soc.*, **90** (8), S68–S73.

Behringer, D. W., M. Ji, and A. Leetmaa, 1998: An improved coupled model for ENSO prediction and implications for ocean initialization. Part I: The ocean data assimilation system. *Mon. Wea. Rev.*, **126**, 1013–1021.

Bell, G. D., and M. Chelliah, 2006: Leading tropical modes associated with interannual and multi-decadal fluctuations in North Atlantic hurricane activity. *J. Climate*, **19**, 590–612.

——, and Coauthors, 1999: The 1998 North Atlantic and eastern North Pacific hurricane season. [in "Climate Assessment for 1998"]. *Bull. Amer. Meteor. Soc.*, **80** (5), S24-S28.

——, and Coauthors, 2000: The 1999 North Atlantic and eastern North Pacific hurricane season [in "Climate Assessment for 1999"]. *Bull. Amer. Meteor. Soc.*, **81** (6), S19–S22.

——, and Coauthors, 2004: Tropical cyclones: Atlantic hurricane season [in "State of the Climate in 2003"]. *Bull. Amer. Meteor. Soc.*, **85** (6), S20–S24.

——, and Coauthors, 2006: Tropical cyclones: Atlantic basin [in "State of the Climate in 2005"]. *Bull. Amer. Meteor. Soc.*, **87** (6), S33–S37.

——, and Coauthors, 2007: Tropical cyclones: Atlantic basin [in "State of the Climate in 2006"]. *Bull. Amer. Meteor. Soc.*, **88** (6), S48–S51.

——, and Coauthors, 2009: Tropical cyclones: Atlantic basin [in "State of the Climate in 2008"]. *Bull. Amer. Meteor. Soc.*, **90** (8), S79–S83.

Bellucci, A., S. Gualdi, E. Scoccimarro, and A. Navarra, 2008: NAO-ocean circulation interactions in a coupled general circulation model. *Climate Dyn.,* **31**, 759–777.

Benedetti, A., and Coauthors, 2009: Aerosol analysis and forecast in the European Centre for Medium-Range Weather Forecasts Integrated Forecast System: 2. Data assimilation. *J. Geophys. Res.*, **114**, D13205, doi:10.1029/2008JD011115.

Béranger, K., L. Siefridt, B. Barnier, E. Garnier, and H. Roquet, 1999: Evaluation of operational ECMWF surface freshwater fluxes of oceans during 1991–1997. *J. Mar. Systems*, **22**, 13–36.

Bergonzini L., Y. Richard, L. Petit, and P. Camberlin, 2004: Zonal circulations over the Indian and Pacific Oceans and the level of Lakes Victoria and Tanganyika. *Int. J. Climatol.*, **24**, 1613–1624.

Bhatt, U. S., M. A. Alexander, C. Deser, J. E. Walsh, J. S. Miller, M. S. Timlin, J. Scott, and R. A. Tomas, 2008: The atmospheric response realistic reduced summer arctic sea ice anomalies. *Arctic Sea Ice Decline: Observations, Projections, Mechanisms, and Implications. Geophys. Monogr.*, Vol. 180, Amer. Geophys.Union, 91–110.

Bindoff, N. L., and Coauthors, 2007: Observations: Oceanic climate change and sea level. *Climate Change 2007: The Physical Science Basis.* S. Solomon et al., Eds., Cambridge University Press, 385–428.

Bingham, R. J., and C. W. Hughes, 2009: Signature of the Atlantic meridional overturning circulation in sea level along the east coast of North America. *Geophys. Res. Lett.*, **36**, 2, doi:10.1029/2008GL036215.

Birkett, C. M., 1995: The contribution of TOPEX/POSEIDON to the global monitoring of climatically sensitive lakes. *J. Geophys. Res.*, **100** (C12), 25 179–25 204.

——, and I. M. Mason, 1995: A new global lakes database for a remote sensing programme studying climatically sensitive large lakes. *J. Great Lakes Res.*, **21**, 307–318.

——, R. Murtugudde, and T. Allan, 1999: Indian Ocean climate event brings floods to East Africa's lakes and the Sudd Marsh. *Geophys. Res. Lett.*, **26**, 1031–1034.

Blake, E. S., E. J. Gibney, D. P. Brown, M. Mainelli, J. L. Franklin, T. B. Kimberlain, and G. R. Hammer, 2009: *Tropical Cyclones of the Eastern North Pacific Basin, 1949-2006.* Historical Climatology Series 6-5, NOAA/National Climatic Data Center, 162 pp.

Blaszczyk, M., J. A. Jania, and J.-O. Hagen, 2009: Tidewater glaciers of Svalbard: Recent changes and estimates of calving fluxes. *Polish Polar Research,* **30**, 85–142.

Böning, C. W., A. Dispert, M. Visbeck, S. R. Rintoul, and F. U. Schwarzkopf, 2008: The response of the Antarctic circumpolar current to recent climate change. *Nature Geosci.*, **1**, 864–869.

Bonjean, F., and G. Lagerloef, 2002: Diagnostic model and analysis of the surface currents in the tropical Pacific Ocean. *J. Phys. Oceanogr.*, **32**, 2938–2954.

Bosilovich, M. G., 2008: NASA's modern era retrospective-analysis for research and applications: Integrating Earth observations. *Earthzine*, posted 26 September 2008. [Available online at http://www.earthzine.org/2008/09/26/nasas-modern-era-retrospective-analysis/.]

Bowman, D. M. J. S., and Coauthors, 2009: Fire in the Earth System. *Science*, **324**, 481–484.

Box, J. E., and A. E. Cohen, 2006: Upper-air temperatures around Greenland: 1964-2005. *Geophys. Res. Lett.*, **33**, L12706, doi:10.1029/2006GL025723.

Boyer, T. P., C. Stephens, J. I. Antonov, M. E. Conkright, R. A. Locarnini, T. D. O'Brien, and H. E. Garcia, 2002: *Salinity.* Vol. 2, *World Ocean Atlas 2001,* NOAA Atlas NESDIS 50, 165 pp.

Brasnett, B., 1999: A global analysis of snow depth for numerical weather prediction. *J. Appl. Meteor.*, **38**, 726–740.

Brennan, C. E., R. J. Matear, and K. Keller, 2008: Measuring oxygen concentrations to improve the detection capabilities of an ocean circulation observation array. *J. Geophys. Res.*, **113**, C01019, doi:10.1029/2007JC004113.

Bretherton, F. P., R. E. Davis, and C. Fandry, 1976: A technique for objective analysis and design of oceanographic instruments applied to MODE-73. *Deep-Sea Res.*, **23**, 559–582.

Brohan, P., J. J. Kennedy, I. Harris, S. F. B. Tett, and P. D. Jones, 2006: Uncertainty estimates in regional and global observed temperature changes: A new data set from 1850. *J. Geophys. Res.*, **111**, D12106, doi:10.1029/2005JD006548.

Bromwich, D. H., and R. L. Fogt, 2004: Strong trends in the skill of the ERA-40 and NCEP-NCAR reanalyses in the high and middle latitudes of the Southern Hemisphere, 1958-2001. *J. Climate*, **17**, 4603–4619.

——, Z. Guo, L.-S. Bai, and Q.-S. Chen, 2004: Modeled Antarctic precipitation. Part I: spatial and temporal variability. *J. Climate*, **17**, 427–447.

——., R. L. Fogt, K. I. Hodges, and J. E. Walsh, 2007: A tropospheric assessment of the ERA-40, NCEP, and JRA-25 global reanalyses in the polar regions. *J. Geophys. Res.*, **112**, D10111 doi:10.1029/2006JD007859.

Bryden, H. L., H. R. Longworth, and S. A. Cunningham, 2005: Slowing of the Atlantic meridional overturning circulation at 25°N. *Nature*, **438**, 655–657.

Butler, J. H., 2009: The NOAA Annual Greenhouse Gas Index (AGGI). [Available online at http://www.esrl.noaa.gov/gmd/aggi/.]

Camargo, S. J., and A. H. Sobel, 2005: Western North Pacific tropical cyclone intensity and ENSO. *J. Climate,* **18**, 2996–3006.

——, K. A. Emanuel, and A. H. Sobel, 2007a: Use of a genesis potential index to diagnose ENSO effects on tropical cyclone genesis. *J. Climate,* **20**, 4819–4834.

——, A. W. Robertson, S. J. Gaffney, P. Smyth, and M. Ghil, 2007b: Cluster analysis of Typhoon tracks. Part II: Large-scale circulation and ENSO. *J. Climate,* **20**, 3654–3676.

——, ——, A. G. Barnston, and M. Ghil, 2008: Clustering of eastern North Pacific tropical cyclone tracks: ENSO and MJO effects. *Geochem. Geophys. Geosys.*, **9**, Q06V05, doi:10.1029/2007GC001861.

Cangialosi, J. P., and L. A. Avila, 2010: Tropical cyclone report: Hurricane Rick (EP202009), 15-21 October 2009. Tropical Cyclone Rep. EP202009. [Available on-line at http://www.nhc.noaa.gov/pdf/TCR-EP202009_Rick.pdf.]

Carlson, A. E., D. W. Oppo, R. E. Came, A. N. LeGrande, L. D. Keigwin, and W. B. Curry, 2008: Subtropical Atlantic salinity variability and Atlantic meridional circulation during the last deglaciation. *Geology*, **36**, 991–994.

Cayan, D. R., 1992: Latent and sensible heat flux anomalies over the northern oceans, driving the sea surface temperature. *J. Phys. Oceanogr.* **22**, 859–881.

Cazenave, A., K. Dominh, S. Guinehut, E. Berthier, W. Llovel, G. Ramillien, M. Ablain, and G. Larnicol, 2009: Sea level budget over 2003-2008: A reevaluation from GRACE space gravimetry satellite altimetry and Argo. *Global Planet. Change*, **65**, 83–88.

Chan, J. C. L., 1985: Tropical cyclone activity in the northwest Pacific in relation to El Niño/Southern Oscillation phenomenon. *Mon. Wea. Rev.*, **113**, 599–606.

Chelliah, M., and G. D. Bell, 2004: Tropical multidecadal and interannual climate variations in the NCEP/ NCAR Reanalysis. *J. Climate*, **17**, 1777–1803.

Chia, H. H., and C. F. Ropelewski, 2002: Interannual variability in the genesis location of tropical cyclones in the northwest Pacific. *J. Climate*, **15**, 2934–2944.

Christy, J. R., and R. T. McNider, 1994: Satellite greenhouse signal. *Nature*, **367**, 325.

——, R. W. Spencer, W. B. Norris, W. D. Braswell, and D. E. Parker, 2003: Error estimates of version 5.0 of MSU-AMSU bulk atmospheric temperatures. *J. Atmos. Oceanic Technol.*, **20**, 613–629.

Chu, P.-S., 2002: Large-scale circulation features associated with decadal variations of tropical cyclone activity over the central North Pacific. *J. Climate*, **15**, 2678–2689.

——, and J. D. Clark, 1999: Decadal variations of tropical cyclone activity over the central North Pacific. *Bull. Amer. Meteor. Soc.*, **80**, 1875–1881.

——, and J. Wang, 1997: Tropical cyclone occurrences in the vicinity of Hawaii: Are the differences between El Niño and non–El Niño years significant? *J. Climate*, **10**, 2683–2689.

——, and ——, 1998: Modeling return periods of tropical cyclone intensities in the vicinity of Hawaii. *J. Appl. Meteor.*, **37**, 951–960.

Clerbaux, C., and D. Cunnold, 2007: Long-lived compounds. *Scientific Assessment of Ozone Depletion: 2006*, Global Ozone Research and Monitoring Project Rep. 50, World Meteorological Organization, 1.1–1.63.

Comiso, J., and F. Nishio, 2008: Trends in the sea ice cover using enhanced and compatible AMSR-E, SSM/I, and SMMR data. *J. Geophys. Res.*, **113**, C02S07, doi:10.1029/2007JC004257.

Conway, T. J., P. P. Tans, L. S. Waterman, K. W. Thoning, D. R. Kitzis, K. A. Masarie, and N. Zhang, 1994: Evidence for interannual variability of the carbon cycle from the NOAA CMDL global air sampling network. *J. Geophys. Res.*, **99** (D11), 22 831–22 855.

Couture, R., S. Smith, S. D. Robinson, M. M. Burgess, and S. Solomon, 2003: On the hazards to infrastructure in the Canadian North associated with thawing of permafrost. *Proc. Geohazards (2003), Third Canadian Conf. on Geotechnique and Natural Hazards*, Edmonton, AB, Canada, The Canadian Geotechnical Society, 97–104.

Crutzen, P. J., A. R. Mosier, K. A. Smith, and W. Winiwarter, 2007: N_2O release from agro-biofuel production negates global warming reduction by replacing fossil fuels. *Atmos. Chem. Phys. Discuss*, **7**, 11 191–11 205.

Cunningham, S., and Coauthors, 2007: Temporal variability of the Atlantic meridional overturning circulation at 26.5°N. *Science*, **317**, 935–938.

——, and Coauthors, 2010: The present and future system for measuring the Atlantic meridional overturning circulation and heat transport. *Proceedings of the OceanObs'09: Sustained Ocean Observations and Information for Society Conference (Vol. 2),* Venice, Italy, 21-25 September 2009, J. Hall et al., Eds., ESA Publication WPP-306.

Curry, R. G., and M. S. McCartney, 2001: Ocean gyre circulation changes associated with the North Atlantic oscillation. *J. Phys. Oceanogr.*, **31**, 3374–3400.

Czaja, A., and C. Frankignoul, 2002: Observed impact of Atlantic SST anomalies on the North Atlantic oscillation. *J. Climate*, **15**, 606–623.

Daniel, J. S., and Coauthors, 2007: Halocarbon scenarios, ozone depletion potentials, global warming potentials. Scientific assessment of ozone depletion: 2006, Global Ozone Research and Monitoring Project Rep. 50, World Meteorological Organization, 8.1–8.39.

Dery, S., M. Hernandez-Henrıquez, J. Burford, and E. Wood, 2009: Observational evidence of an intensifying hydrological cycle in northern Canada. *Geophys. Res. Lett.*, **36**, L13402, doi:10.1029/2009GL038852.

Deser, C., and M. L. Blackmon, 1993: Surface climate variations over the North Atlantic Ocean during winter: 1900–1989. *J. Climate*, **6**, 1743–1753.

Dhomse, S., M. Weber, J. P. Burrows, I. Wohltmann, and M. Rex, 2006: On the possible cause of recent increases in NH total ozone from a statistical analysis of satellite data from 1979 to 2003. *Atmos. Chem. Phys.*, **6**, 1165–1180.

Di Girolamo, L., A. Menzies, G. Zhao, K. Mueller, C. Moroney, and D.J. Diner, 2010: Multi-angle imaging spectroradiometer level 3 cloud fraction by altitude algorithm theoretical basis document. JPL Publ. D-62358, 23 pp.

Di Grigorio, A., and L. J. M. Jansen, 2000: Land cover classification system, concepts and user manual. GCP/RAF/287/ITA, Africover, Food and Agricultural Organization of the United Nations Publishing Service, Rome, Italy, 179 pp.

Dlugokencky, E. J., and Coauthors, 2009: Observational constraints on recent increases in the atmospheric CH_4 burden. *Geophys. Res. Lett.*, **36**, L18803, doi:10.1029/2009GL039780.

DNM, 2009: Fuertes precipitaciones en noviembre de 2009 en Uruguay. [Available online at http://www.meteorologia.com.uy/Anomalias_Lluvias_noviembre_2009.pdf.]

Domingues, C. M., J. A. Church, N. J. White, P. J. Gleckler, S. E. Wijffels, P. M. Barker, and J. R. Dunn, 2008: Improved estimates of upper-ocean warming and multi-decadal sea-level rise. *Nature*, **453**, 1090–1093.

Drozdov, D. S., G. V. Malkova, and V. P. Melnikov, 2008: Recent advances in Russian geocryological research: A contribution to the International Polar Year. *Proc. 9th Int. Conf. on Permafrost, Fairbanks, Alaska, 29 June – 3 July 2008*, Vol. 1, D. L. Kane and K. M. Hinkel, Eds., Institute of Northern Engineering, University of Alaska Fairbanks, 379–384.

Durre, I., R. S. Vose, and D. B. Wuertz, 2006: Overview of the Integrated Global Radiosonde Archive. *J. Climate*, **19**, 53–68.

Easterling, D. R., and T. C. Peterson, 1995: A new method for detecting undocumented discontinuities in climatological time series. *Int. J. Climatol.*, **15**, 367–377.

Egleston, E. S., C. L. Sabine, and F. M. M. Morel, 2010: Revelle revisited: Buffer factors that quantify the response of ocean chemistry to changes in DIC and alkalinity. *Global Biogeochem. Cycles*, **24**, GB1002, doi:10.1029/2008GB003407.

Elliott, W. P., and D. J. Gaffen, 1991: On the utility of radiosonde humidity archives for climate studies. *Bull. Amer. Meteorol. Soc.*, **72**, 1507–1520.

Emanuel, K. A., 1986: An air-sea interaction theory for tropical cyclones. Part I: Steady-state maintenance. *J. Atmos. Sci.*, **43**, 585–605.

Enfield, D. B., and A. M. Mestas-Nuñez, 1999: Multi-scale variabilities in global sea surface temperatures and their relationships with tropospheric climate patterns. *J. Climate*, **12**, 2719–2733.

Eyring, V., and Coauthors, 2006: Assessment of temperature, trace species, and ozone in chemistry-climate model simulations of the recent past. *J. Geophys. Res.*, **111**, D22308, doi:10.1029/2006JD007327.

Fairall, C. W., E. F. Bradley, J. E. Hare, A. A. Grachev, and J. B. Edson, 2003: Bulk parameterization on air–sea fluxes: Updates and verification for the COARE algorithm. *J. Climate.,* **16**, 571–591.

Fargione, J., J. Hill, D. Tilman, S. Polasky, and P. Hawthrone, 2008: Land clearing and the biofuel carbon debt. *Science*, **319**, 1235–1238.

Fekete, B. M., C. J. Vörösmarty, and W. Grabs, 2002: High resolution fields of global runoff combining observed river discharge and simulated water balances. *Global Biogeochem. Cycles*, **16**, doi:10.1029/1999GB001254.

Fetterer, F., K. Knowles, W. Meier, and M. Savoie, 2009: Sea ice index. National Snow and Ice Data Center, Boulder, CO, digital media. [Available online at http://nsicd.org/data/seaice_index/.]

Fettweis, X., G. Mabille, M. Erpicum, S. Nicolay, and M. Van den Broeke, 2010: The 1958-2009 Greenland ice sheet surface melt and the mid-tropospheric atmospheric circulation. *Climate Dyn.*, doi:10.1007/s00382-010-0772-8, in press.

Fioletov, V. E., G. E. Bodeker, A. J. Miller, R. D. McPeters, and R. Stolarski, 2002: Global and zonal total ozone variations estimated from ground-based and satellite measurements: 1964–2000. *J. Geophys. Res.*, **107**, 4647, doi:10.1029/2001JD001350.

Foelsche, U., B. Pirscher, M. Borsche, G. Kirchengast, and J. Wickert, 2009: Assessing the climate monitoring utility of radio occultation data: From CHAMP to FORMOSAT-3/COSMIC. *Terr. Atmos. Oceanic Sci.*, **20**, 155–170.

Fogt, R. L., and D. H. Bromwich, 2006: Decadal variability of the ENSO teleconnection to the high latitude South Pacific governed by coupling with the Southern Annular Mode. *J. Climate*, **19**, 979–997.

——, and Coauthors, 2009a: Antarctica [in "State of the Climate in 2008"]. *Bull. Amer. Meteor. Soc.*, **90** (8), S113–121.

——, J. Perlwitz, S. Pawson, and M. A. Olsen, 2009b: Intra-annual relationships between polar ozone and the SAM. *Geophys. Res. Lett.*, **36**, L04707, doi:10.1029/2008GL036627.

Francis, J. A., W. Chan, D. J. Leathers, J. R. Miller, and D. E. Veron, 2009: Winter northern hemisphere weather patterns remember summer Arctic sea-ice extent. *Geophys. Res. Lett.*, **36**, L07503, doi:10.1029/2009GL037274.

Francis, P., and S. Gadgil, 2010: Towards understanding the unusual Indian monsoon in 2009. *J. Earth Syst. Sci.*, in press.

Frank, W. M., and G. S. Young, 2007: The interannual variability of tropical cyclones. *Mon. Wea. Rev.*, **135**, 3587–3598.

Frankignoul, C., A. Czaja, and B. L'Heveder, 1998: Air-sea feedback in the North Atlantic and surface boundary conditions for ocean models. *J. Climate*, **11**, 2310–2324

Free, M., D. J. Seidel, J. K. Angell, J. R. Lanzante, I. Durre, and T. C. Peterson, 2005: Radiosonde Atmospheric Temperature Products for Assessing Climate (RATPAC): A new dataset of large-area anomaly time series. *J. Geophys. Res.*, **110**, D22101, doi:10.1029/2005JD006169.

Frith, S., R. Stolarski, and P. K. Barthia, 2004: Implications of Version 8 TOMS and SBUV data for long-term trend. *Proc. Quadrennial Ozone Symposium-2004*, C. Zerefos, Ed., IAMAS, 65–66. [Available online at http://acdb-ext.gsfc.nasa.gov/Data_services/merged/.]

Ganachaud, A., and C. Wunsch, 2003: Large-scale ocean heat and freshwater transports during the World Ocean Circulation Experiment. *J. Climate*, **16**, 696–705.

GCOS, 2003: The second report on the adequacy of the Global Observing Systems for Climate in support of the UNFCCC. GCOS-82, WMO/TD No. 1143, 74 pp. [Available online at http://www.wmo.int/pages/prog/gcos/Publications/gcos-82_2AR.pdf.]

——, 2004: Implementation plan for the Global Observing System for Climate in support of the UNFCCC. GCOS-92, WMO/TD No. 1219, 136 pp. [Available online at http://www.wmo.ch/pages/prog/gcos/Publications/gcos-92.pdf.]

Giles, K. A., S. W. Laxon, and A. L. Ridout, 2008: Circumpolar thinning of Arctic sea ice following the 2007 record ice extent minimum. *Geophys. Res. Lett.*, **35**, L22502, doi:10.1029/2008GL035710.

Gillett, N. P., D. A. Stone, P. A. Stott, T. Nozawa, A. Y. Karpechko, G. C. Hegerl, M. F. Wehner, and P. D. Jones, 2008: Attribution of polar warming to human influence. *Nature Geosci.*, **1**, 750–754.

Goldenberg, S. B., and L. J. Shapiro, 1996: Physical mechanisms for the association of El Niño and West African rainfall with Atlantic major hurricane activity. *J. Climate*, **9**, 1169–1187.

——, C. W. Landsea, A. M. Mestas-Nuñez, and W. M. Gray, 2001: The recent increase in Atlantic hurricane activity: Causes and implications. *Science*, **293**, 474–479.

Goni, G., and I. Wainer, 2001: Investigation of the Brazil current front dynamics from altimeter data. *J. Geophys. Res.*, **106** (C12), doi:10.1029/2000JC000396.

——, and J. A. Trinanes, 2003: Ocean thermal structure monitoring could aid in the intensity forecast of tropical cyclones. *Eos, Trans. Amer. Geophys. Union*, **84** (51), doi:10.1029/2003EO510001.

——, and Coauthors, 2009: Applications of satellite-derived ocean measurements to tropical cyclone intensity forecasting. *Oceanography*, **22**, 176–183.

Gould, W. A., and J. A. Mercado-Díaz, 2008: Twenty year record of vegetation change from long-term plots in Alaskan tundra. *Eos, Trans. Amer. Geophys. Union*, **89** (Fall Meeting Suppl.), Abstract C11C-0524.

Gouretski, V., and K. P. Kolterman, 2007: How much is the ocean really warming? *Geophys. Res. Lett.*, **34**, L01610, doi:10.1029/2006GL027834.

Gray, W. M., 1984: Atlantic seasonal hurricane frequency: Part I: El Niño and 30-mb quasi-biennial oscillation influences. *Mon. Wea. Rev.*, **112**, 1649–1668.

Gruber, N., and Coauthors, 2009: Ocean sources, sinks, and transport of atmospheric CO_2. *Global Biogeochem. Cycles*, **23**, GB1005, doi:10.1029/2008GB003349.

Haas, C., A. Pfaffling, S. Hendricks, L. Rabenstein, J.-L. Etienne, and I. Rigor, 2008: Reduced ice thickness in Arctic transpolar drift favors rapid ice retreat. *Geophys. Res. Lett.*, **35**, L17501, doi:10.1029/2008GL034457.

Haeberli, W., and M. Hoelzle, 1995: Application for inventory data for estimating characteristics of and regional climate-change effects on mountain glaciers: a pilot study with the European Alps. *Ann. Glaciol.*, **21**, 206–212.

Hagemann, S., and L. Dümenil, 1998: A parameterization of the lateral waterflow for the global scale. *Climate Dyn.*, **14**, 17–31.

Hahn, C. J., and S. G. Warren, 2007: A gridded climatology of clouds over land (1971–1996) and ocean (1954–1997) from surface observations worldwide. ORNL/CDIAC-153, NDP-026E. [Available online from http://cdiac.ornl.gov/epubs/ndp/ndp026e/ndp026e.html.]

Haimberger, L., C. Tavola, and S. Sperka, 2008: Toward elimination of the warm bias in historic radiosonde temperature records. Some new results from a comprehensive intercomparison of upper air data. *J. Climate*, **21**, 4587–4606.

Hajj, G. A., and Coauthors, 2004: CHAMP and SAC-C atmospheric occultation results and inter-comparisons. *J. Geophys. Res.*, **109**, D06109, doi:10.1029/2003JD003909.

Hakkinen, S., and P. B. Rhines, 2009: Shifting surface currents in the northern North Atlantic Ocean. *J. Geophys. Res.*, **114**, C04005, doi:10.1029/2008JC004883.

Hansen, J., R. Ruedy, J. Glascoe, and M. Sato, 1999: GISS analysis of surface temperature change. *J. Geophys. Res.*, **104** (D24), 30 997–31 022.

——, ——, M. Sato, M. Imhoff, W. Lawrence, D. Easterling, T. Peterson, and T. Karl, 2001: A closer look at United States and global surface temperature change. *J. Geophys. Res.*, **106** (D20), 23 947–23 963.

Harris, C., and W. Haeberli, 2003: Warming permafrost in European mountains. *World Meteorol. Org. Bull.*, **52**, 252-257.

Harris, N. R. P., and Coauthors, 2008: Ozone trends at northern mid- and high latitudes – a European perspective. *Ann. Geophys.*, **26**, 1207–1220.

Hawkins, E., and R. Sutton, 2007: Variability of the Atlantic thermohaline circulation described by three-dimensional empirical orthogonal functions. *Climate Dyn.*, **29**, 745–762.

He, W., S. Ho, H. Chen, X. Zhou, D. Hunt, and Y. Kuo, 2009: Assessment of radiosonde temperature measurements in the upper troposphere and lower stratosphere using COSMIC radio occultation data, *Geophys. Res. Lett.,* **36**, L17807, doi:10.1029/2009GL038712.

Heidinger, A. K. and M. J. Pavolonis, 2009: Gazing at cirrus clouds for 25 years through a split window, part 1: Methodology. *J. Appl. Meteor. Climatol.*, **48**, 1110–1116.

Held, I. M., and B. J. Soden, 2006: Robust response of the hydrological cycle to global warming. *J. Climate*, **19**, 5686–5699.

Hendon, H., C. Zhang, and J. Glick, 1999: Interannual variation of the Madden-Julian Oscillation during Austral Summer. *J. Climate*, **12**, 2538–2550.

Henson, S. A., J. L. Sarmiento, J. P. Dunne, L. Bopp, I. Lima, S. C. Doney, J. John, and C. Beaulieu, 2009: Is global warming already changing ocean productivity? *Biogeosciences Discuss.*, **6**, 10 311–10 354.

Hilburn, K. A., and F. J. Wentz, 2008: Intercalibrated passive microwave rain products from the Unified Microwave Ocean Retrieval Algorithm (UMORA). *J. Appl. Meteor. Climatol.*, **47**, 778–794.

Hill, G. B., and G. H. R. Henry, 2010: Responses of high Arctic wet sedge tundra to climate warming since 1980. *Global Change Biol.*, doi:10.1111/j.1365-2486.2010.02244.x, in press.

Ho, S.-P., Y. H. Kuo, Z. Zeng, and T. Peterson, 2007: A comparison of lower stratosphere temperature from microwave measurements with CHAMP GPS RO data. *Geophy. Res. Lett.,* **34**, L15701, doi:10.1029/2007GL030202.

——, M. Goldberg, Y.-H. Kuo, C.-Z. Zou, and W. Schreiner, 2009a: Calibration of temperature in the lower stratosphere from microwave measurements using COSMIC radio occultation data: Preliminary results. *Terr. Atmos. Oceanic Sci.*, **20**, 87–100.

——, and Coauthors, 2009b: Estimating the uncertainty of using GPS radio occultation data for climate monitoring: Inter-comparison of CHAMP refractivity climate records 2002-2006 from different data centers. *J. Geophys. Res.*, **114**, D23107, doi:10.1029/2009JD011969.

——, W. He, and Y.-H. Kuo, 2009c: Construction of consistent temperature records in the lower stratosphere using global positioning system radio occultation data and microwave sounding measurements. *New Horizons in Occultation Research*, A. K. Steiner et al. Eds., Springer, 207–217.

Hobgood, J. S., 2003: Maximum potential intensities of tropical cyclones near Isla Socorro, Mexico. *Wea. Forecasting*, **18**, 1129–1139.

Hofmann, D. J., and S. A. Montzka, 2009: Recovery of the ozone layer: The ozone depleting gas index. *Eos, Trans. Amer. Geophys. Union,* **9**, 1–2.

——, J. H. Butler, E. J. Dlugokencky, J. W. Elkins, K. Masarie, S. A. Montzka, and P. Tans, 2006: The role of carbon dioxide in climate forcing from 1979 to 2004: Introduction of the Annual Greenhouse Gas Index. *Tellus*, **58B**, 614–619.

Holland, G. J., 1993: Ready reckoner. *Global Guide to Tropical Cyclone Forecasting*, WMO/TD-No. 560, TCP-31, World Meteorological Organization, 9.1–9.32.

Holliday, N. P., and Coauthors, 2008: Reversal of the 1960s to 1990s freshening trend in the northeast North Atlantic and Nordic seas. *Geophys. Res. Lett.*, **35**, L03614, doi:10.1029/2007GL032675.

Hollingsworth, A., and Coauthors, 2008: Toward a monitoring and forecasting system for atmospheric composition: The GEMS Project. *Bull. Amer. Meteor. Soc.*, **89**, 1147–1164 .

Honda, M., J. Inoue, and S. Yamane, 2009: Influence of low Arctic sea-ice minima on anomalously cold Eurasian winters. *Geophys. Res. Lett.*, **36**, L08707, doi:10.1029/2008GL037079.

Hu, Y., and Q. Fu, 2009: Stratospheric warming in Southern Hemisphere high latitudes since 1979. *Atmos. Chem. Phys.*, **9**, 4329–4340.

Hudson, J. M. G., and G. H. R. Henry, 2009: Increased plant biomass in a high arctic heath community from 1981 to 2008. *Ecology*, **90**, 2657–2663.

Huffman, G. J., and Coauthors, 2007: The TRMM multi-satellite precipitation analysis: Quasi-global, multi-year, combined-sensor precipitation estimates at fine scale. *J. Hydrometeor.*, **8**, 38–55.

Hurrell, J. W., Y. Kushnir, G. Ottersen, and M. Visbeck, 2003: An overview of the North Atlantic Oscillation. *The North Atlantic Oscillation: Climate Significance and Environmental Impact. Geophys. Monogr.*, Vol. 134, Amer. Geophys. Union, 1–37.

ICU, 2009: *The Island Climate Update*. National Institute of Water and Atmospheric Research, New Zealand. [Available online at http://www.niwa.co.nz/ncc/icu.]

Ingleby, B., and M. Huddleston, 2007: Quality control of ocean temperature and salinity profiles - historical and real-time data. *J. Mar. Systems,* **65**, 158–175.

Irwin, R. P., and R. Davis, 1999: The relationship between the southern oscillation index andtropical cyclone tracks in the eastern North Pacific. *Geophys. Res. Lett.*, **26**, 2251–2254.

Isaksen, K., D. Vonder Mühll, H. Gubler, T. Kohl, and J. L. Sollid, 2000: Ground surface temperature reconstruction based on data from a deep borehole in permafrost at Janssonhaugen, Svalbard. *Ann. Glaciol.,* **31**, 287–294.

Ishii, M., and M. Kimoto, 2009: Reevaluation of historical ocean heat content variations with time-varying XBT and MBT depth bias corrections. *J. Oceanogr.*, **65**, 287–299.

——, ——, K. Sakamoto, and S.-I. Iwasaki, 2006: Steric sea level changes estimated from historical ocean subsurface temperature and salinity analyses. *J. Oceanogr.*, **62**, 155–170.

Jackson, J. M., E. C. Carmack, F. A. McLaughlin, S. E. Allen, and R. G. Ingram, 2010: Identification, characterization, and change of the near-surface temperature maximum in the Canada Basin, 1993-2008. *J. Geophys. Res.*, **115**, C05021, doi:10.1029/2009JC005265.

Janowiak, J. E., and P. Xie, 1999: CAMS–OPI: A global satellite-rain gauge merged product for real-time precipitation monitoring applications. *J. Climate*, **12**, 3335–3342.

Jauregui, E., 2003: Climatology of landfalling hurricanes and tropical storms in Mexico. *Atmósfera*, **16**, 193–204.

Jia, G. J., H. E. Epstein, and D. A. Walker, 2009: Vegetation greening in the Canadian Arctic related to decadal warming. *J. Environ. Monit.*, **11**, 2231–2238.

Johns, W. E., L. M. Beal, M. O. Baringer, J. R. Molina, S. A. Cunningham, T. Kanzow, and D. Rayner, 2008: Variability of shallow and deep western boundary currents off the Bahamas during 2004-2005: Results from the 26ºN RAPID-MOC array. *J. Phys. Oceanogr.,* **38**, 605–623.

Johnson, D. R., T. P. Boyer, H. E. Garcia, R. A. Locarnini, O. K. Baranova, and M. M. Zweng, 2009: *World Ocean Database 2009 Documentation*. NODC Internal Report 20, 175 pp. [Available online at http://www.nodc.noaa.gov/OC5/WOD09/pr_wod09.html.]

Johnson, D. R., S. Villarreal, M. Lara, P. J. Webber, T. Callaghan, D. Hik, and C. E. Tweedie, 2009: IPY-Back to the Future: Determining decadal time scale change in ecosystem structure and function in high latitude and high altitude tundra ecosystems. *Eos, Trans. Amer. Geophys. Union*, **90** (Fall Meeting Suppl.), Abstract B33A-0372.

Johnson, G. C., and S. C. Doney, 2006: Recent western South Atlantic bottom water warming. *Geophys. Res. Lett.*, **33**, L14614, doi:10.1029/2006GL026769.

——, S. Mecking, B. M. Sloyan, and S. E. Wijffels, 2007: Recent bottom water warming in the Pacific Ocean. *J. Climate*, **20**, 5365–5375.

——, S. G. Purkey, and J. L. Bullister, 2008a: Warming and freshening in the abyssal southeastern Indian Ocean. *J. Climate*, **21**, 5351–5363.

——, ——, and J. M. Toole, 2008b: Reduced Antarctic meridional overturning circulation reaches the North Atlantic Ocean. *Geophys. Res. Lett.*, **35**, L22601, doi:10.1029/2008GL035619.

Jones, A., and Coauthors, 2009: Evolution of stratospheric ozone and water vapour time series studied with satellite measurements. *Atmos. Chem. Phys.*, **9**, 6055–6075.

Jones, B. M., C. A. Kolden, R. Jandt, J. T. Abatzoglou, F. Urban, and C. D. Arp, 2009: Fire behavior, weather, and burn severity of the 2007 Anaktuvuk River tundra fire, North Slope, Alaska. *Arctic Antarct. Alpine Res.*, **41**, 309–316.

Jones, P. D., T. J. Osborn, and K. R. Briffa, 1997: Estimating sampling errors in large-scale temperature averages. *J. Climate*, **10**, 2548–2568.

Kaiser, J. W., M. Suttie, J. Flemming, J.-J. Morcrette. O. Bouchner, and M. G. Schultz, 2009: Global real-time fire emission estimates based on space-borne fire radiative power observations. *AIP Conf. Proc.*, **1100**, 645–648.

Kalnay, E., and Coauthors, 1996: The NCEP/NCAR 40-year reanalysis project. *Bull. Amer. Meteor. Soc.,* **77**, 437–471.

Kanzow, T., and Coauthors, 2007: Observed flow compensation associated with the meridional overturning circulation near 26.5°N in the Atlantic. *Science*, **317**, 938–941.

——, U. Send, and M. McCartney, 2008: On the variability of the deep meridional transports in the tropical North Atlantic. *Deep-Sea Res. I,* **55**, 1601–1623.

——, H. Johnson, D. P. Marshall, S. A. Cunningham, J. J-M. Hirschi, A. Mujahid, H. L. Bryden, and W. E. Johns, 2009: Basin-wide integrated volume transports in an eddy-filled ocean. *J. Phys. Oceanogr.*, **39**, 3091–3110.

Karl, T. R., S. J. Hassol, C. D. Miller, and W. L. Murray, Eds., 2006: Temperature trends in the lower atmosphere: Steps for understanding and reconciling differences. U.S. Climate Change Science Program Final Rep., Synthesis and Assessment Product 1.1, Subcommittee on Global Change Research, Washington, DC, 164 pp. [Available online at http://www.climatescience.gov/Library/sap/sap1-1/finalreport/default.htm.]

Karoly, D. J., 1989: Southern Hemisphere circulation features associated with El Niño-Southern Oscillation events. *J. Climate,* **2**, 1239–1252.

Kasischke, E. S., and Coauthors, 2000: Contributions of 1998 fires in the boreal forest to atmospheric concentrations of carbon monoxide and methane. *Eos, Trans. Amer. Geophys. Union*, **81**, 260.

Kayano, M., and V. Kousky, 1999: Intraseasonal (30-60 day) variability in the global tropics: principal modes and their evolution. *Tellus*, **51A**, 373–386.

Khatiwala, S., F. Primeau, and T. Hall, 2009: Reconstruction of the history of anthropogenic CO_2 concentrations in the ocean. *Nature*, **462**, 346–350.

Knapp, K. R., M. C. Kruk, D. H. Levinson, H. J. Diamond, and C. J. Neumann, 2010: The International Best Track Archive for Climate Stewardship (IBTrACS): Unifying tropical cyclone data. *Bull. Amer. Meteor. Soc.*, **91**, 363–376.

Knight, J., and Coauthors, 2009: Do global temperature trends over the last decade falsify climate predictions? [in "State of the Climate in 2008"]. *Bull. Amer. Meteor. Soc.*, **90** (8), S22–S23.

Knorr, W., N. Gobron, M. Scholze, T. Kaminski, R. Schnur, and B. Pinty, 2007: Impact of terrestrial biosphere carbon exchanges on the anomalous CO_2 increase in 2002-2003. *Geophys. Res. Lett.*, **34**, L09703, doi:10.1029/2006GL029019.

Knutti, R., and L. Tomassini, 2008: Constraints on the transient climate response from observed global temperature and ocean heat uptake. *Geophys. Res. Lett.*, **35**, L09701, doi:10.1029/2007GL032904.

Köhl, A., and D. Stammer, 2008: Variability of the meridional overturning in the North Atlantic from the 50-year GECCO state estimation. *J. Phys. Oceanogr.*, **38**, 1913–1930.

Kokelj, S. V., T. C. Lantz, J. Kanigan, S. L. Smith, and R. Coutts, 2009: Origin and polycyclic behavior of tundra thaw slumps, Mackenzie delta region, Northwest Territories, Canada. *Permafrost Periglacial Processes*, **20**, 173–184.

Kossin, J. P., and D. J. Vimont, 2007: A more general framework for understanding Atlantic hurricane variability and trends. *Bull. Amer. Meteor. Soc.*, **88**, 1767–1781.

Kouketsu, S., M. Fukasawa, I. Kaneko, T. Kawano, H. Uchida, T. Doi, M. Aoyama, and K. Murakami, 2009: Changes in water properties and transports along 24°N in the North Pacific between 1985 and 2005. *J. Geophys. Res.*, **114**, C01008, doi:10.1029/2008JC004778.

Kousky, V., and M. Kayano, 1994: Principal modes of outgoing longwave radiation and 250-mb circulation for the South American sector. *J. Climate*, **7**, 1131–1143.

Krishnamurti, T. N., A. Thomas, A. Simon, and V. Kumar, 2010: Desert air incursions, an overlooked aspect, for the dry spells of Indian summer monsoon. *J. Atmos. Sci.*, doi:10.1175/2010JAS3440.1, in press.

Kuo, Y.-H., T. K. Wee, S. Sokolovskiy, C. Rocken, W. Schreiner, and D. Hunt, 2004: Inversion and error estimation of GPS radio occultation data. *J. Meteor. Soc. Japan*, **82**, 507–531.

——, W. S. Schreiner, J. Wang, D. L. Rossiter, and Y. Zhang, 2005: Comparison of GPS radio occultation soundings with radiosondes. *Geophy. Res. Lett.*, **32**, L05817, doi:10.1029/2004GL021443.

Kwok, R., 2007: Near zero replenishment of the Arctic multiyear sea ice cover at the end of 2005 summer. *Geophys. Res. Lett.*, **34**, L05501, doi:10.1029/2006GL028737.

——, G. F. Cunningham, M. Wensnahan, I. Rigor, H. J. Zwally, and D. Yi, 2009: Thinning and volume loss of the Arctic Ocean sea ice cover: 2003–2008. *J. Geophys. Res.*, **114**, C07005, doi:10.1029/2009JC005312.

Labitzke, K., and M. Kunze, 2009: On the remarkable Arctic winter in 2008/09. *J. Geophys. Res.*, **114**, D00I02, doi:10.1029/2009JD012273.

Lagerloef, G. S. E., R. Lukas, F. Bonjean, J. T. Gunn, G. T. Mitchum, M. Bourassa, and A. J. Busalacchi, 2003: El Niño Tropical Pacific Ocean surface current and temperature evolution in 2002 and outlook for early 2003. *Geophys. Res. Letters*, **30**, 1514, doi:10.1029/2003GL017096.

Landsea, C. W., and W. M. Gray, 1992: The strong association between Western Sahel monsoon rainfall and intense Atlantic hurricanes. *J. Climate*, **5**, 435–453.

——, G. D. Bell, W. M. Gray, and S. B. Goldenberg, 1998: The extremely active 1995 Atlantic hurricane season: Environmental conditions and verification of seasonal forecasts. *Mon. Wea. Rev.*, **126**, 1174–1193.

Langbein, W.B., 1961: Salinity and hydrology of closed lakes. US Geol. Surv. Prof. Pap. 412, 20 pp.

Langenfelds, R. L., R. J. Francey, B. C. Pak, L. P. Steele, J. Lloyd, C. M. Trudinger, and C. E. Allison, 2002: Interannual growth rate variations of atmospheric CO_2 and its $\delta^{13}C$, H_2, CH_4, and CO between 1992 and 1999 linked to biomass burning. *Global Biogeochem. Cycles*, **16**, 1048, doi:10.1029/2001GB001466.

Lantz, T. C., 2008: Relative influence of temperature and disturbance on vegetation dynamics in the Low Arctic: An investigation at multiple scales. Ph.D. thesis, Faculty of Graduate Studies (Forestry), University of British Columbia (Vancouver), 153 pp.

——, and S. V. Kokelj, 2008: Increasing rates of retrogressive thaw slump activity in the Mackenzie delta region, N.W.T. Canada. *Geophys. Res. Lett.*, **35**, L06502, doi:06510.01029/02007GL032433.

Lawrence, D. M., A. G. Slater, R. A. Tomas, M. M. Holland, and C. Deser, 2008: Accelerated Arctic land warming and permafrost degradion during rapid sea ice loss. *Geophys. Res. Lett.*, **35**, L11506, doi:10.1029/2008GL033985.

LeBel, D. A., and Coauthors, 2008: The formation rate of North Atlantic deep water and eighteen degree water calculated from CFC-11 inventories observed during WOCE. *Deep-Sea Res. I,* **55**, 891–910.

L'Ecuyer, T. S., N. B. Wood, T. Haladay, G. L. Stephens, and P. W. Stackhouse, 2008: Impact of clouds on atmospheric heating based on the R04 CloudSat fluxes and heating rates data set. *J. Geophys. Res.*, **113**, D00A15, doi:10.1029/2008JD009951.

Lehner, B., and P. Döll, 2004: Development and validation of a global database of lakes, reservoirs and wetlands. *J. Hydrol.*, **296**, 1–22.

Leibman, M. O., and A. I. Kizyakov, 2007: *Cryogenic Landslides of the Yamal and Yugorsky Peninsulas* (in Russian). Earth Cryosphere Institute, Siberian Branch, Russian Academy of Science, 206 pp.

Lenton, A., F. Codron, L. Bopp, N. Metzl, P. Cadule, A. Tagliabue, and J. Le Sommer, 2009: Stratospheric ozone depletion reduces ocean carbon uptake and enhances ocean acidification. *Geophys. Res. Lett.*, **36**, L12606, doi:10.1029/2009GL038227.

LeQuere, C., and Coauthors, 2009: Trends in the sources and sinks of carbon dioxide. *Nature Geosci.*, **2**, 831–836.

Leuliette, E., and L. Miller, 2009: Closing the sea level rise budget with altimetry, Argo, and GRACE. *Geophys. Res. Lett.*, **36**, L04608, doi:10.1029/2008GL036010.

Levinson, D. H., and J. H. Lawrimore, Eds., 2008: State of the climate in 2007. *Bull. Amer. Meteor. Soc.*, **89** (7), S1–S179.

——, K. Hilburn, and M. C. Kruk, 2009: Global precipitation [in "State of the Climate in 2008"]. *Bull. Amer. Meteor. Soc.*, **90** (8), S24–S28.

Levitus, S., J. I. Antonov, and T. P. Boyer, 2005: Warming of the world ocean, 1995-2003. *Geophys. Res. Lett.*, **32**, L02604, doi:10.1029/2004GL021592.

——, ——, ——, R. A. Locarnini, H. E. Garcia, and A. V. Mishonov, 2009: Global ocean heat content 1955–2008 in light of recently revealed instrumentation problems. *Geophys. Res. Lett.*, **36**, L07608, doi:10.1029/2008GL037155.

L'Heureux, M., G. Bell, and M. Halpert, 2009: ENSO and the tropical Pacific [in "State of the Climate in 2008"]. *Bull. Amer. Meteor. Soc.*, **90** (8), S75–S77.

Li, W. K., F. A. McLaughlin, C. Lovejoy, and E. C. Carmack, 2009: Smallest algae thrive as the Arctic Ocean freshens. *Science*, **326**, 539.

Liljedahl, A., L. Hinzman, R. Busey, and K. Yoshikawa, 2007: Physical short-term changes after a tussock tundra fire, Seward Peninsula, Alaska. *J. Geophys. Res.*, **112**, F02S07, doi:10.1029/2006JF000554.

Lin, I.-I., C.-C. Wu, I.-F. Pun, and D.-S. Ko. 2008: Upperocean thermal structure and the western North Pacific category 5 typhoons. Part I: Ocean features and the category 5 typhoons' intensification. *Mon. Wea. Rev.*, **136**, 3288–3306.

——, I.-F. Pun, and C.-C. Wu. 2009: Upper ocean thermal structure and the western North Pacific category-5 typhoons. Part II: Dependence on translation speed. *Mon. Wea. Rev.*, **137**, 3744–3757.

Lin, P., Q. Fu, S. Solomon, and J. M. Wallace, 2009: Temperature trend patterns in Southern Hemisphere high latitudes: Novel indicators of stratospheric change. *J. Climate*, **22**, 6325–6341.

Liu, H., L. Wang, and K. Jezek, 2005: Wavelet-based edge detection approach to derivation of snow-melt onset, duration and extent from satellite passive microwave measurements. *Int. J. Remote Sens.*, **26**, 4639–4660.

——, ——, and ——, 2006: Spatio-temporal variations of snow melt zones in Antarctic Ice Sheet derived from satellite SMMR and SSM/I data (1978-2004). *J. Geophys. Res.*, **111**, F01003, doi:10.1029/2005JF000318.

Lohmann, G., H. Haak, and J. H. Jungclaus, 2008: Estimating trends of Atlantic meridional overturning circulation from long-term hydrographic data and model simulations. *Ocean Dyn.,* **58**, 127–138.

Lohmann, K., H. Drange, and M. Bentsen, 2009: Response of the North Atlantic subpolar gyre to persistent North Atlantic oscillation like forcing. *Climate Dyn.,* **32**, 273–285.

Luers, J. K., and R. E. Eskridge, 1998: Use of radiosonde temperature data in climate studies. *J. Climate*, **11**, 1002–1019.

Lumpkin, R., and K. Speer, 2007: Global ocean meridional overturning. *J. Phys. Oceanogr.*, **37**, 2550–2562.

——, ——, and K. P. Koltermann, 2008: Transport across 48°N in the Atlantic Ocean. *J. Phys. Oceanogr.*, **38**, 733–752.

Lungu, T., and P. S. Callahan, 2006: QuikSCAT science data product user's manual: Overview and geophysical data products. D-18053-Rev A, version 3.0, 91 pp. [Available from Jet Propulsion Laboratory, 4800 Oak Grove Dr., Pasadena, CA 91109.]

Luo, J.-J., S. Behera, Y. Masumoto, H. Sakuma, and T. Yamagata, 2008: Successful prediction of the consecutive IOD in 2006 and 2007. *Geophys. Res. Lett.,* **35**, L14S02, doi:10.1029/2007GL032793.

——, R. Zhang, S. K. Behera, Y. Masumoto, F.-F. Jin, R. Lukas, and T. Yamagata, 2010: Interaction between El Niño and extreme Indian Ocean dipole. *J. Climate,* **23,** 726–742.

Lyman, J. M., and G. C. Johnson, 2008: Estimating global upper ocean heat content despite irregular sampling. *J. Climate*, **21**, 5629–5641.

Madden, R., and P. Julian, 1971: Detection of a 40-50 day oscillation in the zonal wind in the tropical Pacific. *J. Atmos. Sci*., **28**, 702–708.

——, and ——, 1972: Description of global-scale circulation cells in the tropics with a 40-50 day period. *J. Atmos. Sci*., **29**, 1109–1123.

——, and ——, 1994: Observations of the 40-50 day tropical oscillation: A review. *Mon. Wea. Rev.*, **122**, 814–837.

Maes, C., K. Ando, T. Delcroix, W. S. Kessler, M. J. McPhaden, and D. Roemmich, 2006: Observed correlation of surface salinity, temperature and barrier layer at the eastern edge of the western Pacific warm pool. *Geophys. Res. Lett*., **33**, L06601, doi:10.1029/2005GL024772.

Mainelli, M., M. DeMaria, L. K. Shay, and G. Goni, 2008: Application of oceanic heat content estimation to operational forecasting of recent Atlantic category 5 hurricanes. *Wea. Forecasting*, **23**, 3–16.

Maloney, E. D., and D. L. Hartmann, 2000: Modulation of eastern North Pacific hurricanes by the Madden-Julian Oscillation. *J. Climate*, **13**, 1451–1460.

Mantua, N. J., S. R. Hare, Y. Zhang, J. M. Wallace, and R. C. Francis, 1997: A Pacific interdecadal climate oscillation with impacts on salmon production. *Bull. Amer. Meteor. Soc*, **78**, 1069–1079.

Marland, G., T. A. Boden, and R. J. Andres, 2008: Global, regional, and national CO_2 emissions. *Trends: A compendium of data on global change*, Carbon Dioxide Information Analysis Center, Oak Ridge National Laboratory, U.S. Department of Energy. [Available online at http://cdiac.esd.ornl.gov/trends/emis/em_cont.html.]

Marsh, R., 2000: Recent variability of the North Atlantic thermohaline circulation inferred from surface heat and freshwater fluxes. *J. Climate*, **13**, 3239–3260.

Marshall, G. J., 2003: Trends in the Southern Annular Mode from observations and reanalyses. *J. Climate*, **16**, 4134–4143.

——, A. Orr, N. P. M. van Lipzig, and J. C. King, 2006: The impact of a changing southern hemisphere annular mode on Antarctic peninsula summer temperatures. *J. Climate*, **19**, 5388–5404.

Maslanik, J. A., C. Fowler, J. Stroeve, S. Drobot, J. Zwally, D. Yi, and W. Emery, 2007: A younger, thinner Arctic ice cover: Increased potential for rapid, extensive sea-ice loss. *Geophys. Res. Lett.*, **34**, L24501, doi:10.1029/2007GL032043.

Mason, I. M., M. A. J. Guzkowska, C. G. Rapley, and F. A. Street-Perrott, 1994: The response of lake levels and areas to climatic change. *Climatic Change*, **27**, 161–197.

McClain, C. R., 2009: A decade of satellite ocean color observation. *Annu. Rev. Mar. Sci.*, **1**, 19–42.

——, S. R. Signorini, and J. R. Christian, 2004: Subtropical gyre variability observed by ocean-color satellites. *Deep-Sea Res. II*, **51**, 281–301.

McDonagh, E. L., H. L. Bryden, B. A. King, and R. J. Saunders, 2008: The circulation of the Indian Ocean at 32°S. *Prog. Oceanogr.,* **79**, 20–36.

McPhaden, M. J., and D. Zhang, 2004: Pacific Ocean circulation rebounds. *Geophys. Res. Lett.*, **31**, L18301, doi: 10.1029/2004GL020727.

Mears, C. A., and F. J. Wentz, 2009a: Construction of the RSS V3.2 lower-tropospheric temperature dataset from the MSU and AMSU microwave sounders. *J. Atmos. Oceanic Technol.*, **26**, 1492–1509.

——, and ——, 2009b: Construction of the Remote Sensing Systems V3.2 atmospheric temperature records from the MSU and AMSU microwave sounders. *J. Atmos. Oceanic Technol.*, **26**, 1040–1056.

Meier, M. F., M. B. Dyurgerov, U. K. Rick, S. O'Neel, W. T. Pfeffer, R. S. Anderson, S. P. Anderson, and A. F. Glazovsky, 2007: Glaciers dominate eustatic sea-level rise in the 21st century. *Science*, **317**, 1064–1067.

Meinen, C. S., M. O. Baringer, and R. F. Garcia, 2010: Florida Current transport variability: An analysis of annual and longer-period signals. *Deep-sea Res. I*, doi:10.1016/j.dsr.2010.04.001, in press.

Menne, M. J., C. N. Williams Jr., and M. A. Palecki, 2010: On the reliability of the U.S. surface temperature record. *J. Geophys. Res.*, doi:10.1029/2009JD013094, in press.

Mercier, F., A. Cazenave, and C. Maheu, 2002: Interannual lake level fluctuations (1993-1999) in Africa from Topex / Poseidon: connection with ocean-atmosphere interactions over Indian Ocean. *Global Planet. Change*, **32**, 141–163.

Metzl, N., 2009: Decadal increase of oceanic carbon dioxide in Southern Indian Ocean surface waters (1991-2007). *Deep-Sea Res. II*, **56**, 607–619.

Mo, K. C., 2000: The association between intraseasonal oscillations and tropical storms in the Atlantic Basin. *Mon. Wea. Rev.*, **128**, 4097–4107.

——, and V. E. Kousky, 1993: Further analysis of the relationship between circulation anomaly patterns and tropical convection. *J. Geophys. Res.*, **98** (D3), 5103–5113.

Montzka, S. A., R. C. Myers, J. H. Butler, J. W. Elkins, L. Lock, A. Clarke, and A. H. Goldstein, 1996: Observations of HFC-134a in the remote troposphere. *Geophys Res. Lett.*, **23**, 169–172.

——, J. H. Butler, J. W. Elkins, T. M. Thompson, A. D. Clarke, and L. T. Lock, 1999: Present and future trends in the atmospheric burden of ozone-depleting halogens. *Nature*, **398**, 690–694.

——, B. D. Hall, and J. W. Elkins, 2009: Accelerated increases observed for hydrochlorofluorocarbons since 2004 in the global atmosphere. *Geophys. Res. Lett.*, **36**, L03804, doi:10.1029/2008GL036475.

Mooers, C. N. K., C. S. Meinen, M. O. Baringer, I. Bang, R. Rhodes, C. N. Barron, and F. Bub, 2005: Florida current response to cold front passages: Comparison of NOAA cable and Navy model volume transports. *Eos, Trans. Amer. Geophys. Union*, **86**, 269, 272–273.

Morcrette, J.-J., and Coauthors, 2009: Aerosol analysis and forecast in the European Centre for Medium-Range Weather Forecasts Integrated Forecast System: Forward modeling. *J. Geophys. Res.*, **114**, D06206, doi:10.1029/2008JD011235.

Mote, T. L., 2007: Greenland surface melt trends 1973-2007: Evidence of a large increase in 2007. *Geophys. Res. Lett.*, **34**, L22507, doi:10.1029/2007GL031976.

Münnich, M., and J. D. Neelin, 2005: Seasonal influence of ENSO on the Atlantic ITCZ and equatorial South America. *Geophys. Res. Lett.*, **32**, L21709, doi:10.1029/2005GL023900.

Murphy, D. M., S. Solomon, R. W. Portmann, K. H. Rosenlof, P. M. Forster, and T. Wong, 2009: An observationally based energy balance for the Earth since 1950. *J. Geophys. Res.*, **114**, D17107, doi:10.1029/2009JD012105.

Neumann, C. J., B. R. Jarvinen, C. J. McAdie, and J. D. Elms, 1993: *Tropical Cyclones of the North Atlantic Ocean, 1871-1992.* Historical Climatology Series 6-2, NOAA/National Climatic Data Center, 193 pp.

Newchurch, M. J., E. S. Yang, D. M. Cunnold, G. C. Reinsel, J. M. Zawodny, and J. M. Russel III, 2003: Evidence for slowdown in stratospheric ozone loss: First stage of ozone recovery. *J. Geophys. Res.*, **108**, 4507, doi:10.1029/2003JD003471.

Newman, P. A., J. S. Daniel, D. W. Waugh, and E. R. Nash, 2007: A new formulation of equivalent effective stratospheric chlorine (EESC). *Atmos. Chem. Phys.*, **7**, 4537–4552.

Niiler, P. P., R. E. Davis, and H. J. White, 1987: Water-following characteristics of a mixed layer drifter. *Deep-Sea Res. A*, **34**, 1867–1881.

Nobre, P., and J. Shukla, 1996: Variations of sea surface temperature, wind stress and rainfall over the tropical Atlantic and South America. *J. Climate*, **9**, 2464–2479.

Novelli, P. C., K. A. Masarie, P. M. Lang, B. D. Hall, R. C. Myers, and J. W. Elkins, 2003: Reanalysis of tropospheric CO trends: Effects of the 1997–1998 wildfires. *J. Geophys. Res.*, **108**, 4464, doi:10.1029/2002JD003031.

NRC, 2007: *Earth Science and Applications from Space: National Imperatives for the Next Decade and Beyond.* National Academies Press, 218 pp.

Oberman, N. G., 2008: Contemporary permafrost degradation of northern European Russia. *Proc. of the 9th International Conf. on Permafrost, Fairbanks, Alaska, 29 June – 3 July 2008*, Vol. 2, D. L. Kane and K. M. Hinkel, Eds., Institute of Northern Engineering, University of Alaska Fairbanks, 1305–1310.

——, and G. G. Mazhitova, 2001: Permafrost dynamics in the northeast of European Russia at the end of the 20th century. *Norw. J. Geogr.*, **55**, 241–244.

——, and I. G. Shesler, 2009: Observed and projected changes in permafrost conditions within the European North-East of the Russian Federation (in Russian). *Problemy Severa I Arctiki Rossiiskoy Federacii* (Problems and Challenges of the North and the Arctic of the Russian Federation), **9**, 96–106.

Oerlemans, J., 1994: Quantifying global warming from the retreat of glaciers. *Science*, **264**, 243–245.

Ohring, G., Ed., 2007: *Achieving Satellite Instrument Calibration for Climate Change.* National Oceanographic and Atmospheric Administration, 144 pp.

Olsen, S. M., B. Hansen, D. Quadfasel, and S. Osterhus, 2008: Observed and modelled stability of overflow across the Greenland-Scotland ridge. *Nature*, **455**, 519–522.

Onogi, K., and Coauthors, 2007: The JRA-25 reanalysis. *J. Meteor. Soc. Japan*, **85**, 369–432.

Orsolini, Y. J., 2004: Seesaw ozone fluctuations between the North Pacific and Atlantic in late winter. *J. Meteor. Soc. Japan*, **82**, 941–948.

Osterkamp, T. E., 2008: Thermal state of permafrost in Alaska during the fourth quarter of the twentieth century (plenary paper). *Proc. of the 9th International Conf. on Permafrost, Fairbanks, Alaska, 29 June – 3 July 2008*, Vol. 2, D. L. Kane and K. M. Hinkel, Eds., Institute of Northern Engineering, University of Alaska Fairbanks, 1333–1338.

Overland, J. E., and M. Wang, 2010: Large-scale atmospheric circulation changes associated with the recent loss of Arctic sea ice. *Tellus*, **62A**, 1–9.

Palmer, M. D., and K. Haines, 2009: Estimating oceanic heat content change using isotherms. *J. Climate*, **22**, 4953–4969.

——, ——, S. F. B. Tett, and T. J. Ansell, 2007: Isolating the signal of ocean global warming. *Geophys. Res. Lett.*, **34**, L23610, doi:10.1029/2007GL031712.

——, S. A. Good, K. Haines, N. A. Rayner, and P. A. Stott, 2009: A new perspective on warming of the global oceans. *Geophys. Res. Lett.*, **36**, L20709, doi:10.1029/2009GL039491.

——, and Coauthors, 2010: Future observations for monitoring global ocean heat content. *Proceedings of the OceanObs'09: Sustained Ocean Observations and Information for Society Conference (Vol. 2),* Venice, Italy, 21-25 September 2009, J. Hall et al., Eds., ESA Publication WPP-306.

Pan, L. W., J. C. Gille, D. P. Edwards, P. L. Bailey, and C. D. Rodgers, 1998: Retrieval of tropospheric carbon monoxide for the MOPITT experiment. *J. Geophys. Res.*, **103** (D24), 32 277–32 290.

Park, G.-H., K. Lee, R. Wanninkhof, and R. A. Feely, 2006: Empirical temperature-based estimates of variability in the oceanic uptake of CO_2 over the last two decades. *J. Geophys. Res.*, **111**, C07S0, doi:10.1029/2005JC003090.

Parker, D. E., 2006: A demonstration that large-scale warming is not urban. *J. Climate*, **19**, 2882–2895.

——, P. D. Jones, T. C. Peterson, and J. J. Kennedy, 2009: Comment on "Unresolved issues with the assessment of multi-decadal global land surface temperature trends" by Roger A. Pielke Sr. et al. *J. Geophys. Research,* **114**, D05104, doi: 10.1029/2008JD010450.

Paul, F., A. Kääb, and W. Haeberli, 2007: Recent glacier changes in the Alps observed by satellite: Consequences for future monitoring strategies. *Global Planet. Change*, **56**, 102–111.

Payne, A. J., P. R. Holland, A. P. Shepherd, I. C. Rutt, A. Jenkins, and I. Joghin, 2007: Numerical modeling of ocean-ice interactions under Pine Island Bay's ice shelf. *J. Geophys. Res.*, **112**, C10019 , doi:10.1029/2006JC003733.

PEAC, cited 2009: Pacific ENSO update newsletter. [Available online at http://www.soest.hawaii.edu/MET/Enso.]

Pelto, M., 2010: Forecasting temperate alpine glacier survival from accumulation zone observations. *The Cryosphere,* **4**, 67–75.

Peterson, B. J., R. M. Holmes, J. W. McClelland, C. J. Vorosmarty, R. B. Lammers, A. I. Shiklomanov, I. A. Shiklomanov, and S. Rahmstorf, 2002: Increasing river discharge to the Arctic Ocean. *Science*, **298**, 2171–2173.

Peterson, T. C. and D. R. Easterling, 1994: Creation of homogeneous composite climatological reference series. *Int. J. Climatol.*, **14**, 671–679.

——, and M. O. Baringer, Eds., 2009: State of the climate in 2008. *Bull. Amer. Meteor. Soc.*, **90** (8), S1–S196.

——, K. P. Gallo, J. Lawrimore, A. Huang, and D. A. McKittrick, 1999: Global rural temperature trends. *Geophys. Res. Lett.*, **26**, 329–332.

Pitts, M. C., L. R. Poole, and L. W. Thomason, 2009: CALIPSO polar stratospheric cloud observations: second-generation detection algorithm and composition discrimination. *Atmos. Chem. Phys.*, **9**, 7577–7589.

Polovina, J. J., E. A. Howell, and M. Abecasis, 2008: Ocean's least productive waters are expanding. *Geophys. Res. Lett.*, **35**, L03618, doi:10.1029/2007GL031745.

Polyakov, I. V., and L. A. Timokhov, 1994: Mean fields of temperature and salinity of the Arctic Ocean. *Russian Meteor. Hydrol.*, **7**, 33–38.

Proshutinsky, A. Y., and M. A. Johnson, 1997: Two circulation regimes of the wind-driven Arctic Ocean. *J. Geophys. Res.*, **102** (C6), 12 493–12 514.

——, and Coauthors, 2009: Beaufort Gyre freshwater reservoir: State and variability from observations *J. Geophys. Res.*, **114**, C00A10, doi:10.1029/2008JC005104.

Ramaswamy, V., M. D. Schwarzkopf, W. J. Randel, B. D. Santer, B. J. Soden, and G. L. Stenchikov, 2006: Anthropogenic and natural influences in the evolution of lower stratospheric cooling. *Science*, **311**, 1138–1141.

Randel, W. J., D. J. Seidel, and L. L. Pan, 2007: Observational characteristics of double tropopauses, *J. Geophys. Res.*, **112**, D07309, doi:10.1029/2006JD007904.

Ratnam, J. V., S. K. Behera, Y. Masumoto, K. Takahashi, and T. Yamagata, 2010: Pacific origin for the 2009 Indian summer monsoon failure. *Geophys. Res. Lett.*, **37**, L07807, doi:10.1029/2010GL042798.

Raupach, M. R., G. Marland, P. Ciais, C. Le Quéré, J. G. Canadell, G. Klepper, and C. B. Field, 2007: Global and regional drivers of accelerating CO_2 emissions. *Proc. Natl. Acad. Sci. USA*, **104**, 10 288–10 293.

Ravishankara, A. R., J. S. Daniel, and R. W. Portmann, 2009: Nitrous oxide (N_2O): The dominant ozone-depleting substance emitted in the 21st century. *Science*, **316**, 123–125.

Rawlins, M. A., and Coauthors, 2010: Analysis of the Arctic system for freshwater cycle intensification: Observations and expectations. *J. Climate*. in press.

Rayner, N. A., P. Brohan, D. E. Parker, C. K. Folland, J. J. Kennedy, M. Vanicek, T. J. Ansell, and S. F. B. Tett, 2006: Improved analyses of changes and uncertainties in sea surface temperature measured in situ since the mid-nineteenth century: The HadSST2 dataset. *J. Climate*, **19**, 446–469.

Reed, R. J., D. C. Norquist, and E. E. Recker, 1977: The structure and properties of African wave disturbances as observed during Phase III of GATE. *Mon. Wea. Rev.*, **105**, 317–333.

Reynolds, R. W., N. A. Rayner, T. M. Smith, D. C. Stokes and W. Wang, 2002: An improved in situ and satellite SST analysis for climate. *J. Climate*, **15**, 1609–1625.

Rigby, M., and Coauthors, 2008: Renewed growth of atmospheric methane. *Geophys. Res. Lett.*, **35**, L22805, doi:10.1029/2008GL036037.

Rignot, E., 2002: Ice-shelf changes in Pine Island Bay, Antarctica, 1947-2000. *J. Glaciol.*, **48**, 247–256.

Ringer, M. A., and S. B. Healy, 2008: Monitoring twenty-first century climate using GPS radio occultation bending angles. *Geophys. Res. Lett.*, **35**, L05708, doi:10.1029/2007GL032462.

Rintoul, S. R., and Coauthors, 2010: Deep circulation and meridional overturning: Recent progress and a strategy for sustained observations. *Proceedings of the OceanObs'09: Sustained Ocean Observations and Information for Society Conference (Vol. 1),* Venice, Italy, 21-25 September 2009, J. Hall et al., Eds., ESA Publication WPP-306.

Rio, M.-H., and F. Hernandez, 2004: A mean dynamic topography computed over the world ocean from altimetry, in situ measurements, and a geoid model. *J. Geophys. Res.*, **109**, C12032, doi:10.1029/2003JC002226.

Rocha, A. V., and G. R. Shaver, 2009: Advantages of a two band EVI calculatled from solar and photosynthetically active radiation fluxes. *Agricultural and Forestry Meteorology*, **149**, 1560–1563.

Roemmich, D., and Coauthors, 2009: The Argo Program: Observing the global oceans with profiling floats. *Oceanography*, **22**, 34–43.

Romanovsky, V. E., M. Burgess, S. Smith, K. Yoshikawa, and J. Brown, 2002: Permafrost temperature records: Indicator of climate change. *Eos, Trans. Amer. Geophys. Union*, **83**, 589.

——, S. Gruber, A. Instanes, H. Jin, S. S. Marchenko, S. L. Smith, D. Trombotto, and K. M. Walter, 2007: Frozen ground. *Global Outlook for Ice and Snow*, J. Eamer, Ed., United Nations Publications, 181–200.

——, and Coauthors, 2008: Thermal state and fate of permafrost in Russia: First results of IPY. *Proc. of the 9th International Conf. on Permafrost, Fairbanks, Alaska, 29 June – 3 July 2008*, Vol. 2, D. L. Kane and K. M. Hinkel, Eds., Institute of Northern Engineering, University of Alaska Fairbanks, 1511–1518.

Ropelewski, C. F., and M. S. Halpert, 1987: Global and regional scale precipitation patterns associated with the El Niño/Southern Oscillation. *Mon. Wea. Rev.*, **115**, 1606–1626.

——, and ——, 1989: Precipitation patterns associated with the high index phase of the Southern Oscillation. *J. Climate*, **2**, 268–284.

Rothrock, D. A., D. B. Percival, and M. Wensnahan, 2008: The decline in arctic sea-ice thickness: separating the spatial, annual, and interannual variability in a quarter century of submarine data. *J. Geophys. Res.*, **113**, C05003, doi:10:1029/2007JC004252.

Sabine, C. L., and Coauthors, 2004: The oceanic sink for anthropogenic CO_2. *Science*, **305**, 367–371.

——, R. A. Feely, R. Wanninkhof, and T. Takahashi, 2008: The global ocean carbon cycle [in "State of the Climate in 2007"]. *Bull. Amer. Meteorol. Soc.*, **89** (7), S52–S56.

——, ——, ——, and ——, 2009: The global ocean carbon cycle [in "State of the Climate in 2008"]. *Bull. Amer. Meteorol. Soc.*, **90** (8), S65–S68.

Saha, S., and Coauthors, 2010: The NCEP climate forecast system reanalysis. *Bull. Amer. Meteor. Soc.*, doi:10.1175/2010BAMS3001.1, in press.

Samelson, R. M., and P. L. Barber, 2008: Low-level jets, orographic effects, and extreme events in Nares Strait: A model-based mesoscale climatology. *Mon. Wea. Rev.*, **136**, 4746–4759.

——, T. Agnew, H. Melling, and A. Munchow, 2006: Evidence for atmospheric control of sea-ice motion through Nares Strait. *Geophys. Res. Lett.*, **33**, L02506, doi:10.1029/2005GL025016.

Santer, B. D., and Coauthors, 2006: Forced and unforced ocean temperature changes in Atlantic and Pacific tropical cyclogenesis regions. *Proc. Natl. Acad. Sci. USA*, **103**, 13 905–13 910.

——, and Coauthors, 2007: Identification of human-induced changes in atmospheric moisture content. *Proc. Natl. Acad. Sci. USA*, **104**, 15 248–15 253.

Scambos, T., H. Fricker, C.-C. Liu, J. Bohlander, J. Fastook, A. Sargent, R. Massom, and A.-M. Wu, 2009: Ice shelf disintegration by plate bending and hydrofracture: Satellite observations and model results of the 2008 Wilkins ice shelf break-ups. *Earth Planet. Sci. Lett.*, **280**, 51–60.

Schneider, U., T. Fuchs, A. Meyer-Christoffer, and B. Rudolf, 2008: Global precipitation analysis products of the GPCC. Deutscher Wetterdienst, 12 pp. [Available online at http://gpcc.dwd.de.]

Schott, F. A., L. Stramma, B. S. Giese, and R. Zantopp, 2009: Labrador Sea convection and subpolar North Atlantic deep water export in the SODA assimilation model. *Deep-Sea Res. I*, **56**, 926–938.

Schultz, M. G., 2002: On the use of ATSR fire count data to estimate the seasonal and interannual variability of vegetation fire emissions. *Atmos. Chem. Phys.*, **2**, 387–395.

Seidel, D. J., and J. R. Lanzante, 2004: An assessment of three alternatives to linear trends for characterizing global atmospheric temperature changes. *J. Geophys. Res.*, **109**, D14108, doi:10.1029/2003JD004414.

Shapiro, L. J., 1989: The relationship of the quasi-biennial oscillation to Atlantic tropical storm activity. *Mon. Wea. Rev.,* **117**, 1545–1552.

——, and S. B. Goldenberg, 1998: Atlantic sea surface temperatures and tropical cyclone formation. *J. Climate*, **11**, 578–590.

Shay, L. K., G. J. Goni, and P. G. Black, 2000: Effects of a warm oceanic feature on Hurricane Opal. *Mon. Wea. Rev.*, **128**, 1366–1383.

Sherwood, S. C., C. L. Meyer, R. J. Allen, and H. A. Titchner, 2008: Robust tropospheric warming revealed by iteratively homogenized radiosonde data. *J. Climate*, **21**, 5336–5352.

Shiklomanov, A. I., and R. B. Lammers, 2009: Record Russian river discharge in 2007 and the limits of analysis. *Environ. Res. Lett.*, **4**, 045015, doi:10.1088/1748-9326/4/4/045015.

——, ——, and C. J. Vörösmarty, 2002: Widespread decline in hydrological monitoring threatens pan-Arctic research. *Eos, Trans. Amer. Geophys.Union*, **83**, 16–17

——, T. I. Yakovleva , R. B. Lammers, I. Ph. Karasev, C. J. Vörösmarty, and E. Linder, 2006: Cold region river discharge uncertainty - estimates from large Russian rivers. *J. Hydrol.*, **326**, 231–256.

Shiklomanov, I. A., and A. I. Shiklomanov, 2003: Climatic change and dynamics of river discharge into the Arctic Ocean. *Water Resources*, **30**, 593–601.

Shindell, D. T., and G. A. Schmidt, 2004: Southern Hemisphere climate response to ozone changes and greenhouse gas increases. *Geophys. Res. Lett.*, **31**, L18209, doi:10.1029/2004GL020724.

Siegel, D. A., S. Maritorena, N. B. Nelson, and M. J. Behrenfeld, 2005: Independence and interdependences among global ocean color properties: Reassessing the bio-optical assumption. *J. Geophys. Res.*, **110**, C07011, doi:10.1029/2004JC002527.

Simmons, A. J., and Coauthors, 2004: Comparison of trends and low-frequency variability in CRU, ERA-40, and NCEP/NCAR analyses of surface air temperature. *J. Geophys. Res.*, **109**, D24115, doi:10.1029/2004JD005306.

——, K. M. Willett, P. D. Jones, P. W. Thorne, and D. P. Dee, 2010: Low-frequency variations in surface atmospheric humidity, temperature, and precipitation: Inferences from reanalyses and monthly gridded observational data sets. *J. Geophys. Res.*, **115**, D01110, doi:10.1029/2009JD012442.

Singh, O. P., T. M. Ali Khan, and S. Rahman, 2000: Changes in the frequency of tropical cyclones over the North Indian Ocean. *Meteor. Atmos. Phys.*, **75**, 11–20.

Smith, D. M., S. Cusack, A. W. Colman, C. K. Folland, G. R. Harris, and J. M. Murphy, 2007: Improved surface temperature prediction for the coming decade from a global climate model. *Science*, **317**, 796–799.

Smith, S. L., M. M. Burgess, D. Riseborough, and F. M. Nixon, 2005: Recent trends from Canadian permafrost thermal monitoring network sites. *Permafrost Periglacial Processes*, **16**, 19–30.

Smith, T. M., and R. W. Reynolds, 1998: A high-resolution global sea surface temperature climatology for the 1961-90 base period. *J. Climate*, **11**, 3320–3323.

——, and ——, 2005: A global merged land-air-sea surface temperature reconstruction based on historical observations (1880-1997). *J. Climate*, **18**, 2021–2036.

——, ——, T. C. Peterson, and J. Lawrimore, 2008: Improvements to NOAA's historical merged land-ocean surface temperature analysis (1880-2006). *J. Climate*, **21**, 2283–2296.

Sobel, A. H., and S. J. Camargo, 2005: Influence of western North Pacific tropical cyclones on their large-scale environment. *J. Atmos. Sci.*, **62**, 3396–3407.

Solomon, S., D. Qin, M. Manning, Z. Chen, M. Marquis, K. B. Averyt, M. Tignor, and H. L. Miller, Eds., 2007: *Climate Change 2007: The Physical Science Basis*. Cambridge University Press, 996 pp.

Speer, K. G., 1997: A note on average cross-isopycnal mixing in the North Atlantic Ocean. *Deep-Sea Res. I*, **44**, 1981–1990.

Stackhouse, P.W., Jr., D. P. Kratz, G. R. McGarragh, S. K. Gupta, and E. B. Geier, 2006: Fast Longwave and Shortwave Radiative Flux (FLASHFlux) products from CERES and MODIS measurements. *Proc. 12th Conf. Atmospheric Radiation*, Madison, WI, Amer. Meteor. Soc., P1.10. [Available online at http://ams.confex.com/ams/pdfpapers/113479.pdf.]

Stammerjohn, S. E., D. G. Martinson, R. C. Smith, X. Yuan, and D. Rind, 2008: Trends in Antarctic annual sea ice retreat and advance and their relation to El Niño–Southern Oscillation and Southern Annular Mode variability. *J. Geophys. Res.*, **113**, C03S90, doi:10.1029/2007JC004269.

Steig, E., D. P. Schneider, S. D. Rutherford, M. E. Mann, J. C. Comiso, and D. T. Shindell, 2009: Warming of the Antarctic ice-sheet surface since the 1957 International Geophysical Year. *Nature*, **457**, 459–462.

Steinbrecht, W., and Coauthors, 2009: Ozone and temperature trends in the upper stratosphere at five stations of the network for the detection of atmospheric composition change. *Int. J. Remote Sens.*, **30**, 3875–3886.

Stolarski, R. S., and S. Frith, 2006: Search for evidence of trend slow-down in the long-term TOMS/SBUV total ozone data record: The importance of instrument drift uncertainty and fingerprint detection. *Atmos. Chem. Phys.*, **6**, 4057–4065.

Street-Perrott, F. A., M. A. J. Guzkowska, I. M. Mason, and C. G. Rapley, 1986: Response of lake levels to climatic change - Past, present, and future. *Effects of Changes in Stratospheric Ozone and Global Climate*, Vol.3, Climate Change, U.N. Environ. Programme, Nairobi, Kenya, 1986.

Sweet, W., C. Zervas, and S. Gill, 2009: Elevated east coast sea levels anomaly: June-July 2009. NOAA Technical Report NOS CO-OPS 051, 30 pp.

Szesztay, K., 1974: Water balance and water level fluctuations of lakes. *Hydrol. Sci. Bull.*, **19**, 73–84.

Takahashi, T., and Coauthors, 2009a: Climatological mean and decadal change in surface ocean pCO$_2$, and net sea-air CO$_2$ flux over the global oceans. *Deep-Sea Res. II*, **56**, 554–577.

——, S. C. Sutherland, and A. Kozyr, 2009b: Global ocean surface water partial pressure of CO$_2$ database: Measurements performed during 1968-2008 (Version 2008). ORNL/CDIAC-152, NDP-088r, Carbon Dioxide Information Analysis Center, Oak Ridge, TN, digital media. [Available online at http://cdiac.ornl.gov/ftp/oceans/LDEO_Database/ or doi:10.3334/CDIAC/otg.ndp088r]

Talley, L. D., 2008. Freshwater transport estimates and the global overturning circulation: Shallow, deep and throughflow components. *Progr. Oceanogr.*, **78**, 257–303.

Tanhua, T., E. P. Jones, E. Jeansson, S. Jutterström, W. M. Smethie Jr., D. W. R. Wallace, and L. G. Anderson, 2009: Ventilation of the Arctic Ocean: Mean ages and inventories of anthropogenic CO$_2$ and CFC-11. *J. Geophys. Res.*, **114**, C01002, doi:10.1029/2008JC004868.

Tedesco, M., and A. J. Monaghan, 2009: An updated Antarctic melt record through 2009 and its linkages to high-latitude and tropical climate variability. *Geophys. Res. Lett.*, **36**, L18502, doi:10.1029/2009GL039186.

——, X. Fettweis, M. van den Broeke, R. van de Wal, and P. Smeets, 2008: Extreme snowmelt in northern Greenland during summer 2008. *Eos, Trans. Amer. Geophys. Union*, **89**, 391.

Thomas, H., A. E. Friederike Prowe, I. D. Lima, S. C. Doney, R. Wanninkhof, R. J. Greatbatch, U. Schuster, and A. Corbière, 2008: Changes in the North Atlantic Oscillation influence CO$_2$ uptake in the North Atlantic over the past 2 decades. *Global Biogeochem. Cycles*, **22**, GB4027, doi:10.1029/2007GB003167

Thompson, D. W., and S. Solomon, 2002: Interpretation of recent Southern Hemisphere climate change. *Science*, **296**, 895–899.

Thoning, K. W., P. P. Tans, and W. D. Komhyr, 1989: Atmospheric carbon dioxide at Mauna Loa Observatory 2: Analysis of NOAA GMCC data, 1974-1985. *J. Geophys. Res.*, **94** (D6), 8549–8565.

Thorne, P. W., and Coauthors, 2005: Revisiting radiosonde upper-air temperatures from 1958 to 2002. *J. Geophys. Res.*, **110**, D18105, doi:10.1029/2004JD005753.

Timokhov, L., and F. Tanis, Eds., 1997: *Environmental Working Group Joint U.S.-Russian Atlas of the Arctic Ocean-Winter Period*. Environmental Research Institute of Michigan in association with the National Snow and Ice Data Center, CD-ROM.

——, and ——, Eds., 1998: *Environmental Working Group Joint U.S.-Russian Atlas of the Arctic Ocean-Summer Period*. Environmental Research Institute of Michigan in association with the National Snow and Ice Data Center, CD-ROM.

Trenberth, K. E., 2009: An imperative for climate change planning: tracking Earth's global energy. *Current Opinion in Environmental Sustainability*, **1**, 19–27.

——, and J. T. Fasullo, 2010: Tracking Earth's energy. *Science*, **328**, 316–317.

——, ——, and L. Smith, 2005: Trends and variability in column-integrated atmospheric water vapor. *Climate Dyn.*, **24**, 741–758.

——, and Coauthors, 2010: Intergovernmental Panel for Climate Change (IPCC) and the attribution and prediction of climate: Progress since the fourth assessment. *Proceedings of the OceanObs'09: Sustained Ocean Observations and Information for Society Conference (Vol. 1),* Venice, Italy, 21-25 September 2009, J. Hall et al., Eds., ESA Publication WPP-306.

Trigo, R. M., I. M. Trigo, C. C. DaCamara, and T. J. Osborn, 2004: Winter blocking episodes in the European-Atlantic sector: Climate impacts and associated physical mechanisms in the reanalysis. *Climate Dyn.*, **23**, 17–28.

Turner, J., 2004: Review: The El Niño-Southern Oscillation and Antarctica. *Int. J. Climatol.*, **24**, 1–31.

——, and Coauthors, 2005: Antarctic climate change during the last 50 years. *Int. J. Climatol.*, **25**, 279–294.

Ukraintseva, N. G., 2008: Vegetation response to landslide spreading and climate change in the west Siberian tundra. *Proc. 9th International Conf. on Permafrost, Fairbanks, Alaska*, D. L. Kane and K. M. Hinkel, Eds., Vol. 2, Institute of Northern Engineering, University of Alaska Fairbanks, 1793–1798.

Uppala, S. M., and Coauthors, 2005: The ERA-40 reanalysis. *Quart. J. Roy. Meteor. Soc.*, **131**, 2961–3012 .

Våge, K., and Coauthors, 2009: Surprising return of deep convection to the subpolar North Atlantic Ocean in winter 2007–2008. *Nature Geosci.*, **2**, 67–72.

Van den Broeke, M. R., W. J. van de Berg, E. van Meijgaard, and C. H. Reijmer, 2006: Identification of Antarctic ablation areas using a regional atmospheric climate model. *J. Geophys. Res.*, **111**, D18110, doi:10.1029/2006JD007127.

Van der Werf, G. R., J. T. Randerson, L. Giglio, G. J. Collatz, P. S. Kasibhatla, and A. F. Arellano, 2006: Interannual variability in global biomass burning emissions from 1997 to 2004. *Atmos. Chem. Phys.*, **6**, 3423–3441.

Van Oldenborgh, G. J., and G. Burgers, 2005: Searching for decadal variations in ENSO precipitation teleconnections. *Geophys. Res. Lett.*, **32**, L15701, doi:10.1029/2005GL023110.

Venegas, S. A., and M. R. Drinkwater, 2001: Sea ice, atmosphere and upper ocean variability in the Weddell Sea, Antarctica. *J. Geophys. Res.*, **106**, C8, doi:10.1029/2000JC000594.

Vörösmarty, C. J., C. A. Federer, and A. L. Schloss, 1998: Potential evaporation functions compared on US watersheds: Possible implications for global-scale water balance and terrestrial ecosystem modeling. *J. Hydrol.*, **207**, 147–169.

——, and Coauthors, 2002: Global water data: A newly endangered species. *Eos, Trans. Amer. Geophys. Union*, **82**, 54,56,58.

Vose, R. S., R. L. Schmoyer, P. M. Steurer, T. C. Peterson, R. Heim, T. R. Karl, and J. Eischeid, 1992: The Global Historical Climatology Network: Long-term monthly temperature, precipitation, sea level pressure, and station pressure data. ORNL/CDIAC-53, NDP-041. [Available online at http://cdiac.ornl.gov/epubs/ndp/ndp041/ndp041.html.]

Vyushin, D., V. E. Fioletov, and T. G. Shepherd, 2007: Impact of long-range correlations on trend detection in total ozone. *J. Geophys. Res.*, **112**, D14307, doi:10.1029/2006JD008168.

Waliser, D. E., and C. Gautier, 1993: A satellite-derived climatology of the ITCZ. *J. Climate*, **6**, 2162–2174.

Walker, D. A., and Coauthors, 2009: Spatial and temporal patterns of greenness on the Yamal Peninsula, Russia: interactions of ecological and social factors affecting the Arctic normalized vegetation index. *Environ. Res. Lett.*, **4**, 045004, doi:10.1088/1748-9326/4/4/045004.

Wang, B., and J. C. L. Chan, 2002: How strong ENSO events affect tropical storm activity over the western North Pacific. *J. Climate*, **15**, 1643–1658.

Wang, C., and S.-K. Lee, 2010: Is hurricane activity in one basin tied to another? *Eos, Trans. Amer. Geophys. Union*, **91**, 93–94.

Wang, J., L. Zhang, A. Dai, T. Van Hove, and J. Van Baelen, 2007: A near-global, 8-year, 2-hourly data set of atmospheric precipitable water from ground-based GPS measurements. *J. Geophys. Res.,* **112**, D11107, doi:10.1029/2006JD007529.

Wang, L., C. Derksen, and R. Brown, 2008: Detection of Pan-Arctic terrestrial snowmelt from QuikSCAT, 2000 – 2005. *Remote Sens. Environ.*, **112**, 3794–3805.

Wann, T. C., 1974: Hurricanes in the Central-Eastern Pacific. *Mon. Wea. Rev.*, **102**, 396–397.

Watson, A., and Coauthors, 2009: Tracking the variable North Atlantic sink for atmospheric CO$_2$. *Science*, **326**, 1391–1393.

Weber, M., S. Dhomse, F. Wittrock, A. Richter, B.-M. Sinnhuber, and J. P. Burrows, 2003: Dynamical control of NH and SH winter/spring total ozone from GOME observations in 1995-2002. *Geophys. Res. Lett.*, **30**, 1853, doi:10.1029/2002GL016799.

——, L. N. Lamsal, and J. P. Burrows, 2007: Improved SCIAMACHY WFDOAS total ozone retrieval: Steps towards homogenising long-term total ozone datasets from GOME, SCIAMACHY, and GOME2. *Proc. Envisat Symposium 2007*, ESA SP-636, Montreux, Switzerland, European Space Agency, 5 pp. [Available online at http://envisat.esa.int/envisatsymposium/proceedings/posters/3P4/463281we.pdf.]

Wentz, F. J., 1997: A well-calibrated ocean algorithm for Special Sensor Microwave / Imager. *J. Geophys. Res.*, **102**, 8703–8718.

——, L. Ricciardulli, K. A. Hilburn, and C. A. Mears, 2007: How much more rain will global warming bring? *Science*, **317**, 233–235.

WGMS, 2007: *Glacier Mass Balance Bulletin No. 9* (2004-2005). World Glacier Monitoring Service, 100 pp.

——, 2008: Global glacier changes: Facts and figures. UNEP-World Glacier Monitoring Service, Zurich, Switzerland, 88 pp.

——, 2009: *Glacier Mass Balance Bulletin No. 10* (2006-2007). World Glacier Monitoring Service, 96 pp.

Wheeler, M., and G. N. Kiladis, 1999: Convectively coupled equatorial waves: Analysis of clouds and temperature in the wavenumber-frequency domain. *J. Atmos. Sci.*, **56**, 374–399.

——, and K. M. Weickmann, 2001: Real-time monitoring and prediction of modes of coherent synoptic to intraseasonal tropical variability. *Mon. Wea. Rev.*, **129**, 2677–2694.

Whitney, L. D., and J. S. Hobgood, 1997: The relationship between sea surface temperatures and maximum intensities of tropical cyclones in the Eastern North Pacific Ocean. *J. Climate*, **10**, 2921–2930.

Wielicki, B. A., and Coauthors, 1998: Clouds and the Earth's Radiant Energy System (CERES): algorithm overview. *IEEE Trans. Geosci. Remote Sens.*, **36**, 1127–1141.

Wijffels, S. E., R. W. Schmitt, H. L. Bryden, and A. Stigebrandt, 1992: Freshwater transport by the ocean. *J. Phys. Oceanogr.*, **22**, 155–162.

——, J. Willis, C. M. Domingues, P. Barker, N. J. White, A. Gronell, K. Ridgway, and J. A. Church, 2008: Changing expendable bathythermograph fall-rates and their impact on estimates of thermosteric sea level rise. *J. Climate*, **21**, 5657–5672.

Williams, W. D., 1993: The worldwide occurrence and limnological significance of falling water-levels in large, permanent, saline lakes. *Verh. Int. Ver. Theor. Angew. Limnol.*, **25**, 980–983.

Willis, J. K., D. Roemmich, and B. Cornuelle, 2004: Interannual variability in upper ocean heat content, temperature, and thermosteric expansion on global scales. *J. Geophys. Res.*, **109**, C12036, doi:10.1029/2003JC002260.

——, J. M. Lyman, G. C. Johnson, and J. Gilson, 2007: Correction to recent cooling of the upper ocean. *Geophys. Res. Lett.*, **34**, L16601, doi:10.1029/2007GL030323.

Willmott, C. J., S. M. Robeson, and M. J. Janis, 1996: Comparison of approaches for estimating time-averaged precipitation using data from the USA. *Int. J. Climatol.*, **16**, 1103–1115.

Wisser, D., S. Frolking, E. M. Douglas, B. M. Fekete, C. J. Vörösmarty, and A. H. Schumann, 2008: Global irrigation water demand: Variability and uncertainties arising from agricultural and climate data sets. *Geophys. Res. Lett.*, **35**, L24408, doi:10.1029/2008GL035296.

——, ——, ——, ——, A. H. Schuman, and C. J. Vörösmarty, 2010: The significance of local water resources captured in small reservoirs for crop production - A global-scale analysis. *J. Hydrol.*, **384**, 264–275.

WMO, 2007: Workshop on the re-design and optimization of the space-based Global Observing System. Final Report. WMO Headquarters, 12 pp. [Available online at http://www.wmo.ch/pages///prog//sat/documents/OPT-2FINAL-Report.pdf.]

——, 2010: WMO statement on the status of the climate in 2009. WMO No.1055, 16 pp. [Available online at http://www.wmo.int/pages/prog/wcp/wcdmp/documents/WMOStatement2009.pdf.]

Woodgate, R. A., T. Weingartner, and R. Lindsay, 2010: The 2007 Bering Strait oceanic heat flux and anomalous Arctic sea ice retreat *Geophys. Res. Lett.*, **37**, L01602, doi:10.1029/2009GL041621.

Wooster, M. J., G. Roberts, G. L. W. Perry, and Y. J. Kaufman, 2005: Retrieval of biomass combustion rates and totals from fire radiative power observations: FRP derivation and calibration relationships between biomass consumption and fire radiative energy release. *J. Geophys. Res.*, **110**, D24311, doi:10.1029/2005JD006318.

Wunsch, C., 2008: Mass and volume transport variability in an eddy-filled ocean. *Nature Geosci.*, **1**, 165–168.

——, and P. Heimbach, 2006: Estimated decadal changes in the North Atlantic meridional overturning circulation and heat flux 1993-2004. *J. Phys. Oceanogr.*, **36**, 2012–2024.

Xie, P., and P. A. Arkin, 1997: Global precipitation: A 17-year monthly analysis based on gauge observations, satellite estimates and numerical model outputs. *Bull. Amer. Meteor. Soc.*, **78**, 2539–2558.

Xue, Y., T. M. Smith, and R. W. Reynolds, 2003: Interdecadal changes of 30-yr SST normals during 1871-2000. *J. Climate*, **16**, 1601–1612.

Yamamoto-Kawai, M., F. McLaughlin, E. Carmack, S. Nishino, and K. Shimada, 2009: Aragonite undersaturation in the Arctic Ocean: Effects of ocean acidification and sea ice melt. *Science*, **326**, 1098–1100.

Yang, E. S., D. M. Cunnold, M. J. Newchurch, and R. J. Salawich, 2005: Change in ozone trends at southern high latitudes. *Geophys. Res. Lett.*, **32**, L12812, doi:10.1029/2004GL022296.

Yashayaev, I., and J. W. Loder, 2009: Enhanced production of Labrador Sea Water in 2008. *Geophys. Res. Lett.,* **36**, L01606, doi:10.1029/2008GL036162.

Yin, J., M. E. Schlesinger, and J. Stouffer, 2009: Model projections of rapid sea-level rise on the northeast coast of the United States. *Nature Geosci.*, **2**, 262–266.

Yu, L., and M. M. Rienecker, 2000: The Indian Ocean warming of 1997-1998. *J. Geophys. Res.*, **105** (C7), 16 923–16 939.

——, and R. A. Weller, 2007: Objectively Analyzed air-sea heat Fluxes (OAFlux) for the global ocean. *Bull. Amer. Meteor. Soc.,* **88**, 527–539.

——, Xin, J., and R. A. Weller, 2008: Multidecade global flux datasets from the Objectively Analyzed Air-sea Fluxes (OAFlux) Project: Latent and sensible heat fluxes, ocean evaporation, and related surface meteorological variables. OAFlux Project Tech. Rep. OA-2008-01, 64 pp.

Zebiak, S. E., 1989: Oceanic heat content variability and El Niño cycles. *J. Phys. Oceanogr.*, **19**, 475–486.

Zhang, C., 2005: Madden-Julian Oscillation. *Rev. Geophys.*, **43**, RG2003, doi:10.1029/2004RG000158.

——, and J. Gottschalck, 2002: SST anomalies of ENSO and the Madden Julian Oscillation in the equatorial Pacific. *J. Climate*, **15**, 2429–2445.

Zhang, R., 2008: Coherent surface-subsurface fingerprint of the Atlantic meridional overturning circulation. *Geophys. Res. Lett.*, **35**, L20705, doi:10.1029/2008GL035463.

Zola, R. P., and L. Bengtsson, 2006: Long-term and extreme water level variations of the shallow Lake Poopo, Bolivia. *Hydrolog. Sci. J.*, **51**, 98–114.

Zou, C.-Z., M. Gao, and M. Goldberg, 2009: Error structure and atmospheric temperature trends in observations of the microwave sounding unit. *J. Climate*, **22**, 1661–1681.
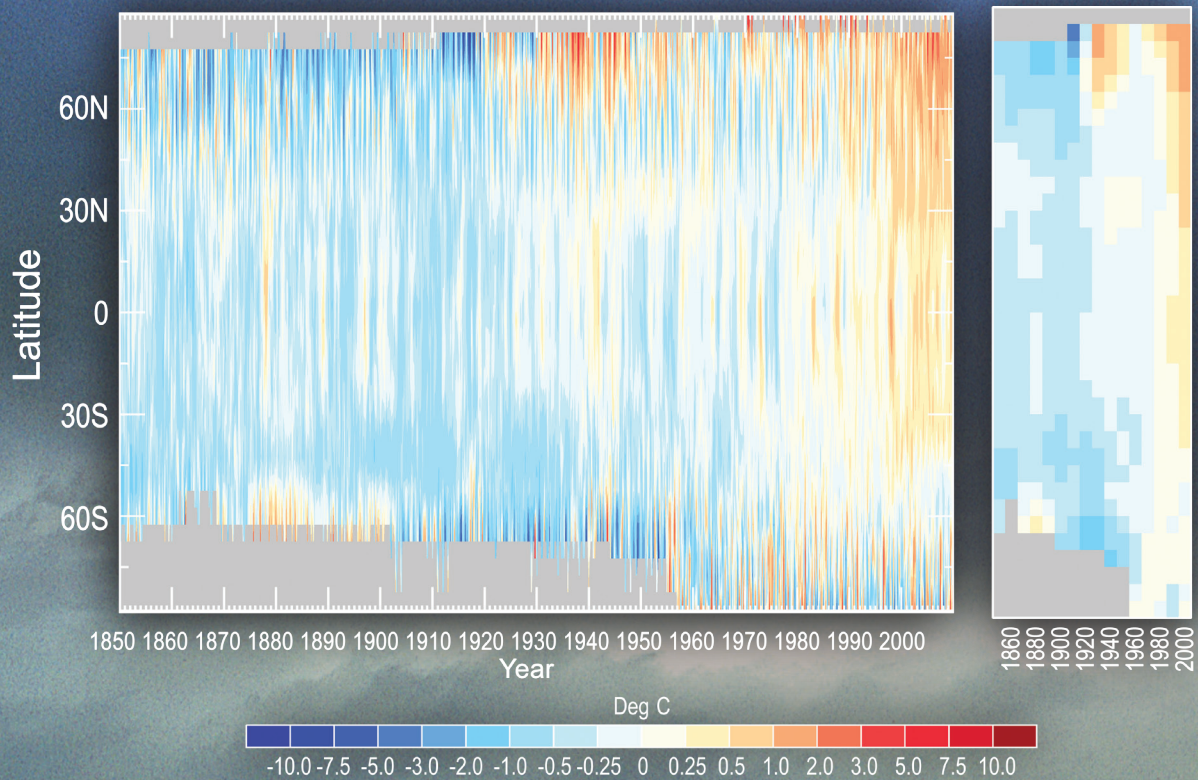
Monthly average temperature anomalies by latitude for the period 1850 to 2009. Decadally-averaged anomalies are shown on the right-hand side where 66% of months are present. Refer to Chapter 2, Figure 2.1 for a more detailed description.